ЧЕТЫРНАДЦАТЫЙ
МОСКОВСКИЙ
МЕЖДУНАРОДНЫЙ
СИМПОЗИУМ
ПО ИССЛЕДОВАНИЯМ
СОЛНЕЧНОЙ СИСТЕМЫ

9–13 ОКТЯБРЯ 2023

ИНСТИТУТ
КОСМИЧЕСКИХ
ИССЛЕДОВАНИЙ
МОСКВА

THE FOURTEENTH
MOSCOW
SOLAR SYSTEM
SYMPOSIUM

9–13 OCTOBER 2023

SPACE RESEARCH
INSTITUTE
MOSCOW

9 OCTOBER:
SESSION MARS
10 OCTOBER:
SESSION MOON AND MERCURY
11 OCTOBER:
SESSION MOON AND MERCURY
SESSION VENUS
12 OCTOBER:
SESSION SMALL BODIES
(INCLUDING COSMIC DUST)
13 OCTOBER:
SESSION EXTRASOLAR PLANETS
SESSION ASTROBIOLOGY

ЧЕТЫРНАДЦАТЫЙ МОСКОВСКИЙ СИМПОЗИУМ ПО ИССЛЕДОВАНИЯМ СОЛНЕЧНОЙ СИСТЕМЫ 14M-S^3

октябрь 9-13, 2023
ИНСТИТУТ КОСМИЧЕСКИХ ИССЛЕДОВАНИЙ РОССИЙСКОЙ АКАДЕМИИ НАУК
МОСКВА, РОССИЯ

THE FOURTEENTH MOSCOW SOLAR SYSTEM SYMPOSIUM 14M-S^3

october 9-13, 2023
SPACE RESEARCH INSTITUTE OF RUSSIAN ACADEMY OF SCIENCES
MOSCOW, RUSSIA

спонсоры:
- Институт космических исследований РАН
- Институт геохимии и аналитической химии им. Вернадского РАН
- Брауновский университет (США)

sponsored by:
- Space Research Institute RAS
- Институт геохимии и аналитической химии им. В.И.Вернадского РАН
- Brown University, USA

ISBN: 978-5-00015-061-0
DOI: 10.21046/14MS3-2023

TABLE OF CONTENT

THE FOURTEENTH MOSCOW SOLAR SYSTEM SYMPOSIUM 14M-S^3

SPACE RESEARCH INSTITUTE
MOSCOW, RUSSIA
october 9-13, 2023

Starting from 2010, the Space Research Institute holds annual international symposia on Solar system exploration. Main topics of these symposia include wide range of problems related to formation and evolution of Solar system, planetary systems of other stars; exploration of Solar system planets, their moons, small bodies; interplanetary environment, astrobiology problems. Experimental planetary studies, science instruments and preparation for space missions are also considered at these symposia.

The Fourteenth Moscow international Solar System Symposium (14M-S^3) will be held from October 9 till 13, 2023.

THE FOLLOWING SESSIONS WILL BE HELD DURING THE SYMPOSIUM:

- Session. MARS
- Session. MOON AND MERCURY
- Session. VENUS
- Session. SMALL BODIES (INCLUDING COSMIC DUST)
- Session. EXTRASOLAR PLANETS
- Session. ASTROBIOLOGY

Space Research Institute holds this symposium with participation of the following organizations:

- Vernadsky Institute of Geochemistry and Analytical Chemistry RAS, Russia
- Brown University, USA
- Schmidt Institute of Physics of the Earth RAS, Russia
- Keldysh Institute of Applied Mathematics RAS, Russia
- Kotelnikov Institute of Radio-engineering and Electronics RAS, Russia
- Sternberg Astronomical institute, Moscow State University, Russia

Symposium website: **https://ms2023.cosmos.ru**
Contact email address: **ms2023@cosmos.ru**

PROGRAM COMMITTEE

chair:
acad. **ZELENYI L.M.** IKI RAS

members:
BAZILEVSKIY A.T. GEOHI RAS
BIBRING J.-P. IAS,CNRS, France
BOROVIN G.K. Keldysh AMI RAS
HEAD III J. Brown University, USA
KORABLEV O.I. IKI RAS
KOSTITSYN Y.A. GEOHI RAS
MAROV M.Ya. GEOHI RAS
MITROFANOV I.G. IKI RAS
RODIN A.V. IKI RAS
SHEVCHENKO V.V. GAISH MSU
SMIRNOV V.M. IRE RAS
TAVROV A.V. IKI RAS
VAISBERG O.L. IKI RAS
VOROBYOVA E.A. MSU
ZAKHAROV A.V. IKI RAS
ZASOVA L.V. IKI RAS

secretary:
ROSTE O.Z. IKI RAS, ms3@iki.rssi.ru

PROGRAM

overview 14M–S³ program
THE FOURTEENTH MOSCOW SOLAR SYSTEM SYMPOSIUM

Space Research Institute, 9–13 October 2023

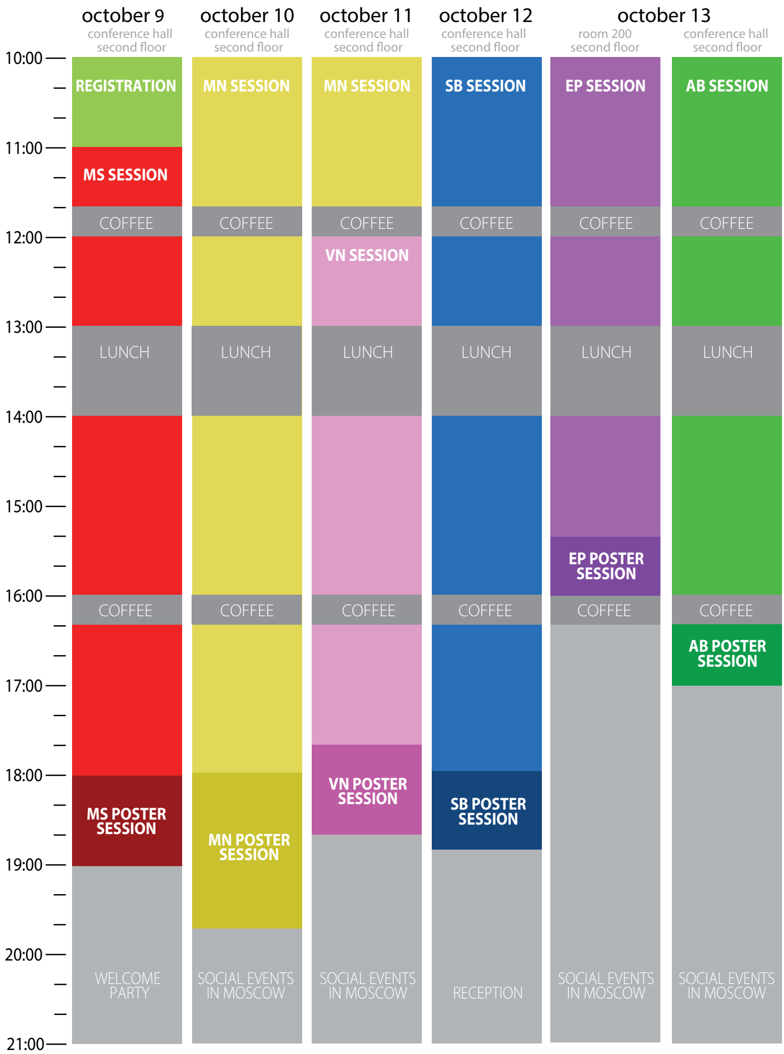

- **MS SESSION**: MARS SESSION
- **MN SESSION**: MOON AND MERCURY SESSION
- **VN SESSION**: VENUS SESSION
- **SB SESSION**: SMALL BODIES (INCLUDING COSMIC DUST) SESSION
- **EP SESSION**: EXTRASOLAR PLANETS SESSION
- **AB SESSION**: ASTROBIOLOGY SESSION

MONDAY, 9 OCTOBER 2023

11.00–19.00

1 MARS SESSION

Convener: **Oleg KORABLEV**
conference hall, second floor

11.00–11:20	**Alina MUKHAMEDZHANOVA**	Valley topography of northeastern Terra Cimmeria on Mars	14MS3-MS-01
11.20–11.40	**Yaowen LUO**	Constraint on paleo hydrological activities from deltas on Mars	14MS3-MS-02
11.40–12.00		COFFEE-BREAK	
12.00–12:20	**Jun CHU et al**	Deposits in the depression west to Eberswalde crater indicate a synchronous hydrogeological history of Holden and Eberswalde craters on Mars	14MS3-MS-03
12.20–12.40	**Boris IVANOV**	New craters on Mars: Updating after 2022 catalog	14MS3-MS-04
12.40–13.00	**Elena PODOBNAYA et al**	Some statistics on fresh Martian clusters	14MS3-MS-05
13.00–14.00		LUNCH	
14.00–14.20	**Zhongchen WU et al**	The gas-solid chemical reaction during Martian dust events	14MS3-MS-06
14.20–14.40	**Anna FEDOROVA et al**	Distribution of atmospheric aerosols during the 2007 Mars dust storm by solar infrared occultation on Mars-Express	14MS3-MS-07
14.40–15.00	**Ekaterina STARICHENKO et al**	Two years of gravity waves observation in the Martian atmosphere by the ACS experiment on board the ExoMars/TGO	14MS3-MS-08
15.00–15.20	**Pavel VLASOV et al**	Martian global water vapor column abundance from ACS TIRVIM nadir observations onboard ExoMars TGO	14MS3-MS-09
15.20–15.40	**Alina MERKULOVA and A.K. PAVLOV**	Possible explanations for seasonal variations of oxygen in the Martian atmosphere	14MS3-MS-10
15.40–16.00	**Dominik BELOUSOV et al**	Possible source of perchlorates on Mars and Europa	14MS3-MS-11
16.00–16.20		COFFEE-BREAK	
16.20–16.40	**Anton SALNIKOV et al**	Analytical continuation of the magnetic field of Mars from satellite data using a combined approach	14MS3-MS-12
16.40–17.00	**Jinsong PING et al**	Mars electron density inversion based on Tianwen-1 radio occultation experiment	14MS3-MS-13
17.00–17.20	**Egor KULIK and Tamara GUDKOVA**	Effects of anelasticity on Chandler period of Mars	14MS3-MS-14

17.20–17.40	**Jordanka SEMKOVA et al**	New results from the radiation investigations aboard ExoMars TGO in 2018-2023	14MS3-MS-15
17.40–18.00	**Elena KARPOVICH et al**	A science Martian airplane: preliminary configurations and radiation loading analysis	14MS3-MS-16
18.00–19.00	**POSTER SESSION, SESSION MARS** 12 posters * 5 min		
18.00–18.05	**Anatoly ZUBAREV et al**	Photogrammetric procession of Mars 2020 Ingenuity data and subsequent obtaining of a 3D surface model	14MS3-MS-PS-01
18.05–18.10	**Alexey BATOV and Tamara GUDKOVA**	On correlation of non-hydrostatic stresses in the interior of Mars with the epicenters of marsquakes	14MS3-MS-PS-02
18.10–18.15	**Sergei KULIKOV et al**	Magnetic field observations at the surface of Mars: the influence of atmospheric/ionospheric phenomena and the interplanetary medium	14MS3-MS-PS-03
18.15–18.20	**Oleg VAISBERG et al**	Recurring magnetic structure in Martian dayside magnetopause	14MS3-MS-PS-04
18.20–18.25	**Marina KUZMICHEVA and Boris IVANOV**	Characteristic features of magnetic anomalies of impact craters on Earth: how they appear on terrestrial planets	14MS3-MS-PS-05
18.25–18.30	**Anatoly MANUKIN et al**	Improvement of the characteristics of the uniaxial seismometer	14MS3-MS-PS-06
18.30–18.35	**Mohamad ABDELAAL et al**	Exploring electromagnetic signatures of dust particles collisions: experimental setup and station construction for signal acquisition	14MS3-MS-PS-07
18.35–18.40	**Vladimir OGIBALOV and G. M. SHVED**	An improved model of radiative transfer for the NLTE problem in the NIR bands of CO_2 and CO molecules in the daytime atmosphere of Mars. 3. An effect of aerosol radiation scattering on the vibrational state populations	14MS3-MS-PS-08
18.40–18.45	**Vladimir OGIBALOV**	Hierarchy of vibrational state sets for solving the NLTE radiative transfer problem in the IR CO_2 bands in the Martian atmosphere	14MS3-MS-PS-09
18.45–18.50	**Petr LYSSENKO et al**	On the role of methane and ammonia absorption in studying Jupiter's atmosphere	14MS3-MS-PS-10
18.50–18.55	**Andrey KIRILLOV**	Electronic kinetics of molecular nitrogen at the altitudes of Titan's middle atmosphere	14MS3-MS-PS-11
18.55–19.00	**Nikolay KASATIKOV**	Integrating IoT with space exploration: Improving Mars missions with Neural networks	14MS3-MS-PS-12
19.00–20.00	WELCOME PARTY		

10.00–19.45

2 MOON AND MERCURY SESSION

Conveners: **Igor MITROFANOV, Maxim LITVAK**
conference hall, second floor

	MERCURY		
10.00–10.20	**Alexander KOZYREV et al**	Three Mercury flybys: observations of neutron and gamma-ray fluxes by MGNS instrument onboard the ESA's BepiColombo mission	14MS3-MN-01
10.20–10.40	**Alexander LAVRUKHIN et al**	Determination of the optimal parameters of the Mercury's magnetosphere for the MESSENGER mission	14MS3-MN-02
	THE STUDIES OF THE MOON AS CELESTIAL BODY		
10.40–11.00	**Alexander GUSEV et al**	Geological exploration of the Moon VI: mineralogy, rheology, heat budget	14MS3-MN-03
11.00–11.20	**Mikhail IVANOV et al**	Thickness of volcanic materials in Mare Fecunditatis	14MS3-MN-04
11.20–11.40	**Alexander BASILEVSKY et al**	Study of the surface morphology of permanently shadowed floor of polar crater Shoemaker: Relative depth of small craters	14MS3-MN-05
11.40–12.00		COFFEE-BREAK	
12.00–12.20	**Alexander BASILEVSKY et al**	Photogeological analysis of the tectonically deformed impact crater in the South Pole region of the Moon	14MS3-MN-06
12.20–12.40	**Xing WANG and James HEAD**	Evidence for extensive cryptomaria in the center of the South-Pole Aitken basin	14MS3-MN-07
12.40–13.00	**Zifeng YUAN et al**	Inversion of global lunar oxides using Chang'E-2 Lunar Microwave Sounder data	14MS3-MN-08
13.00–14.00		LUNCH	
14.00–14.20	**James HEAD and Mikhail IVANOV**	Mare mesas in Mare Fecunditatis: characteristics of a newly documented class of mare volcanic feature	14MS3-MN-09
14.20–14.40	**James HEAD et al**	Ina shield volcano summit pit crater: forward-modeling major stages in its evolution and comparison with surface morphology and sequence	14MS3-MN-10
14.40–15.00	**Maya DJACHKOVA et al**	Studies of the floor of Zeeman lunar polar crater with LRO and Luna-25 data	14MS3-MN-11

15.00–15.20	**Maxim LITVAK et al**	The experiment LEND: 14 years observations of lunar neutron albedo	14MS3-MN-12
15.20–15.40	**Ilia KUZNETSOV et al**	Investigation of the cosmic dusty plasmas with dust monitoring instruments	14MS3-MN-13
15.40–16.00	**Vladimir DUDCHENKO and Evgeny SLYUTA**	A temperature distribution model in the lunar soil at the Polar Regions	14MS3-MN-14
16.00–16.20		COFFEE-BREAK	
		THE EARTH BASED EXPERIMENTS AND STUDIES OF THE MOON	
16.20–16.40	**Daniil MIRONOV et al**	VI-LH1 – Lunar highlands simulant for large scale experiments	14MS3-MN-15
16.40–17.00	**Yuri BONDARENKO et al**	Earth-based radar observations of permanently shadowed regions on the lunar South Pole	14MS3-MN-16
17.00–17.20	**Artem KRIVENKO et al**	Features of isotopic fractionation of water ice during sublimation under lunar conditions	14MS3-MN-17
		LUNAR EXPLORATION PERSPECTIVES	
17.20–17.40	**Dmitry GOLOVIN et al**	The gamma-ray spectroscopy of Rare Earth elements in lunar subsurface	14MS3-MN-18
17.20–18.00	**Anton SANIN et al**	On the neutron emission from the south polar region of the Moon	14MS3-MN-19
18.00–19.45		**POSTER SESSION, SESSION MOON AND MERCURY** 21 posters * 5 min	
18.00–18.05	**Alexander BASILEVSKY et al**	Regional and local geology and Moon Mineralogy Mapper data analysis for the Luna 24 landing site	14MS3-MN-PS-01
18.05–18.10	**Alexander KRASILNIKOV et al**	Model stratigraphy in the Artemis landing sites region	14MS3-MN-PS-02
18.10–18.15	**Mikhail IVANOV et al**	Sources of materials in the Luna-16 sample	14MS3-MN-PS-03
18.15–18.20	**Zhiguo MENG et al**	New findings of surface deposits in cryptomare region revealed by CE-2 MRM data	14MS3-MN-PS-04
18.20–18.25	**Xeniya KOCHUBEY and Mikhail IVANOV**	Degradation of fresh-looking craters on the Moon	14MS3-MN-PS-05
18.25–18.30	**Ekaterina GRISHAKINA et al**	Absolute model age estimates of the Plaskett crater	14MS3-MN-PS-06
18.30–18.35	**Michael SHPEKIN and V.S. SHISHKINA**	The structure features of young impact craters in the area of “bulbous fields” on the Aitken crater floor	14MS3-MN-PS-07

18.35–18.40	**Nadezhda CHUJKOVA et al**	Dynamics of the Earth-Moon and Venus-Mercury systems: a comparative analysis	14MS3-MN-PS-08
18.40–18.45	**Ekaterina KRONROD et al**	Numerical simulation of the thermal evolution of the Moon. Consistency with the presence of a low-viscosity zone at the core-mantle boundary	14MS3-MN-PS-09
18.45–18.50	**Jing YANG and Lianghui GUO**	An omnidirectional filtering method for destriping lunar satellite gravity data	14MS3-MN-PS-10
18.50–18.55	**Jinsong PING et al**	To promote a joint space-time reference datum on the Moon	14MS3-MN-PS-11
18.55–19.00	**Andrey SHUGAROV et al**	Astrophysical UV-Optical-IR telescope for the International Lunar Research Station	14MS3-MN-PS-12
19.00–19.05	**Ekaterina GRISHAKINA et al**	Creating the map of the polar regions of the Moon	14MS3-MN-PS-13
19.05–19.10	**Boris EPISHIN and Michael SHPEKIN**	The situation in the lunar sky in the landing area of the Russian «Luna-25» station from August 2023 to August 2024	14MS3-MN-PS-14
19.10–19.15	**Imant VINOGRADOV et al**	Design of a compact multichannel diode laser spectrometer for the Luna-27 mission: challenges and achievements	14MS3-MN-PS-15
19.15–19.20	**Alexander KOSOV et al**	Luna-27 lander and Luna-26 orbiter navigation by means of Radio Beacon deployed on the Luna-27 lander	14MS3-MN-PS-16
19.20–19.25	**Alexandra UVAROVA**	Studying the suitability of the Kamchatka peninsula as natural testing site for lunar missions based on the properties of soils	14MS3-MN-PS-17
19.25–19.30	**Mohamad ABDELAAL et al**	Investigating high-voltage charging effects and substrate material on dust particle dynamics and electromagnetic signatures in a low-pressure conditions: lunar regolith analogue study	14MS3-MN-PS-18
19.30–19.35	**Ivan AGAPKIN and Alexandra UVAROVA**	Experimental research of the lunar soil-analogue VI-75 under negative temperature	14MS3-MN-PS-19
19.35–19.40	**Egor SOROKIN et al**	Thermal reduced Si and P in metallic iron nanospherules: experimental data	14MS3-MN-PS-20
19.40–19.45	**Azariy BARENBAUM**	New interpretation of "true polar wander" phenomenon: conclusions for terrestrial planets	14MS3-MN-PS-21

10.00–11.40

2 MOON AND MERCURY SESSION

Conveners: **Igor MITROFANOV, Maxim LITVAK**
conference hall, second floor

LUNAR EXPLORATION PERSPECTIVES

10.00–10.20	**Anatoly ZUBAREV et al**	Processing technique for the image data from Service Television Camera System - Luna (STS-L) at the landing stage	14MS3-MN-20
10.20–10.40	**Huijuan WANG et al**	Optimizing scientific objectives for the Lunar-based UV-Optical-IR telescope for ILRS	14MS3-MN-21
10.40–11.00	**Denis LISOV et al**	In-flight selection of landing site for lunar polar lander	14MS3-MN-22
11.00–11.20	**Tatiana TOMILINA et al**	Laboratory Testing for ISRU of Regolith by SLM technology	14MS3-MN-23
11.20–11.40	**Lev ZELENYI et al**	Russian Lunar Program: Difficult beginning	14MS3-MN-24
11.40–12.00		COFFEE-BREAK	

12.00–18.40

3 VENUS SESSION

Convener: **Ludmila ZASOVA**
conference hall, second floor

12.00–12.20	**Lev ZELENYI et al**	Venera-D Mission Update	14MS3-VN-01
12.20–12.40	**Takehiko SATOH et al**	Updates of Akatsuki Venus Orbiter	14MS3-VN-02
12.40–13.00	**Igor KHATUNTSEV et al**	Twelve years cycle in the cloud top winds on Venus	14MS3-VN-03
13.00–14.00		LUNCH	
14.00–14.20	**Ludmila ZASOVA et al**	Some peculiarities of the Venusian mesosphere dynamics	14MS3-VN-04
14.20–14.40	**Mikhail LUGININ et al**	Retrieval of upper haze aerosol properties at Venus from SPICAV–UV and –IR data	14MS3-VN-05
14.40–15.00	**Daria EVDOKIMOVA et al**	Venus lower cloud variations by SPICAV-IR/VEX night emission observations and supplemented radiative transfer model	14MS3-VN-06
15.00–15.20	**Evgenij ZUBKO and Y. J. LEE**	Retrieving microphysics of aerosols in the atmosphere of Venus using the glory phenomenon	14MS3-VN-07

15.20–15.40	**Mikhail IVANOV and James HEAD**	Morphological and topographical groups of large volcanoes on Venus	14MS3-VN-08
15.40–16.00	**Piero D'INCECCO et al**	Introducing the "Analogs for VENus' GEologically Recent Surfaces" initiative: an opportunity for identifying and analyzing recently active volcano-tectonic areas of Venus trough a comparative study with Terrestrial analogs	14MS3-VN-09
16.00–16.20		COFFEE-BREAK	
16.20–16.40	**Denis BELYAEV et al**	Scientific concept of VOLNA experiment to study spectroscopy of Venus atmosphere	14MS3-VN-10
16.40–17.00	**Pavel KLIMOV et al**	SONET scientific equipment for the Venera-D project	14MS3-VN-11
17.00–17.20	**Piero D'INCECCO et al**	The Campo Imperatore ADvanced VEnus' Night Airglows Near-infrared Telescope (ADVENANT) Project as a ground-based segment for future missions to Venus	14MS3-VN-12
17.20–17.40	**Dargilan Oliveira AMORIM and Tamara GUDKOVA**	Earth-like viscoelastic models of Venus interior structure	14MS3-VN-13
17.40–18.40		**POSTER SESSION, SESSION VENUS** 12 posters * 5 min	
17.40–17.45	**Marina PATSAEVA et al**	Influence of the underlying surface on the zonal and meridional speed at the cloud top level near noon from VMC/Venus Express and UVI/Akatsuki images	14MS3-VN-PS-01
17.45–17.50	**Artem NEPOP et al**	Study of aerosol properties in the Venus' upper haze from SOIR data	14MS3-VN-PS-02
17.50–17.55	**Elizaveta FEDOROVA et al**	Study of the HDO/H_2O isotope ratio in the mesosphere of Venus based on SOIR observations for 2006–2014	14MS3-VN-PS-03
17.55–18.00	**Imant VINOGRADOV et al**	Optical design of a high-resolution IR spectrometer ISCRA-V for the Venera-D mission	14MS3-VN-PS-04
18.00–18.05	**Vladislav ZUBKO et al**	Study of flight scenarios to Venus followed by a passage of an asteroid	14MS3-VN-PS-05
18.05–18.10	**Dmitry MOISEENKO et al**	Venus in solar wind: scientific goals and concepts of plasma analyzers for Venera-D mission	14MS3-VN-PS-06

18.10–18.15	**Vladimir GUBENKO and I.A. KIRILLOVICH**	Comparison of internal wave characteristics in the Venus's atmosphere deduced by two independent methods from the Magellan radio occultation measurements	14MS3-VN-PS-07
18.15–18.20	**Evgeniya GUSEVA and Mikhail IVANOV**	Coronae of Venus: topography and volcanic productivity	14MS3-VN-PS-08
18.20–18.25	**Ivan BORONIN and Tamara GUDKOVA**	Computer realization of algorithm for inversion of Venusian interiors based on Monte Carlo method: 1. testing on classical example of gravitational field data	14MS3-VN-PS-09
18.25–18.30	**Tamara GUDKOVA and Alexey BATOV**	On stress state of Venus	14MS3-VN-PS-10
18.30–18.35	**Valery KOTOV**	Motion of Venus and Earth, and Fibonacci numbers	14MS3-VN-PS-11
18.35–18.40	**Natalia BULATOVA**	Cosmic rays are initiators of strong earthquakes	14MS3-VN-PS-12

10.00–18.50

4 SMALL BODIES SESSION including cosmic dust

Conveners: **Alexander BASILEVSKY**, **Alexander ZAKHAROV**
conference hall, second floor

10.00–10.20	**Vacheslav EMEL'YANENKO**	The origin of distant trans-Neptunian objects	14MS3-SB-01
10.20–10.40	**Vladislav GUSEV and Eduard KUZNETSOV**	The accuracy of methods for estimating the ages of pairs of trans-Neptunian objects in close orbits	14MS3-SB-02
10.40–11.00	**Vladimir BUSAREV et al**	Spectral signs and probable mechanisms of optically thin and thick dusty exosphere of active asteroids	14MS3-SB-03
11.00–11.20	**Tatyana GALUSHINA et al**	The study of mean motion resonance multiplet for near-Sun asteroids	14MS3-SB-04
11.20–11.40	**Alexander MELNIKOV and K.S. LOBANOVA**	On perturbations in the rotational motion of the asteroid (99942) Apophis during its 2029 Earth encounter	14MS3-SB-05
11.40–12.00	COFFEE-BREAK		
12.00–12.20	**Evgenij ZUBKO and G. VIDEEN**	What we can learn about dust in comets from their polarimetry /**Invited talk**/	14MS3-SB-06
12.20–12.40	**Wentao LUO et al**	The 2.5 meter Wide Field Survey Telescope (WFST) design and hunting for NEOs	14MS3-SB-07
12.40–13.00	**Dominik BELOUSOV and A.K. PAVLOV**	Distant cometary outbursts: a non-gravitational mechanism of orbit perturbation	14MS3-SB-08
13.00–14.00	LUNCH		
14.00–14.15	**Ilia KUZNETSOV et al**	UV-influence on dust particles electrostatic lift-off processes in experimental set-up	14MS3-SB-09
14.15–14.30	**Valentin BORZOSEKOV et al**	Microwave discharge experiments on samples of a meteorite substance and lunar regolith simulants for plasma-dust cloud modelling	14MS3-SB-10

14.30–14.45	**Tatyana GAYANOVA et al**	Simulation experiments on the deposition of charged particles of LMS-1D regolith on the solar panels of spacecraft	14MS3-SB-11
14.45–15.00	**Yulia IZVEKOVA et al**	Specific features of dusty plasma and wave processes in the exosphere of Mercury	14MS3-SB-12
15.00–15.15	**Sergey POPEL and Lev ZELENYI**	Manifestations of anomalous dissipation in dusty plasmas of our Solar system: celestial bodies without atmosphere	14MS3-SB-13
15.15–15.30	**Yulia REZNICHENKO et al**	Dusty plasma clouds in the atmosphere of Mars: significance of Rayleigh-Taylor instability	14MS3-SB-14
15.30–15.45	**Olga POPOVA et al**	Energy release of large impactors in the terrestrial atmosphere	14MS3-SB-15
15.45–16.00	**Sergei IPATOV**	Migration of bodies ejected from the Earth and the Moon	14MS3-SB-16
16.00–16.15		COFFEE-BREAK	
16.15–16.30	**Tatiana SALNIKOVA and E.I. KUGUSHEV**	Possibility of space debris escape from the Earth – Moon system	14MS3-SB-17
16.30–16.45	**Roman ZOLOTAREV and Boris SHUSTOV**	On the dynamics of meteoroid streams originating from NEA collisions	14MS3-SB-18
16.45–17.00	**Nikolai KISELEV et al**	Polarimetry of NEAs at the Crimean astrophysical observatory and the Peak Terskol observatory in 2019–2023	14MS3-SB-19
17.00–17.15	**Alexander SAMOKHIN et al**	About the GTOC XII problem	14MS3-SB-20
17.15–17.30	**Anton SOKOLOV et al**	Mapping of Hyperion in the triaxial ellipsoid projections	14MS3-SB-21
17.30–17.45	**Vladimir TCHERNYI et al**	Saturn's magnetism in the origin of dense rings and in their peculiarities recorded by the Cassini probe. The Tchernyi-Kapranov effect	14MS3-SB-22
17.45–18.00	**Phiilipp VYSIKAYLO**	Vysikaylo' cumulative plasma cannon on the protection of the Earth from meteoroids	14MS3-SB-23

18.00–18.50	**POSTER SESSION, SESSION SMALL BODIES (INCLUDING COSMIC DUST)** 10 posters * 5 min		
18.00–18.05	**Mohammad MADANI**	An overview of Pluto's atmospheric studies	14MS3-SB-PS-01
18.05–18.10	**Dmitriy SHOKHRIN et al**	2D-description of nonlinear wave perturbations in the dusty magnetosphere of Saturn	14MS3-SB-PS-02
18.10–18.15	**Marina SHCHERBINA et al**	Gaia Data Release 3: distribution by spectral groups of near-Earth asteroids	14MS3-SB-PS-03
18.15–18.20	**Elena PETROVA**	On the evaluation possibility for the properties of the exosphere of an active asteroid from polarimetric data	14MS3-SB-PS-04
18.20–18.25	**Tatiana MOROZOVA and Sergey POPEL**	Instabilities in meteoroid tails associated with ion acoustic mode	14MS3-SB-PS-05
18.25–18.30	**Tatiana MOROZOVA and Sergey POPEL**	Manifestations of modulation instability in meteoroid tails	14MS3-SB-PS-06
18.30–18.35	**Maksim KHOVRICHEV and D.A. BIKULOVA**	Calculation of the non-gravitational A2 parameter using ground-based observations of the apparent close approaches between near-earth asteroids and Gaia stars	14MS3-SB-PS-07
18.35–18.40	**Mariia VASILEVA and Eduard KUZNETSOV**	Asteroid cluster of (338073) 2002 PY38: membership and age estimation	14MS3-SB-PS-08
18.40–18.45	**Vladimir EFREMOV et al**	Application of the small meteors ablation model to Perseid meteors	14MS3-SB-PS-09
18.45–18.50	**Vladislav ZUBKO et al**	Concept of planetary defense system using a projectile asteroid	14MS3-SB-PS-10
19.00–21.00	**RECEPTION**		

10.00–15.50

5 EXTRASOLAR PLANETS SESSION

Convener: **Alexander TAVROV**
room 200, second floor

10.00–10.20	**Ildar SHAIKHISLAMOV et al**	Modelling absorption in lines of hydrogen and oxygen of Super-Hot massive Jupiter Kelt9b	14MS3-EP-01
10.20–10.40	**Marina RUMENSKIKH et al**	The emission spectrum of the host star and transit absorptions of Hot Jupiters in the metastable helium line	14MS3-EP-02
10.40–11.00	**Olga OLEYNIK and Vacheslav EMEL'YANENKO**	The role of Earth-mass planets in the origin of debris disks	14MS3-EP-03
11.00–11.20	**Boris KONDRATYEV et al**	Modified method of round Gaussian rings. Application to the two-planetary problem	14MS3-EP-04
11.20–11.40	**Arina SIMONOVA and Valery SHEMATOVICH**	Calculation of thermal atmospheric loss for a Hot exoplanet on elliptic orbit	14MS3-EP-05
11.40–12.00	COFFEE-BREAK		
12.00–12.20	**Anastasia AVTAEVA and Valery SHEMATOVICH**	Kinetic model of the effect of stellar wind on the extended hydrogen atmosphere of the exoplanet π Men c	14MS3-EP-06
12.20–12.40	**Vladislava ANANYEVA et al**	The refined method for taking into account observational selection for planets detected by the radial velocity technique	14MS3-EP-07
12.40–13.00	**Yisi LIU and Volker PERDELWITZ**	One reliable method for stellar parameter determination based on space photometry and the PHOENIX spectral library	14MS3-EP-08
13.00–14.00	LUNCH		
14.00–14.20	**Anastasiia IVANOVA et al**	Telluric absorption correction and radial velocity method	14MS3-EP-09
14.20–14.40	**Artem SHEPELIN et al**	Statistical equilibrium code for exoplanet atmospheres simulations	14MS3-EP-10
14.40–15.00	**Sergei IPATOV**	Mixing of planetesimals in the Glisse 581 planetary system	14MS3-EP-11
15.00–15.20	**Eduard KUZNETSOV and A.S. PERMINOV**	Investigation of dynamic evolution of the compact planetary system Kepler-51	14MS3-EP-12

15.20–15.50	**POSTER SESSION, SESSION EXTRASOLAR PLANETS** 6 posters * 5 min		
15.20–15.25	**Ilia MIROSHNICHENKO et al**	Simulation of absorption in the Hα line of exoplanet KELT-9b	14MS3-EP-PS-01
15.25–15.30	**Maksim GOLUBOVSKY et al**	Oxygen 777.4 nm triplet absorption simulation in KELT-9b atmosphere	14MS3-EP-PS-02
15.30–15.35	**Stanislav SHARIPOV et al**	Simulation of Hα absorption for hot Jupiter WASP-12b	14MS3-EP-PS-03
15.35–15.40	**Artem BEREZUTSKY et al**	3D aeronomy of the HD 63433 system planets and absorption in Lya line	14MS3-EP-PS-04
15.40–15.45	**Ailar ALIZADEHSABEGH**	Planetary Mass-Radius Relation	14MS3-EP-PS-05
15.45–15.50	**Esfandiar JAHANGIRI**	Ephemeris Updates for Seven Selected HATNet Survey Transiting Exoplanets	14MS3-EP-PS-06
16.00–16.20	COFFEE-BREAK		

10.00–17.00

6 ASTROBIOLOGY SESSION

Convener: **Oleg KOTSYURBENKO**
conference hall, second floor

10.00–10.20	**Vladimir KOMPANICHENKO**	Concept of thermodynamic inversion as a model of the origin of life on planets and satellites	14MS3-AB-01
10.20–10.40	**Valery SHEMATOVICH et al**	Non-thermal nitric oxide formation in polar regions of N_2–O_2 atmospheres	14MS3-AB-02
10.40–11.00	**Sergey BULAT et al**	Searching for extraterrestrial thermophiles on icy moons with subglacial oceans?	14MS3-AB-03
11.00–11.20	**Alexander GURIDOV et al**	Resistance of bacteria Bacillus licheniformis of "EXPOSE-R2" space experiment to the extreme space factors	14MS3-AB-04
11.20–11.40	**Daniil MIRONOV et al**	Development of biomining technology using Aspergillus niger: application to the Lunar program	14MS3-AB-05
11.40–12.00		COFFEE-BREAK	
12.00–12.20	**Elena DESHEVAYA et al**	Planetary protection of Mars in missions for searching possible life forms	14MS3-AB-06
12.20–12.40	**Elena DESHEVAYA et al**	Survival of microorganisms over two years of exposure in the near-ISS space	14MS3-AB-07
12.40–13.00	**Vyacheslav ILYIN and S.V.PODDUBKO**	Exobiological studies in the interests of ensuring planetary quarantine	14MS3-AB-08
13.00–14.00		LUNCH	
14.00–14.20	**Sohan JHEETA**	Irradiation of Methyl Cyanide (CH3CN) with 200 keV at 15 K temperature	14MS3-AB-09
14.20–14.40	**Oleg KOTSYURBENKO**	Main directions and prospects for the development of astrobiology in Russia	14MS3-AB-10
14.40–15.00	**Ximena ABREVAYA et al**	Astrophysical sources of radiation and habitability in the universe	14MS3-AB-11
15.00–15.20	**Richard B. HOOVER and Alexey ROZANOV**	Life in the universe: extraterrestrial water, cyanobacteria and diatoms	14MS3-AB-12
15.20–15.40	**Andrey B. RUBIN et al**	Strategy for using fluorimetric methods in the search for extraterrestrial life forms	14MS3-AB-13
15.40–16.00	**Ivan KONYUKHOV et al**	Using fluorimetric methods to search for extraterrestrial photosynthetic organisms	14MS3-AB-14
16.00–16.20		COFFEE-BREAK	

16.20–17.00	**POSTER SESSION, SESSION ASTROBIOLOGY** 4 posters * 10 min		
16.20–16.30	**Daniil BARBASHIN et al**	Bacterial tolerance to the influence of sodium perchlorate: estimation in extreme ecotopes communities	14MS3-AB-PS-01
16.30–16.40	**Marina GRINBERG et al**	Effect of low intensity ionizing radiation and magnetic fields on the functional status of plants	14MS3-AB-PS-02
16.40–16.50	**Mehdi KHODADADILORI**	2D and 3D parameter relationships for W UMa-type systems revisited	14MS3-AB-PS-03
16.50–17.00	**Alexander SAFRONOV**	Scanning for habitable stellar systems on behalf of future space missions	14MS3-AB-PS-04

ABSTRACTS

SESSION 1. MARS (MS)
ORAL SESSION

VALLEY TOPOGRAPHY OF NORTHEASTERN TERRA CIMMERIA ON MARS

A.E. Mukhamedzhanova
Vernadsky Institute of Geochemistry and Analytical Chemistry RAS, Moscow, Russia, alinam2001@gmail.com

KEYWORDS:
Mars, Terra Cimmeria, river valleys, valley forms, fast deep erosion

INTRODUCTION:

On Mars, there are landforms that visually resemble river valleys and watercourse beds. One of the possible explanations for this fact is the fluvial character of these formations, suggesting the presence of liquid water as an agent of formation of this kind of relief. The most important questions in such a case are about the sources of water, the duration of its active operation, the age of these forms, and the receiving basins.

Terra Cimmeria is a large Martian region located in the southern hemisphere of the planet. To the north of it there is a transition zone with specific relief between the ancient southern cratered continent and relatively younger and lower plains of the northern hemisphere [1]. The choice of the key study area is conditioned by the presence of this specific transition zone and implied the study of the valley relief of the northeastern part of the Terra Cimmeria with consideration of the peculiarities of the structure of a specific part of the transition zone on Mars.

GOALS OF THE STUDY, DATA, AND METHODS:

The purpose of this work is to identify the most probable variant of the origin of the valleys of the northeastern Terra Cimmeria (98.79–179.66° E, 12.13–73.54° N). The main methods used in this work are geomorphologic interpretation of Mars remote sensing data and geomorphologic mapping of the area, as well as morphometric constructions using GIS-technologies. The methodology of valley forms research included: interpretation of valley thalwegs, study of valley network structure, study of morphology of separate valleys, study of valley correlation with relief forms of another genesis.

Based on the Global Geological Map of Mars [2], Geological Map of Aeolis Quadrant [3], as well as visual interpretation of CTX space images with a spatial resolution of 6 m, a geomorphological map of the study area was made. It was revealed that the northeastern Terra Cimmeria is a combination of plains of different morphology formed on ancient (presumably of Early and Middle Noahian age) rock complexes and substantially reworked in the Hesperian and Amazonian times by complex denudation and impact-explosion processes. These plains are cut through by two submeridionally oriented valley systems - Ma'adim and Durius.

RESULTS:

A set of characteristics that helped to identify and describe this type of relief was used as deciphering features of valley forms. Thus, for example, narrow and deep valleys indicate that the conditions of formation of this type of forms existed for a short time, but with active processes of incision. Wide valleys testify about long time of their formation. In some cases, the valleys have a rather clear appearance, by which one can determine their structure, pattern and morphology. Thus, in both the Ma'adim and Durius valley systems the main valleys and their tributaries are clearly distinguished by their shape, size and albedo. During interpretation, the structure of the valley network was coded. The system of valley order determination by Straller was used, where each river tributary is classified according to its position in the overall network. The main characteristics of the network were obtained: valley lengths, widths, and gradients, as well as morphological characteristics of the valleys: longitudinal profile, depths and widths along the banks and bottoms, and the shape of the transverse profile. Changes in the shape and parameters of the cross-sectional profile down the valleys were also analyzed to elucidate the patterns of valley development.

DISCUSSION:

The study revealed that both valley systems are characterized by branching (presence of watercourses of several orders) together with weak development of upper links of the erosion network: tributaries of low orders have insignificant length and insufficient morphological expression compared to the main valley. A general trend of incision from south to north was revealed. Both main valleys tend to develop a U-shaped profile and to widen their bottoms as they approach the mouth. Correlative landforms (outcrop cones, terraces) in the Ma'adim valley may indicate flowing water activity.

The valleys cut through background plains composed of rocks of Early and Middle Noachian age, which automatically excludes the possibility of valley formation at this time. There are areas where valley systems are partially destroyed as a result of impact events, and there is a rather low morphological preservation of the Ma'adim valley paleodelta. These facts allow us to assume a rather ancient bedding of the valley and the cessation of its active functioning in the pre-Amazonian time.

Thus, the most probable time interval for the formation of these valley systems is the Early Noachian-Hesperian time (4.5–3 billion years ago), which does not contradict the existing estimates for some other valleys. Most likely, the considered valleys were formed by relatively fast deep erosion by geologic standards. The relatively simple morphological structure of the valleys under consideration does not imply multiple cycles of incision and alluvium filling and is reduced to relatively fast and directed erosion. At the same time, the terraces and partially eroded fragments of the ancient accumulative valley floor noted in the Ma'adim valley do not exclude individual episodes of partial filling of the valleys with sediment, probably due to the intensification of regressive development of the uppermost links of the valley network that supplied sediment to the main valley.

References:

[1] *Hynek B.M., Beach M., Hoke M.R.T.* Updated global map of martian valley networks and implications for climate and hydrologic processes // J. Geophysical Research. 2010. V. 115. Iss. 9. Art. No. E09008. https://doi.org/10.1029/2009JE003548.

[2] *Tanaka K.L., Skinner T.J.A. Jr., Dohm J.M. et al.* Geologic map of Mars: U.S. Geological Survey Scientific Investigations Map 3292, scale 1:20,000,000 / USGS. 2014. 43 p. http://dx.doi.org/10.3133/sim3292.

[3] *Scott D.H., West M.N.* Geologic map of the Aeolis Quadrangle of Mars: U.S. Geological Survey Miscellaneous Investigations Series Map 1-1111. 1978. https://doi.org/10.3133/i1111.

CONSTRAINT ON PALEO HYDROLOGICAL ACTIVITIES FROM DELTAS ON MARS

Yaowen Luo
Deep Space Exploration Lab, Hefei, 230031, China

KEYWORDS
Mars, deltas, quantitative analysis, hydrologic process, sedimentary processes

Deltas record fluvial and sedimentary activities on the early Mars. However, quantitative hydrologic and sedimentary processes related with the formation of the Martian deltas still need further investigation. We quantitatively analysed the fluvial and sedimentary process of seven deltas with various morphologies in different locations on Mars in order to constrain their formation. Paleo discharge, sediment transport rate, timescale and amount of water needed to construct the deltas were estimated. The volume between deltas and carved valleys are compared, and the absolute age of the delta/valley relation is approximated by crater counting. Different processes of water supply are considered. The seven deltas were divided into three types based on their supplying valleys and water source. We assume that the formation of the deltas can be associated with various scenarios, including retreating erosion, groundwater sapping, ice melting, precipitation, impact events and variations of the Martian obliquity. Based on mass balances, the continuous formation timescale of the deltas can range from days to thousands of Martian years. Considering the intermittency of water supply and flow power, it can reach hundreds of million years. The results suggest that a warm climate is not fundamental requirement for the formation of the Martian deltas.

DEPOSITS IN THE DEPRESSION WEST TO EBERSWALDE CRATER INDICATE A SYNCHRONOUS HYDROGEOLOGICAL HISTORY OF HOLDEN AND EBERSWALDE CRATERS ON MARS

J. Chu[1], M.A. Ivanov[2], A.M. Nikishin[1]

[1] *Lomonosov Moscow State University, Faculty of Geology, Moscow, Russia, vladimirchujun@yandex.ru*

[2] *Vernadsky Institute of Geochemistry and Analytical Chemistry RAS, Moscow, Russia, Mikhail_Ivanov@brown.edu*

KEYWORDS:
Mars, Eberswalde, Holden, channel, chronology

INTRODUCTION:
Eberswalde crater is located to the north of the Holden crater and is characterized by the presence of well-developed delta [1, 2]. The delta in Eberswalde indicates the presence of sustain water flows that carried suspended fine-grained materials into the crater from outside, from a broad depression westward of Eberswalde, the western depression, into the sink of the crater [3]. To study the modes and timescale of the formation of the delta, we investigated the morphological characteristics of the western depression in detail. Our study was based on the topographic data (MOLA gridded topography, 1/128° resolution) and the mosaics of the CTX images (6 m/px resolution).

MORPHOLOGICAL UNITS:
The depression to the west of Eberswalde crater can be divided to three morphological units (Fig. 1): (1) Peripheral channelized unit: it is located in the western and southern part of study area; its surface is cut by narrow channels. (2) Northern light unit: it has a smooth surface with higher albedo and lacks channels. (3) Central dark unit: it is a topographically the lowest area, which is cut by a broader valley and show the presence of outcrops of layered deposition.

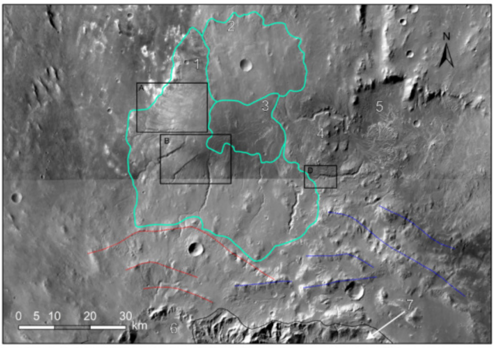

Fig. 1. Morphological units: (1) Peripheral valleyed unit; (2) Northern light unit; (3) Center dark unit; (4) Impact ejection from Holden crater; (5) Eberswalde crater; (6) Bigbee crater; (7) Holden crater. The red and blue dotted lines represent the remnant Bigbee and Holden crater ring, respectively (CTX images)

DESCRIPTION OF OUTCROPS:
The layered outcrops of layered deposited appear to be similar to the outcrop in Holden craters and can be divided into two subunits [4]: (a) the lowed subunit is layered and consisted of light-toned coarse-grained materials. The polygonal cracks on the surface of the subunit are filled with dark materials. The edges of the subunits are step-like with small pits. (b) Dark, fine-grained mantle which unconformably overlays the lower layered subunit.

MORPHOLOGICAL DESCRIPTION OF THE CHANNELS:

There are three types of channels in the study area: (1) channels with funnel-like sources (Fig. 2A): they occur in the western part of the peripheral channelized unit and are characterized by many branches in their upper stretches. (2) long and deep V-like channels (Fig. 2B): they occur in the southern part of the peripheral channelized unit. (3) short and shallow channels (Fig. 2B): they also occur in the southern part of the peripheral channelized unit.

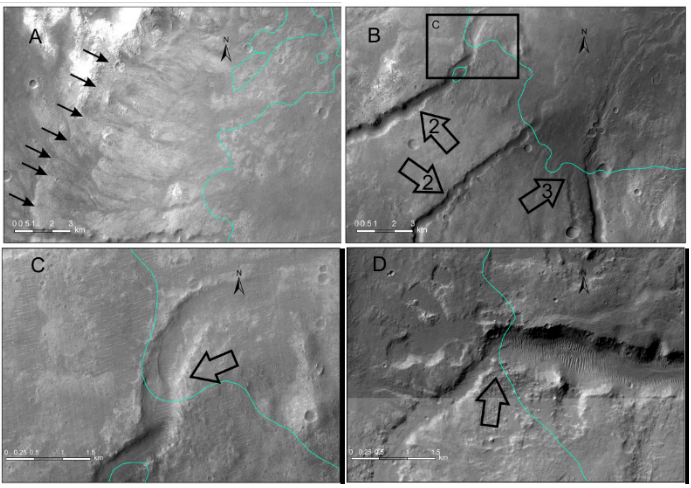

Fig 2. Type of channels: A. channels with funnel-like sources (indicated by black arrows); B. arrows 2 indicate the long and deep V-like channels; arrow 3 indicates the short and shallow channels. C and D. arrow indicate the knickpoint in long and deep V-like channels. The light blue line represents the -280-contour line. (CTX images)

CHRONOLOGY:

In order to reconstruct the sequence of the geological events, we have performed crater size-frequency distribution (CSFD) measurements for the defined units: (1) the southern part of the peripheral channelized units shows a single absolute model age, AMA, of 3.3(+0.06, –0.1) Ga; the western part of peripheral channelized unit with the funnel-like valleys shows a single AMA of 610(+100, –100) Ma; (2) the northern light unit shows two AMAs of 3.8(+0.05, –0.07) Ga and 3.4(+0.04,–0.1) Ga; (3) the central dark unit shows a single AMA of 3.6(+0.07, –0.1) Ga. We also performed CSFD measurements for the floor of Eberswalde crater and obtained two AMAs of 3.8(+0.08, –0.2) Ga and 3.3(+0.1, –0.5) Ga. The southern part of the floor of the Holden crater shows a single AMA of 3.4(+0.05, –0.6) Ga.

DISCUSSION AND CONCLUSION:

1) The presence of layered deposits in the western depression indicates the presence of a stable water body in this area. Morphologically similar outcrops of layered deposits occur in Holden crater and likely contain clay minerals [5]. The later fluvial activity westward of Eberswalde eroded the layered deposits and transported their materials to form the delta.
2) The funnel-like channels morphologically disappear at the contour line of -280 m, and the knickpoints of the V-shaped valleys are also located at the same contour line (see Fig. 2). Thus, the level of –280 m probably indicates the highest water level in the western depression. The water body was ponding by a dam formed by ejecta of the Holden crater deposited between the western depression and Eberswalde crater (see Fig. 1). Later, the dam was breached, and the water level dropped, causing the formation of the second type of the channels (the long deep V-like channel). The boulder-bearing deposits in the Eberswalde delta likely formed by the collapse of the dam [6] and the other parts of the delta may be related to the upper water level (–280 m) in the western depression. The whole process may resemble that of the fan-shaped deposit where Uzboi Vallis entering the Holden crater [7].

3) The AMAs derived from CSFD measurements show that the water flow activity in the west depression began around 3.7 Ga and ended at 3.4 Ga. The AMA of 3.8 Ga may indicate the formation of the lowest strata in the Eberswalde crater. Later, seepage of water from the western depression has filled the floor of the crater and caused formation of the delta; these processes were ended at 3.3 Ga. The southern plain on the floor of the Holden crater represents the lowest layer visible in floor layered sequence, indicating that the filling of Holden crater was basically completed by 3.4 Ga, which is close to the AMAs for the western depression. Previous studies [7–9] indicated that the Holden crater was partly filled by flows from Uzboi Vallis. The western depression is not connected with Uzboi. Thus, the layered deposits on the floors of the Holden and Eberswalde craters have different sources that, however, existed at about the same time.

Acknowledgements:
This work is supported by China Scholarship Council and represents a part of the state order of GEOKHI for MAI.

References:

[1] *Malin M.C., Edgett K.S.* Evidence for persistent flow and aqueous sedimentation on early Mars // Science. 2003. V. 302. Iss. 5652. P. 1931–1934. DOI: 10.1126/science.10905.

[2] *Pondrelli M., Rossi A.P., Marinangeli L. et al.* Evolution and depositional environments of the Eberswalde fan delta, Mars // Icarus. 2008. V. 197. Iss. 2. P. 429–451. https://doi.org/10.1016/j.icarus.2008.05.018.

[3] *Howard A.D., Moore J.M., Irwin R.P. et al.* Boulder transport across the Eberswalde delta // 38th Lunar and Planetary Science Conference, (Lunar and Planetary Science XXXVIII). March 12–16, 2007, League City, Texas. LPI Contribution No. 1338. 2007. Abs. No. 1168.

[4] *Grant J.A., Irwin III R.P., Grotzinger J.P.* HiRISE imaging of impact megabreccia and sub-meter aqueous strata in Holden Crater, Mars // Geology. 2008. V. 36. P. 195–198. HiRISE imaging of impact megabreccia and sub-meter aqueous strata in Holden Crater, Mars.

[5] *Milliken R.E., Grotzinger* J., Grant J. *et al.* Clay minerals in Holden crater as observed by MRO CRISM. // 7th Intern. Conf. Mars. 2007. Art. No. 3282.

[6] *Mangold N., Kite E.S., Kleinhans M.G. et al.* The origin and timing of fluvial activity at Eberswalde crater, Mars // Icarus. 2012. V. 220. Iss. 2. P. 530–551. https://doi.org/10.1016/j.icarus.2012.05.026.

[7] *Grant J.A., Irwin III R.P., Wilson S.A. et al.* A lake in Uzboi Vallis and implications for Late Noachian-Early Hesperian climate on Mars // Icarus. 2011. V. 212. Iss. 1. P. 110–122. https://doi.org/10.1016/j.icarus.2010.11.024.

[8] *Pondrelli M., Baliva A., Di Lorenzo S. et al.* Complex evolution of paleolacustrine systems on Mars: An example from the Holden crater // J. Geophysical Research. 2005. V. 110. Iss. E4. Art. No. E04016. https://doi.org/10.1029/2004JE002335.

[9] *Grant J.A., Irwin III R.P., Wilson S.A.* Aqueous depositional settings in Holden crater, Mars // Lakes on Mars / eds. Cabrol N.A., Grin E.A. Oxford, UK: Elsevier, 2010. P. 323–346. DOI:10.1016/B978-0-444-52854-4.00012-X.

NEW CRATERS ON MARS: UPDATING AFTER 2022 CATALOG

B.A. Ivanov
Institute of Geosphere Dynamics RAS, Moscow, Russia, baivanov@idg.chph.ras.ru

KEYWORDS:
Mars, impact craters, atmospheric shock waves, dust, HiRise

INTRODUCTION:

Numerous orbital spacecrafts continue to investigate Mars to study ongoing planetary processes. One of them is ongoing impact bombardment of the Martian surface with small celestial bodies. In dusty regions new impact craters are easily recognized in high-resolution images allowing us to find impacted sites with low-resolution CTX images. The following HIRISE imaging fixes new craters with the resolution of 25 to 30 cm per pixel. The pioneer study by Malin [1] revealed first twenty of small impact craters formed within the known period of time. The continuation of this activity allows us to find 1221 dated impact cites imaged until 11.02.2021 [2]. The continuation of the published catalog for "new" crater formed after this data allows us to improve estimates of the current impact flux to Mars.

"NEW" (DATED) IMPACT CRATERS:

Impact craters on Mars could be dated with images before and after an impact. Such impact cites are commonly designated as "new' craters. The interval between "before" and "after" images could vary from a few days to a few years. A simple estimate of the origin date is typically the middle date between dates of "before" and "after" images. More sophisticated study of the impact cite decay could be used in a future to better constrained the impact feature age.

The next problem is to estimate the projectile size from the impact records seeing in images. In contrast to the Moon, small celestial bodies could be shuttered in the Martian atmosphere, and approximately in 30% of impacts we have a cluster of craters from one entered projectile. In some extreme cases HiRISE images reveal more than a thousand individual craters in a cluster [3]. By convention we use an equivalent crater diameter as $D_{eq} = (SD_i^3)^{1/3}$ for a cluster of craters with individual diameters D_i (see more details in [2]).

Having ahead more sophisticated representation of craters, taking into account possible difference in the surface mechanical properties, we could discuss some general results from the "new" crater's database. Fig. 1 shows a differential size-frequency distribution, separating the whole collection by the approximate origin data in two large groups — "new" (dated) impacts occurred before and after 2007. We do not make a "fine" tune of the separating date, but this

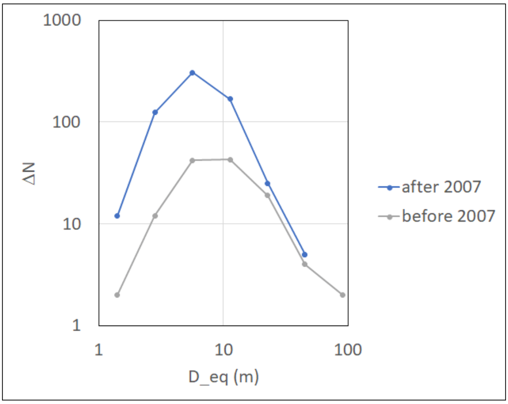

Fig. 1. Differential number DN of "new" impact craters in diameter bins 1 to 2 m, 2 to 4 m, etc. for catalogized ~1800 "new" craters ([2] plus author's data). The "boundary" year 2007 is chosen to have approximately same number of craters in equivalent diameter bins 16 to 32 m and 32 to 64 m

"boundary" date give a good impression of a relative stability of the recorded impact flux during the HiRISE observational period. At the same time, we see how the continuous imaging of the Martian surface results in a better count of small impacts with equivalent crater diameter below 16 m. Above this size we totally accumulated data about ~60 impacts during the whole MRO mission. With a proper selection of a dusty areas we hope to have a reliable impact rate of small bodies on Mars to compare with the Lunar impact rate [4].

NEW CASES OF ATMOSPHERIC SHOCK WAVES:
A very interesting example of a new impact site was recently imaged by the HiRISE (ESP_078372_2020, imaged16 April 2023, D_{main} ~ 11.8 m, lat = 21.929°, lon = 2.381°, "before" image — THEMIS I87237002, 08.14.2021 "after" image HiRise ESP_078372_2020, 04.16.2023, dust index 0.94094, altitude —1.932 km, thermal inertia 120 (Fig. 2).

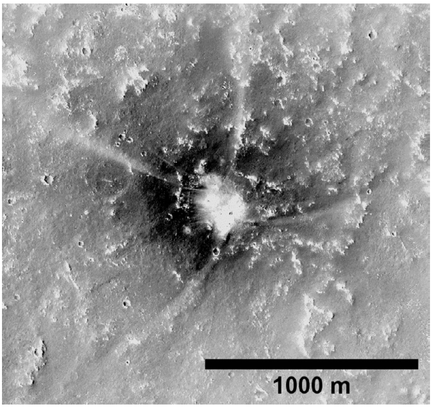

Fig. 2. The impact site formed between August 14, 2021 and April 16, 2023. The main crater is about 10 m with the attached scimitar, recorded the impact trajectory direction from SE to NW. A dozen of smaller crater are seen around the main crater. Fragment impacts created a couple of small craters north of the main one also created "parabolas" (strictly speaking — hyperbolas), giving some data to restrict the impact angle, impact velocity and projectile density

Estimates made with standard gas-dynamic description of air-shock waves propagation in the Martian atmosphere, approximated with CO_2 gas, allow us estimate the size of the main body as ~30 cm (iron) to ~60 cm (stony), impacting the surface with the velocity ~8 km/s at an angle ~36° (iron) or 5.5 to 6.5 km/s at an angle of ~30 to 40° (stony). Smaller impacts, created "parabolas" (hyperbolas) occurred ~0.5 s later than the main impact. More modeling is anticipated to improve our understanding of a complex picture of multiple atmospheric shock wave interaction in Martian conditions.

CONCLUSIONS:
The long-term observations of the bombardment of Mars with a constant flux of small celestial bodies give an unique opportunity to see the interaction between space objects and the planetary surface and atmosphere.

References:
[1] *Malin M.C., Edgett K.S., Posiolova L.V. et al.* Present-day impact cratering rate and contemporary gully activity on Mars // Science. 2006. V. 314(5805). P. 1573–1577.
[2] *Daubar I.J., Dundas C.M., McEwen A.S. et al.* New Craters on Mars: An Updated Catalog // J. Geophys. Research: Planets. 2022. V. 127. No. 7. Art. No. e2021JE007145.
[3] *Ivanov B.A., Melosh H.J., McEwen A.S.* Small Impact Crater Clusters in High Resolution HiRISE Images — II // 40th Lunar and Planetary Science Conf. 2009. Woodlands, Texas, Abs. No. 1410. https://www.lpi.usra.edu/meetings/lpsc2009/pdf/1410.pdf.
[4] *Speyerer E.J., Povilaitis R.Z., Robinson M.S. et al.* Quantifying crater production and regolith overturn on the Moon with temporal imaging // Nature. 2016. V. 538. No. 7624. P. 215–218.

SOME STATISTICS ON FRESH MARTIAN CLUSTERS

E.D. Podobnaya, O.P. Popova, D.O. Glazachev
Institute of Geosphere Dynamics RAS, Moscow, Russia, epodobnaya@gmail.com

KEYWORDS:
Mars, craters, clusters, catalog

INTRODUCTION:

On the Earth, as a rule, meteoroids 1–10 m in scale are observed during a short flight through the atmosphere, and most of their mass remains in the atmosphere due to fragmentation and ablation, in rare cases, their fragments are found as meteorites. On Mars, similar objects would lead to the formation of crater or crater clusters due to rarefied martian atmosphere [1]. The density of the atmosphere near the surface of Mars corresponds to about 30 km altitude in the Earth's atmosphere, so the consideration of crater fields on Mars allows us to study details of fragmentation that cannot be detected in Earth conditions. The properties of space objects are estimated from observational data within certain assumptions with not very high accuracy, the study of Martian clusters provides an opportunity to evaluate the properties of meteoroids independently.

CRATERS ON MARS:

Previously, it was predicted that meteoroids in the Martian atmosphere could disintegrate and form clusters of craters on the Martian surface [2–3]. Later fresh crater clusters were discovered [4]. Currently detailed data for more than 1200 recent dated impact sites are published [5–6]. These data include information about the size and location of craters in the cluster. About 58 % of impact sites are clusters, and the rest are individual craters [6]. New data are permanently released by HiRISE project, so our current catalog is supplemented by about 650 new impact sites.

TYPES OF IMPACT SITES:

Authors of the article [7] suggested to divide impact sites into 4 types based on small statistics available at that time (about 20 cases). First type (Type 0) combined single craters, pairs and clusters with one major crater and few (<9) much smaller ones. Clusters with major crater supplemented by numerous small ones (>10) were marked as Type 1; other clusters refer to the Type 2, but densely populated clusters (with more than 400 craters) were marked as Type 3.

This presentation will apply initially suggested classification to the essentially updated catalog and will discuss its applicability to extended data.

Acknowledgements:
The research was supported by RSF (project No. 23-27-00432).

References:

[1] *Hartmann W.K., Daubar I.J., Popova O.P. et al.* Martian cratering 12. Utilizing primary crater clusters to study crater populations and meteoroid properties // Meteoritics and Planetary Science. 2018. V. 53. Iss. 4. P. 672–686. https://doi.org/10.1111/maps.13042.

[2] *Popova O., Nemtchinov I., Hartmann W.K.* Bolides in the present and past martian atmosphere and effects on cratering processes // Meteoritics and Planetary Science. 2003. V. 38. Iss. 6. P. 905–925. https://doi.org/10.1111/j.1945-5100.2003.tb00287.x.

[3] *Popova O.P., Hartmann W.K., Nemtchinov I.V. et al.* Crater clusters on Mars: Shedding light on martian ejecta launch conditions // Icarus. 2007. V. 190. Iss. 1. P. 50–73. https://doi.org/10.1016/j.icarus.2007.02.022.

[4] *Malin M.C., Edgett K.S., Posiolova L.V. et al.* Present-day impact cratering rate and contemporary gully activity on Mars // Science. 2006. V. 314. Iss. 5805. P. 1573–1577. DOI: 10.1126/science.1135.

[5] Daubar I.J., McEwen A.S., Byrne S., Kennedy M.R., Ivanov B. The current Martian cratering rate // Icarus. 2013. V. 225. No. 1. P. 506-516.

[6] *Daubar I.J., Dundas C.M., McEwen A.S. et al.* New Craters on Mars: An Updated Catalog // J. Geophysical Research: Planets. 2022. V. 127. Iss. 7. Art. No. e2021JE007145. https://doi.org/10.1029/2021JE007145.

[7] *Ivanov B.A., Melosh H.J., McEwen A.S., HIRISE Team.* Small impact crater clusters in high resolution HiRISE images // Proc. 39th Annual Lunar and Planetary Science Conf. Texas. USA. 2008. Abs. No. 1221.

THE GAS-SOLID CHEMICAL REACTION DURING MARTIAN DUST EVENTS

Zhongchen Wu, Yuheng Ni, Wenshuo Mao, Xianyang Sun
School of Space Science and Physics, Institute of Space Sciences, Shandong University, Weihai, Shandong, China, z.c.wu@sdu.edu.cn

KEYWORDS:
Mars, dust events, electrostatic discharge, electrochemical reactions, (per) chlorate, carbonate

INTRODUCTION:
Mars dust events (dust storms, dust devils, and grain saltation) occur frequently on the surface of present-day Mars which generate strong electric field and very likely trigger the electrochemical reactions during electrostatic discharge (ESD). For instance, the ESD on Martian dust has been recently proposed as a geological process producing (per)chlorate [1], carbonate [2], and it may also contribute to the transient HCl in the Martian atmosphere during dust events.

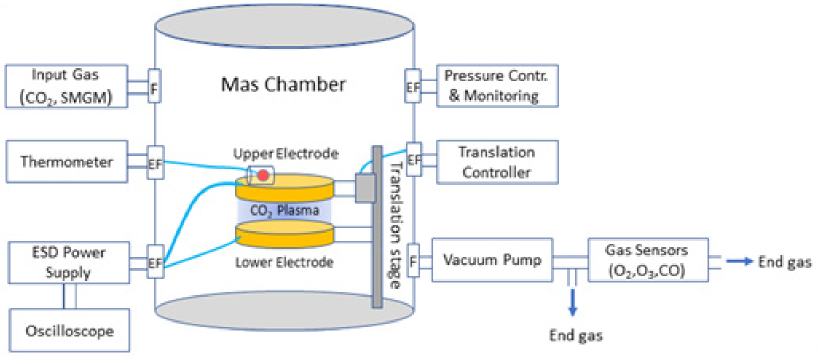

Fig. 1. Experiment setup of ESD CO2 glow discharge for the study of chemical reaction under simulated Martian conditions (F: Flange; EF: Electrical feedthrough; SMGM: Simulated Martian Gas Mixture)

Our studies were conducted in the Mars environmental simulation chamber (cylinder-shaped; diameter 150 mm; height 400 mm) (Fig. 1), where the atmospheric components and pressure resembled those of Mars surface. Two homemade disc-shaped copper parallel planes were used as discharge electrodes with a gap of 2.0–5.0 mm. The CO_2 gas plasma could be generated between two electrodes when certain high A.C. voltages were applied to the two electrodes. Then the chemical reactions will take place in this plasma conditions. For in-time detection of the newly generated gas product during the plasma reaction, a mini air pump and an electronic gas flowmeter were used to pump the end gas of the Mars chamber into several series gas sensors(such as CO, O_3, O_2) at a fixed flow rate.

In this study, several experimental results by ESD chemical reaction using this setup, such as O_2, oxychloride and carbonate aerosol generation, were reported. The new experimental phenomenon and its reaction mechanism were also discussed. Our study indicates that electrochemistry during Martian dust storms leads to the chemical transformation in the Martian atmosphere-surface, and it is also a potential and practicable technology for O_2 and CO generation for in-situ resource utilization (ISRU) on the Martian surface.

References:
[1] *Zhongchen Wu, Alian Wang, William M. Farrell et al.* Forming perchlorates on Mars through plasma chemistry during dust events // Earth and Planetary Science Letters. 2018. V. 504. P. 94–105. https://doi.org/10.1016/j.epsl.2018.08.040.
[2] *Wenshuo Mao, Xiaohui Fu, Zhongchen Wu et al.* Solid-gas carbonate formation during dust events on Mars // National Science Review. 2023. V. 10. Iss. 4. Art. No. nwac293. https://doi.org/10.1093/nsr/nwac293.

DISTRIBUTION OF ATMOSPHERIC AEROSOLS DURING THE 2007 MARS DUST STORM BY SOLAR INFRARED OCCULTATION ON MARS-EXPRESS

A.A. Fedorova[1], O.I. Korablev[1], F. Montmessin[2], J.-L. Bertaux[2], D.S. Betsis[1], F. Lefèvre[2]

[1] *Space Research Institute, Moscow, Russia, fedorova@cosmos.ru*

[2] *Laboratoire Atmosphères, Milieux, Observations Spatiales (LATMOS) Université de Versailles — Saint-Quentin-en-Yvelines (UVSQ), Guyancourt, France*

KEYWORDS:
Mars, atmospheres, solar occultations, spectroscopy, dust, clouds

Solar occultation measurements by the SPICAM IR on Mars-Express have been used to study aerosol vertical distribution during the 2007 global dust storm (GDS) of Mars Year 28. The spectrometer working in the near-IR spectral range from 1 to 1.7 μm provides information about aerosol optical properties like opacity, extinction coefficient, particle size and number density [1–2]. The observations were performed at *Ls* = 254–302° of MY28 and latitudes from 65° S to 65° N. SPICAM IR cannot distinguish between absorption due to dust or water ice. The particle size distribution and its parameters, the effective radius and variance, are retrieved assuming either mineral dust or water ice refraction indices. Before the GDS *Ls* < 265° the aerosol was extended from 20 to 60 km with dust particle size about 0.7 μm below 50 km and decreasing with altitude above. The detached layers, presumably water ice, have been found at altitudes of 60 km in the Southern hemisphere and 45 km in the northern and southern hemispheres with opacity <0.01 and 0.01–0.04, respectively. With the development of the GDS the dust lifted to 80 km and higher, r_{eff} tends to increase with altitude and stay about 1–1.2 μm up to 70–80 km. At the high latitudes of the Northern hemisphere at *Ls* = 268–275° the optically thin high altitude water ice clouds were detected at 80–90 km with r_{eff} < 0.3 μm and number density 2–7 cm^{-3}. The dependence of the effective variance on altitude and season has been found. Before the beginning GDS v_{eff} varied from 0.4–0.6 below 40–55 km to v_{eff} ≈ 0.2 above. During the GDS, the wide distribution propagated higher, with v_{eff} ~ 0.5–0.6 up to 70 km in both hemispheres. This suggests profound modification of the dust particle size distribution during a GDS.

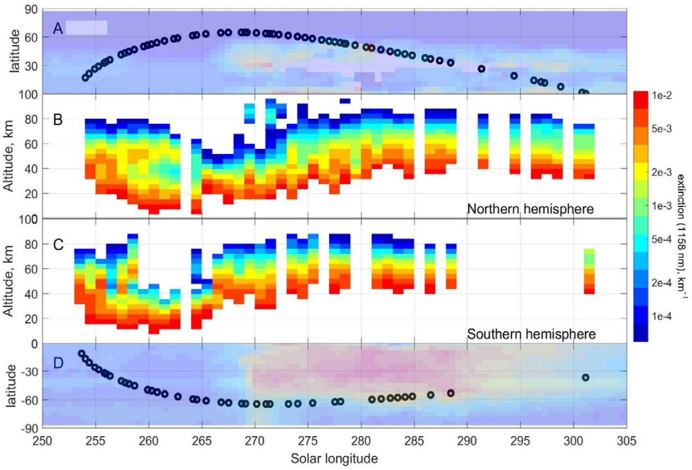

Fig. 1. Evolution of extinction coefficient profiles at 1152 nm. A — latitudinal trend of occultations in the Northern hemisphere; B — vertical distribution of the SPICAM extinctions in km–1 for the Northern hemisphere; C — vertical distribution of the SPICAM extinctions in km–1 for the Southern hemisphere; D — latitudinal trend of occultations in the Southern hemisphere. The background of panels A and D corresponds to the column dust optical depth at 9.3 μm from [3] with red colors corresponding to τ > 1 and dark blue to τ < 0.1

Acknowledgements:
We acknowledge RSF grant no. 23-12-00207.

References:

[1] *Korablev O., Bertaux* J.-L., *Fedorova A.A. et al.* SPICAM IR acousto-optic spectrometer experiment on Mars Express // J. Geophysical Research: Planets. 2016. V. 111. Iss. E9. Art. No. E09S03. https://doi.org/10.1029/2006JE002696.
[2] *Fedorova A.A., Korablev O.I., Bertaux* J.-L. *et al.* Solar infrared occultations by the SPICAM experiment on Mars Express: Simultaneous observations of H_2O, CO_2 and aerosol vertical distribution // Icarus. 2009. V. 200. Iss. 1. P. 96–117. https://doi.org/10.1016/j.icarus.2008.11.006.
[3] *Montabone L., Forget* F., *Millour* E. *et al.* Eight-year climatology of dust optical depth on Mars // Icarus. 2015. V. 251. P. 65–95. https://doi.org/10.1016/j.icarus.2014.12.034.

TWO YEARS OF GRAVITY WAVES OBSERVATION IN THE MARTIAN ATMOSPHERE BY THE ACS EXPERIMENT ON BOARD THE EXOMARS/TGO

E.D. Starichenko[1], D.A. Belyaev[1], A.S. Medvedev[2], A.A. Fedorova[1], O.I. Korablev[1], F. Montmessin[3], A. Trokhimovskiy[1]

[1] *Space Research Institute RAS, Moscow, Russia, starichenko.ed@phystech.edu*
[2] *Max Planck Institute for Solar System Research, Göttingen, Germany*
[3] *Laboratoire Atmosphères, Milieux, Observations Spatiales (LATMOS) Université de Versailles — Saint-Quentin-en-Yvelines (UVSQ), Guyancourt, France*

KEYWORDS:
Martian Atmosphere, Gravity Waves, Trace Gas Orbiter, Atmospheric Chemistry Suite, ExoMars, Solar Occultation

INTRODUCTION:
Internal Gravity waves (GWs) represent the oscillations of air in the atmosphere that originate from the displacement of balance between gravity and buoyancy forces. Since they redistribute energy and momentum between atmospheric layers, GWs greatly affect atmospheric dynamics. In this work, we study the parameters of GWs [1] and their various distributions. These parameters are retrieved from the vertical profiles of Martian atmosphere temperature, which is obtained from the solar occultation experiments conducted by the infrared spectrometers of Atmospheric Chemistry Suite (ACS) [2] on board the Trace Gas Orbiter (TGO). In this study we analyze waves' amplitude, potential energy and the GW drag. It is found that the activity of GWs is symmetrically distributed around the equator during the seasons of equinoxes, while during solstices periods the maxima of activity is shifted towards the winter hemisphere. Maxima of GW drag is aligned with the weak zonal wind areas along the border of seasonally varying zonal jets modeled with the MAOAM Martian general circulation model (MGCM) [3]. The increased GW activity in the polar regions during the Global Dust Storm event of 34 Martian Year (MY34) is seen. A diurnal and semidiurnal modulation of the GW activity and drag is found in both equinoctial seasons.

ACS is a part of the TGO, which represents the ESA-Roscosmos ExoMars 2016 collaborative mission. The instrument consists of three infrared channels [1]: near-IR (NIR, 0.73–1.6 µm), middle-IR (MIR, 2.3–4.2 µm) and thermal-IR (TIRVIM, 1.7–17 µm). In this work, we use the data obtained from the MIR and NIR instruments. Both spectrometers can retrieve temperature and density vertical profiles in the absorption bands of CO_2 transmission spectra covering the broad altitude range of 10-180 km (MIR) [4] and 10–100 km (NIR) [5] with the vertical resolution ~0.5–2.5 km. Presently, we report the observations for 2 Martian years (MY), from the middle of MY34 (April 2018) to the middle of MY36 (February 2022), counting ~760 occultations of MIR and ~8550 occultations of NIR.

References:

[1] *Starichenko E., Belyaev* D.A., *Medvedev* A.S. *et al.* Gravity wave activity in the Martian atmosphere at altitudes 20–160 km from ACS/TGO occultation measurements // J. Geophysical Research: Planets. 2021. V. 126. Art. No. e2021JE006899. DOI: 10.1029/2021JE006899.

[2] Korablev O., Montmessin F., ACS Team. The Atmospheric Chemistry Suite (ACS) of three spectrometers for the ExoMars 2016 Trace Gas Orbiter // Space Science Reviews. 2018. V. 214. Art. No. 7. DOI 10.1007/s11214-017-0437-6.

[3] *Medvedev A.S., Hartogh P.* Winter polar warmings and the meridional transport on Mars simulated with a general circulation model // Icarus. 2007. V. 186. P. 97–110. https://doi.org/10.1016/j.icarus.2006.08.020.

[4] *Belyaev D., Fedorova A.A., Trokhimovskiy A.V. et al.* Thermal Structure of the Middle and Upper Atmosphere of Mars from ACS/TGO CO2 Spectroscopy // J. Geophysical Research: Planets. 2022. V. 127. Art. No. e2022JE007286. DOI: 10.1029/2022JE007286.

[5] Fedorova A., Montmessin F., Trokhimovskiy A. et al. A two-Martian year survey of the water vapor saturation state on Mars based on ACS NIR/TGO occultations // Submitted to J. Geophysical Research: Planets. 2022. V. 128. Iss. 1. Art. No. e2022JE007348. DOI: 10.1029/2022JE007348.

MARTIAN GLOBAL WATER VAPOR COLUMN ABUNDANCE FROM ACS TIRVIM NADIR OBSERVATIONS ONBOARD EXOMARS TGO

P. Vlasov[1], N. Ignatiev[1], O. Korablev[1], A. Fedorova[1], S. Guerlet[2], D. Grassi[3], A. Grigoriev[4], A. Shakun[1], D. Patsaev [1], I. Maslov[1], F. Montmessin[5], L. Zasova[1]

[1] *Space Research Institute RAS, Moscow, Russia, pavel.vlasov@phystech.edu*
[2] *Laboratoire de Météorologie Dynamique/IPSL, Sorbonne Université, PSL Research Université, École Normale Supérieure, École Polytechnique, CNRS, Paris, France*
[3] *Istituto di Astrofisica e Planetologia Spaziali — Istituto Nazionale di Astrofisica, Rome, Italy*
[4] *Research School of Astronomy and Astrophysics, Australian National University, Canberra, Australia*
[5] *Laboratoire Atmosphères, Milieux, Observations Spatiales (LATMOS) Université de Versailles — Saint-Quentin-en-Yvelines (UVSQ), Guyancourt, France*

KEYWORDS:
ExoMars TGO, ACS TIRVIM, nadir observations, Martian atmosphere, water vapor column abundance, 6 μm H_2O band, H_2O–CO_2 collisional broadening

The Thermal InfraRed channel (TIRVIM) [1] is a double-pendulum Fourier-transform spectrometer and one of the three instruments (NIR, MIR, TIRVIM) of the Atmospheric Chemistry Suite (ACS) designed by Space Research Institute of the Russian Academy of Sciences (IKI) in Moscow [2] onboard the joint ESA-Roscosmos mission ExoMars Trace Gas Orbiter (TGO) [3]. ACS TIRVIM is designed to observe the Martian atmosphere in the 1.7–16.7 μm spectral range in nadir and solar occultation modes at a great variety of local times, covering almost a complete Martian Year (MY) during its operation from March 2018 till December 2019. The main scientific goal of TIRVIM in nadir mode is long-term monitoring of thermal structure of the atmosphere up to 60 km of altitude, surface temperature and column dust and water ice clouds content from measurements in 5–16 μm spectral range with 1.17 cm^{-1} resolution.

TIRVIM is also capable of observing 6 μm H_2O band which provides information about water vapor column abundance in the Martian atmosphere at the daytime. The nighttime nadir observations of water vapor are not available due to the low signal-to-noise ratio. Another significant problem of nadir water vapor retrieval is correct H_2O spectroscopic parameters in CO_2-rich atmospheres since there are not enough measurements for H_2O broadened by CO_2 in this spectral region (1400–1800 cm^{-1}). The most of approaches use simple scaling of H_2O line parameters from HITRAN database [4] based on observations of other H_2O bands [5,6], and there are also attempts to measure and simulate H_2O–CO_2 collision broadening in the considered 5–8 μm spectral range [7,8].

In this work we present an overview of of the daytime atmospheric water vapor column abundance seasonal variability from ACS TIRVIM nadir observations in the 1400–1800 cm^{-1} spectral range onboard ExoMars TGO, which includes both of zonal mean map and the set of spatial maps in different seasons during almost a complete MY (from L_s = 142° of MY 34 to L_s = 115° of MY 35). We also demonstrate that different H_2O–CO_2 broadening affects the retrieved column water vapor abundance with content varying by 25% in some cases, so it is important to know exact line parameters for H_2O broadened by CO_2 in order to reduce inaccuracy and get correct atmospheric water vapor abundance on Mars.

Acknowledgments:
This work is supported by the Ministry of Science and Higher Education of the Russian Federation.

References:

[1] *Shakun A., Ignatiev I., Luginin M., Grigoriev A., Moshkin B., Grassi D., Arnold G., Maturilli A., Kungurov A., Makarov V., et al.* ACS/TIRVIM: Calibration and first results // Conf. Infrared remote sensing and instrumentation XXVI. SPIE. 2018. id. 107650E. https://doi.org/10.1117/12.2322163

[2] *Korablev O., Montmessin F., Trokhimovskiy A., Fedorova A.A., Shakun A.V., Grigoriev A.V., Moshkin B.E., Ignatiev N.I., Forget F., Lefèvre F., et al.* The Atmospheric Chemistry Suite (ACS) of three spectrometers for the ExoMars 2016 Trace Gas Orbiter // Space Science Reviews. 2018. V. 214. id. 7. https://doi.org/10.1007/s11214-017-0437-6

[3] *Vago J., Witasse O., Svedhem H., Baglioni P., Haldemann A., Gianfiglio G., Blancquaert T., McCoy D.,* de Groot R. ESA ExoMars program: The next step in exploring Mars // Solar System Research. 2015. V. 49. № 7. P. 518–528. https://doi.org/10.1134/S0038094615070199

[4] *Gordon I.E., Rothman L.S., Hargreaves R.J., Hashemi R., Karlovets E., Skinner F., Conway E.K., Hill C., Kochanov R.V., Tan Y., et al.* The HITRAN2020 molecular spectroscopic database // Journal of Quantitative Spectroscopy and Radiative Transfer. 2022. V. 277. id. 107949. https://doi.org/10.1016/j.jqsrt.2021.107949

[5] *J.B. Pollack, J.B. Dalton, D. Grinspoon, R.B. Wattson, R. Freedman, D. Crisp, D.A. Allen, B. Bezard, C. DeBergh, L.P. Giver, et al.* Near-Infrared Light from Venus' Nightside: A Spectroscopic Analysis // Icarus. 1993. V. 103. № 1. P. 1–41. https://doi.org/10.1006/icar.1993.1055

[6] *M.D. Smith.* The annual cycle of water vapor on Mars as observed by the Thermal Emission Spectrometer // Journal of Geophysical Research. 2002. V. 107. № E11. id. 5115. https://doi.org/10.1029/2001JE001522

[7] *Brown L R.* CO_2-broadened water in the pure rotation and ν_2 fundamental regions // Journal of Molecular Spectroscopy. 2007. V. 246. № 1. P. 1–21. https://doi.org/10.1016/j.jms.2007.07.010

[8] *Gamache R.R., Farese M., Renaud C.L.* A spectral line list for water isotopologues in the 1100–4100 cm^{-1} region for application to CO_2-rich planetary atmospheres // Journal of Molecular Spectroscopy. 2016. V. 326. P. 144–150. https://doi.org/10.1016/j.jms.2015.09.001

POSSIBLE EXPLANATIONS FOR SEASONAL VARIATIONS OF OXYGEN IN THE MARTIAN ATMOSPHERE

A.Y. Merkulova, A.K. Pavlov
Ioffe Institute, Saint Petersburg, Russia, alinamer@icloud.com

KEYWORDS:
Mars, clathrate, ozone, oxygen, atmosphere, seasonal variations, photodissociation, polar cap

INTRODUCTION:
Using The Sample Analysis at Mars (SAM) instrument onboard the Mars Science Laboratory Curiosity rover, it was observed that the amount of oxygen increases by 30 % during the spring and summer and decreases to the predicted values of known photochemistry by the fall [1]. At present, no atmospheric or surface process has been found to explain the seasonal variations in oxygen.

RESULTS:
Clathrate compounds of CO_2+O_3+O_2 formation in Polar Regions during a winter season is considered as a possible reason for the seasonal oxygen variations. The clathrate compound dissociates and releases the previously stored ozone, when the temperature rises in spring. which dissociates to O_2 under the action of ultraviolet radiation.

Using the thermodynamic model of the CO_2+O_3+O_2 clathrate [2], we estimated the mass of ozone that could be accumulated in the clathrate compound within Martian winter. We demonstrate that the mass is sufficient to provide seasonal variations of oxygen in the Mars atmosphere. The ozone transport from low and middle latitudes to Polar Regions was analyzed as possible powerful source of ozone in polar region during winter season

According to the results of this study, it was revealed that the formation of ozone clathrates in the polar regions of Mars may be the cause of seasonal variations in oxygen.

References:
[1] *Trainer M.G., Wong M.H., Mcconnochie T.H.* Seasonal Variations in Atmospheric Composition as Measured in Gale Crater, Mars // J. Geophysical Research: Planets. 2019. V. 124. Iss. 11. P. 3000-3024. https://doi.org/10.1029/2019JE006175.
[2] *Muromachi S., Nagashima H.D., Herri J.-M.* Thermodynamic modeling for clathrate hydrates of ozone // J. Chemical Thermodynamics. 20013. V. 64. P. 193–197. https://doi.org/10.1016/j.jct.2013.05.020.

POSSIBLE SOURCE OF PERCHLORATES ON MARS AND EUROPA

D.V. Belousov[1], V.S. Cheptsov[2,3], A.K. Pavlov[1]
[1] *Ioffe Institute, Saint Petersburg, Russia, dom.999.bel@gmail.com*
[2] *Lomonosov Moscow State University, Soil Science Faculty, Moscow, Russia*
[3] *Space Research Institute RAS, Moscow, Russia*

KEYWORDS:
Mars, Europa, perchlorates, ionizing radiation

INTRODUCTION:

The presence of perchlorate salts is an important feature of the Martian regolith, which affects the preservation of organic matter and survival of microorganisms. Perchlorates can act as a strong oxidation agent, therefore destroying organic matter. On the other hand, perchlorate-containing solutions preserve liquid state at low temperatures as liquid brines, which contribute to survival and growth of microorganisms [1]. In addition, perchlorates could be a crucial indicator of geological and climatical processes on Mars. Indeed, due to high hygroscopicity and solubility of perchlorates, local concentration of perchlorates may indicate the planet's water regime in different geological epochs. It is worth mentioning that Mars is not the only object in the Solar system where perchlorates were detected. Indeed, the IR survey of Europa showed magnesium and potassium perchlorates present on the moon's surface [2].

It is well known that the formation of perchlorates on the Earth occurs by photochemical reactions of atmospheric chlorine with ozone. However, the photochemical mechanism yields an order of magnitude lower concentration of perchlorate on Mars compared to that found. Due to the absence of a dense atmosphere and an internal magnetic field, the surface of Mars is exposed to intense radiation by galactic cosmic rays. Taking into account high doses of radiation, it is assumed that the main mechanism of perchlorate formation is the radiolysis of Martian soil [3]. Europa's surface is also irradiated intensively by energetic charge particles (electrons and various ions) captured by Jupiter's magnetosphere. In addition to the synthesis, irradiation leads to the destruction of perchlorates [4]. The fact that surface of Europa has a stable concentration of perchlorates clearly indicates the existence of sustainable mechanism for the formation of perchlorates in a non-atmospheric environment.

Here we present an experimental work on synthesis and destruction of perchlorates by energetic electrons in conditions close to Europa and Mars.

METHODS AND RESULTS:

To study the synthesis and destruction of perchlorates under the influence of high doses of ionizing radiation, sodium perchlorate and sodium chloride in various mediums (water ice and sand) are irradiated by 0.9 MeV electrons at doses up to 10 MGy. Irradiation with accelerated electrons is carried out in the previously described climatic chamber [5] at a pressure of about 0.01 Torr and temperatures of about –120 and –50° C. Perchlorate concentrations are determined in irradiated and non-irradiated (control) samples using: the perchlorate-selective electrode and the photometric method. In the irradiated samples of perchlorides and chlorides, the content of gaseous ClO_2 is determined by the method of time-of-flight mass spectrometry. Chlorine dioxide is both a precursor of perchlorates and a product of their degradation.

To date, our group has developed an experimental methodology and is currently conducting necessary calibrations of analytical methods. We have received preliminary results of the destruction of pure perchlorates, which are in good agreement with the results of [4].

Acknowledgements:
Preliminary experiments were carried out last year in the frame of the finished Russian Foundation for Basic Research grant 20-02-00470.

References:

[1] *Cheptsov V., Belov A., Soloveva O. et al.* Survival and Growth of Soil Microbial Communities under Influence of Sodium Perchlorates // International J. Astrobiology. 2020. V. 20. Iss. 1. P. 33–47. https://doi.org/10.1017/S1473550420000312.

[2] *Ligier N., Poulet F., Carter J. et al.* VLT/SINFONI observations of Europa: new insights into the surface composition // The Astronomical Journal. 2016. V. 151. No. 6. Art. No. 163. 16 p. DOI: 10.3847/0004-6256/151/6/163.

[3] *Wilson E.H., Atreya S.K., Kaiser R.I., Mahaffy P.R.* Perchlorate formation on Mars through surface radiolysis-initiated atmospheric chemistry: A potential mechanism // J. Geophysical Research Planets. 2016. V. 121. P. 1472–1487. DOI: 10.1002/2016JE005078.

[4] *Turner A.M., Abplanalp M.J., Kaiser R.I.* Mechanistic studies on the radiolytic decomposition of perchlorates on the Martian surface // The Astronomical J. 2016. V. 820. Art. No. 127. 8 p. DOI: 10.3847/0004-637X/820/2/127.

[5] *Pavlov A.K., Belousov D.V., Tsurkov D.A., Lomasov V.N.* Cosmic ray irradiation of comet nuclei: a possible source of cometary outbursts at large heliocentric distances // Monthly Notices of the Royal Astronomical Society. 2022. V. 511. Iss. 4. P. 5909–5914. DOI: 10.1093/mnras/stac497.

ANALYTICAL CONTINUATION OF THE MAGNETIC FIELD OF MARS FROM SATELLITE DATA USING A COMBINED APPROACH

A.M. Salnikov[1,2], A.V. Batov[1,2], I.E. Stepanova[1], T.V. Gudkova[1]
[1] *Schmidt Institute of Physics of the Earth RAS, Moscow, Russia, amsalnikov@hotmail.com*
[2] *Trapeznikov Institute of Control Sciences RAS, Moscow, Russia*

KEYWORDS:
Mars, magnetic field, analytical continuation, regularization method

INTRODUCTION:
Mars possesses no global magnetic field as is the case for the Earth or Mercury. However, the satellite data derived from Mars Global Surveyor (MGS) and Mars Atmosphere and Volatile Evolution (MAVEN) missions indicate an intense and localized magnetic field of crustal origin.

The latest model of the crustal magnetic field [1] that uses MGS and MAVEN data has spatial resolution of ~160 km at the surface, corresponding to spherical harmonic degree 134. The magnetic field at the InSight landing site turned out to be ten times stronger than predicted by satellite-based models [2]. The Zhurong rover measured an extremely weak magnetic field at 16 locations in the Utopia Basin along a 1,089 m track [3].

METHOD AND RESULTS:
We have built analytical models of the magnetic field of Mars from satellite data in the landing area of the Zhurong rover of the Chinese Tianwen-1 mission using a combined approach [4]. We analyzed satellite measurements and introduced several criteria for selecting and using data for further building magnetic field models. To form grids of samples, both regular grids and SREAG (Spherical Rectangular Equal-Area Grid) grids were used [5]. We have performed an analytical continuation of the magnetic field towards the sources at different depths and compared the model values with the measurements received from Zhurong rover.

Acknowledgements:
The study was supported by a grant from the Russian Science Foundation No. 23-27-00392 (https://rscf.ru/project/23-27-00392/).

References:
[1] *Langlais B., Thébault E., Houliez A. et al.* A new model of the crustal magnetic field of Mars using MGS and MAVEN // J. Geophysical Research: Planets. 2019. V. 124. Iss. 6. P. 1542–1569. https://doi.org/10.1029/2018JE005854.
[2] Johnson C.L., Mittelholz A., Langlais B. et al. Crustal and time-varying magnetic fields at the InSight landing site on Mars // Nature Geoscience. 2020. V. 13. Iss. 3. P. 199–204. DOI:10.1038/s41561-020-0537-x.
[3] *Du A., Ge Y., Wang H. et al.* Ground magnetic survey on Mars from the Zhurong rover // Nature Astronomy. 2023. https://doi.org/10.1038/s41550-023-02008-7.
[4] *Stepanova I.E., Salnikov A.M., Gudkova T.V. et al.* On finding the analytical continuation of the magnetic field of Mars from satellite data using a combined approach // Geophysical research. 2023. V. 24. No. 2. P. 58–83. https://doi.org/10.21455/gr2023.2-4.
[5] *Malkin Z.* A New Equal-area Isolatitudinal Grid on a Spherical Surface // The Astronomical J. 2019. V. 158. Iss. 4. Art. No. 158. DOI: 10.3847/1538-3881/ab3a44.

MARS ELECTRON DENSITY INVERSION BASED ON TIANWEN-1 RADIO OCCULTATION EXPERIMENT

J.S. Ping[1], Q.Q. Han[2], L. Chen[1,2], K. Jing[2], M. Wang[2], M.Y. Wang[1]
[1] *National Astronomical Observatories, Chinese Academy of Sciences, Beijing, jsping@bao.ac.cn*
[2] *Beijing Aerospace Control Center, Beijing, China*

KEYWORDS:
radio occultation, Tianwen-1; Martian ionosphere, ionosphere electron density profile, Open-loop velocity measurement

INTRODUCTION:
The orbit of Tianwen-1 around Mars has created favorable conditions for the inversion of the Martian ionosphere based on satellite-ground radio occultation. The orbital position of Tianwen-1, the Martian body, and the ground station meet specific positional relationships within a specific arc segment: that is, the Martian body gradually blocks the downlink signal of Tianwen-1, and the downlink signal passes through the Martian atmosphere and ionosphere, and can be received by the ground station. This provides necessary conditions for conducting Martian radio occultation scientific experiments.

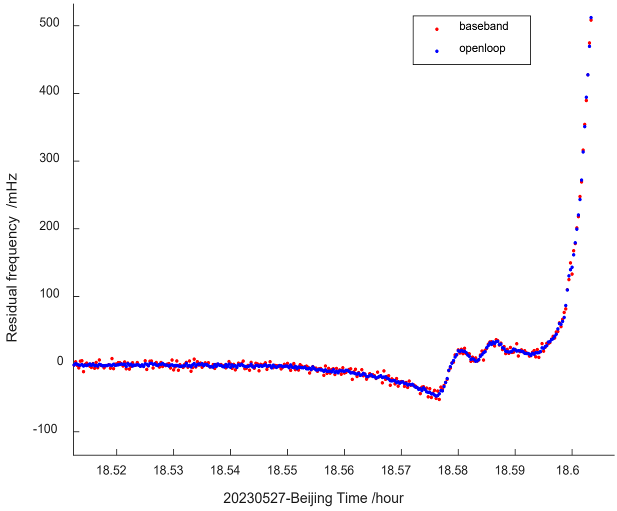

Fig. 1. The orbit determination residual error of the open-loop velocity measurement result during radio occultation procedure

In this paper, open-loop velocity measurement data during radio occultation is used for the inversion of the Martian ionosphere, as shown in Figure 1, it is the orbit determination residual error of the open-loop velocity measurement result. The preliminary results are shown in Figure 2, which is the preliminary Martian structure of the ionosphere electron density profile. The main feature of the Martian ionosphere is the main layer controlled by photochemistry, namely the M2 layer, generated by solar EUV radiation. The peak height of the M2 layer at the sunset point is about 120 km, which varies with the solar zenith angle. The M2 peak height in this radio occultation observation experiment was 126 km. The second layer, the M1 layer, has a relatively low density and is located about 20 km below the M2 layer. The M1 layer is generated by absorbing solar soft X-ray radiation and varies greatly over time. The height of the M1 layer observed in this time is 107 km. The inverted Martian electron density profile well conforms to the vertical structural characteristics of the Martian ionosphere.

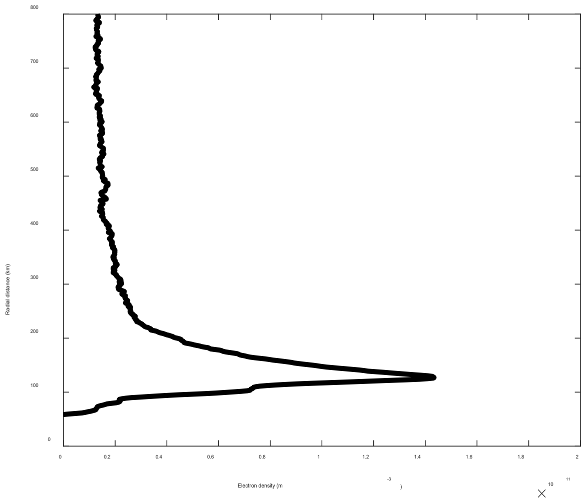

Fig. 2. Inversion Results of Electron Content and Density in the Martian Ionosphere

EFFECTS OF ANELASTICITY ON CHANDLER PERIOD OF MARS

E.A. Kulik, T.V. Gudkova
Schmidt Institute of Physics of the Earth RAS, Moscow, Russia,
kulik.ea@phystech.edu; gudkova@ifz.ru

KEYWORDS:
Mars, interior structure models, anelasticity, Love numbers, Chandler period

INTRODUCTION:

Seismic data obtained during the successful seismic experiment SEIS on Mars in the InSight Mission posted a number of significant restrictions on the internal structure of the planet: the average thickness of the crust is from 32 to 70 km, and its average density of not more than 3100 kg/m^3 [1, 2], the radius of the core (1830±40 km) [3]. The Chandler Wobble (CW) (206.9±0.5 days) has been detected for Mars from radio tracking observations of Mars Odyssey, Mars Reconnaissance Orbiter, and Mars Global Surveyor [4]. CW of Mars provides a measure of the body to deform at very long periods. Its value is determined mainly by temperature, rheology and the composition of the mantle and CW period can be used as an additional constraint on the interior structure model.

INTERIOR STRUCTURE MODELS:

As constraints for models of the Mars interior structure we use the measured geodesy parameters: the mass, mean radius, the normalized polar moment of inertia (0.3640±0.0006) and the Love number k_2 (0.174±0.008) [4] and the values obtained by seismic data: the crust thickness and the core radius [1–3]. The interior structure models are built following [5]. The models are based on the Wanke — Dreibus mineralogy.

The variable parameters of the models: ferrous number of the mantle Fe# (Fe# = $Fe^{2+}/(Fe^{2+} + Mg)$) is 0.18-0.25, density and radius of the core, crustal density (Fig. 1).

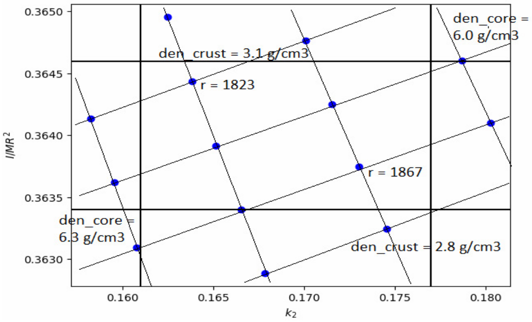

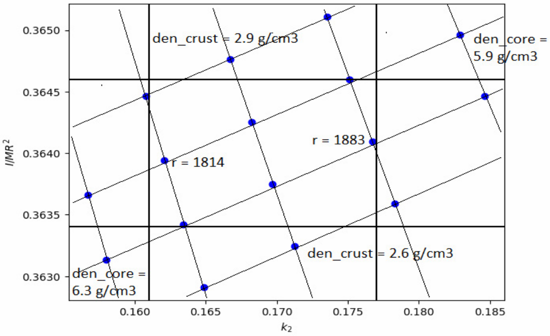

Fig. 1. The selection of the models: the horizontal solid lines indicate admissible values of the moment of inertia, the vertical solid lines — of Love number k_2. Fe# = 0.18 on the top, Fe# = 0.20 on the bottom

ANELASTICITY:

The models of the internal structure of Mars are elastic. When interpreting the k_2 value, knowledge is required about the rheological properties of planetary interiors, which is definitely not determined even for the Earth. Excluding the rheology, the obtained model values of the Love number k_2 are underestimated. The shear module and the tidal number k_2 are the functions of frequency. When describing the viscoelastic model of Andrada, the complex shift module $\hat{\bar{\mu}}$ is equal to $1/\hat{\bar{J}}$, where $\hat{\bar{J}}$ is called complex compliance and set by the formula [6]

$$\hat{\bar{J}}(\chi) = J\left[1 + (i\tau_M \chi)^{-\alpha}\Gamma(1+\alpha)\right] - \frac{i}{\eta\chi},$$

where $J = 1/\mu$, $\tau_M = \eta/\mu$ — Maxwell time; χ — tide frequency; Γ — gamma function; α — Andrada parameter.

Andrada parameter lies in the interval of 0.2–0.5 [6], although α = 0.3 is often used for a mantle in the planets. Using the Andrade rheology, for the trial values of viscosity in the interiors of Mars, the model Love numbers are calculated.

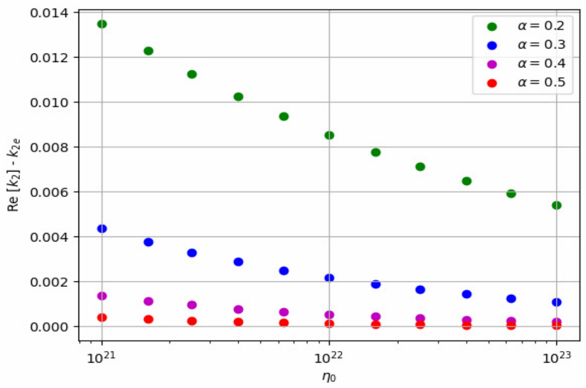

Fig. 2. The increase of Love number k_2 due to anelasticity (in the crust the viscosity is taken η_0, in the olivine mantle $10^{-2}\eta_0$, in the β-layer $10^{-1}\eta_0$, in the γ-layer η_0)

CHANDLER PERIOD CALCULATIONS:

The CW period for a triaxial elastic body with a liquid core is given by [7]

$$T_W = T_E\left(1 - \frac{(A_c B_c)^{1/2}}{(AB)^{1/2}}\right)\Big/\left(1 - k/k_0\right), \quad T_E = \tau_M(\alpha\beta)^{-0.5}, \quad \alpha = \frac{C-A}{A},$$

$$k_0 = \frac{3G(C-\bar{A})}{R^5\omega^2},$$

where T_E is the Eulerian period, τ_M is the period of the rotation of Mars; A, B and C are the principal moments of inertia of the planet, A_c, B_c — the principal moments of inertia of the core, k_0 is a smaller secular Love number.

RESULTS:

The CW period was calculated for a set of interior structure models of Mars. As noted above, in all calculations of the interior models only elastic models were considered. The rheological behaviour of the mantle rock in tidal/rotational periods is frequency dependent. Although all models corresponded to the value of the Love number of k_2, some of them did not quite satisfy the period of the CW. The values of α are in the interval (0.08–0.35) reported in [7]. The period of the CW is sensitive not only to the Andrada parameter α, but to a number of other factors, such as rheological models or grains size. Anelastic behaviour of the mantle decreases the mantle rigidity and leads to the increase of k_2 and the CW period. As a result, anelasticity lengthens the CW period with respect to an elastic model by several days. The viscosity of the mantle is highly dependent on the temperature. The CW serves as an additional restriction on the distribution of elastic parameters in the interiors of the planet obtained from observation data.

ACKNOWLEDGEMENTS:
The study was performed based on funding of Russian Scientific Foundation No. 23-22-00074 (https://rscf.ru/project/23-22-00074).

REFERENCES:
[1] *Knapmeyer-Endrun B., Panning M.P., Bissig F. et al.* Thickness and structure of the Martian crust from insight seismic data // Science. 2021. V. 373. Iss. 6553. P. 438–443. DOI: 10.1126/science.abf896.
[2] *Wieczorek M.A., Broquet A., McLennan S.M. et al.* InSight constraints on the global character of the Martian crust // J. Geophysical Research: Planets. 2022. V. 127. Iss. 5. Art. No. e2022JE007298. https://doi.org/10.1029/2022JE007298.
[3] *Stähler S.C., Khan A., Banerdt W.B. et al.* Seismic detection of the martian core // Science. 2021. V. 373. Iss. 6553. P. 443–448. DOI: 10.1126/science.abi7.
[4] *Konopliv A.S., Park R.S., Rivoldini A. et al.* Detection of the Chandler wobble of Mars from orbiting spacecraft // Geophysical Research Letters. 2020. V. 47. Iss. 21. Art. No. e2020GL090568. https://doi.org/10.1029/2020GL090568.
[5] *Zharkov V.N., Gudkova T.V.* Construction of Martian interior model // Solar System Research. 2005. V. 39. Iss. 5. P. 343–373. DOI: 10.1007/s11208-005-0049-7.
[6] *Castillo-Rogez J.C., Efroimsky M., Lainey V.* The tidal history of Japetus: Spin dynamics in the light of a refined dissipation model // J. Geophysical Research: Planets. 2011. V. 116. Iss. E9. https://doi.org/10.1029/2010JE003664.
[7] *Zharkov V.N., Gudkova T.V.* The period and Q of the chandler wobble of Mars // Planetary and Space Science. 2009. V. 57. Iss. 3. P. 288–295. https://doi.org/10.1016/j.pss.2008.11.010.
[8] *Harada Y.* Reconsideration of the anelasticity parameters of the Martian mantle: Preliminary estimates based on the latest geodetic parameters and seismic Models // Icarus. 2022. V. 383. P. 114917. https://doi.org/10.1016/j.icarus.2022.114917.

NEW RESULTS FROM THE RADIATION INVESTIGATIONS ABOARD EXOMARS TGO IN 2018–2023

J. Semkova[1], R. Koleva[1], V. Benghin[3], K. Krastev[1], Yu. Matviichuk[1], B. Tomov[1], N. Bankov[1], St. Maltchev[1], Ts. Dachev[1], I. Mitrofanov[2], D. Golovin[2], M. Mokrousov[2], M. Litvak[2], A. Kozyrev[2], V. Shurshakov[3], S. Drobyshev[3], J. Guo[4,5], J. Zhang[4], W. Liu[4,6]

[1] *Space Research and Technology Institute, Bulgarian Academy of Sciences, Sofia, Bulgaria, jsemkova@stil.bas.bg*
[2] *Space Research Institute RAS, Moscow, Russia*
[3] *Institute of Biomedical Problems RAS, Moscow, Russia*
[4] *Deep Space Exploration Laboratory/School of Earth and Space Sciences, University of Science and Technology of China, Hefei, China*
[5] *CAS Center for Excellence in Comparative Planetology USTC, Hefei, China*
[6] *Department of Climate and Space Sciences and Engineering, University of Michigan, Ann Arbor, MI, USA*

KEYWORDS:
Mars, ExoMars TGO, radiation measurements, galactic cosmic rays (GCR), solar energetic particle (SEP) event, simulation

INTRODUCTION:
The dosimetric telescope Liulin-MO for measuring the radiation environment onboard the ExoMars Trace Gas Orbiter (TGO) is a module of the Fine Resolution Epithermal Neutron Detector (FREND) [1–2].

Presented are the main results from the measurements in TGO Mars science orbit (400 km altitude, 74° inclination) of the radiation characteristics of the galactic cosmic rays (GCR) and solar energetic particle (SEP) events provided by Liulin-MO during different phases of the solar cycle in the period 2018–2023. The results show that the dose rate and particle flux of GCR in June 2023 during the increasing phase of the 25th solar cycle are about 55 % of the corresponding values measured during the 24th solar cycle minimum in March – August 2020. Eight SEP events are registered in Mars orbit from July 2021 to June 2023. The 15–19 February 2022 SEP event is the most powerful in our data. During this event the SEPs dose is equal to the dose for 38 days from GCR in undisturbed conditions, the biologically significant dose equivalent from SEPs is equal to the dose equivalent for 13 days from GCR in undisturbed conditions. The doses from 28–31 October 2021 SEP event are about 2 times less. Measurements by Liulin-MO during SEP events are compared to measurements by other instruments in the heliosphere.

Discussed are comparisons between the measured and simulated dose rates and particle flux from GCR and albedo radiation in Mars orbit [3–4].

The results of the radiation measurements on TGO are of importance for benchmarking of the space radiation environment models and for assessment of the radiation risk to future manned and robotic missions to Mars.

REFERENCES:
[1] *Mitrofanov I., Malakhov A., Bakhtin B. et al.* Fine Resolution Epithermal Neutron Detector (FREND) onboard the ExoMars Trace Gas Orbiter // Space Science Reviews. 2018. V. 214. Art. No. 86. https://doi.org/10.1007/s11214-018-0522-5.
[2] *Semkova J., Koleva R., Benghin V. et al.* Charged particles radiation measurements with Liulin-MO dosimeter of FREND instrument aboard ExoMars Trace Gas Orbiter during the transit and in high elliptic Mars orbit // Icarus. 2018. V. 303. P. 53–66. https://doi.org/10.1016/j.icarus.2017.12.034.
[3] *Semkova J., Benghin V., Guo J. et al.* Comparison of the flux measured by Liulin-MO dosimeter in ExoMars TGO science orbit with the calculations // Life Sciences in Space Research. 2022. https://doi.org/10.1016/j.lssr.2022.08.007
[4] *Weihao L., Guo J., Zhang J., Semkova J. et al. Modeling the Radiation Environment of Energetic Particles at Mars Orbit and a First Validation against TGO Measurements // The Astrophysical J.* 2023. V. 949. No. 2. P. 949–77. **DOI:** 10.3847/1538-4357/acce3c.

A SCIENCE MARTIAN AIRPLANE: PRELIMINARY CONFIGURATIONS AND RADIATION LOADING ANALYSIS

E.A. Karpovich,T.S. Kombaev, D. Gueraiche
Moscow Aviation Institute, Moscow, Russia, karpovichea@mai.ru, kombaew@ya.ru

KEYWORDS:
aircraft for Mars exploration, radiation tolerance, COTS

INTRODUCTION:

The study of Mars provides a deeper insight into the evolution of the universe and enables a better prediction of the environmental conditions for future Mars missions. Though there are several probes of different types currently operating on Mars, our understanding of Mars evolution and climate is still limited. The success of the Ingenuity helicopter mission based on COTS (Commercial off-the-shelf) electronic components [1] inspired the scientists and engineers to include flying vehicles in future Mars missions, for example, the Mars Sample Return project [2].

In contrast to helicopters and surface-based probes, a fixed-wing aircraft can perform modes of observation that require the airborne acquisition of data at a longer range and a larger payload [3].

An aircraft intended for Mars exploration can be designed to perform single-flight or multiple-flight missions.

A single-flight aircraft will conduct in-flight measurements and, if equipped with a device to perform a single controlled vertical landing, it will also serve as a lander, measuring parameters of interest on the planet's surface.

A multiple-flight vertical take-off and landing vehicle will be able to either perform profile measurements on the required timescales, or carry instruments to the prescribed sites and conduct on-surface measurements. The first option will allow for the determination of turbulent and radiative fluxes over the lowest 2–5 km of the atmosphere. The authors of [4] emphasize that such measurements are needed to capture the strong temporal variations anticipated in this part of the atmosphere. The second option will widen the geographical and temporal coverage of measurements.

Out of the scientific targets for a Martian probe, for an airplane, the walls of canyons and craters can be considered, for the following reasons:

- The relatively high atmospheric pressure expected below the topographical datum (which would allow reducing the airplane's cruise speed and exploring the hypothesis of the water persisting in a liquid state deep inside craters).
- The high scientific significance of analyzing the inner sides of the crater rim; walls of craters and canyons might unveil millions of years of Mars's history.
- The impossibility of studying crater walls by rovers and landers.

Another target for exploration may be the Martian boundary layer. The direct observational measurements within the Martian boundary layer remain relatively sparse, with the vast majority of in situ measurements on Mars having been obtained at altitudes a little higher than 1 m.

In addition to more typical constraints, the feasible design area for a Martian aircraft may be limited by:

- The aeroshell shape and size, with the consequence of using rigid or inflatable unconventional airframe structures with high technical risk.
- The launch and entry g-load, with the consequence of increased structural weight;.
- The aeroshell center-of-gravity constraint, which may also exert a significant influence on the "big" decisions, like that of the aerodynamic layout selection.

- The high turbulence intensity, low temperature, dust.
- The radiation load.

The use of COTS for the aircraft's equipment calls for the estimation of their tolerance to external ionizing radiation and the displacement effects due to the internal radiation sources. In the analysis reported in this paper, a Mars mission is considered, with the airplane mounted in the descent module as a primary or secondary payload. The analysis accounts for the fact that a portion of the radiation load comes from the internal radiation sources of the descend module.

Depending on its vertical takeoff and landing capabilities, the UAV can either be released from the descend module once the rear jacket (with the parachute system) is separated, or perform a vertical takeoff from the landing platform resting on the Mars surface.

Assuming that in either case, after completing its flight mission, the airplane can act as a stationary platform, its overall service life is set to be 5 years.

The assessment of the external space environment was carried out using the COSRAD software [5]. The calculations were performed on the spectra of fluxes of protons and electrons from solar and galactic cosmic rays and secondary particles generated during the interaction of primary cosmic radiation with spacecraft and UAV materials. Calculations of fluxes were performed for different thicknesses of spherical mass shielding. The assessment of the non-ionization dose from internal sources of radiation on board the descent module and UAV was also performed.

References:

[1] *Balaram B., Canham T., Duncan C. et al.* Mars Helicopter Technology Demonstrator // 2018 AIAA Atmospheric Flight Mechanics Conf. 8–12 Jan. 2018, Kissimmee, Florida. Art. No. AIAA 2018-0023. DOI: 10.2514/6.2018-0023

[2] *Withrow-Maser* Sh.*, Grip H., Young L. et al.* Mars Sample Recovery Helicopter: Rotorcraft to Retrieve the First Samples from the Martian Surface // Vertical Flight Society's 79th Annual Forum and Technology Display. West Palm Beach, FL, USA, May 16–18, 2023.

[3] *Bouskela A., Kling A., Schuler T. et al.* Mars Exploration Using Sailplanes // Aerospace. 2022. V. 9. Iss. 6. Art. No. 306. https://doi.org/10.3390/aerospace9060306.

[4] *Petrosyan A., Galperin B., Larsen S.E. et al.* The Martian atmospheric boundary layer // Rev. Geophysics. 2011. V. 49. Iss. 3. Art. No. RG3005. DOI: 10.1029/2010RG000351.

[5] *Kuznetsov N.V., Malyshkin Yu.M., Nikolaeva N.I. et al.* Software complex COSRAD for radiation environment forecasting onboard spacecraft // Problems of Atomic Science and Technology. Series: Physics of Radiation Effects on Electronic Equipment. 2011. P. 72–78 (in Russian).

SESSION 1. MARS (MS)
POSTER SESSION

PHOTOGRAMMETRIC PROCESSION OF MARS 2020 INGENUITY DATA AND SUBSEQUENT OBTAINING OF A 3D SURFACE MODEL

A.E. Zubarev [1,2], I.E. Nadezhdina [1], N.A. Kozlova [1], N.A. Slodarzh [1]

[1] *Moscow State University of Geodesy and Cartography (MIIGAiK), MIIGAiK Extraterrestrial Laboratory (MExLab), 105064, Gorokhovsky per, 4, Moscow, Russia (fair-max@yandex.ru);*

[2] *Space Research Institute RAS, Moscow 117997, Russia*

KEYWORDS:

Mars, Mars 2020, Ingenuity, photogrammetric remote sensing, DTM

INTRODUCTION:

In 2020, the Mars 2020 Rover mission was launched from Cape Canaveral SLC-41. As payloads, the rover Perseverance and the helicopter Ingenuity were launched. Ingenuity is equipped with 2 cameras: #1 navigation camera NAV with a frame size of 640x480 pixels and #2 a full-format survey nadir camera RTE with a frame size of 4208x3120 pixels [1]. The SPICE database [2] does not contain data on the parameters of these cameras, however, using data from the MRO HIRISE camera, it is possible to restore the surface topography and determine the geometric characteristics of each of these cameras. On the PDS website, color-synthesized images from a #2 camera are available as pre-products, with metadata indicating pixel size and focal length [3]. This data was taken as preliminary when determining the distortion also for the navigation camera #1.

To determine the camera parameters, the longest flight with the largest number of frames was chosen. Then the tie points were measured and the image block was adjusted with self-calibration. The parameters determined at this stage were used to link all the images available at the time of August 2022, i.e. over 7000 images. As an example, the result of processing one of the flights with duration of 200 frames is presented and the technical feasibility of obtaining a DTM from this data is shown.

References:

[1] *Balaram, B., Canham, T., Duncan, C. et al.* Mars Helicopter Technology Demonstrator // 2018 AIAA Atmospheric Flight Mechanics Conference. (https://doi.org/10.2514/6.2018-0023).

[2] https://naif.jpl.nasa.gov/naif/data.html

[3] https://planetarydata.jpl.nasa.gov/img/data/mars2020

ON CORRELATION OF NON-HYDROSTATIC STRESSES IN THE INTERIOR OF MARS WITH THE EPICENTERS OF MARSQUAKES

A.V. Batov[1,2], T.V. Gudkova[1]
[1] *Schmidt Institute of Physics of the Earth RAS, Moscow, Russia, gudkova@ifz.ru*
[2] *Trapeznikov Institute of Control Sciences RAS, Moscow, Russia, batov@ipu.ru*
KEYWORDS:
Mars, gravity, topography, stress state, epicenters of marsquakes

INTRODUCTION:
It is shown that the location of most of the epicenters of marsquakes, recorded during the SEIS experiment of the InSight mission, is located in the zones of extension and sufficiently large shear stresses resulting from the deviation of the planet from the state of hydrostatic equilibrium.

DATA:
The modeling is based on the data of the gravitational field and the topography of Mars, which are present on the website of the Planetary Data System (http://pds-geosciences.wustl.edu). We use the MRO120D model [1] and topography data up to 90° and order [2], since at harmonics above 90, the correlation of the gravitational field data and the topography of Mars deteriorates markedly. The catalog of marsquakes is available in [3].

INTERIOR STRUCTURE MODELS:
For calculations, a model of the internal structure of Mars M_50 from the work [4] was chosen, which has an average crust thickness of 50 km with a density of 2900 kg/m^3, the radius of the core is 1821 km. This value is within the range of determining the radius of the core of Mars by seismic methods (1830±40 km) [5].

METHOD:
A planet is modeled as an elastic, self-gravitational spherical body. It is assumed, that deformations and stresses which obey Hooke's law are caused by the pressure of relief on the surface of the planet and anomalous density, distributed by a certain way in the crust. Numerical simulation is based on a static approach (see for details [4, 6–8]). The criterion for the selection of possible epicenters of marsquakes was the large values of shear stresses against the background of significant tensile stresses. It was assumed that it is the significant shear stresses in the extension zones that represent the most probable source regions of marsquakes.

RESULTS:
Most of the foci of marsquakes were found east of the seismometer, in the area of the Cerberus graben system (Cerberus Fossae) [3, 9], a large tectonic structure. The Cerberus Fossae area is thought to be a formation that is possibly associated with recent volcanic activity due to the Elysium Mons uplift. The seismic events of this group are located at an epicentral distance of 26–27°, have a magnitude of 3.5-4, and the focal mechanism of these events corresponds to extensional tectonics [10].

Comparison of the theoretically calculated non-hydrostatic stresses in the Elysium Planitia region with data on the location of the epicenters of seismic events on Mars in this region is shown in the Fig. 1. The figure corresponds

to the model of the internal structure of Mars with a crustal thickness of 50 km, the thickness of the lithosphere is 300 km, under the lithosphere there is a weakened layer $\mu = 0.1\mu_0$ to a depth of 1140 km (μ_0 is the value of the shear modulus for a purely elastic model).

The stress field under the Elysium shield is dominated by the compressional stress field, while east of the Elysium Planitia there are significant extensional stresses in the lithosphere, indeed sufficient to trigger seismic events. Significant shear stresses in extension zones correlate well with the identified marsquake epicenters.

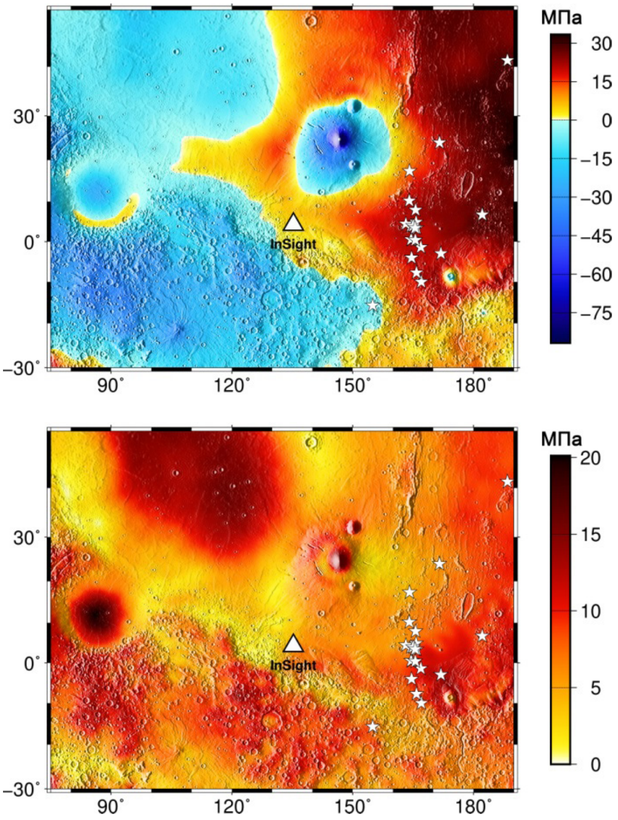

Fig 1. Model non-hydrostatic stresses in the Martian crust at a depth of 25 km in the Elysium Planitia region: extensional-compression stresses (top) and shear stresses (bottom) in MPa. Designations: Δ — geophone position, ☆ — epicenters of marsquakes

The previously accepted criterion for selecting zones with high shear stresses against the background of significant tensile stresses as the most probable areas of marsquake sources has justified expectations. Possible plume activity in this area [11] can lead to a release of accumulated stresses.

Acknowledgements:
This work is financially supported by Budget funding of Schmidt Institute of the Earth RAS.

References:

[1] *Konopliv A.S., Park R.S., Folkner W.M.* An improved JPL Mars gravity field and orientation from Mars orbiter and lander tracking data // Icarus. 2016. V. 274. P. 253–260.

[2] *Smith D.E., Zuber M.T., Frey H.V. et al.* Mars Orbiter Laser Altimeter: Experimental summary after the first year of global mapping of Mars // J. Geophysical Research. 2001. V. 106(E10). P. 23689–23722.

[3] InSight Marsquake Service. Mars Seismic Catalogue, InSight Mission 2023. V14 2023-04-01.ETHZ, IPGP, JPL, ICL, Univ. Bristol. https://doi.org/10.12686/a21.

[4] *Gudkova T.V., Batov A.V., Zharkov V.N.* Model estimates of non-hydrostatic stresses in the Martian crust and mantle: 1. Two-level model // Solar System Research. 2017. V. 51. No. 6. P. 457–478.

[5] *Stähler S.C., Khan A., Banerdt W. B.et al.* Seismic detection of the martian core // Science. 2021. V. 373. P. 443–448.

[6] *Zharkov V.N., Koshlyakov E.M., Marchenkov K.I.* Composition, structure and gravitational field of Mars // Sol. Syst. Res. 1991. V. 25. P. 515–547.

[7] *Zharkov V.N. Marchenkov K.I., Lyubimov V.M.* On long-waves shear stresses in the lithosphere and the mantle of Venus // Sol. Syst. Res. 1986. V. 20. P. 202–211.

[8] *Batov A.V., Gudkova T.V., Zharkov V.N.* Nonhydrostatic stress state in the Martian interior for different rheological Models // Izvestiya, Physics of the solid Earth. 2019. V. 55. No. 4. P. 688–700.

[9] *Giardini D., Lognonné P., Banerdt W.B. et al.* The Seismicity of Mars // Nature Geoscience. 2020. V. 13. No. 3. P. 205–212.
[10] *Brinkman N., Stähler S.C., Giardini D. et al.* First focal mechanisms of Marsquakes // J. Geophysical Research: Planets. 2021. V. 126. Art. No. e2020JE006546.
[11] *Broquet A., Andrews-Hanna J.C.* Geophysical evidence for an active mantle plume underneath Elysium Planitia on Mars // Nature Astronomy. 2022. https://doi.org/10.1038/s41550-022-01836-3.

MAGNETIC FIELD OBSERVATIONS AT THE SURFACE OF MARS: THE INFLUENCE OF ATMOSPHERIC/IONOSPHERIC PHENOMENA AND THE INTERPLANETARY MEDIUM

S.V. Kulikov, A.A. Skalsky, S.I. Klimov
Space Research Institute RAS, Moscow, Russia, sv.kulikov93@yandex.ru

KEYWORDS:
Mars, magnetic field, MAVEN, InSight, solar wind

INTRODUCTION:

Simultaneous observations from the orbiter and lander on the surface of Mars permit studies of interactions between the solar wind and the Martian plasma environment (magnetosphere and ionosphere).

Observations performed onboard the InSight lander and MAVEN spacecraft indicate that the magnetic field at the planet's surface depends on the dynamic pressure of the solar wind, mostly seen near the terminator on both flanks of Mars. It seems that phenomenon is related to the motion of the upper boundary of the Martian magnetosphere as a response to interplanetary conditions, which strongly affect the position of that, particularly at flanks.

Two types of variations are found at the surface of Mars in the nightside sector:

- 30-minute variations, possibly related to gradients of ionospheric density caused by atmospheric gravity waves;
- 100-second variations whose origin is tentatively associated with the processes in the Mars magnetotail.

14MS3-MS-PS-04
POSTER

RECURRING MAGNETIC STRUCTURE IN MARTIAN DAYSIDE MAGNETOPAUSE

O.L. Vaisberg[1], S.D. Shuvalov[2], A.Yu. Shestakov[1], R.H. Zhuravlev[1], A. Ramazan[3]

[1] *Space Research Institute RAS, Moscow, Russia, olegv@iki.rssi.ru*
[2] *University of Colorado, Boulder, USA*
[3] *Moscow Institute of Physics and Technology (National Research University), Dolgoprudny, Moscow Region, Russia*

KEYWORDS:
Mars, magnetosheath, magnetopause, magnetosphere

The high temporal measurements of the magnetic field and plasma of Mars are provided by Atmosphere and Volatile Evolution (MAVEN, [1]) which allow analyzing the fine layers of Mars plasma envelope. This paper describes magnetic structure associated with dayside Martian magnetopause.

It was shown that the shocked solar wind at the dayside of Mars does not directly interact with ionosphere of Mars. The plasma and magnetic field layer of 200–300 km thickness form the dayside magnetosphere which is defined as a region between magnetosheath and ionosphere [2].

Dayside magnetosphere is of two types: (1) the more frequent type magnetosphere consists of heated and accelerated O^+ and O_2^+ ions having kinetic structure and (2) other type of dayside magnetosphere consists of accelerated O^+ and O_2^+ ions towards the magnetosheath where they form continue accelerated beam forming the plume.

Between the magnetosheath and the magnetosphere there is magnetic structure which rotates almost unchanging its magnitude. This structure is located within second part of transition of $n_p/(n_p + n_h)$ from ~1 to ~10^{-2}.

The transition between magnetosheath and magnetosphere occurs smoothly including energy density and composition. At the same time the flux of protons diminishes and the flux of heavy ions increases.

There is repeating phenomenon usually called attractor. It can be calling Recurring.

References:

[1] *Jakosky B.M., Grebowsky J.M., Luhmann J.L., Brain D.A.* Initial results from the MAVEN mission to Mars // Geophysical Research Letters. 2015. V. 42. Iss. 21. P. 8791–8802. https://doi.org/10.1002/2015GL065271.

[2] *Vaisberg O., Shuvalov S.* Properties and sources of the dayside Martian magnetosphere // Icarus. 2021. V. 354. Art. No. 114085. https://doi.org/10.1016/j.icarus.2020.114085.

CHARACTERISTIC FEATURES OF MAGNETIC ANOMALIES OF IMPACT CRATERS ON EARTH: HOW THEY APPEAR ON TERRESTRIAL PLANETS

M.Y. Kuzmicheva, B.A. Ivanov
Institute of Geosphere Dynamics RAS, Moscow, Russia, mukuzmgm@gmail.com

KEYWORDS:
impact crater, shock wave, magnetic anomaly, impact demagnetization, paleomagnetic field

INTRODUCTION:
The impact craters found on the Earth are characterized by the presence of gravitational and magnetic anomalies [1], mostly negative. Magnetic anomalies associated with craters have been found on the surface of Mars [2]. The demagnetization of the lunar surface is also associated with the process of impact cratering [3].

TYPICAL FEATURES OF IMPACT CRATER MAGNETIC ANOMALIES:
The authors have previously carried out numerical simulations of the magnetic anomaly of the Bosumtwi crater [4], which makes it possible to generalize the results obtained in relation to other impact craters including on Mars and Mercury. On the one hand, the ejection of target rocks as a result of a high-speed impact of an asteroid on the surface and the passage of a shock wave into the target that destroys and weakens the magnetic properties leads to the formation of a negative magnetic anomaly. On the other hand, as a result of the impact, impactites are formed — rocks with increased magnetic susceptibility, capable of creating a positive magnetic anomaly in the presence of a planetary magnetic field. The parameters of the magnetic field at the time of the formation of the crater are manifested in the resulting magnetic anomaly, so it possible to determine the paleomagnetic field.

References:
[1] *Grieve R.A.F., Robertson P.B., Dence M.R.* Constraints on the formation of ring impact structures // Multiring Basins: Formation and evolution: Proc. Lunar and Planetary Science Conf. Houston, TX, Nov. 10–12, 1980 / eds. P.H. Schultz, R.B. Merrill. . N.Y.; Oxford: Pergamon Press, 1981. P. 37–57. Art. No. A82-39033 19-91.
[2] *Mohit P.S., Arkani-Hamed J.* Impact demagnetization of the martian crust // Icarus. 2004. V. 168. Iss. 2. P. 305–317. https://doi.org/10.1016/j.icarus.2003.12.005.
[3] *Wieczorek M.A.* Strength, Depth, and Geometry of Magnetic Sources in the Crust of the Moon from Localized Power Spectrum Analysis // J. Geophysical Research: Planets. 2018. V. 123. Iss. 1. P. 291–316. https://doi.org/10.1002/2017JE005418.
[4] *Kuzmicheva M., Ivanov B.* Simulation of the Magnetic Anomaly Associated with a Complex Crater Using the Example of the Bosumtwi Crater // Solar System Research. 2020. V. 54. Iss. 5. P. 372–383. DOI: 10.1134/S0038094620050056.

IMPROVEMENT OF THE CHARACTERISTICS OF THE UNIAXIAL SEISMOMETER

A.B. Manukin, N.A. Chernogorova, N.F. Sayakina, A.K. Tonshev
Space Research Institute RAS, Moscow, Russia, amanukin@yandex.ru, natalia@cosmos.ru, n.sayakina@gmail.com, tonshev@skbkp.tarusa.ru

KEYWORDS:
uniaxial seismometer, test body, foil, measuring capacity, elastic modulus, accidental emissions, capacitive converter, small accelerations

INTRODUCTION:
As a result of the work within the ExoMars project, a new version of the three-coordinate seismogravimeter SEM was developed and created, in which three identical uniaxial seismometers with mutually perpendicular axes of sensitivity were installed in one housing so that their axes of sensitivity were at an angle of 54.736 degrees with a vertical [1]. The measuring system was distinguished by the fact that in it the uniaxis is provided by the elements of mechanical rigidity themselves. The scheme of such a system is shown in Figure 1.

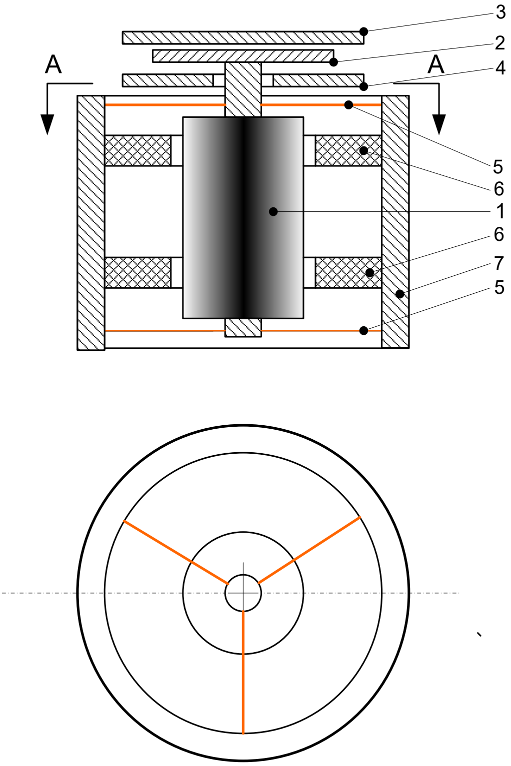

Fig. 1.

The test body 1 in the form of a cylinder is held along the *Z* axis (sensitivity axis), as well as along the X and Y axes using two stretch blocks 5 installed near the two ends of the cylinder. Each block consists of three thin foil films (beryllium bronze was used) placed at an angle of 120° and connected at one end to the test mass, and the other to the housing element of the device (7), having the shape of a hollow cylinder, coaxial with the test mass. The movements of the test body 1 along the *Z* axis are measured using a capacitive transducer. The figure shows only the rotary plate 2 of the measuring differential capacity connected to the test mass 1 and the fixed plates 3 and 4 of the measuring capacity.

The elastic element is a thin foil — stretching and is the most important part of the sensor. For its manufacture, a material is required for which the magnitude of the elastic modulus weakly depends on the influence of factors such as temperature, time, vibrations, workloads, etc. Since there are no ideal materials, it is necessary to choose a material whose temperature characteristic of the elastic modulus in the required temperature range is linear and sufficiently stable. Then the temperature error of the sensor, which appears due to changes in the modulus of elasticity, can be taken into account.

Another important requirement for the elastic element material is the high stability of the elastic modulus over time.

The instability of the elastic modulus is associated with the processes of aftereffect and relaxation occurring in the material after its mechanical or thermal treatment. Therefore, metals that do not receive significant residual stresses as a result of processing have the least time instability of the elastic modulus.

Such metals include dispersion-hardening alloys. A characteristic feature of these alloys is that in the quenched state they have high plasticity, and an increase in elastic properties is achieved during tempering. Beryllium bronze is just such a dispersion-hardening alloy. In addition, the change in the Young's modulus in a wide temperature range from minus 200 to plus 600° C is almost linear. For beryllium bronze, thermoelastic coefficient ~$(-2{,}4\cdot10^{-4})$ K^{-1}. Therefore, a thin beryllium bronze foil was used in the device as elastic elements – stretch marks.

WAYS TO IMPROVE THE CHARACTERISTICS OF THE SEISMOMETER

After conducting all the tests of the design and finishing (KDO) and standard (SHO) samples of the SEM device, some characteristics were revealed that, if possible, I would like to improve. Of course, the tests showed the readiness of the SHO to carry out a mission on Mars, but the feeling of being able to improve something else, to improve - always remains. Analyzing the results of the tests carried out, primarily functional, physical tests, you understand that there is something to improve in the device.

First of all, this applies to the systems of suspensions – extensions of the test mass. Stretch marks are elastic elements made of a thin ribbon with a thickness of 30-50 microns made of beryllium bronze BrB– 2, which are soldered to the massive elements of the rake. For various reasons, these relatively massive 1.5 mm thick elements were made of brass. The main reason is the most banal: at that moment there was no material in stock — a bar from BrB-2, and there was not enough time to order a bar as usual. The manufacture of an elastic element from a thin tape from BrB-2, and massive suspension elements from brass, materials with similar but different coefficients of thermal expansion can lead to undesirable instabilities of the suspension system, which was observed in some samples of sensitive elements. And the criterion for choosing suspensions for their installation in the SHO was the fact that there were no unwanted accidental emissions. If it were possible, first of all, the availability of the necessary time, then the first thing that could be redone in the prepared samples would be the replacement of the material of the massive suspension elements — brass, with BrB–2. This would greatly simplify the selection of suspensions and practically eliminate the appearance of unwanted accidental emissions.

The second important change in the design of the device is the reduction of gaps in the measuring capacitors of capacitive converters from 0.25 to 0.1–0.15 mm, which would significantly increase their conversion steepness. This is an important characteristic that allows you to increase the resolution of the device when registering small accelerations affecting its base.

The noted improvements can qualitatively improve the operation of the device and do not require serious processing of design documentation.

The third change concerns the technology of setting up the device for measurements on the planets of the Solar System, where the acceleration of gravity is significantly different. The experience of such work has shown that inserting the parts of the seismometer "separately" into the body of a special device designed to adjust the device in terrestrial conditions is very inconvenient and involves a high probability of failure of a number of parts.

The main thing is to keep the old developments as much as possible. It is proposed to make a device that will allow placing the sensitive part of the device into the device for its entire configuration. To do this, it is necessary to make three recesses in the upper and lower suspensions of the test mass, where rigid vertical parts are inserted on the screws that hold the entire structure (see the sketch in Figure 2). The outer size together with the vertical parts is the same as that of the suspensions. All this design, together with the test mass, is placed in the housing of the device for tuning. (the lower suspension shines through the mass in the sketch)

In the section (Figure 3), the vertical parts (1) are gray, with the help of screws (2) they are screwed to the suspensions. As before, the gap between the suspension part (3) and the part (4) in which the test mass is fixed is 30–50 microns. The movable plate of the capacitive sensor is conventionally shown in red, and a permanent magnet is shown below. The whole structure remains unchanged. The only change is that it is necessary to slightly reduce the inner radius of the suspension ring by 0.5–0.7 mm and use a BrB2 foil with a thickness of 10–20 microns.

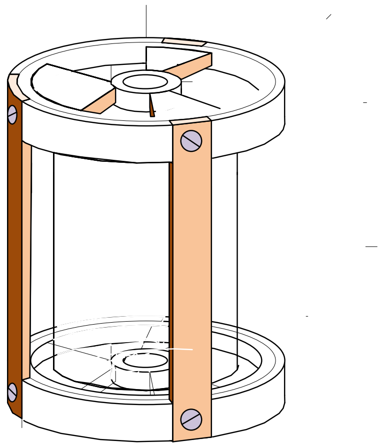

Fig. 2.

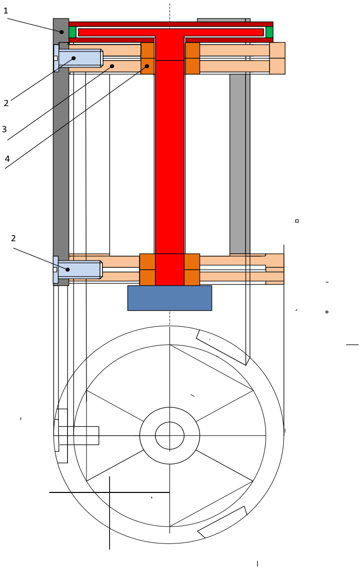

Fig. 3.

REPORT

Improvement of the uniaxial seismogravimeter, which allows to significantly improve the characteristics of the device. Firstly, it is the use of one material – beryllium bronze BrB-2 — for the manufacture of massive suspension elements of a test mass with a thickness of 1.5 mm and an elastic element made of a thin tape with a thickness of 10–20 microns, which reduces the likelihood of instability. Secondly, it reduces the gap in capacitors of capacitive converters from 0.25 to 0.1–0.15 mm to significantly increase the steepness of the conversion of the capacitive sensor. Thirdly, a change in the technology of setting up the device, for which to combine all the elements of the sensitive part of the uniaxial seismogravimeter with the help of special vertical inserts. This allows you to place the device as a whole in the system for its configuration, eliminating the possibility of failure of individual elements, thereby increasing the reliability of the device.

Acknowledgements:

The study was performed based on funding of ExoMars project.

References:

[1] *Manukin A.B., Kazantseva O.S., Kalinnikov I.I.* New Version of Highly Sensitive Single-Axis Sensor for Seismic Accelerometer // Seismicheskie pribory. 2018. V. 54. No. 4. P. 66–76.

EXPLORING ELECTROMAGNETIC SIGNATURES OF DUST PARTICLES COLLISIONS: EXPERIMENTAL SETUP AND STATION CONSTRUCTION FOR SIGNAL ACQUISITION

M.E. Abdelaal[1,2], I.V. Dokuchaev[2], I.A. Kuznetsov[2], G.G. Dolnikov[2], A.N. Lyash[2], A.E. Dubov[2], A.A. Kartasheva[2], A.V. Zakharov[2]

[1] *Moscow Institute of Physics and Technology (National Research University), Dolgoprudny, Moscow Region, Russia, mohamad.essam@phystech.edu*

[2] *Space Research Institute RAS, Moscow, Russia, zakharov@iki.rssi.ru*

KEYWORDS:
electromagnetic signatures, dust particles, signal processing, dust monitoring, Martian atmosphere, dust devils, dust storms

INTRODUCTION:
This study presents the results of experiments conducted using an Electromagnetic Analyzer (EMA) to analyze the registered signals generated from the collision of dust particles. The aim was to characterize the interactions between dust particles and investigate their electromagnetic signatures. To

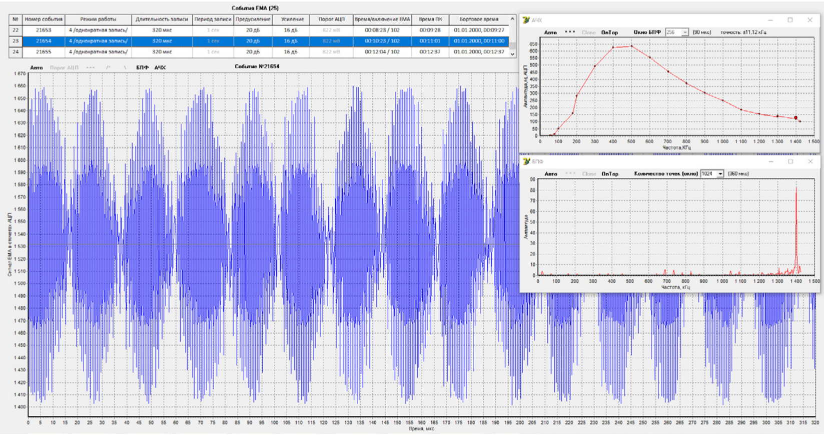

Fig. 1. Device calibration

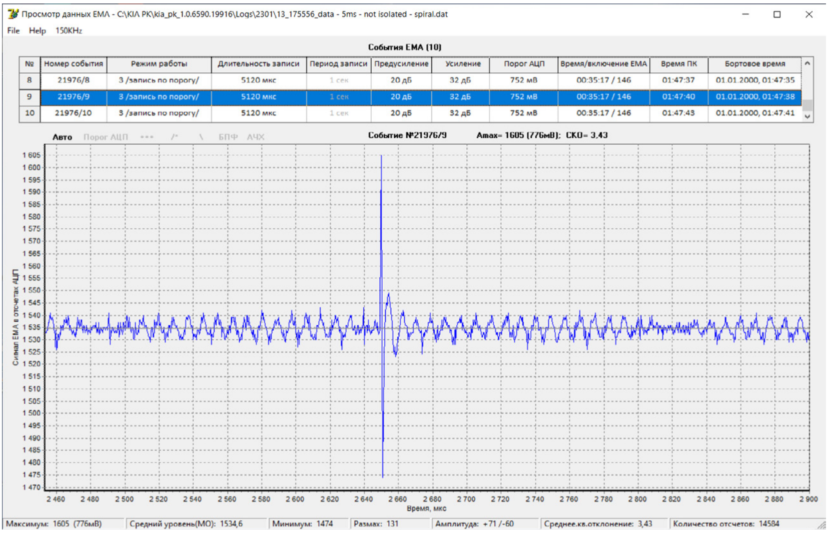

Fig. 2. Electromagnetic signal signature

ensure accurate measurements, various experimental setups were implemented to mitigate interference and optimize data acquisition. Moreover, a robust station construction was developed to provide a controlled environment for conducting the experiments. The obtained results shed light on the electromagnetic properties of dust particle collisions, offering valuable insights into their behavior and potential applications in diverse fields such as astrophysics, environmental science, and particle dynamics. The methodologies employed in this study serve as a foundation for future research in this area, enabling further exploration and understanding of dust particle dynamics through electromagnetic analysis.

References:

[1] *Newman C.E., Lewis S.R., Read P.L., Forget F.* Modeling the Martian dust cycle. 1. Representations of dust transport processes // J. Geophysical Research. Planets. 2002. V. 107. Iss. E12. P. 6-1–6–18. https://doi.org/10.1029/2002JE001910.

[2] *Kwetkus B.A., Sattler K., Siegmann H.-C.* Gas breakdown in contact electrification // J. Physics D: Applied Physics. 1992. V. 25. Iss. 2. P. 139. DOI:10.1088/0022-3727/25/2/002.

[3] *Yair Y., Fischer G., Simões F. et al.* Updated review of planetary atmospheric electricity // Planet. Atmospheric Electr. 2008. P. 29–49. https://doi.org/10.1007/s11214-008-9349-9.

[4] *Zhai Y., Cummer S.A., Farrell W.M.* Quasi-electrostatic field analysis and simulation of Martian and terrestrial dust devils // J. Geophysical Research. Planets. 2006. V. 111. Iss. E6. Art. No. E06016. https://doi.org/10.1029/2005JE002618.

[5] *Atreya S.K., Wong* A.-S., *Nilton R.O. et al.* Oxidant enhancement in martian dust devils and storms: implications for life and habitability // Astrobiology. 2006. V. 6. Iss. 3. P. 439–450. https://doi.org/10.1089/ast.2006.6.439.

[6] *Renno N.O., Kok J.F.* Electrical activity and dust lifting on Earth, Mars, and beyond // Planetary Atmospheric Electricity. 2008. P. 419–434. https://doi.org/10.1007/s11214-008-9377-5.

AN IMPROVED MODEL OF RADIATIVE TRANSFER FOR THE NLTE PROBLEM IN THE NIR BANDS OF CO_2 AND CO MOLECULES IN THE DAYTIME ATMOSPHERE OF MARS. 3. AN EFFECT OF AEROSOL RADIATION SCATTERING ON THE VIBRATIONAL STATE POPULATIONS

V.P. Ogibalov[1,2], G.M. Shved[2]
[1] *Admiral Makarov State University of Maritime and Inland Shipping, Saint Petersburg, Russia, vpo563@mail.ru*
[2] *Saint Petersburg State University, Department of Atmospheric Physics, Saint Petersburg, Petrodvorets, Russia*

KEYWORDS:
radiative transfer, infrared molecular bands, vibrational non-LTE, carbon dioxide, Martian atmosphere, aerosol extinction.

INTRODUCTION:
The problem of radiative transfer in the IR ro-vibrational bands of the CO_2 and CO molecules is the fundamental one for the atmosphere of Mars, since the heating due to the emissions in these bands has a dominant value in establishing the energy balance, structure, and dynamic properties throughout the entire atmosphere of this planet.

The Martian atmosphere consisting of almost 95 % carbon dioxide has a relatively low density. Therefore, the rarity of molecular collisions, on the one hand, and the high rate of excitation of the vibrational states of the CO_2 and CO molecules due to the absorption of solar radiation in the near-infrared (NIR) spectral range of ~1.05–5 µm, on the other hand, result in the breakdown of the Boltzmann distribution in values of the concentrations (populations) of the vibrational states of these molecules. By another words, the breakdown of the local thermodynamic equilibrium (LTE) over the vibrational degrees of freedom of these molecules (vibrational non-LTE) takes place. The altitude of the level in the Martian atmosphere, lower which one needs to take into account for the vibrational non-LTE effects when assessing the populations of vibrational states of the CO_2 and CO molecules, varies depending on the wavelengths of the fundamental band (FB) in which the excitation of these states by absorption of the solar NIR radiation from the molecular ground state takes place. Thus, these altitude levels may even descend to the planet's surface for vibrational states of the main isotopologue $^{12}C^{16}O_2$ (or 626, in the HITRAN notification) which are excited by solar radiation in the ro-vibrational (R-V) transitions of the CO_2 molecule with the wavelengths shorter than 1.6 µm.

Since the Martian atmosphere is sufficiently rarified already at the surface, the breakdown of vibrational local thermodynamic equilibrium (LTE) for the CO_2 and CO molecules starts in the daytime from the troposphere. As the Mars lower atmosphere is dusty, the scattering of infrared solar radiation by aerosols should affect the vibrational state populations of these molecules.

The paper presents the results of modeling the radiative transfer under non-LTE conditions in the CO_2 and CO bands in the wavelength range of 1–5 µm, taking into account the radiation scattering by aerosols. The populations were studied depending on the optical thickness both of the aerosol layer and of the bands, the vertical distribution of aerosols, the solar zenith angle, and the aerosol parameters describing the scattering and absorption of radiation. The weaker the band, the stronger the aerosol effect on a population. This effect manifests as an increase and a decrease in population above and below a certain altitude level, respectively.

The present study is a continuation of the papers [1–2].

References:

[1] *Ogibalov V.P., Shved G.M.* An improved model of radiative transfer for the NLTE problem in the NIR bands of CO_2 and CO molecules in the daytime atmosphere of Mars. 1. Input data and calculation method // Solar System Research. 2016. V. 50. No. 5. P. 316–328. DOI: 10.7868/S0320930X16050042.

[2] *Ogibalov V.P., Shved G.M.* An improved model of radiative transfer for the NLTE problem in the NIR bands of CO_2 and CO molecules in the daytime atmosphere of Mars. 2. Population of vibrational states // Solar System Research. 2017. V. 51. No. 5. P. 373–385. doi:10.1134/S0038094617050070.

 14MS3-MS-PS-09
POSTER

HIERARCHY OF VIBRATIONAL STATE SETS FOR SOLVING THE NLTE RADIATIVE TRANSFER PROBLEM IN THE IR CO_2 BANDS IN THE MARTIAN ATMOSPHERE

V.P. Ogibalov
Admiral Makarov State University of Maritime and Inland Shipping, Saint Petersburg, Russia, vpo563@mail.ru

KEYWORDS:
Radiative transfer, infrared molecular bands, vibrational non-LTE, carbon dioxide, Martian atmosphere, aerosol extinction

INTRODUCTION:

The problem of radiative transfer in the IR ro-vibrational bands of the CO_2 and CO molecules is the fundamental one for the atmosphere of Mars, since the heating due to the emissions in these bands has a dominant value in establishing the energy balance, structure, and dynamic properties throughout the entire atmosphere of this planet. Also, the emissions in some bands of the CO_2 and CO molecules are used for remote sensing of the Martian atmosphere.

The Martian atmosphere consisting for 95 % of the CO_2 molecules has a rather low density. Therefore, both a rarity of molecular collisions, on one hand, and the high rate of excitation of the vibrational states of the CO_2 and CO molecules due to an absorption of the solar radiation in the near-IR spectral range, on another hand, result in a breakdown of the Boltzmann distribution of the excited vibrational state populations of these molecules within wide altitude intervals of the Martian atmosphere, i.e. the vibrational non-local thermodynamic equilibrium (vibrational NLTE) takes place. So, a development of sophisticated NLTE models for evaluating the values of the Martian atmosphere emissions in the IR bands of the CO_2 and CO molecules is required.

THE EXTENDED MODEL:

In the paper [1], the extended model used for solving the NLTE problem of radiative transfer in the IR bands of the CO_2 and CO molecules in the Martian atmosphere has included the 321 excited vibrational states belonging to the 7 isotopologues of CO_2 molecules and the 10 ro-vibrational bands rising between the 8 vibrational states of 2 isotopologues of the CO molecules. The most upper state is 2003 of the principal CO_2 isotopologue with energy of about 9500 cm^{-1}. In total, the 779 radiative vibrational transitions (about 100 000 lines) in the ro-vibrational bands of the CO_2 molecules (near 4.3, 2.7, 2.0, 1.6, 1.4, 1.25, 1.2 and 1.05 μm) and of the CO molecules (near 4.7, 2.3, 1.6 and 1.2 μm) were included into the extended NLTE model.

In the study [2], the NLTE model has been further improved to solve the above radiative transfer problem in the following directions. 1) The radiative transfer in all the bands of CO_2 and CO within the 15–1.02 μm spectral interval is taken into account with an exact treatment of overlapping of the spectral lines in frequency. 2) The processes of scattering and absorption of radiation by aerosol particles at the frequencies of the IR bands of the CO_2 and CO molecules were taken into account. 3) A reflection of the IR radiation by the Martian surface is also taken into account. 4) The accelerated lambda-iteration technique (the so-called ALI-method) used for solving the NLTE radiative transfer problem has been modified for the case of the aerosol extinction presence. The ALI-method allows to take into account the processes of scattering (with a phase function of general type) and absorption of radiation by aerosols at the frequencies belonging to the spectral ranges of the CO_2 and CO ro-vibrational bands.

The above features of the extended NLTE model demand significant computational resources. For the case, when one is interested in evaluation with given satisfied accuracy of non-equilibrium populations of only the relatively low excited vibrational states of the most abundant isotopologues of the CO_2 and CO molecules, which contribute substantially into the IR emissions and the net radiative heating of the Martian atmosphere, and one does not need to know the populations of the high excited states with the same accuracy, it is desirable to find more simple sets with reduced number of the vibrational states of the CO_2 and CO molecules.

THE METHODOLOGY:

Taking into account the intrinsic features of the NLTE radiative transfer problem in molecular bands mentioned above, an important question is how to select correctly both the vibrational states and vibrational bands of different isotopologues of the CO_2 and CO molecules in order to provide the necessary accuracy of the solution of the NLTE problem. In the paper [3–4], the procedure for reducing the amount of vibrational states which bases itself onto more or less reasonable criteria was suggested for solving the NLTE problem in the Earth middle atmosphere using the approximation of isolated ro-vibrational lines belonging to the CO_2 bands.

In this study, these criteria were updated to take into account the overlapping over frequency of lines within a given ro-vibrational band as well as lines belonging to different bands. It is important for the optically thick bands of the CO_2 and CO molecules in the atmosphere of Mars. Now, in particular, all the possible vibrational states with given numbers of the ν_2 and ν_3 quanta, which belong to the given Fermi family and interact by the Fermi resonance are proposed to be included into the set of vibrational states.

RESULTS:

A hierarchy of three vibrational state models, which are more simplier than the extended model but provide a reliable accuracy of estimating the values of the non-equilibrium vibrational populations, is proposed. In direction of decreasing accuracy, the two first (R1 and R2) models include, respectively, the 208 and 119 vibrational states of 7 isotopologues of the CO_2 molecules as well as the 8 vibrational states of 2 isotopologues of the CO molecules.

The third set for the most simple model (R3) contains the 62 vibrational states of 5 isotopologues of the CO_2 molecules as well as the 3 vibrational states of the principal isotopologue of the CO molecules. For a number of both the vertical profiles of the kinetic temperature and the solar zenith angle, the numerical errors in estimating the values of the integral non-equilibrium limb radiance of the 4.3 and 15 µm bands using the R3 model do not exceed of order of 10 and 1 %, respectively. As it concerns of evaluating the rate of net radiative heating within all the IR bands arising between the included vibrational states, the use of the R3 model gives error which does not exceed of about 0.5 K/day above altitudes with pressure of 0.001 mbar and increases down to the Martian surface up to about 2 K/day.

References:

[1] *Ogibalov V.P., Shved G.M.* An improved optical model for the non-LTE problem for the CO_2 molecule in the atmosphere of Mars: Nighttime populations of vibrational states and the rate of radiative cooling of the atmosphere // Solar System Research. 2003. V. 37. No. 1. P. 23–33. DOI: 10.1023/A:1022343620953.

[2] *Ogibalov V.P.* Non-equilibrium radiation in the infrared bands of the CO_2 and CO molecules in the planetary atmospheres (in the application to Mars) // Proc. SPIE. V. 10466. Pt. 1: 23rd Intern. Symp. Atmospheric and Ocean Optics: Atmospheric Physics. Irkutsk, Russia, 3–7 July 2017. P. 1–14. https://doi.org/10.1117/12.2292238.

[3] *Ogibalov V.P., Shved G.M.* The CO_2 non-LTE problem taking account of the multiquantum transitions on the ν_2-mode during CO_2-O collisions // Physics and Chemistry of the Earth. Pt B. Hydrology, Oceans and Atmosphere. 2000. V. 25. No. 5–6. P. 485–492. 10.1016/S1464-1909(00)00051-4.

[4] *Ogibalov V.P., Shved G.M.* Non-local thermodynamic equilibrium in CO_2 in the middle atmosphere. III. Simplified models for the set of vibrational states // J. Atmospheric and Solar-Terrestrial Physics. 2002. V. 64. Iss. 4. P. 389-396. https://doi.org/10.1016/S1364-6826(01)00113-4.

ON THE ROLE OF METHANE AND AMMONIA ABSORPTION IN STUDYING JUPITER'S ATMOSPHERE

P.G. Lysenko, V.D. Vdovichenko, A.M. Karimov, V.G. Tejfel, V.A. Filippov, G.A. Kharitonova
Fesenkov Astrophysical Institute, Almaty, Kazakhstan, lyssenko_petr@mail.ru

KEYWORDS:
Jupiter, troposphere, clouds, methane, ammonia

INTRODUCTION:
The weak methane and ammonia absorption bands that are present in Jupiter's visible spectrum are important for understanding the structural properties of its cloud cover and deeper regions of the troposphere. The study of spatiotemporal variations in the intensity of absorption bands of methane and ammonia on Jupiter has been a traditional line of work of the Laboratory of Physics of the Moon and Planets for more than 60 years. From 2004 to the present, a program of systematic homogeneous spectral observations of Jupiter has been carried out, the material of which covers more than one complete period of Jupiter's revolution around the Sun. In recent years, some previously unknown interesting features have been discovered that deserve attention and further study.

RESULTS OF OBSERVATIONS
In our observations since 2004, we have used a diffraction spectrograph (SGS) equipped with an ST7XE CCD camera (both manufactured by the Santa-Barbara Instrument Group). The spectral dispersion is 4.3 Å/pixel. The scale of the image on the spectrogram was 4.08 pixels per one arc second, so the diameter of Jupiter, on the spectrogram, was about 160 pixels. Two methods of observation were used: recording spectra with the slit oriented along the central meridian of Jupiter or recording zonal spectra when scanning Jupiter's disk from the south pole to the north. Variations in the intensity of the absorption bands of methane (CH4) at 619, 702, and 725 nm and separately of the band (CH4) at 887 nm were studied. The profiles and intensities of the absorption bands of ammonia (NH3) at 645 and 787 nm were also measured.

The detailed technique and results of these measurements are described in a number of our articles, for example [1] and in the monograph [2].

Figure 1 shows a comparison of extinction variations in the latitudinal direction and along the equator, as an illustration of a well-defined difference in the change in extinction from the center of the disk to its edges to the east and west, to the south and north. Here are the relative values of the equivalent widths of the absorption bands normalized to the center of the disk and the corresponding profiles of the relative brightness of the disk of Jupiter in the continuous spectrum.

For each extinction curve, the plots show the characteristic absolute values of the equivalent widths at the center of Jupiter's disk. As can be seen, the meridional course of absorption differs significantly from the course of brightness, while the course of absorption along the equator is similar to the change in brightness from the center of the disk to its edge, to a greater extent for ammonia and to a lesser extent for methane.

Moreover, for the absorption bands of methane, the following is observed: dark zones correspond to increased absorption, and light zones correspond to reduced absorption.

Ammonia is characterized by an increased uptake in the southern dark belt SEB and a reduced uptake throughout the northern hemisphere.

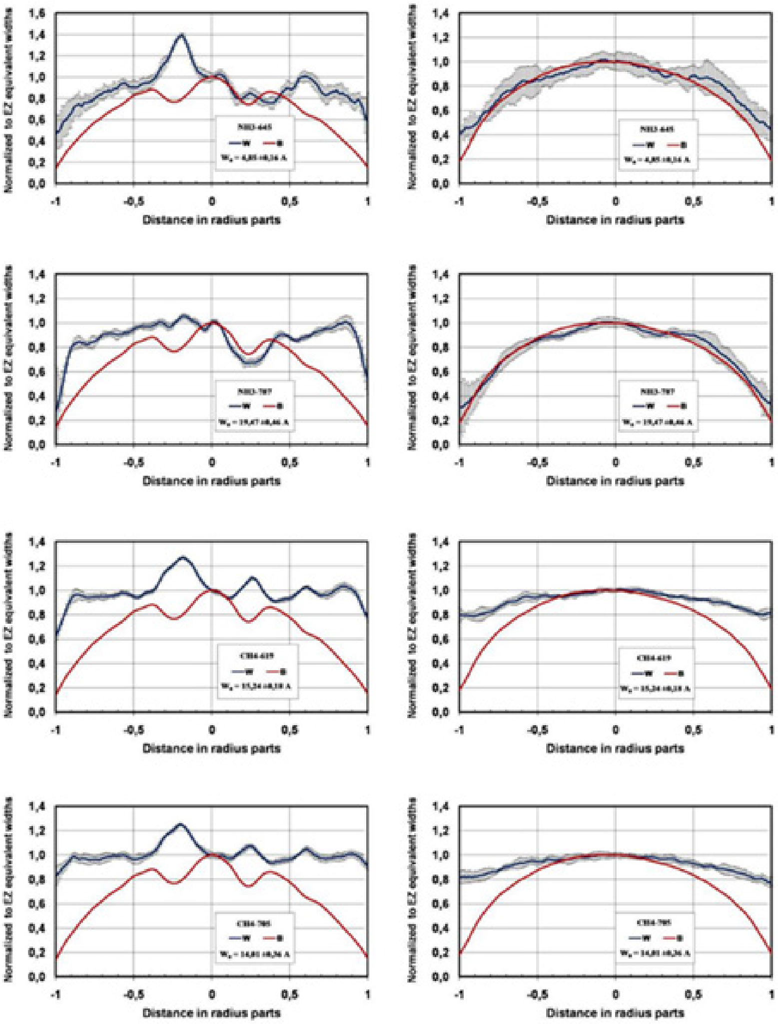

Fig. 1. Comparison of relative intensities of CH4 and NH3 absorption bands and brightness profiles observed in the continuous spectrum along Jupiter's central meridian and equator.

The similarity of the change in absorption of both methane and ammonia along the equator to the edges of the disk with a decrease in brightness towards the edges is mainly associated and determined by the geometry of illumination and reflection from the scattering layer of clouds. However, meridional absorption variations do not obey this rule and should be mainly due to latitudinal structural changes in the cloud layer itself. Interestingly, in different absorption bands, there are divergences in the positions of the extrema of the equivalent widths in latitude. This feature was discovered by us earlier [3] based on observations of Jupiter in 1999, covering all longitudes of the planet.

BRIEF DISCUSSION

Over the past decades, new technology has made it possible to significantly expand the spectral range of measurements of reflected and intrinsic thermal radiation in Jupiter observations. Now, in addition to infrared radiation, measurements are also being made in microwave radio emission with the VLA radio telescope system, and a centimeter section of the spectrum has also been reached from the JUNO [4] space probe, which makes it possible to study the depths of the Jovian atmosphere up to a thousand or more bar.

But this in no way detracts from the value of observations in the visible and near infrared regions of the spectrum, especially when it comes to studies of Jupiter's cloud cover. Therefore, here we again pay attention to some features in the observed variations in the molecular absorption bands, which are most associated precisely with variations in the structure of the ammonia cloud layer. So far, this structure itself, its connection with dynamic processes in the troposphere, remains unclear. It is also not yet possible to confidently determine which model is closest to reality in terms of the thickness and density of the planet's cloud cover. Are we dealing with a geometrically and optically thick layer of clouds, according to the most popular models [5], or should we accept the model of a translucent cloud, according to direct sounding data from GALILEO [6].

Until the next experiment of this kind, the main role remains with studies in the visible and near-IR spectral regions, as an integral part of the overall complex of all-wave observations of the planet.

Acknowledgement
This research is funded by the Science Committee of the Ministry of Science and Higher Education of the Republic of Kazakhstan (Grant No. BR20280974)

References:

[1] *Vdovichenko V.D., Karimov A.M., Kirienko G.A., Lysenko P.G., Tejfel V.G., Filippov V.A., Kharitonova G.A., Khozhenetz A.P.* Zonal Features in the Behavior of Weak Molecular Absorption Bands on Jupiter // Solar System Research, 2021, V. 55, No. 1, P. 35 - 46.

[2] *Vdovichenko V.D., Tejfel V.G.* The stadies planet on Kazakstan. Almaty, 2018 (in rus)

[3] *Tejfel V.G., Kharitonova G.A, Glushkova E.A., Sinyaeva N.V.,* 2001. Variation of the methane absorptions on Jupiter's disk from zonal CCD spectrofotometry data. Solar System Research 35, P. 261-277.

[4] *Bhattacharya A., Li C., Atreya S.K., et al.* Highly depleted alkali metals in Jupiter's deep Atmosphere arXiv:2306.12546v1 [astro-ph.EP] 21 Jun 2023 P. 17

[5] *Weidenschilling S.J., Lewis J.S.,* 1973. Atmospheric and cloud structures of the Jovian planets. Icarus 20, 465-476.

[6] *Ragen B., Colburn D.S., Rages K.A., Knight T.C.D., Avrin P., Orton G.S., Yanamandra-Fisher P.A., Grams G.W.,* 1998. The clouds of Jupiter: Results of the Galileo Jupiter mission probe nephelometer experiment. J. Geophys. Res. 103, 22891-22910.

14MS3-MS-PS-11
POSTER

ELECTRONIC KINETICS OF MOLECULAR NITROGEN AT THE ALTITUDES OF TITAN'S MIDDLE ATMOSPHERE

A.S. Kirillov
Polar Geophysical Institute, Apatity, Murmansk region, Russia, kirillov@pgia.ru

KEYWORDS:
Titan, middle atmosphere, molecular nitrogen, triplet states, cosmic rays, radicals

Molecular nitrogen is the main molecular gas in the Titan's atmosphere. We study the electronic kinetics of triplet states of N_2 at the altitudes of 50–250 km during the precipitation of cosmic rays. Intramolecular and intermolecular electron energy transfer processes during inelastic molecular collisions with N_2, CH_4, CO are taken into account. We present vibrational populations of triplet states at different altitudes of Titan's middle atmosphere. The important role of molecular collisions in the population of metastable molecular nitrogen is shown.

We study the inelastic interaction of electronically excited N_2 molecules with acetylene C_2H_2 and ethylene C_2H_4 molecules at the altitudes of the middle atmosphere. It was shown for the first time that the inelastic interaction dominates in the formation of C_2H and C_2H_3 radicals at the altitudes. The main contribution in the radical formation is related with collisions of metastable molecular nitrogen with acetylene and ethylene molecules. The possible role of the reactions in hydrocarbon production is discussed.

INTEGRATING IOT WITH SPACE EXPLORATION: IMPROVING MARS MISSIONS WITH NEURAL NETWORKS

N.N. Kasatikov
Moscow Aviation Institute, Moscow, Russia, Nick925@yandex.ru

KEYWORDS:
IoT technologies, Neural networks, artificial intelligence, astronauts, Mars

INTRODUCTION:
The use of Internet of Things (IoT) technologies has revolutionized various industries, and space exploration is no exception. Expeditions to Mars require real-time monitoring of environmental conditions, equipment operation, and the well-being of astronauts. In this presentation, we will look at the potential benefits of IoT integration for the safety of astronauts on Mars exploration missions. We will discuss the deployment of sensor networks on Mars to collect valuable data on atmospheric conditions, astronaut health, radiation levels, geological features, and more. We will also look at the challenges and considerations for implementing IoT in harsh Martian environments, including power management, communication protocols, and data storage limits. In addition, we will explore how the IoT can improve the safety and well-being of astronauts by monitoring vital signs, providing feedback to the environment, and enabling efficient resource management. The integration of IoT technologies with space exploration on Mars holds great promise for expanding our understanding of the Red Planet and enabling future long-range missions.

References:
[1] *Yousefpour A., Fung C., Nguyen T. et al.* All one needs to know about fog computing and related edge computing paradigms: A complete survey // J. Systems Architecture. 2019. V. 98. P. 289–330. https://doi.org/10.1016/j.sysarc.2019.02.009.
[2] *Talari S., Shafie-Khah M., Siano P. et al.* A review of smart cities based on the internet of things concept // Energies. 2017. V. 10. Iss. 4. Art. No. 421. https://doi.org/10.3390/en10040421.

SESSION 2. MOON AND MERCURY (MN)
ORAL SESSION

THREE MERCURY FLYBYS: OBSERVATIONS OF NEUTRON AND GAMMA-RAY FLUXES BY MGNS INSTRUMENT ONBOARD THE ESA'S BEPICOLOMBO MISSION

A.S. Kozyrev [1], B. Bakhtin [1,2], J. Benkhoff [3], M.L. Litvak [1], I.G. Mitrofanov [1], A.B. Sanin [1]

[1] *Institute for Space Research, Profsojuznaja 84/32, 117997 Moscow, Russian Federation*

[2] *Mechanical Engineering Research Institute, Maly Kharitonyevsky Pereulok 4, 101000, Moscow, Russian Federation*

[3] *European Space Agency, ESTEC, Keplerlaan 1, 2201 AZ Noordwijk, The Netherlands*

KEYWORDS:
BepiColombo, Mercury, Venus, MGNS, nuclear planetology.

INTRODUCTION:
The trajectory of the BepiColombo spacecraft on its cruise to Mercury involves a series of gravitational maneuvers on Earth, Venus and Mercury [1, 2]. This report analyses the data for the second Venus flyby and the first, second and third Mercury flybys. Data from the first Fly-by of Venus was not used, as the BepiColombo spacecraft was at a large distance at the moment of closest approach, so that the signal from the planet could be detected by the MGNS instrument [3, 4] with reliable statistics. Special sessions of measurements were performed during Venus and Mercury fly-bys during which the MGNS instrument measured neutron flux with a time resolution of 20 seconds. In the case of Mercury, neutron fluxes with energies of about 1–100 MeV are produced in the shallow surface layer under the exposure to Galactic Cosmic Rays radiation. These neutrons interact with the nuclei of the main soil-forming elements through inelastic scattering reactions (if the neutron has high energy) or neutron capture reactions (if the neutron is slowed down to thermal energies). For Venus the processes of generation and moderation of secondary neutrons are the same as for Mercury except that the neutron flux is not generated on the surface of Venus but in its atmosphere at altitudes above about 50–60 km. For the atmosphere of Venus, the element that best absorbs thermal neutrons is nitrogen, of which there is about 3.0-3.5 wt% in the upper layers of the atmosphere. In order to obtain model estimates of Mercury's surface composition and interpret the MGNS instrument measurement, Monte Carlo based simulations also will presented for the Fly-bys environmental conditions.

References:
[1] *J. Benkhoff, G. Murakami, W. Baumjohann, et al.* BepiColombo - Mission Overview and Science Goals // Space Science Reviews. P. 217. 2021.

[2] *Valeria Mangano, Melinda Dósa, Markus Fränz, Anna Milillo, et al.* BepiColombo Science Investigations During Cruise and Flybys at the Earth, Venus and Mercury // Space Sci Rev 2021. 217:23.

[3] *I.G. Mitrofanov at al*, The Mercury Gamma and Neutron Spectrometer (MGNS) onboard the Planetary Orbiter of the BepiColombo mission // Planetary and Space Science 58. 2010. P. 116–124.

[4] *Mitrofanov I.G., Kozyrev A.S., Lisov D.I., et al.* The Mercury Gamma-Ray and Neutron Spectrometer (MGNS) Onboard the Mercury Planetary Orbiter of the BepiColombo Mission: Design Updates and First Measurements in Space // Space Science Reviews. 2021. V. 217, Iss. 5, Art. No. 67.

DETERMINATION OF THE OPTIMAL PARAMETERS OF THE MERCURY'S MAGNETOSPHERE FOR THE MESSENGER MISSION

A.S. Lavrukhin[1], I.I. Alexeev[1], D.V.Neskii [1,2]
[1] *Skobeltsyn Institute of Nuclear Physics Lomonosov Moscow State University, Moscow, Russia, lavrukhin@physics.msu.ru*
[2] *Lomonosov Moscow State University, Faculty of Physics, Moscow, Russia*

KEYWORDS:
Mercury, magnetosphere, MESSENGER

INTRODUCTION:

Mercury, the planet closest to the Sun, has its own magnetic field, sufficient to create its own magnetosphere around the planet. It has been studied in detail during the MESSENGER (MERcury Surface, Space ENvironment, GEochemistry, and Ranging) mission. This spacecraft completed more than 4,000 revolutions around the planet from 2011 to 2015. We use the paraboloid model of Mercury's magnetospheric magnetic field to determine the optimal parameters of Mercury's magnetosphere current systems and internal planetary dipole parameters for all MESSENGER orbits.

The formation of the magnetosphere is associated with the currents flowing in the space around the planet, which create their own magnetic field, superimposed on the planetary internal magnetic field. These currents, and hence the magnetic field they create, can change from flyby to flyby, or even on the scale of one spacecraft orbit, due to the short reconfiguration time of the Mercury's magnetosphere, which is on the order of several minutes [1]. To take into account these contributions and to refine the estimate of the planetary magnetic moment, a model of the magnetospheric field is required. In this work, we use a paraboloid model of the Mercury magnetosphere. It was introduced in [2] for the Mariner 10 data analysis, and then for the analysis of the first two MESSENGER flybys in [3], where the effect of dipole tilt was included. In [4], the paraboloid model was used to describe the erosion of Mercury's magnetosphere.

METHOD:

We use an updated implementation of the chi^2 functional minimization method FUMILIM [5]. The FUMILI code algorithm was made available for use as part of the CERN library. The program for finding the minimum of the functional of the sum of squared differences between the components of the experimental and model magnetic fields calculates the model magnetic field vector using a theoretical paraboloid model with free parameters, which allows one to calculate the magnetic field in the planetary magnetosphere and compare it with the obtained experimental data. The FUMILIM code is used for determination of the best fitting model parameters that minimize the RMS standard deviation between the model field vector and the measured magnetic field.

For the dataset used, when searching for the minimum of the functional, it makes sense to take into account not only the modulus of the difference vectors, but also the angle between the two vectors. The approach used in [3] took into account only the modulus of the residual vector and lost sensitivity to the sign of the difference between experiment and theory. This effect was especially pronounced for a parameter that is significant only for one of the components of the vector function (such parameters include the values of the corresponding IMF components penetrating the magnetosphere). The new version of the FUMILIM minimum functionality search program can accurately work with vector functions as well. In the new version of the package, all three components of the residual vector are transferred to the program.

Our task is to find six parameters that determine the magnitude of the planetary magnetic field of Mercury. As a first approximation, we neglect secular variations and assume that these parameters do not change from one revolution to another. In addition, each orbit is characterized by seven local parameters that describe the state of magnetospheric current systems formed during the interaction of the solar wind plasma with the planetary field.

DISCUSSION:

As a result of the magnetic field vector fitting, the magnitude and direction of the magnetic moment of Mercury, as well as its displacement relative to the center of the planet for each of the orbits of the satellite, were redefined. In this case, there is a small secular variation of the dipole moment, but these changes are at the limit of errors, more precisely, beyond the limits: in order to isolate a possible effect, it is necessary to increase the reliability of the method for solving the inverse problem by an order of magnitude. The parameters of the current systems of the magnetosphere model were also determined for each individual orbit. For each revolution of MESSENGER around Mercury, we considered the parameters of the magnetosphere to be unchanged during the entire magnetospheric part of the trajectory, which lasted about an hour on average. We have considered only two magnetospheric current systems — the currents at the magnetopause, which screen the dipole field from penetrating into the transition layer, and the current system of the magnetotail. As a result, the state of the magnetosphere at each orbit was described by 4 parameters: B_t is the field of the current sheet at its leading edge in *nT*, R_1 is the distance to the subsolar point at the magnetopause in R_M, R_2 is the distance to the inner edge of the current sheet in R_M, Z_0 is the displacement of the current sheet in the vertical direction relative to the equatorial plane of the magnetospheric coordinate system in R_M. Three more constants specify three components of a constant (changing from one orbit to another, but constant along a fixed MESSENGER orbit) vector of the magnetic field, which makes the discrepancy between the model and measurements minimal. This B_{MF} vector is formed by the vector of the interplanetary magnetic field penetrating from the transition layer into the magnetosphere and as a result of the regular deviation of the rotation paraboloid from the real magnetosphere, which gives a “correcting constant” in the field of currents at the magnetopause. However, uncertainty now remains both in the spatial distribution of the penetrating interplanetary field and in the relative value of the penetration coefficient for different components. In order to evaluate the effectiveness of the dipole parameters selected for fitting, the pairwise cross-correlation of the parameters among themselves was calculated, the smaller the pairwise correlation coefficients, the better the selected set of parameters. As expected, for the vertical displacement and the dipole value, the correlation is the highest, but in this case, the residual minimum is well manifested, and the accuracy of its determination is quite high.

References:

[1] *Slavin J.A., Krimigis S.M., Acuña M.H. et al.* MESSENGER: Exploring Mercury’s Magnetosphere // Space Sciences Reviews. 2007. V. 131. P. 133–160. https://doi.org/10.1007/s11214-007-9154-x.

[2] *Alexeev I.I., Belenkaya E.S., Bobrovnikov S.Yu. et al.* Paraboloid model of Mercury’s magnetosphere // J. Geophysical Research. 2008. V. 113. Iss. A12. Art. No. A12210. https://doi.org/10.1029/2008JA013368.

[3] *Alexeev I.I., Belenkaya E.S., Slavin J.A. et al.* Mercury’s magnetospheric magnetic field after the first two MESSENGER flybys // Icarus. 2010. V. 209. No. 1. P. 23–39.

[4] *Heyner D., Nabert C., Liebert E., Glassmeier K.-H.* Concerning reconnection-induction balance at the magnetopause of Mercury // J. Geophysical Research. Space Physics. 2016. V. 121. Iss. 4. P. 2935–2961. https://doi.org/10.1002/2015JA021484.

[5] *Sitnik I.M., Alexeev I.I., Selugin O.V.* The final version of the FUMILIM minimization package // Computer Physics Communications. 2020. V. 251. Art. No. 107202. DOI: 10.1016/j.cpc.2020.107202.

GEOLOGICAL EXPLORATION OF THE MOON VI: MINERALOGY, RHEOLOGY, HEAT BUDGET

A. Gusev[1], Z.G. Meng[2], J.S. Ping[3]
[1] *Kazan Federal University, Department of Mathematical Methods in Geology, Kazan, Tatarstan, Russia, agusev33@gmail.com*
[2] *College of Geoexploration Science and Technology, Jilin University, Changchun, China*
[3] *National Astronomical Observatory of China CAS, Beijing, China*

KEYWORDS:
crust, regolith, marine basalts, petrology, rheology, heat budget of the Moon

INTRODUCTION:

The review discusses 1) the new results of laboratory studies of the lunar regolith within new dates of the Chinese mission Chang'E-5, 2) the new realistic estimations of the water concentration in the bound state of lunar rocks, 3) the last mysteries of the long-term generation of a powerful thermal budget of the Moon. A new era of scientific and applied research of the Moon is coming, and dozens of lunar missions of various space agencies are already planned for the next decade [1–2].

Currently, Chinese scientists and engineers are working on the next series of lunar missions: the Chang'E-6 spacecraft will collect the first samples of lunar soil from the far side of the Moon in 2025, the Chang'E-7 multi-purpose spacecraft, which is scheduled to launch in 2026 and among other tasks will look for water ice in the shadowed craters of the Moon. The Chang'E-8 spacecraft, due to land on the moon around 2028, will lay the groundwork for the larger ILRS project that China plans to build in the 2030s. The ILRS will consist of a lander, a habitable bunker, an orbiter and a rover, and will include testing the first technologies for exploiting lunar resources on the lunar surface. Also, Chinese colleagues are considering the possibility of 3D printing lunar bricks using materials from the lunar surface. A nuclear facility will be used to power the Chinese lunar base. 3D printing for space activities has been considered and tested for years: the European Space Agency is working on making lunar bricks that mimic lunar regolith.

CHANG'E-5 MISSION ON THE MOON: MINERALOGY:

The origin of the young lunar basalts of Chang'E-5 (CE-5) is highly debated. The authors [3] present the results of high pressure, high temperature (P-T) phase equilibrium experiments and petrological modeling to limit the source depth and temperature of these unique marine basalts. Experimental results indicate that CE-5 basalts could have been formed either by the melting of clinopyroxene and cumulates rich in single bond Fe oxide Ti in the shallow lunar mantle, or by extreme fractional crystallization of the hot Mg-rich parent melt. The results of Chinese scientists confirm the local retention of significant heat (at least 1200 °C) in the lunar mantle, which is necessary for the formation of basaltic melts of CE-5 composition at the age of 2 billion years. The authors of the paper argue that CE-5 basalts are formed by the melting of Fe and rich Ti accumulate in the shallow lunar mantle, since the extreme fractional crystallization of olivine and plagioclase from the original picritic melts requires too high temperatures in the lunar mantle (>1500 °C) for approximately 2 Gyr.

The successful Chang'E-5 mission returned to Earth 1731 g of lunar soil from the northeastern ocean Oceanus Procellarum [4]. The author's study starts with a comparison of the mineralogy and geochemistry of the CE-5 soil with the Apollo and Luna samples. Samples CE-5 have the same mineral content as the Apollo Sea soils. Geochemically, the CE-5 soil is characterized by a high content of FeO, an average content of TiO_2, and an increased content of geologically incompatible elements. New returned lunar samples CE-5 is a unique type of marine soil that expands the variety of returned lunar samples. Their gross chemistry suggests that the CE-5 soil is composed of crushed local marine basalt. Lunar Samples CE-5 provides an additional iron-rich basaltic composition and significantly expands the chemical range of existing calibration soils for lunar remote sensing. The CE-5 lunar samples, together with the topographic localization of the landing site, can serve as a new ground standard in both mineralogy and geochemistry. Based on the general chemical data of the CE-5 samples and the pyroxene compositions in the CE-5 marine basalt clasts, the authors conclude that the CE-5 marine basalt has a fractional crystallization history like the high-Ti Apollo basalts.

RHEOLOGY AND HEAT BUDGET OF THE MOON:

In the article [5, Fig. 1], the modernized rheological models of Andrade (1910) and Sandberg and Cooper (2010) are compared with the Maxwell model in order to better understand the mechanisms of tidal heat generation inside rocks. The authors found that both Andrade and Sandberg-Cooper rheology's [6] can produce at least 10 times more tidal heating compared to the traditional Maxwell model for a warm 1400–1600 K lunar-like celestial body. Sandberg-Cooper rheology can also cause even more heat generation in the vicinity of the critical temperature and tidal frequency.

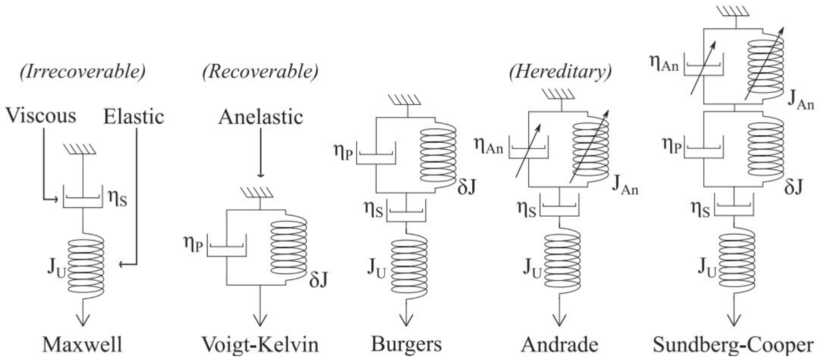

Fig. 1. Rheology

These models allow cooler planets and their moons to remain tidally active in the face of orbital disturbances, a condition the authors call "tidal stability."

This has implications for the temporal evolution of tidally active worlds and the long-term orbital-rotational equilibrium in which they are trapped. The authors also show that Andrade inelasticity, which is contained in both Andrade and Sandberg-Cooper rheological models, can generate much greater dissipation energy at lower temperatures in the mantles of planets and their resonant moons. The authors provide detailed reference tables for the general initial dissipation equations that other scientists need to incorporate the Andrade and Sandberg-Cooper models into standard tide formulas. The authors show that advanced modern rheology strongly influence the heating of short-period exoplanets and exo-moons, while tidal stability properties may mean more tidally active worlds among all extrasolar systems. In the past, the area of planetary tidal dynamics has been moderately separated from the nuances of laboratory materials science. New papers [7–8] attempts to best combine these two regions through careful modeling of the planetary geometry and layered interior compositions of their moons. Tidal forces are generated by a non-zero gravitational potential gradient across the planet's moon. These forces result in internal stress, which is counteracted by the strength of the satellite material. Changing this gradient over time due to an eccentric orbit, non-synchronous rotation (NSR), non-zero inclination, or some combination results in the dissipation of orbital and/or spin frictional energy into internal heat. All rheological models are attempts to represent the microphysical interactions between atoms and grains of the planet's basic material on a macro scale, usually with a compact set of equations. Burgers rheology is better able to capture certain interfacial interactions at grain boundaries. They become relevant at moderately high frequencies and are usually described by a peak or plateau in the response. Grain boundary sliding is a phenomenon that occurs on a shorter relaxation time scale than Maxwell-like diffusion creep and moreover is recoverable, which is represented by a pair of parallel spring-ash (Voigt-Kelvin) elements in Burgers. The use of parameters proposed by ground-based observations [8] leads to a rheological response in the temperature range similar to Maxwellian, except for temperatures in the range of 1200–1600 K, where a moderate secondary peak of tidal dissipation occurs.

The Andrade model was originally developed to describe the tensile response of laboratory specimens of metallic copper (Andrade, 1910). It has since expanded and become particularly successful in describing a wide range of laboratory studies, including silicate minerals, metals, and ices, and has recently made inroads into planetary science. One of the features of Andrade's rheology is the goal of "softening" the too steep frequency dependence of the Maxwell model with a function that is a power law in the frequency domain with fractional powers less than 1. This allows the model to describe the very real phenomenon that few materials the real world consist of grains for the same size; they usually contain impurities along with a spatially varying defect range and defect density. Since neither Burgers' formalism nor Andrade's formalism could account for this feature, they developed a complex rheological model combining features of both.

The authors of [5] call their composite model Sandberg-Cooper rheology [6] and found that the use of Andrade and Sandberg-Cooper rheology leads to an increase in a property which is called tidal stability, or the ability of ongoing tidal activity to persist for a long time in the face of disturbances.

In general, recommend considering Andrade and Sandberg-Cooper rheology for any solid-state tidal application where minimal errors are desired with the tides. Likewise, continued observation of the heat flux leaving tidally active worlds such as Io will allow us to better constrain internal states. In general, we recommend that Andrade and Sandberg-Cooper rheology be seriously considered for any solid-state tidal application where errors of less than 10 are desired when mapping the results back to internal conditions. This is especially true for masses from 1 MIo to 10ME, for temperatures from 1000 to 1600 K, and for all periods of action associated with tides.

References:

[1] *Tang T., Meng Z.G., Lian Y. et al.* Extracting Mare-like Cryptomare Deposits in Cryptomare Regions Based on CE-2 MRM Data Using SVM Method // Remote Sensing. 2023. V. 15. Iss. 8. P. 2010–2021. https://doi.org/10.3390/rs15082010.

[2] *Meng Z.G., Tang T.Q., Dong X.G., Gusev A.* Analyzing the microwave thermal emission features of lunar regolith in Chang'E landing sites and its geologic significance. SCIENTIA SINICA Physica // Mechanica and Astronomica. 2023. V. 53. Iss. 3. Art. No. 239609. 17 p. (In Chinese). https://doi.org/10.1360/SSPMA-2022-0303.

[3] *Haupt C.P., Renggli C.J., Klaver M. et al.* Experimental and petrological investigations into the origin of the lunar Chang'e-5 basalts // Icarus. 2023. V. 402. Art. Id. 115625. 8 p. https://doi.org/10.1016/j.icarus.2023.115625.

[4] *Fu X., Yin Ch., Jolliff B.L. et al.* Understanding the mineralogy and geochemistry of Chang'E-5 soil and implications for its geological significances // Icarus. 2022. V. 388. Iss. 1. Art. No. 15254. 11 p. https://doi.org/10.1016/j.icarus.2022.115254.

[5] *Renaud J.P., Henning W.G.* Increased tidal dissipation using advanced rheological models: Implications for Io and tidally active exoplanets // The Astrophysical J. 2018. V. 857. No. 98. Art. No. 98. 29 p. DOI: 10.3847/1538-4357/aab784.

[6] *Sundberg M., Cooper R.F.* A composite viscoelastic model for incorporating grain boundary sliding and transient diffusion creep; correlating creep and attenuation responses for materials with a fine grain size // Philosophical Magazine. 2010. V. 90. Iss. 20. P. 2817–2840. https://doi.org/10.1080/14786431003746656.

[7] *Tobie G.,* Čadek O., *Sotin* C. Solid tidal friction above a liquid water reservoir as the origin of the south pole hotspot on Enceladus // Icarus. 2008. V. 196. Iss. 2. P. 642–652. https://doi.org/10.1016/j.icarus.2008.03.008.

[8] *Henning W.G., O'Connell R.J., Sasselov D.D.* Tidally heated terrestrial exoplanets: viscoelastic response models // Astrophysical J. V. 707. No. 2. P. 1000-1015. DOI: 10.1088/0004-637X/707/2/1000.

THICKNESS OF VOLCANIC MATERIALS IN MARE FECUNDITATIS

M.A. Ivanov[1], J.W. Head[2], H. Hiesinger[3]
[1] *Vernadsky Institute of Geochemistry and Analytical Chemistry, RAS, Moscow, Russia, mikhail_ivanov@brown.edu*
[2] *Brown University, Providence, RI, USA, James_Head@brown.edu*
[3] *University of Münster, Münster, Germany, hiesinger@uni-muenster.de*

KEYWORDS:
Moon, Mare Fecunditatis, mare fill, impact craters, thickness

INTRODUCTION:

The thickness of the volcanic fill within lunar maria is an important characteristic of the volcanic evolution of the Moon. There are several approaches to estimating the nature, geometry and thickness of volcanic flooding of cratered planetary surfaces (e.g., [1]). Modern data, including high-resolution photographs of the surface, topography, and spectroscopy provide the means to refine previous estimates (e.g., [2–3]) of total thickness of mare materials. Here we present our estimates of the thickness of volcanics within Mare Fecunditatis.

THICKNESS ESTIMATES AT THE LOCAL SCALE:

Several lines of evidence suggest that the thickness of mare materials in Mare Fecunditatis may be relatively small locally [4]. (1) Within Mare Fecunditatis there are a number of outcrops of highlands that occur in the SW and NE portions of the mare. The highlands outside the mare in both regions have standard deviations from the mean elevation of ~290 m (SW region) and ~620 m (NE region). The mean elevation of the highland outcrops in the SW region is ~200±130 m and in the NE region is ~60±30 m. These values suggest that near the outcrops in the SW portion of Mare Fecunditatis, the mare thickness is several tens of meters, whereas in the NE portion, the thickness may approach a few hundred meters. (2) In the area around the Luna 16 landing site, exposures of pre-mare craters are seen. These craters are about 10-12 km diameter and their rim heights are estimated to be a few hundred meters (e.g., [5]), which introduces additional constraints on the mare thickness in the vicinity of the landing site. Autors [5] have estimated the thickness of the mare fill near craters Webb-B (~60 km WSW of the Luna-16 landing site) and Webb-H (~100 km SW of the Luna-16 landing site) to be about 33 and 95 m, respectively. (3) About 30 km SW of the landing site there is a fresh crater with a distinctly low abundance of FeO in its interior and ejecta. The crater diameter is ~1.5 km, which suggests that the thickness of the mare fill near the landing site is less than ~150 m.

LARGER FLOODED CRATERS:

An independent way of estimating the local mare thickness comes from comparison of the topographic configuration of craters affected and not-affected by volcanism. Crater Webb-P (~50 km diameter) at the NE edge of Mare Fecunditatis has an actual depth of ~0.7 km. The crater Kapteyn is similar in size and is as deep as ~2.5 km, thus, the thickness of mare in Webb-P is ~1.8 km. The flooded crater that forms Sinus Successus (~130 km) is ~0.8 km deep and non-embayed crater Langrenus (123 km) has a depth of ~3.5 km, which provides an estimated thickness of mare in Sinus Successus to be ~2.7 km. The partly flooded crater Gutenberg (70 km), at the western edge of Mare Fecunditatis, is ~1.25 km deep and crater Stevinus (~77 km) is ~2.5 km deep; thus, an estimated mare thickness in Gutenberg is ~1.25 km.

Within Mare Fecunditatis, there are a number of almost completely flooded craters. Comparison of their actual depth with the depth of non-filled craters within the highlands nearby the Fecunditatis basin provides mare thickness estimates varying over a narrow interval from ~1.8 to ~2 km.

THICKNESS ESTIMATES AT REGIONAL SCALE:

The small values of mare basalt thickness determined locally suggest that if they are representative for the entire Mare Fecunditatis, then remnants of larger craters from the pre-mare population should be visible within the mare if they indeed formed in this region. To test this hypothesis, we selected a large area on the farside between 60°N – 60°S and 150°E – 115°W, which has only small and dispersed mare occurrences (mostly in the northern portion of the South Pole – Aitken basin). In this area, which represents a non-modified crater population of the highlands, we have measured the mean distances between craters in different diameter ranges using the catalogue of lunar craters larger than 20 km [6]. These distances are as follows: ~280±160 km (for craters in 128–256 diameter range), ~110±50 km (64–128 diameter range), and ~65±30 km (32–64 diameter range).

We then calculated an expected number of these craters within the inner ring of the Fecunditatis basin (~700 km diameter) as a ratio of the area within the inner ring to an area of a circle with the radius equal to the mean nearest distance. The expected number of craters 128–256 km diameter is ~2, which is equal to the actual number of such craters within the rim (Langrenus, 132 km and Sinus Successus, 130 km). For the smaller craters, however, a significant deficiency of craters within the ring is observed. The expected number of craters in the 64–128 km range is ~10, whereas only one crater of such size (unnamed crater at 64.58°E, 1.76°N, 70 km diameter) is present, near the western edge of Mare Spumans. The expected number of craters in the 32–64 km range is ~30 and only 11 craters of this size are seen within the inner ring.

The differences between the expected and actual number of craters suggest that a composite layer of mare materials within the inner ring is sufficiently thick to hide a significant portion of craters smaller than ~100 km diameter. Crater Ansgarius (79.72°E, 12.92°S, 95 km) eastward of the Fecunditatis basin is not flooded/embayed; the height of its rim is ~1.5 km, which provides a minimal estimate of the thickness of mare in the basin.

CONCLUSIONS:

The calculated thicknesses suggest that the mare basalt volcanic fill of Mare Fecunditatis is highly variable. At the regional scale, it must be at least ~1.5 km to be able to hide a significant number of ancient larger craters. In areas of partly or completely flooded craters the thickness increases up to ~2–2.7 km. In the vicinity of the Luna-16 landing site, however, the mare thickness appears to be much smaller, and is likely to be less than a few hundred meters. These variations appear to be due to the complex topography of the pre-mare surfaces which was significantly affected by initial viscous relaxation followed by ejecta from both the Nectaris and Crisium basins. The highly variable thickness of mare materials (and range of ages and locations) is consistent with significant lateral variations of the time of different volcanic phases, which can reflect eruptions of different duration, rate, and age (e.g., [7]).

Acknowledgements:

The work is supported by the Russian Science Foundation grant no. 21-17-00035: Estimates of the rate of exogenous resurfacing on the Moon.

References:

[1] *Whitten J.L., Head J.W.* Detecting volcanic resurfacing of heavily cratered terrain: Flooding simulations on the Moon using Lunar Orbiter Laser Altimeter (LOLA) data // Planetary and Space Science. 2013. V. 85. P. 24–37. https://doi.org/10.1016/j.pss.2013.05.013.

[2] *De Hon R.A.* Thickness of mare material in the Tranquillitatis and Nectaris basins // Proc. 5th Lunar Science Conf. 1974. V. 1. P. 53–59.

[3] *De Hon R.A.* Thickness of the western mare basalts // Proc. 10th Lunar Science Conf. 1979. V. 3. P. 2935–2955.

[4] *De Hon R.A., Waskom J.D.* Geologic structure of the eastern mare basins // Proc. 7th Lunar Science Conf. 1976. V. 3. P. 2729–2746.

[5] *Du J., Fa W., Wieczorek M.A. et al.* Thickness of lunar mare basalts: New results based on modeling the degradation of partially buried craters // J. Geophysical Research. 2019. V. 124. P. 24–37. https://doi.org/10.1029/2018JE005872.

[6] *Kadish S.J., Fassett C.I., Head J.W. et al.* A global catalog of large lunar craters (>20 km) from the Lunar Orbiter Laser Altimeter // Lunar and Planetary Science Conf. 2011. V. 42. abs. #1006.

[7] *Head J.W., Wilson L.* Generation, ascent and eruption of magma on the Moon: New insights into source depths, magma supply, intrusions and effusive/explosive eruptions (Pt. 2: Predicted emplacement processes and observations) // Icarus. 2017. V. 283. P. 176–223. https://doi.org/10.1016/j.icarus.2016.05.031.

STUDY OF THE SURFACE MORPHOLOGY OF PERMANENTLY SHADOWED FLOOR OF POLAR CRATER SHOEMAKER: RELATIVE DEPTH OF SMALL CRATERS

A.T. Basilevsky[1], Li Y.[2]

[1] *Vernadsky Institute of Geochemistry and Analytical Chemistry, RAS, Moscow, Russia, atbas@geokhi.ru*

[2] *Suzhou Vocational University, SuZhou, China, yuanli_scires@outlook.com*

KEYWORDS:

Moon, permanently shadowed area, digital terrain model (DTM), craters, relative depth, water ice in regolith

INTRODUCTION:

This is continuation of our study of permanently shadowed floor of polar crater Shoemaker reported at the 13th Moscow Solar System Symposium [1].

Crater Shoemaker (88.14°S, 44.91°E) is superposed on the rim of South Pole – Aitken impact basin. It has rather mature morphology. Its rim is pitted by numerous small craters of a few km in diameter, whose spatial density corresponds to model age 4.15±0.02 Ga [2]. Inside crater Shoemaker, at its floor and lower parts of its inner slopes is permanently shadowed area within which we outlined four study areas, each about 4.5×6 km, — two on the floor and two on the lower parts of inner slopes.

This time we report on measurements of relative depth (*d*/*D*) of craters with diameters of 150-400 m in the Shoemaker floor (Study areas 1 and 2) and compare the results with similar measurements in the Lunokhod-2 and Apollo-16 areas.

MEASUREMENTS:

For that in the cases of Shoemaker and Apollo-16 craters were used DTMs based on the LOLA measurements [3] and for the Lunokhod-2 area — DTM based on stereometric analysis of LROC NAC images [4]. The crater depth was obtained by calculating the difference between the maximum and minimum values of the elevation within the considered crater area. Results of these *d*/*D* measurements are shown in Fig. 1.

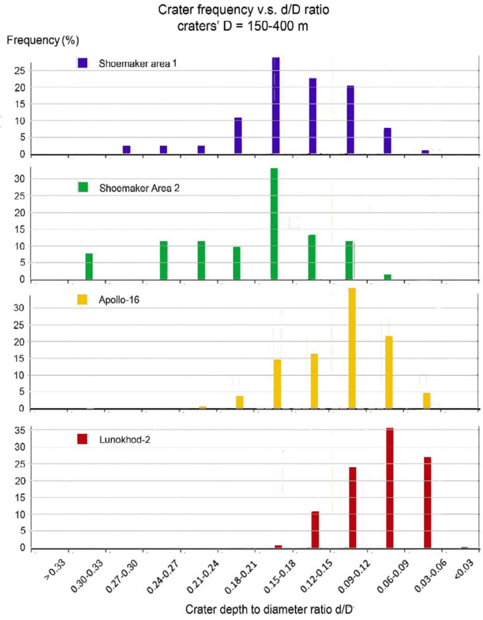

Fig. 1. Histograms of the relative depth (*d*/*D*) values for craters of the Shoemaker floor Areas 1 and 2 and the Apollo-16 and Lunokhod-2 sites

It is seen in Fig. 1 (see next page) that small craters on the permanently shadowed floor of Shoemaker are systematically deeper than craters in the Lunokhod-2 and Apollo-16 areas “normally” illuminated by the Sun. The deepest craters, which are obviously the youngest in their size range, of the Shoemaker floor Areas 1 and 2 have d/D values ~0.3, while the deepest craters of the Lunokhod-2 and Apollo-16 sites have d/D values ~0.2. Mean d/D for 74 craters of Area 1 with D = 150–400 m is 0.147, for 60 craters of Area 2 it is 0.18, for 130 craters of Apollo-16 site it is 0.114, and for 288 craters of Lunokhod-2 working area it is 0.082.

DISCUSSION:

We suggest that this may be due to presence of water ice in the target material of the Shoemaker floor. LCROSS experiment in the floor of polar crater Cabeus showed that content of water ice in the crater floor material may be ~5 mass% [5]. It looks obvious that presence of water ice in the upper 1–2 m of the polar regolith (0.51±0.04 mass% in the case of Shoemaker crater [6]) cannot influence the cratering mechanics for craters 150–400 m in diameter. Thickness of the ice-containing material in the case of Shoemaker floor should be commensurate with the depth of penetration for craters of the considered size (D = 150–400 m), that is ~30–80 m.

Some numerical simulations considering cratering in target with ice layer on top of basalts [7] and cratering experiments with dry and water-saturated sandstones [8] showed influence of water ice and liquid water presence on the cratering process. But the situations considered in these publications differ from our case. So, they do not explain the concrete mechanism of crater deepening due to admixture of water ice in the Shoemaker case.

Interesting that [9] measured the depth/diameter ratio of approximately 12 000 lunar craters of 2.5–15 km in diameter using Lunar Reconnaissance Orbiter data and found that craters become shallower near the south pole of the Moon. They found than near the south pole, craters become ~15 % shallower. The average shallowing is ~10±1 m. They concluded that it is due to the presence inside these craters of rather thick ice deposits. Our observations show the opposite trend, but craters considered by us are by 1 to 1.5 orders of magnitude smaller than those considered by [9] and suggested by them ice in the crater floor material even may be the factor of deepening of considered by us craters of 150 to 400 m in diameter.

CONCLUSION:

Craters of the Shoemaker floor are systematically deeper than those in the Lunokhod-2 and Apollo-16 areas. This maybe an effect of presence of water ice in the Shoemaker target material. Similar studies in other permanently shadowed areas are necessary to understand if the mentioned crater deepening is present there too.

Acknowledgements:

In this work A.T. Basilevsky was supported by the Russian Science Foundation grant no. 21-17-00035: Estimates of the rate of exogenous resurfacing on the Moon, and Yuan Li was supported by the grant from JiangSu education department with project no. 20KJD160001. Authors are grateful to B.A. Ivanov, S.S. Krasilnikov, I.P. Karachevtseva and A.B. Sanin for their help.

References:

[1] *Basilevsky A.T. Li Yuan, Fang Li Gang.* Surface morphology inside the PSR area of polar crater Shoemaker in comparison with that of the sunlit areas // The 13th Moscow Solar System Symposium 2022. Moscow. Russia. Abs. 13MS3-MN-08-ORAL.

[2] *Tye A.R., Fassett C.I., Head J.W. et al.* The age of lunar south circumpolar craters Haworth, Shoemaker, Faustini, and Shackleton: Implications for regional geology, surface processes, and volatile sequestration // Icarus. 2015. V. 255. P. 70–77. https://doi.org/10.1016/j.icarus.2015.03.016.

[3] http://pds-geosciences.wustl.edu/lro/lro-l-lola-3-rdr-v1/lrolol_1xxx/browse/lola_gdr/

[4] *Karachevtseva I.P., Kozlova N.A., Kokhanov A.A. et al.* Cartography of the Luna-21 landing site and Lunokhod-2 traverse area based on Lunar Reconnaissance

Orbiter Camera images and surface archive TV-panoramas // Icarus. 2017. V. 283. P. 104–121. https://doi.org/10.1016/j.icarus.2016.05.021.

[5] *Colaprete A., Schultz P., Heldmann J. et al.* Detection of water in the LCROSS ejecta plume // Science. 2010. V. 330. Iss. 6003. P. 463–468. DOI: 10.1126/science.1186986.

[6] *Sanin A.B., Mitrofanov I.G., Litvak M.L. et al.* Hydrogen distribution in the lunar polar regions // Icarus. 2017. V. 283. P. 20–30. https://doi.org/10.1016/j.icarus.2016.06.002.

[7] *Senft L.E., Stewart S.T.* Impact crater formation in icy layered terrains on Mars // Meteoritics and Planetary Science. 2008. V. 43. iss. 12. P. 1993–2013. https://doi.org/10.1111/j.1945-5100.2008.tb00657.x.

[8] *LaJeunesse J.W., Hankin M., Kennedy G.B. et al. Dynamic* response of dry and water-saturated sand systems // J. Applied Physics. 2017. V. 122. Art. No. 015901. 11 p. https://doi.org/10.1063/1.4990625.

[9] *Rubanenko L., Venkatraman J., Paige D.A.* Thick ice deposits in shallow simple craters on the Moon and Mercury // Nature Geoscience. 2019. V. 12(8). P. 597–601.

PHOTOGEOLOGICAL ANALYSIS OF THE TECTONICALLY DEFORMED IMPACT CRATER IN THE SOUTH POLE REGION OF THE MOON

A.T. Basilevsky[1], S.S. Krasilnikov[2], M.A. Ivanov[1]
[1] *Vernadsky Institute of Geochemistry and Analytical Chemistry, RAS, Moscow, Russia, atbas@geokhi.ru*
[2] *Planetary Remote Sensing Laboratory, Department of Land Surveying and Geo-Informatics, The Hong Kong Polytechnic University, Hong Kong, PR China, sergey.krasilnikov@polyu.edu.hk*

KEYWORDS:
The Moon, crater, fractured floor, galley, surface texture, crater age, age of the crater floor, magmatic activity

INTRODUCTION:
Space agencies of a number of countries plan for near future studies in the South Pole region of the Moon. This is because there in regolith are present ices of volatiles (that typical for the North Pole region too) and because there is rim of South Pole – Aitken impact basin, the largest and the most ancient on the Moon. South Pole region is highlands with predominance of impact craters. Among the latter sometimes are observed craters with gullies (fractures) on their floors. Such floor-fractured craters are also observed in other lunar regions and their floors' fracturing is considered as resulted from magmatic activity beneath the crater floor [1–2]. Such combination of impact and magmatic processes is very interesting and we study one of such craters located in south polar area (Fig. 1). Coordinates of its center are 126.59°W, 64.32°S and diameter is 34 km. Our method is photogeological analysis of images. More extended description of this study is presented in [3].

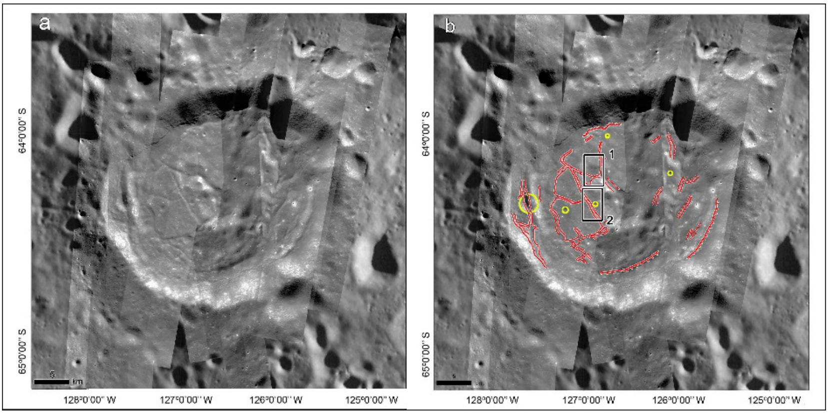

Fig. 1. Mosaic of LROC NAS images showing the considered crater (*a*); the same with shown on the floor gullies and scarps (red) and prominent craters (yellow) (*b*). Black rectangles outline areas shown in Fig. 2 and 3.

OBSERVATIONS AND MEASUREMENTS:
In the vicinities of the considered crater, besides numerous craters with diameters up to several tens of kilometers, there are chains of secondary craters. It is seen in Fig. 1 that the considered crater floor is complicated by hills, gullies and scarps. Central peak is absent and in morphologic classification the considered crater belongs to class Dawes [4]. Hills, gullies and scarps are gentle-sloped with slope steepness <10–15°, rarely up to 20° and with no shadows on the used for this mosaic NAC images. Shadows are seen only in a few craters with diameters 300–500 m and smaller. In a number of places, the inner slope of the considered crater merges into arcuate gullies.

Gullies near the inner slopes and within the floor area are more numerous in the western part of the floor. They are 2 to 20 km long, 0.3–1 km wide and 50–150 m deep. Planimetrically they form a polygonal system. Scarps are observed close to inner slope of the crater in its northern, southern and south-eastern parts. Their length is 6–10 km, height 50–150 m.

To estimate age of the considered crater we counted in the south-western part of its rim craters of 300 m to 2 km in diameter. To estimate age of the considered crater floor we counted craters of 500 to 900 m in diameter in two areas where the surface slopes were <5°. It was found that the crater age is ~3.85 Ga. But here we cannot exclude presence of mentioned above secondary craters so this value may be overestimation. Estimates for the crater floor showed two values: ~1 and ~3.5 Ga. The first value probably relates to the age of the crater floor reworking by the suggested magma intrusion, while value ~3.5 Ga relates to the considered crater age.

Below is analyzed surface morphology in two subareas of the considered crater floor (black rectangles in Fig. 1*b*) using the NAC images with resolution ~1 m taken at the Sun elevations 14.3 and 24.1°.

Figure 2 shows subarea 1, where one of the gullies is forking. It is seen that at the gulley edges there are no scarps. Steepness of their inner slopes first downslope increases, then decreases. Texture of the regolith surface is wrinkled. This is typical for the inclined surfaces and is resulted due to the downslope regolith material movement provoked by meteorite impacts and moonquakes. There are seen craters up to 50-100 m in diameter, but they are rather rare probably due to their accelerated destruction on the slopes [5].

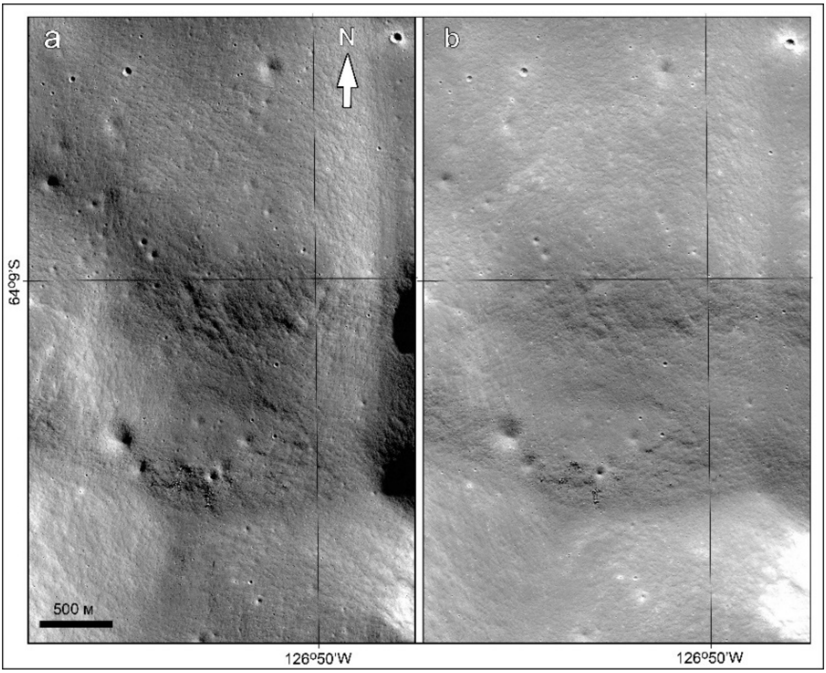

Fig. 2. Fragments of NAC images M1122039053LE/RE (*a*) and M135960042LE (*b*) with resolution 0,88 m and height of the Sun above the horizon 14,3 and 24,1°, correspondingly.

Figure 3 shows subarea 2, where is present the NW-SE oriented gulley which characteristics are the same as for gullies in subarea 1. Near the NE edge of this gulley is 700-m crater. Based on position of shadow in it (see Fig. 3*a*) its relative depth is ~0.25 and steepness of the slopes is 15-25°, that related it to morphologic class B, but with unusually large depth. Its age should be <1 Ga [5]. Absence of its ejecta in the adjacent part of the gulley suggests that that the crater is older than the gulley.

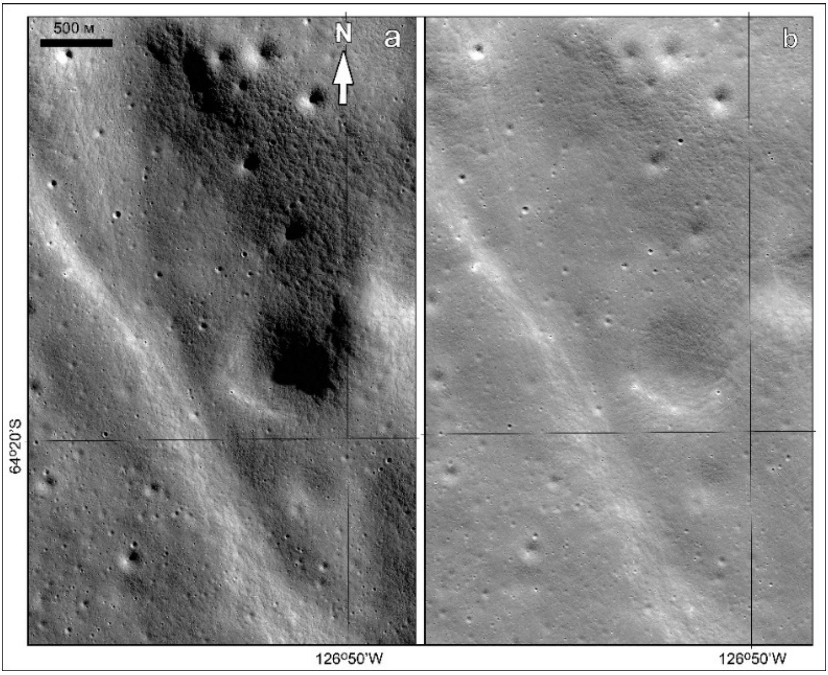

Fig. 3. Fragments of NAC images M1122039053LE/RE (*a*) and M135960042LE (*b*) with resolution 0,88 m and height of the Sun above the horizon 14,3 and 24,1°, correspondingly.Conclusion:

The considered 34-km crater certainly deserves further studies: It is interesting to look if the suggested young magmatic activity influenced details of the mineralogic composition as well as concentrations of water ice and chemically bound water in the crater floor regolith. We plan to apply to International Astronomical Union suggesting to name this crater “Galimov” in honor of late geochemist and planetologist academician Eric Galimov, who was director of the Vernadsky Institute of Geochemistry and Analytical Chemistry of Russian Academy of Sciences. We believe that there will be many publications about the considered crater and name of Galimov will be often mentioned.

Acknowledgements:
A.T. Basilevsky and M.A. Ivanov were supported by the Russian Science Foundation grant no. 21-17-00035: Estimates of the rate of exogenous resurfacing on the Moon.

References:
[1] *Schultz P.H.* Floor-fractured lunar craters // Moon. 1976. V. 15. P. 241-273.
[2] *Jozwiak L.M., Head J.W., Zuber M.T. et al.* Lunar floor-fractured craters: Classification, distribution, origin and implications for magmatism // J. Geophysical Research. 2012. V. 117. Iss. E11. Art. No. E11005. https://doi.org/10.1029/2012JE004134.
[3] *Basilevsky A.T. et al.* Impact crater with of tectonic deformations in south polar region of the Moon // Solar System Research. 2024. V. 58. No 1. (In Press).
[4] *Basilevsky A.T., Ivanov B.A., Florensky K.P. et al.* Impact Craters on the Moon and Planets. M.: Nauka. 1983. 232 p. (In Russian).
[5] *Basilevsky A.T.* On the evolution rate of small lunar craters // 7th Lunar Science Conference: Proc. 1976. V. 1. P. 1005–1020.

EVIDENCE FOR EXTENSIVE CRYPTOMARIA IN THE CENTER OF THE SOUTH POLE–AITKEN BASIN

X. Wang[1,2], J.W. Head[2]
[1] *Key Laboratory of Lunar and Deep Space Exploration, National Astronomical Observatories, Chinese Academy of Sciences, Beijing, China, wangx01@nao.cas.cn*
[2] *Department of Earth, Environmental, and Planetary Sciences, Brown University, Providence, RI, USA, James_Head@brown.edu*

KEYWORDS:
South Pole-Aitken (SPA) basin, Central South Pole-Aiken basin compositional anomaly (SPACA), cryptomare; SPA impact melt, lunar farside volcanism, crater size-frequency distribution (CSFD) analysis

INTRODUCTION:
Most lunar farside maria were identified as concentrated within the SPA basin, which is the largest observable basin on the Moon. Nevertheless, these identified mare patches within this largest basin appears to be spotty [1], and have relatively young ages (Imbrian and younger) [2]. Are there still some buried or obscured old maria/cryptomaria within the basin, especially in the center of the basin where mare deposits are usually observed in the large nearside basins? Previous spectral investigation reported a compositional anomaly in the center of the SPA basin named SPACA [3]. SPACA exhibits a pervasive high-Ca pyroxene (HCP) feature, while the surrounding unit is dominated by abundant Mg-rich low-Ca pyroxene (LCP). In addition, its albedo is slightly higher than the typical maria but lower than the surroundings. These characteristics might indicate that SPACA represent potential cryptomaria occurring in the center of the SPA basin. However, SPACA has also been interpreted to originate from the differentiated SPA impact melt [4], or non-mare volcanisms induced by the SPA impact [5]. Due to these uncertainties, we reassess these theories for the origin of SPACA.

COULD SPACA ORIGINATE FROM DIFFERENTIATED IMPACT MELT?
We reconsider the differentiated impact melt origin for SPACA from the perspective of the scale of the SPA impact melt sheet. The large-scale topography of the SPA basin in Figure 1a shows that SPACA is confined only within ~350 km from the center; yet the SPA central depression is much larger, ~700 km from the center. In addition, the entire central depression has a relatively thin crust (Fig. 1*b*). We compare the SPA basin to the Orientale basin, the best-preserved multi-ring basin on the Moon. A central depression also occurs in the Orientale basin with a characteristic thin crust (Fig. 1*c*, *d*), lying within the Inner Rook ring (IR). Two best-fit topographic ellipses of the SPA basin were previously identified [6] (E1, E2 in Fig. 1*a*, *b*). These two ellipses appear to correspond to the Outer Rook ring (OR) and the Cordillera ring (CD) of the Orientale basin, respectively. Given that large basin with concentric rings often shows ring spacing roughly proportional to √2 [7], the location of SPA inner ring could be approximated (the dashed ellipse in Fig. 1*a*, *b*), which is coincident with the edge of the central depression as observed in the topography. In Orientale, impact melt deposits occupy the entire central depression [8]. The SPA central depression may be analogous to this, suggesting the scale of SPACA may be much smaller than a region representing a differentiated SPA impact melt sheet.

COULD SPACA EXTENSIVE SPA CENTRAL CRYPTOMARIA?
We perform CSFD analyses on craters with diameters over 5 km in the three SPA interior compositional zones. The crater data used is from LROC database (5–20 km in diameter) and [9] (>20 km in diameter). As shown in Figure 2, the Mg-pyroxene Anulus (MA) and the Heterogeneous Anulus (HA) of the SPA basin show comparable patterns, and a clear, separable distinction can be observed between SPACA and these two. The obvious deflection at the

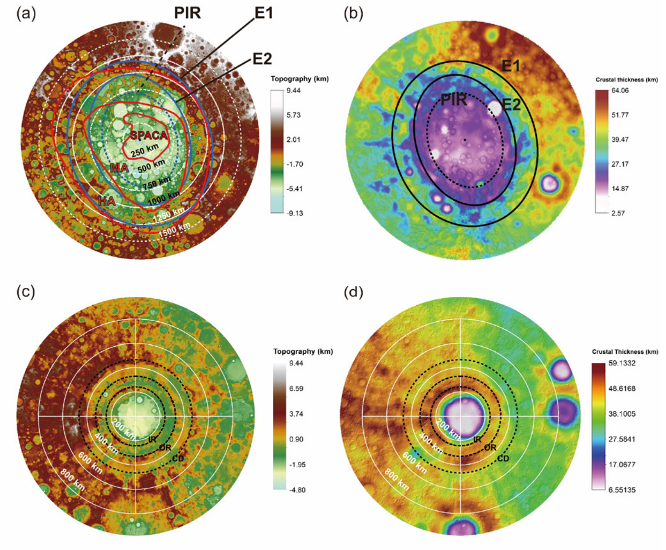

Fig. 1. Topography and Crustal Thickness maps for SPA and Orientale. E1, E2 and PIR in (*a*) and (*b*) refer to the two ellipses from [6] and the potential location of SPA inner ring, respectively. The compositional zones in red outlines are from [3]. IR, OR and CD in (*c*) and (*b*) refer to the Inner Rook ring, Outer Rook ring and Cordillera ring of the Orientale basin, respectively

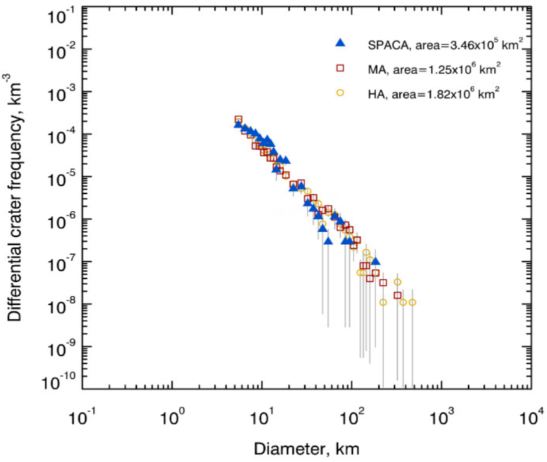

Fig. 2. CSFD analysis for craters with diameters over 5 km in the three SPA interior compositional zones

SPACA CSFD plot strongly suggests that resurfacing events have occurred here before. The HCP composition of SPACA further supports the interpretation that resurfacing events are likely to be associated with basalt filling. In addition, impact rays (e.g., from Orientale) and secondary crater chains are widely recognizable within SPACA, indicating that this area was also modified by subsequent impact craters and basins. This may account for the increased albedo. Eventually, the extensive SPA central cryptomaria were formed.

The thickness of this potential SPA central cryptomaria can also be determined from the CFSD analysis. The deflection occurs at ~70 km for SPACA (see Fig. 1), suggests that the pre-resurfacing craters with diameters below 70 km may have been completely buried by the subsequent volcanic activities [10]. Therefore, the rim heights for 70 km diameter craters are taken to represents the average thickness of the cryptomaria in the SPA basin center, which is ~1.29 km according to the rim height/diameter relationship [11].

This is consistent with the 1–2 km thick cryptomare deposits in the SPA center predicted by the lava flooding model [12]. On the basis of the regional geological mapping [13], we infer that these SPA central cryptomaria may be no younger in age than the Early Imbrian period.

CONCLUSIONS:

We conclude that the central region of the SPA basin has experienced widespread resurfacing events. SPACA likely originates from extensive cryptomaria deposits in the basin center rather than the differentiated impact melt sheet. These old mare basalts were modified and buried by ejecta deposits from nearby or distant craters or basins, increasing their albedo and eventually forming cryptomaria. This work also demonstrates that SPA basin can be placed into the population of virtually all other impact basins on the Moon in having been filled with voluminous and potentially continuous post-basin formation mare deposits.

References:

[1] *Yingst R.A., Head J.W.* Volumes of lunar lava ponds in South Pole-Aitken and Orientale Basins: Implications for eruption conditions, transport mechanisms, and magma source regions // J. Geophysical Research: Planets. 1997. V. 102. Iss. E5. P. 10909–10931. https://doi.org/10.1029/97JE00717.

[2] *Pasckert J.H., Hiesinger H., van der Bogert C.H.* Lunar farside volcanism in and around the South Pole – Aitken basin // Icarus. 2018. V. 299. P. 538–562. https://doi.org/10.1016/j.icarus.2017.07.023.

[3] *Moriarty D.P., Pieters C.M.* The Character of South Pole-Aitken Basin: Patterns of Surface and Subsurface Composition // J. Geophysical Research: Planets. 2018. V. 123. Iss. 3. P. 729–747. https://doi.org/10.1002/2017JE005364.

[4] *Uemoto K., Ohtake* M., *Haruyama* J. *et al.* Evidence of impact melt sheet differentiation of the lunar South Pole-Aitken basin: Observation of the SPA Impact Melt Sheet // J. Geophysical Research: Planets. 2017. V. 122. Iss. 8. P. 1672–1686. https://doi.org/10.1002/2016JE005209.

[5] *Moriarty D.P., Pieters C.M.* The nature and origin of Mafic Mound in the South Pole-Aitken Basin // Geophysical Research Letters. 2015. V. 42. Iss. 19. P. 7907–7915. https://doi.org/10.1002/2015GL065718.

[6] *Garrick-Bethell I., Zuber M.T.* Elliptical structure of the lunar South Pole – Aitken basin // Icarus. 2009. V. 204. Iss. 2. P. 399–408. https://doi.org/10.1016/j.icarus.2009.05.032.

[7] *Pike R.J., Spudis P.D.* Basin-ring spacing on the Moon, Mercury, and Mars // Earth, Moon and Planets. 1987. V. 39. Iss. 2. P. 129–194.

[8] *Vaughan W.M., Head J.W., Wilson L., Hess P.C.* Geology and petrology of enormous volumes of impact melt on the Moon: A case study of the Orientale basin impact melt sea // Icarus. 2013. V. 223. Iss. 2. P. 749–765. https://doi.org/10.1016/j.icarus.2013.01.017.

[9] *Head J.W., Fassett A.I., Seth J.K. et al.* Global Distribution of Large Lunar Craters: Implications for Resurfacing and Impactor Populations // Science. 2010. V. 329. Iss. 5998. P. 1504–1507. DOI: 10.1126/science.11950.

[10] *Hiesinger H., Head III J.W., Wolf U. et al.* Lunar mare basalt flow units: Thicknesses determined from crater size-frequency distributions // Geophysical Research Letters. 2002. V. 29. Iss. 8. 89-1–89-4. https://doi.org/10.1029/2002GL014847.

[11] *Pike R.J.* Geometric interpretation of lunar craters: Report. 1980. Ser. Prof. Paper. No. 1046-C. P. C1–C77.

[12] *Whitten J.L., Head J.W.* Detecting volcanic resurfacing of heavily cratered terrain: Flooding simulations on the Moon using Lunar Orbiter Laser Altimeter (LOLA) data // Planetary and Space Science. 2013. V. 85. P. 24–37. https://doi.org/10.1016/j.pss.2013.05.013.

[13] *Poehler C.M., Ivanov M.A., van der Bogert C.H. et al.* The Lunar South Pole – Aitken Basin Region: A New Geological Map // Europlanet Science Congress 2020. V. 14. Art. No. EPSC2020-600. https://doi.org/10.5194/epsc2020-600

INVERSION OF GLOBAL LUNAR OXIDES USING CHANG'E-2 LUNAR MICROWAVE SOUNDER DATA

Z. Yuan[1,2], Y. Li[1,2], Y. Zhang[2,3], J. Ping[2,3]

[1] *Beijing University of Technology, Faculty of Information Technology, Beijing, China, yuli@bjut.edu.cn*

[2] *Key Laboratory of Lunar and Deep Space Exploration, National Astronomical Observatories, Chinese Academy of Sciences, Beijing China*

[3] *School of Astronomy and Space Science, University of Chinese Academy of Sciences, Beijing, China*

KEYWORDS:

Chang'e-2 satellite, lunar oxides, machine learning, quantitative inversion, microwave radiation, brightness temperature

INTRODUCTION:

The study of the abundance of the major lunar oxides plays a key role in understanding the evolution and formation of the Moon. Till now, several studies concentrated on the inversion of major Lunar oxides based on multi-spectral data [1–4]. However, multi-spectral remote sensing can only observe the shallow layer of the Lunar surface. This shortcoming limits the effective abundance inversion under the lunar surface.

Chang'e-2 Lunar Microwave Sounder (CELMS) has been proved a complementary tool to study both the Lunar surface and sub-surface for its penetration depth ranging from several centimeters to several meters by four operation frequencies: 3.0, 7.8, 19.35 and 37.0 GHz [5–6]. In this study, we use eight normalized brightness temperature features including four noon features (nT_B) and four brightness temperature difference features (ndT_B) between noon and midnight (shown in Figure 1) to inverse global oxides including Al_2O_3, CaO, FeO, MgO and TiO_2 based on small-patch convolutional neural network (SP-CNN) model [3, 7]. The training and testing samples include 40 in-situ returned regolith samples from Apollo, Luna and Chang'e missions [2–3]. To the best of our knowledge, this is the first study and product to comprehensively inverse the serial oxides with CELMS data.

The scatter plots of five major oxides of both training and validation sets by SP-CNN model are shown in Figure 2. And the corresponding mapping results are displayed in Figure 3. Our results generally agree with those derived from previous studies from multi-spectral data, which demonstrates the feasibility of the proposed method, but presents some brand-new important hints:

1) Compared with other multi-spectral-based machine learning inversion results [2–4], our oxide maps exhibit more various changes in major maria regions that highly related to the period of the basalt eruption, such as Oceanus Procellarum, Mare Imbrium, Mare Nubium, Mare Tranquillitatis, and Mare Fecunditatis. The possible reason is that CELMS data can reflect the characteristic of deep-layer structure, so yields specific changes of oxide abundances effected by basalt eruption period.

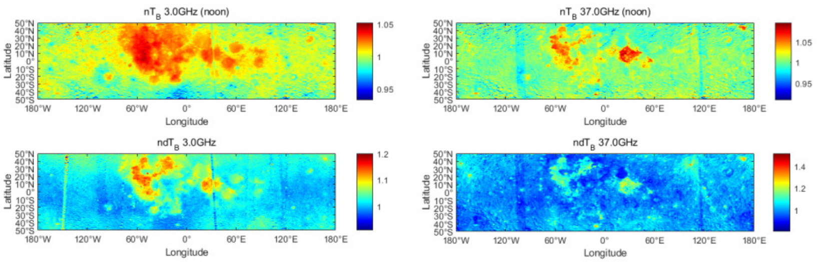

Fig. 1. Normalized noon (nT_B) and difference (ndT_B) maps of 3.0 GHz and 37.0 GHz (50° N ~ 50 °S)

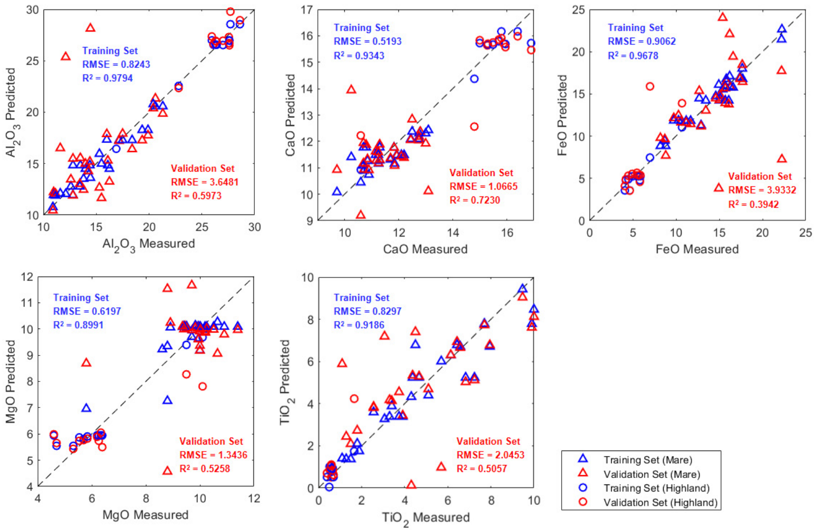

Fig. 2. Scatter plots of five major oxides

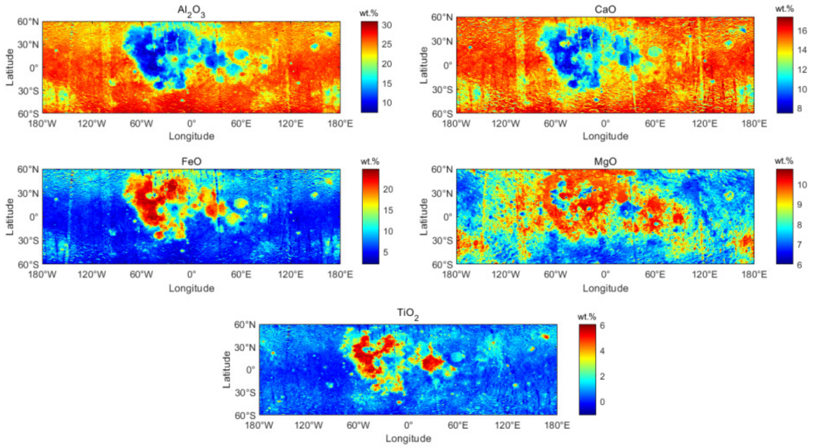

Fig. 3. Maps of five lunar global major oxides by our approach (60° N ~ 60 °S).

2) The abundances of MgO in eastern Oceanus Procellarum, western Mare Imbrium and Mare Tranquillitatis are shown relatively lower values than their vicinities compared with the previous studies [2-4]. One of the hypothesis is that deep-layer brightness temperature difference (ndT_B) is an impact factor because lower MgO abundances in maria regions show high correlations with 3.0 GHz ndT_B. But the exact relationships between MgO abundance and CELMS brightness temperature should be further investigated in future studies.

3) The abundance of TiO_2 in maria regions by our study are distinct from the previous results by multi-spectral data. In the TiO_2 maps by [2–3], the TiO_2 abundance of Mare Tranquillitatis is outstandingly higher than other mares. However, in our results, Oceanus Procellarum, Mare Imbrium and Mare Tranquillitatis exhibit the three highest TiO_2 abundance regions in the whole lunar surface and their differences are obviously less than previous results. Spectral information only reflects the shallow surface characteristic. In 37.0 GHz nT_B and ndT_B maps (shown in Figure 1) which reflect approximate depths with spectral information, it is obvious that Mare Tranquillitatis shows higher brightness temperature than other mares. But in 3.0 GHz nT_B and ndT_B maps, the brightness temperature distributions are quite different: Oceanus Procellarum presents the highest brightness temperature in 3.0 GHz nT_B map, and Oceanus Procellarum, Mare Imbrium and Mare

Tranquillitatis exhibit similar difference temperature value. This deep-layer information has never been revealed by spectral data before. And the abundance of Ti is one of the most important factors of the change of brightness temperature [8]. Accordingly, the depth information from CELMS data is crucial in understanding the composition of lunar regolith.

In conclusion, CELMS data provides both reliable and complementary information in studying lunar geological structure. This study presents five new lunar oxide maps that contains surface and sub-surface regolith characters. Further studies will be conducted on the influence of the difference depth of the brightness temperature on the oxide inversion.

Acknowledgement:
This work was supported in part by the National Key Research and Development Program of China (2021YFA0715101), the Strategic Priority Program of the Chinese Academy of Sciences (XDB41020104) and the Natural Science Foundation of China (41706201).

References:

[1] *Wu S., Chen J., Li L., Zhang C. et al.* Quantitative inversion of lunar surface chemistry based on hyperspectral feature bands and extremely randomized trees algorithm // Remote Sensing. 2022. V. 14. No. 20. Art. No. 5248. https://doi.org/10.3390/rs14205248.

[2] *Wang X., Zhang J., Ren H.* Lunar surface chemistry observed by the KAGUYA multiband imager // Planetary and Space Science. 2021. V. 209. P. 105360. https://doi.org/10.1016/j.pss.2021.105360

[3] *Zhang L., Zhang X., Yang M. et al.* New maps of major oxides and Mg# of the lunar surface from additional geochemical data of Chang'E-5 samples and KAGUYA multiband imager data // Icarus. 2023. V. 397. Art. No. 115505. https://doi.org/10.1016/j.icarus.2023.115505.

[4] *Ma M., Li B., Chen S. et al.* Global estimates of lunar surface chemistry derived from LRO diviner datam // Icarus. 2022. V. 371. Art. No. 114697. https://doi.org/10.1016/j.icarus.2021.114697.

[5] *Cai Z., Lan T.* Lunar brightness temperature model based on the microwave radiometer data of Chang'E-2 // IEEE Trans. Geoscience and Remote Sensing. 2017. V. 55. No. 10. P. 5944–5955. DOI: 10.1109/TGRS.2017.2718027.

[6] *Li Y., Yuan Z., Meng Z. et al.* A unified brightness temperature features analysis framework for mapping mare basalt units using Chang'e-2 Lunar Microwave Sounder (CELMS) data Remote Sensing, 2023. V. 15. No. 7. Art. No. 1910. https://doi.org/10.3390/rs15071910.

[7] *LeCun Y., Bottou L., Bengio Y., Haffner P.* Gradient-based learning applied to document recognition // Proc. IEEE. 1998. V. 86. Iss. 11. P. 2278–2324. DOI: 10.1109/5.726791.

[8] *Meng Z., Chen S., Wang Y. et al.* Reevaluating Mare Moscoviense and its vicinity using Chang'e-2 microwave sounder data // Remote Sensing. 2020. V. 12. No. 3. Art. No. 535. https://doi.org/10.3390/rs12030535.

MARE MESAS IN MARE FECUNDITATIS: CHARACTERISTICS OF A NEWLY DOCUMENTED CLASS OF MARE VOLCANIC FEATURE

J.W. Head[1], M.A. Ivanov[2]
[1] *Department of Earth, Environmental and Planetary Sciences, Brown University, Providence, USA, james_head@brown.edu*
[2] *Vernadsky Institute of Geochemistry and Analytical Chemistry RAS, Moscow, Russia*

KEYWORDS:
Lunar volcanism, Mare Fecunditatis, mesas, flood basalts, early volcanic fill.

INTRODUCTION:
A wide diversity of lunar mare volcanic features has been identified in previous studies of global lunar volcanism and shown to be related to the characteristics of dikes approaching and reaching the surface [1]. In our recent detailed geological mapping of the Mare Fecunditatis region of the Moon [2], we documented an unusual type of feature noted earlier [3–4] but not previously described with recent image/topography data. Here we describe several occurrences of these features, which we call “mare mesas” due to their generally relatively steep sides and often flat tops (Figures 1–3). We explore several candidate origins for “mare mesas” and encourage the search for similar features in other parts of the maria.

GEOLOGICAL SETTING:
On the basis of our regional and local studies of the Fecunditatis basin and Mare Fecunditatis (location of the Luna-16 sample return landing site), we find that: 1) crater size-frequency measurements yield an absolute model age (AMA) of ~3.81 Ga, suggesting resurfacing after the Fecunditatis impact event but before the latest mare emplacement; 2) Mare Fecunditatis mare surface AMAs are ~3.45 Ga, consistent with most radiometric age determinations from Luna-16 samples (clustered at ~3.5–3.4 Ga); 3) Mare Fecunditatis current surface is likely to represent the latter episodes of volcanism, but the presence of older basalts in the Luna-16 sample should not be ruled out, taking into account the likely multiple sources of its materials and the complex nature of the emplacement of lavas in Mare Fecunditatis.

Fecunditatis mare materials have been subdivided into unit mMF and include materials of flat-topped mesas (unit mm). The mesas are defined by flat-topped hills less than a few kilometers across and tens of meters high (up to a few hundred meters) with scarp-like angular or scalloped edges (see Figs. 1–3). This unit corresponds to the table-like hills described earlier in the NE portion of Mare Fecunditatis [3] and elsewhere [4]. Steep-sided dome-like features and a narrow sinuous ridge, which is morphologically different from the mare wrinkle ridges, occur on the summit of the largest mesa. Several elongated, flow-like features extend from the mesa and appear to be embayed by the surrounding mare. The surface of the mesa is draped by a regolith layer that obscures details of the mesa internal structure. High-resolution NAC images, however, show that the steeper slopes of the mesa expose numerous large (a few meters across) boulders arranged in layers and the body of the mesa appears to consist of stacks of meters-thick layers. The high-resolution, Kaguya based map of FeO abundance [5] shows that the mesa has the same abundance of iron as the surrounding mare. These characteristics suggest that the mesa represent a volcanic feature that pre-dates the emplacement of vast Fecunditatis volcanic mare plains.

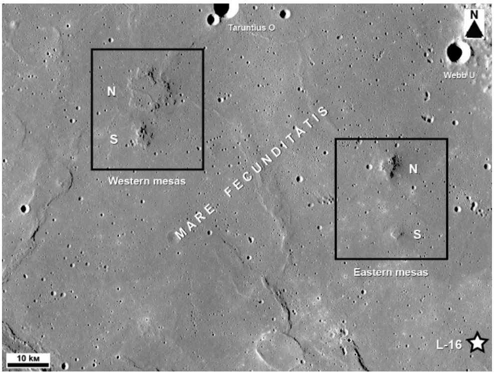

Fig 1. Fecunditatis Mare Mesas

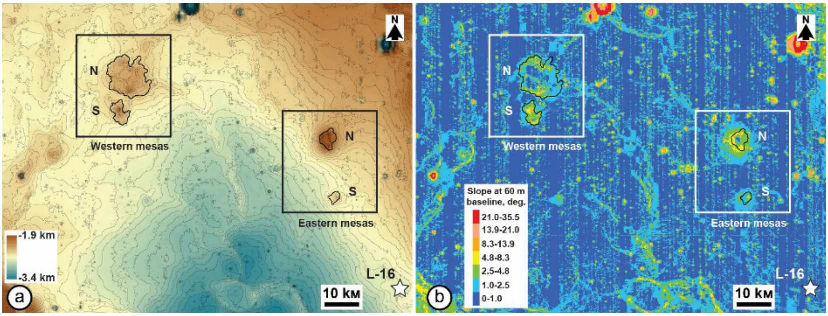

Fig. 2. Fecunditatis Mare Mesas: (a) topography; (b) slope. LOLA topography

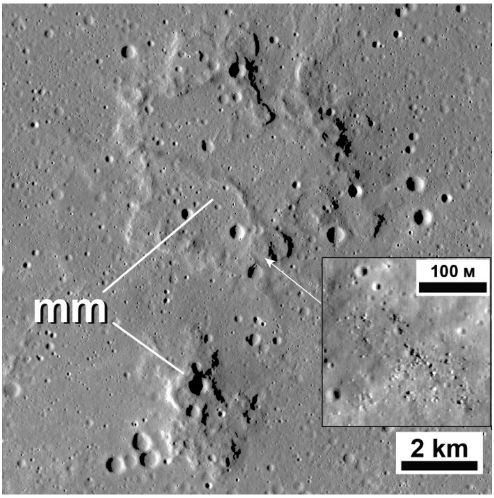

Fig. 3. Western Fecunditatis Mare Mesas. Mosaic of the Kaguya images (inset: LROC NAC image_)

REFERENCES:

[1] *Head J.W., Wilson* L. Generation, ascent and eruption of magma on the Moon: New insights into source depths, magma supply, intrusions and effusive/explosive eruptions. Part 2: Predicted emplacement processes and observations // Icarus. 2017. V. 283. P. 176–229. https://doi.org/10.1016/j.icarus.2016.05.031

[2] *Ivanov* M.A., *Head J.W., Hiesinger* H. New insights into the regional and local geological context of the Luna 16 landing site // Icarus. 2023. V. 400. Art. No. 115579. https://doi.org/10.1016/j.icarus.2023.115579.

[3] *Florensky K.P., Bazilevsky A.T., Pronin A.A.* Geological and morphological characteristics of the landing area of the automatic lunar station "Luna-16" // Lunar soil from the Sea of Plenty. Moscow: Nauka, 1974. P. 19–22 (in Russian).

[4] *Schultz P.H.* Moon morphology: interpretations based on Lunar Orbiter photography. Austin; London: Univ. Texas Press. 626 p.
[5] *Lemelin M., Lucey P.G., Miljković K. et al.* The compositions of the lunar crust and upper mantle: Spectral analysis of the inner rings of lunar impact basins // Planetary and Space Science. 2019. V. 165. P. 230–243. https://doi.org/10.1016/j.pss.2018.10.003.

INA SHIELD VOLCANO SUMMIT PIT CRATER: FORWARD-MODELING MAJOR STAGES IN ITS EVOLUTION AND COMPARISON WITH SURFACE MORPHOLOGY AND SEQUENCE

J.W. Head[1], L. Wilson[2], L. Qiao[3]
[1] *Brown University, Providence, USA, james_head@brown.edu*
[2] *Lancaster University, Lancaster, UK*
[3] *Shandong University, Weihai, China*

KEYWORDS:
Ina, strombolian, pit crater, shield volcano, mounds, vesicles, magmatic foams.

INTRODUCTION:
The enigmatic Ina feature is a 2×3 km D-shaped pit crater (Figure 1) at the summit of an ~22 km diameter shield volcano on the central lunar nearside. Ina consists of a rough, optically immature floor, with a population of smooth, meniscus-like, convex-upward optically-mature, irregularly shaped mounds [1]. Recently defined as a large "Irregular Mare Patch" (IMP), analysis of superposed impact craters revealed an Absolute Model Age (AMA) of the Ina floor mounds of ~33 Ma [2], younger that the crater Tycho and virtually all regional lunar mare deposits [3]. Two other large IMP AMAs (Sosigenes, ~18 Ma; Cauchy 5, ~58 Ma) suggested that lunar mare volcanism has continued until geologically recently [2] and may indeed be continuing today, in conflict with virtually all lunar thermal evolution models [4]. While the basic definition and observations [1–2] are not contested, interpretation of the ages fall into two categories (summarized in [5]): Ina and related IMPs represent: 1) recent lunar volcanic activity (<100 Ma), consistent with their fresh surfaces, sharp boundaries, and modern AMAs [2]; or 2) ancient volcanic activity (~3.5 Ga) consistent with their surroundings and geologic settings, with their young AMAs explained by unique substrate characteristics [6]. Here we follow our earlier theoretical work [7–9] and forward-model the late-stage behavior of a lunar shield volcano summit pit crater, as a basis for testing against observations.

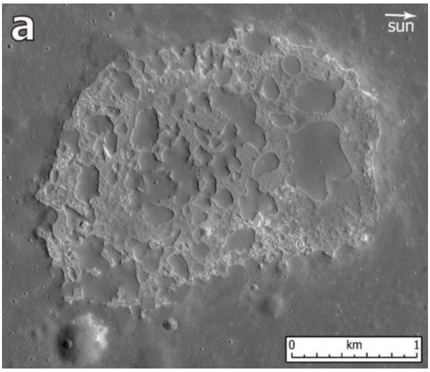

Fig. 1. Ina pit crater. LROC NAC image

THEORETICAL PREDICTIONS AND FORWARD MODELING:
Modeling of the generation, ascent, and eruption of lunar basaltic magma [7–9] has shown that eruptions progress through four basic phases [9], with the highest flux and volume occurring during the Phase 2 lava flow extrusion/shield-building stage. We therefore construct a forward-model of this process to make predictions to compare to observations. Of interest here is Stage 3 and 4, the strombolian stages, where magma rise rates decrease dramatically and strombolian activity dominates in the pit crater. *Phase 3*. (Transition to strombolian activity; occurs quickly). The main driving process is the horizontal reduction in the dike thickness due to decrease in dike excess pres-

sure and forced host rock relaxation/deformation. Magma vertical rise speed decreases greatly to <1 m/s; reduced vertical magma flow speed means that gas bubbles nucleating throughout the vertical dike extent can now rise at an appreciable rate through the liquid, and there is time for larger bubbles, especially CO bubbles being produced at great depths, to overtake smaller bubbles leading to coalescence and even greater growth. The result is very large bubbles — gas slugs — filling almost all of the dike width and producing strombolian explosions at the surface. *Phase 4*. (Dike closing, strombolian vesicular phase). Activity is entirely strombolian; tectonic stresses continue to close dike, magma extrusion at a low flux. Magma is still being forced up to lower pressure, and bubble production continues. Very minor strombolian explosive activity continues above the vent. However, a stable crust will have formed on the magma still emerging from the vent (the lid). We utilize this baseline as a forward model to assess the terminal cooling and solidification stages of the volcanic activity at Ina in order to provide more quantitative tests of the hypotheses for the formation of the pit crater interior, rough floor and mounds (Figure 2). We explore the following questions:

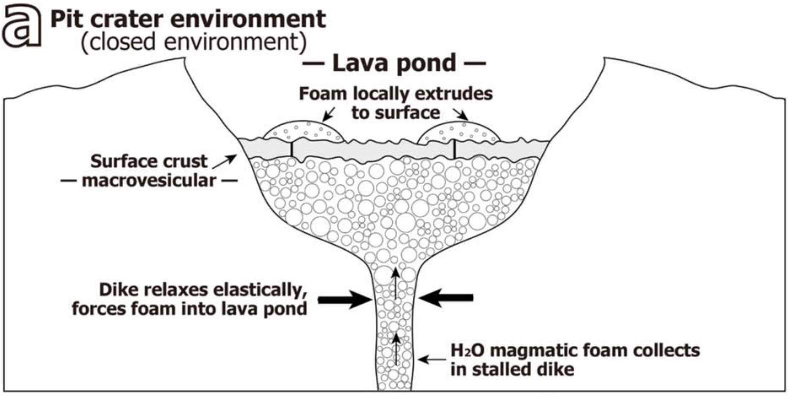

Fig. 2. Conceptual model for pit crater formation [7]

1. What is the predicted total time for cooling and solidification of the entire lava lake and feeder dike?
2. How long does strombolian activity continue before the lava lake floor (lid) is sufficiently thick that its disruption is precluded?
3. What is the fate of the volatiles degassed after lid disruption ceases?
4. What is the size of gas slugs rising from depth as the dike solidifies?
5. What is the time delay before lava lake second boiling occurs and can the exsolved volatiles disrupt the lid at this point.
6. How does the 3-D geometry of the lava lake change with time during progressive cooling and solidification?
7. What topographic changes are predicted during lava lake solidification processes?
8. What is the nature and fate of the volatiles degassed during cooling and solidification (lid, lava lake, etc.)?

On the basis of these considerations, our forward-model makes the following predictions: Radiative cooling of the upper lava lake surface causes the lava lake lid to grow to a thickness of 10–11 m in less than a year, a thickness that would generally preclude disruption due to rising gas slugs. We therefore predict a final lava lake stratigraphy consisting of an upper very rough vesicular lid surface, with vesicularity growing in volume and vesicle size with depth in the lid. At the base of the lid, exsolved volatiles would collect, varying in size from coalesced bubbles to flattened gas slugs. If the lid precluded significant diffusive loss until solidification a wide range of macrovesicles should survive, the upper limit dictated by the evolving slug volumes. A phase of second boiling occurs in the cooling lava lake in the weeks after lid stabilization.

Exsolved volatiles collect above and below the evolving solidification fronts in the central lake, their expansion offsetting subsidence due to solidification. The resulting flexure and fracturing of the lid can provide potential pathways for the underlying highly vesicular magmas to reach the surface; ensuing eruptions into the vacuum are predicted to further vesiculate the magmas, producing an 'autoregolith' overlying magmatic foams and vesicular lavas.

COMPARISON OF PREDICTIONS AND OBSERVATIONS: We apply this forward model to observed topography and morphology. We interpret the observed topography of the Ina interior (Fig. 3) to be consistent with progressive cooling and subsidence of an ancient lava lake in the terminal stage of evolution of the associated shield volcano. The rough, relatively flat floor unit represents the upper surface of the cooling lava lake lid, modified by subsequent impact cratering and vertical sifting of regolith into the predicted abundant internal voids. The stratigraphically younger floor mounds are interpreted to represent extrusions of highly vesicular magma from second boiling, extruded through late-stage flexural cracks associated with cooling and volatile inflation. The current extremely young AMAs of the mounds and floor unit, and their sharp contacts are interpreted to be due to the changes in impact cratering energy partitioning from that seen in normal dense basaltic flows, favoring vertical crushing and penetration, over lateral excavation and bowl-shaped crater formation; an unusual vertical diffusions processes (sifting of impact-generated regolith into subsurface voids [10]) dominates over lateral diffusions of traditional regolith. These predictions and interpretations can be further tested in association with the upcoming DIMPLE PRISM Mission to Ina.

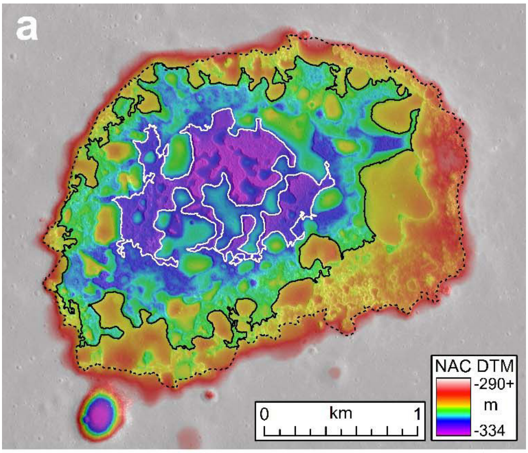

Fig. 3. Topography of Ina interior. LROC NAC DTM on LROC NAC M119815703 [6]

References:

[1] *Whitaker,* Apollo-15: Preliminary Science Report. 1972. NASA SP-289.
[2] *Braden S.E., Stopar* J.D., *Robinson M.S. et al.* Evidence for basaltic volcanism on the Moon within the past 100 million years // Nature Geoscience. 2014. V. 7. Iss. 11. P. 787–791. https://doi.org/10.1038/ngeo2252.
[3] *Hiesinger et al.*, 2014, GSA SP-477, 1.
[4] *Shearer et al.*, 2006, NVM. MSA 60.
[5] *Qiao* L., *Head J.W., Wilson* L., *Ling* Z. Ina Lunar Irregular Mare Patch Mission Concepts: Distinguishing between Ancient and Modern Volcanism Models // Planetary Science J. 2006. V. 2. Art. No. 66.
[6] *Qiao L. et al.* // J. Geophysical Research: Planets. 2019. V. 124.
[7] *Wilson L., Head J.W.* Generation, ascent and eruption of magma on the Moon: new insights into source depths, magma supply, intrusions and effusive/explosive eruptions (Part 1: Theory) // Icarus. 2017. V. 283. P. 146–175. doi: 10.1016/j.icarus.2015.12.039.
[8] *Head J.W., Wilson L.* Generation, ascent and eruption of magma on the Moon: new insights into source depths, magma supply, intrusions and effusive/explosive eruptions (Part 2: Predicted emplacement processes and observations). // Icarus. 2017. V. 283. P. 176–223. https://doi.org/10.1016/j.icarus.2016.05.031.

[9] *Wilson L., Head J.W.* Controls on Lunar Basaltic Volcanic Eruption Structure and Morphology: Gas Release Patterns in Sequential Eruption Phases // Journal of Geophysical Research Letters. 2018. V. 45. Iss. 12. P. 5852–5859. https://doi.org/10.1029/2018GL078327.
[10] *Kreslavsky M. A. Head J. W.*. "Spiders" on the Moon: Sites of Regolith Drainage into Subsurface Voids // 53rd Lunar and Planetary Science Conf. 2022. Art. No. 1830.

STUDIES OF THE FLOOR OF ZEEMAN LUNAR POLAR CRATER WITH LRO AND LUNA-25 DATA

M.V. Djachkova[1], A.B. Sanin[1], Y.D. Elyashev[1], I.G. Mitrofanov[1], M.L. Litvak[1], I.V. Polyansky[1], A.E. Zubarev[2]

[1] *Space Research Institute of the Russian Academy of Sciences, 117997 Profsoyuznaya 84/32, Moscow, Russia, djachkova@np.cosmos.ru*

[2] *Moscow State University of Geodesy and Cartography, 105064 Gorokhovsky per. 4, Moscow, Russia*

KEYWORDS:

Moon, South Polar region of the Moon, Zeeman crater, LOLA, LEND, LRO

Zeeman crater is a lunar impact crater located on the far side of the Moon in the south polar region. This crater is among the deepest craters in the southern hemisphere of the Moon and has has an unusual size ratio: its diameter is about 190 km and its depth is about 8 km. Its formation is associated with a very strong impact, which is possible if the impactor's speed is very high or its substance is very dense.

Landing cameras of the STS-L system of Luna-25 spacecraft took the images of the Zeeman crater on August 17 [1] during a flight in the orbit of an artificial satellite of the Moon. The resulting images significantly complement the currently available information about this crater.

The images revealed the different roughness features of the crater that was analyzed using the LOLA data [2]. We interpreted the differences according to the lunar geological features and examined the WEH content according to the LEND data [3].

References

[1] "Luna-25" took the first image of the lunar surface URL: https://iki.cosmos.ru/news/avtomaticheskaya-stanciya-luna-25-sdelala-pervyy-snimok-lunnoy-poverkhnosti

[2] *Smith D.E., Zuber M.T., Neumann G.A., Mazarico E., Lemoine F.G., Head J.W., Lucey P.G., Aharonson O., Robinson M.S., Sun X., Torrence M.H., Barker M.K., Oberst J., Duxbury T.C., Mao D., Barnouin O.S., Jha K., Rowlands D.D., Goossens S., Baker D., Bauer S., Gläser P., Lemelin M., Rosenburg M., Sori M.M., Whitten J., Mcclanahan T.* Summary of the results from the lunar orbiter laser altimeter after seven years in lunar orbit // Icarus. 2017. V. 283. P. 70–91.

[3] *Sanin A.B., Mitrofanov I.G., Litvak M.L., Bakhtin B.N., Bodnarik J.G, Boynton W.V., Chin G., Evans L.G., Harshman K., Fedosov F., Golovin D.V., Kozyrev A.S., Livengood T.A., Malakhov A.V., McClanahan T.P., Mokrousov M.I., Starr R.D., Sagdeev R.Z., Tret'yakov V.I., Vostrukhin A.A.* Hydrogen distribution in the lunar polar regions // Icarus. 2017. V. 283. P. 20–30.

THE EXPERIMENT LEND: 14 YEARS OBSERVATIONS OF LUNAR NEUTRON ALBEDO

M.L. Litvak, I.G. Mitrofanov, A.B. Sanin
Space Research Institute RAS, Moscow, Russia, litvak@mx.iki.rssi.ru

KEYWORDS:
LEND; LRO; Moon; neutrons; water

INTRODUCTION:
The LRO spacecraft started orbital mapping of the Moon on 15 September 2009 using circular polar orbit with ~50 km altitude [1]. In December 2011 the circular orbit was transformed into a stable elliptical orbit to maximize spacecraft lifetime. The mapping is continued until now allowing to collect a lot of science data that is very important for the lunar studies and preparation future lunar missions.

LEND is a neutron spectrometer integrated onboard LRO spacecraft to provide mapping of lunar neutron albedo with a rather high spatial resolution [2]. It uses collimated neutron detectors with a selection of lunar neutrons coming in with angles 0°–14° of the nadir direction. It provides possibility to distinguish major permanent shadowed regions and test if they/their vicinities contain subsurface water ice [3].

In this study we present the updated map of subsurface water ice in southern polar regions of the Moon based on a summary of 14 years of orbital observations.

References:
[1] *Chin G. et al.* Lunar Reconnaissance Orbiter Overview: The Instrument Suite and Mission // Space Sci. Rev. 2007. V. 129. P. 391-419.
[2] *Mitrofanov I.G. et al.* Lunar exploration neutron detector for the NASA Lunar Reconnaissance Orbiter // Space Sci. Rev. 2010. V. 150. P. 183–207.
[3] *Sanin A. B. .et al.* Hydrogen distribution in the lunar polar regions // Icarus. 2017. V. 283. P. 20-30.

INVESTIGATION OF THE COSMIC DUSTY PLASMAS WITH DUST MONITORING INSTRUMENTS

I. Kuznetsov[1], A. Zakharov[1], G. Dolnikov[1], I. Dokuchaev[1], A. Lyash[1], A. Dubov[1], M. Essam[1], V. Grushin[1], A. Kartasheva[1], E. Kronrod[3,4], T. Morozova[1], S. Popel[1], A. Poroykov[2], I. Shashkova[1], O. Voshchan[1]

[1] *Space Research Institute RAS, Moscow, Russia, kia@cosmos.ru*
[2] *National Research University "Moscow Power Engineering Institute", Moscow, Russia*
[3] *Vernadsky Institute of Geochemistry and Analytical Chemistry RAS, Moscow, Russia*
[4] *Kazan Federal University, Kazan, Russia*

KEYWORDS:
dust, lunar dust, dusty plasma, lunar lander, Luna-25, Luna-27, Phobos, Moon, asteroids

INTRODUCTION:
One of the complicating factors of the deep space exploration is the influence of the dust. The upper regolith layer of the atmosphereless bodies is electrically charged by the solar ultraviolet radiation and the flow of solar wind particles. Therefore, electric charge and thus surface potential depend on the local time, latitude and the electrical properties of the regolith.

DUST MONITORING INSTRUMENT:
Based on the ideas of the PmL instrument for Luna-25 mission a number of improvements for the next generation dusty plasma monitoring instrument is suggested. The possible orbit or in-situ configuration for the instrument is proposed.

A TEMPERATURE DISTRIBUTION MODEL IN THE LUNAR SOIL AT THE POLAR REGIONS

V.A. Dudchenko, E.N. Slyuta
Vernadsky Institute of Geochemistry and Analytical Chemistry RAS, Moscow, Russia, dudchenko@geokhi.ru

KEYWORDS:
thermal conductivity, diurnal temperature fluctuations, lunar soil, Moon exploration, polar regions

INTRODUCTION:

The diurnal temperature fluctuations in the lunar soil in the equatorial region completely attenuate at a depth of about 80 cm, where a constant temperature of about –20 °C is observed [1, ref. there in]. In the Moon Polar Regions, the Sun shines tangentially and, depending on the relief, the degree of illumination can vary from its complete absence to 80 % [2], and the temperature on the surface from 273 to 27 K [3]. Estimating the temperature distribution in the lunar soil in the Polar Regions is one of the urgent tasks at the present stage of lunar exploration and is necessary, among other things, for the development and creation of scientific equipment and various lunar soil sampling and drilling devices.

EQUATORIAL REGION:

In the equatorial region, the daily temperature variation on the surface from the minimum (night) to the maximum (day) reaches 300°. The lunar soil thermophysical properties, the diurnal variation and distribution of temperature in the lunar soil were measured in the area of the Hadley Rille in Mare Imbrium and in the Taurus Littrow in Mare Serenitatis at Apollo-15 and 17 landing sites of [4–5]. It was found that daily temperature fluctuations in the lunar soil in the equatorial region completely attenuate at a depth down to 80 cm, while annual temperature fluctuations can be traced to a depth of 2 m or more (Figure 1).

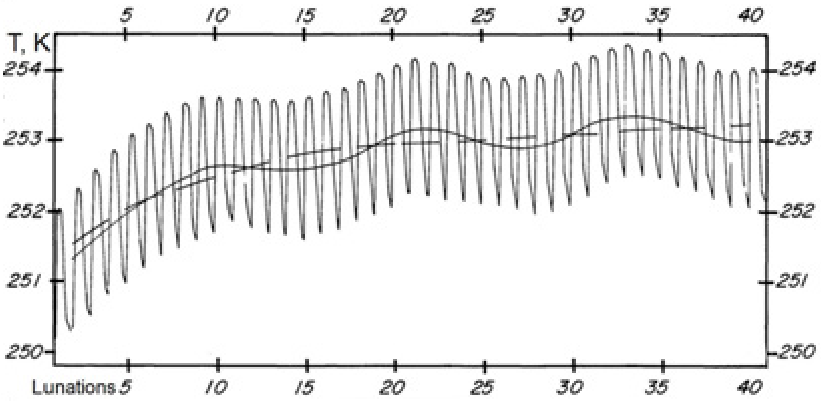

Fig. 1. Daily temperature variation (y) at a depth of 45 cm during 38 lunations (lunar days) (x) according to [6]. The smoothed solid line reflects annual temperature fluctuations minus daily variations with a resolution of ±0.015 K. The dashed line after subtracting annual temperature variations reflects the transition to an equilibrium state disturbed by the activity of astronauts on the surface

Thus, the average temperature established at depth is known, as well as daily and annual temperature fluctuations depending on depth, and the periodic dependence of the heat wave on time, i.e. function $T(z, t)$, where z is depth, t is time. To calculate a thermal wave in the lunar soil, boundary conditions and thermophysical properties of an inhomogeneous solid body (lunar soil) are required [1, ref. there in]: thermal conductivity,

$K_e(T) = (1{,}66{\cdot}10^{-2}z^{3/5}) + (8{,}4{\cdot}10^{-11}T^3)$, heat capacity,

$$c = -23.173 + 2.1270T + 1.5009\cdot10^{-2}T^2 - 7.3699\cdot10^{-5}T^3 + 9.6552\cdot10^{-8}T^4,$$

density,

$$\rho = 1.92(z + 12.2)/(z + 18).$$

The boundary conditions for the nonlinear one-dimensional heat equation are determined by the step function of the surface heating temperature from 80 to 380 K (Figure 2). Since the thermal conductivity of the upper loose soil layer with a thickness of about 3–5 cm is almost an order of magnitude less than the underlying layer [1, ref. there in], then to simplify the problem, the conditional surface is set at a depth of z = 5 cm. The next boundary condition in the form of a fixed temperature is set at a conditionally large depth, since annual temperature fluctuations at a depth of 2 m become negligible [6]. Thermal waves decay exponentially (see Fig. 2). At a depth of z ~ 30 cm, a clear asymptotic line of the average temperature value is already visible, around which oscillations occur. The straight horizontal line indicates the establishment of an equilibrium constant temperature in the lunar soil. An upward slope would indicate heating, and a downward slope would indicate cooling.

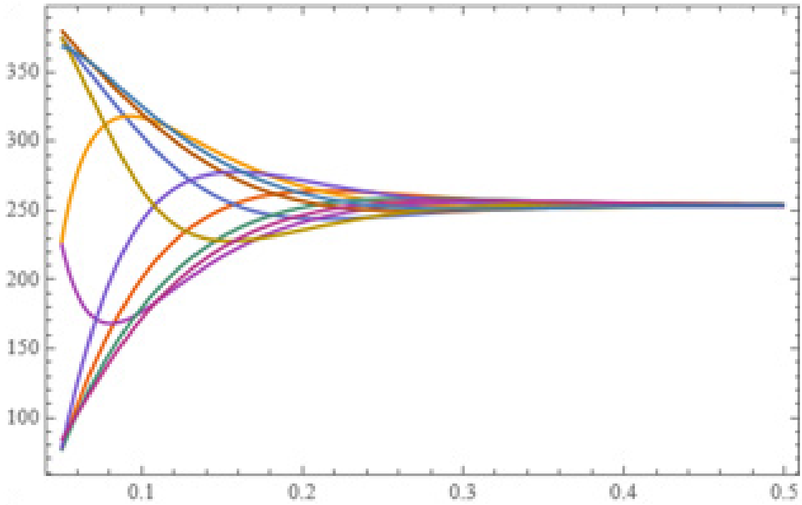

Fig. 2. Model of the daily course of temperature distribution in the lunar soil (*x*) of the equatorial region depending on the temperature on the surface (*y*) with superimposed fluctuations in the region of all possible values

The $T(z)$ model, taking into account the known thermophysical properties of the lunar soil and depending on the specified conditions on the surface (duration of day and night, average day and night temperatures on the surface), allows solving the inverse problem to determine the steady-state equilibrium temperature in the lunar soil at depth. For example, according to this model, the calculated constant temperature in the equatorial region at a depth of 45 cm is estimated at 254 K with a fluctuation of 1 K, which is in good agreement with the measured data [6] (see Fig. 1).

Polar Region: According to a comparative analysis of several sites at the South Pole, the most preferable site for accommodating a lunar scientific station [7] is site #2, a flat hill on the rim of the Shackleton crater (Figure 3), where the degree of illumination reaches 80 %, i.e., the lunar day lasts 80 %, and the night 20 % [2]. In the summer season, the average temperature is 165 K, the maximum is 255 K, and the minimum is 90 K (Figure 4) [3]. Given these conditions on the surface, the calculated constant temperature at a depth of 45 cm in the lunar soil is 230 K. In the winter season, the average temperature is 130 K, the maximum is 240 K, and the minimum is 80 K (see Fig. 4). Given these conditions on the surface, the calculated constant temperature at a depth of 45 cm in the lunar soil is 210 K.

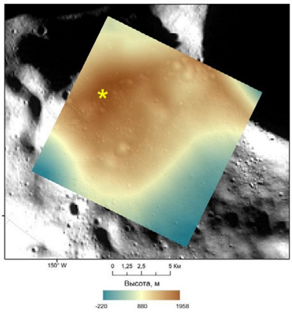

Fig. 3. Digital elevation models of sites #2 by data on LRO spacecraft (NASA) [7]. The asterisk shows the location of the temp. estimate in the lunar soil

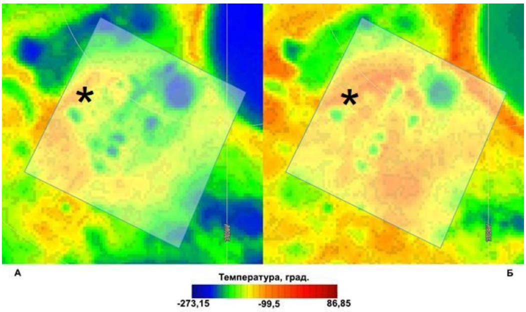

Fig. 4. Average winter (left) and summer (right) temperatures at site #2 [4]. The asterisk shows the location of the temperature estimate in the lunar soil

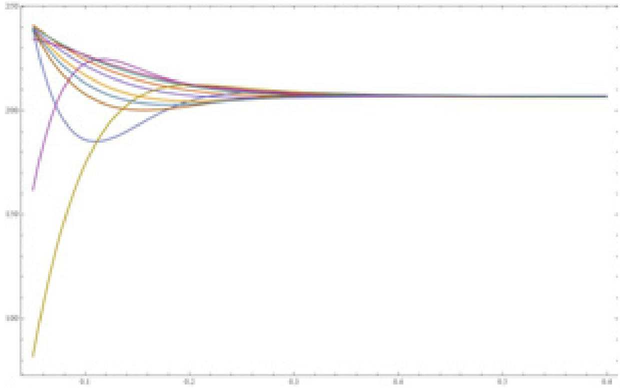

Fig. 5. Model of the daily course of temperature distribution in the lunar soil (x) at site #2 in the winter season (see Fig. 4) depending on the temperature on the surface (y) with superimposed fluctuations in the region of all possible values

SUMMARY:

The T(z) model, depending on the given conditions on the surface (duration of day and night, average day and night temperatures on the surface), allows solving the inverse problem for determining the steady-state equilibrium temperature in the lunar soil at depth. The estimated constant equilibrium temperature in the lunar soil at a depth of about 45 cm on a hill near the Shackleton crater with a degree of illumination of about 80 % in the summer season is about 230 K, and in the Winter season it drops to 210 K, which is 40° lower than in the equatorial areas where there is no change of seasons.

References:

[1] *Slyuta E.N., Marov M.Ya., Dunchenko A.G. et al.* TERMO-LR Experiment on the Luna-27 Lander: Study of Thermophysical, Physicomechanical, and Electromagnetic Properties of the Lunar Soil // Solar System Research. 2021. V. 55. Iss. 5. P. 446–466. DOI: 10.1134/S0038094621050051.

[2] *Mazarico E., Neumann G.A., Smith D.E., Zuber M.T., Torrence M.H.* Illumination conditions of the lunar polar regions using LOLA topography // Icarus. 2011. V. 211. P. 1066–1081.

[3] *Williams J.-P., Greenhagen B.T., Paige D.A. et al.* Seasonal Variations in South Polar Temperatures on the Moon // 50th Lunar and Planetary Science Conf. 2019. Abs. No. 2852.

[4] *Langseth M.G. Jr., Clark S.P. Jr. Chute J.L. Jr. et al.* Heat Flow Experiment // Apollo-15 : Preliminary Science Report. Washington, DC: NASA, 1972. P. 11-1–11-23.

[5] *Langseth M.G. Jr., Keihm S.J., Chute J.L. Jr.* Heat Flow Experiment // Apollo-17: Preliminary Science Report. Washington, DC: NASA, 1973. P. 9-1–9-24.

[6] Langseth M.G., Keihm S.J., Peters K. Revised Lunar Heat-Flow Values // Proc. 7th Lunar Science ConfVII. 1976. P. 3143–3171.
[7] *Slyuta E.N., Grishakina E.A., Turchinskaya O.I. et al.* To the site Selection for A Lunar Research Station // 54th Lunar and Planetary Science Conf. 2023. Abs. No. 1092.

VI-LH1 — LUNAR HIGHLANDS SIMULANT FOR LARGE SCALE EXPERIMENTS

D.D. Mironov[1,2], A.V. Uvarova[1], E.N. Slyuta[1], E.M. Sorokin[1], I.A. Agapkin[1], E.A. Grishakina[1]

[1] *Vernadsky Institute of Geochemistry and Analytical Chemistry RAS, Moscow, Russia, d.mironov@geokhi.ru*

[2] *Institute of Environmental Engineering, RUDN University, Moscow, Russia*

KEYWORDS:
Lunar highland simulant, Moon, lunar exploration, geochemical properties, mineralogy, grain size

INTRODUCTION:

For various experiments, where, unlike analogs of lunar soil in terms of physical and mechanical properties, for example, VI-75 [1], the chemical and mineralogical properties of the lunar highlands, as well as the particle size distribution, are important, a new simulator of the lunar highlands soil VI-LH1 was developed (Institute named after A.I. VI Vernadsky — Lunar Highlands 1), made from natural labradoritic anorthosite complex without adding any other components. This analogue is not close enough to the lunar highland rocks in terms of the content of anorthite molecule, but its content is close enough (compared to other available analogues). In addition, the geochemical weathering of the material is relatively minimal. This material is available in large volumes, which allows it to be used in large-scale experiments. The geotechnical properties such as chemical and mineralogical compositions, particle morphology, grain size distribution and bulk density were determined. The results were compared with data obtained during the Apollo-16 and Luna-20 missions and with other analogues.

MATERIALS AND METHODS:

A sample of labradoritic anorthosite was delivered from the Osnykovskoye deposit, located in Zhytomyr region, Ukraine. This deposit is located on the northern part of the Ukrainian crystalline shield. All the oldest rocks of magmatic origin are concentrated within its boundaries. Rocks from the Osnykovskoye deposit, such as labradoritic anorthosite, are the best-selling ornamental stones of this rock in the CIS, and are also used in European countries. To determine the composition and study the properties, the material was preliminarily crushed to powdery state. Chemical analysis of the rock was determined by x-ray fluorescence analyses on an Axious Advanced PW 4400/04 (Philips) using a basalt standard. X-ray diffraction analysis of powder preparations was performed using a MiniFlex 600 X-ray diffractometer. Interpretation and phase diagnostics of the samples were performed using the Jade 6 software package with connected PDF-2 powder databases. The composition of accessory minerals as well as the morphology of particles were determined by scanning electron microscopy on a TESCAN MIRA 3 instrument. The data obtained by electron microscopy were analysed in Aztec program. The grain size distribution was determined according to standard methods [2] by sieve method for fractions larger than 0.1 mm and areometric method for smaller fractions, using areometer AG (0995-1030). The density of hard particles was determined by pycnometric method, with the volume of 100 ml container, according to [3].

RESULTS:

The bulk chemistry of material of the Osnykovskoye deposit is similar to lunar rocks in many aspects, but the difference is the higher alkaline concentration (K_2O+Na_2O), and in comparison with some analogues it is closer to lunar rocks (Table 1). It is noted that most analogues of lunar highlands soils have similar alkalinity [4–7]. This material is classified as intermediately related to basaltic tracheandesites-andesites of normal and moderate alkalinity [8].

The main minerals, according to X-ray diffraction analysis, are plagioclase, which accounts for 80 % (Table 2), biotite, quartz. Pyroxene and ilmenite are also common, pyrrhotite, apatite, chromite are represented as accessory minerals, olivine and magnetite are relatively rare, and hornblende is presumably also found. The composition of plagioclases: 54 % of the rock is labradorite with the concentration of anorthite molecule mainly 56–61 %, reaching 72 % in some phases, 26 % is represented by andesine, the content of anorthite molecule is 30–50 %. It is noted that the contained minerals are characteristic of anorthosites in general [11].

Table 1. Chemical composition of VI-LH1 and comparison with Apollo-16 regolith samples, Luna-20 regolith samples and some analogues of lunar highlands

	VI-LH1	A-16 [9]	Luna-20 [10]	JLU-H [4]	UoM-W [5]
Loi	1,06			0,77	
Na2O	4,25	0,43	0,40	4,95	13,40
MgO	0,83	6,00	9,15	0,06	5,21
Al2O3	23,74	26,80	22,90	19,28	1,40
SiO2	52,69	45,10	45,60	65,15	68,24
P2O5	0,81	0,10		0,01	0,33
K2O	1,20	0,14	0,07	2,74	1,07
CaO	10,20	15,60	14,50	6,45	9,06
TiO2	0,49	0,75	0,46	0,04	0,06
MnO	0,06	0,22	0,10	0,01	0,01
FeO(t)	4,64	5,40	7,50	1,18	1,40
Sum	99,98	100,54	100,68	100,64	100,18

Table 2. Mineralogy of VI-LH1 during the XRD and SEM data

	wt, %
Labradorite (An 50–70 %)	54
Andesine (An 30–50 %)	26
Biotite	10
Quartz	8
Other (olivine, pyroxene, ilmenite, etc.)	2

Due to the permanent bombardment of the Moon by meteorites and absence of weathering processes, most of the particles have a sharp shape [12]. To give this shape, the process of particle erasing is used. Based on visual SEM analysis (Figure 1*a*), the developed analog has such particles, which is consistent with the characteristics of lunar soil particles. Grain size distribution modeling demonstrated that the particle size is generally similar to that of lunar regolith, based on Apollo-16 data (Figure 1*b*).

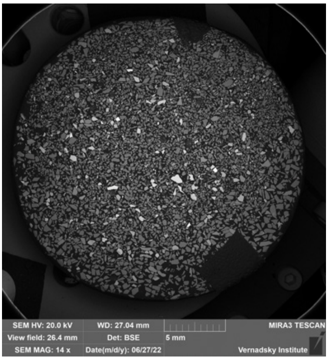

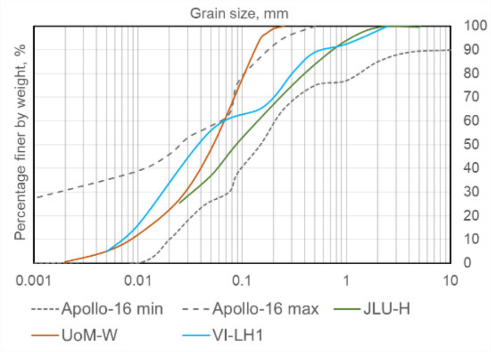

a **b**

Fig. 1. Image of crushed sample using SEM (**a**); Cumulative curves of particle size distribution for continental lunar regolith (Apollo-16 [13]) and lunar soil analogues (**b**)

SUMMARY:
VI-LH1 is one of the most available and cheapest analogues of lunar highlands soil. This analogue is very similar in chemical and mineralogical composition to most other analogs, having some advantages. Most of the other parameters of VI-LH1 are similar to the Apollo 16 lunar highland regolith and match well with other highland simulants, confirming the high ability to simulate many lunar rock properties in the development of this analogue. This analogue is supposed to be used for various experiments, including large-scale ones, in which the main and most important requirement is the imitation of lunar soil in terms of chemical, mineral, and granulometric composition. Also, such analogue will be useful for development and testing of new methods and technologies, for example, lunar regolith sintering and lunar biomining, as the development of new technologies at the first stage requires a large amount of material. Such an analogue is also suitable for biological and astrobiological experiments, since it is close to the most common lunar highlands rocks in terms of chemical and mineralogical composition.

References:
[1] *Slyuta E., Grishakina E., Makovchuk V.Y., Agapkin I.J.* Lunar Soil-Analogue VI-75 for Large-Scale Experiments // Acta Astronautica. 2021. V. 187. P. 447–457. https://doi.org/10.1016/j.actaastro.2021.06.047.
[2] GOST 12536-2014. Soils. Methods of laboratory granulometric (grain-size) and microaggregate distribution. Standartinform. M., 2019. 23 p. (in Russian).
[3] GOST 5180-2015. Soils. Methods for Laboratory Determination of Physical Characteristics. Standardinform. M., 2016. 20 p. (in Russian).
[4] Xumin Sun, Rui Zhang, Xiujuan Li, Meng Zou, Chu Wang, Lei Chen, JLU-H: A novel lunar highland regolith simulant for use in large-scale engineering experiments // Planetary and Space Science. 2022. V. 221. https://doi.org/10.1016/j.pss.2022.105562.
[5] *Just G.H., Joy K.H., Roy M.J., Smith K.L.* Geotechnical characterisation of two new low-fidelity lunar regolith analogues (UoM-B and UoM-W) for use in large-scale engineering experiments // Acta Astronautica. 2020. V. 173. P. 414–424. https://doi.org/10.1016/j.actaastro.2020.04.025.
[6] *Battler M.M., Spray J.G.* The Shawmere anorthosite and OB-1 as lunar highland regolith simulants // Planetary and Space Science. 2009. V. 57. Iss. 14–15. P. 2128–2131. https://doi.org/10.1016/j.pss.2009.09.003.
[7] *Linke S., Windisch L., Kueter N. et al.* TUBS-M and TUBS-T based modular Regolith Simulant System for the support of lunar ISRU activities, Planetary and Space Science. 2020. V. 180. https://doi.org/10.1016/j.pss.2019.104747.
[8] Igneous Rocks: A Classification and Glossary of Terms: Recommendations of the International Union of Geological Sciences Subcommission on the Systematics of Igneous Rocks / eds. Le Maitre R., Streckeisen A., Zanettin B., Le Bas M., Bonin B., Bateman P. 2nd ed.). Cambridge: Cambridge University Press, 2002. https://doi.org/10.1017/CBO9780511535581.
[9] *McKay D.S., Blacic J.D.* Workshop on Production and Uses of Simulated Lunar Materials // Lunar and Planetary Institute technical report (1981-1998). 1991. Art. No. 19910016787.
[10] *Korotev R.L., Haskin L.A., Lindstrom M.M.* A synthesis of lunar highlands compositional data // Proc. 11th Lunar Planet. Science Conf. 1980. P. 395–429.
[11] Anorthosites of the Earth and the Moon / ed. A.V. Peive. M.: Nauka, 1984. 272 p. (in Russian).
[12] *Carrier III W.D., Olhoeft G.R., Mendell W.* Physical Properties of the Lunar Surface // Lunar Sourcebook: A User's Guide to the Moon / eds. Heiken G., Vaniman D.T., French B.M. Cambridge: Cambridge University Press, 1991. P. 475–594.
[13] *Graf J.C.* Lunar Grain Size Catalog / NASA Reference Publication 1265.1993. 464 p.

EARTH-BASED RADAR OBSERVATIONS OF PERMANENTLY SHADOWED REGIONS ON THE LUNAR SOUTH POLE

Yu.S. Bondarenko[1], D.A. Marshalov[1], B.M. Zinkovsky[2], A.G. Mikhailov[1]
[1] *Institute of Applied Astronomy RAS, Saint Petersburg, Russia, bondarenko@iaaras.ru*
[2] *Special design bureau of the National Research University "Moscow Power Engineering Institute", Moscow, Russia*

KEYWORDS:
Moon, PSR, Lunas South Pole, Radar Images, Polarimetry, CPR

INTRODUCTION:

Earth-based radar observations of the lunar South Pole provide detailed topographic and polarimetric data for areas that are in permanent shadow from solar illumination. Such areas may contain water-ice deposits as well as various surface and subsurface features hidden from optical images [1–4]. Here we present new radar images (Fig. 1) and polarimetry data of the South Polar Region of the Moon with a surface resolution of 75 m.

Earth-based radar observations were conducted in May 2023 using the 64-meter diameter antenna (TNA-1500) at the Bear Lakes Satellite Communi-

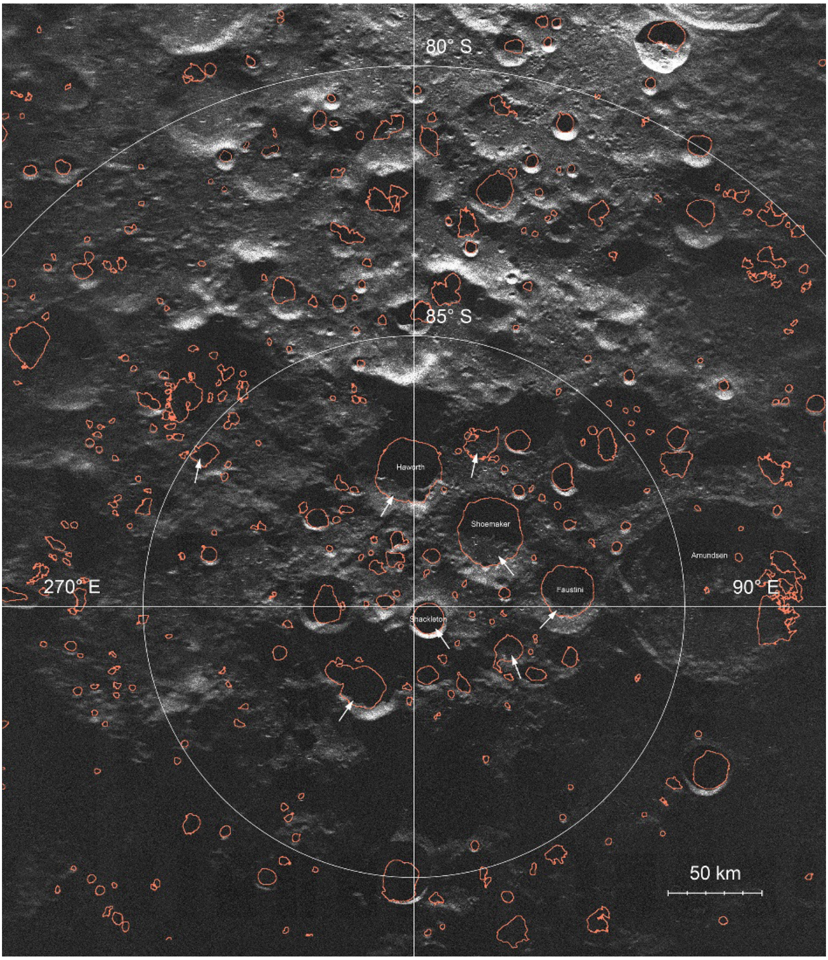

Fig. 1. Opposite-sense circular polarization radar backscatter image of the south polar region of the Moon in orthographic projection. PSRs are circled in red [6], while white arrows indicate several areas visible to the radar

cations Center of the SDB MPEI and the 13.2-meter diameter radio telescope (RT-13) at Svetloe observatory of the IAA RAS in a bistatic configuration at a wavelength of 4.2 cm. At this wavelength, radar signals penetrate to a depth of 1 m into the lunar regolith and are sensitive to surface and suspended material with a diameter of about 1 cm and larger.

During our observations, the radar incidence angle at the south pole was close to the maximum of 84°, which allowed the radar to illuminate as much of the permanently shadowed regions (PSRs) as possible. The TNA-1500 antenna was used to transmit a circularly polarized modulated signal, and the RT-13 radio telescope received reflections in both senses of circular polarization. Circular polarization of the signal is reversed after reflection from smooth, radar-facing parts of the surface and the maximum power of the reflected signal is expected in the opposite circular (OC) polarization, though some of the signal is received in the same circular (SC) polarization as transmitted, due to multiple reflections or diffuse scattering by surface or subsurface features with wavelength-scale roughness, such as rocks or cracks. The circular polarization ratio (CPR) defined as the ratio between SC and OC is a measure of roughness, rock abundance and material composition at the lunar surface and below. Low CPR values correspond to smooth at wavelength scales surfaces, while CPR values approaching one indicate targets with high diffuse scattering such as impact crater rocky ejecta and fractured melt [5]. Measurements of receiving system noise temperature during the radar observations provided a reliable estimate of the CPR.

Analysis of the obtained radar images revealed areas with high backscatter and CPR within permanently shadowed regions. The number and distribution of rocks and irregularities at wavelength scales, on the surface and near-surface layer of the regolith were estimated.

Acknowledgements:
We want to thank the technical staff at the Bear Lakes Satellite Communications Center of the SDB MPEI and the Svetloe Radio Astronomical Observatory of the Institute of Applied Astronomy of the Russian Academy of Sciences for their assistance in organizing and conducting radar observations of the Moon. This work was supported by the Russian Science Foundation (project No. 23-22-00254).

References:
[1] *Stacy N.J.S., Campbell D.B., Ford P.G.* Arecibo radar mapping of the lunar poles: A search for ice deposits // Science. 1997. V. 276. Iss. 5318. P. 1527–1530. DOI: 10.1126/science.276.5318.1527.
[2] *Margot J.L., Campbell D.B., Jurgens R.F., Slade M.A.* Topography of the Lunar Poles from Radar Interferometry: A Survey of Cold Trap Locations // Science. 1999. V. 284. Iss. 5420. P. 1658–1660. DOI: 10.1126/science.284.5420.16.
[3] *Patterson G.W., Stickle A.M., Turner F.S. et al.* Bistatic radar observations of the Moon using Mini-RF on LRO and the Arecibo Observatory // Icarus. 2017. V. 283. P. 2–19. https://doi.org/10.1016/j.icarus.2016.05.017
[4] *Kumar S., Singh A., Sharma A. et al.* Polarimetric analysis of L-band DFSAR data of Chandrayaan-2 mission for ice detection in permanently shadowed regions (PSRs) of lunar South polar craters // Advances in Space Research. 2022. V. 70. Iss. 12. P. 4000–4029. https://doi.org/10.1016/j.asr.2022.01.038.
[5] *Campbell B.A.* High circular polarization ratios in radar scattering from geologic targets // J. Geophysical Research. 2012. V. 117. Iss. E6. Art. No. E06008. https://doi.org/10.1029/2012JE004061.
[6] *Mazarico E., Neumann G.A., Smith D.E. et al.* Illumination conditions of the lunar polar regions using LOLA topography // Icarus. 2011. V. 211. Iss. 2. P. 1066–1081. https://doi.org/10.1016/j.icarus.2010.10.030.

FEATURES OF ISOTOPIC FRACTIONATION OF WATER ICE DURING SUBLIMATION UNDER LUNAR CONDITIONS

A.P. Krivenko, V.S. Sevastyanov, S.A. Voropaev
Vernadsky Institute of Geochemistry and Analytical Chemistry RAS, Moscow, Russia, voropaev@geokhi.ru

KEYWORDS:
water ice, isotopes, fractionation, sublimation, Moon

INTRODUCTION:
One of the processes that define conditions for the retention of water ice in the Moon' regolith is the sublimation and condensation of water vapor with a daily change in the temperature of the regolith surface. This process involves free water, which, unlike chemically bound water, is not part of the crystal lattice of minerals, but is retained by regolith, mainly in the pores of mineral grains due to adsorption-desorption or by adhesion in high vacuum conditions.

EXPERIMENTS AND RESULTS:
The physics of the processes is essentially similar to the processes occurring in the pore space of the comet nucleus [1]. However, obtaining quantitative estimates of the contribution of (re) sublimation to water retention in the lunar regolith is associated with great uncertainties, since the known measurements of vapor diffusion and condensation were carried out mainly under atmospheric conditions. In solving this problem, conducting experiments on laboratory vacuum installations in conditions as close as possible to those existing on the lunar surface can help.

Proper experimental facility has been created at GEOKHI RAS to analyze the processes of (re) sublimation of water ice in vacuum at low temperatures. The range of (re) sublimation temperature is from -100 to 0 °C [2]. The device is connected to an isotope ratio mass spectrometer (IRMS), which allows measuring the isotopic composition of vapors of an evaporating substance and estimating the rate of sublimation under specified physico-chemical conditions. The presence of direct gas input into the mass spectrometer in real time distinguishes the developed installation from foreign analogues.

The IRMS setup revealed the strong dependence of stable hydrogen D/H isotopes fractionation value of the water ice during sublimation under lunar conditions. It means low total pressure and temperatures from –20 to –60° C. It turned out that not only the temperature has an important role, but also the mineral composition on which the water ice was located. The effect is associated with the features of condensation and adsorption of water vapor on silicate minerals with different types of crystal lattices [3]. In particular, a comparison was made with the known data on the isotopic composition of water at lunar regolith minerals delivered by the Luna-20, -21, -22, -23, -24 and Apollo-14, -15, -16, -17 missions.

Acknowledgments:
This work was supported by the RSCF grant no. 21-17-00120.

References:
[1] *Marov M.Ya., Kolesnichenko A.V., Skorov Y.V.* Numerical simulation of the gas-dust flow in the near-surface layer of the cometary atmosphere // Solar System Research. 1995. V. 26. No. 3. P. 243–252.
[2] *Sevastyanov V.S., Krivenko A.P., Voropaev S.A, Marov M.Ya.* Studies of isotopic fractionation of D/H water ice of the lunar regolith // Solar System Research. 2023 V. 57. Iss. 6 (in print).
[3] *O'Neil J.R.* Stable isotopes in mineralogy // Physics and Chemistry of Minerals. 1977. V. 2. Iss. 1–2. P. 105–112. DOI: 10.1007/BF00307527.

GAMMA-RAY SPECTROSCOPY OF RARE EARTH ELEMENTS IN THE LUNAR SUBSURFACE

D.V. Golovin[1], I.G. Mitrofanov[1], M.L. Litvak[1], S.Y. Nikiforov[1], A.B. Sanin[1], V.N. Shvetsov[2], E.E. Pavlik[2]

[1] *Space Research Institute, IKI. Profsoyuznaya st. 84/32, 117997, Moscow, Russia. golovin@np.cosmos.ru*

[2] *Joint Institute for Nuclear Research, JINR. 6 Joliot-Curie St, 141980, Dubna, Moscow Region, Russia*

KEYWORDS:
Moon, Rare earth elements, Gamma-ray sensing, In-situ exploration

The laboratory experiment was conducted at Joint Institute for Nuclear Research with a prototype of planetary gamma-ray spectrometer (GRS) based on a High Purity Germanium (HPGe) detector and a proton detector configured with the GRS [1]. The main objective was to conduct experiment with an irradiation of 11 samples of Rare Earth Elements (REEs) with high energy protons (170 MeV) to find a set of uniquely characterized gamma-ray lines that confidently indicate the presence of the given REE.

These measurements are acquired to understand the conditions of a hypothetical space experiment on the lunar surface aimed for the reconnaissance of lunar resources [2]. In this experiment, ambient gamma radiation is produced by charged particles of Galactic Cosmic Rays [3]. 45 significant gamma-ray lines were found for 11 tested samples of REEs in total.

The obtained experimental results were used to predict the expected intensities of the REEs gamma-ray lines in a future gamma-ray spectrometric experiment on the lunar surface. In particular, for a hypothetical lunar ore field [4] it is estimated that a planetary GRS may detect Cerium after 1.6 h of signal accumulations.

Acknowledgements:
This study is performed under the Russian Science Foundation Grant 8-12-00487.

References:

[1] *A.B. Sanin et al.* On the study of the spatial variability of the composition of the lunar material in experiments on gamma spectroscopy onboard a mobile spacecraft using the tagged-cosmic-rays method // Solar system research, 54, 6. (2020).

[2] *L.A. Haskin et al.* Rare-earths and other trace elements in Apollo 11 lunar samples // Proceedings of the Apollo 11 Lunar Science Conference, 2, 1213-1231. (1970).

[3] *I.G. Mitrofanov et al.* Cosmic Gamma-Ray Spectrometer with Tagged Charged Particles of Galactic Cosmic Rays // Nuclear Inst. and Methods in Physics Research, 953, (2020).

[4] *L.J. Drew et al.* The Bayan-Obo iron-rare-earth-niobium deposits, inner Mongolia, China // Lithos 26, 1-2, 43–65. (1990).

THE NEUTRON EMISSION FROM THE SOUTH POLAR REGION OF THE MOON

A.B. Sanin, I.G. Mitrofanov, M.L. Litvak
Space Research Institute RAS, Profsoyusnaya street, 84/32, Moscow, Russian Federation

KEYWORDS:
Moon, neutron, Galactic Cosmic Rays, soil, neutron spectrum, radiation hazard.

A manned expedition to the Moon is fraught with a number of difficulties and risks. One of them is hazard radiation on the surface. The absence of an atmosphere and a global magnetic field allows particles of Galactic Cosmic Rays (GCRs) to freely bombard the lunar soil. GCR particles interact with nuclei in the shallow subsurface to produce secondary nuclei, charged particles and neutrons [1]. Not only charged particles, but also neutrons pose a radiation hazard to cosmonauts. The energies of these newly produced neutrons are distributed over a wide range from tens of MeV up to tens of GeV. The process of random diffusive propagation of neutrons occurs in the subsurface layer with multiple collisions with rock-forming nuclei. The energy of neutrons decreases at collisions and they are moderating during propagation in the subsurface. Thus, the energy spectrum of secondary neutrons emitted from the surface is ranging from tens of GeV, as an initial energy of produced particles, down to the thermal energy with the temperature of the subsurface material. It is obvious that the temperature of the subsurface soil is a determining factor in the properties of the thermal neutron flux. The presence of light nuclei such as hydrogen in the lunar soil reduces the flux of epithermal and fast neutrons and increases flux of thermal neutrons. On the other hand, the presence in the soil of nuclei with a large neutron absorption cross-section may dramatically decrease the flux of the thermal and low-energy epithermal neutrons.

We present the results of numerically simulations of neutron spectra on the surface of the Moon in the southern high-latitude region. Changes in the obtained spectra depending on the temperature of the lunar soil, its composition, and hydrogen content are discussed.

Acknowledgment:
This study was supported by the grant #23-12-00321 of the Russian Science Foundation.

References:

[1] *Reedy R.C., Arnold J.R*. Interaction of solar and galactic cosmic-ray particles with the Moon // J. Geophys. Res. 1972. V. 77. No. 4. P. 537–555.

PROCESSING TECHNIQUE FOR THE IMAGE DATA FROM SERVICE TELEVISION CAMERA SYSTEM — LUNA (STS-L) AT THE LANDING STAGE

A.E. Zubarev [1,2], I.E. Nadezhdina[1], N.A. Kozlova[1], Ya.D. Elyashev[2]
[1] *Moscow State University of Geodesy and Cartography, MIIGAiK Extraterrestrial Laboratory, Moscow, Russia fair-max@yandex.ru*
[2] *Space Research Institute RAS, Moscow, Russia*

KEYWORDS:
Moon, Luna-Resurs, service television system, STS-L, lunar topography

In August 2023 the Russian lunar landing mission Luna-Resurs (Luna-25) is to launch. Onboard Service Television System (STS-L) consists of 8 cameras, including four wide-angle cameras in the optical range, located on its side panels and providing a 360-degree view of the surrounding surface. Images obtained by these cameras will be used to get the topography of the landing site.

All cameras were calibrated in the laboratory with an RMS not worse than 0.5 pixels. Relative calibration of the cameras was performed after the system was installed on board the spacecraft. The maximum relative calibration error did not exceed 1 image pixel (RMS 0.4 pixels). The STS-L was referenced to the spacecraft coordinate system with an absolute RMS of 7.3 cm along all 3 axes. This makes it possible to determine the position and orientation of each STS-L camera in the Moon coordinate system (MOON ME) based on transmitted telemetry data (obtained images).

During the controlled descent of the Luna-25 spacecraft, the STS-L system will conduct operational survey of the landing till the touchdown. All obtained data will be transmitted to Earth during the first weeks after landing. The design of the STS-L system allows building stereo pairs from neighboring cameras, but stereo covers narrow overlapping areas — up to 20 % of the field of view. During the landing, due to vertical movement, it will be possible to build stereo pairs from images obtained at adjacent time points, which will increase the stereo coverage up to 80%. The entire set of images can be used to obtain the topography of the landing site, as well as general information about the distant terrain around the touchdown point.

The study will present the image processing technique and digital terrain models obtained based on modeled image data (used for testing the technique) and first results of processing STS-L data (if available).

OPTIMIZING SCIENTIFIC OBJECTIVES FOR THE LUNAR-BASED UV-OPTICAL-IR TELESCOPE FOR ILRS

H. Wang[1,2], M. Sachkov[3], S. Dong[4], X. Bai[1,2], A. Shugarov[3], X. Jiang[1,2], H. Tian[5], N. Jiang[6], Y. Deng[1,2], G. Zhao[1,2], T. Li[1], V. Shmagin[3], B. Shustov[3], S. Sichevskij[3], A. Buslaeva[3], I. Savanov[3], X. Zhang[1,2], J. Wang[1,2]

[1] *National Astronomical Observatories, Chinese Academy of Sciences, Beijing, China, wanghj@nao.cas.cn*

[2] *University of Chinese Academy of Sciences, Beijing, China, xybai@nao.cas.cn*

[3] *Institute of Astronomy RAS, Moscow, Russia, msachkov@inasan.ru*

[4] *Department of Astronomy, School of Physics, Peking University, Beijing, China, dongsubo@pku.edu.cn*

[5] *School of Earth and Space Sciences, Peking University, Beijing, China, huitian@pku.edu.cn*

[6] *Department of Astronomy, University of Science and Technology of China, Hefei, China, jnac@ustc.edu.cn*

KEYWORDS:
ILRS, evolution of galaxies, transients, habitability, UV-Optical-IR telescope, lunar-based telescope, space weather

Taking the advantages of the lunar-based environment, we could perform multi-wavelength observations with an ultra-wide wavelength coverage, especially from extreme ultraviolet (EUV) to infrared (IR). A proposal to build a Lunar-based UV-Optical-IR telescope/array for the International Lunar Research Station (ILRS) was submitted by our collaborative research groups from Russia and China in 2021. We kept on prompting it since then, and we focus on optimizing the scientific objectives during the past year.

The optimized scientific objectives of this telescope focus on:

1) To carry out lunar-based UV sky survey and fine observations, obtain a dynamically updated and complete UV catalog, conduct research on galaxy formation and evolution, and construct a picture of galaxy evolution within 80 % of the universe's evolution history;
2) To shoot dynamic cosmic "movies" in the near UV band, explore high-energy transients in the local universe and systematically study the ultraviolet characteristics of variable sources in the Milky Way;
3) To investigate the habitability of exoplanets from a new and unique perspective, both space weather phenomena and the influence of small bodies in planetary systems will be considered; discover new terrestrial exoplanets in the habitable zones, study the characters of them, and explore the future livable homes for mankind.

The optimization of the scientific objectives, some new simulations about the scientific capabilities, and some new considerations about payload requirements over the past year will be introduced in this talk, as its concept and preliminary science have been introduced in our previous talks and paper [1–6].

References:

[1] *Wang H., Chen X., Sachkov M. et al.* A brief introduction to the astronomical research for ILRS // Intern. Workshop on Overall Science Objectives of ILRS. Hefei, China, Apr. 26, 2023.

[2] *Shugarov A.S., Wang H., Dong S. et al.* The concept of Lunar-based astrophysical telescope for international lunar research station // Vestnik NPO Lavochkina. 2022. No. 1(55). P. 3–9. DOI: 10.26162/LS.2022.71.64.001 (in Russian).

[3] *Shugarov A., Dong S., Wang H. et al.* The Concept of Moon-Based UV Survey to Study Transients and Variables // 13th Moscow Solar System Symposium 13M-S3. IKI RAS, Moscow, Russia, Oct. 10–14, 2022: Abs. book. 2022. P. 106–107. DOI: 10.21046/13MS3-2022.

[4] *Wang H., Sachkov M., Dong S. et al.* Science of the Lunar-Based UV-Optical-IR Telescope for ILRS // 13th Moscow Solar System Symposium 13M-S3. IKI RAS, Moscow, Russia, Oct. 10–14, 2022: Abs. book. 2022. P. 108. DOI: 10.21046/13MS3-2022.

[5] *Shugarov A., Sachkov M., Wang H. et al.* The concept of Lunar-based UV-Optical-IR Telescope for ILRS // 12th Moscow Solar System Symposium 12M-S3. IKI RAS, Moscow, Russia, Oct. 11–15, 2021: Abs. book. 2021. P. 441–443. DOI: 10.21046/12M-S3.
[6] *Sachkov M., Shugarov A., Shmagin V., Gómez de Castro A.I.* The concept of lunar-based astrophysical telescope for international lunar research station (ILRS) // Proc. SPIE. 2022. V. 12181. Art. No. 121812V. DOI: 10.1117/12.2629619.

IN-FLIGHT SELECTION OF LANDING SITE FOR LUNAR POLAR LANDER

D.I. Lisov, M.V. Djachkova, I.G. Mitrofanov, A.B. Sanin
Space Research Institute of the Russian Academy of Sciences

KEYWORDS:
lunar lander, landing site selection, software, Luna-25, LOLA, LEND.

INTRODUCTION:

Modern lunar lander missions often target the polar areas of the Moon due to high scientific interest to high latitudes including the possibility of water ice deposits being present in these areas. This constraint makes landing noticeably more challenging[1]. Both lighting and radio visibility conditions are more complex and variable at higher latitudes. In addition, the lunar surface in these areas is more rough, with more slopes and obstacles that could cause a landing failure, than at lower latitudes usually targeted before.

The planned landing site of a mission, while chosen well before launch, can be modified at multiple points in the mission timeline including after launch. The initial landing area can be refined based on the predicted or actual final orbit before landing, and the spacecraft may be capable of autonomously adjusting the landing point for safety reasons.

During the development of the Luna-25 mission we created special software for optimizing the mission success chance and expected science value by choosing the target landing site based on the actual orbit measurements taken during flight, including precise measurements of the final orbit. The software takes into account mission requirements, surface properties that affect safety and scientific value (slopes and roughness from LOLA[2], hydrogen/water content from LEND[3]), illumination and radio visibility conditions for the mission dates based on simulated horizon[4], and ballistic restrictions on the points where landing is possible. The software operator is provided with a user interface for exploring this dataset and listing candidate landing sites. The software uses a multi-factor ranking algorithm that enables the operator to quickly produce a list of best landing site candidates for further simulation, final landing site selection and implementation.

The software is not specific to the Luna-25 mission and can be used for future lunar landing missions including, but not limited to, the planned Luna-27 and Luna-28 landers if necessary.

References:

[1] *Djachkova M.V., Litvak M.L., Mitrofanov I.G. et al.* Selection of Luna-25 landing sites in the South Polar Region of the Moon // Sol Syst Res. 2017. V. 51, P. 185–195.
[2] *Barker, M.K., Mazarico, E., Neumann et al.* A new lunar digital elevation model from the Lunar Orbiter Laser Altimeter and SELENE Terrain Camera // Icarus. 2016. V. 273. P. 346–355.
[3] *Sanin, A.B., Mitrofanov, I.G., Litvak, M.L. et al.* Hydrogen distribution in the lunar polar regions // Icarus. 2017. V. 283. P. 20-30.
[4] *Djachkova, M.V., Mitrofanov, I.G., Sanin, A.B. et al*. Characterization of the Luna-25 Landing Sites // Sol Syst Res. 2021. V. 55. P. 509–528.

LABORATORY TESTING FOR ISRU OF LUNAR REGOLITH BY SLM TECHNOLOGY

T.M. Tomilina, A.A. Kim, A.M. Lysenko
A.A. Blagonravov Mechanical Engineering Research Institute (IMASH) of Russian Academy of Sciences, 4, M. Kharitonyevskiy Str., Moscow, Russia, 101000

KEYWORDS:
Moon exploration, lunar regolith, additive technology

Lunar regolith may become important resource for future lunar exploration. As a raw material, it may be used for making components of lunar infrastructure, also the artificial surfaces of regolith may become a protection of mechanisms of lunar dust. Therefore, development and technology for ISRU of regolith is a subject of study for many research centers around the world [1,2].

Such technology consists of three basic elements: preparing of regolith as raw material, manufacture of particular elements and ensuring the necessary mechanical properties of final products.

These three items will be discussed in this report: a short overview of already obtained results will be presented as well as recent results obtained at A.A. Blagonravov Mechanical Engineering Research Institute using additive SLM technology.

Acknowledgments:
The work was supported by RSF (grant № 22-22-00840).

References:

[1] *K.W. Farries, P. Visintin, S.T. Smith et al.* Sintered or melted regolith for lunar construction: state-of-the-art review and future research directions// Construction and Building Materials. 2021. V.296. 123627. https://doi.org/10.1016/j.conbuildmat.2021.123627
[2] *T.M. Tomilina, A.A. Kim, D.I. Lisov et al.* A Lunar Printer Experiment of the Lunar Regolith in the Luna-Grunt Space Project. Cosmic Res **61,** 314-323 **(**2023). https://doi.org/10.1134/ S0010952523700302

RUSSIAN LUNAR PROGRAM: DIFFICULT BEGINNING

L.M. Zelenyi, I.G. Mitrofanov, V.I. Tretyakov, M.L. Litvak
Space Research Institute RAS, Profsojuznaja 84/32, 117997 Moscow, Russian Federation;

KEYWORDS:
Moon, Russian lunar program, Luna-25

INTRODUCTION:
First spacecraft “Luna-25” of the new Russian program for the investigation of Lunar polar regions was launched from the new cosmodrom “Vostochnyi” August, 11, 2023.

During 9 days of spacecraft operations’ in interplanetary space and circular Lunar orbit scientific payload of this mission was successfully tested and some instruments even provided some valuable results. Some of them will be reported in this talk. However at August, 19, spacecraft braking for the transition to the lower prelanding orbit was erroneously too strong and the mission was aborted due to collision with the Lunar surface.

However, despite this tragic failure Russian Lunar program continues and current plans for the next “Luna-26” – “Luna-27” – “Luna-28” mission are updated and their scientific and operational plans will be presented during this talk.

SESSION 2. MOON AND MERCURY(MN) POSTER SESSION

REGIONAL AND LOCAL GEOLOGY AND MOON MINERALOGY MAPPER DATA ANALYSIS FOR THE LUNA-24 LANDING SITE

A.T. Basilevsky[1], D. Dhingra[2], J.W. Head[3], M.A. Ivanov[1], G. Michael[4], C.M. Pieters[3]

[1] *Vernadsky Institute of Geochemistry and Analytical Chemistry RAS, Moscow, Russia, atbas@geokhi.ru*
[2] *Indian Institute of Technology Kanpur (IIT-K), Kalyanpur, Kanpur, India*
[3] *Department of Earth, Environmental and Planetary Sciences, Brown University, Providence, RI, USA*
[4] *Freie Universität Berlin, Berlin, Germany*

KEYWORDS:
sample return, Luna-24, Mare Crisium, basalt, local geology, regolith

INTRODUCTION:

Luna-24 was the last Soviet sample return robotic mission to the Moon. It landed in 1976 in the SE part of Mare Crisium, drilled a bore-hole, loaded the 2-m long core of regolith material into the returned capsule and delivered it to Earth. The samples received extended and intensive studies which showed that the returned material is representive of a new very low-Ti (VLT) type of mare basalts (e.g., [1–3]), which based on then-available remote sensing data, were not expected in that place [4]. Later remote sensing studies did not result in an explicit understanding of surface composition of that area (e.g., [5–7]). The analysis was complicated by the lack in understanding of the local geology of the landing site. Special searches in Lunar Reconnaissance Orbiter Narrow Angle Camera (LROC NAC) images led to discovery of the location of the Luna-24 lander on the lunar surface, sitting on the rim a of 65-m crater, Lev [8] (Fig. 1). Roscosmos plans to send the Luna-28 mission to the South polar area of the Moon to return samples from this very interesting region (frozen volatiles in regolith and location on the rim of the largest and most ancient from known South Pole – Aitken basin) [12-13], it is thus worthwhile to recollect the last Soviet sample return from the Moon, the Luna-24 mission.

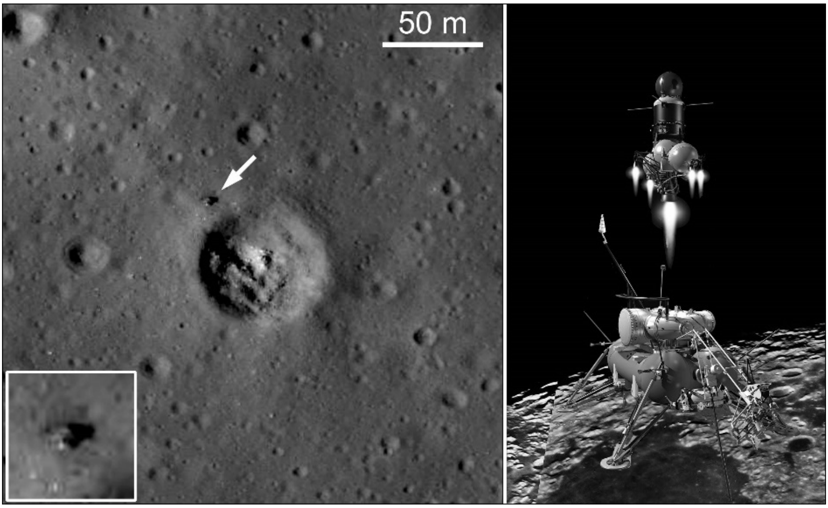

Fig. 1. Surface of Mare Crisium at the Luna-24 site; portion of LROC NAC image M119449091RE. Arrow shows the lander at the rim of crater Lev, see also inlet (*left*). Artistic representation of the Luna-24 liftoff, rendered from the image provided by http://russianspaceweb.com/luna24.html (*right*)

DESCRIPTION:

In this paper we consider the results of photogeologic analysis of LROC WAC and NAC images, Kaguya Terrain Camera images, as well as Lunar Obiter Laser Altimeter (LOLA) data. Also analyzed were data taken by the Moon Mineralogy Mapper (M3) [9]. The analysis of LOLA gridded topography with spatial resolution of 512 px/deg covers area ~200×200 km while analysis of LROC WAC mosaic (100 m/px) covers the area from 10 to 15° N and from 60 to 65° E (~150×150 km). These data provide the regional context of the study: This area includes the SE part of Mare Crisium and part of the Crisium basin highland rim. The analysis of the Kaguya Terrain Camera mosaic (7.7 m/px) covers the area 31.5×41 km around the Luna-24 landing site including the 6.5 km crater Fahrenheit, whose ejecta probably reached the Luna-24 site, and the adjacent mare plains. Our goal was to understand geology in the vicinity of the Luna-24 site, aiming to select the sites to study the surface composition based on the data gained by the Moon Mineralogy Mapper [9]. The analysis of the LROC NAC images (0.5 to 1.4 m/px) was intended to understand details of the geology of the Giordano Bruno rays and secondary craters, including those in the close vicinity of the Luna-24 site [10].

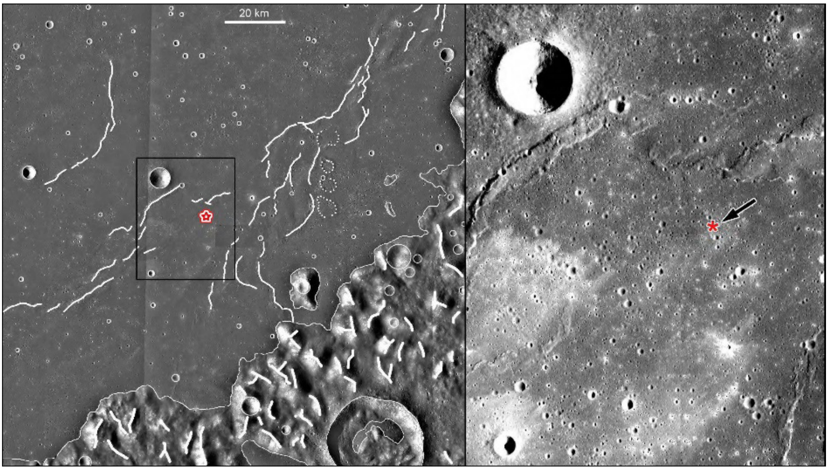

Fig. 2. The vicinity of the Luna-24 site seen on the LROC WAC mosaic. The black box outlines the area shown on the right (*left*). : Portions of the Kaguya Terrain Camera mosaics, morning version. Crater Fahrenheit (6 km diameter) is in the upper left. Red stars show the landing site (*right*)

The analysis of LROC WAC mosaic showed that Luna-24 landed on the mare surface with craters of various size and wrinkle ridges. Relatively bright, diffuse features considered to be rays from the distant highland 22-km crater Giordano Bruno crater [10] are observed near the landing site and at great distances. Outcrops of highland terrain are observed ~40 km SE of the landinte site are probably one source of the minor admixture of highland material in the Luna-24 core. Study of the Kaguya mosaic combined with other information revealed no evidence for distinct individual lava flows or mare units r. It was also shown that the area was affected by ejecta from the 6 km diameter Fahrenheit crater, which should be well-mixed with local regolith; its percentage in the regolith should be rather small. Study of LROC NAC images within the Luna-24 landing area led to better understanding of the structure of Giordano Bruno rays [10]. An overview of the region using M3 data [11] indicates that local craters have excavated two types of mare basalt in the region, one of which is distinctly olivine-rich. The spatial resolution of M3 data and limited number of measurable craters near the Luna-24 site, however, is insufficient to determine which basalt type is likely to dominate the Luna-24 sample from M3 data alone.

CONCLUSIONS:

The above consideration suggests that Luna-24 landed about 7 m northwest of its rimcrest of the 65 m crater Lev (one of the secondaries formed 5–10 m.y ago by ejecta from the distant farside crater Giordano Bruno). Earlier events likely are recorded in the sample including ejecta from 6.5 km crater Fahrenheit. They should be derived from a depth ~100–400 m; models suggest that they should be deposited at the Luna-24 site in an amount equivalent to a layer ~0.5 m thick. This depth suggests that at least part of the ejecta could have been derived from the central to lower parts of mare forming lava flows (for example, potentially both types of maria detected by M3 data [11]) and that they should be relatively coarse-grained. At the Luna-24 landing point, the estimated thickness of crater Lev ejecta is 0.5 to 1 m. During the landing event an unknown upper part of the surface material was likely to have been blown away by the descent engine plume. Taken together, these data provide new insights into the characteristics and provenance of the Luna-24 core materials, and provide a model for the sequence of event represented by changes of sample characteristics with depth in the core. A concentrated re-examination of Luna-24 results, together with new Luna-24 sample analyses should be undertaken with these results as an interpretive framework.

Acknowledgments:
A.T. Basilevsky and M.A. Ivanov were supported by the Russian Science Foundation grant no. 21-17-00035: Estimates of the rate of exogenous resurfacing on the Moon. Many thanks to J Plescia and B.A. Ivanov for their contributions.

References:
[1] *Barsukov V.L., Florensky C.P.* The lunar soil from Mare Crisium: Preliminary data // Lunar and Planetary Science Conf. 1976. V. 8. P. 61–63.
[2] *Barsukov V.L., Tarasov L.S., Dmitriev L.V. et al.* The geochemical and petrochemical features of regolith and rocks from Mare Crisium // 8th Lunar Science Conference: Proc. 1977. V. 3. P. 3319–3332.
[3] *Taylor G.J., Warren P., Ryder G. et al.* Lunar rocks // Lunar Sourcebook: A User's Guide to the Moon. Cambridge University Press, 1991. P. 183–284.
[4] *Pieters C.M., McCord T.B., Adams J.B.* Regional basalt types in the Luna-24 landing area as derived from remote observations // Geophysical Research Letters. 1976. V. 3. Iss. 11. P. 697–700. https://doi.org/10.1029/GL003i011p00697.
[5] *Adams J.B., Head* III *J.W., McCord T.B. et al.* Mare Crisium: Regional stratigraphy and geologic history // Geophysical Research Letters. 1978. V. 5. Iss. 4. P. 313–316. https://doi.org/10.1029/GL005i004p00313.
[6] *Head* III *J.W., Adams, J.B., McCord et al.* Regional stratigraphy and geologic history of Mare Crisium // 9th Lunar and Planetary Science Conference: Proc. 1978. P. 43–74.
[7] *Pieters C.M., McCord T.B., Head J.W. et al.* Mare Crisium geologic units — Implications of additional remote sensing data // 10th Lunar and Planetary Science Conference: Proc. 1979. V. 3. P. 2967–2973.
[8] *Robinson M.S., Plescia J.B., Jolliff B.L., Lawrence S.J.* Soviet lunar sample return missions: Landing site identification and geologic context // Planetary and Space Science. 2012. V. 69. Iss. 1. P. 76–88. https://doi.org/10.1016/j.pss.2012.03.013.
[9] *Pieters C.M., Boardman J., Buratti B. et al.* The Moon Mineralogy Mapper (M^3) on Chandrayaan-1 // Current Science. 2009. V. 96. No. 4. P. 500–505.
[10] *Basilevsky A.T., Head J.W.* Age of Giordano Bruno crater as deduced from the morphology of its secondaries at the Luna-24 landing site // Planetary and Space Science. 2012. V. 73. Iss. 1. P. 302–309. https://doi.org/10.1016/j.pss.2012.08.017.
[11] *Pieters C.M., Basilevsky A.T., Dhingra* D., Head *J.W.* Diversity Of Materials at Luna-24 Site from Moon Mineralogy Mapper (M^3) // 8th Moscow Solar System Symposium. 2017. Art. No. 8MS3-PG-09.
[12] *Marov M.Ya., Slyuta E.N.* Early steps toward the lunar base deployment: Some prospects // Acta Astronautica. 2021. V. 181. P. 28–39. https://doi.org/10.1016/j.actaastro.2021.01.002.
[13] *Mitrofanov I.G., Zelenyi L.M., Tret'yakov V.I., Kalashnikov D.V.* Luna-25: The first polar mission to the Moon // Solar System Research. 2021. V. 55. Iss. 6. P. 485–495. DOI: 10.1134/S0038094621060095.

MODEL STRATIGRAPHY IN THE ARTEMIS LANDING SITES REGION

A.S. Krasilnikov[1], M.A. Ivanov[1], S.S. Krasilnikov[1,2], J.W. Head[3]
[1] *Vernadsky Institute of Geochemistry and Analytical Chemistry, RAS, Moscow, Russia, krasilnikov_as@geokhi.ru*
[2] *Hong Kong Polytechnic University, Hong Kong, PRC, sergey.krasilnikov@polyu.edu.hk*
[3] *Brown University, Providence, RI, USA, James_Head@brown.edu*

KEYWORDS:
Luna, Artemis, landing sites, crater ejecta, SPA

INTRODUCTION:

The southern circumpolar region of the Moon (SCR) is a geologically complex area [1] whose topography was largely formed by four major impact events [2–3]: the South Pole-Aitken (SPA), Bailly, Amundsen-Ganswindt, and Schrödinger basins. The close areal clustering of the four basins suggests that their ejecta came from similar crustal (and possibly mantle) domains of the Moon [4].

The Artemis region [5] is in a zone interpreted to be on the rim of the SPA basin where the ejecta could be contiguous and thick. Their estimated model thickness is ~5.4 km. Most of successive impacts [1] caused excavation and re-distribution of the SPA ejecta materials, which therefore could potentially be found throughout the SCR and in all Artemis sites as well.

Diameters of the post-SPA basins, Bailly, Amundsen-Ganswindt, and Schrödinger vary from ~300 to ~350 km. This means that the excavation depth of their impacts exceeded the model thickness of the SPA ejecta, and ejecta deposits of these basins likely contain a significant proportion of materials characterizing the earliest (pre-SPA) stages of lunar evolution. Thus, ejecta of these basins has very high scientific potential.

The region of the Artemis landing sites is near the southern portion of the Amundsen-Ganswindt basin. This basin is thus likely to represent the major contributor of materials that have been deposited at the landing sites. The Amundsen-Ganswindt basin (AGB, ~350 km diameter) is within the Mg-pyroxene zone of the SPA, away from the central compositional anomaly of the basin [6]. The AGB impact likely excavated materials that are not contaminated by SPA impact melt.

DIGITAL FORMATS FOR FIGURES:

In order to estimate a model thickness of ejecta of impact craters and basins within the Artemis region, we used models proposed in [7] for craters <45 km, [8] for craters 45–300 km, and [9] for basins >300 km. The relative ages of the deposits with the estimated thickness were derived from the recently published geological map of the SCR [1].

In all landing sites studied in our work, the model thickness of ejecta of the Amundsen-Ganswindt basin exceeds several hundred meters, ranging from ~400–500 to 1500–2000 m. Ejecta of the younger craters that overlay deposits of the basin are relatively thin, with the mean model thickness ranging from zero to ~650 m. The usually adopted estimate of the excavation depth (1/10 of crater diameter, e.g., [10]) suggests that relatively small craters (several kilometers diameter) formed on the surface of the pre-Nectarian deposits can excavate ejecta of the of Amundsen-Ganswindt basin. These craters could represent targets of higher priority.

Although the composite layer of deposits from the smaller craters that mantles the Amundsen-Ganswindt ejecta was derived from different sources, it still represents a generalized sample of materials ejected from the SPA basin. Because most of the craters responsible for the formation of the composite layer are concentrated in the SPA rim zone, they re-distributed materials ejected by the SPA impact from the upper portions of the ancient lunar crust. Thus, the suites of deposits in the Artemis sites allow analysis of both the lower (the Amundsen-Ganswindt ejecta) and the upper (the SPA ejecta) horizons of the ancient lunar interior.

The other intriguing feature of the SCR is the local enhanced concentration of hydrogen in the regolith [11–16], which is usually interpreted as a constituent of water [12]. Within the Artemis region, ejecta of four craters, Cabeus, Shoemaker, Haworth, and Faustini are characterized by the higher concentration of hydrogen, which can be as high as 0.5 mas% of water equivalent hydrogen, WEH [15]. The higher values of the WEH characterize both the interior and the zone of contiguous ejecta of these craters. The hydrogen-bearing phases are likely to represent extremely friable components of the regolith. Still, it is important to analyze ejecta of craters with the high WEH in order to constrain both the physical state of hydrogen, its sources, and possible modes of its accumulation and preservation in the regolith. In several proposed landing sites, ejecta from craters Shoemaker, Haworth, and Faustini comprise the upper portion of the regolith layer and the hydrogen-bearing materials may be present on the surface of these sites. The total model thickness of ejecta of these craters may be up to 150–250 m.

Acknowledgements:
The work is supported by the Russian Science Foundation grant no. 21-17-00035: Estimates of the rate of exogenous resurfacing on the Moon.

References:

[1] *Krasilnikov S.S., Ivanov M.A., Head J.W., Krasilnikov A.S.* Geologic history of the south circumpolar region (SCR) of the Moon // Icarus. 2023. V. 394. Art. No. 115422. https://doi.org/10.1016/j.icarus.2022.115422.

[2] *Fassett C.I., Head J.W., Kadish S.J. et al.* Lunar impact basins: Stratigraphy, sequence and ages from superposed impact crater populations measured from Lunar Orbiter Laser Altimeter (LOLA) data // J. Geophysical Research. 2012. V. 117. Iss. E12. Art. No. E00H06. DOI: 10.1029/2011JE003951.

[3] *Neumann G.A., Zuber M.T., Wieczorek M.A. et al.* Lunar impact basins revealed by Gravity Recovery and Interior Laboratory measurements // Science Advances. 2015. V. 1. Iss. 9. Art. No. e1500852. DOI: 10.1126/sciadv.150085.

[4] *Jollif B.L., Gillis J.J., Haskin L.A. et al.* Major lunar crustal terranes: Surface expressions and crust-mantle origins // J. Geophysical Research. 2000. V. 105. Iss. E2. P. 4197–4216. https://doi.org/10.1029/1999JE001103.

[5] https://www.nasa.gov/press-release/nasa-identifies-candidate-regions-for-landing-next-americans-on-moon.

[6] *Moriarty D.P., Pieters C.M.* The character of South Pole-Aitken Basin: Patterns of surface and subsurface composition // J. Geophysical Research: Planets. 2018. V. 123. Iss. 3. P. 729–747. https://doi.org/10.1002/2017JE005364.

[7] *Sharpton V.L.* Outcrops on lunar crater rims: Implications for rim construction mechanisms, ejecta volumes and excavation depths // J. Geophysical Research. 2014. V. 119. Iss. 1. P. 154–168. DOI: 10.1002/2013JE004523.

[8] *Housen K.R., Schmidt R.M., Holsapple K.A.* Crater ejecta scaling laws: fundamental forms based on dimensional analysis // J. Geophysical Research. 1983. V. 88. Iss. B3. P. 2485–2499. DOI: 10.1029/JB088iB03p02485.

[9] *Fassett C.I., Head J.W., Smith D.E. et al.* Thickness of proximal ejecta from the Orientale Basin from Lunar Orbiter Laser Altimeter (LOLA) data: Implications for multiring basin formation // Geophysical Research Letters. 2011. V. 38. Iss. 17. Art. No. L17201. DOI: 10.1029/2011GL048502.

[10] *Melosh H.J.* Impact Cratering: A Geologic Process. N.Y.: Oxford University Press, 1989. 254 p.

[11] *Mitrofanov I.G., Bartels A., Bobrovnitsky Y.I. et al.* Lunar Exploration Neutron Detector for the NASA Lunar Reconnaissance Orbiter // Space Science Review. 2010. V. 150. Iss. 1–4. P. 183–207. DOI: 10.1007/s11214-009-9608-4.

[12] *Mitrofanov I., Litvak M., Sanin A. et al.* Testing polar spots of water-rich permafrost on the Moon: LEND observations onboard LRO // J. Geophysical Research. 2012. V. 117. Iss. E12. Art. No. E00H27. DOI: 10.1029/2011JE003956.

[13] *Boynton W.V., Droege G.F., Mitrofanov I.G. et al.* High spatial resolution studies of epithermal neutron emission from the lunar poles: Constraints on hydrogen mobility // J. Geophysical Research. 2012. V. 117. Iss. E12. Art. No. E00H33. DOI: 10.1029/2011JE003979.

[14] *Litvak M.L., Mitrofanov I.G., Sanin A.B. et al.* LEND neutron data processing for the mapping of the Moon // J. Geophysical Research. 2012. V. 117. Iss. E12. Art. No. E00H32. DOI: 10.1029/2011JE004035.

[15] *Sanin A.B., Mitrofanov I.G., Litvak M.L. et al.* Testing lunar permanently shadowed regions for water ice: LEND results from LRO // J. Geophysical Research. 2012. V. 117. Iss. E12. Art. No. E00H26. DOI: 10.1029/2011JE003971.

[16] *Sanin A.B., Mitrofanov I.G., Litvak M.L. et al.* Hydrogen distribution in the lunar polar regions // Icarus. 2017. V. 283. P. 20–30. https://doi.org/10.1016/j.icarus.2016.06.002.

SOURCES OF MATERIALS IN THE LUNA-16 SAMPLE

M.A. Ivanov[1], J.W. Head[2], H. Hiesinger[3]
[1] *Vernadsky Institute of Geochemistry and Analytical Chemistry, RAS, Moscow, Russia, mikhail_ivanov@brown.edu*
[2] *Brown University, Providence, RI, USA, James_Head@brown.edu*
[3] *University of Münster, Münster, Germany, hiesinger@uni-muenster.de*

KEYWORDS:
Moon, Mare Fecunditatis, Luna-16, provenance, absolute ages

INTRODUCTION:

Luna-16 drilled and returned to Earth a core sample that represents the uppermost 35 cm of lunar regolith at the landing site [1]. Although the Luna-16 drill core shows no distinctive layering, it was divided into several zones according to changes in the median grain sizes of the regolith particles [1]. The vertical distribution of particles of different types shows that agglutinates are the dominant type of particles in zones A, C, and D. Zone B is dominated by breccias, and agglutinates in this zone are as abundant as gabbro particles. The presence of such contrasting components as gabbro/basalt and anorthosite indicates different sources of materials deposited in the landing site region.

NON-MARE COMPONENTS:

The non-mare components of the sample are obviously sourced from numerous rays extending radially from craters within the highlands. In the landing site area, the rays are mostly oriented in the SW-NE and SE-NW directions (Fig. 1). The most likely source of the NW-trending rays is the crater Langrenus (~300 km SE of the landing point), whose rays and secondary craters can be traced to the landing site region. In the vicinity of the landing site there are no rayed craters that could have been the sources of the NE-trending rays. One of the rays of Tycho crater (~2,500 km SW of the landing site), however, extends in the northeastern direction and is recognizable near the landing site within about 5–10 km. Tycho crater may thus represent a potential additional source for the non-mare materials in the Luna 16 regolith, similar to soil fragment at the Apollo-17 site in SW Serenitatis [2], even further from Tycho.

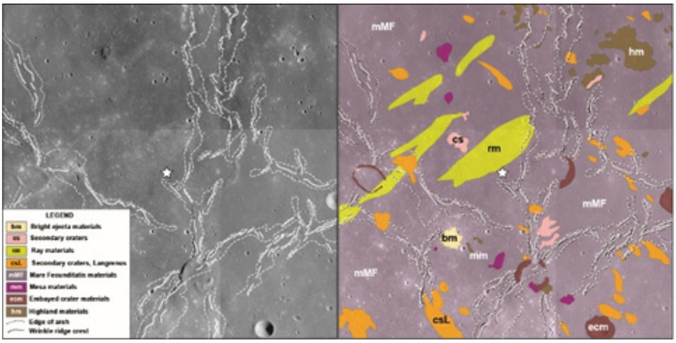

Fig. 1. Geological map of the Luna-16 landing site and its immediate surroundings

MARE COMPONENTS:

The gabbro and basalt particles in the Luna 16 sample obviously represent fragments of volcanic materials that had different thermal histories. They may have been brought to the landing site from different sources within Mare Fecunditatis. Alternatively, the gabbro and basalt particles may represent fragments of a single lava flow(s) that experienced different cooling history. For example, basalts may correspond to the rapidly chilled boundary layers, whereas the gabbroic particles could form in the slow cooling interior of the flow(s). The mutual occurrence of basalt and gabbro particles in one core may be additional evidence of mixing of materials composing the Luna-16 core. The apparent emplacement of multiple flows of volcanic materials in Mare Fecunditatis suggests that their absolute radiometric ages can vary depending upon duration and time separation of different volcanic phases.

AGE DETERMINATIONS:

The large error bars of the earlier determinations of the absolute age, 3.5±0.6 Ga (Fig. 2) could be partly the result of mixing of materials with different emplacement times in one analytical sample, which was derived from gabbro particles analyzed from different zones of the sample [3]. In contrast, the absolute age of a single basalt particle [4] is much more well-constrained (see Fig. 2). Later studies of the absolute ages of volcanic particles in the Luna 16 sample (see Fig. 2) showed either ranges of ages [5,6] or a bimodal distribution of ages [7]. These results suggest that the volcanic materials in the Luna-16 sample have different sources that probably were active at different times.

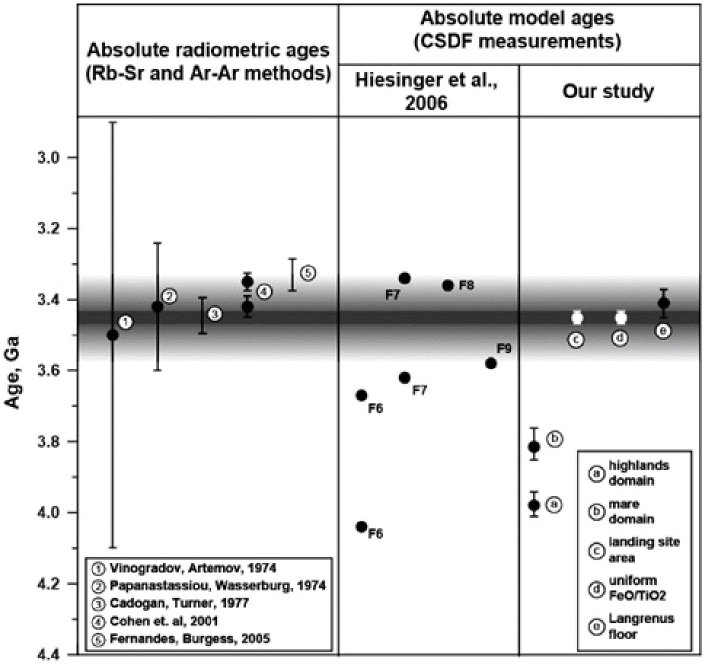

Fig. 2. Comparison of the radiometric ages of particles in the Luna-16 sample and collection of the results of the AMA determinations in different parts of Mare Fecunditatis

CONCLUSIONS:

This conclusion seems to be in agreement with the results of AMA determinations from CSFD measurements. The different spectrally defined units in Mare Fecunditatis are characterized by a variety of AMAs [8] and these ages have a bimodal distribution. The younger AMAs are clustered at ~3.35 Ga and the older AMAs are around ~3.65 Ga (see Fig. 2).

Our determinations of AMAs in the area around the landing site and in the region with uniform distribution of FeO and TiO_2 (see Fig. 2) are consistent with most radiometric age determinations and we conclude that they are likely to reflect the latter stage of emplacement of volcanic materials in Mare Fecunditatis, between about 3.5–3.4 Ga ago (see Fig. 2). Although older radiometric ages have not yet been reported, the presence of older basalts in the Luna-16 sample cannot be ruled out, taking into account the well-mixed character of the sample and, thus, multiple sources of its materials and evidence for the emplacement of multiple phases of lavas in Mare Fecunditatis. Further analyses of Luna-16 samples and radiometric age determinations on a larger number of fragments should be undertaken.

References:

[1] *Vinogradov A.P.* Preliminary data on lunar ground brought to Earth by automatic probe Luna-16 // Proc. 2nd Lunar Science Conf. 1971. V. 2. 16 p.

[2] *Vaniman D.T., Labotka T.C., Papike J.J. et al.* The Apollo-17 drill core: Petrologic systematics and the identification of a possible Tycho component // Proc. 10th Lunar Science. Conf. 1979. V. 10. P. 1185–1227.

[3] *Vinogradov A.P., Artjemov Yu.M.* Absolute age of lunar regolith material from Sea of Fertility // Lunar soil from Sea of Feritility. M.: Nauka, 1974. P. 455–467. (In Ruassian)/

[4] *Papanastassiou D.A., Wasserburg G.J.* Rb-Sr age of Luna-16 basalt and the model age of lunar soil // Lunar soil from Sea of Feritility. M.: Nauka, 1974. P. 471–477.

[5] *Cadogan P.H., Turner G.* ^{40}Ar-^{39}Ar dating of Luna-16 and Luna-20 samples // Philosophical Trans. Royal Society. 1977. V. 284. Iss. 1319. P. 167–177. https://doi.org/10.1098/rsta.1977.0007.

[6] *Fernandes V.A., Burgess R.* Volcanism in Mare Fecunditatis and Mare Crisium: Ar-Ar age studies // Geochimica et Cosmochimica Acta. 2005. V. 69. Iss. 20. P. 4919–4934. https://doi.org/10.1016/j.gca.2005.05.017.

[7] *Cohen B.A., Snyder G.A., Hall C.M. et al.* Argon-40-argon-39 chronology and petrogenesis along the eastern limb of the Moon from Luna 16,20 and 24 samples // Meteoritics Planetary Science. 2001. V. 36. No. 10. P. 1345–1366.

[8] *Hiesinger H., Head J.W., Wolf U. et al.* New ages for basalts in Mare Fecunditatis based on crater size-frequency measurements // 37th Lunar Planetary Science Conf. 2006. abs. 1151.

NEW FINDINGS OF SURFACE DEPOSITS IN CRYPTOMARE REGION REVEALED BY CE-2 MRM DATA

Z.G. Meng[1], W.Q. Chang[1], T.Q. Tang[1], J.S. Ping[2,3], Y.Z. Zhang[2,3], A. Gusev[4]
[1] *College of Geoexploration Science and Technology, Jilin University, Changchun, China, mengzg@jlu.edu.cn, changwq20@mails.jlu.edu.cn*
[2] *National Astronomical Observatory, Chinese Academy of Sciences, Beijing, China, jsping@bao.ac.cn, zhangyz@nao.cas.cn*
[3] *School of Astronomy and Space Science, University of Chinese Academy of Sciences, Beijing, China*
[4] *Kazan Federal University, Department of Mathematical Methods in Geology, Kazan, Tatarstan, Russia*

KEYWORDS:
cryptomare region, microwave radiometer, surface deposits, thermophysical parameter, normalized brightness temperature

INTRODUCTION:

The Cryptomare is a mare basalt deposits covered by impact ejecta, which records early lunar volcanic activity (3.8 ~ 4.35 Ga) [1], and can provide important information on the thermal evolution of the moon [2, 3]. Currently, the recognition of the Cryptomare is mainly based on the Dark Haloed Crater (DHC) by using the visible data [4]. However, the recognition is heavily affected by shadow effects in images and by space weathering [5].

In China's Chang'E (CE)-1/2 missions, a microwave radiometer (MRM) was onboard to passively measure the brightness temperature (TB) of the regolith. The MRM data are sensitive to the thermophysical features of surface deposits within the penetration depth [6]. Thus, MRM data were tried to way to assess the distribution and dielectric properties of surface deposits in the cryptomare, sampled by the Balmer-Kapteyn region.

METHODOLOGY:

The CE-2 MRM data were used in this work. The instrument obtained a total of approximately 3650 observation records in one orbital period (118 min). The observation angle of the instrument was 0°. The radiometric sensitivity of the MRM data was better than 0.5 K [6]. After ascribing the the observed MRM points into 24 lunation hours, the Delaunay triangulation linear interpolation method was used to generate TB maps of the Balmer-Kapteyn region with a spatial resolution of 0.25×0.25°. Then, The normalized TB (nT_B) mapping method, defined by Z. Meng et al. [7], were applied to weaken the change of the TB with latitude (Figure 1).

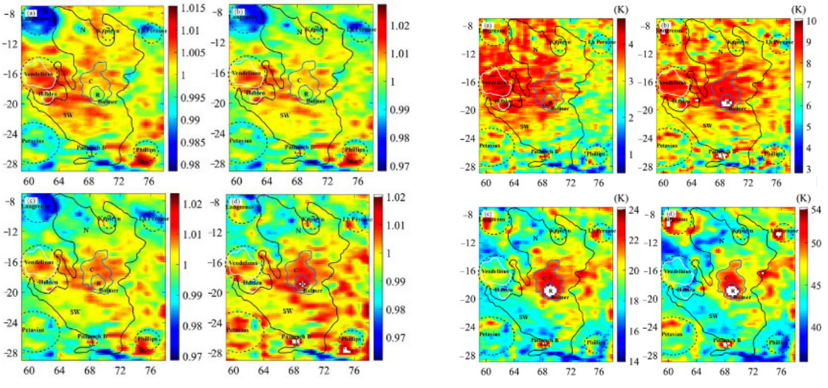

a b c d

Fig. 1. nT_B maps of the Balmer-Kapteyn region at noon (left) and night (right): *a* — 3.0 GHz; *b* — 7.8 GHz; *c* — 19.35 GHz; *d* —37 GHz. Black line: cryptomare unit, white line: mare unit [2]

FINDINGS:

1. DEFINING MARE-LIKE CRYPTOMARE DEPOSIT

In cryptomare unit, the regular T_B performances occur in the central part marked C (see Fig. 1), which indicates relatively high nT_B values at noon, relatively low nT_B values at night, and relatively high dT_B values. Similar T_B performances are also found in the basaltic deposits of the Maria Imbrium, Moscoviense, Apollo Basin, and Rümker regions [7, 8]. That is, the material in Region C appears to be mare deposit. However, in the Balmer-Kapteyn cryptomare region, the existence of mare deposits is impossible, because the impact ejecta is as thick as at 33 m [3]. Thus, we denote the materials found in Region C as mare-like cryptomare deposit (MCD).

The discovery of MCD is helpful for improving our understanding of basaltic volcanism in the Balmer-Kapteyn region. Here, the buried mare deposits in Region C were lacking in the Th element, indicating that the buried mare deposits in this region are in a younger episode compared with the northern part of the Balmer-Kapteyn region. Thus, there are at least two kinds of buried mare deposits in the Balmer-Kapteyn region, which erupted during different episodes.

2. FINDING A CONSTRUCT-LIKE VOLCANIC FEATURE

In Region R, at daytime, the nT_B is relatively low at 3.0 and 7.8 GHz, similar at 19.35 GHz, and is clearly higher at 37 GHz compared with the nearby regions; at night, the nTB is clearly lower than its vicinity. The nT_B behaviors evidence that there are abundant rocks in Region R.

Considering that the penetration depth of the MRM microwave is at least several tens of centimeters and is much larger than the micrometer-scale penetration depth of the RA-related thermal infrared data, this phenomenon implies that there likely exists a hidden construct in Region R.

Based on Clementine UV–VIS data and M3 spectra data, B.R. Hawke et al. [2] and X. Wang and D. Qiu [3] both mentioned the special compositions in crater S, which are gabbro and monzogabbro enriched in high-Ca pyroxene. Considering that Region R is located just within Region C and that they both represent late-episode volcanic activity, we propose that the hidden construct in Region R is probably a construct-like volcanic feature.

3. DISCOVERING SPECIAL MATERIALS WITH LOW T_B DIFFERENCE

When generating the T_B difference (dTB) map between the T_B maps at daytime and at night (Figure 2), there exists low dT_B anomaly in the mare unit within the Vendelinus crater and the northwest and southwest ports of the study area, marked by the yellow line in Figure 2.

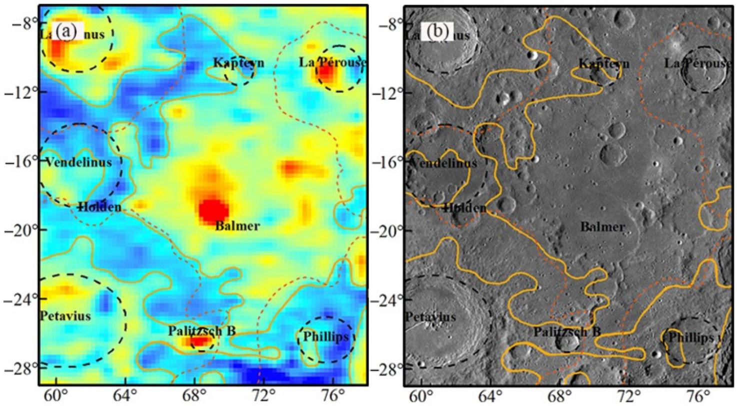

Fig. 2. (a) Low-dT_B anomaly outlined (orange line) in the dT_B map at 37 GHz. (b) Boundary of the low-dTB anomaly expressed in the WAC image. The dashed lines are boundaries of the impact ejecta identified by B.R. Hawke et al. [2].

The regional geochemistry and chemical components of the Balmer-Kapteyn region have been fully studied by B.R. Hawke et al. [2] and X. Wang and

D. Qiu [3], but none of the components appear to be responsible for the low-dT_B anomaly, at least in geographical position. That is, there probably exists a new chemical component that has not been identified, at least in the Balmer-Kapteyn region, which causes the low-dT_B anomaly.

When projecting the boundary of the low-dT_B anomaly and the boundaries of the ejecta interpreted by B.R. Hawke et al. [2] on the WAC images in Figure 2b, a strong correlation between the low-dT_B anomaly and the impact ejecta identified by B.R. Hawke et al. [2] was observed. We mentioned that the low-dT_B anomaly in the western part comprises large portions of the ejecta from the Langrenus and Petavius craters. In the southeastern area, the special material mainly exists in the ejecta from the Humboldt crater. In particular, the boundary of the low-dT_B anomaly largely agrees with the northeastern margin of the ejecta from the Petavius crater in the southwestern area. These agreements suggest that the special material is probably the ejecta of large craters. Considering the large excavation depth of large craters such as Langrenus, Petavius, and Humboldt, according to the cratering numerical simulation [8], the special material should originate in the deep layer of the lunar crust [9].

Acknowledgements:
This research was funded by the National Key R&D Program of China (no. 2021YFA0715104), the National Natural Science Foundation of China (no. 42071309), and the Natural Science Foundation of Jilin Province (no. 20220101159JC).

References:
[1] *Whitten J.L., Head J.W.* Lunar cryptomaria: Physical characteristics, distribution, and implications for ancient volcanism // Icarus. 2015. V. 247. P. 150–171. https://doi.org/10.1016/j.icarus.2014.09.031.
[2] *Hawke B.R., Gillis J.J., Giguere T.A. et al.* Remote sensing and geologic studies of the Balmer-Kapteyn region of the Moon // J. Geophysical Research. Planets. 2005. V. 110, Iss. E6. https://doi.org/10.1029/2004JE002383.
[3] *Wang X., Qiu D.* Lunar Cryptomare: New Insights Into the Balmer-Kapteyn Region // J. Geophysical Research. Planets. 2018. V. 123. Iss. 12. P. 3238–3255. https://doi.org/10.1029/2018JE005693.
[4] *Kaydash V., Shkuratov Y., Videen G.* Dark halos and rays of young lunar craters: A new insight into interpretation // Icarus. 2014. V. 231. P. 22–33. https://doi.org/10.1016/j.icarus.2013.11.025.
[5] *Lucey P.G., Blewett D.T., Taylor G.J., Hawke B.R.* Imaging of lunar surface maturity // J. Geophysical Research. Planets. 2000. V. 105. P. 20377–20386. https://doi.org/10.1029/1999JE001110.
[6] *Zheng Y., Chan K.L., Tsang K.T. et al.* Analysis of Chang'E-2 brightness temperature data and production of high spatial resolution microwave maps of the Moon // Icarus. 2019. V. 319. P. 627–644. DOI: 10.1016/j.icarus.2018.09.036.
[7] *Meng Z., Hu S., Wang T. et al.* Passive Microwave Probing Mare Basalts in Mare Imbrium Using CE-2 CELMS Data // IEEE J. Selected Topics in Applied Earth Observations and Remote Sensing. 2018. V. 11. Iss. 9. P. 3097–3104. DOI:10.1109/JSTARS.2018.2845417.
[8] *Yue Z., Johnson B.C., Minton D.A. et al.* Projectile remnants in central peaks of lunar impact craters // Nature Geoscience. 2013. V. 6. Iss. 6. P. 435–437. DOI:10.1038/ngeo1828.
[9] *Tang T., Meng Z., Lian Y., et al.* New Insights into Surface Deposits in the Balmer-Kapteyn Cryptomare Region Provided by Chang'E-2 Microwave Radiometer Data // J. Remote Sensing. 2022. V. 14. Iss. 18. Art. No. 4556. https://doi.org/10.3390/rs14184556.

DEGRADATION OF FRESH-LOOKING CRATERS ON THE MOON

X. Kochubey[1], M. Ivanov[2]
[1] *Lomonosov Moscow State University, Moscow, Russia, kochubey.ksenia@yandex.kz*
[2] *Vernadsky Institute of Geochemistry and Analytical Chemistry, RAS, Moscow, Russia*

KEYWORDS:
Moon, craters, slope, erosion, erosion rate, crater degradation

INTRODUCTION:

Impact craters are the most common type of landform on the Moon. Small lunar craters are susceptible to changes in topography and surface processes. The study of crater degradation provides new data on lunar erosion. Recent orbiters have provided higher-resolution remote sensing data of the lunar surface, which enable reliable and accurate estimation of morphometric parameters for even small craters [1–2].

We present results of a study of morphologically prominent craters on the Moon in four regions: Mare Fecunditatis, Mare Crisium, Mare Serenitatis and Montes Apenninus. Aim of our research is to receive quantitative estimates of different aspects of crater degradation.

APPROACH:

In order to work out a methodic of the study and to pursue the main goal of our study, we have selected 24 morphologically prominent craters in a diameter range from ~5 km (Webb-U) to 14.4 km (Greaves). For each crater, we have conducted crater size-frequency distribution measurements (CSFD) both on the rim and walls using the Kaguya mosaics with resolution ~7 m/px. On the rim, measurements were made in four polygons within a one-radius-wide zone around the crater rim crest. Inside the craters, measurements were conducted on the northern and southern portions of the wall where illumination conditions permitted confident identification of craters. Along with CSFD measurements, we also have measured steepness of the northern and southern walls of the studied craters by constructing topographic profiles and then by linear best-fit approximation of the walls. We used the LOLA gridded topography map with spatial resolution of ~60 m/px.

RESULTS/DISCUSSION:

In the vast majority, the density of small craters in the rim areas of the larger ones is higher than on the crater walls and its ratio (*Dr*/*Dw*) varies from ~0.6 up to 124 for all diameter bins (root-2 binning). Compared sections differ in steepness. The difference in crater densities on rims and walls of larger craters is due to the higher erosion rates on the inner slopes of craters compared to the lower erosion activity on the subhorizontal rim areas. Values of *Dr*/*Dw*, which are less than 1, are rare and are found for the smallest crater diameters (11–23 m). These craters are underrepresented in the data sample due to the spatial resolution of the images. Thus, these values may not reflect certain trends and have random nature.

There is a tendency of increasing of the *Dr*/*Dw* ratio as the mean diameter of the superimposed craters increases. This tendency may suggest that the larger craters on the walls are more effectively erased compared with the smaller craters. Such an explanation does not seem plausible and we believe that an observational effect is responsible for the increase of the ratio. The mass-wasting processes on the steep-sloped walls (23–33° for the studied craters) constantly modify the older crater populations erasing the smaller craters and modifying the larger ones. The larger craters are losing their distinctive morphologies and are not recognized as impact structures. The smaller craters on the walls represent the younger crater populations that had more chances to survive as recognizable features. That tendency is weakly manifested for the Apenninus craters (Marco Polo-H, Galen, Conon-A). That may be due to the fact that geological structure of the Apenninus region (ejecta from Mare Imbrium) differs from other areas (mare basalts).

There is a noticeable correlation (Spearman's correlation coefficient = –0.64) between the crater age and the steepness of crater walls (Fig. 1) for mare regions. The estimated rate of mare basalts' craters wall flattening is 1.7 deg/Gyr, which is extremely low. Addition of Apenninus craters into the sample leads to decreasing of correlation coefficient (–0.50).

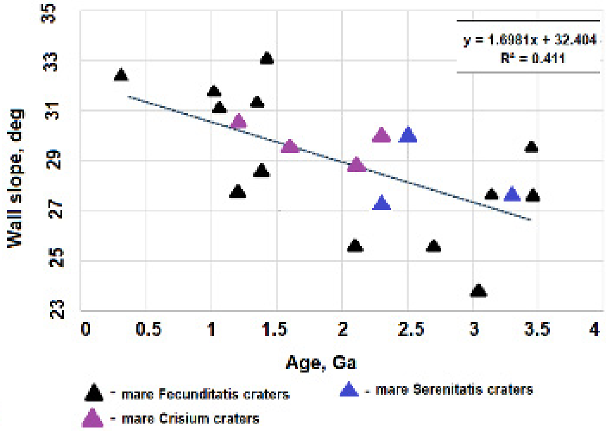

Fig. 1. Correlation between crater AMA and the slope of its walls

Comparison of the densities of the superposed craters on the northern (equatorward) and southern (poleward) walls of the studied craters illustrates how the wall exposition and different thermal regimes affect mass-wasting processes. For 8 out of 13 craters in Mare Fecunditatis the density of superposed craters on the equatorward wall is systematically lower (Fig. 2 *left*). For these craters the difference is pronounced and a deficiency of the smaller craters (35–80 m diameter) on the equatorward wall is sufficient. These differences suggest that on the northern wall mass-wasting processes were more effective compared with the southern wall and removed a layer ~3.5–8 m thick. These estimates suggest erosion rate as high as ~2 mm/Myr. Some craters located at 0° latitude show no difference in the crater density on the walls (Fig. 2 *right*). There are also no significant differences in crater densities on the inner slopes of the craters in other regions such as Mare Crisium, Mare Serenitatis and Apennines. Consequently, the effect of surface exposure on the intensity of mass wasting is ambiguous.

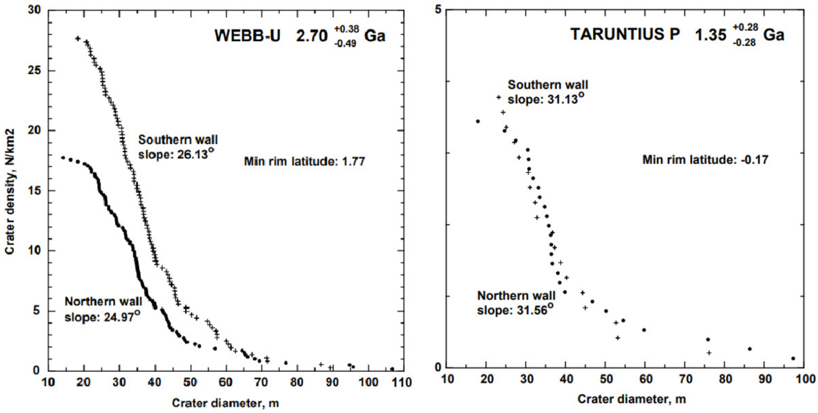

Fig. 2. Crater cumulative densities on the northern and southern walls. Cumulative crater density on the southern (poleward) wall of crater Webb-U (2.70 Ga) is significantly higher for the superposed craters larger than ~60 m (*left*). Identical densities of the crater Taruntius-P (1.35 Ga) which is located at 0° latitude (*right*)

To estimate the erosion rates on crater slopes relative to the flat rim areas (Fig. 3), we used Dr/Dw ratio in all diameter ranges of superposed craters.

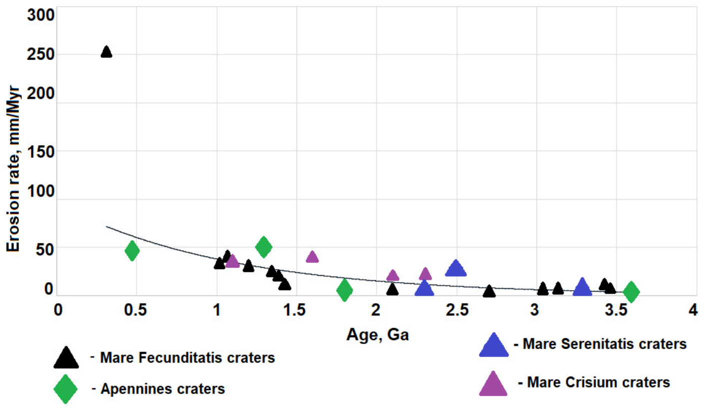

Fig. 3. Erosion rates on craters inner slopes

The erosion rates (*Er*) were calculated using the formula:

$Er = (Mdw \times 0.1 \times Dr/Dw)/(\mathrm{Ac} - \mathrm{A}w)$,

where *Mdw* is the median diameter of the population of superposed craters on the walls; *Ac* is the absolute model age, AMA, of the study crater (from CSFD measurements in the crater rim areas); *Aw* is the AMA on the inner walls of key crater. Estimated erosion rates vary over large ranges and decline sharply with time (see Fig. 3). Thus, for our youngest crater, Messier (0.31 Ga), the calculated rate is 275 mm/Myr, and for our oldest crater, Conon-A (3.6 Ga), the rate is 3.6 mm/Myr. Our estimates are an order magnitude higher than the rates reported earlier [3–5]. However, our estimates are related to the steep-sloped walls where the higher erosion rate is expected.

Acknowledgements:
The work is supported by the Russian Science Foundation grant no. 21-17-00035: Estimates of the rate of exogenous resurfacing on the Moon.

References:

[1] *Mahanti P., Robinson M.S., Thompson T.J. et al.* Small lunar craters at the Apollo-16 and -17 landing sites — morphology and degradation // Icarus. 2018. V. 299. P. 475–501. https://doi.org/10.1016/j.icarus.2017.08.018.

[2] *Vijayan S., Vani K., Sanjeevi S.* Topographical analysis of lunar impact craters using SELENE Images // Advances in Space Research. 2013. V. 52. Iss. 7. P. 1221–1236. https://doi.org/10.1016/j.asr.2013.06.025.

[3] *Craddock R.A., Howard A.D.* Simulated degradation of lunar impact craters and a new method for age dating farside mare deposits // J. Geophysical Research. 2000. V. 105. Iss. E8. P. 20387–20401. https://doi.org/10.1029/1999JE001099.

[4] *Fassett C.I., Combellick J.R.* The rate of crater degradation and topographic evolution on the Moon: Results from the maria and initial comparisons with the highlands // 45th Lunar and Planetary Science Conf. 2014. abs. 1429.

[5] *Fassett C.I., Thomson B.J.* Crater degradation on the lunar maria: Topographic diffusion and the rate of erosion on the Moon // J. Geophysical Research: Planets. 2014. V. 119. Iss. 10. P. 2255–2271. DOI: 10.1002/2014JE004698.

ABSOLUTE MODEL AGE ESTIMATES OF THE PLASKETT CRATER

E.A. Grishakina[1], M.A. Ivanov[1], S.S. Krasilnikov[2]
[1] *Vernadsky Institute of Geochemistry and Analytical Chemistry RAS, Moscow, Russia, grishakina@geokhi.ru*
[2] *The Hong Kong Polytechnic University, Hong Kong, China*

KEYWORDS:
Moon, crater Plaskett, absolute model age, crater size-frequency distribution

INTRODUCTION:

Crater Plaskett (81.63° N, 176.71° E, 114.34 km diameter) is a pre-Imbrian impact structure in the northern subpolar region of the Moon. It has a pronounced steep and terraced walls, flat floor, and a massive central peak. In each of the three areas boulders are exposed both as individual rocks and clusters; some boulders have rolling marks. The flat floor of the crater suggests that it is covered by either impact melt or basaltic flows. In any case, the floor is paved by stronger rocks compared to material that makes up the walls of the crater that likely represent masses of megaregolith displaced during the Plaskett impact event. In this paper, we present our estimates of the absolute model age (AMA) of the crater.

METHOD:

Available data on the surface composition in the polar regions [1] do not show the presence of basaltic lava flows on the floor of Plaskett. Because of this, we presume that the flat floor of the crater is covered by impact melt and, thus, represent an ideal area for crater size-frequency distribution (CSFD) measurements [2] and estimates of the crater's AMA [3, 4]. For CSFD measurements we used medium (WAC, 100 m/px) and high (NAC, 0.5–1.5 m/px) spatial resolution images obtained by the LRO orbiter [5]. A mosaic of WAC images was the main photographic base for our measurements. Its resolution is sufficient to identify craters larger than 500 m diameter. However, significant portions of the floor are in shadows in the WAC mosaics. For these areas, we used both mosaics of NACs and the LOLA LRO DEM with resolution of 20 m/pixel [6].

We used the ArcGIS CraterTool [7] to map primary craters (>0.1–0.5 km) and exported their measured diameters to the Craterstat software [3], which provides the possibility to fit measured CSFD by isochrons [4, 8]; obvious clusters of secondary craters were excluded from the count areas.

In our CSFD measurements we used three data sets with different spatial resolution. Data with the coarser resolution (WACs) allows measurements of craters larger than 400–500 m, which is the lower lower limit of measurements on our study.

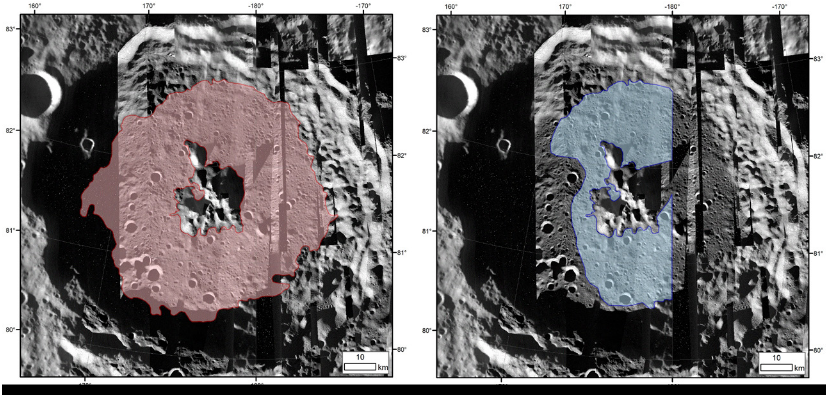

Fig. 1. LROC WAC mosaic partially overlaid with LROC NAC images to interpret craters. On the left, the area of the floor of the Plaskett is bounded in translucent pink, on the right, in translucent blue, the part of the floor is shown, on which the LRO WAC mosaic is informative for CSFD of the floor

In our work, we determined CSFD within the entire floor of Plaskett imaged by the WAC, NAC, and LOLA DEM data (area is 3790.6 km^2, 515 measured craters) and within a part of the floor imaged by the WAC images only (area is 1619.5 km^2, 280 measured craters) in order to see if there are significant/systematic differences between the AMAs obtained with the help of the slightly different data sets. In both cases, the count areas are large enough to provide reliable estimates of the AMAs [9].

RESULTS AND DISCUSSIONS:

The AMA of Plaskett was estimated to be 4.00±0.01 Ga based on CSFD for the entire floor area and 4.00±0.02 Ga based on data for the area where analysis was performed using only LROC WAC images (Figure 2).

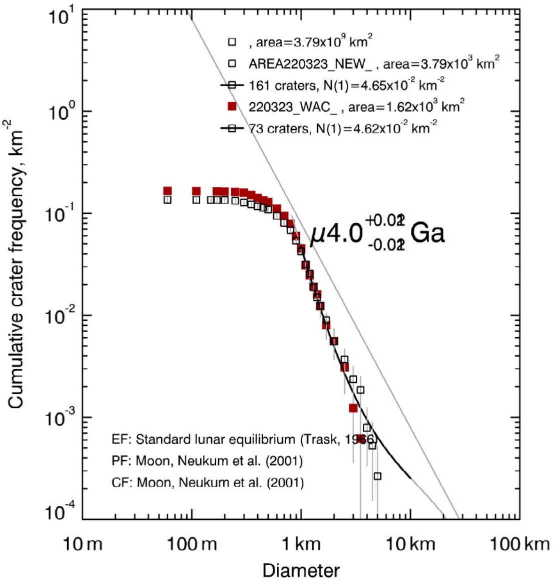

Fig. 2. Size-frequency distribution of superposed primary craters: black-white squares - on the floor of the Plaskett, red squares - on the floor part of the Plaskett on which the LRO WAC mosaic is informative

The differences in dating are practically absent, which is an exopected results. The AMA of Plaskett estimated in our study corresponds to pre-Nectarian epoch according to the chosen chronology model [4, 8] and, thus, is strongly different from the age ascribed to the crater in [10]. We believe that our estimate of the Plaskett AMA is more robust because it is based on the results of direct CSFD measurements.

Acknowledgements:

The work is supported by the Russian Science Foundation grant No. 21-17-00035: Estimates of the rate of exogenous resurfacing on the Moon.

References:

[1] *Lemelin M., Lucey P.G., Camon A.* Compositional maps of the lunar Polar regions derived from the Kaguya spectral profiler and the Lunar Orbiter Laser Altimeter Data // The Planetary Science J. 2022. V. 3. No. 3. Art. No. 63. 14 p. DOI 10.3847/PSJ/ac532c.

[2] *van der Bogert C.H., Hiesinger H., Dundas C.M. et al.* Origin of discrepancies between crater size-frequency distributions of coeval lunar geologic units via target property contrasts // Icarus. 2017. V. 298. P. 49–63. https://doi.org/10.1016/j.icarus.2016.11.040.

[3] *Michael G.G., Neukum G.* Planetary surface dating from crater size-frequency distribution measurements: Partial resurfacing events and statistical age uncertainty // Earth and Planetary Science Letters. 2010. V. 294. Iss. 3–4. P. 223–229. https://doi.org/10.1016/j.epsl.2009.12.041.

[4] *Neukum G., Ivanov B.A., Hartmann W.K.* Cratering records in the inner solar system in relation to the lunar reference system // Space Science Reviews. 2001. V. 96. Iss. 1–4. P. 55–86. https://doi.org/10.1023/A:1011989004263.

[5] *Robinson M.S., Brylow S.M., Tschimmel M. et al.* Lunar Reconnaissance Orbiter Camera (LROC) instrument overview // Space Science Reviews. 2010. V. 150. Iss. 1–4. P. 81–124. https://doi.org/10.1007/s11214-010-9634-2.
[6] *Smith D.E., Zuber M.T., Neumann G.A. et al.* Initial observations from the Lunar Orbiter Laser Altimeter (LOLA) // Geophysical Research Letters. 2010. V. 37. Iss. 18. Art. No. L18204. https://doi.org/10.1029/2010GL043751.
[7] *Kneissl T., van Gasselt S., Neukum G.* Map-projection-independent crater size-frequency determination in GIS environments — New software tool for ArcGIS // Planetary and Space Science 2011. V. 59. Iss. 11–12. P. 1243–1254. https://doi.org/10.1016/j.pss.2010.03.015.
[8] *Stöffler D., Ryder G., Ivanov B.A. et al.* Cratering history and lunar chronology // Reviews in Mineralogy and Geochemistry. 2006. V. 60. Iss. 1. P. 519–596. https://doi.org/10.2138/rmg.2006.60.05.
[9] *van der Bogert C.H., Michael G., Kneissl T., Hiesinger H., Pasckert J-H.* Effects of count area size on absolute model ages derived from random crater size-frequency distributions // 46th Lunar and Planetary Science Conf. 2015. Abs. No. 11554.
[10] *Losiak A., Wilhelms D.E., Byrne C. J., Thaisen K., Weider S.Z., Kohout T., O'Sullivan K., Kring D.A.* A new lunar impact crater database // 40th Annual Lunar and Planetary Science Conf. 2009. Abs. No. 1532.

THE STRUCTURE FEATURES OF YOUNG IMPACT CRATERS IN THE AREA OF "BULBOUS FIELDS" ON THE AITKEN CRATER FLOOR

M.I. Shpekin, V.S. Shishkina
Kazan Federal University, Kazan, Tatarstan, Russia, MichaelS1@yandex.ru

KEYWORDS:
impact crater, impact crater structure, Aitken crater floor, bulbous fields, crater topography, Lunar guickmap, crater diameter, crater deep, crater formation process, lunar soil melt, impactor, domes formation

The studied section of the Aitken crater floor is a compact group of 5 small craters. This area is located about 20 km east of the central peak of the Aitken crater and is clearly visible on all orbital images, starting with the Lunar Orbiter spacecraft (1967–1968), and on maps. The surface of three of the five mentioned craters attracts attention with its unusual topography, as it is covered with domes. In some publications the relief of this type was called "bulbous fields". Figure 1 shows a general view of the studied area (~20×16 km) on a map fragment. Table 1 shows the dimensions of all 5 craters. The map fragment and the data in the table are obtained on the basis of LQM (https://quickmap.lroc.asu.edu).

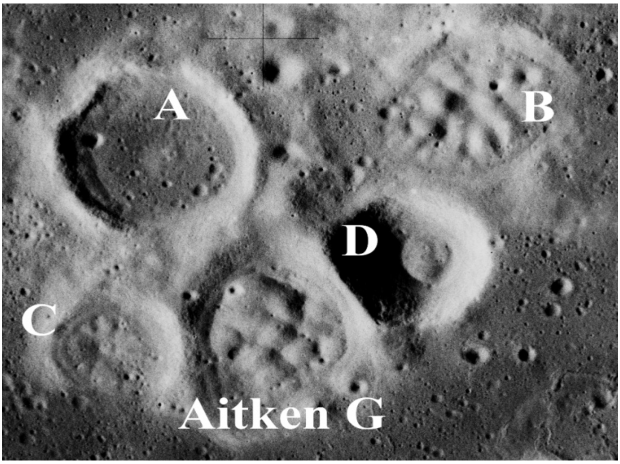

Fig. 1. General view of the Aitken crater floor in the area of the "bulbous fields". The conditional unofficial names of the four craters, which are used within the text of these theses, are indicated in capital letters. **Aitken G** crater is the generally accepted official name on lunar maps

The images and the map show that the material covering the floor of crater **A** is noticeably darker than all the other 4 craters. However, the structure of the floor in craters **B**, **C** and **G** attracts the most attention. Craters **B** and **G**, completely covered with pronounced domes, look especially impressive.

Table 1. Approximate dimensions of the five craters discussed. Craters **B** and **G** have an oval shape, so two values are indicated for them in the "diameter" column. Approximate average depth values are given for the craters **B**, **C** and **G** due to their complex topography

Crater	Diameter, km	Floor diameter, km	Depth, m
A	5.9	4.2	270
B	5×6	4.0	200
C	3.8	3.0	160
D	4.3	1.5	570
G	5×6	4.2	100

It follows from the table that crater **D**, yielding to crater **A** in diameter by one and a half times, exceeds it in depth by more than two times. While its floor is more than three times smaller in diameter. Also striking is the large shadow from the southwestern part of the wall of crater **D**, as well as the small size of its floor. These characteristics served as the basis for a more thorough consideration of crater **D**.

On the 3D-model [1], built by us from the images of the Apollo Spacecraft (https://wms.lroc.asu.edu/apollo/browse), it is clearly visible that crater **D** is noticeably deeper than the rest in the studied area. The great depth of the crater just did not allow us to examine its structure in detail on our model. Then we turned to the LQM database in order to better understand its topography. To begin with, we built high-altitude profiles using the Arc tool. Figure 2 shows the cross-section profiles of crater **D** constructed by us in two different directions. The graphs below show that the slopes of the crater wall and its floor are distinguished by a clearly defined relief. At the same time, the slopes of the wall are quite steep, and a rather curious relief is visible on the floor of the crater, the shape of which attracts attention.

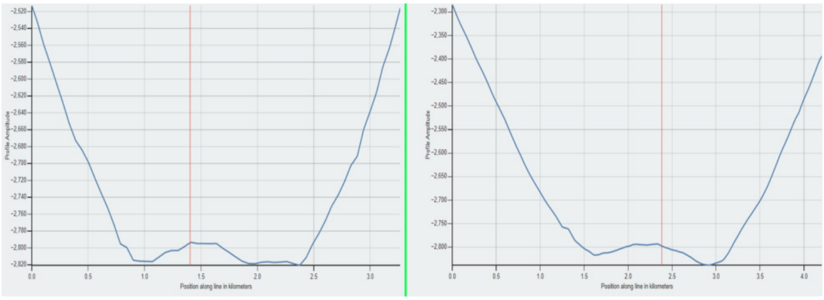

Fig. 2. High-altitude profiles of crater **D** in two sections, built on the basis of LQM map: on the left — along the meridian passing through the center of the crater floor; on the right — along the circle of latitude through the same center

The first thing to note is the absence of a flat bottom flooded with cooled lava from the melt of the lunar soil. Instead, a fairly smooth convex surface is clearly visible, covering the entire territory of the floor within the foot of the inner slope of the crater wall. There is no melt substance on this surface, which is characteristic of the crater formation process. There is no pronounced peak in the central part of the floor, as it happens in the so-called complex craters, and the vicinity of the crater itself is not covered with lunar soil emissions, which usually accompany the explosive process.

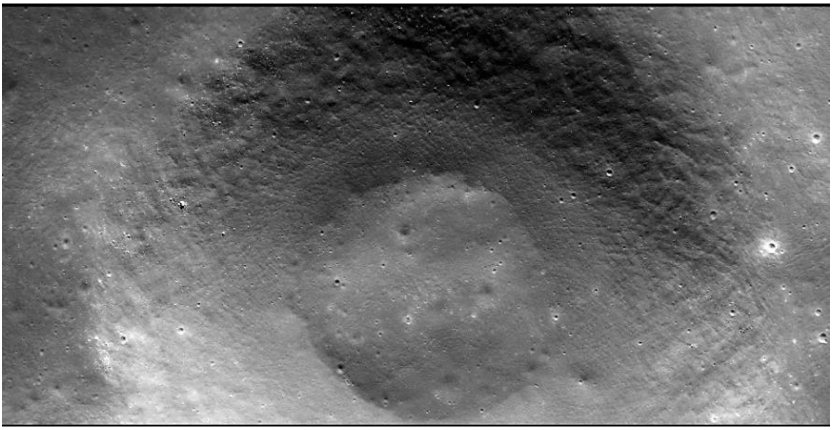

Fig. 3. The crater **D** view in high-resolution image taken by the NAC camera aboard the low-orbit LRO station. Image M176494896LC 11/21/2011, 06:07 (https://wms.lroc.asu.edu/lroc/search)

The properties of crater **D** that we have discovered, listed above, allow us to make the assumption that in the case of this crater we are dealing not with the usual, but with a unique case of crater formation. Apparently, the velocities of the impactor's fall, and therefore the energy of the impact itself, were small enough to lead to the melting of the soil at the point of the fall, as well as to the destruction of the impactor itself. Most likely, it is a slow asteroid, the energy of which was enough to penetrate into the lava lake of Aitken to a considerable depth of several kilometers. But it was not enough to lead to the formation of an explosive process with significant heating of the substance at the point of contact and the release of the substance around the crater **D**.

Apparently, the substance of the asteroid-like impactor turned out to be quite dense, as a result of which excessive pressure was created in the subsurface layer in the vicinity of the "drowned" asteroid, which led to the formation of domes in three nearby neighboring craters: crater **B**, crater **C** and crater **Aitken G**. The combination of domes on the floors of the three named craters formed a rather rare geological phenomenon on the Moon, called "bulbous fields".

Acknowledgements:
The work is performed according to the Russian Government Program of Competitive Growth of Kazan Federal University.

We acknowledge the use of imagery from Lunar QuickMap (https://quickmap.lroc.asu.edu), a collaboration between NASA, Arizona State University and Applied Coherent Technology Corp.

References:
[1] *Shishkina V.S.* Investigation of selected elements of the lunar relief in the Aitken crater using 3D- models: Bachelor thesis. Kazan Federal University, 2023. 56 p.

DYNAMICS OF THE EARTH-MOON AND VENUS-MERCURY SYSTEMS: A COMPARATIVE ANALYSIS

N.A. Chujkova, L.P. Nasonova, T.G. Maksimova
Sternberg Astronomical Institute Lomonosov Moscow State University, Moscow, Russia, chujkova@sai.msu.ru, nason@sai.msu.ru, max@sai.msu.ru

KEYWORDS:
Earth, Moon, Venus, Mercury, evolution of orbits, internal structure, tectonic development

INTRODUCTION:

The dynamics of the Earth-Moon system is considered in detail in our several articles [1–3] and presented in our report at the 13th Moscow Symposium on the Solar System (2022). The questions of the dynamics of the Venus-Mercury system are discussed in detail in the articles in the collection “Solar System” (2017) [4–5], in the article in the collection “Essays on Geophysical Research” (2003) [6], as well as in some articles by other authors.

DYNAMICS OF THE EARTH-MOON SYSTEM:

An analysis of a huge amount of geological and geomorphological data, carried out by a number of researchers and summarized in [7], indicates the latest (over the past 3–1 million years) synchronous uplifts of the Earth’s surface. Our analysis shows that modern uplifts of the earth’s surface in the circumpolar regions are mainly associated with a decrease in the compression of the earth’s surface due to a decrease in the Earth’s rotation rate due to tidal braking due to the gravitational influence of the Moon. Similar conclusions were made in the book [8] in the section “Tectonic Consequences of the Moon’s Tidal Interaction with the Earth”. Consequently, lunar-terrestrial tidal interactions primarily played the role of a “trigger” mechanism that launched tectonic processes on Earth. This is a very important and, apparently, the main consequence of the influence of the moon on our planet. If the Moon did not exist and the preliminary heating of our planet occurred only due to the decay of radioactive elements, then the Earth would still remain for about 2–2.5 billion years. Years as a tectonically passive planet and the cryptotectonic (Katarchean) epoch would have lasted not 600 million years, but all 2.6–3.1 billion years in a row and the first tectonic movements of the earth’s interior appeared only about 2.0–1.5 billion years ago.

It follows that if the Earth did not have its large satellite, then now it would have been dominated by tectonic conditions of the early Proterozoic or even late Archean. Thus, we can conclude that all dynamic phenomena and climate change on Earth are due to the presence of the Moon and the evolution of the Earth-Moon system.

DYNAMICS OF THE VENUS-MERCURY SYSTEM:

Desiring to understand the nature of the planet, we inevitably return to the question of the contamination of the solar system. The processes that took place 4.5 billion years ago, unfortunately, are not complete enough. One of the problems is heat sources for the formation of liquid lava filled with impact craters on Mercury and the Moon. An analysis of lunar rocks shows that the age of the laurel frozen on the surface has decreased to 4 billion years. For the calculation of Mercury, based on the unification of the rate of decay of radioactive elements, it is shown that the preceding natural differentiation of the heating of Mercury should have taken 1.0–4.5 billion years, which covers the age of the lava. Another hypothesis — an attempt to explain the rapid heating by meteorite bombardment — is also refuted by calculations.

In the article by L.V. Ksanfomality [4] on Mercury considered the hypothesis that Mercury could be a lost satellite of Venus. In 1976, a mathematical experiment was set up in which the evolution of the orbit of Mercury, which was initially placed in the orbit of Venus, was calculated. The experiment not only did not disprove the assumptions about the possible escape of Mercury through one of the Lagrangian points of the Venus – Sun system, but also showed that it inevitably had to happen in a very short time on a cosmogonic scale — less than 500 million years. Before escape, the period of Mercury's orbit should have been about 40 days. All this is quite close to the period of revolution of our Moon (27 days) and the distance to it (385 thousand kilometers).

During the previous 500 million years (or less), the tides in the body of Venus, due to the impact of a satellite 4.5 times more massive than our Moon, released a lot of thermal energy in the crust and bowels of Venus. There must have been crustal shifts and rapid degassing of the bowels of Venus, resulting in a hot planet with a dense, hot atmosphere, huge mountains and very slow rotation, which is observed today. This is an interesting hypothesis, but it cannot be considered proven.

Such an interpretation of the early history of Venus and Mercury explains a number of facts, in particular, the resonant, but not synchronous period of Mercury's revolution around the Sun (3/2 of the rotation period), the loss of the angular momentum of Venus and Mercury, and the absence of satellites for these planets.

According to its mechanical parameters (mass, radius, average density and model of the internal structure), Venus is a twin planet of the Earth. However, one of the sensations revealed during the study of the planet with the help of spacecraft was that in many respects Venus differs significantly from the Earth. The pressure at the bottom of the atmosphere of Venus is 90 bar, it does not have its own magnetic field, it has no satellites, it passed by chance, the history of tidal evolution. Unlike the Earth, Venus is a dry planet, and perhaps the most significant difference is the youthfulness of the rocks on its surface, whose age does not exceed 300-500 million people. years. There are no traces of global plate tectonics on Venus. A large number of works devoted to Venus were carried out at the Institute of Physics of the Earth.

These studies are summarized in a large review [9], based on original studies carried out at the Institute of Physics of the Earth.

In the early 1980s, it became clear that the interpretation of the anomalous gravitational field depended on the rheological model of the planetary interior. For this purpose, the Green's function method was developed. The Green's function technique was used for the joint interpretation of the topography and the gravitational field. The long-wave relief of the crust-mantle boundary and the thickness of the crust were determined. The tangential stresses in the lithosphere of Venus are calculated, the correlation of these stresses with surface structures is revealed.

Models of thermal evolution of Venus are constructed in the approximation of parametrized convection [10]. For this purpose, the well-known work [11] of Western authors was substantially generalized. An important feature of [10] is that it allows obtaining an asymptotic solution of the problem under consideration in an analytical form and thus revealing in a visual form all the features of the cooling of Venus or the Earth. The modern temperature of the upper layers of the Venusian mantle is approximately 1700 K, the temperature at the mantle boundary is 3500–4000 K and is close to that for the Earth.

The most likely reason for the absence of its own magnetic field in Venus is due to the fact that the core of Venus has not yet begun to solidify; as a result, convection does not occur in it, and the magnetohydrodynamic dynamo mechanism does not work. The magnetic field near the planet could be excited in the first ~2 billion years.

CONCLUSION:

Venus is the second planet from the Sun. It occupies a special position among the terrestrial planets. Until recently, it was called the twin of the Earth. The similarity between Venus and Earth in size and mass (and hence in average density and gravity) suggests that the internal structure of the two planets is similar. However, as Venus was studied, it had less and less traits of a "double". In the early epoch, Venus, which was almost a "double" of the Earth, in its further evolution took a different path. Therefore, like no other planet, it allows us to see what could (or could not) be the evolution of our planet under the influence of not yet fully understood external or internal causes.

References:

[1] *Chuikova N.A., Maksimova T.G., Chesnokova T.S., Grushinsky A.N.* Vertical movements of the earth's crust according to ITRF2000, ITRF2005, ITRF2008, ITRF2014 data and their comparative analysis // On Sat. "Astronomy, geodesy and geophysics". M., 2018. P. 78–89.
[2] *Chuikova N.A., Nasonova L.P., Maksimova T.G.* A new solution of the inverse problem of gravimetry for the terrestrial planets and its verification for the Earth // On Sat. "Astronomy, geodesy and geophysics". M., 2018. P. 90–113.
[3] *Chuikova N.A., Nasonova L.P., Maksimova T.G.* Density, stress, and gravity anomalies in the interiors of the Earth and Mars and the probable geodynamical implications: comparative analysis // Izvestiya, Physics of the Solid Earth. 2014. V. 50. No. 3. P. 427–443.
[4] *Ksanfomaliti L.V.* Mercury // Solar system. M.: Fizmatlit, 2017. 458 p. Ch. 4. P. 106–132. (In Russian).
[5] Ksanfomaliti L.V. Venus // Solar system. M.: Fizmatlit, 2017. Ch. 5. P. 136–174. (In Russian).
[6] *Zharkov V.N.* On Sat. "Essays on Geophysical Research". M.: OIFZ (IPhE) RAN, 2003, P. 439–440.
[7] *Artyushkov E.V.* Neotectonic uplifts of the earth's crust on the continents as a result of infiltration into the lithosphere of a large volume of mantle fluid // Tectonophysics and topical issues of Earth sciences. M.: IPE RAS, 2012. V. 1. P. 30–35.
[8] *Sorokhtin O.G., Ushakov S.A.* Origin of the Moon and its influence on the global evolution of the Earth. M.: MSU, 1989. 111 p. (In Russian).
[9] Venus geology, geochemistry, and geophysics research results from the USSR / eds. Barsukov V.L., Basilevsky A.T., Volkov V.P., Zarkov V.N. 1992. Pt. 111. Geophysics / ed. V.N. Zharkov. P. 208–319.
[10] *Solomatov V.S, Zarkov V.N.* The thermal regime of Venus // Icarus. 1990. V. 84. Iss. 2. P. 280–295. https://doi.org/10.1016/0019-1035(90)90038-B.
[11] *Stevenson D.L., Spohn T., Schubert G.* Magnetism and thermal evolution of terrestrial planets // Icarus. 1983. V. 54. Iss. 3. P. 466–483. https://doi.org/10.1016/0019-1035(83)90241-5.

NUMERICAL SIMULATION OF THE THERMAL EVOLUTION OF THE MOON. CONSISTENCY WITH THE PRESENCE OF A LOW-VISCOSITY ZONE AT THE CORE-MANTLE BOUNDARY

E.V. Kronrod, V.A. Kronrod, O.L. Kuskov
Vernadsky Institute of Geochemistry and Analytical Chemistry RAS, e.kronrod@gmail.com

KEYWORDS:
Moon, thermal evolution, heat transfer, numerical simulation, temperature profile, geophysical constraints

THE MODEL OF THE MOON:
The model of the Moon consists of a 35 km thick crust [1], the upper and the lower mantle, the layer of low-velocity/low-viscosity (LVZ), liquid outer core, and solid inner core. It is assumed that the upper-middle mantle boundary marks the base of the lunar magma ocean (LMO), and below is the primarily undifferentiated mantle, unaffected by partial melting processes.

LVZ (LOW-VELOCITY/VISCOSITY ZONE):
The existence of a partially molten zone in the lowermost mantle is evidenced by selenophysical data and seismic wave attenuation at the base of the lower mantle [2, 3]. The LVZ layer is believed to contain ilmenite-bearing cumulates (IBC) containing radioactive sources. Initially formed in the crust, the cumulates descended through the mantle layers into the LVZ layer as a result of a mantle overturn (IBC overturn, [4]). According to (Zhang et al., 2013), half of the KREEP material from the crust enters the IBC layer. The content of ilmenite in LVZ can reach 20 wt.% [6, 4]. The presence of additional heat sources in the mantle, as well as the reduced viscosity of ilmenite, make it possible to provide conditions for partial melting in the LVZ [7]. The LVZ layer is believed to contain ilmenite-bearing cumulates (IBC) containing radioactive sources. Initially formed in the crust, the cumulates descended through the mantle layers into the LVZ layer as a result of a mantle overturn (IBC overturn) [4]. According to [5], half of the KREEP material from the crust enters the IBC layer. The content of ilmenite in LVZ can reach 20 wt.% [4, 6]. The presence of additional heat sources in the mantle, as well as the smaller viscosity of ilmenite, make it possible to provide conditions for partial melting in the LVZ [7].

HEAT SOURCES IN MANTLE AND LVZ:
The content of radioactive sources in the mantle was set in accordance with the estimates obtained in [8]. In accordance with the magma ocean hypothesis, the heat release in the lower mantle is assumed to be equal to the bulk heat release. Following the concept of “IBC overturn”, the sources in the crust identified in [8] will be divided equally between the crust and LVZ [5].

METHOD OF CALCULATION:
Calculation of the thermal evolution of the Moon was carried out within the one-dimensional non-stationary model of thermal conductivity, taking into account the restrictions on the existence of a low-viscosity zone in the mantle near the core–mantle boundary. Both conductive and convective heat transfer were taken into account, as well as the processes of heating of the mantle matter due to the energy of radioactive decay.

RESULTS:
Calculations were carried out for a nonstationary thermal model from 0.5 billion years from CAI formation to the present time. The temperature distributions obtained as a result of calculations (Fig. 1) are consistent with geophysical data, as well as with previous estimates of the temperature distribution in the Moon, calculated from seismic data [9].

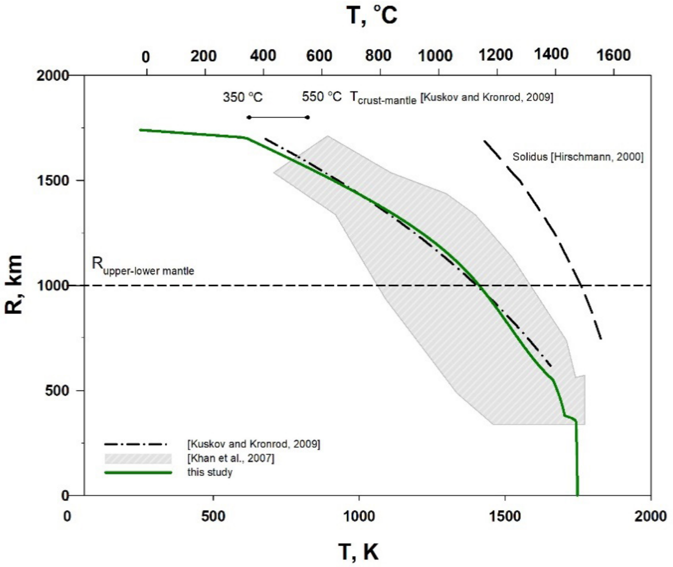

Fig. 1. Estimated current temperature distribution

Acknowledgements:
This study was carried out under government-financed research project for the Vernadsky Institute of Geochemistry and Analytical Chemistry, Russian Academy of Sciences

References:
[1] *Wieczorek M.A., Neumann G.A., Nimmo F. et al.* The crust of the Moon as seen by GRAIL // Science. 2013. V. 339. Iss. 6120. P. 671–675. https://doi.org/10.1126/science.1231530.
[2] *Khan A., Connolly J.A.D., Pommier A., Noir J.* Geophysical evidence for melt in the deep lunar interior and implications for lunar evolution // J. Geophysical Research. Planets. 2014. V. 119. P. 2197–2221. http://dx.doi.org/10.1002/2014JE004661.
[3] *Williams J.G., Konopliv A.S., Boggs D.H. et al.* Lunar interior properties from the GRAIL mission // J. Geophysical Research. Planets. 2014. V. 119. No. 7. P. 1546–1578. https://doi.org/10.1002/2013JE004559.
[4] *Zhao Y., de Vries J., van den Berg A.P. et al.* The participation of ilmenite-bearing cumulates in lunar mantle overturn // Earth and Planetary Science Letters. 2019. V. 511. P. 1–11. https://doi.org/10.1016/j.epsl.2019.01.022.
[5] *Zhang N., Dygert N., Liang Y., Parmentier E.M.* The effect of ilmenite viscosity on the dynamics and evolution of an overturned lunar cumulate mantle // Geophysical Research Letters. 2017. V. 44. P. 6543–6552. DOI: 10.1002/2017GL073702.
[6] *de Vries J., van den Berg A., van Westrenen W.* Formation and evolution of a lunar core from ilmenite-rich magma ocean cumulates // Earth and Planetary Science Letters. 2010. V. 292. P. 139–147. https://doi.org/10.1016/j.epsl.2010.01.029.
[7] *Tan Y., Harada Y.* Tidal constraints on the low-viscosity zone of the Moon // Icarus. 2021. V. 365. Art. No. 114361. https://doi.org/10.1016/j.icarus.2021.114361.
[8] *Kronrod E.V., Kronrod V.A., Kuskov O.L.* Constraints on the thermal regime and uranium content in the Moon for a magma ocean model with conditions for partial melting of mantle matter in the vicinity of the core // Solar System Study: Some Milestones: Proc. V.: IKI RAS. 2015. P. 89–101 (in Russian).
[9] *Kuskov O.L., Kronrod V.A.* Geochemical constraints on the model of the composition and thermal conditions of the Moon according to seismic data. 2009 // Izv. Phys. Solid Earth. V. 45. P. 753–768. https://doi.org/10.1134/S1069351309090043.

AN OMNIDIRECTIONAL FILTERING METHOD FOR DESTRIPING LUNAR SATELLITE GRAVITY DATA

J. Yang[1], L. Guo[2]
[1] *School of Geophysics and Information Technology, China University of Geosciences Beijing, Beijing, China, yang_jing0122@email.cugb.edu.cn*
[2] *School of Geophysics and Information Technology, China University of Geosciences Beijing, Beijing, China, guo_lianghui@163.com*

KEYWORDS:
satellite gravity data, destriping, Moon, GRAIL, data preprocessing

INTRODUCTION:

The high-resolution lunar gravity field model of high degree and order established by Gravity Recovery and Interior Laboratory (GRAIL) provides crucial insights into the internal structure and evolutionary processes of the Moon. However, high-resolution gravity anomalies solved from gravity field models are often disrupted by complex interference such as multi-directional striping and random noise. These disruptions arise due to correlations among high-degree and high-order coefficients, variations in satellite orbits, and instrument-related random errors. These issues present challenges for subsequent analysis and interpretation.

The interference, characterized by multi-directional striping and high-frequency noise, is mainly affected by the high-order terms of the gravity field model. Prior approaches [1] often directly manipulate these high-degree and high-order terms, such as discarding or reducing their significance, to mitigate striping interference and errors. Yet, these methods typically yield limited denoising effects and may sacrifice valid signals. Processed grid satellite gravity anomaly data hold physical significance. As a harmonic field, gravity data should exhibit smooth transitions between neighboring points without abrupt Sudden changes or spikes. In other words, when using the same polynomial fitting method, the results of one-dimensional polynomial fitting on a certain point and its adjacent points should be consistent with the results of two-dimensional polynomial fitting in principle. Thus, deviations between data fitting using the same approach signify striping interference.

Consequently, we develop the omnidirectional filtering method for destriping lunar satellite gravity data upon the DPF method developed [2] for airborne geophysical data. Our method introduces angle parameters to address the multi-directional nature of satellite gravity data striping. Through data segmentation and iterative steps involving sliding subregions, a novel omnidirectional filtering method for destriping lunar satellite gravity data is devised. The method follows these steps: (1) Dividing the gravity anomaly grid data into subregions; (2) Selecting suitable filter window sizes, employing one- and two-dimensional polynomial fitting to eliminate striping errors, achieving single-direction denoising for each subregion; (3) Based on the actual striping distribution, rotating coordinates and regridding using preset angle parameters, returning to step (2) until denoising is completed for all preset angle directions, yielding denoised subregion data for all directions; (4) Merging denoised subregion data; (5) Assessing whether error conditions are met. If satisfied, denoising results are output; otherwise, return to step (2) for iterative refinement until the output is viable.

Through theoretical model experiments and high-precision satellite gravity data tests in the Moon's Rümker region, this study demonstrates our method has superior performance in striping and random noise removal compared to previous methods. The omnidirectional filtering method effectively denoises high-resolution satellite gravity data and holds potential for application to satellite gravity data of other planets or other satellite geophysical data.

References:

[1] *Swenson S., Wahr J.* Methods for inferring regional surface-mass anomalies from Gravity Recovery and Climate Experiment (GRACE) measurements of time-variable gravity // J. Geophysical Research. 2002. V. 107. Iss. B9. Art. No. 2193. P. ETG 3-1–ETG 3-13. https://doi.org/10.1029/2001JB000576.

[2] *Beiki* M., *Bastani* M., *Pedersen L.* Leveling HEM and aeromagnetic data using differential polynomial fitting // Geophysics. 2010. V. 75. Iss. 1. P. L13–L23. DOI: 10.1190/1.3279792.

TO PROMOTE A JOINT SPACE-TIME REFERENCE DATUM ON THE MOON

J.S. Ping[1], A. Kosov[2], W.X. Li[1], A. Gusev[3], M.Y. Wang[1], J. Sun[1], L. Chen[1], Z.R. Wang[1], H.B. Jin[1]

[1] *National Astronomical Observatories, Chinese Academy of Sciences, Beijing, China, jsping@bao.ac.cn*
[2] *Space Research Institute RAS, Moscow, Russia*
[3] *Kazan Federal University, Kazan, Russia*

KEYWORDS:
space, time, reference, datum, Moon, LLR, clock, beacon

INTRODUCTION:

Following the rapid progress of lunar space and lunar surface activities of human beings, the request of a lunar space local datum for Space-Time reference has been becoming urgent and necessary.

For a lunar surface space-reference, we suggest to set a key selenodetic site with multi space-geodetic displines, like astronomy, the lunar laser ranging (LLR), space geodesy, radio beacon and GNSS, for constructing the lunar dynamical reference frame or ephemeris, and a lunar fixed reference frame. At the same place, to realize lunar space local time standard, atomic clock is suggested as time-frequency reference, with the support of radio link and calibration between GNSS satellite and the site clock. This datum can be used as a key station for PNT service in lunar space and on the surface of the moon, the relevant method has also been considered carefully. This lunar reference frame can be closely tied to the ITRF, and to various ICRFs.

A simple combination of an S/X band radio beacon with PLL transponder, a GNSS receiver, a CCR, and a chip Rb clock with USO will be mature technology for the suggested lunar surface Space-Time Datum hardwares. When keeping this datum operation, it can be used to study the lunar and planetary evolution. The observation of lunar physical libration (LPhL) or rotation in longitude and latitude and lunar pole wobble, plays a key role on study the lunar interior structure and layered dynamical evolution. In the past 50 years, the lunar laser ranging (LLR) method by measuring the distance variation between the lunar surface laser retro-reflectors and ground stations.

Both Russian and French scientists have been arranged top level research teams, parallel with NASA JPL team, on study the LPhL and on providing good constraints on the lunar structure of the Moon. Large progress has been made on finding two and multi-layer Moon. LLR, and the suggested space techniques also can contribute to test the general relativity in the Earth-Moon space, in various dimensions. Teams from other nations are catching up with the top level ones.

ASTROPHYSICAL UV-OPTICAL-IR TELESCOPE FOR THE INTERNATIONAL LUNAR RESEARCH STATION

A. Shugarov[1], M. Sachkov[1], H. Wang[2,3], S. Dong[4], X. Bai[2,3], Y. Deng[2,3], X. Jiang[2,3], V. Shmagin[1], B. Shustov[1], S. Sichevskij[1], A. Buslaeva[1], I. Savanov[1], T. Li[2,3], X. Zhang[2,3], N. Jiang[5]

[1] *Institute of Astronomy RAS, Moscow, Russia, shugarov@inasan.ru*
[2] *National Astronomical Observatories, Chinese Academy of Sciences, Beijing, China, wanghj@nao.cas.cn*
[3] *University of Chinese Academy of Sciences, Beijing, China, xybai@nao.cas.cn*
[4] *Department of Astronomy, School of Physics, Peking University, Beijing, China, dongsubo@pku.edu.cn*
[5] *Department of Astronomy, University of Science and Technology of China, Hefei, China, jnac@ustc.edu.cn*

KEYWORDS:
UV astronomy, moon-based telescope, ILRS, MCP detector, solar blind detector

INTRODUCTION:
A Moon-based UV-Optical-IR telescope will be an important research tool for astronomers to study the evolution of the universe, dark matter, dark energy and the evolution of stars and galaxies. Moon-based telescopes can also perform an all-sky survey in UV and discover transients/variables, search and characterize comets and near-Earth objects in the Solar system and explore the habitability of exoplanets.

The first Chinese Moon-based telescope LUT (Chang'E-3 mission) has demonstrated its efficiency in near-UV region. In 2021 China and Russia signed an agreement to build a future International Lunar Research Station, which provides new exciting opportunities for Moon-based astronomy. The main advantages of placing a telescope on the Moon are:

- stable position of the telescope (no micro-disturbances);
- absence of an atmosphere;
- longer duration of uninterrupted observations (the rotation of the Moon is much slower than that of the Earth);
- location outside the geocorona (the glow of the geocorona in UV affects observations from the low Earth orbit).

We are considering several approaches to building up a Moon-based astrophysical telescope, depending on the available mass budget.

- 15–30 cm telescope with pre-aperture repointing system. We have different approaches: moderate wide-field imaging telescope, multiband imaging telescope.
- 60–100 cm multipurpose UV-optical-IR telescope with two independent focal planes for FUV spectroscopy and broad-band imaging and spectroscopy.
- Extra wide field UV lens array to capture the whole visible sky in near UV with high time resolution (~ few minutes).
- A small-scale extreme UV telescope.
- A small-scale extra wide field telescope (prototype).

In all cases, the main design drivers for the Moon-based telescope are: to have a simple and lightweight design, 2–3 different detectors without an optical relay system and space for filter wheels for each detector.

For the large-scale ILRS-5 mission, we propose a full reflective telescope with one relatively large focal plane to accommodate several detectors and spectrographs and another narrow field-of-view focal plane for high-sensitivity spectrograph.

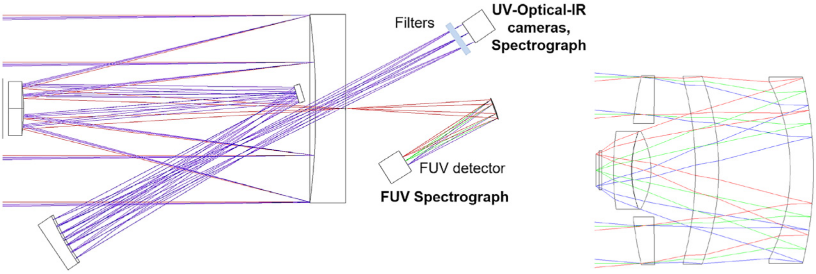

Fig. 1. 60–100 cm telescope for ILRS-5 with two independent focal planes (*left*), extra wide-field 16 cm UV telescope (*right*)

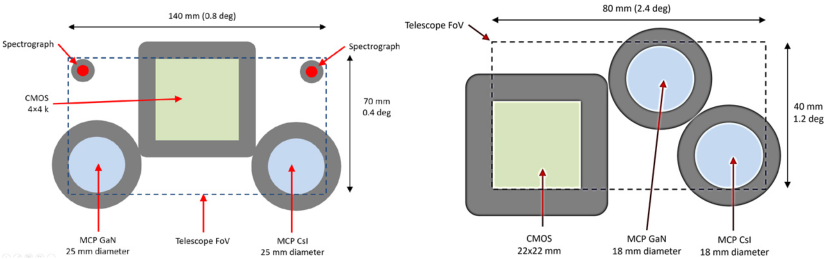

Fig. 2. Focal plane layouts for: 60–100 cm multipurpose telescope (*left*), 15–30 cm multiband imaging telescope (*right*)

Table 1. Summary of different proposals for ILRS astrophysical telescope

Parameter	20 cm imaging telescope	15–30 cm multiband imaging telescope	60–100 cm multipurpose telescope ILRS-5	Extra wide field UV lens array
Aperture, cm	20	15–30	60–100	16
Cameras	1 camera	2-3 cameras FUV, NUV, Optical, IR	3–5 cameras EUV, FUV, NUV, Optical, IR	1 NUV
Spectrographs	–	0-1	2-3	-
Focal length, cm	300	180	Focus 1:1000 Focus 2:500	16
Field of view, deg	0.4	2.4×1.2	Focus 1:0.4×0.8 Focus 2: 0.1	10
Pixel scale, arcsec/pixel	0.3	0.5	Focus 1: 0.1 Focus 2: 0.2	14

For FUV and NUV observations, we need solar blind photon counting MCP detectors to allow long exposures. In addition, a UV-enhanced CMOS/CCD is needed for high dynamic range and broad spectral range observations. The expected performance of the UV MCP detectors for an ILRS telescope is:

- Image format: 2k×2k pixels (2.5k — goal) for 25 mm MCP with 6 **μm pore**;
- Equivalent pixel size: 10 **μm**;
- Solar-blind NUV 170–320 nm, QE > 25 % (goal);
- Solar-blind FUV 115–176 nm, QE > 15 % (goal);
- Local count rate 20/200 cps in full-frame/window mode (photon-counting);
- Dynamic range over 10 000 using HV gating.

We suggest using scientific CMOS GSENSE400BSI in TE-cooled package with UV window; it has 2k×**2k** format, 11 μm pixel, readout noise $<2e^-$. 5k×5k small pixel size (4 **μm)** CMOS with very low readout noise ($<1e^-$) are expected to be available in the future. The small pixel size of CMOS can improve the sampling and angular resolution of the small aperture Moon telescope.

For the wide field telescope, we consider a custom MCP detector with 3 µm pore to achieve 4k×4k pixels (5k — goal) resolution in UV.

For a long-term mission, Moon dust may affect the telescope's performance. Preliminarily we suggest the following methods for preventing the telescope's efficiency degradation due to dust:

- To use pressurized air to blow dust away from the telescope optics, for example, to put nozzles close to the entrance optics;
- To design a protective cover to close the telescope according to the "Moon's dust forecast";
- To consider using magnetic traps and blinds around entrance optics.

References:

[1] *Shugarov* A.S., Wang H., Dong S. et al. The concept of Lunar-based astrophysical telescope for international lunar research station // Vestnik NPO Lavochkina. 2022. No. 1(55). P. 3–9. DOI: 10.26162/LS.2022.71.64.001 (in Russian).

[2] *Shugarov* A., Dong S., Wang H. et al. The Concept of Moon-Based UV Survey to Study Transients and Variables // 13th Moscow Solar System Symposium 13M-S3. IKI RAS, Moscow, Russia, Oct. 10–14, 2022: Abs. book. 2022. P. 106–107. DOI: 10.21046/13MS3-2022.

[3] *Wang H., Sachkov* M., Dong S. *et al.* Science of the Lunar-Based UV-Optical-IR Telescope for ILRS // 13th Moscow Solar System Symposium 13M-S3. IKI RAS, Moscow, Russia, Oct. 10–14, 2022: Abs. book. 2022. P. 108. DOI: 10.21046/13MS3-2022.

[4] *Shugarov* A., *Sachkov* M., Wang H. et al. The concept of Lunar-based UV-Optical-IR Telescope for ILRS // 12th Moscow Solar System Symposium 12M-S3. IKI RAS, Moscow, Russia, Oct. 11–15, 2021: Abs. book. 2021. P. 441–443. DOI: 10.21046/12M-S3.

[5] *Sachkov* M., *Shugarov* A., *Shmagin* V., Gómez de Castro *A.I.* The concept of lunar-based astrophysical telescope for international lunar research station (ILRS) // Proc. SPIE. 2022. V. 12181. Art. No. 121812V. DOI: 10.1117/12.2629619.

CREATING THE MAP OF THE POLAR REGIONS OF THE MOON

E.A. Grishakina[1], Zh.F. Rodionova[2], E.N. Slyuta[1], E.A. Feoktistova[2], V.V. Shevchenko[2]

[1] *Vernadsky Institute of Geochemistry and Analytical Chemistry RAS, Moscow, Russia, grishakina@geokhi.ru*

[2] *Sternberg Astronomical Institute Lomonosov Moscow State University, Moscow, Russia, marss8@mail.ru*

KEYWORDS:
map of the Moon, polar regions, digital terrain model, craters, depth

INTRODUCTION:

In the near future, several countries are planning flights to the Moon. In the southern polar region of the Moon, the landing of the Russian Luna-25 (Luna-Glob) spacecraft is scheduled for August 2023. The main tasks of this mission are to develop the soft landing technology, study the soil by the contact method, and also confirm the presence of water. For this, a manipulator complex is designed to take lunar rock with a bucket and transfer it to a special analyzer device [1]. After this station, more complex spacecraft will follow to the Moon: the Luna-26 lunar orbiter [2], the Luna-27 lander for studying frozen volatile components in lunar soil and studying its chemical and mineral composition, as well as thermophysical, physical-mechanical and electromagnetic properties [3], and the Luna-28 lander for the delivery of lunar soil to the Earth [4–6]. On August 1, 2023, the Chandrayaan-3 spacecraft entered the circumlunar orbit. Landing of the descent module with the lunar rover is scheduled for August 23–24. Further, India is preparing, in cooperation with the Japanese JAXA, the Chandrayaan-4 mission also to the South Pole of the Moon, where India will provide the lander, and Japan the launcher and lunar rover. China also plans to search for frozen water near the Moon's South Pole. In 2024, the Chang'e-6 spacecraft will be launched to collect soil samples from the far side of the Moon, and then, in 2026, the Chang'e-7 spacecraft will land in the South Pole zone. CNSA believes that the flying vehicle, unlike traditional rovers, will be able to reach the bottom of the crater. Using a drilling tool, the probe will take a sample of ice, and the manipulator will move it to the apparatus for spectral analysis. The launch of the Chang'e-8 apparatus is scheduled for 2028 to conduct experiments on the use of lunar resources and create a basic model of the International Lunar Research Station. Japan hopes to perform a precision landing on the surface of the moon using an orbiter and land a lunar rover at the South Pole. The UK will launch its first lunar lander by 2024, with an orbiting probe to study regolith chemistry, provide communications and map the lunar surface. South Korea, together with ESA, intends to launch a lunar orbiter and lander in 2025. NASA will send several spacecraft to the Moon in 2024, including the new VIPER rover. The purpose of the device will be a detailed mapping of the distribution and concentration of water in the region of the South Pole of the Moon. The NASA Artemis program aims to land astronauts on the Moon, including the first female astronaut. The main goal of the program is to return people to the surface of the Moon and ensure a long-term human presence on the Moon.

CONTENTS OF THE MAP OF THE POLAR REGIONS OF THE MOON:

It became possible to process large amounts of data received by spacecraft in automatic mode and present them in the form of various overview and thematic maps [7, 8]. We used ESRI ArcGIS 10.1 software. The map of the circumpolar regions of the Moon was compiled on a scale of 1:5 000 000 in a polar stereographic projection and is limited by ±60 ° parallels so that the landing site of the Luna-25 ALS could be displayed. Particular interest in the circumpolar regions of the Moon is due to the fact that there is ice in permanently shaded places. The Kaguya and LRO laser altimeters determined the heights of the lunar surface with high accuracy. We used a digital terrain model built according to the laser altimeter (LOLA) data of the Lunar Reconnaissance Orbiter (LRO) spacecraft with an accuracy of 64 pixels per degree (0.5 km per pixel) [9]. The heights on the map are measured from a sphere with an average radius of 1737,4 km. Detailed "hillshading" by the cut-off method was carried out by Grishakina E.A. The height scale includes 17 levels. The total elevation difference on the Moon is almost 20 km. During the development of a color scale for displaying heights on a map, the problem of showing characteristic landforms at all height intervals was solved. With the help of cartographic research methods, it was possible to determine the depth of craters and large basins located on the visible and far sides of the Moon. The South Pole – Aitken Basin turned out to be the deepest (the average depth of which is 9 km). The deepest 20 craters in the northern and southern subpolar regions are presented in Table 1. It follows from the table that the craters of the southern polar region are, on average, 1–2 km deeper than those in the northern polar region. In addition to the relief, the map shows the names of major moon formations in IAU Latin and in Russian. Named craters are indicated by dots in the center. The largest craters in the northern polar region are: Bel'kovich 215 km, Schwarzschild 211 km, Rozhdestvenskiy 181 km, Plaskett 177 km, W. Bond 170 km, and in the south: Schrodinger 316 km, Bailly 301 km, Zeeman 187 km, Haysen 163 km. There are several other large unnamed craters (see Table 1). Symbols on the map show the hard landing sites of the vehicles: GRAILA and GRAILB in the northern polar region, as well as: Kaguya, Lunar Prospector, Chandrayaan-1, LCROSS, Vikram in the southern polar region [10]. It is proposed to map new landing sites for Luna 25 and Chandrayaan-1. It is interesting that the number of craters with a diameter of 10 km or more in the northern polar region is 2302 craters, while in the southern polar region there are only 1320 craters (http://selena.sai.msu.ru/Rod/Publications/morph-catalog-craters-moon-nord/ morph-catalog-craters-moon-nord.htm; http://selena.sai.msu.ru/Rod/Publications/morph-catalog-craters-moon/ morph-catalog-craters-moon.htm) [11]. Figure 1 shows dependence of the number of craters on the ratio of depth to diameter in two polar regions. The structure of the distribution of craters is generally the same in both hemispheres, but differs in number.

Table 1. The deepest craters in the northern and southern polar regions of the Moon

Northern Polar Region					Southern Polar Region			
N	Name	Diameter, km	Depth, km	h/D	Name	Diameter, km	Depth, km	h/D
1	–	337,2	10,8	0,032	Cabeus	103,9	10,1	0,097
2	Sommerfeld	138,8	7,9	0,057	–	353,5	9,6	0,027
3	Stebbins	132,0	7,7	0,058	Zeeman	198,8	9,5	0,048
4	Milankovic	105,9	7,3	0,069	Planck	318,0	9,3	0,029
5	–	248.8	7,1	0,028	Boussingault	124,9	9,2	0,074
6	–	118,8	7,1	0,060	Petzval	110,0	9,2	0,083
7	–	158,6	7,0	0,044	Sikorskiy	98,7	8,7	0,085
8	Rozhdestvenskiy	177,7	6,9	0,039	Drigalski	173,5	8,7	0,050
9	Schwarzschild	212,8	6,8	0,032	Amundsen	104,5	8,5	0,082
10	Cremona	92,0	6,6	0,072	Demonax	128,4	8,3	0,065
11	Hayn	88,9	6,6	0,074	Le Gentil	115,2	8,1	0,070
12	Belcovich	215,0	6,3	0,029	Casatus	108,7	7,8	0,072
13	Tikhov	81,6	6,2	0,089	Hausen	182,5	7,8	0,043
14	Avogadro	127,3	6,2	0,048	Ashbrook	152,0	7,7	0,051
15	Hayn F	66,6	6,2	0,093	Schrodinger	313,8	7,7	0,025
16	Poinsot	68,3	6,2	0,091	Antoniadi	165,3	7,4	0,045
17	Plaskett	115,0	6,1	0,053	Curtius	101,4	7,4	0,073
18	Seares	109,7	6,0	0,054	Malapert	75,6	7,2	0,095
19	Karpinskiy	96,2	6,0	0,062	–	91,5	7,2	0,079
20	-	153,9	6,0	0,039	Scheiner	108,4	7,1	0,065

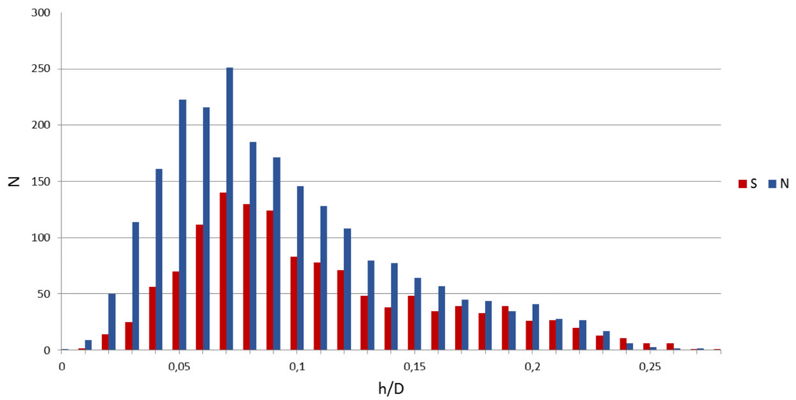

Fig. 1. Graphs of the dependence of the number of craters on the ratio of h/D in the northern and southern polar regions of the Moon

References:

[1] *Marinin I.* God do zapuska: Luna-25 gotovitsya k startu (One year to launch, Luna-25 prepares for liftoff) // Russkiy kosmos. 2020. No. 20. Iss. 5. P. 38–41 (in Russian).

[2] *Slyuta E.N., Vysochkin V.V., Ivanov V.V. et al.* “Meteor-L” device on the lunar orbital vehicle “Luna-26”: space dust detector // Solar System Research. 2021. V. 55. No. 5. P. 437–445. DOI: 10.1134/S003809462105004X.

[3] *Slyuta E.N., Marov M.Ya., Dunchenko A.G. et al.* TERMO-LR Experiment on the Luna-27 Lander: Study of Thermophysical, Physicomechanical, and Electromagnetic Properties of the Lunar Soil // Solar System Research. 2021, V. 55. Iss. 5. P. 446–466. DOI: 10.1134/S0038094621050051.

[4] *Marov M.Ya., Slyuta E.N.* Early steps toward the Lunar base deployment: Some prospects // Acta Astronautica. 2021. V. 181. P. 28–39. https://doi.org/10.1016/j.actaastro.2021.01.002.

[5] *Slyuta E.N.* The scientific tasks of the Luna-Grunt project (Luna-28) // 8th Moscow Solar System symposium, 2017. P. 247–249.

[6] *Slyuta E.N.* The Luna program // Sample Return Missions: The Last Frontier of Solar System Exploration / ed. A. Longobardo. Amsterdam: Elsevier, 2021. P. 37–78.

[7] *Grishakina E.A., Rodionova Zh.F., Slyuta E.N., Shevchenko V.V.* Obzornaya karta Luny 1:13 000 000 (An overview map of the Moon). M.: Sternberg Astronomical Institute MGU; Vernadsky Institute of Geochemistry and Analytical Chemistry, RAS, 2018, 2021, 2022 (in Russian).

[8] *Nass A., Hargitai H.* Participants and initiatives in planetary cartography // Planetary Cartography and GIS. Cham: Springer Nature, 2019. P. 355–374. DOI:10.1007/978-3-319-62849-3_21.

[9] *Smith D.E., et al*. The Lunar Orbiter Laser Altimeter investigation on the Lunar Reconnaissance Orbiter mission // Space Science Reviews. 2010. V. 150. P. 209–241, DOI: 10.1007/s11214-009-9512-y.

[10] *Phil Stooke.* Lunar Landing and Impact Sites. University of Western Ontario. 2019. https://publish.uwo.ca/~pjstooke/.

[11] *Slodarzh N.A., Rodionova Zh.F.* Comparison of the cratering of the north and south polar regions of the Moon // 13th Moscow Solar System Symposium. 2021. Art. No. 13MS3-MN-PS-26.

SITUATION IN THE LUNAR SKY IN THE LANDING AREA OF THE RUSSIAN LUNA-25 STATION FROM AUGUST 2023 TO AUGUST 2024

B.A. Epishin, M.I. Shpekin
Kazan Federal University, Kazan, Tatarstan, Russia, epishin.boris@yandex.ru, MichaelS1@yandex.ru

KEYWORDS:
russian station Luna-25, electronic lunar yearbook, development software, physical libration, occultation and eclipses, topocentric coordinates, rising and setting ephemeris, lunar day duration, lunar night duration, South Pole area, lunar sky

Earlier, we reported on our results aimed at developing our own computer program that would allow ephemeris calculations of the position of any celestial bodies, including stars and bodies of the Solar System, in the lunar sky for an arbitrary position of an observer on the surface of the Moon at large time intervals [1–8]. Such program has been developed and tested in a number of the above-mentioned publications. The main difference of the developed program is that it is autonomous and does not depend on other programs. The program uses ASCII JPL DE 440 text files [9] and takes into account the physical libration according to the algorithm published in the almanac [10]. The values of the horizontal coordinates of our program coincide with the values of “Horizons Web Application” [11] up to hundredth of arc second.

We have performed calculations for the main landing site. Figure 1 shows graph of the Earth’s movement for one lunar day (Earth month). Figure 2 shows graph of the Earth’s movement across the sky at intervals of one Earth day for the period from August 2023 to August 2024. The movement of the Earth across the sky for one lunar day occurs in a counterclockwise direction. Figure 3 shows graph of the movement of the Sun during the year for the period from July 2023 to July 2024 at the main landing site of the spacecraft. The sun rises in the east, passes the upper culmination in the north about 20° above the horizon and sets in the west.

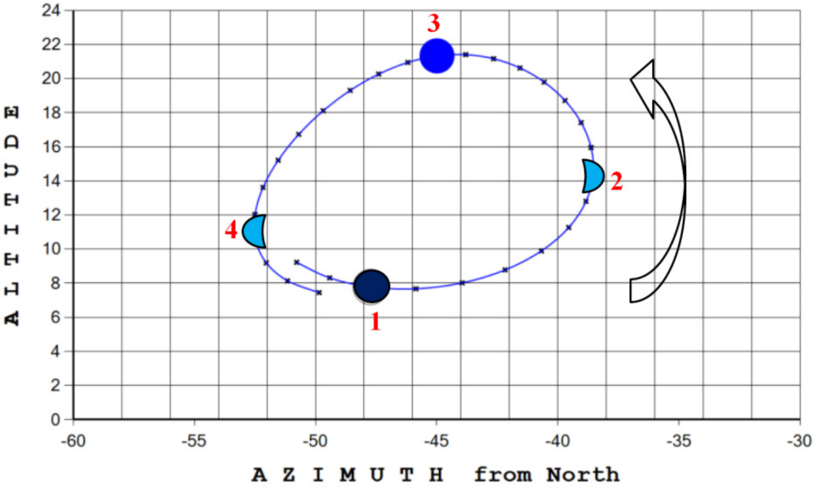

Fig. 1. The apparent motion graph of Earth across the lunar sky in July 2023 in the topocentric horizontal coordinate system for the main landing site. Black crosses indicate the position of the Earth’s disk with an interval of one day. The red numbers indicate the degree of illumination: 1 — “new Earth” on July 3; 2 — the first quarter on July 10; 3 — “full Earth” on July 18; 4 — the last quarter on July 26. The arrow shows the direction of movement. The coordinates are signed in degrees

This graph shows that the movement of the Sun during the year is slightly different with each lunar day. For clarity, Figure 5 shows graph of the lunar days (in red) and lunar nights (in black) duration in hours for the period from August 2023 to August 2024 for the main landing site. The columns on the graph show the days and nights calculated for the moments of sunrise and sunset for the Sun's disk center. Curved lines show the duration of lunar days and nights, taking into account the upper edge of the Sun's disk at sunrise and sunset. The time interval from the sunrise of the upper edge of the disk to the sunrise of the Sun's disk center is about one and half hours. It is important to note that the duration of the lunar day or lunar night will differ, as can be seen from the graph, by three hours when taking into account the sunrise and sunset of the upper edge of the Sun, than when calculating for the center of the disk.

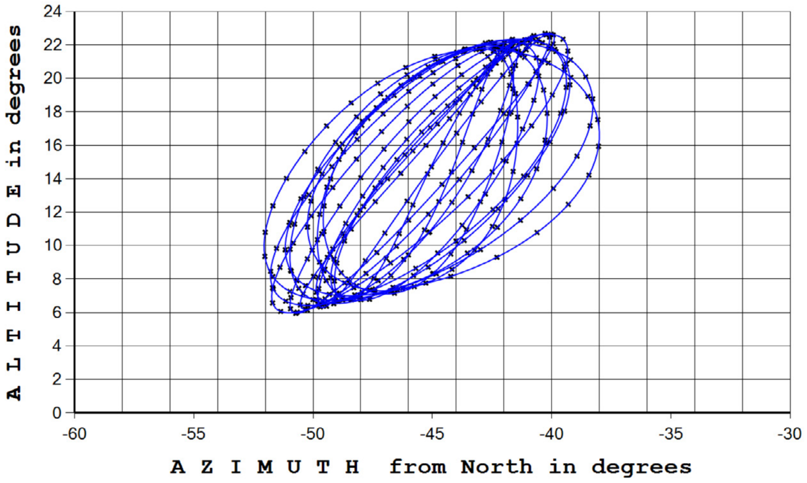

Fig. 2. The apparent motion graph of Earth across the lunar sky during the year (August 2023 – August 2024) at the main landing site

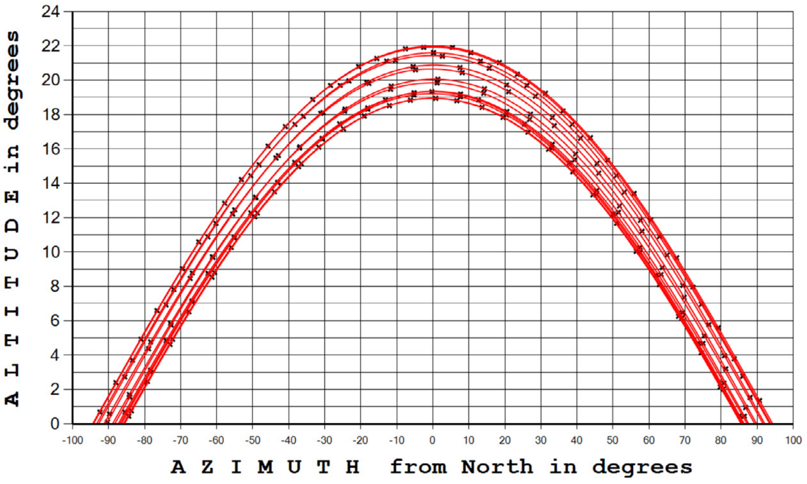

Fig. 3. The apparent motion graph of Sun across the lunar sky during the year (August 2023 – August 2024) at the main landing site

Figure 4 shows the graph of the movement of the Sun and the Earth for the period October – December 2021 for comparison with the paper [12]. In our calculations, the positions of the Sun and the Earth were calculated for the mathematical horizon (without taking into account the relief). As a result of comparing these graphs, it can be concluded that, taking into account the relief, the duration of the lunar day at the main landing site decreases by about 30 Earth hours. In general, the comparison shows that our calculations are consistent with the work of the authors of 2021.

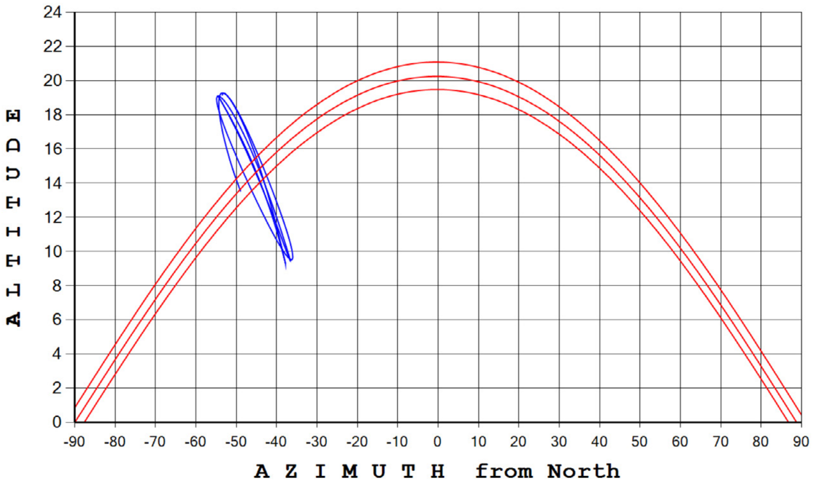

Fig. 4. The apparent motion graph of Sun and Earth across the lunar sky in the period October – December 2021 for the main landing site

It is important to note that the brightest star in the lunar sky, Sirius, will be constantly visible above the horizon at an altitude of approximately 17 to 58° for the main and backup points. Together with the Earth, this star will serve as an excellent navigator in the lunar sky not only during long cold nights, but also during the daytime due to the absence of an atmosphere.

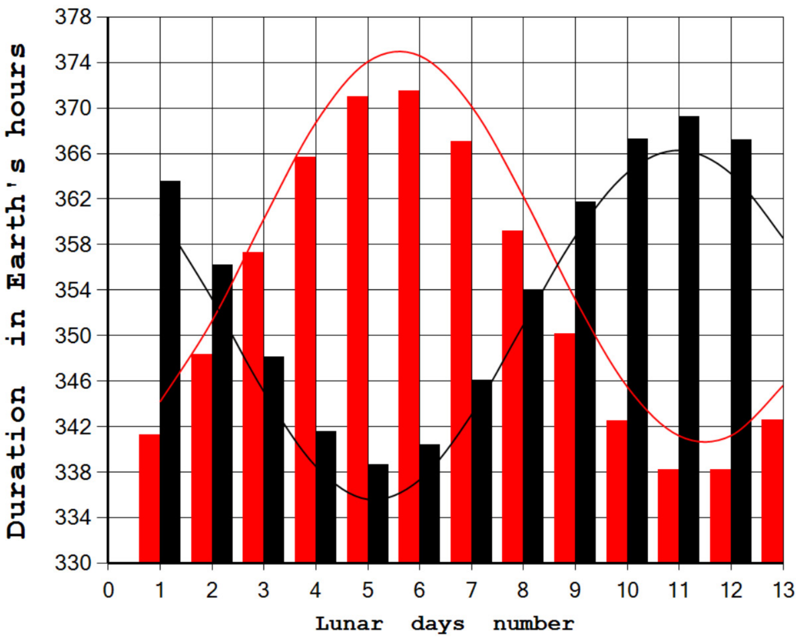

Fig. 5. The duration of the lunar day and night in hours for the main landing site is from August 2023 to August 2024. Red is day, black is night

It is interesting to note that during the annual period, three solar eclipses will occur in the area of the main landing site. According to our calculations, a total solar eclipse is expected on October 28, 2023. Partial solar eclipse is expected on March 25, 2024 with magnitude = 0.87 and once more partial solar eclipse — on September 18, 2024 with magnitude = 0.12. Table 1 shows the local circumstances of the total eclipse for the main landing point. For all calculations, the universal time was used, taking into account the difference between the ephemeris and the universal time of 71 s.

Table 1. Total Solar Eclipse 28 October 2023. P, V — position angles relatively lunar pole and zenith in degrees

Contacts	Universal Time	P	V	Az_N	Alt
1-st contact: Beginning partial phase	$18^h\ 26^m\ 38^s$	244	77	–40	16
2-st contact: Beginning total phase	$19^h\ 56^m\ 50^s$	27	220	–41	16
Middle eclipse	$20^h\ 23^m\ 47^s$	187	20	–41	16
3-st contact: End total phase	$20^h\ 50^m\ 41^s$	347	181	–41	16
4-st contact: End partial phase	$22^h\ 21^m\ 00^s$	130	323	–42	16

References:

[1] *Epishin B.A., Shpekin M.I.* Analysis of apparent motion of Sun, Earth and stars on the lunar sky // The 8th Moscow Solar System Symp. 2017.

[2] *Epishin B.A., Shpekin M.I.* Analysis of occultations of stars by the Earth on the lunar sky // The 9th Moscow Solar System Symp. 2018.

[3] *Epishin B.A., Shpekin M.I.* Occultations of Stars by the Earth on the Lunar Sky // PhysikA.SPb: Abs. 2019. 576 p. P. 22–23. ISBN 978-5-7422-6681-5.

[4] *Epishin B.A., Shpekin M.I.* Lunar territories with the Earth direct visibility // The 12th Moscow Solar System Symp. 2021.

[5] *Epishin B.A., Shpekin M.I.* Autonomous electronic Yearbook for observations from the surface of the Moon // The 13th Moscow Solar System Symp. 2022.

[6] *Shpekin M.I., Epishin B.A.* Project of a long-term astrometric observatory on the Moon // 66th All-Russian Scientific Conf. Architecture and Construction: Abs. Kazan: KGASU, 2014. P. 331.

[7] *Shpekin M.I.* Some principles of creating astrometric observatory on the Moon territory // The 5th Moscow Solar System Symp. 2014. P. 207ab-208ab.

[8] *Shpekin M.I., Barenbaum A.A., Mukhametshin Ch.R.* Some objectives of the study and exploration of the Moon // The 6th Moscow Solar System Symp. 2015. P. ab-210–211-ab.

[9] JPL planetary and lunar ephemerides https://ssd.jpl.nasa.gov/ftp/eph/planets/ascii/.

[10] *Taylor D.B., Bel S.A., Hilton J.L.* Computation of the Quantities Describing the Lunar Librations in the Astronomical Almanac.

[11] JPL Horizons on-line ephemeris syst. https://ssd.jpl.nasa.gov/horizons/app.html#/.

[12] *Djachkova M.V., Mitrofanov I.G., Sanin A.B. et al.* Characterization of the Luna-25 Landing Sites // Solar System Research. 2021. V. 55. Iss. 6. P. 509–528. DOI: 10.1134/S0038094621060034.

DESIGN OF A COMPACT MULTICHANNEL DIODE LASER SPECTROMETER FOR THE LUNA-27 MISSION: CHALLENGES AND ACHIEVEMENTS

I.I. Vinogradov[1], M.V. Spiridonov[1], V.V. Meshcherinov[2,1], V.A. Kazakov[1,2], Yu.V. Lebedev[1], A.A. Venkstern[1], V.V. Barke[1], Ya.Ya. Ponurovskiy[3]

[1] *Space Research Institute RAS, Moscow, 117997 Russia, imant@iki.rssi.ru*

[2] *Moscow Institute of Physics and Technology (National Research University), Dolgoprudny, Moscow Region, Russia, meshcherinov@phystech.edu*

[3] *Prokhorov General Physics Institute RAS, Moscow, Russia, ponur1960@yandex.ru*

KEYWORDS:
Luna-Resource; Lunar soil; chemical composition; isotopic ratios; tunable diode laser absorption spectroscopy.

INTRODUCTION:

Lunar soil studies are planned aboard the Luna-27 heavy landing station, planned for a mission under the Luna-Resource program. Scientific instruments of the Luna-27 lander will perform a wide range of experiments, including in situ analysis of an ice sample from below the lunar surface to determine its nature and form of distribution. A spectrometer, called DLS-L, was designed as an integral part of a versatile Gas Analytical Package (GAP) for independent study of products that will be extracted from soil, sampled at the Luna-27 landing site. The purpose of DLS-L is to measure the yield dynamics and integral content of pyrolytically evolved soil components H_2O and CO_2, and in retrieving the corresponding isotopic ratios D/H, $^{18}O/^{17}O/^{16}O$, $^{13}C/^{12}C$.

EXPERIMENT ENVIRONMENT AND METHOD OF MEASUREMENT:

There are three main sources of volatiles on the Moon: degassing of the lunar mantle, interaction of solar wind protons with surface rocks, and shock degassing of falling meteorites and comets [1]. The composition of the forming volatiles and their isotopologues will be unique in each case. The DLS-L data will help for further understanding of physics and chemistry of the Lunar regolith, as original data of near-polar soil direct study.

The DLS-L instrument is based on tunable diode laser absorption spectroscopy (TDLAS) technique in the mid-IR range [2–5]. Laboratory testing and calibration of the DLS-L have been carried out for IR regions of:

- 2.64 µm (for H_2O isotopologues absorption lines),
- 2.68 µm (H_2O and CO_2 basic molecules),
- 2.78 µm (CO_2 isotopologues),

using pure H_2O and CO_2 under low pressure of 5–15 mbar at 300 K in a so-called “static” operation mode. Actual molecular content values and isotopic ratios were retrieved while fitting of recorded optical transmission spectra and molecular absorption data with simulated spectral data. DLS-L accuracy was verified by cross-calibrations while comparing with mass-spectrometer data of same samples measurement, however, not for the ^{17}O content.

Existing layout of the DLS-L instrument is quite miniature, matching well with ultimate compactness of the Gas Chromatograph instrument, a host unit for DLS-L in GAP. Compactness of the DLS-L optics and of the analytical cell is challenging for achieving of good accuracy and precision of measurements; the cell is 19 cm long with 3 mm diameter clearance and lets the laser beam go only one path through it, see Fig. 1.

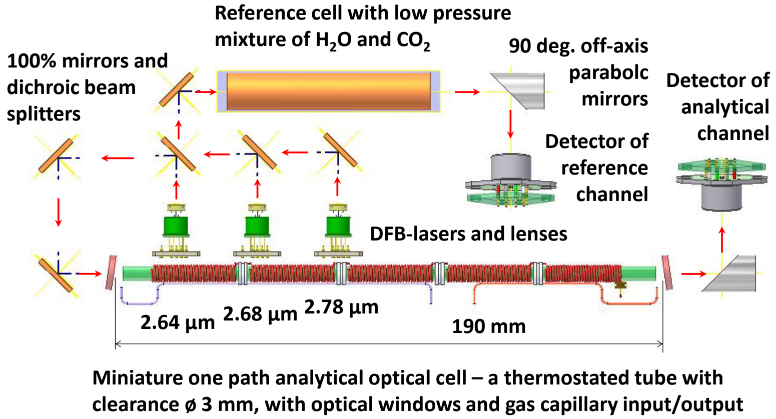

Fig. 1. DLS-L optics layout

Calculations confirm the sub-percentage potential of the DLS-L measurements accuracy and precision. However, it was found for spectral contours of HDO lines with weak absorption, that variations of accuracy and precision have sometimes exceeded the expected value of 10 ‰, see Table 1. Origin of these variations' magnitude was studied with special attention to laser light scattering and its interference with the main laser beam in a highly miniaturized optical layout, contributing to appearance of a strong so-called "fringing" noise component in the output signal.

For the output signal processing, there were used mathematical methods, which improve accuracy and precision by:

- better fitting experimental line contours with line shape models of not only Voigt, but also of Galatry, Rautian, Hartman models;
- an option of revising HITRAN database molecular absorption parameters;
- better compensation of spectra baseline and of specific pseudo periodical "fringing" noise components.

Table 1. Measurement results of the DLS-L spectrometer in the GC-L instrument, data from the end of 2022.

Gas mixture / Reference data source	Isotope	"Isotopic signature" reference values, ‰	"Isotopic signature" retrieved values by DLS-L in GC-L, ‰	Difference of "isotopic signature" mean values, ‰
CO_2, test sample / GEOKhI	$\delta_{VPDB}{}^{13}C$ (CO_2)	–47,55±0,06	–39,64±11,97	7,91
	$\delta_{VSMOW}{}^{18}O$ (CO_2)	20,17±0,27	14,28±16,37	–5,89
H_2O, test sample / GEOKhI	$\delta_{VSMOW}{}^{18}O$ (H_2O)	–9,8±0,8	–11,24±5,25	–1,44
Perrier water / [6] (Delta, XM)	$\delta_{VSMOW}{}^{18}O$ (H_2O)	–5,23±0,05	–5,82±7,75	–0,59
Perrier water / [7] (Picarro L1102-i)		–6,33±0,02		0,51
Perrier water / [6] (Delta, XM)	$\delta_{VSMOW}D$ (H_2O)	–35,83±1,01	–43,37±23,88	–7,54
Perrier water / [7] (Picarro L1102-i)		–39,82±0,2		–3,55

Simple hardware improvements were preliminary tested for the aim of damping scattered light and reducing associated output signal noise; resulting data series of spring'2023 are under calculation and analysis. The results, obtained with a similar spectrometer laboratory breadboard, confirm good potential of the used technique. When designing DLS for the following missions, it should be possible to include in the DLS scheme an additional optical cell with an optical path several meters long to radically improve the exactness of isotopic ratio measurements.

Nearest team's activity concentrates on searching and testing of both hardware and mathematical methods for further reducing of noise, extending of dynamic range and enhancing accuracy and precision of measurements. Technology transfer by import substitution should be carried out.

Acknowledgements:
Authors are grateful to Prof. Leonid N. Sinitsa, V. E. Zuev Institute of Atmospheric Optics SB RAS, Tomsk, for fruitful discussions and for his help in understanding of specific spectroscopy parameters.

The work is kindly supported by subsidy "Planeta" for IKI RAS and by Roscosmos for the industrial design and realization of the instrument.

References:
[1] *Basilevsky A.T., Abdrakhimov A.M., Dorofeeva V.A.* Water and other volatiles on the moon: A review // Solar System Research, 2021, V. 46(2), P. 89–107. https://doi.org/10.1134/S0038094612010017.
[2] *Durry G., Vinogradov I., Korablev O, et al.* Near infrared diode laser spectroscopy of C_2H_2, H_2O, CO_2 and their isotopologues and the application to TDLAS, a tunable diode laser spectrometer for the Martian PHOBOS-Grunt space mission // Applied Physics B, 2010, V. 99, P. 339–351. https://doi.org/10.1007/s00340-010-3924-y.
[3] *Rodin A., Vinogradov I., Zenevich S. et al.* Martian Multichannel Diode Laser Spectrometer (M-DLS) for In-situ Atmospheric Composition Measurements on Mars onboard ExoMars-2022 Landing Platform // Applied Sciences, 2020, V. 10(24), P. 8805. https://doi.org/10.3390/app10248805.
[4] *Meshcherinov* V, *Vinogradov* I., *Gerasimov M. et al.* Lunar multichannel diode laser spectrometer DLS-L for in-situ study of samples pyrolytically evolved from regolith onboard Luna-27 mission // Proc. SPIE, 27th International Symposium on Atmospheric and Ocean Optics, Atmospheric Physics, 2021, V. 11916, P. 119162O. DOI: 10.1117/12.2602144.
[5] *Vinogradov* I., *Spiridonov* M., *Meshcherinov* V. *et al.* Multichannel diode laser spectrometer DLS-L for Luna-27 mission // XX Symposium on High Resolution Molecular Spectroscopy HighRus-2023 2023, Lake Baikal, Abstract L4, P. 104.
[6] Private communication // MS-Analytica, 2020, https://analytica.ms/
[7] *Godoy J.M., Godoy M.L.D.P., Neto* A. et al. Direct determination of δ(D) and $\delta(^{18}O)$ in water samples using cavity ring down spectrometry: Application to bottled mineral water // J. Geochemical Exploration, 2012, V. 119–120, P. 1–5. https://doi.org/10.1016/j.gexplo.2012.05.007.

LUNA-27 LANDER AND LUNA-26 ORBITER NAVIGATION BY MEANS OF RADIO BEACON DEPLOYED ON THE LUNA-27 LANDER

A.S. Kosov[1], A.V. Gusev[2], J.S. Ping[3], L.S. Roshkov[1], V.S. Roshkov[1]
[1] *Space Research Institute RAS, Moscow, Russia, kosov@coscos.ru*
[2] *Kazan Federal University, Kazan, Tatarstan, Russia, agusev33@gmail.com*
[3] *National Astronomical Observatories Chinese Academy of Sciences, China, jsping@bao.ac.cn*

KEYWORDS:
ranging, radio beacon, microwaves, coherent transponder, H2 maser, dilator

INTRODUCTION:

One of the objectives of Radio Beacon Instrument (RBI) on board of Luna-27 lander is navigation support of the lander. The navigation includes precise position and relative velocity measurement. Scientific objectives also based on the precise position and velocity measurements. Scientific objectives of RBI have reported in [1].

RBI can operate in two modes: free running mode and coherent transponder mode. In free running mode, RBI irradiates monochromatic signals in two frequency bands: X-band — about 8400 MHz and Ka-band — about 32 000 MHz. Frequency stability of the signals determines by the performance of local reference quartz oscillator. The Precision Low Phase Noise OCXO MV341 is plan to use in RBI. The short-term frequency stability (Allan deviation) of the reference is $<2\cdot10^{-13}$ per 1 s; the long-term frequency stability is $\pm1\cdot10^{-8}$ per year.

RBI could use for navigation measurements of lander position and orbit parameters of Moon-Glob orbiter. Figure 1 shows navigation measurements of Luna-26 (Moon-Glob Orbiter) and Luna-27 (Lander).

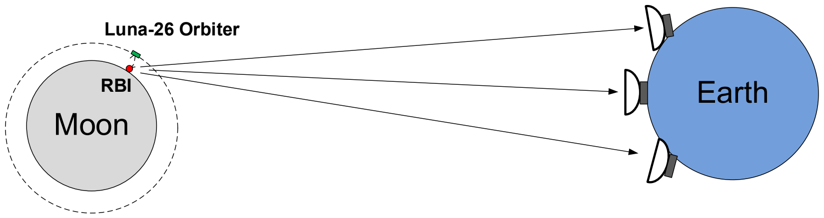

Fig. 1. Navigation measurements for Luna-26 Orbiter and Luna-27 Lander

Russian VLBI Quasar-KWO network plan to use for lander position measurement. The DELTA-DOR [2] technology can used to measure the Lander coordinates. The target accuracy of Lander position measurements is 0.1 m.

RBI free running mode of operation allows precision measurements on Luna-26 Orbiter parameters. PKD instrument on board of Luna-26 Orbiter can record the Doppler frequency shift of Ka-band signal irradiated by RBI and measure the relative velocity between Lander and Orbiter. Due to the very high stability of the reference frequency sources both RBI and PKD the relative velocity can measured with high accuracy, better 1 mm/s. The retrieval procedure can provide unprecedented accuracy for orbit parameters measurements.

Coherent transponder mode of operation implies external reference source for RBI. RBI receives reference signal at uplink frequency and irradiate the signal back at downlink frequency without loss of coherency. The up/down frequencies ratio is equal to 749/880. Uplink signal could pseudo noise modulated, which allows precise ranging [3]. It is possible to measure distance between host instrument and RBI. Master instrument can deployed on both any spacecraft and ground station. Measuring accuracy depends upon total phase noise of the both systems and propagation trace and is equal to $\Delta R = \lambda\Delta\phi/2\pi$, where $\Delta\phi$ is total phase fluctuation. For regular systems, $\Delta\phi$ could estimate as $\leq0.1\pi$ and ΔR as ≤0.05 m [4].

Scientific experiment will be proceeded with Earth ground station like “Bear Like” in Moscow region. In the case then H2 Maser will used as reference source the unprecedented accuracy of distance and velocity measurements could be achieved. Frequency stability (Alan variance) of “Bear Like” reference source shown below on Fig. 2.

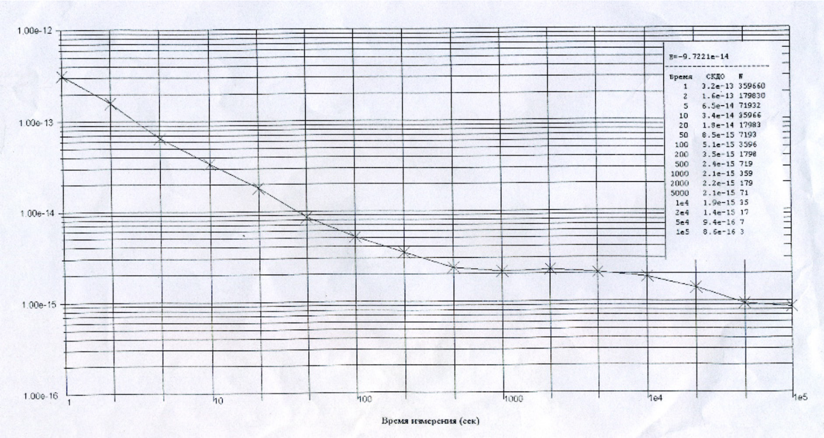

Fig. 2. Frequency stability (Alan variance) of “Bear Like” H2 Maser

Navigation measurements and scientific experiments with “Bear Like” ground station can perform with accuracy 1 mm for ranging and 0.1 mm/s for velocity. The accuracy allows getting new fundamental scientific data.

References:

[1] *Gromov V.D., Kosov A.S.* The Objectives of the Radioscience Experiment in Luna-Resource and Luna-Glob Space Projects // The 6th Moscow Solar System Symp. 2015.

[2] Delta-Dor Raw Data Exchange Format. June 2013. CCSDS 506.1-B-1. https://public.ccsds.org/Pubs/506x1b1.pdf.

[3] Pseudo-Noise (PN) Ranging Systems: Recommended Standard. CCSDS 414.1-B-3. 2022. https://public.ccsds.org/Pubs/414x1b3.pdf.

[4] *Gromov V.D., Kosov A.S.* The Ranging Accuracy of the Radioscience Experiment with the Radio-Beacon Transponder in Comparison with Laser Ranging // The 7th Moscow Solar System Symp. 2016.

STUDYING THE SUITABILITY OF THE KAMCHATKA PENINSULA AS NATURAL TESTING SITE FOR LUNAR MISSIONS BASED ON THE PROPERTIES OF SOILS

A.V. Uvarova
Vernadsky Institute of Geochemistry and Analytical Chemistry RAS, Moscow, Russia, uvarova@geokhi.ru

KEYWORDS:
lunar testing site, lunar soil, lunar regolith, volcanic ash, Kamchatka peninsula, soil-analogue

INTRODUCTION:
Natural testing sites are used to test space rovers in different countries in conditions that imitate lunar or martian landscapes. The Laboratory of Geochemistry of the Moon and planets of Vernadsky Institute proposes to consider the Kamchatka Peninsula as a possible test site for lunar missions. Soil analogues are currently used for Russian missions within covered hangars. However, the creation of large-scale sites may be economically impractical as the volumes and difficulty of production of soil analogues increase. The choice was made in favor of the Kamchatka Peninsula, because this region rich in the most unweathering volcanic material. Especially, samples of ash from the Tolbachik volcano and the Khalaktyrsky beach have the chemical composition close to marine lunar regolith [1].

LUNAR SOIL'S PROPERTIES:
The lunar regolith of marine areas is a silty sand with an admixture of rubble and boulders. The median particle size is about 0.07 mm [2], [3]. The natural density of lunar regolith on the surface down to a depth of 15 cm, according to data from the Luna-16 and Luna-20 missions, varies from 1.12 to 1.7 g/cm^3 with an average value of about 1.5 g/cm^3. The average density of regolith on the surface, according to data from the Apollo missions, is 1.3 g/cm^3, but then increases sharply with depth according to a hyperbolic dependence. Deeper than 60 cm, the density of the regolith soil increases slightly, and at a depth of about 3 m it approaches the value of 1.92 g/cm^3 [2, 4].

Scientists' assessment [5, 6] of bore hole resilience against caving from Apollo-16 and Apollo-17 missions showed that the specific cohesion at landing sites is 1.1–1.8 kPa and the angle of internal friction is 46.5°. Lunokhod-2 in Lemonnier crater near the eastern coast of the Sea of Clarity also measured the following parameters: specific cohesion — 0.40 kPa, angle of internal friction – 40° [2].

Experimental studies of the lunar soil delivered from the landing sites of the manned Apollo expeditions showed a strong dependence of cohesion and the angle of internal friction on the density of the soil and, accordingly, on the depth [6]. When the density changed from 1.115 to 1.87 g/cm^3, the cohesion varied within 0.3–3.0 kPa and the angle of internal friction was 13–56° [6, 3].

The total deformation modulus was evaluated on the imported samples. Loose samples, which correspond to the upper layer of regolith to a depth of 15 cm, are strongly deformed even under a small pressure and have a low modulus of deformation, about 24 kPa. The compact samples, corresponding to regolith from a depth of 30 cm and further, have a significantly higher deformation modulus, about 420 kPa. Poisson's ratio in the studies was calculated through the coefficient of lateral expansion, it amounted to 0.2 f.u. [7].

METHODS:
The main physical and mechanical properties were determined by standardized methods. Loose density (ρ) was determined by the method of free pouring into a container of a known volume, and density in a compact state by layer-by-layer tamping. The strength characteristics, the angle of internal friction (φ) and specific cohesion (c) were determined by a shear strength

test. The normal stress was set depending on the density of the samples in the range from 10 to 50 kPa for loose and from 50 to 200 kPa for compact samples. The shear stress was defined as the maximum value at which the sample failed. The destruction rate was 2 mm/min.

Deformation modulus (*E*) and Poisson's ratio (ν) were determined using triaxial compression test with a load application rate of 0.15 mm/min. The initial all-round pressure was set to 0.1 MPa.

RESULTS:

There were 5 imported samples: Gorely (lower part of the slope), Gorely (1390 m) (upper part of the slope), Khalaktyrsky beach, Mutnovsky, Tolbachik. The samples of Kamchatka ash were sandy soils with an admixture of dust and a coarse-grained fraction in different proportions, which is close in description to lunar rocks. However, tephra from the Tolbachik volcano was too large-grained; it had previously been crushed. Ashes from the upper part of the Gorely volcano and crushed ash of Tolbachik are closest in particle size distribution to the lunar regolith [1]. The samples had a different range of density and, therefore, strength characteristics, as shown in Table. 1.

Table 1. Comparison of properties of volcanic aches and lunar soil

Samples	ρ, g/cm^3	ϕ, grad	c, kPa	E, MPa	ν, f.u.
Mutnovsky	1.34–1.65	43.7–50.8	3.1–18.1	14.6–23.4	0.12–0.19
Gorely (1390 m)	1.27–1.57	33.8–36.1	1.7–12.8	12.1–49.7	0.11–0.21
Gorely (foot)	1.36–1.66	34.8–33.1	3.9 –16.9	10.9–36.9	0.19–0.15
Tolbachik (<0.1 mm)	1.18–1.54	10–34.5	11.9–23.6	4.2–21.5	0.15–0.09
Khalaktyrsky beach	1.68–1.87	29.9–40.3	4.2–14.6	31.9–52.7	0.23–0.31
Lunar soil	1.12—1.92	46.5–25	0–1.8	(13–420)·10^{-3}	0.2

The density range of all samples does not completely correspond to the lunar one; their properties are close to those of the near-surface layer of the lunar regolith.

The mechanical properties of the ashes are different in some measure. All samples have values of the angle of internal friction comparable to those of the lunar soil, however, the specific cohesion of all samples is much higher than the cohesion of regolith in compact state.

The ash deformation modulus is much higher than the characteristic values of the lunar regolith. This difference may be related to the conditions of the experiment; the ash samples were tested with a significantly larger sample size than the lunar regolith and a larger range of loads. The values of the mechanical properties of the ashes themselves correlate with past studies of the properties of the ashes [8].

At this stage of research, the results show that the ashes from volcanoes can be used to practice the landing of landers, which was previously implemented for moon rovers. The upper part of Gorely volcano and Tolbachik volcano are best suited for these purposes, in terms of physical and mechanical properties. However, the sample from the Tolbachik volcano is too large-grained. Further studies of this volcano are required in order to find a suitable site with finer-grained soil.

References:

[1] *Slyuta E.N., Sorokin E.M., Agapkin I.A., Grishakina E.A., Makovchuk V.Yu., Mironov D.D., Turchinskaya O.I., Tretyukhina O.S.* Natural lunar test site on Earth // 13th Moscow Solar System Symp. 2022. P. 165–167.

[2] *Carrier W.D. III.* Apollo drill core relationships // The Moon. 1974. V. 10. P. 183–194. DOI: 10.1007/BF00655719.

[3] *Slyuta E.N.* Physical and mechanical properties of the lunar soil (A review) // Solar System Research. 2014. V. 48. Iss. 5. P. 330–353. https://doi.org/10.1134/S0038094614050050.
[4] *Carrier W.D. III, Olhoeft G.R., Mendell W.* Physical properties of the lunar surface // Lunar Sourcebook / eds. Heiken G., Vaniman D., French B.M. Cambridge: Cambridge Univ. Press, 1991. Ch. 9. P. 475–594.
[5] *Mitchell J.K., Houston W.N., Scott R.F., Costes N.C., Carrier W.D. III, Bromwell L.G.* Mechanical properties of lunar soil: density. porosity. cohesion. and angle of friction // Proc. 3rd Lunar Scirnce Conf. 1972. P. 3235–3253.
[6] *Jaffe L.D.* Shear strength of lunar soil from Oceanus Procellarum // The Moon. 1973. V. 8. P. 58–72.
[7] *Leonovich A.K., Gromov V.V., Dmitriev A.D., Penetrigov V.N., Semenov P.S., Shvarev V.V.* The main features of the processes of deformation and destruction of the lunar soil // Cosmochemistry of the Moon and planets / ed. Vinogradov A.P. M.: Science. 1975. P. 585–592 (in Russian).
[8] *Girina O.A.* Pyroclastic deposits of modern eruptions of andesitic volcanoes of Kamchatka and their engineering-geological features / Institute of Volcanic Geology and Geochemistry FEB RAS. Vladivostok: Dalnauka. 1998. 174 p. (in Russian).

INVESTIGATING HIGH-VOLTAGE CHARGING EFFECTS AND SUBSTRATE MATERIAL ON DUST PARTICLE DYNAMICS AND ELECTROMAGNETIC SIGNATURES IN A LOW-PRESSURE CONDITIONS: LUNAR REGOLITH ANALOGUE STUDY

M.E. Abdelaal[1,2], I.V. Dokuchaev[2], I.A. Shashkova[2], A.Y. Poroykov[3], I.A. Kuznetsov[2], G.G. Dolnikov[2], A.N. Lyash[2], A.E. Dubov[2], A.A. Kartasheva[2], A.V. Zakharov[2]

[1] *Moscow Institute of Physics and Technology, Moscow, Russia, mohamad.essam@phystech.edu*

[2] *Space Research Institute RAS, Moscow, Russia, zakharov@iki.rssi.ru*

[3] *National Research University "Moscow Power Engineering Institute", Moscow, Russia*

KEYWORDS:
dust particle dynamics, Low pressure conditions, high voltage charging, particle-to-particle interactions, electromagnetic signals, interdisciplinary approach

INTRODUCTION:
This research study delves into the realm of dust particle dynamics within a vacuum chamber under extremely low pressure conditions. By applying high voltage charging to diverse dust particles, including a lunar regolith analogue, we explore the influence of electrical potential as a power source on their behavior and kinematics. Furthermore, our investigation encompasses the examination of direct particle-to-particle interactions with connector and dielectric substrates. Notably, we assess the potential for registering electromagnetic signals emanating from the levitation and collision of these charged particles. Through an interdisciplinary approach combining physics, materials science, and electrical engineering, our findings aim to shed light on the complex interplay between high voltage, dust particles, and their electromagnetic manifestations, paving the way for advancements in fields such as astrophysics, space exploration, and particle dynamics research.

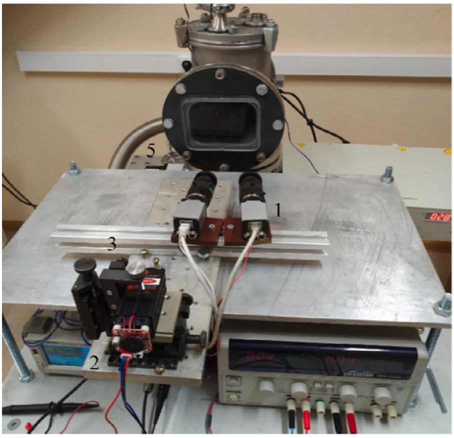

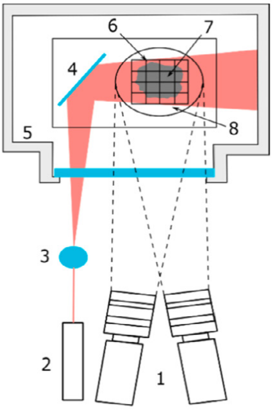

Fig. 1. Picture and scheme (*top*) of the experimental setup for investigating the dust particles trajectories: 1 — CMOS cameras, 2 — laser, 3 — beam expander, 4 — mirror, 5 — vacuum chamber, 6 — steel mesh, 7 — dust particles, 8 — conductive substrate

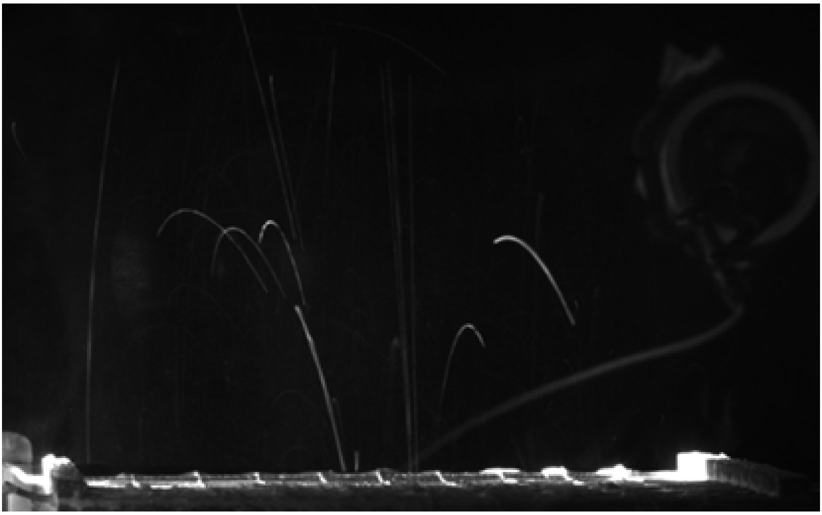

Fig. 2. Visualization of the levitation of Lunar Regolith Analogue particles

References:

[1] *Zakharov A.V., Zelenyi L.M., Popel S.I.* Lunar Dust: Properties and Potential Hazards // Solar System Research. 2020. V. 54. Iss. 6. P. 455–476. DOI: 10.1134/S0038094620060076.

[2] *Wang X., Horányi M., Robertson S.* Experiments on dust transport in plasma to investigate the origin of the lunar horizon glow // J. Geophysical Research: Space Physics. 2009. V. 114. Iss. A5. https://doi.org/10.1029/2008JA013983.

[3] *Rennilson J.J., Criswell D.R.* Surveyor observations of lunar horizon-glow // The Moon. 1974. V. 10. Iss. 2. P. 121–142. https://doi.org/10.1007/BF00655715.

[4] Lunar Sourcebook: A User's Guide to the Moon / eds. Heiken G.H., Vaniman D.T., French B.M. Cambridge University Press, 1991. 778 p.

EXPERIMENTAL RESEARCH OF THE LUNAR SOIL-ANALOGUE VI-75 UNDER NEGATIVE TEMPERATURE

I.A. Agapkin, A.V. Uvarova
Vernadsky Institute of Geochemistry and Analytical Chemistry RAS, 15331533@mail.ru

KEYWORDS:
Lunar soil analogue, frozen regolith, strength properties

INTRODUCTION:

Modern studies of the moon are aimed, among other things, at the study of the Polar Regions. In these areas, ice may be present and, according to various estimates, its content can reach 4 % by weight [1]. It greatly affects the mechanical properties of soils [2] and can increase the strength properties by several times. This fact should not be neglected during missions, the purpose of which is drilling and sampling of soil, as well as its sounding. In this regard, the research is aimed at studying the lunar soil analogue with different water contents at low temperatures. The lunar soil analogue VI-75 [3], previously developed by the Laboratory of Geochemistry of the Moon and Planets, was used as an analogue soil, which imitates the physical and mechanical properties of the surface lunar soil.

RESEARCH METHODS:

The main strength properties in soil mechanics are the angle of internal friction (ϕ) and specific cohesion (c). The first parameter characterizes the ratio of normal (σ) and tangential (τ) forces required to destroy the sample, while the second shows the resistance to tangential forces, without the influence of normal forces. These characteristics were determined by a shear test. This method is based on the Mohr-Coulomb theory: the destruction of materials occurs at a certain ratio of normal and shear stresses.

The experiments were carried out at three values of the vertical load according recommendations of Russian standards 12248.1-2020 [4], the minimum stress was taken to be 50 kPa, since it is close to the natural pressure of dense soils at a depth of 60 cm and further. Subsequent stages of loading are chosen as doubled values of the previous stage. The Shear load was set kinematically at a velocity of 2 $mm \cdot s^{-1}$. All experiments were done using testing equipment the GEOTEK Company.

A sample of VI-75 was mixed evenly with the required amount of water, until the same water content was reached inside the sample. Water content values were set at 5 and 10 % by weight. The resulting mixture was placed in cylindrical rings 35 mm high and 71 mm in diameter, these are special forms for preparing samples for shear tests, and compacted to $\rho = 1.75\ g \cdot cm^{-3}$. The rings were pre-lubricated with petroleum jelly to make it easier to push the frozen samples into the test setup.

The prepared samples were placed in a box made of insulating material. Liquid nitrogen was poured into a separate container to quickly freeze the samples. They froze to the lowest possible temperature from –110 to –120 °C within 2 hours (Fig. 1).

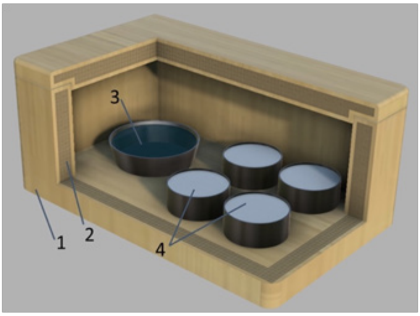

Fig. 1. Scheme of preparing samples for testing: **1** — hardboard box, **2** — heat insulator, **3** — liquid nitrogen, **4** — samples in metal rings

The initial stage of the research did not involve the use of freezers for a single-plane cut could fit there with a large capacity, so that the whole device, besides, it was not designed to work with such low temperatures, so the experiments were carried out at a temperature of +13 °C. Such conditions inevitably led to an increase in the temperature of the samples; therefore, the rate of thawing of the samples was additionally measured. As a result of a large number of experiments (about 20), 9 closest to each other were selected, 3 results for each level of normal load.

RESULTS:

Measurement of the thawing rate showed a significant increase in temperature from –120 to –50 °C in 5 minutes, then the rate decreases and, when approaching zero, the graph asymptotically approaches zero, which is quite explainable by the beginning of the phase transition of water ice (Fig. 2).

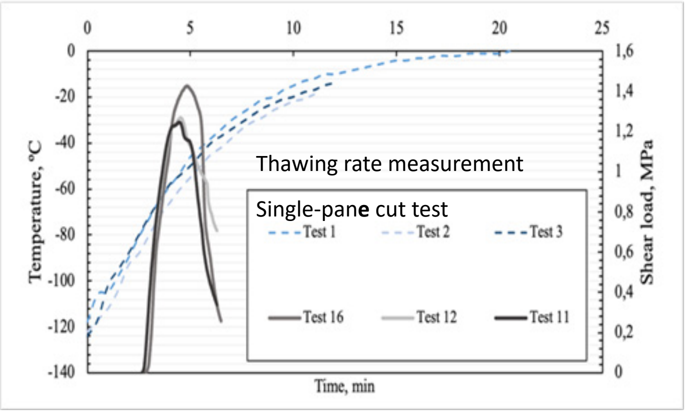

Fig. 2. Graph of thawing samples with 10 % water content and test results of 3 samples at a normal load of 0.1 MPa

Comparison of the results of the cut with the thawing rate graph shows that the peak value of the shear load is reached at the 5th minute of the experiment, while the temperature of the samples is from –45 to –55 °C. Shear stress also varies from 1.26 to 1.42 MPa. Samples with a large spread of shear stress values and outside the statistical error were excluded from the total sample. Thus, due to a large number of experiments, it can be assumed that all the selected tests were on samples with a temperature from –45 to –55 °C at the time of destruction.

Tests with a one-plane cut of samples with a 5 % water content showed that the angle of internal friction is 66.8±0.9° and the specific cohesion is 163.9±28.4 kPa. These characteristics increased to the values ϕ = 74.9±0.67° and c = 486.2±72.9 kPa with an increase in the total weight moisture to 10% (Fig. 3).

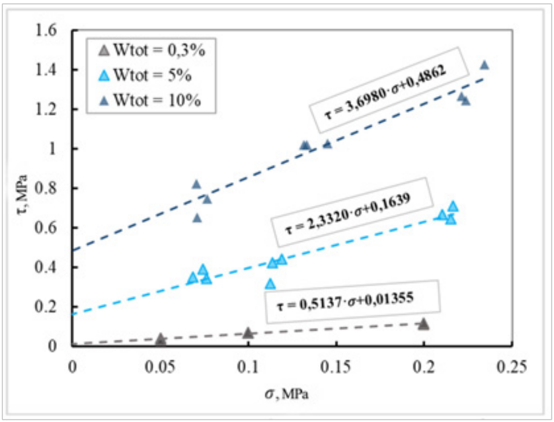

Fig. 3. Test results for samples with a density of 1.75 g/cm^3 and various water contents

CONCLUSION:

The experiments carried out with a shear test on the VI-75 frozen soil with 5% and 10% water contents at a temperature from –45 to –55 °C, as well as its comparison of the results with a dry sample, the water content of which is not more than 0.3 %, showed that the angle of internal friction increased greatly at 5 % water content up to 66.8° and up to 74.9° at $W = 10$ %. Specific cohesion increased even more and became 163.9 at $W = 5$ %, and at 10 % water content it is equal to 486.2 kPa. Thus, the presence of ice in the lunar regolith can significantly increase its strength characteristics.

Further research will focus on ways to test samples at constant temperature, as well as to determine other mechanical characteristics.

References:

[1] *Grishakina E.A., Slyuta E.N.* Probable reserves of water ice in the lunar polar regions // Proc. 18th Conf. young scientists "Fundamental and applied space research". M.: IKI RAN, 2021. P. 20–24. DOI: 10.21046/KMU-2021-20-24.

[2] *Roman L.T.* Mekhanika merzlykh gruntov [Mechanics of Frozen Soils]. M.: Nauka/ Interperiodika, 2002. 426 p. (In Russian).

[3] *Slyuta E.N., Grishakina E.A., Makovchuk V.Yu, Agapkin I.A.* Lunar soil-analogue VI-75 for large-scale experiments // Acta Astronautica. 2021. V. 187. P. 447–457. https://doi.org/10.1016/j.actaastro.2021.06.047.

[4] Russian standard 12248.1-2020 Standartinform, 2020. 20 p.

THERMAL REDUCED SI AND P IN METALLIC IRON NANOSPHERULES: EXPERIMENTAL DATA

E.M. Sorokin[1], O.I. Yakovlev[1], E.N. Slyuta[1], M.V. Gerasimov[2], M.A. Zaitsev[2], K.M. Ryazantsev[1]
[1] *Vernadsky Institute of Geochemistry and Analytical Chemistry RAS, Moscow, Russia, egorgeohim@ya.ru*
[2] *Space Research Institute RAS, Moscow, Russia*

KEYWORDS:
Lunar soil, space weathering, np-Fe^0, laser experiment, micrometeorite bombardment, thermal reduction

INTRODUCTION:
As a result of micrometeorite bombardment, nano- and submicroscopic spherules of metallic iron (npFe^0) are formed in regolith grains of airless bodies. The presence of nanophase iron (npFe^0) significantly changes the spectrum of reflection from airless bodies - it subdued the characteristic absorption bands in the visible and near-IR ranges, shifts the intensity of reflected light toward longer wavelengths and reduces the total albedo [1–3]. During micrometeorite bombardment, it is formed as a result of condensation of vapor arising from the shock evaporation of lunar rocks. Especially often, nanophase iron can be observed in a thin amorphous film on the surface of mineral particles [4–5].

EXPERIMENTAL METHODS, TECHNIQUE AND STUDY OF THE SAMPLES:
For the experiment a pulsed neodymium glass laser was used. The laser radiation wavelength was 1.06 µm, the pulse duration was 10–3s, and the pulse energy was ~600–700 J. The energy flux density was ~106–107 $W \cdot cm^{-2}$. The temperature at the “impact” point was of the order of 4000–5000 K, which corresponded to the evaporation temperature during high-speed impact processes with collision velocities of the order of 10–15 km/s [6–7]. In the experiment, we used several types of targets - tholeiite recrystallized basalt, basalt glass, several types of olivines, several pyroxenes, and peridotite. Numerous placers of iron nanospherules with different shapes and textures were found in all targets. Spherules up to 5 µm in size were analyzed by the EDS method. To determine the chemical composition of submicron iron spherules, we analyzed craters in targets made of ferruginous olivine and basalt glass. When studying the composition of large spherules, the method of sequential fourfold rotation of the sample and the direct determination method of oxygen was used.

The analysis was performed on a TESCAN MIRA 3 scanning electron microscope with an X-MAX 80 EDS analyzer (Vernadsky institute).

RESULTS:
In our experiments, very large spherules with sizes of a few microns up to 5 were obtained: in the basalt glass 19 spherules, in the Fe-olivine - 36 spherules. Such spherules are amenable to analysis in a scanning electron microscope (Figure 1). Although the determination of oxygen by the EDS method occurs at a semi-quantitative level, and taking into account the effect of the oxidation of the metal phase in air and even in the chamber of a scanning electron microscope. For example, up to 1.5 % oxygen is found in the cobalt standard, that is, an oxide film is formed. We can indirectly show that high abundances of elements in the reduced state are found (Table 1); even taking into account the possible contamination from condensate material that could be deposited from the vapor cloud above the crater.

Among the impurity elements in such micron spherules, Ni (<1 %), Si (up to 5 %), P (up to 14 %), S (up to 0.2 %) and some other elements were found (Table 1). The content of elements such as Al, Mg, Ca show a direct correlation with the content of oxygen, while the content of P, Si, Ni does not (Figure 2).

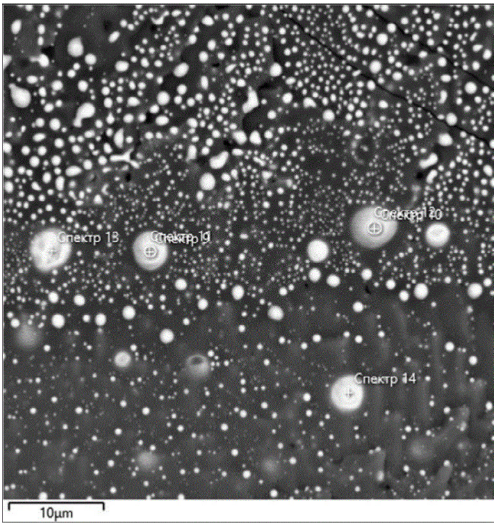

Fig. 1. Large spherules of metallic iron in a crater of ferruginous olivine, scanning electron microscope

Table 1. Average content of chemical elements in submicrospherules in targets made of ferruginous olivine and basalt glass

Element	Fe-olivine	Basalt glass
O	1,90	6,91
Na	0,00	0,71
Mg	1,95	1,32
Al	0,06	1,74
Si	1,44	9,23
S	0,01	0,00
P	0,00	3,86
Ca	0,03	1,03
Mn	0,04	0,45
Fe	90,39	70,76
Ni	0,27	0,19
Total	96,10	96,41

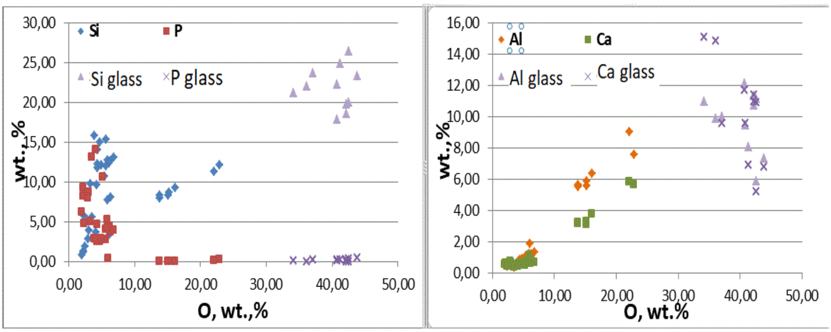

Fig. 2. Contents of various elements in iron submicrospherules with respect to oxygen, for a basalt glass target. Purple markers are responsible for the content of these elements in the glass, which is the matrix for these nanospherules

CONCLUSION:
Metallic iron spherules were obtained in a laser experiment. The largest ones were measured by the EDS method on a scanning electron microscope. The analyzes performed indirectly showed that in a short time of the experiment, on the order of a millisecond, not only the thermal reduction of iron oxide, but also silica, with subsequent dissolution of silicon in the iron melt, as well as enrichment in siderophilic elements (P,S) of this melt, has time to occur.

References:
[1] *Hapke B.* Space weathering from Mercury to the asteroid belt // J. Geophys. Res. 2001. V. 106. Iss. E5. P. 10039–10073. https://doi.org/10.1029/2000JE001338.
[2] *Pieters C.M., Taylor L.A., Noble S.K. et al.* Space weathering on airless bodies: Resolving a mystery with lunar samples // Meteoritics and Planetary Science . 2000. V. 35. Iss. 5. P. 1101–1107. https://doi.org/10.1111/j.1945-5100.2000.tb01496.x
[3] *Pieters C.M., Noble S.K.* Space weathering on airless bodies // J. Geophysical Research: Planets. 2016. V. 121. Iss. 10. P. 1865–1884. https://doi.org/10.1002/2016JE005128.
[4] *Keller L., McKay D.* Discovery of vapor deposits in the lunar regolith // Science. 1993. V. 261. Iss. 5126. P. 1305–1307. DOI: 10.1126/science.261.5126.1305.
[5] *Keller L.P., McKay D.S.* The nature and origin of rims on lunar soil grains // Geochimica et Cosmochimica Acta. 1997. V. 61. Iss. 11. P. 2331–2341. https://doi.org/10.1016/S0016-7037(97)00085-9.
[6] *Sorokin E.M., Yakovlev O.I., Slyuta E.N. et al.* Laser experimental modeling of the formation of nanophase iron (np-Fe^0) // Proc. 52nd Lunar and Planetary Science Conf. 2021. Art. No. 1975.
[7] *Gerasimov M.V, Ivanov B.A., Yakovlev O.I., Dikov Yu.P.* Physics and Chemistry of Impacts // Laboratory Astrophysics and Space Research / eds. P. Ehrenfreund, K. Krafft, H. Kochan, V. Pirronello. Ser. Astrophysics and Space Science Library (ASSL). Kluwer Academic Publishers, 1999. V. 236. P. 279–330. 51 p.

NEW INTERPRETATION OF "TRUE POLAR WANDER" PHENOMENON: CONCLUSIONS FOR TERRESTRIAL PLANETS

A.A. Barenbaum
Oil and Gas Research Institute RAS, Moscow, Russia, azary@mail.ru

KEYWORDS:
TPW phenomenon, Earth's lithospheric shell, plate movement, Coriolis force

ANNOTATION:
A new physical interpretation of phenomenon of "true polar wander (TPW)" is proposed, which explains the TPW phenomenon by bombardments of Solar System by galactic comets. This explanation assumes that Earth has an autonomous convective lithospheric shell in which plates form and move. Three questions are considered: 1) cosmogonical grounds for existence of a convective shell on Earth; 2) the TPW phenomenon and its explanation by falls of galactic comets; 3) theoretical model that takes into account the Coriolis force influence on plates movement.

ORIGIN OF EARTH CONVECTIVE SHELL AND LITHOSPHERIC PLATE:
We closely connect the question of existence of an autonomous convective lithospheric shell on Earth with the origin Moon problem. This problem is solved by us from the standpoint of cosmogonical concept "Cosmogony of Open Solar System" [1], which, unlike the cosmogony of Kant-Laplace, takes into account powerful bombardments of Solar System by galactic comets.

According to COSS concept, our Solar system formed in two main stages. At the first stage ~6.6 Ga ago, the Sun and planets arose, while satellites of planets, including Moon, as well as asteroid bodies belt formed at second stage ~4.6 Ga ago, caused by the planet Phaethon destruction. At this point in time, Earth already had a solid Fe-Ni core, a fairly thick anorthosite crust, and a system of mantle silicate shells similar to those existing today [2].

Calculations show [2] that as a result of fall on Earth of large Phaeton fragments, our planet lost 245±10 km of the surface layer of rocks, which consisted on ~1/3 of primary anorthosite crust and on ~2/3 of mantle rocks. Most of this matter was lost forever, about 18 % was ejected into near-Earth orbit and became part of the Moon, and about the same amount fell back to Earth, melting it to a depth of ~100 km. After cooling, these molten rocks differentiated into crust and mantle. However, due to the loss of ~2/3 of primary crust, the remaining refractory crustal material was only enough to cover ~1/3 of Earth's surface with continents. This lack of crustal matter today manifests itself in existence of oceanic and continental hemispheres on our planet, as well as a system of continental ("old") and oceanic ("young") lithospheric plates moving along the plastic layer of asthenosphere rocks.

The uppermost layer of rocks today is Earth's lithospheric shell. As we can see, this previously molten rocks layer has not yet cooled down and continues to be in a state of partial melting and convective mixing. An important role in maintaining the lithospheric shell in this state is played by cyclic bombardments of Earth by galactic comets [2]. Falls of comets split lithospheric plates and cause their movement, and also lead to heating of the layer of asthenosphere rocks [3], along which individual plates and the lithospheric shell as a whole move.

THE "TRUE POLAR WANDER" PHENOMENON:
An analysis of lithospheric plates movement shows that disparate continental plates with period of 400 Myr [4] unite into supercontinents either in southern or in northern Earth's hemisphere. At the same time, over ~10^6–10^7 years, not only individual plates change their direction and speed, but also Earth's rotation pole. The latter phenomenon is called "True Polar Wander (TPW)".

It is believed that TPW phenomenon is inherent in all planets [5]. On our planet, this phenomenon is explained by change in orientation of Earth's main axis of inertia, due to moving of density inhomogeneities in mantle [6].

It is known from mechanics that in a free state, all rotating bodies tend to take position in which the axis of their largest (principal) moment of inertia is the axis of their rotation and coincides in direction with the momentum vector of body. If the latter condition is not met, then, during the transition to a stable state, the body rotation axis can perform a complex reciprocating motion [7].

Although our Earth is not a "solid" body, such its model is currently used to determine of TPW magnitude. The traditional approach to estimating TPW effect is to compare [8] for specific plates the position of Earth's magnetic pole, established by magnetic methods, with movement of this plate in the frame of reference corresponding to Earth's mantle. The procedure is carried out in several stages. At first, using magnetic methods, by measurements on different plates find the average position of the magnetic pole, which is identified with the axis of Earth's rotation. Then, for all plates, the trajectory of movement of Earth's rotation axis is constructed, which is considered as the sum of movement of this plate relative to mantle (1) and rotation of mantle itself around Earth's axis (2) — TPW effect. The TPW value is found by subtracting the movement of plate (1) from the sum of two movements.

It must be said that determining of TPW in this way is not quite correct. First, the variation of Earth's main axis of inertia over a time of ~10^7 years is physically problematic [6]. Secondly, the changes in angular momentum and velocity of Earth's rotation under influence of cyclic cometary bombardments are not taken into account [2]. And thirdly, other important factors affecting the movement of lithospheric plates, in particular, Earth's axis precession, and the Coriolis force influence on movement of plates, is ignored.

ALTERNATIVE APPROACH TO EXPLAINING TPE PHENOMENON:

In [9], the new approach to explaining TPW phenomenon is proposed, which makes it possible to take these factors into account. It is shown that TPW phenomenon should be explained by variations not of Earth's rotation axis, but only of its lithospheric shell. In this case, shell (or significant part of it) rotates relative to mantle with higher angular velocity than Earth as a whole.

This approach is based on mechanism of supercontinental cyclicity, which is explained by bombardments of Earth by galactic comets [10]. Taking into account [11–12], supercontinents are formed in Earth's subpolar zones at a very high density of galactic comets falls and cease to exist in middle latitudes under conditions of a much lower density of comet falls.

It is also taken into account that the ecliptic plane makes an angle ~62° with Galaxy plane, in which Sun and galactic comets move. Therefore, after half period of Sun's revolution in Galaxy, galactic comets alternately bombard the southern and northern hemisphere of planets in Solar System.

As a result, rotation axes of planets deviate from the perpendicular to ecliptic plane by angle ϑ equal to the difference of 90° and angle of 62°. In particular, angle ϑ is equal to 23.44° for Earth, 25.19° for Mars, 26.73° for Saturn, and 28.32° for Neptune. The value of angle ϑ explains by recent cometary bombardment of Solar System, which took place in period from ~5.0 to 0.7 Ma [2].

Another conclusion [13] is that the period of supercontinental cyclicity of 400 Myr is due to precession of ecliptic plane with a period of 2000 Myr, which is in resonance with Sun's orbital motion in Galaxy. Therefore, reason for supercontinental cyclicity is the processes in Galaxy and Solar System, and not in deep Earth's bowels.

INFLUENCE OF CORIOLIS FORCE ON MOVEMENT OF PLATES:

The Coriolis force is the force of inertia acting on objects moving in a frame of reference rotating about an inertial frame of reference. Under the action of this force in a rotating reference frame, objects receive acceleration:

$$\alpha = 2[V\times\omega] = 2V\omega\cdot\sin(\phi), \tag{1}$$

where V is velocity vector of object in the rotating reference frame; ω is vector of angular rotation velocity of the rotating reference frame relative to inertial frame; ϕ is angle between vectors V and ω. The Coriolis force is directed perpendicular to plane of vectors V and ω. In Northern hemisphere of Earth, Coriolis force deflects objects to the right of their movement direction, and in Southern hemisphere — to the left.

The question of Coriolis force effect on motion of lithospheric plates was first raised by us in [14] when analyzing the results of [15]. Studying the heat fluxes along nine geotraverses crossing Mid-Ocean Ridges (MORs) in Atlantic, Indian, and Pacific Oceans at different latitudes, the authors of [15] found that average heat fluxes on western and eastern flanks of geotraverses in Northern and Southern hemispheres systematically differ.

The authors of [15] associated these differences with Coriolis force, which, in their opinion, deflects ascending magma flows in the MOR zones in opposite directions in Southern and Northern hemispheres.

Consideration of this issue showed [14] that Coriolis force acts not on magma, but on lithospheric plates. At the same time, all plates (oceanic and continental) form a single lithospheric shell on Earth, which, apparently, rotates as a whole in asthenosphere with an angular velocity ω_o, which differs from mantle rotation ω_m. In Phanerozoic, velocity of lithospheric shell rotation ω_o was higher than ω_m, and at the same time plates shifted to the north. Therefore, lithosphere and mantle do not necessarily have a common rotation axis.

THEORETICAL MODEL

Let us express velocity of plates relative to mantle by sum of velocities $\tilde{V} = V' + V''$, where V' is vector of velocity of plates in lithospheric shell, and V'' is vector of shell velocity relative to mantle. We will also consider the lithospheric shell as a rotating frame of reference, and mantle with Earth's axis fixed in it (as well as axis of geomagnetic dipole) as an inertial frame of reference [9].

Let the lithospheric shell and mantle rotate around the same axis with velocities $\omega_o > \omega_m$. In this case, the plates in inertial frame of reference will move west along the latitude with a velocity

$$V = R(\omega_o - \omega_m) \cdot \cos(\phi), \tag{2}$$

and under Coriolis force influence they will acquire acceleration in longitude

$$\alpha = 2R\, \omega_m(\omega_o - \omega_m) \cdot \cos(\phi), \tag{3}$$

where R is Earth's radius; φ is latitude of the place.

Formula (3) shows that the Coriolis force effect on plates movement caused by difference in velocities ω_o and ω_m, is maximum at latitude ϕ = ±45°, and at equator (ϕ = 0°) and at poles (ϕ = ±90°) this force stops acting. At the same time, due to general movement of lithospheric shell to the north, plates experience greatest tensile and shift stresses at equator.

Testing of this simplest model showed [9] that it quite well reflects the specifics of Pangaea supercontinent fragmentation and also explains the structure of Mid-Atlantic Ridge and its transform faults.

CONCLUSIONS:

- The reason for orientation change of Earth rotation axis and other planets is the processes in Galaxy and Solar System, and not in bowels of planets.
- The "true polar wandering" phenomenon should be attributed not to Earth as a whole, but to the rotation pole of its lithospheric shell (or a significant part of this shell), which can change position for time ~10^6–10^7 years.

The author believes that the transition to a new interpretation of TPW phenomenon and taking into account the Coriolis force effect on movement of lithospheric plates will expand the range of problems being solved today in the Earth sciences and planetology.

REFERENCES:

[1] *Barenbaum A.A.* Origin of asteroids and meteorites (new cosmogony concept) // Conceptual foundations of geology: Proc. St. Petersburg Mining Institute. 1992. V. 134. P. 9–27. (In Russian).

[2] *Barenbaum A.A.* Galactocentric paradigm in geology and astronomy. M., 2010. 544 p. (In Russian).
[3] *Barenbaum A.A.* Possible mechanism of heating of lithospheric rocks by galactic comets // Uralian Geological J. 2013. No. 1(91). P. 21–39. (In Russian).
[4] *Bozhko N.A.* Supercontinental cyclicity in Earth evolution // Vestnik MGU. Geol. 2009. No. 2. P. 13–28. (In Russian).
[5] *Mitchell R.N., Thissen C.J., Evans D. et al.* A Late Cretaceous true polar wander oscillation // Nature Communication. 2021. V. 12. Iss. 1. Art. No. 3629.
[6] *Goldrreich P., Toomre A.* Some remarks on polar wandering // J. Geophysical Research. 1969. V. 74. Iss. 10. P. 2555–2567.
[7] *Greenwood D.T.* Principles of Dynamics. Prentice-Hall, 1988. 552 p.
[8] *Steinberger B., Torsvik T.H.* Absolute plate motions and true polar wander in the absence of hotspot tracks // Nature. 2008. V. 452. P. 620–623. https://doi.org/10.1038/nature06824.
[9] *Barenbaum A.A.* Rotation of Earth's lithosphere shell relative to mantle: new explanation of "true polar wander" phenomenon, participation of the Coriolis force in lithosphere plates movement // Proc. All-Russia An. Seminar on Experimental Mineralogy, Petrology and Geochemistry (RASEMPG-2023). Vernadsky Inst. Geochemistry and Analytical Chemistry RAS. Moscow. 2023. (In Press).
[10] *Barenbaum A.A.* Supercontinental cyclicity as a result of bombardment of Earth by galactic comets in Galaxy spiral arms // Proc. All-Russia An. Seminar on Experimental Mineralogy, Petrology and Geochemistry (RASEMPG-2022). Vernadsky Inst. Geochemistry and Analytical Chemistry RAS. Moscow. 2022. P. 258–264. (In Russian).
[11] *Barenbaum A.A.* Geological structures created by falls of galactic comets // J. Physics: Conf. Series. 2015. V. 653. Art. No. 012073. 9 p.
[12] *Barenbaum A.A., Shpekin M.I.* To the development of the mechanism of interaction of galactic comets with terrestrial planets // J. Physics: Conf. Series. 2016. V. 774. Art. No. 012096. DOI: 10.1088/1742-6596/774/1/012096.
[13] *Barenbaum AA.* Measuring the precession period of Solar System ecliptic plane using Galactic model // The 13 Moscow Solar System Symp; Book of abstracts. Space Research Institute RAS, Moscow. 2022. Art. No. 13MS3-GP-PS-04.
[14] *Barenbaum A.A.* Displacement of heat flows in mid-ocean ridges by the Coriolis force // Geology of Seas and Oceans: Proc. 32nd Intern. Sci. Conf. (School) on Marine Geology. Shirshov Institute of Oceanology RAS. Moscow. 2019. V. 5. P. 37–40. (In Russian).
[15] *Khutorskoy M.D., Teveleva E.A.* Heat flow asymmetry at mid-ocean ridges in the Northern and Southern hemispheres of Earth // Georesursy. 2018. V. 20. Iss. 2. P. 122–132.

SESSION 3. VENUS(VN)
ORAL SESSION

VENERA-D MISSION UPDATE

L.M. Zelenyi[1], L.V. Zasova[1], O.I. Korablev[1], D.A. Gorinov[1], M.V. Gerasimov[1], N.I. Ignatiev[1], N.A. Eismont[1], M.A. Ivanov[2], D.V. Strelnikov[1], and the Venera-D team

[1] *Space Research Institute RAS, Profsouznaya 84/32, Moscow 117997, Russia zasova@cosmos.ru*

[2] *Vernadsky Institute of Geochemistry and Analytical Chemistry*

KEYWORDS:

Venus, mission, orbiter, lander, balloon.

INTRODUCTION:

Venera-D is a mission to study atmosphere, surface, and surrounding plasma of Venus, in order to resolve the fundamental question of why our sister planet Venus is so different from Earth, and what lessons we can learn from the understanding of the evolution of Venus climate as applied to the Earth. It can also help understand environments of the terrestrial planets of the Solar System and Venus-like exoplanets as well as with the question of their potential habitability. Venera-D includes an orbiter, a lander, and an aerial platform (balloon) [1].

ORBITER:

The Orbiter on the polar orbit is focused on studying a) thermal structure of the atmosphere, winds, thermal tides, and solar locked structures; the dynamics and the nature of superrotation, radiative balance, and the source of the greenhouse effect; b) composition of the atmosphere; clouds, their structure, composition, microphysics and chemistry; c) composition of the lower atmosphere, and surface emissivity on the night side. A suite of plasma instruments on the Orbiter is aimed to study the upper atmosphere, ionosphere, electrical activity, magnetosphere, the atmospheric escape rate, and solar wind interaction.

LANDER:

The most important element of the Venera-D mission contains scientific payload to study the elemental and mineralogical composition of the surface and near-subsurface materials after drilling to a few cm depth and taking samples. During descent it will study structure and chemical composition of the atmosphere down to the surface, including the abundances and isotopic ratios of trace and noble gases, direct chemical analysis of cloud aerosols, and geomorphology of the landing site.

AERIAL PLATFORM:

A balloon with variable altitude of floating (within 53-57 km) is planned to operate for up to three months. Such module can provide unique in situ information on the meteorological parameters, composition of the atmosphere and cloud structure.

SUMMARY:

The Venera-D project is planned to be launched in 2031. Venera-D has unique capabilities such as surface sampling, long-term in situ cloud measurements, and instrumentation that could work in synergy with the parallel missions (Rocket Lab's mission [2], DAVINCI [3], VERITAS [4], EnVision [5], possibly Shukrayaan-1 and VOICE). A coordination of efforts with other missions (and their scientific instruments) is crucial to answer the most important fundamental questions about our mysterious neighbor planet.

Acknowledgements:

We acknowledge Ministry of Science and Higher Education grant 122042500018-9. The Venera-D team acknowledges our previous work with NASA for invaluable joint discussions and collaborative work during Pre-phase A.

References:

[1] *Zelenyi L.M. et al*. The Venera-D mission for comprehensive study of Venus // 44th COSPAR Scientific Assembly, Athens, Greece. 2022. id B4.1-0027-22.

[2] *French R. et al.* Rocket Lab Mission to Venus // Aerospace. 2022. V. 9. I. 8. Id 445.
[3] *Garvin J.B. et al.* Revealing the Mysteries of Venus: The DAVINCI Mission // The Planetary Science Journal. 2022. V. 3. I. 5. id 117.
[4] *Smrekar S.E. et al.* VERITAS (Venus Emissivity, Radio Science, InSAR, Topography, and Spectroscopy): A Selected Discovery Mission // 54th Lunar and Planetary Science Conference, Woodlands, USA. 2023. id 1198.
[5] *Widemann T. et al.* EnVision: Understanding Why Earth's Closest Neighbor Is So Different // 54th Lunar and Planetary Science Conference, Woodlands, USA. 2023. id 1764.

UPDATES OF AKATSUKI VENUS ORBITER

T. Satoh, A. Yamazaki, N. Ishii, AKATSUKI Team
Institute of Space and Astronautical Science, Japan Aerospace Exploration Agency, Sagamihara, Japan, satoh@stp.isas.jaxa.jp

KEYWORDS:
Venus, meteorology, atmospheric dynamics, super rotation, AKATSUKI

INTRODUCTION:

AKATSUKI (aka Venus Climate Orbiter) was launched on 21 May 2010, and was successfully inserted to the Venus' orbit at the second attempt (VOI-R) happened on 7 December 2015. Since then, AKATSUKI has been regularly acquiring Venus' data for nearly 8 earth years to date. This duration almost compares that achieved by ESA's Venus Express (from 2006 to 2014).

AKATSUKI is unique because it is the first "meteorological" satellite orbiting around a planet other than the earth. To investigate the peculiar dynamics of Venusian atmosphere (the super-rotation, in particular), AKATSUKI is equipped with 5 cameras (UVI, IR1, IR2, LIR, and LAC) plus the ultra-stable oscillator for radio science (RS) experiments. These instruments were so designed to perform best when the spacecraft is in an equatorial plane orbit of retrograde direction (the same as Venus rotates). AKATSUKI has actually been in an elongated and retrograde orbit (~11 earth day period) near the equatorial plane of Venus [1].

The onboard instruments, together with its preferred orbit, perform almost as we anticipated, achieving remarkable discoveries such as the stationary gravity-wave features in the cloud-top temperature [2], the equatorial jets in the middle-to-low clouds [3], etc. Unfortunately, IR1 and IR2 stopped working due to the malfunction of their shared control electronics (IR-AE) in December 2016. All other instruments, as well as the spacecraft bus system, still maintain good health condition.

AKATSUKI's high-precision measurements of the wind fields at the cloud-top level revealed that the super-rotation, at least near the equator to low latitudes, is maintained by the thermal tides excited by the solar heating in the day hemisphere [4]. Thermal imaging by LIR provides uniform coverage of

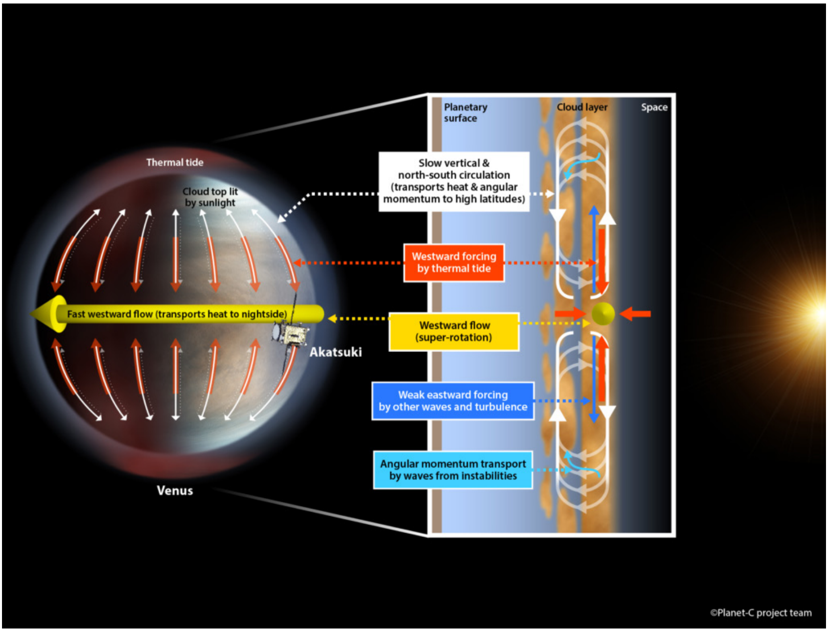

Fig. 1. The schematic of mechanisms how super-rotation of Venus' atmosphere is maintained (a press release illustration for [4])

both day and night side of the cloud-top level. A new feature-tracking method applied to such data revealed the global circulation pattern for the first time ever: while equator to poleward divergence is seen in the day, the equatorward convergence was observed [5]. The "true" meridional Hadley circulation seems to be far weaker than was estimated before.

Long-term and consistent data acquisition is essential for studies of meteorology and climatology. Now, AKATSUKI is entering the phase to provide valuable data to study secular variability and/or periodicity related (or not) to the solar cycle or other external influences [6]. Although uncertainties in the remaining fuel is the biggest concern, we AKATSUKI team will continue careful operation and data acquisition as long time period as possible for better understanding of the earth twin planet's atmosphere.

References:

[1] *Nakamura M., Imamura* T, *Ishii* N. *et al.* AKATSUKI returns to Venus // Earth, Planets and Space. 2016. V. 68. Art. No. 75. https://doi.org/10.1186/s40623-016-0457-6.
[2] *Fukuhara T., Futaguchi* M., Hashimoto G. *et al.* Large stationary gravity wave in the atmosphere of Venus // Nature Geoscience. 2017. V. 10. P. 85–88. https://doi.org/10.1038/ngeo2873.
[3] *Horinouchi T., Murakami* S.*-ya, Satoh T. et al.* Equatorial jet in the lower to middle cloud layer of Venus revealed by Akatsuki // Nature Geoscience. 2017. V. 10. P. 646–651. https://doi.org/10.1038/ngeo3016.
[4] *Horinouchi T., Hayashi* Y.-Y., *Watanabe* S. *et al.* How waves and turbulence maintain the super-rotation of Venus' atmosphere // Science. 2020. V. 368. P. 405–409. DOI: 10.1126/science.aaz4439.
[5] *Fukuya K., Imamura* T., *Taguchi* M. *et al.* Unveiling of nightside cloud-top circulation of Venus atmosphere // Nature. 2021. V. 595. P. 511–515. DOI: 10.1038/s41586-021-03636-7.
[6] *Khatuntsev I.V., Patsaeva M.V., Titov D.V. et al.* Twelve-Year Cycle in the Cloud Top Winds Derived from VMC/Venus Express and UVI/Akatsuki Imaging // Atmosphere. 2022. V. 13. Iss. 12. https://doi.org/10.3390/atmos13122023.

TWELVE YEARS CYCLE IN THE CLOUD TOP WINDS ON VENUS

I.V. Khatuntsev[1], M.V. Patsaeva[1], L.V. Zasova[1], D.V. Titov[2], N.I. Ignatiev[1], D.A. Gorinov[1], A.V. Turin[1]
[1] *Space Research Institute RAS, Moscow, Russia, khatuntsev@cosmos.ru*
[2] *Leiden Observatory, Leiden University, Leiden, The Netherlands*

KEYWORDS:
atmospheres, venusian atmosphere, atmospheric dynamics. solar cycle

INTRODUCTION:

We present the long-term variations of both zonal and meridional components of the cloud top winds. For the first time, we jointly analyze the wind fields derived from the VMC/Venus Express and UVI/Akatsuki UV cameras using the same digital cloud-tracking technique that resulted in the longest-to-date and almost continuous temporal coverage of approximately 24 Venusian years (2006–2022). To focus the study on the long-term changes and exclude the influence of spatial and local time variations, we limited the latitude range to 20±2.5° S and local time to 11–13 h. More than 46,000 wind vectors were derived from the VMC and UVI images using the digital cloud tracking technique developed by I.V. Khatuntsev et al. [1] and described by M.V. Patsaeva et al. [2], enabling intercomparison of the results obtained by both cameras.

The time series $u_i(t)$ was analyzed for long-term periodicities. We used the Lafler – Kinman method [3], which is widely applied in astronomy for detection of periodicities. The method is also referred to as the epoch folding method. For any trial period P' a phase curve is created, where for every measurement u_i made at the time t_i a phase ϕ_i is determined as the fractional part of $E = (t_i - t_0)/P'$. Thus, for a periodical time series all measurements performed at different moments are brought together within one cycle.

As a result, the observation date t_i and initial Julian date t_0 = 2456314.26 (ϕ_0 = 0) are related to the period P = 4576.21 and phase (fractional part of E) as follows:

$$t_i = 2456314.26 + 4576.21E.$$

The phase curves for the zonal and meridional components were calculated for the period of 4576.21±180 days (12.5±0.5 years). The measurements from the earlier missions fit the zonal wind phase curve for the 13- and 12-year period quite well. However, decreasing the trial period to 11 years results in a higher dispersion and the mismatch with OCPP/Pioneer Venus measurements becomes critically large. This is where we can see the strong difference between 12–13 years and 11 years due to the much longer time scale.

Thus, the long-term variations (Figure 1) of the mean zonal and the meridional wind speed in the upper cloud show periodical behavior within the period of 12.5±0.5 years. The zonal wind component is characterized by an annual mean of −98.6±1.3 m/s and an amplitude of 10.0±1.6 m/s. The mean meridional wind velocity is –2.3±0.2 m/s and has an amplitude of 3.4±0.3 m/s.

Plausible physical explanations of the periodicity include both internal processes and external forcing. Both missions observed periodical changes in the UV albedo correlated with the circulation variability. This could result in acceleration or deceleration of the winds due to modulation of the deposition of the radiative energy in the clouds. The circulation can be also affected by the solar cycle that has a period of approximately 11 years with a large degree of deviation from the mean. The solar cycle correlated with the wind observations can probably influence both the radiative balance and chemistry of the mesosphere.

See more details in our publication [4].

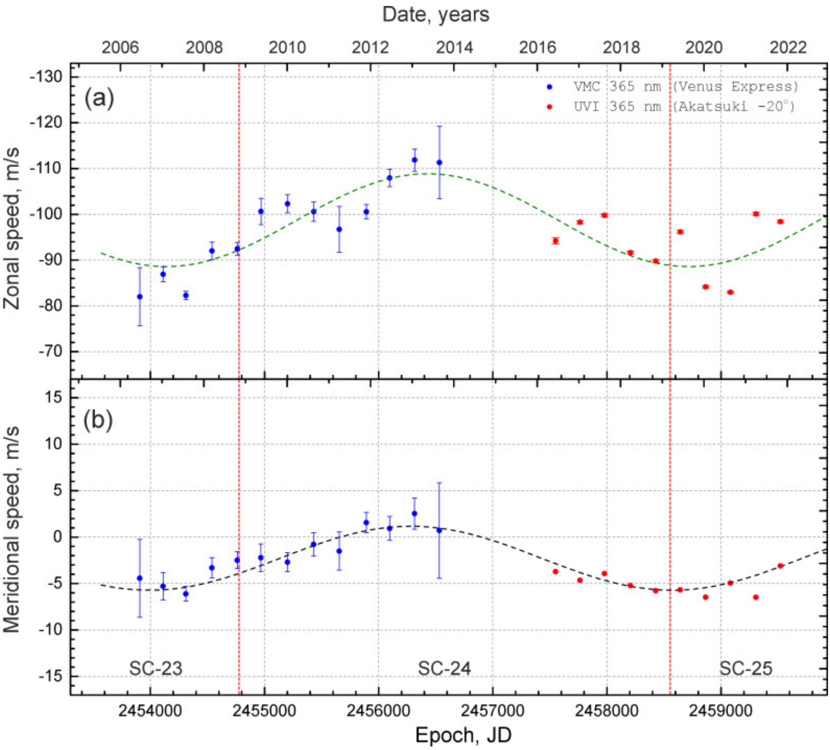

Fig. 1. Long-term variations of the mean zonal (a) and meridional (b) wind speed at 20±2.5° S at around noon (12±1 h LT) derived from VMC/ Venus Express (blue) and UVI/ Akatsuki (red) images. Error bars correspond to 99.6 % confidence interval $(3\sigma_{\overline{x}})$. The zonal wind component is negative, indicating east-west retrograde circulation. The negative sign of the meridional speed corresponds to north-south motions.

References:

[1] *Khatuntsev I.V., Patsaeva M.V., Titov D.V. et al.* Cloud level winds from the Venus Express Monitoring Camera imaging // Icarus. 2013. V. 226. P. 140–158. https://doi.org/10.1016/j.icarus.2013.05.018.

[2] *Patsaeva M.V., Khatuntsev I.V., Patsaev D.V. et al.* The relationship between mesoscale circulation and cloud morphology at the upper cloud level of Venus from VMC/Venus Express // Planetary and Space Science. 2015. V. 113. P. 100–108. https://doi.org/10.1016/j.pss.2015.01.013.

[3] *Lafler J., Kinman T.D.* An RR Lyrae Star Survey with Ihe Lick 20-INCH Astrograph II. The Calculation of RR Lyrae Periods by Electronic Computer // Astrophysical J. Supplement Ser. 1965. V. 11. Art. No. 216. https://doi.org/10.1086/190116.

[4] *Khatuntsev I.V., Patsaeva M.V., Titov D.V. et al.* Twelve-Year Cycle in the Cloud Top Winds Derived from VMC/Venus Express and UVI/Akatsuki Imaging // Atmosphere. 2022. V. 13. Iss. 12. Art. No. 2023. https://doi.org/10.3390/atmos13122023.

SOME PECULIARITIES OF THE VENUSIAN MESOSPHERE DYNAMICS

L.V. Zasova[1], I.V. Khatuntsev[1], M.V. Patsaeva[1], D.A. Gorinov[1], N.I. Ignatiev[1], D.V. Titov[2]
[1] *Space Research Institute RAS, Profsouznaya 84/32, Moscow 117997, Russia zasova@cosmos.ru;*
[2] *Leiden Observatory, Leiden University, The Netherlands*

KEYWORDS:
Mesosphere, dynamics, thermal tides, Hadley cells

INTRODUCTION:
Venus has a massive atmosphere characterized by complex dynamic properties. Here we discuss the processes which affect the dynamics of Venus mesosphere.

THERMAL TIDES:
The distribution of the O_2 emission on the night side of Venus characterizes the atmospheric circulation at about 100 km altitude, the main mode of which is SS-AS circulation [1]. The VIRTIS-M/VEx mapping of the 1.27 μm O_2 band shows that the convergent area of the horizontal flow peaks at 22-23 hours local time (LT) instead of midnight as one could expect from the SS-AS circulation [2]. This shift is occurring in the opposite direction to the superrotation. Local time of the convergent area coincides with the maximum of the temperature vs LT tidal curve at a given altitude [3].

HADLEY CIRCULATION:
An existence of a Hadley cell in the upper cloud layer became apparent after demonstration of the temperature fields in the mesosphere by Pioneer Venus [4] and Venera-15 [5]: the temperature vs latitude curve rises from the equator to the polar region above 65 km and decreases below this altitude level. The midlatitude jet attributed to Hadley circulation was also observed. Meridional wind speed data were obtained from VMC/VEx data [6,7]. Its direction indicates the motion of the horizontal flow towards the pole at the upper boundary of clouds, and backward to the equator deeper in the clouds, the so-called “direct Hadley cell”. Fragments of the direct Hadley cell (analogous to that in the upper clouds) were also found on the night side of Venus in the lower cloud layer from VIRTIS-M 1.74 μm data [8].

SURFACE INFLUENCE:
The other factor, which affects the dynamics of the mesosphere is a surface relief. At the “continental” highlands, such as Aphrodite Terra, orographic waves generated by the near-surface atmospheric flow influence the atmospheric flow in the equatorial latitudes of the southern hemisphere [9].

SOLAR CYCLES:
From the combined set of VMC/VEx and UVI/Akatsuki data the 12.3±0.5 yr. periodicity of the mean velocity of horizontal wind was revealed [10]. Note that this set of observations covers the 24th cycle of solar activity. As it was shown previously [11], the UV albedo of Venus decreases from solar minimum to solar maximum. From VMC data it was also found that the increase of the zonal wind speed at low latitudes runs parallel with the increase of the solar activity [10]. However, the ambiguity remains because in both sets of data near solar maximum the Aphrodite Terra was also observed. During VMC observations the altitude of upper boundary of the upper clouds increased by several kilometers between minimum and maximum of the solar cycle.

References:
[1] *Bougher S.W. and Borucki W.J.* Venus O_2 visible and IR nightglow: Implications for lower thermosphere dynamics and chemistry // Journal of Geophysical Research. 1994. V. 99. P. 3579.

[2] *Shakun A.V., Zasova L.V., Gorinov D.A. et al.* O_2 ($a^1\Delta_g$) Airglow at 1.27 μm and Upper Mesosphere Dynamics on the Night Side of Venus // Solar System Research. 2023. V. 57. I. 3. P. 200-213.
[3] *Zasova L.V., Ignatiev N., Khatuntsev I. et al.* Structure of the Venus atmosphere // Planetary and Space Science. 2007. V. 55. I. 12. P. 1712-1728.
[4] *Taylor F.W., Beer R., Chahine M.T. et al.* Structure and meteorology of the middle atmosphere of Venus Infrared remote sensing from the Pioneer orbiter // Journal of Geophysical Research. 1980. V. 85. P. 7963-8006.
[5] *Zasova L.V., Khatountsev I.A., Moroz V.I. et al.* Structure of the Venus middle atmosphere: Venera 15 fourier spectrometry data revisited // Advances in Space Research. 1999. V. 23. I. 9. P. 1559-1568.
[6] *Khatuntsev I.V., Patsaeva M.V., Titov D.V. et al.* Cloud level winds from the Venus Express Monitoring Camera imaging // Icarus. 2013. V. 226. I. 1. P. 140-158.
[7] *Khatuntsev I.V., Patsaeva M.V., Zasova L.V. et al.* Winds From the Visible (513 nm) Images Obtained by the Venus Monitoring Camera Onboard Venus Express // Journal of Geophysical Research. 2022. V. 127. I. 4. id. e07032.
[8] *Gorinov D.A., Zasova L.V., Khatuntsev I.V. et al.* Winds in the Lower Cloud Level on the Nightside of Venus from VIRTIS-M (Venus Express) 1.74 μm Images // Atmosphere. 2021. V. 12. I. 2. P. 186.
[9] *Bertaux J.-L., Khatuntsev I.V., Hauchecorne A. et al.* Influence of Venus topography on the zonal wind and UV albedo at cloud top level: The role of stationary gravity waves // Journal of Geophysical Research: Planets. 2016. V. 121. P. 1087–1101.
[10] *Khatuntsev I.V., Patsaeva M.V., Titov D.V. et al.* Twelve-Year Cycle in the Cloud Top Winds Derived from VMC/Venus Express and UVI/Akatsuki Imaging // Atmosphere. 2023. V. 13. I. 12. P. 2023.
[11] *Lee Y.J., Jessup K.-L., Perez-Hoyos, S. et al.* Long-term Variations of Venus's 365 nm Albedo Observed by Venus Express, Akatsuki, MESSENGER, and the Hubble Space Telescope // The Astronomical Journal. 2019. V. 158. I. 3. id. 126.

RETRIEVAL OF UPPER HAZE AEROSOL PROPERTIES AT VENUS FROM SPICAV–UV AND –IR DATA

M. Luginin[1], A. Fedorova[1], D. Belyaev[1], F. Montmessin[2], O. Korablev[1], J.-L. Bertaux[2]
[1] *Space Research Institute RAS, Moscow, Russia mikhail.luginin@phystech.edu*
[2] *Laboratoire Atmosphères, Milieux, Observations Spatiales Université de Versailles — Saint-Quentin-en-Yvelines (LATMOS UVSQ), Guyancourt, France*

KEYWORDS:
Infrared observations, atmosphere of Venus, solar occultation, upper haze

INTRODUCTION:

Venus is covered by a thick layer of clouds extending from 40 to 70 km with tenuous upper haze layer lying above. Particles at the cloud top are spherical and consist of sulfuric acid droplets [1]. Clouds are stratified into three layers, the upper cloud region is populated by mode 1 (~0.2 µm) and mode 2 (~1 µm) particles. Before Venus Express, the upper haze was believed to consist of only mode 1 [1].

Early independent study of three channels of SPICAV/SOIR instrument with data set from a few selected orbits showed presence of bimodality in size distribution [2]. Analysis of aerosol properties from single SPICAV−IR spectrometer for the whole data set obtained from May 2006 till November 2014 has proved it [3]. In this work, we report retrieval of upper haze aerosol properties from joint SPICAV−UV and –IR solar occultation observations for the whole data set.

OBSERVATIONS:

We analyzed spectra from 101 simultaneous solar occultation observations from SPICAV−UV and −IR instruments that were measured between March 2007 (orbit #339) and January 2013 (#2464). Aerosol properties are determined using 6 wavelengths in 200−300 nm range from SPICAV−UV and 10 wavelengths in 650−1550 nm range for SPICAV−IR.

METHOD OF ANALYSIS:

The first step in retrieval procedure is calculation of aerosol extinction. Inversion method for SPICAV−UV is identical to the one used for SO_2 abundance retrievals [4]. Aerosol extinction retrieval of SPICAV−IR data was described in [3].

The second step is retrieval of particle size distribution by fitting spectral dependence of experimental normalized aerosol extinctions to their corresponding theoretical values. The aerosol extinction is modeled according to Mie theory, adopting refractive indices for 75 % H_2SO_4 sulfuric acid aqueous solution. In our retrieval procedure unimodal and bimodal lognormal size distributions were considered independently.

The final step is to calculate aerosol number density as a ratio of experimental extinction coefficient to modeled extinction cross section.

RESULTS:

A joint analysis of the data from two spectrometers allowed us to characterize the size distribution ~10 km higher in the atmosphere compared to previous analysis and to detect bimodal distribution in ~50 % of observations previously believed to be unimodal. At altitudes 81−92 km, bimodality is observed in >50 % of cases. Mode 2 particles are detected up to 98 km and mode 1 up to 100 km. Mean radius equals 0.16±0.02 µm for mode 1 and 0.78±0.18 µm for mode 2. Number density profiles for both modes of particles exponentially decrease with altitude, starting from 50 cm^{-3} and 0.3 cm^{-3} at 82 km for mode 1 and mode 2, respectively, and reaching 3 cm^{-3} at 98 km for mode 1 and 0.03 cm^{-3} at 94 km for mode 2. Resulting mean profiles of effective radius and number density alongside the results from the [3] and [5] are shown in Fig. 1.

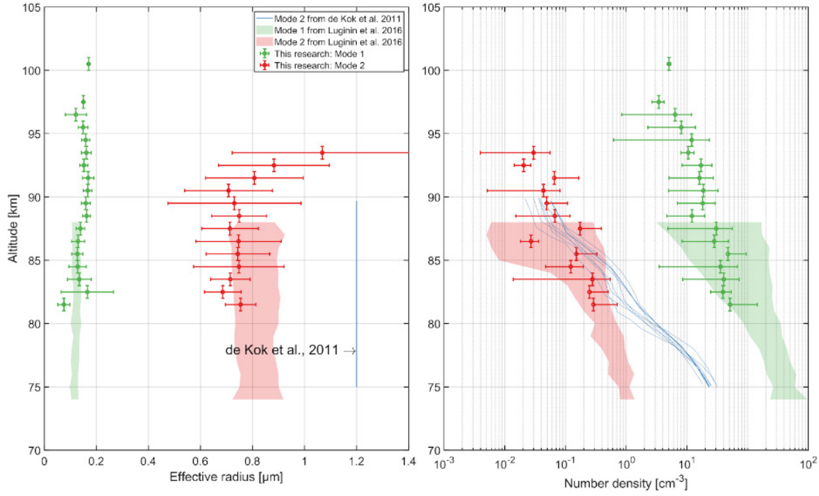

Fig. 1. Comparison of vertical profiles of effective radius (*left panel*) and number density (*right panel*) of mode 1 (green) and mode 2 (red) from this work (crosses), [3] (shaded area) and [5] (blue lines)

Acknowledgments:
This work has been funded by grant no. 23-12-00207 of the Russian Science Foundation.

References:

[1] *Esposito L.W., Knollenberg R.G., Marov M.Ia. et al.* 1983. The Clouds and Hazes on Venus // Venus (A83-37401 17-91). Tucson, AZ, Univ. Arizona Press, 1983. P. 484–564.
[2] *Wilquet V., Fedorova A., Montmessin F. et al.* Preliminary characterization of the upper haze by SPICAV/SOIR solar occultation in UV to mid-IR onboard Venus Express // J. Geophysical Research. 2009. V. 114. Iss. 12. Art. No. E00B42. DOI: 10.1029/2008JE003186.
[3] *Luginin* M., *Fedorova* A., *Belyaev* D. *et al.* Aerosol properties in the upper haze of Venus from SPICAV IR data // Icarus. 2016. V. 277. P. 154–170. https://doi.org/10.1016/j.icarus.2016.05.008.
[4] *Belyaev D.A., Evdokimova D.G., Montmessin F. et al.* Night side distribution of SO_2 content in Venus' upper mesosphere // Icarus. 2017. V. 294. P. 58–71. https://doi.org/10.1016/j.icarus.2017.05.002.
[5] *de Kok R., Irwin P.G.J., Tsang C.C.C. et al.* Scattering particles in nightside limb observations of Venus' upper atmosphere by Venus Express VIRTIS // Icarus. 2011. V. 211. Iss. 1. P. 51–57. https://doi.org/10.1016/j.icarus.2010.08.023.

VENUS LOWER CLOUD VARIATIONS BY SPICAV-IR/VEX NIGHT EMISSION OBSERVATIONS AND SUPPLEMENTED RADIATIVE TRANSFER MODEL

D.G. Evdokimova[1], A.A. Fedorova[1], M.S. Zharikova[1], O.I. Korablev[1], J.-L. Bertaux[2]

[1] *Space Research Institute RAS, Moscow, Russia, daria.evdokimova@cosmos.ru*

[2] *Laboratoire Atmosphères, Milieux, Observations Spatiales (LATMOS), CNRS, Sorbonne Université, Université de Versailles — Saint-Quentin-en-Yvelines (UVSQ), France*

KEYWORDS:
Venus, aerosol particles, water vapour, transparency windows

INTRODUCTION:

Venus clouds surrounding the planet with a thick layer at 46–70 km bounded by upper (>70 km) and lower (<46 km) haze are the largest aerosol system of all the terrestrial planets [1]. Cloud layer plays a great role in energy balance and, thus, current climate on Venus. The main component of the aerosol particles is an aqueous solution of sulphuric acid (75–90 %) [2]. Aerosol formation primarily occurs in the upper cloud layer, where SO_2 and H_2O transferred from the deep atmosphere recombine [1]. Variations in the cloud system can indicate changes in complex dynamics and coupling between the lower and upper atmosphere. Short- and long-term changes in the clouds have been noted previously [3–5].

In-situ experiments on board descent modules allowed us to identify four modes in the size distribution of aerosol particles: mode 1, 2, 2′ and 3 [2, 6]. Each is characterized by a modal radius: <0.4 μm for mode 1, 1.05 and 1.25 μm for modes 2 and 2′ respectively, 3–4 μm for mode 3. The size distribution dispersions are 1.56, 1.29, 1.23, 1.28 [2]. Depending on modes of the dominant aerosol particles, three cloud sub-layers can be specified [6]. The modes 1 and 2 constitute the upper cloud layer (50–70 km) and haze (>70 km). Aerosol particles of modes 2′ and 3 prevail in the middle and lower clouds (46–50 km) and the lower haze. The biggest aerosol particles of mode 3 determine the opacity and bulk of the Venus cloud layer [6].

SPICAV-IR/VENUS EXPRESS OBSERVATIONS:

Remote sensing of middle and lower cloud layers is obstructed by the aerosol opacity. Measurements of the surface and deep atmosphere thermal radiation, modulated by scattering in the clouds, are another way to study aerosol behaviour. However, a strong absorption by the dominant (96.5%) atmospheric constituent, carbon dioxide (CO_2), leaves only a few narrow spectral intervals in the near infrared, i.e., «transparency windows», where a part of the radiation can be observed remotely [2].

The IR channel of the SPICAV instrument on board the Venus Express spacecraft performed observations from the orbit around the planet in 2006–2014 with a high resolving power of ~1400 [7]. The spectral range covered five transparency windows at 1.0, 1.10, 1.18, 1.28, 1.31 μm [7] where thermal emission originated from the hot surface and the first-scale height of the atmosphere (0–20 km) [2]. The windows' intensity is defined by cloud optical properties, surface emissivity and H_2O absorption at 0.9–1.0 and 1.10–1.20 μm. The 1.28-μm window is contaminated by an oxygen airglow at 1.27 μm produced at 95 km [2].

MODELLING THE VENUS NIGHT SIDE EMISSION:

The SPICAV IR data is analysed using an updated approach to define Venus night-side emission spectra. Thermal radiance of the Venus surface and deep atmosphere is simulated by a multiple scattering radiative transfer model. The model is based on the SHDOMPP program implementing the spherical harmonic discrete ordinate method for plane-parallel geometry [8]. It was adjusted for the Venus observations [7, 9]. The vertical profiles of the atmospheric temperature, pressure and density are taken from the VIRA database [7]. CO_2, H_2O and HDO absorption parameters are taken from the «High-T» database, VTT and BT2 line lists [7]. Water vapour is assumed to have a constant volume mixing ratio, and the HDO/H_2O ratio is 127 times lower than the terrestrial value [7]. The aerosol particles are restricted to be spherical and the concentration of H_2SO_4 in the solution is set to 75 %. Optical depth, single scattering albedo and parameter of asymmetry are calculated according to the Mie theory based on the vertical number density profiles of aerosol modes by R. Haus et al. in 2016 [10]. Free parameters of the model are water vapour mixing ratio, cloud opacity and surface emissivity. The SPICAV IR spectrum simulation also includes modelling of the O_2 ($\alpha^1\Delta_g$) airglow. The airglow contribution is a spectrum computed line by line based on spectral line parameters from the HITRAN database [11].

RESULT:

The work presents an updated model to reproduce Venus night-side emission spectra in the 1.0–1.3 μm wavelength range. It includes a radiative transfer model and a line-by-line computation of the O_2 ($\alpha^1\Delta_g$) airglow overlapping the Venus thermal emission spectrum. This increases the accuracy of the 1.28-μm transparency window intensity retrieval, and the 1.28-μm transparency window is only modulated by changes in aerosol optical depth. Analysis of the full SPICAV IR dataset shows high variability in the lower clouds observed from 2006 to 2014.

Acknowledgements:

D.G. Evdokimova acknowledges a support from the grant Russian Science Foundation no. 23-72-01064.

References:

[1] *Titov D.V., Ignatiev N.I., McGouldrick* K. *et al.* Clouds and Hazes of Venus // Space Science Reviews. 2018. V. 214. No. 126. https://doi.org/10.1007/s11214-018-0552-z.

[2] *Pollack J.B., Dalton J.B., Grinspoon* D. *et al.* Near-infrared light from Venus' nightside: a spectroscopic analysis // Icarus. 1993. V. 103. Iss. 1. P. 1–42. DOI: 10.1006/icar.1993.1055.

[3] *McGouldrick K., Momary T.W., Baines K.H. et al.* Quantification of middle and lower cloud variability and mesoscale dynamics from Venus Express/VIRTIS observations at 1.74 μm // Icarus. 2011. V. 217. Iss. 2. P. 615–628. https://doi.org/10.1016/j.icarus.2011.07.009.

[4] *McGouldrick K., Toon O.B.* Investigation of possible causes of the holes in the condensational Venus cloud using a microphysical cloud model with radiative dynamical feedback // Icarus. 2007. V. 191. Iss. 1. P. 1–24. DOI: 10.1016/j.icarus.2007.04.007.

[5] *McGouldrick K., Toon O.B.* Modeling the effects of shear on the evolution of the holes in the condensational clouds of Venus // Icarus. 2008. V. 196. Iss. 1. P. 35–48. DOI: 10.1016/j.icarus.2008.02.020.

[6] *Esposito L.W., Bertaux J.-L., Krasnopolsky V.A. et al.* Chemistry of lower atmosphere and clouds. Venus II. Tucson, Arizona: The Univ. Arizona Press, 1997. P. 415–458.

[7] *Fedorova A., Bézard B., Bertaux J.-L. et al.* The CO_2 continuum absorption in the 1.10- and 1.18-μm windows on Venus from Maxwell Montes transits by SPICAV IR onboard Venus express // Planetary and Space Science. 2015. V. 113–114. P. 66–77. https://doi.org/10.1016/j.pss.2014.08.010.

[9] *Bézard B., Fedorova A., Bertaux J.-L. et al.* The 1.10- and 1.18-lm nightside windows of Venus observed by SPICAV-IR aboard Venus Express // Icarus. 2011. V. 216. Iss. 1. P. 173–183. DOI:10.1016/j.icarus.2011.08.025.

[8] Evans K.F. The spherical harmonic discrete ordinate method for three-dimensional atmospheric radiative transfer // J. Atmospheric Sciences. 1998. V. 55. P. 429–446. https://doi.org/10.1175/1520-0469(1998)055<0429:TSHDOM>2.0.CO;2.

[10] *Haus R., Kappel* D., *Tellmann* S. *et al.* Radiative energy balance of Venus based on improved models of the middle and lower atmosphere // Icarus. 2016. V. 272. P. 178–205. https://doi.org/10.1016/j.icarus.2016.02.048.

[11] *Bertaux J.-L., Hauchecorne A, Lefèvre F. et al.* The use of the 1.27 μm O_2 absorption band for greenhouse gas monitoring from space and application to MicroCarb // Atmospheric Measurement Techniques. 2020. V. 13. P. 3329–3374. https://doi.org/10.5194/amt-13-3329-2020.

RETRIEVING MICROPHYSICS OF AEROSOLS IN THE ATMOSPHERE OF VENUS USING THE GLORY PHENOMENON

E. Zubko, Y.J. Lee
Planetary Atmospheres Group, Institute for Basic Science (IBS), Daejeon, South Korea, zubko@ibs.re.kr

KEYWORDS:
Venus, atmosphere, phenomenon of glory, aerosols, modeling, Mie theory, retrieval, microphysics

INTRODUCTION:

Venus reveals phenomenon of the *glory* near opposition. On the phase function of the scattered light intensity $p(\alpha)$, this phenomenon appears in a form of surge at the phase angles $\alpha < 10°$ (e.g., [1]). While its origin is barely understood yet, all existing explanations refer to particles whose radius r significantly exceeds the wavelength of incident radiation λ, $r >> \lambda$ (e.g., [2]), so the geometric-optics concept to hold true. On the other hand, the currently existing models of the glory in the Venusian atmosphere all assume that the aerosol radius spans the range up to less than several micrometers (e.g., [3]). Nevertheless, the glory phenomenon provides important clues for better understanding microphysics of the aerosol particles (e.g., [4]). We investigate impact of three parameters characterizing a differential power-law size distribution r^{-n} of the aerosol particles, its bottom limit r_{min}, upper limit r_{max}, and the index n, on appearance of the glory.

MODELING:

We model shape of an aerosol particle with a perfect sphere and compute its light-scattering response using our own implementation of the Mie theory. Light scattering by a sphere is governed by ratio of its radius r to wavelength λ that is often quantified in terms of the *size parameter* $x = 2\pi r/\lambda$. Another important characteristic of a scatterer is the complex refractive index m, whose real and imaginary parts quantify refraction and absorption of the incident electromagnetic wave within constituent-material volume. We investigate sulfuric-acid composition of the aerosol particles. The modelign was conducted at $\lambda = 0.365$ µm, where its complex refractive index is $m = 1.47 + 0i$ (e.g., [3] and references therein). Radius of the sulfuric-acid particles r was ranging from 0.01 µm up to 7.5 µm, with the increment $\Delta r = 0.01$ µm.

RESULTS AND DISCUSSION:

We first investigate effect of the bottom limit in size distribution r_{min}, considering $r_{min} = 0.01$ µm, 0.1 µm and 1 µm; whereas, the upper limit was set to $r_{max} = 5$ µm. The power index was varying from $n = 1$ to 4 with step of 0.1. We found that the light-scattering responses obtained at $r_{min} = 0.01$ µm and 0.1 µm appear to be virtually the same. Interestingly, the same effect also was found for irregularly shaped particles [5]. Thus, r_{min} does not affect the light-scattering response when it is sufficiently small, $r_{min} < 0.1$ µm. However, value of r_{min} still has an impact on the *effective radius* r_{eff} and the *effective variance* ν_{eff}, two characteristics of a polydisperse system of particles introduced in [6] and currently used in various atmospheric applications (e.g., [3, 4]). It clearly reveals ambiguity of characteristics r_{eff} and ν_{eff}.

While $r_{min} = 1$ µm considerably changes amplitude of the glory compared to what emerges at $r_{min} = 0.01$ µm and 0.1 µm, it hardly affects its location on the phase function. Furthermore, a significant change in the power index n, from 1 to 4, only slightly shifts the glory along the phase function (±1°). As a consequence, at given m, position of the glory is almost solely governed by the upper limit of size distribution r_{max}. We find that $r_{max} \approx 2$ µm yields the best fit to position of the glory observed in Venus at $\lambda = 0.365$ µm.

Figure 1 demonstrates the phase function $p(\alpha)$ computed for the sulfuric-acid spheres with radius ranging from $r = 0.01$ µm up to 2.01 µm. Three curves here present results obtained at different values of the power index n = 1.8, 2, and 2.2. It is worth noting that these size distributions quantitatively reproduce the Pioneer-Venus findings in the Venusian atmosphere [7]. The corresponding values of r_{eff} and ν_{eff} are given in the legend and they indeed match what was inferred *in situ* [7]. The curves in Fig. 1 do reproduce location of the glory on the phase function of Venus (e.g., [1]). However, oscillations on the phase functions shown in Figure 1 exceed what is observed in Venus. Such a discrepancy is fully expected because our modeling does not take into account multiple scattering among the aerosol particles yet. It is a subject for further research.

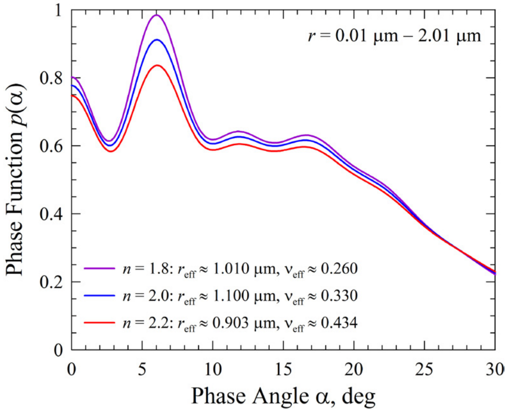

Fig. 1. Phase function $p(\alpha)$ of poly disperse particle systems of the sulfuric-acid sphere simulated at λ = 0.365 μm using the Mie theory

References:

[1] *Lee Y.J., Yamazaki A., Imamura T. et al.* Scattering properties of the Venusian clouds observed by the UV imager on board Akatsuki // Astronomical J. 2017. V. 154. No. 2. Art. No. 44. DOI 10.3847/1538-3881/aa78a5.

[2] *Adam J.A.* The mathematical physics of rainbows and glories // Physics Reports. 2002. V. 356. Iss. 4. P. 229–365. DOI:10.1016/S0370-1573(01)00076-X.

[3] *Petrova E.V.* Glory on Venus and selection among the unknown UV absorbers // Icarus. 2018. V. 306. P. 163–170. https://doi.org/10.1016/j.icarus.2018.02.016.

[4] *Markiewicz W.J., Petrova E., Shalygina O. et al.* Glory on Venus cloud tops and the unknown UV absorber // Icarus. 2014. V. 234. P. 200–203. https://doi.org/10.1016/j.icarus.2014.01.030.

[5] *Zubko E., Videen G., Arnold J.A. et al.* On the small contribution of supermicron dust particles to light scattering by comets // Astrophysical J. 2020. V. 895. Iss. 2. Art. No. 110. 9. p. DOI: 10.3847/1538-4357/ab8ae4.

[6] *Hansen J.E., Hovenier J.W.* Interpretation of the polarization of Venus // J. Atmospheric Sciences. 1974. V. 31. P. 1137–1160. https://doi.org/10.1175/1520-0469(1974)031<1137:IOTPOV>2.0.CO;2.

[7] *Knollenberg R.G., Hunten D.M.* The microphysics of the clouds of Venus: Results of the Pioneer Venus particle size spectrometer experiment // J. Geophysical Research. 1980. V. 85. Iss. A13. P. 8039–8058. https://doi.org/10.1029/JA085iA13p08039.

MORPHOLOGICAL AND TOPOGRAPHICAL GROUPS OF LARGE VOLCANOES ON VENUS

M.A. Ivanov[1], J.W. Head[2]
[1] *Vernadsky Institute of Geochemistry and Analytical Chemistry RAS, Moscow, Russia, mikhail_ivanov@brown.edu*
[2] *Brown University, Providence RI, USA, James_Head@brown.edu*

KEYWORDS:
Venus, large volcanoes, volcanism principal component analysis, discriminant function analysis

INTRODUCTION:

Large volcanoes (basal diameter exceeds ~100 km [1]) are important components of the volcanic evolution of Venus [2–3]. They show a variety of shapes that likely reflect a variety of processes responsible for the volcano formation and evolution. Can the volcanoes be classified in distinct groups according to their gross shape? Or do they form a sequence that is continuous and gradational morphologically and topographically? The presence of gradual changes would suggest that the processes/environments that controlled the volcano formation changed systematically as a function of size and that the entire population of the volcanoes represent a single class of features that different from the other volcanic landforms. In contrast, the existence of distinct groups within the population of the volcanoes would suggest that specific combinations of processes/environments governed growth of the large volcanoes.

DATA AND METHODS:

In our study, we used a revised catalogue of the large volcanoes [1], the SAR F-MIDR images (75 m/px resolution), and available topographic data (the Magellan gridded topography, ~5 km/px resolution) to collect various morphological and topographical characteristics of the volcanoes. We used these characteristics to test the morphological continuity of the volcano population with the help of multidimensional methods such as principal component (PCA) and discriminant function (DF) analyses.

RESULTS/DISCUSSION:

The independent input parameters for the multidimensional methods were as follows: edifice diameter (D), background elevation (Be), mean elevation of the summit area, and diameter of the summit caldera (caldera complex, C). The last parameter is a diameter of a circle the area of which is equal to the caldera area.

At the first step, we applied a PCA that does not require preliminary grouping (Fig. 1*a*). The areal distribution of points in the Factor1/Factor2 plane suggests the existence of two groups of volcanoes.

To test if these groups are stable clusters of features, we applied the DF analysis using the groups defined by the PCA (Fig. 1*b*). The components of both groups defined by the PCA were correctly classified by the DF procedure. Thus, exactly the same results produced by two different and independent methods of multidimensional analysis suggest that there are indeed two different morphological and topographical groups of large volcanoes (Fig. 2).The first group (G1) consists of volcanoes that have much larger basal diameter (~500 km) and a very large summit area, about 140 km across. These volcanoes are relatively low (~1.2 km high) and have a low aspect ratio ((h/D)×1000 = ~2.6). The summit area of the G1-volcanoes typically has a large caldera (caldera complex) the mean diameter of which is 4-5 times larger than that of the G2-volcanoes. The G1 calderas appear as broad and apparently shallow depressions surrounded by concentric zones of grooves and, thus resemble coronae (Fig. 3*a*). The G2-volcanoes (see Fig. 2) are somewhat smaller, have much smaller summit area, and a significantly larger aspect ratio (~6–7). The summit calderas of these volcanoes are preferentially of either trapdoor or piston-like types (do you have a reference for the different caldera types to put here?). The size-frequency distribution of the G2-volcanoes shows a prominent break of slope at ~200 km, which suggests that there are two subpopulation of features within Group 2 (see Fig. 2): the larger (G2 large, Fig. 3*b*) and smaller (G2 small, Fig. 3*c*) volcanoes.

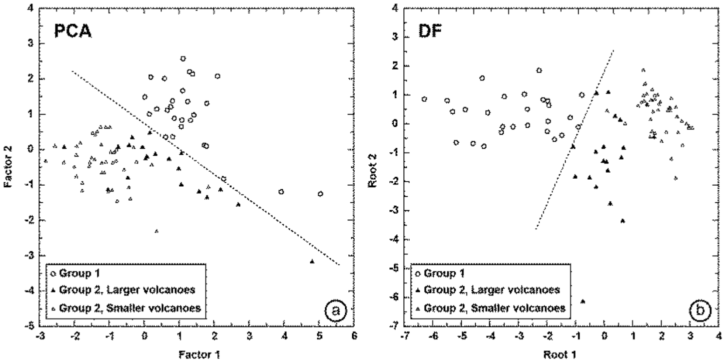

Fig. 1. Results of the principal component (PCA) and discriminant function (DF) analyses of parameters characterizing the gross shape of large volcanoes on Venus

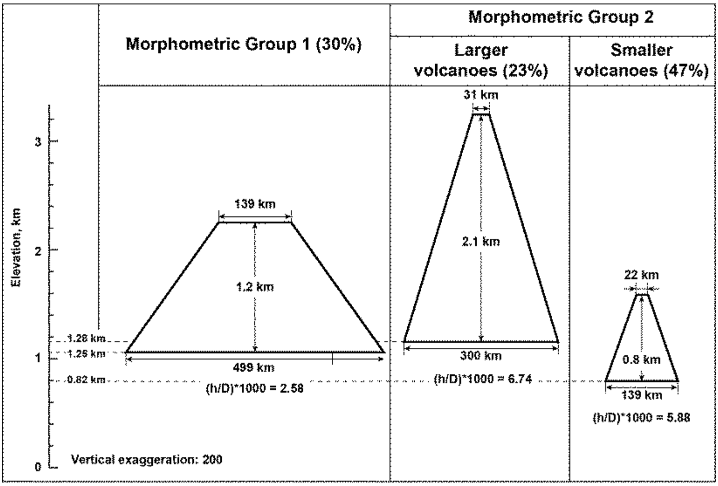

Fig. 2. Generalized shape of different morphological and topographical groups of large volcanoes

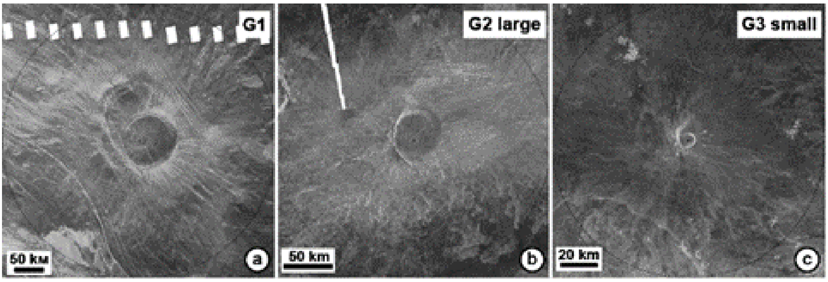

Fig. 3. Typical examples of large volcanoes from the different morphological and topographical groups

CONCLUSIONS:

The multidimensional analyses of four independent and important parameters that characterize the gross shape of the large volcanoes reveal that the volcanoes form two distinct groups of features (see Fig. 1). These groups contradict to the first formulated hypothesis about the existence of continuous morphological and topographical sequences of the volcanoes. In contrast, the alternative hypothesis about the existence of discrete groups of large volcanoes is supported by the analyses. Thus, it is likely that specific combinations of internal magmatic processes and external environments have governed growth of the large volcanoes on Venus. Currently, we are assessing the stratigraphic and areal distributions of the large volcanoes from different groups. Because the G1 and G2 volcanoes appear to occur in broadly the same regions, the conditions that caused formation of different groups of volcanoes should occur rather at local scale and likely are related to characteristics of the magmatic plumbing systems of each large volcano and potentially the size, age and depth of the magma source region.

References:

[1] *Crumpler L.S., Aubele J.* Volcanism on Venus // Encyclopedia of Volcanoes / eds. Sigurdsson H., Houghton B., McNutt S.R. et al. Academic Press: 2000. 1111 p. P. 727–770. https://handwiki.org/wiki/Astronomy:Volcanology_of_Venus.
[2] *Ivanov M.A., Head J.W.* Global geological map of Venus // Planetary and Space Science. 2011 V. 59. Iss. 13. P. 1559–1600. https://doi.org/10.1016/j.pss.2011.07.008.
[3] *Ivanov M.A., Head J.W.* The history of volcanism on Venus // Planetary and Space Science. 2013 V. 84. P. 66–92. https://doi.org/10.1016/j.pss.2013.04.018.

INTRODUCING THE "ANALOGS FOR VENUS' GEOLOGICALLY RECENT SURFACES" INITIATIVE: AN OPPORTUNITY FOR IDENTIFYING AND ANALYZING RECENTLY ACTIVE VOLCANO-TECTONIC AREAS OF VENUS TROUGH A COMPARATIVE STUDY WITH TERRESTRIAL ANALOGS

P. D'Incecco[1], J. Filiberto[2], J.B. Garvin[3], G.N. Arney[3], S.A. Getty[3], I. López[4], R. Ghail[5], P. Mason[6], L. M. Zelenyi[7], L.V. Zasova[7], M.A. Ivanov[8], D.A. Gorinov[7], J. Brossier[9], S. Bhattacharya[10], S.S. Bhiravarasu[10], D. Putrevu[10], C. Monaco[11,12], S. Branca[12], D. Trang[13], J.R. Crandall[14], S. Aveni[15], G.L. Eggers[16], N. Mari[17], M. Blackett[18], G. Komatsu[19], A. Kosenkova[20], G. Di Achille[1]

[1] *National Institute for Astrophysics – Astronomical Observatory of Abruzzo, Teramo, Italy, piero.dincecco@inaf.it*
[2] *Astromaterials Research and Exploration Science Division, NASA Johnson Space Center, Houston, TX, 77058, USA*
[3] *NASA Goddard Space Flight Center, Greenbelt, USA*
[4] *Departamento de Biología, Geología, Física y Química Inorgánica. Universidad Rey Juan Carlos, Madrid, Spain*
[5] *Earth Sciences, Royal Holloway, University of London, Egham, United Kingdom*
[6] *Department of Earth Science and Engineering, Imperial College London, Prince Consort Road, London, United Kingdom*
[7] *Space Research Institute RAS, Moscow, Russia*
[8] *Vernadsky Institute of Geochemistry and Analytical Chemistry RAS, Moscow, Russia*
[9] *National Institute for Astrophysics – Institute for Space Astrophysics and Planetology, Rome, Italy*
[10] *Space Applications Centre, Indian Space Research Organization, Ahmedabad, India*
[11] *Dipartimento di Scienze Biologiche Geologiche e Ambientali, Università di Catania, Catania, Italy*
[12] *Istituto Nazionale di Geofisica e Vulcanologia, Osservatorio Etneo — Sezione di Catania, Italy*
[13] *Hawai'i Institute of Geophysics and Planetology, University of Hawai'i at Mānoa, Honolulu, USA; Space Science Institute, Boulder, USA*
[14] *Eastern Illinois University, Department of Geology and Geography, Charleston, IL, USA*
[15] *Department of Civil, Constructional and Environmental Engineering, Sapienza University of Rome, Italy*
[16] *Lunar and Planetary Institute, USRA, Houston, TX, USA*
[17] *Department of Earth and Environmental Sciences, University of Pavia, Pavia, Italy*
[18] *Centre for Agroecology, Water and Resilience, Coventry University, United Kingdom*
[19] *Università G. d'Annunzio, Pescara, Italy*
[20] *Bauman Moscow State Technical University, Moscow, Russia*

KEYWORDS:
Venus, Earth, volcanism, analogues, geology, missions, radar interferometry

INTRODUCTION:

Several missions to Venus have been recently selected for launch [1–6], opening a new era for the exploration of the planet. One of the key questions that the future missions need to address is whether Venus is presently volcanically active [7–15]. Studying areas of active volcanism and tectonism on Venus is crucial to reveal clues about the geologic past of the planet, as well as provide information about the volatile content of its interior and the formation of its dense atmosphere. The "Analogs for VENus' GEologically Recent Surfaces" (AVENGERS) initiative aims to build a comprehensive database of terrestrial analog sites for the comparative study of recent and possibly ongoing volcanic activity on Venus. Besides its scientific relevance, the AVENGERS initiative also acts as a bridge for international scientific collaboration, including the leadership and/or team members from the currently selected missions to Venus.

MAIN OBJECTIVES OF THE AVENGERS INITIATIVE:

COMPARATIVE STUDY THROUGH GEOLOGIC MAPPING AND STRATIGRAPHIC RECONSTRUCTION AT REGIONAL LEVEL OF THE SELECTED VOLCANIC STRUCTURES:

Using GIS tools, we are performing morpho-structural mapping and topographic analysis of the selected volcanic structures both on Earth and on Venus. For the geologic interpretation and mapping, we are using radar images of both terrestrial and Venusian volcanoes.

DATING VENUSIAN VOLCANIC ACTIVITY USING ALTERATION OF TERRESTRIAL ANALOG SITES:

Orbital spectroscopy of weathered versus fresh lava flows, specifically the 1-micron absorption band in nighttime emissivity, has been suggested as a tool for age dating lava flows [refs]. Therefore, several lava flow samples of different age, texture, and alteration state have been and will be retrieved during the field trips on easily accessible volcanic structures, such as Mount Etna or Kīlauea. The retrieved samples from Mount Etna are currently being analyzed with the infrared spectrometer of the laboratories at the Lunar and Planetary Institute (TX, USA) (Eggers et al.).

RADIOMETRIC PROPERTIES AND INTERFEROMETRY (CHANGE DETECTION) ANALYSIS ON ACTIVE VOLCANOES ON EARTH AND ON VENUS:

The analysis of the radiometric properties (i.e., radar emissivity, dielectric constant) can also inform about composition and relative age of volcanic surface deposits [11–13]. For this reason, we will use variations in radar emissivity on active volcanoes on Earth as a further parameter to identify areas of possibly ongoing volcanism on Venus.

CRITERIA OF SELECTION OF THE AVENGERS INITIATIVE:

In the project, three main criteria of selection will be considered: a) Sites of ongoing volcanic activity on Earth, b) Ease of access, and c) Applicability of bulk composition.

ANALOG SITES ON EARTH FOR THE IDENTIFICATION AND STUDY OF RECENT VOLCANO-TECTONIC ACTIVITY ON VENUS:

At the present state, we selected four active volcanoes on Earth that may represent suitable "end-member" analogs for covering a good part of the spectrum of possible types of active volcanism and volcanic products on Venus that may be identified with the new datasets from the future missions.

MOUNT ETNA: A SUITABLE ANALOGUE FOR ITS VARIETY OF VOLCANIC PRODUCTS AND ITS EASE OF ACCESS:

Mount Etna (37°30′ to 37°55′ N, 14°47′ to 15°15′ E) located in Sicily, Italy is the largest and most active volcano in Europe (i.e., [18–19]). It is a composite volcano characterized by multiple phases of effusive and explosive volcanism (i.e., [18–19]). For these reasons, Mount Etna offers the unique opportunity to study at the same time a wider range of possible eruptive styles. Given its ease of access, Mount Etna also represents a suitable landing site analog area for the preparation of the drilling operations and in-situ elemental analyses to be performed by future Venus's landers.

KĪLAUEA: A SUITABLE TERRESTRIAL END-MEMBER FOR THE STUDY HOTSPOT-LIKE VOLCANISM ON VENUS:

Kīlauea (19° N, 155° W, Figure 1) located in Hawai'i, USA, is an active shield volcano fed by a magma reservoir arriving up to 60 km depth. Kīlauea is an example of terrestrial hotspot volcanism, thus not related to the interaction between the tectonic plates. The hotspot style of volcanism has been fre-

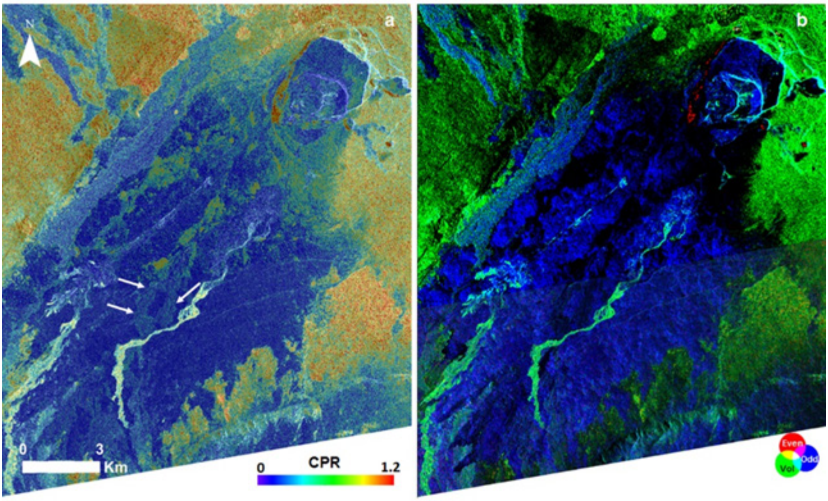

Fig. 1. Kīlauea region shown here in a) circular polarization Ratio (CPR) and b) NNED images. These polarimetric products are generated from RISAT-1A C-band SAR data at a resolution of 7 m/pixel. The CPR image is stretched to a colour scale and overlaid on HV-pol data and the colour wheel in the decomposition image *(*b) highlights the colours for each scattering regime (red: even bounce; blue: single (odd) bounce; green: volume/diffuse scattering). Notice the December 1974 pāhoehoe flows (indicated with arrows in (a)) that have a CPR contrast with the background and are not readily visible from other polarization images

quently used to describe volcanism on Venus, since this planet does not show clear evidence of Earth-like plate tectonics. For this reason, active hotspot volcanoes, such as Kīlauea, can be used as a suitable terrestrial analog for identifying active volcanism on Venus. Moreover, Kīlauea is also easily accessible, so that it is possible to retrieve lava flow samples for laboratory analyses.

EAST AFRICAN RIFT SYSTEM AS A SUITABLE ANALOG FOR VOLCANO-RIFT SYSTEMS ON VENUS:
Another suitable area is represented by the East African Rift System (EARS) (10° N, 40° E, Figure 7), an active rift zone located in East Africa with multiple volcanoes that could be potential analogues. The EARS is a divergent plate boundary, where the African plate is being split into two parts. Given its structural frame, the EARS can help us to better study the mechanism behind the formation of the volcano-rift systems, which can be considered among the most recently active areas on Venus.

MOUNT MERAPI: AN OPPORTUNITY FOR STUDYING PLUME-INDUCED "CRUSTAL-RECYCLING" VOLCANISM ON VENUS:
Mount Merapi (7° S, 110° E) in Indonesia is also a terrestrial analog site that we intend to investigate. It is the most active stratovolcano of Indonesia, and it is the youngest of a group of volcanoes situated in southern Java. It is located at the "subduction zone" where the Indo-Australian plate is subducting under the Sunda plate. Despite Venus the lack of evidence of Earth-like plate tectonics today, some spatially limited plume-induced crustal recycling activity cannot be excluded on Venus [20]. For this reason, it is also important to analyze an active subduction zone explosive volcano like Mount Merapi.

References:
[1] *Garvin J.B., Getty S.A., Arney G.N. et al.* Revealing the Mysteries of Venus: The DAVINCI Mission // Planetary Science J. 2022. V. 3. No. 5. Art. No. 117. 11 p. DOI: 10.3847/PSJ/ac63c2.
[2] *Ghail* R. *et al.* EnVision Assessment Study Report (Yellow Book). 2021. 109 p.
[3] *Smrekar* S., *Dyar* D., *Helbert* J. *et al.* VERITAS (Venus Emissivity, Radio Science, InSAR, Topography And Spectroscopy): A Proposed Discovery Mission // Europlanet Science Congress 2020. Virtual meeting. 21 Sept. – 9 Oct. 2020. Art. No. EPSC2020-447.

[4] *Senske D., Zasova L., Economou T. et al.* The Venera-D Mission Concept, Report on the Activities of the Joint Science Definition Team // 15th Meeting of the Venus Exploration and Analysis Group (VEXAG). 14–16 Nov., 2017, Laurel, Maryland. LPI Contribution No. 2061. 2017. Art. No. 8014.

[5] *Zasova L.V., Gorinov* D.A., *Eismont N.A. et al.* Venera-D: A Design of an Automatic Space Station for Venus Exploration// Solar System Research. 2019. V. 53. 506–510. https://doi.org/10.1134/S0038094619070244.

[6] *Sundararajan V.* Tradespace Exploration of Space System Architecture and Design for India’s Shukrayaan-1, Venus Orbiter Mission // ASCEND 2021. Nov. 15–17, 2021, Las Vegas, Nevada. 2021. Art. No. AIAA 2021-4103. https://doi.org/10.2514/6.2021-4103.

[7] *Smrekar S.E., Stofan E.R., Mueller N. et al.* Recent hotspot volcanism on Venus from VIRTIS emissivity data // Science. 2010. V. 328. Iss. 5978. P. 605–608. DOI: 10.1126/science.1186785

[8] *D’Incecco P., Müller N., Helbert* J., *D’Amore* M. Idunn Mons on Venus: Location and extent of recently active lava flows // Planetary and Space Science. 2017. V. 136. 25–33. https://doi.org/10.1016/j.pss.2016.12.002.

[9] *Filiberto J., Trang D., Treiman* A.H., Gilmore M.S. Present-day volcanism on Venus as evidenced from weathering rates of olivine // Science Advances. 2020. V. 6. Iss. 1. Art. No. eaax7445. DOI: 10.1126/sciadv.aax7445.

[10] *D’Incecco P., Filiberto J., López* I. *et al.* Idunn Mons: Evidence for Ongoing Volcano-tectonic Activity and Atmospheric Implications on Venus // Planetary Science J. 2021. V. 2. Iss. 5. Art. No. 215. DOI 10.3847/PSJ/ac2258.

[11] *Brossier J., Gilmore M.S., Head J.W.* Extended rift-associated volcanism in Ganis Chasma, Venus detected from Magellan radar emissivity // Geophysical Research Letters. 2022. V. 49. Iss. 15. Art. No. e2022GL099765. https://doi.org/10.1029/2022GL099765.

[12] *Brossier J., Gilmore M.S., Toner K., Stein A.J.* Distinct Mineralogy and Age of Individual Lava Flows in Atla Regio, Venus Derived from Magellan Radar Emissivity // J. Geophysical Research: Planets. 2021. V. 126. Iss. 3. Art. No. e2020JE006722. https://doi.org/10.1029/2020JE006722.

[13] *Brossier J.F., Gilmore M.S., Toner K.* Low radar emissivity signatures on Venus volcanoes and coronae: New insights on relative composition and age // Icarus. 2020. V. 343. Art. No. 113693. https://doi.org/10.1016/j.icarus.2020.113693.

[14] *López I., D’Incecco* P., Filiberto J., Komatsu G. The volcanology of Idunn Mons, Venus: The complex evolution of a possible active volcano // J. Volcanology and Geothermal Research. 2022. V. 421. https://doi.org/10.1016/j.jvolgeores.2021.107428.

[15] *Herrick R.R., Hensley S.* Surface changes observed on a Venusian volcano during the Magellan mission // Science. 2023. V. 379(6638). P. 1205–1208. DOI: 10.1126/science.abm7735.

[16] *Cutler K.S., Filiberto J., Treiman* A.H., Trang D. Experimental Investigation of Oxidation of Pyroxene and Basalt: Implications for Spectroscopic Analyses of the Surface of Venus and the Ages of Lava Flows // Planetary Science J. 2020. V. 1. Iss. 1. Art. No. 21. 10 p. DOI 10.3847/PSJ/ab8faf.

[17] *Teffeteller H., Filiberto J., McCanta M.C. et al.* An experimental study of the alteration of basalt on the surface of Venus // Icarus. 2022. V. 384. Art. No. 115085. https://doi.org/10.1016/j.icarus.2022.115085.

[18] *Branca S., Coltelli M., Groppelli G.* Geological map of Etna volcano, 1:50,000 scale // Italian J. Geosciences. 2011. V. 130. Iss. 3. P. 265–291. DOI: https://doi.org/10.3301/IJG.2011.15.

[19] *Branca S., Coltelli M., Groppelli G.* Geological evolution of a complex basaltic stratovolcano: Mount Etna // Italian J. Geosciences. 2011. V. 130. Iss. 3. P. 306–317. https://doi.org/10.3301/IJG.2011.13.

[20] *Davaille A., Smrekar* S.E., Tomlinson S. Experimental and observational evidence for plume-induced subduction on Venus // Nature Geoscience. 2017. V. 10. P. 349–355. https://doi.org/10.1038/ngeo2928.

SCIENTIFIC CONCEPT OF VOLNA EXPERIMENT TO STUDY SPECTROSCOPY OF VENUS ATMOSPHERE

A. Belyaev, Yu.S. Dobrolenskiy, N.I. Ignatiev, D.G. Evdokimova , I.A. Dzuban, N.A. Viazovatskiy, O.I. Korablev
Space Research Institute (IKI), Moscow, Russia, dbelyaev@cosmos.ru

KEYWORDS:
Venus atmosphere, spectroscopy, UV absorbers, solar occultation, albedo of clouds.

VOLNA - Venus Occultation, Limb and Nadir Analysis - is a spectrometer proposed for the orbital module of the Roskosmos “Venera-D” mission. The instrument will operate in the ultraviolet (UV) and visible wavelength range, from 190 to 490 nm, with spectral resolution of 0.2 nm. The observation modes include solar occultations, to analyse vertical structure of the upper atmosphere, and nadir soundings, to study spectral albedo of Venus clouds and to measure the column density of atmospheric species. The field of view and optics of the instrument will allow for imaging of spatial distribution and variations of the retrieved components.

In the present paper we discuss scientific potential of the VOLNA spectrometer, that is up to date to study the composition, structure and dynamics of Venus clouds and the upper atmosphere in the UV-visible wavelength range. Here, we highlight the following aspects: 1) search for components as candidates into the “unknown” UV-absorber in the clouds from the measured spectral albedo 2) the day-side mapping of SO_2, SO and O_3 content (plus detection of OCS and OSSO) and their correlation with the “unknown” UV-absorber; 3) vertical profiling of SO_2, SO and O_3 content at altitudes from 80 to 110 km from solar occultation measurements; 4) characterization of molecular limb glows from NO, CO, and O_2. 5) study of the atmospheric dynamics from the UV imaging. Sensitivity of the proposed measurements is analysed as well, comparing with previous analogous experiments.

SONET SCIENTIFIC EQUIPMENT FOR THE VENERA-D PROJECT

P.A. Klimov[1], A.A. Belov[1,2], A.S. Murashov[1], D.V. Chernov[1]
[1] *Skobeltsyn Institute of Nuclear Physics Lomonosov Moscow State University, Moscow, Russia, pavelklimov@eas.sinp.msu.ru;*
[2] *Lomonosov Moscow State University, Faculty of Physics, Moscow, Russia*

KEYWORDS:
Venus lightning, transient luminous events, SiPM, imaging photometer

Observations of potential lightning flashes on Venus have been undertaken for more than 40 years using optical and radio wave instruments, both on spacecraft and by ground-based telescopes [1—3]. However, there is no definitive answer about the existence of lightning on this planet yet. The main reason for the uncertainty is the problem with distinguishing natural lightning patterns from transient noise caused by other sources in the measuring equipment [4]. But the conditions for the lightning discharges exist. Despite the density of the atmosphere and the difficulty of detecting an optical signal, the possibility of such measurements must be used to study and understand the complex of processes occurring on Venus. One of the promising channels of information about processes in the low atmosphere are the so-called transient luminous events (TLEs) — the optical response of the upper atmosphere to powerful electromagnetic discharges in clouds and below them [5]. These phenomena occur high up and are not shielded by dense cloud cover.

For this reason, the SONET telescope (System for Observation of Energetic Transients) was proposed as part of the scientific equipment of the Venera-D project. The detector is an imaging photometer (telescope) capable to perform spectral measurements in various emission lines of nitrogen, oxygen, and carbon dioxide. The photodetector is a matrix of highly sensitive silicon photomultipliers operating in the photon counting mode, and the optical system is represented by a compact and thin Fresnel lens. The time resolution of the instrument is 1 µs. The combination of measuring the space-time pattern and the emission spectrum makes it possible not only to detect optical flashes, but also to distinguish their type. The report presents the scientific goals and objectives, as well as the composition of the SONET equipment.

References:

[1] *Krasnopolsky V.A.* Lightnings and nitric oxide on Venus // Planetary and Space Science. 1983. V. 31. Iss. 11. P. 1363–1369. https://doi.org/10.1016/0032-0633(83)90072-7.
[2] *Hansell S.A., Wells W.K., Hunten D.M.* Optical detection of lightning on Venus // Icarus. 1995. V. 117. Iss. 2. P. 345–351. https://doi.org/10.1006/icar.1995.1160.
[3] *Takahashi Y., Sato M., Imai M. et al.* Initiation of a lightning search using the lightning and airglow camera onboard the Venus orbiter Akatsuki // Earth, Planets and Space. 2018. V. 70. No. 1. Art. No. 88. https://doi.org/10.1186/s40623-018-0836-2.
[4] *Lorenz R.D.* Lightning detection on Venus: a critical review // Progress in Earth and Planetary Science. 2018. V. P. No. 1. Art. No. 34. https://doi.org/10.1186/s40645-018-0181-x.
[5] *Yair Y., Takahashi Y., Yaniv* R. *et al.* A study of the possibility of sprites in the atmospheres of other planets // J. Geophysical Research: Planets. 2009. V. 114. Iss. E9. Art. No. 09002. https://doi.org/10.1029/2008JE003311.

THE CAMPO IMPERATORE ADVANCED VENUS' NIGHT AIRGLOWS NEAR-INFRARED TELESCOPE (ADVENANT) PROJECT AS A GROUND-BASED SEGMENT FOR FUTURE MISSIONS TO VENUS

P. D'Incecco[1], D.A. Gorinov[2], M. Dolci[1], L. Tartaglia[1], F. De Luise[1], G. Valentini[1], M. Cantiello[1], J. Filiberto[3], S.S. Bhiravarasu[4], E. Brocato[1], G. Di Achille[1]

[1] *National Institute for Astrophysics — Astronomical Observatory of Abruzzo, Teramo, Italy, piero.dincecco@inaf.it*
[2] *Space Research Institute RAS, Moscow, Russia*
[3] *Astromaterials Research and Exploration Science Division, NASA Johnson Space Center, Houston, TX, USA*
[4] *Space Applications Centre, Indian Space Research Organization, Ahmedabad, India*

KEYWORDS:
Venus, atmosphere, near-infrared spectroscopy, oxygen nightglows, Campo Imperatore Observatory

INTRODUCTION:

The thick atmosphere of Venus presents a puzzling and complex dynamic structure. While the cloud layer (approximately from 50 to 70 km altitude) can be thoroughly studied using cloud images in UV, visible and IR [1], the region from 80 to 120 km largely remains a mystery. It neither has no clouds to allow motion tracking, nor it is possible to measure winds using in situ probes due to engineering constraints. Yet this region is important for Venus atmospheric dynamics because there occurs the transition from the global retrograde zonal superrotation (RZS) mode below to the subsolar-antisolar (SS-AS) cell circulation above [2].

However, this transition region can be studied using nightside airglows — NO and O_2, which peak at 110 and 97 km, and can be observed in UV and near-IR (Figures 1–3), respectively [3–4]. In this work we focus on the infrared observa-

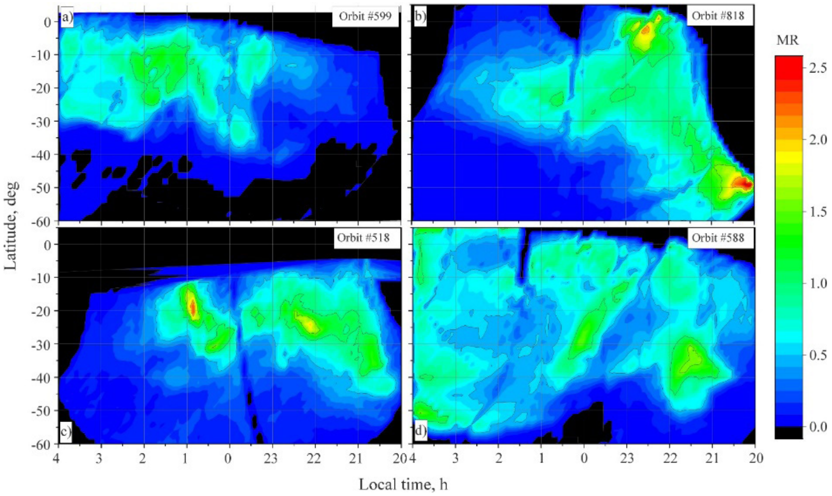

Fig. 1. Examples of O_2 ($a^1\Delta_g$) airglow emission on Venus nightside in local time — latitude coordinates. Emission intensity is calculated after removing the input of the lower atmosphere and surface, cloud scattering and water vapor absorption: (a) orbit 599 (images 00-07): peak emission is at 1–2 h, most of the bright areas are located on the morning side; (b) orbit 818 (images 00-10): two maxima on the evening side, one of which is near the equator, the other one is in the middle latitudes; (c) orbit 518 (images 00-01): two maxima on both sides of the midnight meridian; the stronger (but also more spatially compact) one is at 1 h, the weaker (but more extended) one is at 22 h; (d) orbit 588 (images 00-06): several local maxima at 22.5, 0 and 3–4 h LT [4].

tions of the O_2 ($a^1\Delta_g$) emission at 1.27 µm (see Figure 1, Table 1). The atomic oxygen forms on the dayside from the dissociation of CO_2 and then travels to the nightside with the SS-AS circulation where it recombines in the downwelling flow and emits around midnight [5]. However, the maximum of the emission is not found directly at the antisolar point, but shifted towards 22 h of local time. Therefore, other dynamic mechanisms such as thermal tides and stationary gravity waves are suspected to play a role at these altitudes [6].

A significant problem with these results is the lack of experimental data, as only Venus Express spacecraft studied this phenomenon as well as a few short ground-based observations. Our presentation aims at addressing this issue and proposing a new series of ground-based observations of the oxygen nightglow on Venus using the AZT-24 telescope at the INAF Campo Imperatore Observatory.

THE INAF CAMPO IMPERATORE AZT-24 TELESCOPE:

THE SITE:

The INAF Campo Imperatore Observatory is located in the Gran Sasso mountains in Abruzzo, Italy, at an altitude of 2150 m above the sea level. The atmospheric transparency, along with the climatic conditions — especially in winter — have always made it a suitable site for observations in the near infrared (1–2 micron) (i.e., [7]).

THE TELESCOPE:

The AZT-24 is a reflecting telescope, Ritchey-Chretien configuration, with an aperture of 1.1 m. The mechanics is very good and a new motorization system — in the commissioning phase - will allow great pointing and tracking accuracy (<0.1 arcs), as well as an uncommon tracking speed (the mechanics is designed to reach 3 deg/s).

THE FUTURE NEAR-INFRARED DETECTOR FOR THE AZT-24 TELESCOPE:

The camera will be based on a commercial InGaAs sensor, sensitive in the entire band from 450 nm to 1.78 micron (Johnson photometric bands: V, R, I, J, H_short), even if in this project we plan to use it only for infrared. The Quantum Efficiency in the J and H bands is around 90 %.

It will be equipped with a forefront optics with a tip-tilt corrector, in order to work in seeing-enhanced mode (it will likely be possible to reach a seeing of 1.5 arcs, from the starting >2.5 arcs). Under these conditions, the pixel scale would be between 0.4 and 0.6 arcs/pixel. With the camera formats available (between 640×480 to 960×1200), this will allow for Field-of-Views of the order of 6×8 arcmin or even greater.

In addition to the broad-band filters (I, J, H_short) appropriate narrow-band filters will be foreseeable, selected on the basis of the scientific programs that will potentially have the greatest impact.

THE CAMPO IMPERATORE ADVENANT PROJECT AS A GROUND-BASED SEGMENT FOR FUTURE MISSIONS TO VENUS:

Considering that we still have to wait for some years before obtaining high-resolution data about the Nightside Airglows of Venus from orbital measurements, the dataset and observation time to be provided from the future

Table 1. Mean O_2 ($a^1\Delta_g$) emission intensities from Earth-based observations and from previous VIRTIS-M measurements that were not accounting for surface influence

Author(s)	Year(s) of observation	Instrument	Mean O2 emission intensity (MR)	Peak 02 emission intensity (MR)
Crisp et al. (1996)	1991–1994	Canada-France Hawaii Telescope	1	6
Ohtsuki et al. (2008)	2002–2007	CSHELL	0.28	5
Krasnopolsky (2010)	2009	CSHELL	0.52	1.2
Piccioni et al. (2009)	200622009	VIRTIS-M	0.52±0.4	1.2

Near-Infrared detector of the AZT-24 telescope will be a unique opportunity to anticipate and complement the wealth of data and studies from the recently selected missions to Venus [8–13]. For this reason, we propose the Campo Imperatore ADVENANT project as a ground-based segment for the future missions to Venus.

References:

[1] *Peralta J., Lee Y.J., McGouldrick* K. *et al.* Overview of useful spectral regions for Venus: An update to encourage observations complementary to the Akatsuki mission // Icarus. 2017. V. 288. P. 235–239. https://doi.org/10.1016/j.icarus.2017.01.027.

[2] *Bougher S.W., Alexander M.J., Mayr H.G. et al.* Upper atmosphere dynamics: global circulation and gravity waves // Venus II: Geology, Geophysics, Atmosphere, and Solar Wind Environment // eds. S.W. Bougher, D.M. Hunten, R.J. Philips. Tucson: Univ. Arizona Press, 1997. 1362 p. P. 259–292. https://doi.org/10.2307/j.ctv27tct5m.13.

[3] *Stiepen A., Soret L., Gérard J.-C. et al.* The vertical distribution of the Venus NO nightglow: Limb profiles inversion and one-dimensional modeling // Icarus. 2012. V. 220. Iss. 2. P. 981–989. https://doi.org/10.1016/j.icarus.2012.06.029.

[4] *Shakun A.V., Zasova L.V., Gorinov* D.A. *et al.* O_2 ($a^1\Delta_g$) Airglow at 1.27 µM and upper Mesosphere Dynamics on the Night Side of Venus // Solar System Research. 2023. V. 57. Iss. 3. P. 200–213. https://doi.org/10.1134/S0038094623030085.

[5] *Gérard J.-C., Saglam A., Piccioni G. et al.* Distribution of the O2 infrared nightglow observed with VIRTIS on board Venus Express // Geophysical Research Letters. 2008. V. 35. Art. No. L02207. DOI:10.1029/2007GL032021.

[6] *Gorinov D., Khatuntsev* I.V., *Zasova L.V. et al.* Circulation of Venusian Atmosphere at 90–110 km Based on Apparent Motions of the O_2 1.27 µm Nightglow From VIRTIS-M (Venus Express) Data // Geophysical Research Letters. 2018. V. 45. Iss. 2. P. 2554–2562.

[7] *Del Principe M., Piersimoni A.M., Bono G. et al.* Near-Infrared Observations of RR Lyrae Variables in Galactic Globular Clusters. I. The Case of M92 // Astronomical J. 2005. V. 129. No. 6. P. 2714–2724. DOI: 10.1086/430148.

[8] *Garvin J.B., Getty S.A., Arney G.N. et al.* Revealing the Mysteries of Venus: The DAVINCI Mission // Planetary Science J. 2022. V. 3. No. 5. Art. No. 117. 11 p. DOI: 10.3847/PSJ/ac63c2.

[9] *Zasova L.V., Gorinov* D.A., *Eismont N.A. et al.* Venera-D: A Design of an Automatic Space Station for Venus Exploration// Solar System Research. 2019. V. 53. 506–510. https://doi.org/10.1134/S0038094619070244.

[10] *Senske D., Zasova L., Economou T. et al.* The Venera-D Mission Concept, Report on the Activities of the Joint Science Definition Team // 15th Meeting of the Venus Exploration and Analysis Group (VEXAG). 14–16 Nov., 2017, Laurel, Maryland. LPI Contribution No. 2061. 2017. Art. No. 8014.

[11] *Ghail R. et al.* EnVision Assessment Study Report (Yellow Book). 2021. 109 p.

[12] *Haider S.A., Bhardwaj A., Shanmugam M. et al.* Indian Mars and Venus missions: Science and exploration // 42nd COSPAR Scientific Assembly. 14–22 July 2018, Pasadena, California, USA. 2018. Abs. No. B4.1-10-18.

[13] *Smrekar S., Dyar* D., *Helbert* J. *et al.* VERITAS (Venus Emissivity, Radio Science, InSAR, Topography And Spectroscopy): A Proposed Discovery Mission // Europlanet Science Congress 2020. Virtual meeting. 21 Sept. – 9 Oct. 2020. Art. No. EPSC2020-447.

EARTH-LIKE VISCOELASTIC MODELS OF VENUS INTERIOR STRUCTURE

D.O. Amorim[1], T.V. Gudkova[2]

[1] *Moscow Institute of Physics and Technology (National Research University), Dolgoprudny, Moscow Region, Russia, amorim.dargilan@gmail.com*

[2] *Schmidt Institute of Physics of the Earth RAS, Moscow, Russia, gudkova@ifz.ru*

KEYWORDS:
Planetary interiors, Venus' core, moment of inertia, tidal Love numbers, Andrade rheology

INTRODUCTION:

Constraining Venus' interior structure is a crucial step to understand the planet's evolution and why it is so different from Earth. In this work we attempt to do so based on the available measurements of its moment of inertia [1] and tidal Love number k_2 [2]. We have made 45 PREM-based models of Venus that differ in core size and density profile. The viscoelasticity of the mantle is accounted by using the Andrade rheology for a wide range of its parameters and viscosity distributions. Unlike our previous works, the heavy Venus' atmosphere is now considered when computing k_2.

VENUS' MODELS:

Our models differ in density profile and core radius R_c (from 2850 to 3550 km). The crust thickness is set equal to 25 km and its density to 2900 kg/m^3 [3]. As it was suggested in [4], the mantle equation of state $p_m(P)$ is defined as $p_m(P) = A\rho_0(P)$, where P is the pressure, $\rho_0(P)$ is the PREM's equation of state and A is a coefficient near 1. Similarly, the liquid core equation of state $\rho_c(P)$ is given by the expression $p_c(P) = B\rho_0(P)$, where B is also a coefficient near 1. We compute models for three values of B: 1.00, 0.98 and 1.02, representing respectfully an Earth-like core, a lighter core and a heavier core. For each model (with specific values of R_c and B) the value of the mantle parameter A is chosen so that the mass condition is satisfied (Venus' mass = $4.8669 \cdot 10^{24}$ kg [5]). Models with large (R_c > 3300 km) and dense (B > 1) cores have considerably light mantles (A < 0.98), while models with small (Rc < 3000) and light (B < 1) cores have dense mantles (A > 1.02).

CORE STATE:

The pressure profile is computed for all models and the obtained values at the center of Venus (P_c) range from 260 to 320 GPa (see Fig. 1). They are lower than the pressure at Earth's inner core boundary (ICB) and indicate that Venus' can't have an inner solid core if its composition is similar to Earth's. This could help explain the absence of an internal magnetic field in Venus.

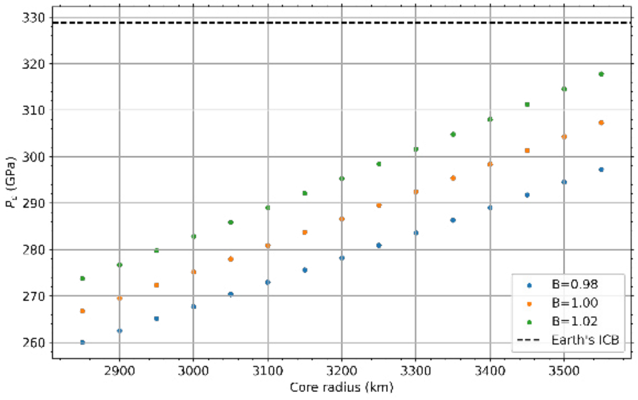

Fig. 1. Pressure at the center of Venus P_c in GPa for all models

MOMENT OF INERTIA:
The computed values of Venus' moment of inertia *I* (see Fig. 2) lie in the range from 0.318 to 0.347, which is in accordance with the measured value [1] 0.337±0.024. However, the low precision of the measurement does not allow us to precisely constrain the interior structure of Venus. For the purpose of doing so, we need more constraints, such as the tidal Love numbers.

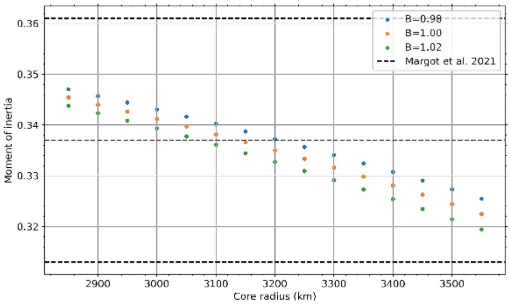

Fig. 2. Moment of inertia values of all 45 models. Dashed lines represent the measured value 0.337±0.024 [1]

VISCOELASTICITY:
In order to account for the viscoelasticity when computing the tidal Love numbers, we use the Andrade rheology as suggested in [6] for a wide range of values of its parameters α and ζ. Venus' solar tide period is 58.4 days.

Since Venus' viscosity profile is not known, we consider two models with low and high viscosity values: $\eta_C = 10^{19}$–10^{22} Pa·s, $\eta_{UM} = 10^{18}$–10^{21} Pa·s, $\eta_{TZ} = 10^{18}$–10^{21} Pa·s and $\eta_{LM} = 10^{18}$–10^{21} Pa·s, where C — stands for crust; UM for upper mantle, TZ for transition zone and LM for lower mantle.

TIDAL LOVE NUMBERS:
The tidal Love number k_2 of all 45 models have been computed for both viscosity profiles and for several combinations of the Andrade parameters α and ζ. We now consider Venus' heavy atmosphere when computing k_2 and, similarly to what is stated in [7], the tidal Love number value is reduced by about 3%, significantly changing the conclusions about Venus' interior structure. The obtained values are shown in Fig. 3.

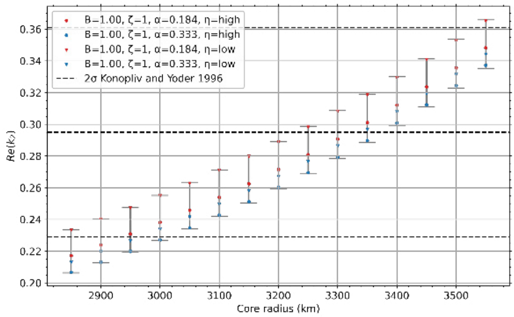

Fig. 3. k_2 values of our Venus' models. Bars represent the variation of k_2 due to the uncertainty in viscosity, α, ζ and B. Dashed lines represent the measured value 0.295±0.066 [2]

ESTIMATING THE BEST MODELS:
The comparison between the computed and the measured [1–2] values of moment of inertia and k_2 allows us to estimate the probability of each model (Fig. 4). By averaging this probability though *I* and k_2 for a certain value of R_c we can get the best estimates of Venus' core radius (Fig. 5).

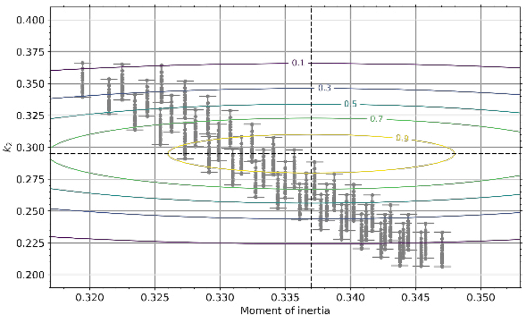

Fig. 4. Probability distribution of all models. Colorful solid lines represent the probability levels of 90, 70, 50, 30 and 10 %, while dashed lines represent the central values $k_2 = 0.295$ and $I = 0.337$

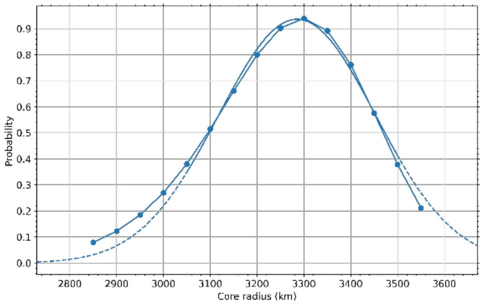

Fig. 5. Probability distribution of Venus' core radius' values. By fitting the highest values to a Gaussian, we get the estimate R_c = 3285±168 km

CONCLUSIONS:

The analysis of the modeled pressure distributions indicates that Venus' core is probably entirely liquid, while the moment of inertia and k_2 values point to a core radius in the range from 3100 to 3450 km.

Acknowledgements:

The study was performed based on funding of Russian Scientific Foundation no. 23-22-00074, https://rscf.ru/project/23-22-00074.

References:

[1] *Margot J.-L., Campbell D.B., Giorgini* J.D. *et al.* Spin state and moment of inertia of Venus // Nature Astronomy. 2021. V. 5. P. 676–683. DOI: 10.1038/s41550-021-01339-7.

[2] *Konopliv A.S., Yoder C.F.* Venusian k_2 tidal Love number from Magellan and PVO tracking data // Geophysical Research Letters. 1996. V. 23. Iss 14. P. 1857–1860. https://doi.org/10.1029/96GL01589.

[3] *Jiménez-Díaz A., Ruiz J., Kirby J.F. et al.* Lithospheric structure of Venus from gravity and topography // Icarus. 2015. V. 260. P. 215–231. https://doi.org/10.1016/j.icarus.2015.07.020.

[4] *Gudkova T.V., Zharkov V.N.* Models of the internal structure of the Earth-like Venus // Solar System Research. 2020. V. 54. Iss. 1. P. 20–27. DOI: 10.1134/S0038094620010049.

[5] *Steinberger B., Werner S.C., Torsvik T.H.* Deep versus shallow origin of gravity anomalies, topography and volcanism on Earth, Venus and Mars // Icarus. 2010. V. 207. Iss. 2. P. 564–577. https://doi.org/10.1016/j.icarus.2009.12.025.

[6] *Efroimsky M.* Tidal dissipation compared to seismic dissipation: In small bodies, Earths, and super-Earths // The Astrophysical J. 2012. V. 746. No. 2. Art. No. 150. DOI 10.1088/0004-637X/746/2/150.

[7] *Dumoulin C., et al.* Tidal constraints on the interior of Venus // J. Geophysical Research: Planets. 2017. V. 122. Iss. 6. P. 1338–1352. https://doi.org/10.1002/2016JE005249.

SESSION 3. VENUS (VN)
POSTER SESSION

INFLUENCE OF THE UNDERLYING SURFACE ON THE ZONAL AND MERIDIONAL SPEED AT THE CLOUD TOP LEVEL NEAR NOON FROM VMC/VENUS EXPRESS AND UVI/AKATSUKI IMAGES

M.V. Patsaeva[1], I.V. Khatuntsev[1], D.V. Titov[2], N.I. Ignatiev[1], L.V. Zasova[1], D.A. Gorinov[1], A.V. Turin[1]
[1] *Space Research Institute RAS, Moscow, Russia, marina@irn.iki.rssi.ru*
[2] *Leiden Observatory, Leiden University, Leiden, The Netherlands*

KEYWORDS:
Venus, mesosphere, dynamics, topography

INTRODUCTION:
UV (365 nm) images obtained by Venus Monitoring Camera (VMC/Venus Express) from 2006 to 2013 and by Ultraviolet Imager (UVI/Akatsuki) from December 2015 to August 2021 were used to study the mesosphere dynamics. Wind vectors were derived by the digital tracking technique [1–2]. We have studied changes in the longitudinal dependence of the zonal and meridional speed at the cloud top (70±2 km) in equatorial latitudes for limited time intervals of Venus Express and Akatsuki missions. Since the maximum deceleration associated with the surface influence is observed at noon [3], studies were carried out for 11–13 local time interval for both missions. Due to the fact that the vectors in the equatorial region obtained from the VMC images have phase angles from 60 to 90°, the vectors obtained from the UVI images were also limited to this range.

RESULTS:
The VMC registered in 2006–2013 the increase of the mean zonal wind speed from 85 to 115 m/s in equatorial latitudes [1]. At 20° S from 2006 to 2020 a periodicity in zonal wind with a period of 12.5±0.5 Earth years was discovered [4]. The amplitude of the approximating sinusoid for the zonal component was 10.0±1.6 m/s relative to the average –98.6±1.3 m/s. The same period was found from 2006 to 2021 at 10°S, corresponding to the maximum height of Aphrodite Terra. The zonal component has an amplitude 10.6±1.0 m/s relative to –98.9±0.7 m/s. The amplitude of the meridional component is –3.4±0.4 m/s relative to –0.8±0.3 m/s.

The dependence of the horizontal flow speed on longitude for two regions is shown in Fig. 1. First region (10±5° S, 60–120° E) corresponds to Ovda Regio, maximum height of Aphrodite Terra, second — to the lowlands (10±5° S, 330–30° E). The maximum height difference between the considered longitudes is about 4.5 km. Above the Ovda region, the amplitude of the sinusoid for the zonal component increased to 16.7±2.4 m/s at an average velocity of –101.2±1.9 m/s, relative to the indicators of the average sinusoid, for the meridional component — up to 5.3±1.4 m/s with an average of 1.6±1.1 m/s. Above the lowland, on the contrary, a decrease in amplitude is observed: for the zonal component to 9.7±4.5 m/s with an average of –99.5±3.2 m/s, for the meridional component to 1.6±0.7 m/s with an average of –1.0±0.7 m/s. Thus, high-altitude regions of the surface have a greater impact on the dynamics of the atmosphere at the cloud top.

It was shown in [5] that the decrease in the zonal speed correlates with the Ovda region. We observe acceleration above the Ovda region approximately from 2009 to 2017, deceleration — before 2009 and after 2017. The longitudinal variations of the zonal speed extend from the equator to the middle latitudes. The meridional speed shows longitude variations associated with topography, regardless of whether the horizontal flow is decelerating or accelerating above the Ovda region. Based on the behavior of the meridional component, we can cautiously assume that the influence of topography on the dynamics of the atmosphere will remain in any case.

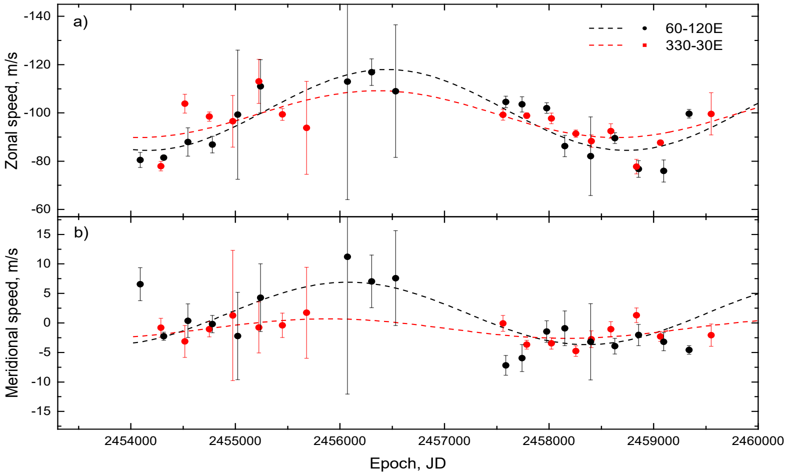

Fig. 1. Long-term variations in the zonal (*a*) and meridional (*b*) components of the mean horizontal flow with a period of 12.5 years at a latitude of 10±5° S near afternoon (12±1 h) above the highland (black color) — Ovda region, 60–120°E and lowland (red color) — Navka Planitia and Tinatin Planitia, 330-30°E. The dots indicate the mean speed over the Venusian year for a sample of measurements with a phase angle 60–90°. The error bars correspond to the 99.6 % confidence interval ($3\sigma_{\overline{X}}$). Dotted lines indicate sinusoids with a period of 12.5±0.5 years

CONCLUSION:

Change in the longitude behavior of the zonal speed was observed from 2009 to 2017. The reasons for this phenomenon require further study.

References:

[1] *Khatuntsev I.V., Patsaeva M.V., Titov D.V. et al.* Cloud level winds from the Venus Express Monitoring Camera imaging // Icarus. 2013. V. 226. Iss. 1. P. 140–158. https://doi.org/10.1016/j.icarus.2013.05.018.

[2] *Patsaeva M.V., Khatuntsev I.V., Patsaev D.V. et al.* The relationship between mesoscale circulation and cloud morphology at the upper cloud level of Venus from VMC/Venus Express // Planetary and Space Science. 2015. V. 113–114. P. 100–108. https://doi.org/10.1016/j.pss.2015.01.013.

[3] *Patsaeva M.V., Khatuntsev I.V., Zasova L.V. et al.* Solar Related Variations of the Cloud Top Circulation Above Aphrodite Terra From VMC/Venus Express Wind Fields // J. Geophysical Research: Planets. 2019. V. 124. Iss. 7. P. 1864–1879. https://doi.org/10.1029/2018JE005620.

[4] *Khatuntsev I.V., Patsaeva M.V., Titov D.V. et al.* Twelve-Year Cycle in the Cloud Top Winds Derived from VMC/Venus Express and UVI/Akatsuki Imaging // Atmosphere. 2022. V. 13. Iss. 13. Art. No. 2023. https://doi.org/10.3390/atmos13122023.

[5] *Bertaux J.-L., Khatuntsev I.V., Hauchecorne A. et al.* Influence of Venus topography on the zonal wind and UV albedo at cloud top level: The role of stationary gravity waves // J. Geophysical Research: Planets. 2016. V. 121. Iss. 6. P. 1087–1101. https://doi.org/10.1002/2015JE004958.

STUDY OF AEROSOL PROPERTIES IN THE VENUS' UPPER HAZE FROM SOIR DATA

A. Nepop[1,2], M. Luginin[2], A. Fedorova[2], F. Montmessin[3], O. Korablev[2], J.-L. Bertaux[3]

[1] *Moscow Institute of Physics and Technology (National Research University), Dolgoprudny, Moscow Region, Russia, nepop.ar@phystech.edu*
[2] *Space Research Institute RAS, Moscow, Russia*
[3] *Laboratoire Atmosphères, Milieux, Observations Spatiales (LATMOS) Université de Versailles — Saint-Quentin-en-Yvelines (UVSQ), Guyancourt, France*

KEYWORDS:
Venus, aerosols, upper haze, solar occultation, SOIR

INTRODUCTION:
The Venus upper haze is mainly formed by sulphuric acid particles. Limbic observations by Venera-9, Venera-10 and Pioneer-Venus orbiters have revealed submicron particles at upper haze altitudes. Bimodal particle size distribution in Venus upper haze was discovered from a few solar occultation observations by SPICAV/SOIR spectrometer onboard Venus Express [1]. [2] analyzed temporal and spatial variations of aerosol extinction at 3 µm from ~200 solar occultations covering period from September 2006 to September 2010 and found aerosol variablity on a time scale of several days. [3] studied >200 solar occultations performed by SPICAV-IR channel in the spectral range of 0.7 to 1.7 µm during the full mission length 2006–2014. They detected bimodal distribution at 75−85 km and retrieved vertical profiles of effective radius and number density of aerosol particles. In this work, we use SOIR data to retrieve microphysical properties of the upper haze aerosols.

SOIR (Solar Occultation in the IR) is a part of SPICAV/SOIR tool (SPICAV — Spectroscopy for Investigation of Characteristics of the Atmosphere of Venus) onboard Venus Express. SOIR is a small and lightweight high-resolution IR spectrometer. It operates in the 2.32 to 4.25 µm wavelength range. SOIR made over 700 observations in solar occultation geometry. In order to retrieve the microphysical properties of the aerosol, measurements must be carried out in a sufficiently wide wavelength range with a high vertical resolution. A total of 111 observations were selected that satisfy these criteria.

SOIR observation dataset includes multiple transmittance spectra. Solar radiation that has passed through the atmosphere is considered to obey Beer-Bouguer-Lambert law. So, the spectral optical depth can be expressed in terms of the transmittance as $\tau(\lambda, L) = -\ln\left(\frac{I(\lambda, z)}{I_0(\lambda)}\right)$. Also, it was shown that Rayleigh scattering and atmospheric refraction do not affect SOIR spectra significantly. So, the vertical profiles of aerosol extinction can be obtained by implementing nothing but onion peeling algorithm. Unimodal and bimodal log-normal distribution functions were used for modeling extinction of aerosol population. The Fortran program from [4] was used to calculate the extinction cross section of aerosol population in accordance with Mie theory. The refractive index values were taken from [5] for mass concentration of 75 % and a temperature of 215 K. Another script had been implemented to retrieve particle size distribution parameters and number density. It solves the optimization problem for the χ^2 objective function via SLSQP algorithm.

Implementation of bimodal distribution does not significantly improve quality of the fitting for most measurements. However, it was shown that implementation of the second mode allows much more accurate experimental data approximation for some measurements (Fig. 1). The retrieved values of the effective radius vary from ~3 to ~0.1 µm. The radius of one of the modes for bimodal distribution model is often close to unimodal radius.

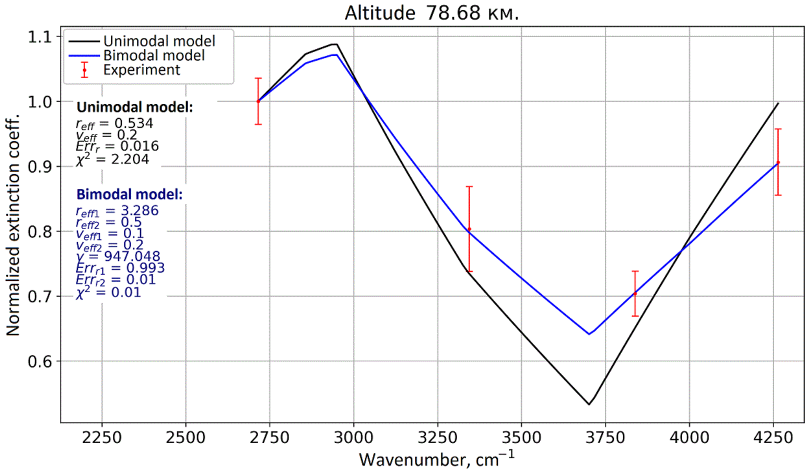

Fig. 1. Normalized extinction coefficient spectrum for unimodal (black), bimodal (blue) models and experiment (red). Observation 2007.08.20. Altitude 78.68 km. Implementation of the second mode allows much more accurate experimental data approximation for this measurement

References:

[1] *Wilquet V., Fedorova A., Montmessin F. et al.* Preliminary characterization of the upper haze by SPICAV/SOIR solar occultation in UV to mid-IR onboard Venus Express // J. Geophysical Research. 2009. V. 114. Iss. 12. Art. No. E00B42. DOI: 10.1029/2008JE003186.

[2] *Wilquet V., Drummond R., Mahieux A. et al.* Optical extinction due to aerosols in the upper haze of Venus: Four years of SOIR/VEX observations from 2006 to 2010 // Icarus. 2016. V. 217. Iss. 2. P. 875–881. https://doi.org/10.1016/j.icarus.2011.11.002.

[3] *Luginin M., Fedorova A., Belyaev D. et al.* Aerosol properties in the upper haze of Venus from SPICAV IR data // Icarus. 2016. V. 277. P. 154–170. https://doi.org/10.1016/j.icarus.2016.05.008.

[4] *Mishchenko M., Dlugach J., Yanovitskij E., Zakharova N.* Bidirectional reflectance of flat, optically thick particulate layers: an efficient radiative transfer solution and applications to snow and soil surfaces // J. Quantitative Spectroscopy and Radiative Transfer. 1999. V. 63. Iss. 2–6. P. 409–432. https://doi.org/10.1016/S0022-4073(99)00028-X.

[5] *Hummel J., Shettle E., Longtin D.* A New Background Stratospheric Aerosol Model for Use in Atmospheric Radiation Models: Scientific Report. No. 8. 1988. 71 p.

STUDY OF THE HDO/H2O ISOTOPE RATIO IN THE MESOSPHERE OF VENUS BASED ON SOIR OBSERVATIONS FOR 2006–2014

E.S. Fedorova, D.A. Belyaev, A.A. Fedorova, M.Luginin, O.I. Korablev
Space Research Institute RAS, Moscow, Russia, lisaoneechan@gmail.com

KEYWORDS:
Venus mesosphere, aerosol, solar occultation, water vapor

In the atmosphere of Venus, aerosol particles are contained not only in the cloud layer (50–70 km above surface), but also in the so-called upper haze layer in the mesosphere (70–100 km above surface). Similarly to the clouds, these particles are, in fact, droplets of sulfuric acid aqueous solution (75–80 % H_2SO_4). Recent Venus Express (VEx) studies showed that the particles are of submicron (~0.2 µm) and micron (~1 µm) sizes and can form separate dense layers at altitudes from 70 to 90 km [1–2]. The mechanism of formation of such layers is not completely studied; it depends on the photochemical interaction of water vapor (H_2O) and sulfur dioxide (SO_2), the HDO/H_2O isotope ratio, and also on the conditions of water condensation in the mesosphere.

In this work, we present the results of processing the transmission spectra of H_2O, HDO, and CO_2 obtained in the SOIR/VEx (Solar Occultation in the InfraRed) experiment in the solar occultation mode, and the HDO/H_2O ratio in the mesosphere of Venus, which is important for understanding the evolution of the planet. This work is a continuation of the data analysis published in 2008 [3], and covers observations for the entire duration of the SOIR experiment, from 2006 to 2014. SOIR is an acousto-optic echelle spectrometer and a part of the Venus Express mission. It carried out measurements in the spectral range of 2.3–4.3 µm with a spectral resolution of about 25000, which made it possible to detect thin absorption lines of such molecules as CO_2, H_2O, HDO, SO_2. The range of available altitudes when operating in solar occultation mode starts at above 65 km (directly above the clouds), which makes SOIR ideally suited for the studies of the upper haze layer [3]. At this stage, the altitude profiles of CO_2, H_2O, HDO and temperature were obtained in this altitude range. In the future, it is planned to use the results of this work to study the mechanisms of formation of dense aerosol layers above the clouds, which will help improving the existing chemical and microphysical models of the atmosphere of Venus and implementing of future experiments on the planet.

References:

[1] *Luginin M., Fedorova A., Belyaev D. et al.* Aerosol properties in the upper haze of Venus from SPICAV IR data // Icarus. 2016. V. 277. P. 154–170. DOI: 10.1016/j.icarus.2016.05.008.

[2] *Luginin M., Fedorova A., Belyaev D. et al.* Scale heights and detached haze layers in the mesosphere of Venus from SPICAV IR data // Icarus. 2018. V. 311. DOI: 10.1016/j.icarus.2018.03.018.

[3] *Fedorova A., Korablev O., Vandaele A.-C. et al.* HDO and H_2O vertical distributions and isotopic ratio in the Venus mesosphere by Solar Occultation at Infrared spectrometer on board Venus Express // J. Geophysical Research. 2008. V. 113. Iss. E5. Art. No. E00B22. DOI: 10.1029/2008JE003146.

OPTICAL DESIGN OF A HIGH-RESOLUTION IR SPECTROMETER ISCRA-V FOR THE VENERA-D MISSION

I.I. Vinogradov, P.A. Volkov, Yu.V. Lebedev, M.V. Spiridonov
Space Research Institute RAS, Moscow, Russia, imant@iki.rssi.ru

KEYWORDS:
Venera-D lander, atmosphere of Venus, sulfur dioxide, laser spectrometer, optical multipass cell

INTRODUCTION:

To continue studies of the atmosphere of Venus [1–3], an experiment ISCRA-V (Investigation of Sulphurous Components of Rarefied Atmosphere of Venus) have been proposed for retrieving of vertical profiles for sulphurous and for several minor gas components of the atmosphere at the descent trajectory of the Venera-D lander.

EXPERIMENT ENVIRONMENT AND METHOD OF MEASUREMENT:

ISCRA-V instrument, being a part of the Venera-D mission lander payload [4–7], is a tunable infrared laser absorption spectrometer. The goal of the ISCRA-V experiment is a study of the Venusian atmosphere (cloud layer, middle, low, and near-surface atmosphere). The issues of investigation are measuring vertical profiles of selected atmosphere gases concentrations at the abundant CO_2 background, such as SO_2, OCS, CO, H_2O, HCl, as well as isotopic ratios $^{34}S/^{33}S/^{32}S$, D/H, $^{18}O/^{17}O/^{16}O$, $^{37}Cl/^{35}Cl$. An active phase of the ISCRA-V experiment will start up when a protective shield of the lander be dropped off at an altitude of nearly 70 km and will be continued during lander's decent until touching down the surface of Venus, and afterwards aboard the lander at the surface of Venus.

Multipass Herriott scheme optical cell together with its laser, photodetector and vacuum interfaces is the core of the ISCRA-V instrument. Probing laser beams will pass many times through the optical cell analytical volume, filled in by a portion of the surrounding atmosphere, rarefied down to the pressure of 20–30 mbar. High-resolution spectra of optical transmission will show true absorption line contours for molecules of interest and make it possible to evaluate molecular concentrations and isotopic ratios.

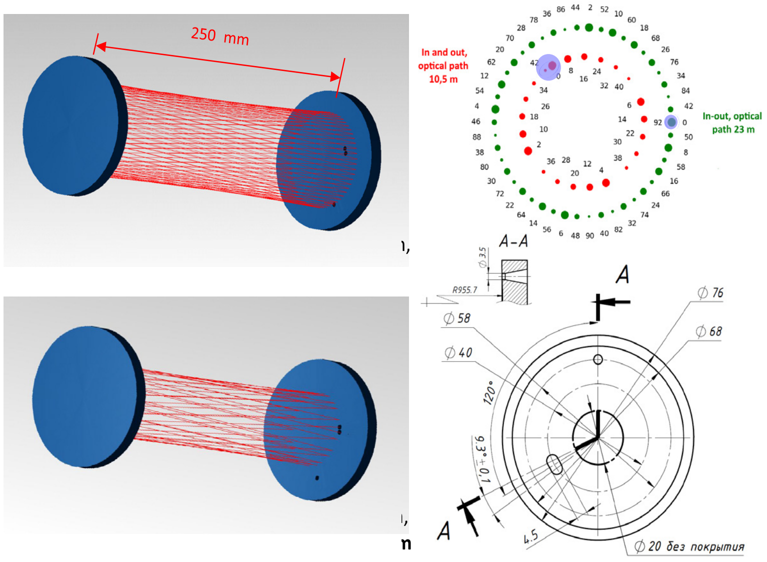

Fig. 1. Moments of mathematical modeling of the optical cell scheme and of its mirrors design

The instrument is supposed to use four lasers with the following wavelengths:

- 7416 or 7280 nm for measurements of SO_2, CO_2, H_2O,
- 4823 nm for measurements of OCS, CO, CO_2,
- 3397 nm for measurements of HCl,
- 2630 or 2657 nm for measurements of H_2O, CO_2.

For the first two spectral regions an optical path complete length of 10 m is quite sufficient, while for the last two spectral regions the optical path of about 25 m is required. For this reason, it is necessary to develop a modified Herriott type multipass optical cell with two different optical path configurations.

Current results of the multipass cell modeling, calculation of key characteristics for some variants are reported, see Figure 1. The inner group of the laser beam reflection points at the mirror's surface, a "pattern", corresponds to the shorter optical path, which takes just a part of the outer pattern's full optical path. That is, the given dual pattern scheme is a concentric one.

Analysis of stability of the multipass configuration is been carried out:

- possible deformations of the configuration due to thermal changes, mechanical impact, as well as due to manufacturing inaccuracy are taken into account;
- scattered laser beams light cross-interference effect has been considered and minimized;
- criteria for the optimal choice of an optical scheme are formulated and optical breadboard is developed for experimental checking out the calculation correctness.

Examples of simulated molecular absorption spectra are shown in the report for the current state of the project development.

Acknowledgements:
The work is kindly supported by subsidy "Planeta" for IKI RAS and by Roscosmos for the experiment's technical proposal writing and submission.

References:

[1] *Bertaux J.-L., Moroz V.I. et al.* VEGA-1 and VEGA-2 entry probes: An investigation of local UV absorption (220–400 nm) in the atmosphere of Venus (SO_2, aerosols, cloud structure) // J. Geophysical Research: Planets. 1996. V. 101. Iss. E5. P. 12709–12745. DOI: 10.1029/96JE00466.

[2] *Zasova L.V., Moroz V.I., Esposito L.W., Na C.Y.* SO_2 in the middle atmosphere of Venus: IR Measurements from Venera-15 and Comparison to UV data // Icarus. 1993. V. 105. No. 1. P. 92–109. DOI: 10.1006/icar.1993.1113.

[3] *Zasova L.V., Gorinov* D.A., *Eismont N.A. et al.* Venera-D: A Design of an Automatic Space Station for Venus Exploration // Solar System Research. 2019. V. 53. No. 7. P. 506–510. DOI: 10.1134/S0038094619070244.

[4] *Vinogradov I.I., Belyaev D.A.* Experiment ISCRA-V (Investigation of Sulphurous Components of Rarefied Atmosphere of Venus) of the national project "Venera-D" // Intern. Conf. DLS-23. 27 Oct. 2015, GPI, Moscow. http://www.dls.gpi.ru/rus/sem/23/1.pdf.

[5] *Vinogradov I. et al.* Investigation of sulphurous components of rarefied atmosphere of Venus: ISCRA-V experiment at the Venera-D lander // Proc. VAK-2021 Conf. 23–28 Aug. 2021, SAI MSU, Moscow. 2022. P. 263. DOI: 10.51194/VAK2021.2022.1.1.096.

[6] *Vinogradov I.I., Barke* V.V.*, Belyaev* D.A. *et al.* Study of sulphurous and other components of the Venus atmosphere by laser absorption spectroscopy at the Venera-D mission // 13th Moscow International Solar System Symposium (13MS3). IKI RAS, Moscow, 2022: Book of abstracts. 2022. Art. No. 13MS3-VN-15. P. 331–333. DOI: 10.21046/13MS3-2022.

[7] *Volkov P., Vinogradov I., Spiridonov M.* Multipass dual pattern optical scheme of the ISKRA-V high resolution IR spectrometer onboard Venera-D mission // 20th Symp. High Resolution Molecular Spectroscopy HighRus-2023. Lake Baikal, 2023: Abs. D25. P. 52. https://symp.iao.ru/ru/hrms/20/progpdf.

14MS3-VN-PS-05
POSTER

STUDY OF FLIGHT SCENARIO OF MISSION TO VENUS FOLLOWED BY A PASSAGE OF AN ASTEROID

V.A. Zubko, N.A. Eismont, K.S. Fedyaev, A.A. Belyaev
Space Research Institute RAS, Moscow, Russia, v.zubko@iki.rssi.ru

KEYWORDS:
Venus, asteroids, flyby mission, mission design

A study of the trajectories of a spacecraft to Venus followed by the passage of asteroids was conducted. To do this, an analysis was made of a prospective flight scheme to Venus that included a gravity assist maneuver to make a landing at any desired point on the surface of Venus. In the frame of this scheme, it is shown that its implementation can be greatly expanded by impulse-free flyby of an asteroid by the spacecraft on its route to landing on the Venus surface. A total of 53 mission scenarios to Venus in the framework of the abovementioned scheme accompanied by an asteroid flyby have been found within the 2029–2050 launch date interval. For these scenarios, 35 asteroids were found out of 117 selected. The main criteria for selection was the object's average diameter, which was supposed to be greater than 1 km. It is shown that a free-impulse asteroid encounter is possible only in the gravity assist scenario and almost impossible in the direct flight i.e. Earth-Venus case. Among the 53 scenarios, the most notable were the ones with the flyby of the M-class asteroids 3554 Amun; 3753 Cruithne, which are in a 1:1 orbital resonance with the Earth, and 5731 Zeus, which is one of the largest objects among the selected ones. It is shown that in the framework of the developed schemes it is possible to perform the free-impulse encounter with comet 2P/Encke for launch in 2032 and 2044. The link between attainable landing points and the possibility of a free impulse passage of an asteroid by a spacecraft moving in a resonant orbit was established.

VENUS IN SOLAR WIND: SCIENTIFIC GOALS AND CONCEPTS OF PLASMA ANALYZERS FOR VENERA-D MISSION

D. Moiseenko, A. Shestakov, O. Vaisberg, A. Petukh
Space Research Institute RAS, Moscow, Russia, modaldi@cosmos.ru

KEYWORDS:
solar wind, Venus, Venera-D, ion mass-analyzer, electron energy analyzer, energetic neutral particle detector, inducted magnetosphere

INTRODUCTION:
Despite the long period of exploration of Venus by spacecrafts, its plasma environment is the object of great scientific interest. Venus, unlike Mars, don't have a large amount of scientific information that causes the interaction of the solar wind with the planet's atmosphere, and at the moment there are no satellites near the planet capable to produce measurements of space plasma parameters. The presence of a modern complex of plasma instruments on board of the perspective Venera-D spacecraft will make it possible to obtain new scientific information and perform detail study of the processes occurring during the interaction of the solar wind with Venus. This report considers the list of scientific goals that will allow to solve with the complex of plasma instruments on board the Venera-D spacecraft, and also describes the structure and principle of operation of three plasma instruments: an ion energy-mass analyzer, an electronic energy analyzer and a detector of energetic neutral atoms.

SCIENTIFIC GOALS OF FUTURE MISSION:
Plasma and magnetic field measurements carried out onboard the Venera-9 and Venera-10 spacecraft in the 1970s made it possible to obtain initial data of the processes of interaction between the solar wind and the formation of an induced magnetosphere. Also, a significant contribution to the study of the interaction of the solar wind with the atmosphere of Venus was made by the results of measurements within the space mission Pioneer-Venus Orbiter [1]. The obtained experimental data made it possible to develop a model of the induced magnetosphere of Venus [2–3]. The processes of interaction between the solar wind and Venus were also studied in the framework of the space missions Pioneer Venus Orbiter (1978), the mission Venus Express (1978) [4–5].

Now the most relevant scientific data are the results of the operation of the plasma complex of the Venus Express spacecraft launched in 2005. During this mission, unique measurements were made in the polar regions and in terminator orbits, and obtained data of the plasma parameters in the tail of Venus [5]. However, despite the fruitful work of this spacecraft, the study of the plasma environment of Venus remains actual.

Since Venus has no own magnetic field, the solar wind interacts directly with the planet's atmosphere. As a result, the upper atmosphere of Venus has a cometary nature of interaction with the solar wind. Because of this nature of the interaction, the particle stream behind Venus is laden with planetary ions trapped in the solar wind stream as a result of ionization by the Sun's ultraviolet radiation. This capture of planetary ions leads to the development of an induced magnetosphere and a shock wave. Losses of heavy ions caused by the impact of the solar wind make a significant contribution to the loss of the Venusian atmosphere.

One of the important scientific goals of the Venera-D space mission is to study the mechanisms that affect the loss of the atmosphere of Venus and the processes leading to this phenomenon. An important goal is also to estimate the rate of erosion of the Venusian atmosphere under various environmental conditions — depending on solar activity, coronal ejections, under the influence of waves in the plasma.

Also, the following positions can be attributed to the urgent tasks of studying the plasma environment of Venus: determination of the mass composition of the planetary ion flux, tracking its changes under various conditions and in various regions of the Venusian magnetosphere; measurement of the distribution function over the velocities of outgoing ions in order to study the mechanisms of loss and acceleration of particles; investigation of fine structures at the boundaries of the magnetosphere using high-frequency measurements of plasma and magnetic field parameters; study of the processes of mass loading on the atmosphere of Venus, determination of the loss rate and the influence of strong solar wind disturbances; evaluation of critical factors affecting atmospheric erosion in order to assess the evolution of the atmosphere over time; study of acceleration processes in current sheets.

INSTRUMENTS FOR PLASMA MEASUREMENTS:

ION ENERGY-MASS ANALYZER ARIES-D

Measuring the velocity distribution function of ions is one of the main tasks that makes it possible to study the processes of interaction between the solar wind and the atmosphere of Venus and to study the processes occurring in the induced magnetosphere of the planet. For this, a wide-angle ion energy-mass analyzer is being developed, which provides registration of the energy and mass spectrum of ions in the energy range from 10 to 10,000 eV with a high time resolution. During the Venera-D mission, the ARIES-L ion energy-mass spectrometer will measure the mass composition of the planetary ion flux, track its changes under various conditions and in various regions of the Venusian magnetosphere.

ELECTRON ENERGY-ANALYZER ELSPEC

The electron analyzer is an important component of the plasma complex that makes it possible to solve problems related with measuring of the solar wind parameters near Venus, to study the processes associated with the interaction of the solar wind and interplanetary plasma with the induced magnetosphere, and to carry out measurements in the tail of Venus. The instrument is designed to measure the distribution function of the electrons in solar wind and in the magnetosphere and ionosphere of Venus. Such measurements will make it possible to study the processes of particle interaction with the Venusian magnetosphere, determine the mechanisms of particle acceleration, and study fine structures at the boundaries of the magnetosphere.

ENERGETIC NEUTRAL PARTICLES DETECTOR NPD

The Neutral Particles Detector will make it possible to obtain information of the mass composition and spatial distribution of neutral particles in different regions of the spacecraft orbit, which will make it possible to study the reconnection processes occurring in the magnetosphere and tail of Venus, to study the interaction of neutral atoms and charged particles with the induced magnetosphere of Venus, to study the processes of interaction of magnetospheric and low-energy ionospheric ions with neutral atoms.

REFERENCES:

[1] *Russell C.T., Vaisberg O.* The interaction of the solar wind with Venus // Venus / ed. D.M. Hunton et al. Tucson: Univ. Arizona Press, 1983. P. 873–894.

[2] *Zelenyi L.M., Malova H.V., Artemyev A.V. et al.* Thin current sheets in collisionless plasma: equilibrium structure, plasma instabilities, and particle acceleration // Plasma Physics Reports. 2011. V. 37. P. 118–160. DOI: 10.1134/S1063780X1102005X.

[3] *Vaisberg O.L., Zeleny L.M.* Formation of the plasma mantle in the Venusian magnetosphere // Icarus. 1984. V. 58. P. 412–430. DOI: 10.1016/0019-1035(84)90087-3.

[4] *Barabash S., Fedorov A., Sauvaud J.J. et al.* The loss of ions from Venus through the plasma wake // Nature. 2007. V. 450. P. 650–653. DOI: 10.1038/nature06434.

[5] *Futaana, Y., Stenberg Wieser G., Barabash S. et al.* Solar Wind Interaction and Impact on the Venus Atmosphere // Space Science Reviews. 2017. V. 212. P. 1453–1509/ https://doi.org/10.1007/s11214-017-0362-8.

COMPARISON OF INTERNAL WAVE CHARACTERISTICS IN THE VENUS'S ATMOSPHERE DEDUCED BY TWO INDEPENDENT METHODS FROM THE MAGELLAN RADIO OCCULTATION MEASUREMENTS

V.N. Gubenko, I.A. Kirillovich
Kotel'nikov Institute of Radio Engineering and Electronics RAS, Fryazino branch, Fryazino, Moscow region, Russia, vngubenko@gmail.com; gubenko@fireras.su

KEYWORDS:
Radio occultation (RO) measurements, Magellan spacecraft, Venus's atmosphere, vertical temperature profiles; internal gravity waves (IGWs)

INTRODUCTION:

Hinson and Jenkins [1] suggested that radiative damping is the principal process to dissipate internal atmospheric waves having vertical wavelengths shorter than 4 km, and this approach was used for an analysis of the Magellan RO temperature data. They showed that the observed wave structures were consistent with pure IGWs that are attenuated by radiative damping during the vertical ascent. It was found that the amplitude and vertical wavelength of temperature variations at altitude of ~65 km are about 4 K and 2.5 km, respectively. A model for radiative damping, developed by Hinson and Jenkins [1], implies that the wave intrinsic frequency is of $\sim 2 \cdot 10^{-4}$ rad/s, and the corresponding ratio between horizontal and vertical wavelengths is of ~100. A similar approach was also used by authors of the work [2] for an analysis of the Venus Express RO temperature data. It should be noted that D.P. Hinson and J.M. Jenkins [1] supposed the wave amplitude is not sufficient to cause convective instability, an alternative damping mechanism. Similarly, they believed (possibly erroneously in our opinion) that wind shear instability is not likely to be the cause of the observed attenuation, since the wave amplitude appears to be insufficient to trigger this effect.

We have developed an alternative independent method of identifying the discrete wave events and reconstructing the IGW parameters from an analysis of the individual vertical temperature, density, or buoyancy (Brunt – Vaisala) frequency squared profile in a planetary atmosphere. Our method does not require any additional information not contained in the profile and can be adopted to analyze vertical profiles obtained by various techniques. The threshold discrimination criterion was formulated and justified for identifying wave events; its fulfillment assumes that the analyzed temperature or density variations to be manifestations of internal waves [3–8]. This method relies on the analysis of the relative wave amplitude, determined from the vertical profile of temperature or density, as well as on the concept of the linear IGW theory, which suggests that the wave amplitude is limited by threshold values due to wind dynamic (shear) instability in the atmosphere of planet. It is expected that when the internal wave amplitude reaches the wind shear instability threshold as the wave propagates upward, the wave energy dissipation occurs so that the IGW amplitude stays at the atmospheric instability threshold (wave amplitude saturation). An application of the method to the analysis of RO temperature data enabled us for the first time to identify wave events in the Earth's and Martian atmospheres and to determine the key characteristics of detected waves, including IGW intrinsic frequency, vertical fluxes of wave energy and momentum [3–6]. Numerical simulation data and an analysis of the independent radar and radiosonde measurements in Earth's atmosphere demonstrate high efficiency of our method and high reliability of scientific results it yields [9].

We used parameters of the temperature variations from Magellan RO profiles, remaining after high-pass filtering for wavelengths <4 km [1], as the input RO data for our reanalysis of IGWs in the Venus's atmosphere. The analyzed temperature data were obtained from the Magellan spacecraft measurements on 5–6 October 1991 during three successive orbits (orbit numbers 3212–3214). The results obtained by two independent methods are presented, compared, and discussed in this work.

Acknowledgements:
This research has been carried out in the framework of the state task no. 075-01110-23-01.

References:
[1] *Hinson D.P., Jenkins J.M.* Magellan radio occultation measurements of atmospheric waves on Venus // Icarus 1995. V. 114. Iss. 2. P. 310–327. https://doi.org/10.1006/icar.1995.1064.
[2] *Tellmann S., Hausler B., Hinson D.P. et al.* Small-scale temperature fluctuations seen by the VeRa Radio Science Experiment on Venus Express // Icarus. 2012. V. 221. Iss. 2. P. 471–480. https://doi.org/10.1016/j.icarus.2012.08.023.
[3] *Gubenko V.N., Pavelyev A.G., Andreev V.E.* Determination of the intrinsic frequency and other wave parameters from a single vertical temperature or density profile measurement // J. Geophysical Research. 2008. V. 113. Iss. D8. Art. No. D08109. DOI: 10.1029/2007JD008920.
[4] *Gubenko V.N., Pavelyev A.G., Salimzyanov R.R., Pavelyev A.A.* Reconstruction of internal gravity wave parameters from radio occultation retrievals of vertical temperature profiles in the Earth's atmosphere // Atmospheric Measurement Techniques. 2011. V. 4. Iss. 10. P. 2153–2162. DOI: 10.5194/amt-4-2153-2011.
[5] *Gubenko V.N., Pavelyev A.G., Salimzyanov R.R., Andreev V.E.* A method for determination of internal gravity wave parameters from a vertical temperature or density profile measurement in the Earth's atmosphere // Cosmic Research. 2012. V. 50. Iss. 1. P. 21–31. DOI: 10.1134/S0010952512010029.
[6] *Gubenko V.N., Kirillovich I.A., Pavelyev A.G.* Characteristics of internal waves in the Martian atmosphere obtained on the basis of an analysis of vertical temperature profiles of the Mars Global Surveyor mission // Cosmic Research. 2015. V. 53. Iss. 2. P. 133–142. DOI: 10.1134/S0010952515020021.
[7] *Gubenko V.N., Pavelyev A.G., Kirillovich I.A., Liou Y.-A.* Case study of inclined sporadic E layers in the Earth's ionosphere observed by CHAMP/GPS radio occultations: Coupling between the tilted plasma layers and internal waves // Advances in Space Research. 2018. V. 61. Iss. 7. P. 1702–1716. DOI: 10.1016/j.asr.2017.10.001.
[8] *Gubenko V.N., Kirillovich I.A.* Diagnostics of internal atmospheric wave saturation and determination of their characteristics in Earth's stratosphere from radiosonde measurements // J. Atmospheric and Solar-Terrestrial Physics. 2018. V. 4. No. 2. P. 41–48. DOI: 10.12737/stp-42201807.
[9] *Rechou A., Kirkwood S., Arnault J., Dalin P.* Short vertical-wavelength inertia gravity waves generated by a jet-front system at Arctic latitudes — VHF radar, radiosondes, and numerical modeling // Atmospheric Chemistry and Physics. 2014. V. 14. Iss. 13. P. 6785–6799. DOI: 10.5194/acp-14-6785-2014.

CORONAE OF VENUS: TOPOGRAPHY AND VOLCANIC PRODUCTIVITY

E.N. Guseva, M.A. Ivanov
Vernadsky Institute of Geochemistry and Analytical Chemistry RAS, Moscow, Russia, guseva-evgeniya@ya.ru

KEYWORDS:
Venus, coronae, lobate plains, topography, volcanism

INTRODUCTION:
Coronae on Venus are large, up to 2500 km, ring-shaped landforms with an annulus consisting of densely spaced grooves and ridges [1–3]. Their topography, volcanism, and nonrandom spatial distribution [3–4] indicate that coronae are surface manifestations of mantle diapirs. The late stages of the diapirs evolution are likely related to volcanic activity at coronae, manifested by lobate flows that form lobate plains [5]. Lobate plains are common inside the annulus and when extend outward they form lava aprons at some coronae. Young volcanic activity at coronae can be important indicator of late mantle convection on Venus.

The goals of this study were: (1) to find how often coronae represent the sources of lobate plains and (2) to estimate areas of lobate plains sourced by coronae.

METHODS:
In our study, we used the published catalogs of coronae [3, 6] and the global geological map of Venus showing fields of lobate plains [5]. For each corona, we noted the presence/absence of lobate plains and features indicating that this corona either is the source of lobate plains or is flooded by them. In this way, we defined a subpopulation of the coronae - sources of lobate plains. Determining if specific fields of lava plains that are genetically related to a specific corona is difficult, as these plains can be formed by flows from different sources. Therefore, we were able to find coronae that are unambiguous sources of lobate plains. For these coronae, the area of the corona itself within its annulus and the total area of the surrounding lobate plains were determined using the Mollweide equal area projection.

SIZE-FREQUENCY AND SPATIAL DISTRIBUTION OF CORONAE
We identified 90 coronae — sources of lobate plains, which is ~17 % of the total population. By size (~100–650 km), they overlap the major part of all coronae of Venus, with the exception of the smallest coronae and corona-like features. The subpopulation with pure cases of coronae — sources of lobate plain includes 41 coronae whose size-frequency distribution (SFD) is bimodal. Such a bimodality is a consequence of the nonrandom nature of the selection of coronae and, obviously, has no physical meaning.

About half of all coronae — sources of lobate plains (40 out of 90 or ~44 %) are located within the Beta-Atla-Themis (BAT) in the region. The coronae — sources of lobate plains, both in the BAT region and beyond, belong to topographic classes *D* (~44 % of the population of coronae-sources), *W* (~28 %), and *U* (~28 %). Class D, dome-shaped coronae, probably reflect the progressive stage of evolution of the parental diapir [7]. Coronae of W- and U-classes are characterized by the presence of a complex (*W*) or simple (*U*) central depression, which probably forms at the late stages of a diapir evolution when its thermal anomaly waned.

AREAS OF LOBATE PLAINS AT THE CORONA-SOURCES
We calculated the areas of lobate plains associated with particular coronae to estimate their volcanic productivity. For calculations, we used a subpopulation of pure cases of corona-sources of lobate plains.

To assess the possible productivity variations, we used the dimensionless parameter *P*, which is a S_a/S_c ratio, where S_a — the area of lobate plains associated with the corona and S_c is the area of the corona itself (within the annulus). In order to characterize the possible changes of *P*, we considered four models: (1) the area of the lava apron increases proportionally to the increase in the corona diameter; (2) the area of the apron increases randomly as the diameter of the corona increases; (3) the area of the apron increases progressively as the diameter of the corona increases; (4) the area of the apron decreases as corona diameter increases. In all cases, the model corona was a circle of a given diameter, and the lava apron was a ring around the corona. The inner diameter of the ring was equal to the diameter of the corona, and the outer diameter increased as the diameter of the corona increased, depending on the model considered (Fig. 1). In all models, the area of lobate plains surrounding the corona increased as the corona diameter increased (see Fig. 1*a*). This result is trivial and is a consequence of the model setup. The expected increase in the apron can either be strictly functional (models 1, 2, and 4) or exhibit some degree of dispersion from the overall trend (model 2).

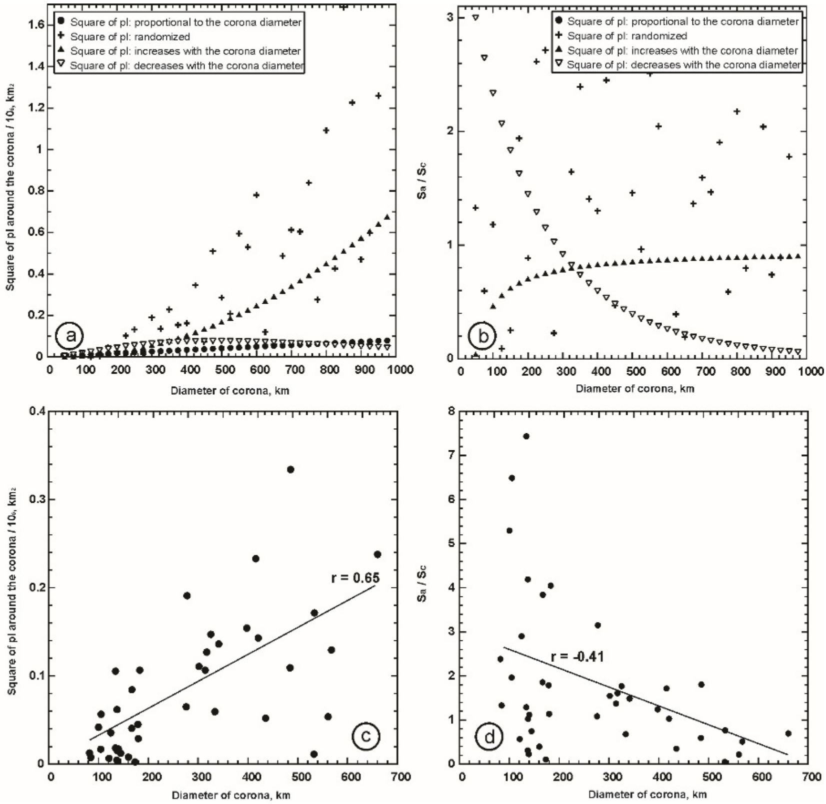

Fig. 1. Models of possible relationships between the corona areas and areas of lobate plains sourced by coronae

Important and diagnostic changes are observed when we compare the changes of the *P* value with the corona diameter (see Fig. 1*b*). There are three types of dependence between *P* and *D*. (1) As the corona diameter increases, the value of the ratio *P* decreases. This type of dependence corresponds to models 1 and 4. The correlation between the values of the parameters *P* and *D* is negative (correlation coefficients for models 1 and 4: $r = -0.67$ and $r = -0.64$, respectively, although the relationship between the parameters is not linear). (2) The values of the *P* ratio change chaotically as the corona diameter increases (see Fig. 1*b*). This case corresponds to model 2. There is no correlation between the values of the parameters **P** and *D* in this case ($r = 0.05$). (3) The values of the P ratio increase with the growth of the corona diameter (see Fig. 1*b*). This case corresponds to model 3. In this case, the correlation between the parameters *P* and *D* is positive ($r = 0.75$, although the relationships between these parameters are not linear).

CONCLUSION:

1) Only 17 % of the entire population of coronae of Venus are sources of lobate plains that characterize the Atlian period of the geologic history of Venus. Such a small fraction of coronae that were volcanically active recently may suggest that either the rate of formation of mantle diapirs decreased with time, or the thickening lithosphere more effectively filtered out rising diapirs, or these factors together influenced the mode of mantle convection.
2) The area of lobate plains that can be unambiguously associated with a particular corona and the area of the corona itself are negatively correlated (see Fig. 1c). Such relationships allow the existence of only two models of the final stages of the evolution of diapirs. (a) All parent diapirs of the corona-sources of the lobate plains were located at approximately at the same depth, corresponding either to the zone of neutral buoyancy or to the base of the rheological barrier of the lithosphere. (b) The depth at which the rise of the diapirs stopped was greater for the larger diapirs. Since there are no obvious physical reasons for this model, we assume that during the Atlian period either there was a single zone of neutral buoyancy, or the base of the lithosphere was located approximately at the same level.

References:

[1] *Barsukov V.L., Basilevsky A.T., Burba G.A. et al.* The geology and geomorphology of the Venus surface as revealed by the radar images obtained by Venera 15 and 16 // J. Geophysical Research. 1986. V. 91. Iss. B4. P. 378–398. https://doi.org/10.1029/JB091iB04p0D378.
[2] *Campbell D.B., Stacy N.J.S., Newman W.I. et al.* Magellan observations of extended impact crater related features on the surface of Venus // J. Geophysical Research. 1992. V. 97. P. 16249–16277. https://doi.org/10.1029/92JE01634.
[3] *Stofan E.R., Sharpton V.L., Shubert G., Baer G.et al.* Global distribution and characteristics of coronae and related features on Venus: implication for origin and relation to mantle processes // J. Geophysical Research. 1992. V. 97. P. 13347–13378. https://doi.org/10.1029/92JE01314.
[4] Phillips R.J., Raubertas R.F., Arvidson R.E.et al. Impact craters and Venus resurfacing history // J. Geophysical Research. 1992. V. 97. Iss. E10. P. 15923–15948. https://doi.org/10.1029/92JE01696.
[5] *Ivanov M.A., Head J.W.* Global geological map of Venus // Planetary and Space Science. 2011. V. 59. Iss. 13. P. 1559–1600. https://doi.org/10.1016/j.pss.2011.07.008.
[6] *Crumpler L.S., Aubele J.* Volcanism on Venus // Encyclopedia of Volcanoes / eds. Sigurdsson H., Houghton B., McNutt S.R. et al. Academic Press: 2000. 1111 p. P. 727–770. https://handwiki.org/wiki/Astronomy:Volcanology_of_Venus.
[7] *Smrekar S.E., Stofan E.R.* Corona formation and heat loss on Venus by coupled upwelling and delamination // Science. 1997. V. 277. Iss. 5330. P. 1289–1294. DOI: 10.1126/science.277.5330.12.

COMPUTER REALIZATION OF ALGORITHM FOR INVERSION OF VENUSIAN INTERIORS BASED ON MONTE CARLO METHOD: 1. TESTING ON CLASSICAL EXAMPLE OF GRAVITATIONAL FIELD DATA

I.A. Boronin, T.V. Gudkova
Schmidt Institute of Physics of the Earth RAS, Moscow, Russia, gudkova@ifz.ru

KEYWORDS:
Monte-Carlo method, inverse problem, Bayesian statistics, Markov chains, internal structure of the planets, Venus

INTRODUCTION:
Until now, the choice of a model of the internal structure of Venus was carried out as a result of solving a direct problem based on data on the gravitational field (mass, moment of inertia, Love tidal numbers k_2) and assumed geochemical data. The solution of the inverse problem has become relevant in order to combine model parameters with the observed values. Methods for solving nonlinear inverse problems [1–5] have been increasingly used to refine the internal structure of planets and satellites. One of the goals of this work is to implement a numerical algorithm with probability distributions that will solve the problem of combining observed data with data obtained from the model.

METHOD:
At the first stage, a numerical algorithm is implemented to determine the distributions of the parameters of the internal structure of the planet from a set of observational data. Using the Bayesian approach to statistics, the inverse problem is formulated, which is solved using the Monte Carlo method with Markov chains (MCMC). The probabilistic approach to solving the inverse problem significantly simplifies the task of combining model parameters that satisfy observational data and a priori data. The Bayesian approach to statistics allows us to take into account the correspondence between the initial information about the model and the observation data. A feature of the algorithm is the complete independence of each Markov chain from the others. With this feature it is easy to use parallel computer calculations to significantly reduce the calculation time.

TESTING MCMC METHOD:
In order to test the implemented numerical algorithm the classical model example of the inversion of gravitational field data is presented. We will use the classical model problem of inversion of gravity data from [3]. Suppose there is a vertical boundary up to a depth of 100 km. To the left of it, the medium is homogeneous and density ρ_1 = 2570 kg/m^3, to the right, the medium is divided into horizontal layers with density ρ(z) depending on depth. The boundary of each layer is parallel to the surface, and below 100 km the medium is homogeneous and has a constant density of 2570 kg/m^3. The inverse problem is to select the medium density distribution function in such a way that the measurement results coincide with the available observational data. According to the Bayesian approach, we must determine a priori information about the system. A priori information is that the distribution of layer thicknesses to the right of the vertical boundary obeys the exponential distribution law with mean value of 4 km. Then it is necessary to create a model that satisfies all a priori assumptions, the parameters of which will be calculated in the process of solving the inverse problem, let's call this model "real" (Fig. 1).

The solution algorithm is as follows: first, a random model is created that satisfies all known a priori information, then a sampling algorithm based on random walks is used, which selects models to construct probabilistic characteristics. In order to coordinate with the observational data, the sampling algorithm of a priori probabilistic quantities is modified into the sampling algorithm of a posteriori probabilistic quantities by calculating the likelihood function value for the model from the current step and for the model from expected next step. If the value of likelihood function is greater at the next step, then the step is taken always, else the step is taken with probability equal to the ratio of likelihood function values of the next step to current (the probability of a successful step is calculated according to the Metropolis rule). 10 Markov chains with a length of 500 000 elements were created and analyzed, 5 for constructing a priori probabilistic characteristics and 5 for constructing a posteriori ones. Approximately half of the first elements of each Markov chain were discarded due to low values of the likelihood function, then an analysis was carried out for autocorrelation of models, since neighboring models are dependent. As a result, there were about 2500 independent models that participated in the construction of probabilistic characteristics.

Figure 1 shows that in the "real" model at depths of 12, 28, and 46 km, the density function has local extrema. As a result of numerical experiments, it turned out that at a depth of 12 km, values of the a posteriori density function are more common than the average value of 2571, and for a depth of 28 km — less, which corresponds to local extrema of the true density function. However, no such phenomenon is observed for a depth of 46 km (Fig. 2).

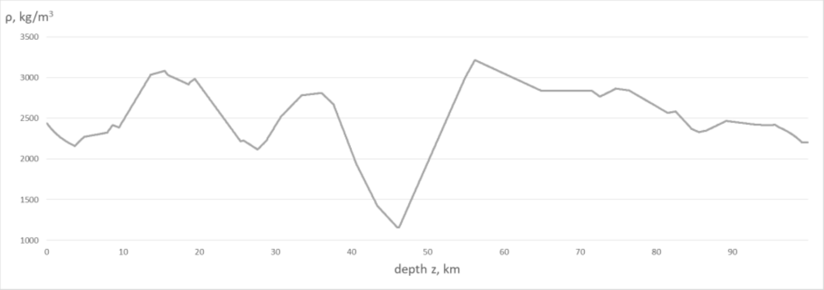

Fig. 1. Averaged density function of the "real" model depending on the depth

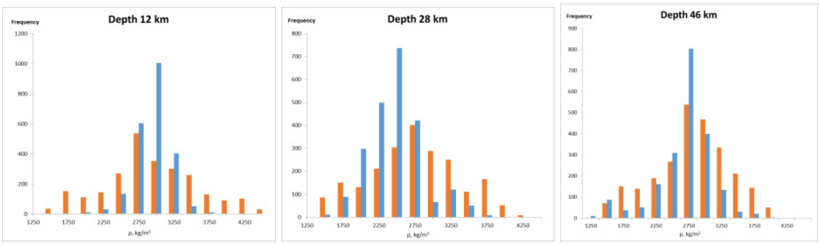

Fig. 2. Histograms of frequencies of values of a priori (orange) and a posteriori (blue) density function for depths of 12, 28 and 46 km

APPLICATION:

At the second stage of the work, the implemented numerical algorithm is planned to be used to find the distribution of parameters in the interiors of Venus according to known observational data.

For Venus, we use geodetic data; these data include mass, mean radius, mean moment of inertia and second degree tidal Love number k2 [6]. Unlike calculating mass and mean moment of inertia, the calculation of tidal Love number k2 from model parameters is a non-linear process. Markov Chain Monte Carlo algorithm is a way to determine the posterior probability distribution and the optimal values of the internal structure parameters of Venus with the geodetic data.

Acknowledgements:

The study was performed based on funding of Russian Scientific Foundation no. 23-22-00074, https://rscf.ru/project/23-22-00074.

References:

[1] *Tarantola A., Valette B.* Inverse problems = Quest for information // J. Geophysics. 1982. V. 50. Iss. 1. P. 159–170.

[2] *Tarantola A.* Inverse Problem Theory: Methods for Data Fitting and Model Parameter Estimation. N.Y.: Elsevier, 1987. 613 p.

[3] *Mosegaard K., Tarantola A.* Monte Carlo sampling of solutions to inverse problems // J. Geophysical. Research. 1995. V. 100. No. B7. P. 12431–12447. https://doi.org/10.1029/94JB03097.

[4] *Mosegaard K.* Resolution analysis of general inverse problemsthrough inverse Monte-Carlo sampling // Inverse Problems. 1998. V. 14. No. 3. P. 405–426. DOI : 10.1088/0266-5611/14/3/004.

[5] *Tarantola A.* Inverse Problem Theory and Methods for Model Parameter Estimation // Society for Industrial and Applied Mathematics. 2005. 342 p.

[6] *Amorim O., Gudkova T.V.* Earth-like viscoelastic models of Venus interior structure // 14th Moscow Solar System Symposium, 14M-S^3: Book of Abs. Moscow, 9–13 *Oct.* 2023.

14MS3-VN-PS-10
POSTER

ON STRESS STATE OF VENUS

T.V. Gudkova[1], A.V. Batov[1,2]
[1] *Schmidt Institute of Physics of the Earth RAS, Moscow, Russia, gudkova@ifz.ru*
[2] *Trapeznikov Institute of Control Sciences RAS, Moscow, Russia, batov@ipu.ru*

KEYWORDS:
Venus, gravity, topography, stress state

INTRODUCTION:

Venus has a global rift system stretching for thousands of kilometers. Moreover, there is now evidence of modern volcanism on Venus [1–2]. Intraplate earthquakes, moonquakes, and marsquakes show that seismic activity can be associated not only with plate tectonic events, volcanism can act as a trigger, and there is no doubt that Venus is a seismically active planet. For upcoming seismic experiments on Venus [3–5] it is important to know in which areas the stresses are large enough to cause quakes.

DATA:

The expansion of the gravity field data in terms of Legendre polynomials is known up to the 180th degree and order (SHGJ180u model) [6], topography data up to the 360th degree and order (SHTJV360u model) [7]. These models, presented as series of fully normalized coefficients, can be found on the Planetary Data System website (http://pds-geosciences.wustl.edu). Here we use the coefficients up to the 70th degree and order, since the correlation between the gravity and topography data decreases for higher harmonics. The topography and gravitational field of Venus are determined with respect to the reference surface, for which the surface of effectively equilibrium Venus is chosen [8]. The topography map is shown in Fig. 1.

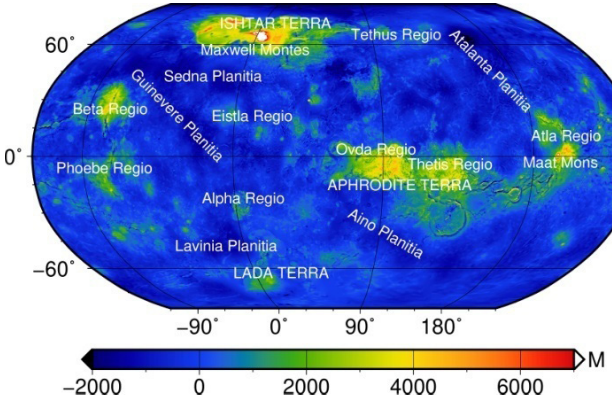

Fig. 1. Topographic map of Venus (in meters). Zero value corresponds to the average radius of the planet. The 60° meridian was chosen as the center of the projection. For clarity, areas with a height of more than 7000 m are marked in white

INTERIOR STRUCTURE MODELS:

Modeling of non-hydrostatic extensional-compression stresses and shear stresses was performed for test models of the internal structure of Venus V_16 and V_5 from [9], which satisfy all currently available observational data for Venus. The average crustal thickness of the models is 30 (V_16) and 70 (V_5) km, the average crustal density is 2800 kg/m^3.

METHOD:

A planet is modeled as an elastic, self-gravitational spherical body. It is assumed, that deformations and stresses which obey Hooke's law are caused by the pressure of relief on the surface of the planet and anomalous density, distributed by a certain way in the crust. Numerical simulation is based on a static approach [10–11]. The method for solving the problem of modeling non-hydrostatic stresses by the static method was described in detail in the Appendix of the work [12].

RESULTS:

Estimates of the stress state of the interior of Venus are carried out for two types of idealized models of inhomogeneous elasticity, which allow us to estimate the order of magnitude of stresses in the planet: 1) an elastic model, 2) a model with an elastic lithosphere of variable thickness (100–500 km) located on weakened layer, which has partially lost its elastic properties. The presence of a weakened layer under the lithosphere is modeled by a tenfold decrease in the value of the shear modulus μ in the layer under the lithosphere, which is considered to extend to the core.

In general, the level of non-hydrostatic stresses on Venus is not too high (Fig. 2). This result is consistent with the values obtained in [10–11], where the calculations were carried out using the data of the gravitational field and topography up to the 18th degree (accuracy of the gravitational field at that time). As expected, on the surface of the planet and in the crust, the greatest shear stresses appear in the region of Maxwell Montes on Ishtar Terra. Under the Maxwell Montes, shear stresses in the crust reach 80 MPa, compression values reach values of 125–150 MPa, depending on the model: 125 MPa for an elastic model, and 150 MPa for a model with a lithosphere of 100 km. Extensional stresses around this area are about 20 MPa.

The greatest extensional stresses occur in areas under such structures as Atalanta Planitia, Guinevere Planitia, Snegurochka Planitia, Lavinia Planitia, the Sedna Planitia, the Aino Planitia. The stress level in the lithosphere depends on the choice of the inhomogeneous elasticity model. Compression-extensional and shear stresses for a model with a lithosphere of 300 km (see Fig. 2) are higher than for an elastic model. The thinner the thickness of the lithosphere, the higher the stresses in it. In the area of the Aino Planitia, extensional stresses are 23 MPa for models with a lithosphere of 100 km, and 20

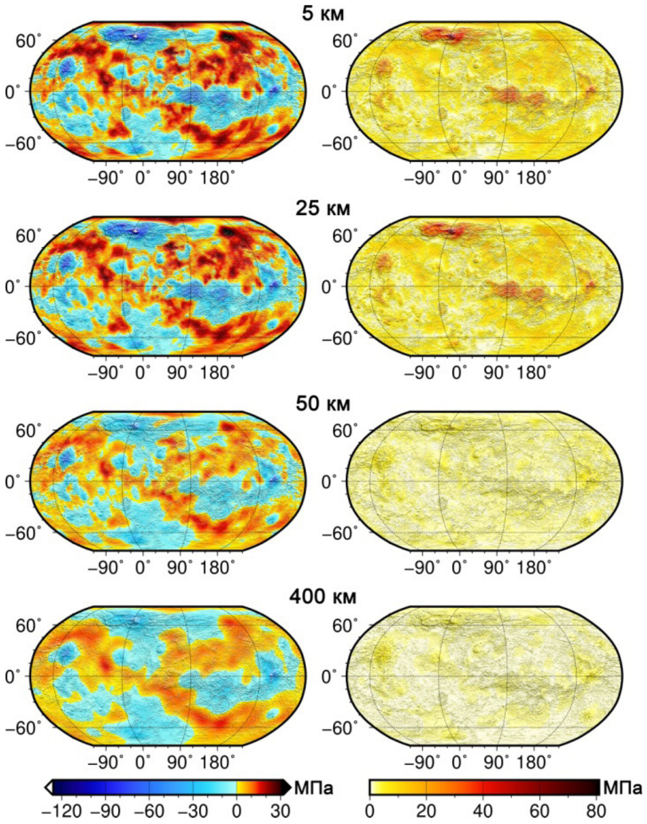

Fig. 2. Extensional-compression stresses (left) and shear stresses (right) (in MPa) in the crust at depths of 5 and 25 km and in the mantle at depths of 50 and 400 km for a model with a lithosphere of 300 km for model V_16 from [9]

MPa for a lithosphere thickness of 500 km. There is no significant difference in the values of stresses obtained for models with a crustal thickness of 30 and 70 km.

The previously accepted criterion for selecting zones with high shear stresses and the significant extensional stresses as the most probable areas of marsquake sources has justified expectations [13]. Here this technique is applied to Venus. The presented calculations can be of interest for choosing the location of the seismometer and interpreting seismic data in connection with the planned seismic experiments on Venus.

Acknowledgements:
The study was performed based on funding of Russian Scientific Foundation no. 23-22-00074 (https://rscf.ru/project/23-22-00074).

References:

[1] *Shalygin E.V., Markiewicz W.J., Basilevsky A.T. et al.* Active volcanism on Venus in the Ganiki Chasma rift zone // Geophysical Research Letters. 2015. V. 42. Iss. 12. P. 4762–4769. https://doi.org/10.1002/2015GL064088.

[2] *Herrick R.R., Hensley S.* Surface changes observed on a Venusian volcano during the Magellan mission // Science. 2023. V. 379. Iss. 6638. P. 1205–1208. DOI: 10.1126/science.abm77.

[3] Zasova L.V., Gorinov D.A., Eismont N.A. et al. Venera-D: A design of an automatic space station for Venus exploration // Solar System Research. 2019. V. 53. Iss. 7. P. 506–510. DOI: 10.1134/S0038094619070244.

[4] *Kremic T., Ghail R., Gilmore M. et al.* Long-duration Venus lander for seismic and atmospheric science // Planetary and Space Science. 2020. V. 190. Art. No. 104961. https://doi.org/10.1016/j.pss.2020.104961.

[5] *Tian Y., Herrick R.R., West M.E., Kremic T.* Mitigating power and memory constraints on a Venusian seismometer // Seismological Research Letters. 2023. V. 94. Iss. 1. P. 159–171. https://doi.org/10.1785/0220220085.

[6] *Konopliv A.S., Banerdt W.B., Sjogren W.L.* Venus gravity:180th degree and order model // Icarus. 1999. V. 139. Iss. 1. P. 3–18. https://doi.org/10.1006/icar.1999.6086.

[7] *Rappaport N.J., Konopliv A.S., Kucinskas A.B.* An improved 360 degree and order model of Venus topography // Icarus. 1999. V. 139. Iss. 1. P. 19–31. https://doi.org/10.1006/icar.1999.6081.

[8] *Zharkov V.N., Gudkova T.V.* On parameters of the Earth-like model of Venus // Solar System Research. 2019. V. 53. Iss. 1. P. 1–4. DOI: 10.1134/S0038094618060084.

[9] *Gudkova T.V., Zharkov V.N.* Models of the Internal Structure of the Earth-like Venus // Solar System Research. 2020. V. 54. Iss. 1. P. 20–27. DOI: 10.1134/S0038094620010049.

[10] *Zharkov V.N. Marchenkov K.I., Lyubimov V.M.* Long-wave tangential stresses in the lithosphere and mantle of Venus // Astronomicheskii Vestnik. 1986. V. 20. No. 3. P. 202–211 (In Russian).

[11] *Marchenkov K.I., Zharkov V.N.* Stresses in the Venus crust and the topography ofthe mantle boundary // Soviet Astronomy Letters. 1989. V. 15. P. 77–81.

[12] *Batov A.V., Gudkova T.V., Zharkov V.N.* Nonhydrostatic stress state in the Martian interior for different rheological Models // Izvestiya, Physics of the Solid Earth. 2019. V. 55. No. 4. P. 688–700. DOI: 10.1134/S1069351319040025.

[13] *Batov A.V., Gudkova T.V.* On correlation of non-hydrostatic stresses in the interior of Mars with the epicenters of marsquakes. // 14th Moscow Solar System Symp. 14M-S^3: Book of Abs. 9–13 Oct. 2023.

MOTION OF VENUS AND EARTH, AND FIBONACCI NUMBERS

V.A. Kotov
Crimean Astrophysical Observatory, Nauchny, Russia, vkotov@craocrimea.ru

KEYWORDS:
The Sun, Venus, Earth, rotation, pulsations, solar system

It is shown that motions of the Sun, Mercury, Venus and Earth are involved in close resonances with the participation of the Fibonacci numbers 2, 3, 5, 8 and 13, — a consequence of the peculiar role of the Hale's cycle P_H = 22.14(8) years [1] and the Sun's spinning with a period of P_S = 27.027(4) days (*synodic*) for our planetary system [2]:

$(1–3/\pi)P_H \approx P_S^{\,2}/2P_D \approx 3^3P_S/2 \approx P_E$,

where P_E is the Earth's orbital period, and P_D — the mean solar day. The remarkable diophantine relations are observed also for Venusian rotation with the sidereal period P_V = 243.023 days:

$P_V \approx 3^2P_S \approx 2P_E/3 \approx 3^5P_D \approx 3^7P_0$ = 243.015 days,

with $P_0 \approx$ 0.111 days, a period of "mysterious" pulsations of the Sun [3].

A hypothesis is advanced that (a) the Hale's cycle, the solar rotation period P_S and those of the Earth's motions (orbital and axial), united by the π number and the above Fibonacci numbers, present in fact fundamental timescales of the World, and (b) cosmic timescales P_S, P_E, P_D and P_0 characterize in fact the striving of objects, structures and processes of the Universe to recur in time and space. True nature of the solar P_0 pulsations and all above relations (precise to 0.2 %), proving singularity of the solar system, is however far from clear.

References

[1] *Kotov V.A., Sanchez F.M.* Solar 22 years cycle // Astrophysics and Space Science. 2017. V. 362. Iss. 1. Art. No. 6. 6 p. DOI: 10.1007/s10509-016-2985-8.
[2] *Kotov V.A.* Is the Earth's orbital motion linked to the spin rotation of the Sun? // Advances in Space Research. 2019. V. 63. Iss. 10. P. 3385–3389. https://doi.org/10.1016/j.asr.2019.01.018.
[3] *Kotov V.A., Haneychuk V.I.* Oscillations of solar photosphere: 45 years of observations // Astronomische Nachrichten. 2020. V. 341. Iss. 6–7. P. 595–599. https://doi.org/10.1002/asna.202013797.

COSMIC RAYS ARE INITIATORS OF STRONG EARTHQUAKES (*M* > 7)

N.P. Bulatova
Independent researcher, n.p.bulatova@mail.ru

KEYWORDS:
strong earthquakes, solar activity, anticorrelation, galactic cosmic rays, spatio-temporal distribution of the arthquakes, global seismicity

ANNOTATION:
Previously, the author investigated the influence of a number of cosmic factors (the Sun, Moon, and cosmic rays) on the number and distribution of earthquake groups characterized by different energies (magnitude from $M = 3$ to $M \geq 6$ in 2080–2000 [1]). At same time, for group with $M > 6.5–7.0$ (0–2000) the predominant role of cyclic changes in solar activity (SA) was revealed. Previously, it was believed that the greater the solar activity, the more earthquakes can occur [2–3]. When comparing the results of statistical analysis of the spatial and temporal distribution of a group of strong earthquakes ($NM \geq 7$) with a cyclical change in solar activity-the author obtained an unexpected result — anticorrelation of the maximum number of strong earthquakes in the minimum of CA solar activity [4]. To explain this phenomenon, the energy source was found — galactic cosmic rays [5–7]. It is obvious that energy particles are required to participate in the initiation of such strong earthquakes. In this study earthquake used (http://www.wdcb.ru/sep/index.html).

INTRODUCTION:
In spatiotemporal studies of the occurrence of earthquakes [1, P. 25; 2], it was concluded that both 1) endogenous (within the land distribution of physical fields) and 2) exogenous (cosmic) influence on global seismicity. Endogenous sources also include mechanical movements both inside and on the Earth's surface (lithospheric plates, uneven rotation of the Earth), and the geospheres themselves relative to each other. Exogenous sources include cosmic sources of gravitational, magnetic, radiation fields, etc. The Sun and Moon, which are closest to the Earth, have always been considered as such traditional sources of influence [1]. When studying the influence of a number of possible cosmic factors (the Sun, the Moon) on the number of earthquakes, the main role of cyclical changes in Solar activity (SA) was revealed [7]. Traditionally, it was believed that the greater the solar activity, the more earthquakes can occur. When comparing the results of statistical analysis of the time distribution of a groupN strong earthquakes with cyclical changes in solar activity — the author obtained an unexpected result-anticorrelation of the maximum number of strong earthquakes and the minimum of solar activity CA (W) [1–2].

To explain it, it was necessary to find an unknown source of energy for this phenomenon.

However, when comparing the distribution of the time series of the quantities N strong earthquakes (magnitude $M \geq 7.0$) from 1973 to 2005 with cyclic changes in solar activity (SA), as the distribution of numerical values W (Wulf numbers), contrary to the traditional view, the fact of anticorrelation of the maxima of the quantities of strong earthquakes (of was established 1).

The conclusion that seemed natural: the more solar activity (SA), the more earthquakes and volcanic eruptions should occur on Earth, was questioned. The author suggested that there may be some factors that have not yet been named and are not taken into account, for example, cosmic rays (CR, GCL). The author of this paper would like to test this probable effect of an increase in CR on the global seismicity of the Earth by studying the factors influencing the preparation and occurrence of strong earthquakes. It is known that the GCR intensity is related tomagnetic field of the solar wind, which significantly weakens it.

Preliminary analysis showed the complexity of the problem. Obviously, it is necessary to solve it in parts, starting with the behavior of the Sun itself, due to the cyclical nature of both the mid-latitude solar activity (moderate intensity component), and the strength and polarity of the high-latitude magnetic fields of the Sun (MPS) (magnetic component), etc. Special attention was paid to the ratio of these components [6].

Scientists have been conducting experiments to regularly monitor cosmic rays in the Earth's atmosphere since 1957 [6]. The indisputable value of studies of long-term variations in the intensity of galactic cosmic rays in the heliosphere and their connection with the solar wind lies in the length of the time series (covering four CA cycles).

References:

[1] *Bulatova N.P.*The latitude distribution of terrestrial seismicity in relation to the locations of the Sun and Moon // J. Volcanology and Seismology. 2005. No. 2. P. 57–78 (in Russian).

[2] *Sytinsky A.D.* On the influence of solar activity on the seismicity of the Earth // Reports of the Academy of Sciences of the USSR. 1973. V. 208. No. 5. P. 1078–1081 (in Russian).

[3] *Chizhevsky A.L.* Cosmic pulse of life. The Earth in the arms of the Sun. M.: Thought. 1965. P. 43–135 (in Russian).

[4] *Bulatova N.P.* Spatial-temporal study of seismicity of the Earth: diss. … candidate of physical and mathematical sciences. M.: Schmidt Institute of Physics of the Earth RAS. 2004. 120 p. (in Russian).

[5] *Bulatova N.P.* On the recognition of cosmic factors that affect the seismicity of the Earth: cosmic rays // Magyar Tudományos J. 2020. No. 42. P. 37–39. (in Russian).

[6] *Bulatova N.P.* Possible influence of GCL on the seismicity of the Earth // 15th Annual Conf. "Plasma Physics in the Solar System". 2020 P. 202. https://plasma2020.cosmos.ru/docs/PLASMA-2020-IKI-AbstractBook.pdf. (in Russian).

[7] *Krainev M.B., Bazilevskaya G.A., Kalinin M.S. et al.* Galactic Cosmic Ray Intensity in the Upcoming Minimum of the Solar Activity Cycle // Geomagnetism and Aeronomy. 2018. V. 58. No. 2. P. 169–177.

SESSION 4. SMALL BODIES (SB) ORAL SESSION

THE ORIGIN OF DISTANT TRANS-NEPTUNIAN OBJECTS

V.V. Emel'yanenko
Institute of Astronomy RAS, Moscow, Russia, vvemel@inasan.ru

KEYWORDS:
Trans-Neptunian objects, planet-disk interactions, N-body symplectic integration

INTRODUCTION:
The discovery of Sedna-type bodies has led to controversial discussions about the structure of the outer Solar system. To find out the origin of these distant trans-Neptunian objects moving in orbits with semimajor axes $a > 150$ au and perihelion distances $q > 40$ au, we study the dynamical evolution of a system consisting of the giant planets and a massive planetesimal disk for the age of the Solar system [1]. We carry out the full N-body symplectic integrations. Our results show that the collective gravity of the giant planets and massive planetesimals produces distant trans-Neptunian objects in a wide range of the initial disk mass. Secular resonances between planetesimals play a major role in increasing their perihelion distances. Distant trans-Neptunian objects are a natural consequence of models that include the migrating giant planets and a self-gravitating planetesimal disk.

References:
[1] *Emel'yanenko V.V.* Dynamical evolution of a self-gravitating planetesimal disk in the distant trans-Neptunian region // Astronomy and Astrophysics. 2022. V. 662. Art. No. L4. 7 p. https://doi.org/10.1051/0004-6361/202243324.

THE ACCURACY OF METHODS FOR ESTIMATING THE AGES OF PAIRS OF TRANS-NEPTUNIAN OBJECTS IN CLOSE ORBITS

V.D. Gusev, E.D. Kuznetsov
Ural Federal University, Ekaterinburg, Russia, vlad06gusev@gmail.com, eduard.kuznetsov@urfu.ru

KEYWORDS:
Trans-Neptunian objects, pairs of trans-Neptunian objects, Kholshevnikov metrics, Kuiper belt, celestial mechanics, numerical simulation

INTRODUCTION:
In the main asteroid belt, a large number of pairs of asteroids with close orbits that have a common origin have been found (see, e.g. [1–2]). The formation of such pairs or groups of small bodies in close orbits can be the result of collisions, high rotation speeds, disintegration of binary systems, and other processes (see, e.g. [3−5]). Secular resonances and mean-motion resonances can also lead to the motion of objects in similar orbits (see, e.g. [6]). The existence of collisional families of small bodies beyond the orbit of Neptune was proposed in [7]. The first family identified in the outer Solar System was associated with the dwarf planet (136108) Haumea [8]. In [9], a systematic search for statistically significant pairs and groups of dynamically correlated objects with semi-major axes of orbits greater than 25 au was carried out. Two pairs of trans-Neptunian objects (TNOs) were confirmed and six candidate pairs were found. The increase in the number of open TNOs has led to the discovery of new pairs. In [10], 26 pairs of TNOs were found in close orbits. 21 pairs of TNOs, in which one of the objects is binary, were found in [11]. All pairs found in [10] and [11] belong to the dynamically cold population of the Kuiper belt.

Standard methods for determining the age of pairs of small bodies in close orbits include: 1) analysis of the minimum distances between the orbits of objects (see, e.g. [12]), 2) analysis of simultaneous approaches of lines of nodes and lines of apsides of orbits of objects (see, e.g. [13]) and 3) low relative-velocity close encounters of objects [14]. In this paper, we study the accuracy of determining the age of model pairs by the first two methods. To estimate the distance between the orbits, one of the Kholshevnikov metrics was chosen [15]. When performing probabilistic modeling of the pair's dynamic evolution, we took into account the uncertainty of orbits, which is typical for trans-Neptunian objects.

To create model pairs, we used the criterion for the disintegration of an ultra-wide TNO binary system. Ultra-wide binary systems can disintegrate at times comparable to the age of the Solar System [16]. These bodies can be sources of pairs of trans-Neptunian objects in close orbits.

We considered several model pairs of TNOs that refer to the dynamically cold population of the Kuiper Belt. The age of the model pair was set by modeling the dynamic evolution of the pair. Age estimation methods were applied to pairs aged 1 and 10 Myr, and the dynamic evolution of pairs was studied at 1.5 and 15 Myr, respectively.

Numerical simulation of the dynamic evolution of the pair components was performed using the Rebound package [17]. A modified 15th order Everhart method with an adaptive step was used [18]. Disturbances from four giant planets and Pluto were taken into account.

The results showed that the accuracy of the age estimate significantly depends on the accuracy of determining the orbits of the pair. The orbit determination accuracy chosen by us is relatively high, but the age determination error is 10–30 % of the age value itself.

Acknowledgements:
The work was supported by the Ministry of Science and Higher Education of the Russian Federation via the State Assignment Project FEUZ-2020-0038 (EDK).

References:

[1] *Vokrouhlický D., Nesvorný D.* Pairs of Asteroids Probably of a Common Origin // The Astronomical J. 2008. V. 136. No. 1. P. 280–290. DOI 10.1088/0004-6256/136/1/280.
[2] *Pravec P., Vokrouhlický D.* Significance analysis of asteroid pairs // Icarus. 2009. V. 204. Iss. 2. P. 580–588. https://doi.org/10.1016/j.icarus.2009.07.004.
[3] *Benz W., Asphaug E.* Catastrophic Disruptions Revisited // Icarus. 1999. V. 142. Iss. 1. P. 5–20. https://doi.org/10.1006/icar.1999.6204.
[4] *Boehnhardt H.* Split comets // Comets II / ed. M.C. Festou, H.U. Keller, H.A. Weaver. 2004. V. 745. P. 301–316.
[5] *Jacobson S.A., Scheeres D.J.* Dynamics of rotationally fissioned asteroids: Source of observed small asteroid systems // Icarus. 2011. Iss. 214. No. 1. P. 161–178. https://doi.org/10.1016/j.icarus.2011.04.009.
[6] *de la Fuente Marcos C., de la Fuente Marcos R.* Far from random: dynamical groupings among the NEO population // Monthly Notices of the Royal Astronomical Society. 2016. V. 456. Iss. 3. P. 2946–2956. https://doi.org/10.1093/mnras/stv2885.
[7] *Chiang E.I.* A Collisional Family in the Classical Kuiper Belt // The Astrophysical J. 2002. V. 573. No. 1. P. L65–L68. DOI: 10.1086/342089.
[8] *Brown M.E., Barkume K.M., Ragozzine D., Schaller E.L.* A collisional family of icy objects in the Kuiper belt // Nature. 2007. V. 446. No. 7133. P. 294–296. DOI: 10.1038/nature05619.
[9] *de la Fuente Marcos C., de la Fuente Marcos R.* Dynamically correlated minor bodies in the outer Solar system // Monthly Notices of the Royal Astronomical Society. 2018. V. 474. Iss. 1. P. 838–846. https://doi.org/10.1093/mnras/stx2765.
[10] *Kuznetsov* E*.D., Al-Shiblawi O.M., Gusev V.D.* Dynamic Evolution of Pairs of Trans-Neptunian Objects // Solar System Research. 2022. V. 56. No. 2. P. 122–134. DOI: 10.1134/S003809462202006X.
[11] *Kuznetsov E.D., Al-Shiblawi O.M., Gusev V.D.* Dynamic evolution of pairs of trans-Neptunian objects: the case of binary and single objects in pair // Contributions of the Astronomical Observatory Skalnate Pleso. 2021. V. 51. No. 3. P. 226–240. https://doi.org/10.31577/caosp.2021.51.3.226.
[12] *Kuznetsov E.D., Rosaev A.E.* A Search for Young Asteroid Pairs with Close Orbits // Solar System Research. 2020. V. 54. No. 3. P. 236–252. DOI:10.1134/S0038094620030077.
[13] Rosaev A., Pl´avalov´a E., On relative velocity in very young asteroid families // Icarus. 2018. V. 304. P. 135-142
[14] Pravec A, Fatka P., D. Vokrouhlický et al. Asteroid pairs: A complex picture // Icarus. 2019. V. 333. P. 429–463. DOI: 10.1016/j.icarus.2019.05.014.
[15] *Kholshevnikov K.V., Kokhirova G.I., Babadzhanov P.B., Khamroev U.H.* Metrics in the space of orbits and their application to searching for celestial objects of common origin // Monthly Notices of the Royal Astronomical Society. 2016. V. 462. Iss. 2. P. 2275–2283. https://doi.org/10.1093/mnras/stw1712.
[16] *Campbell H.M., Stone L.R., Kaib N.A.* Close Trans-Neptunian Object Passages as a Driver of the Origin and Evolution of Ultrawide Kuiper Belt Binaries // The Astronomical J. V. 165. No. 1. Art. No. 19. 11 p. DOI: 10.3847/1538-3881/aca08e.
[17] *Rein H., Liu S.F.* REBOUND: an open-source multi-purpose N-body code for collisional dynamics // Astronomy and Astrophysics. 2012. V. 537. Art. No. A128. https://doi.org/10.1051/0004-6361/201118085.
[18] *Rein H., Spiegel D.S.* IAS15: a fast, adaptive, high-order integrator for gravitational dynamics, accurate to machine precision over a billion orbits // Monthly Notices of the Royal Astronomical Society. 2015. V. 446. Iss. 2. P. 1424–1437. https://doi.org/10.1093/mnras/stu2164.

SPECTRAL SIGNS AND PROBABLE MECHANISMS OF OPTICALLY THIN AND THICK DUSTY EXOSPHERE OF ACTIVE ASTEROIDS

V.V. Busarev[1,2], V.B. Puzin[2], S.I. Barabanov[2], M.P. Shcherbina[2,1]
[1] *Sternberg Astronomical Institute Lomonosov Moscow State University, Moscow, Russia, busarev@sai.msu.ru*
[2] *Institute of Astronomy RAS, Moscow, Russia*

KEYWORDS:
sublimation activity of asteroids, reflectance spectra, optically thin and thick dust exosphere, radiative transfer models, solar activity influence

INTRODUCTION:

During the previous decade, more than 30 objects with some signs of activity were found in Main asteroid belt (MAB) (e.g., [1] and references therein). Nearly a half of them are bodies of ~1-km or less in size, so called main-belt comets (MBCs), which had signs of a stronger (comet-like) activity [2]. We consider results of new spectrophotometric observations of eight main-belt primitive asteroids, in the depths of which water ice can survive, passed near perihelion distances in the present period of solar activity rise. Some of them displayed different signs of sublimation activity judging by the changes of their reflectance spectra (RS). Analysis of the RS are based on our previous observational data and results, as well as on their numerical simulations [3–5]. Possible reasons of formation of a thin or thick dusty exosphere around the asteroids are discussed.

SUMMARY OF OUR PREVIOUS RESULTS:

Here we briefly remind our former important results. Figure 1 shows normalized RS of four main-belt active asteroids (AAs) of primitive types (145, 704, 779, and 1474) in September 2012. Results of our numeric simulation (using the light-scattering and radiative-transfer theories) are presented in Figure 2 as model RS of a conditional primitive asteroid enveloped by a thin dusty exosphere (DE) with optical thickness of 0.5. The latter is assumed to contain aggregate particles of submicron constituents with different composition (water ice, tholins, and olivine).

One can see a good agreement of observational and model reflectance spectra of AAs surrounded by a thin DE in the period of a high solar activity in 2012, which made the DE more pronounced due to frequent solar flashes in the UV-range and related coronal mass ejections (CME) [4].

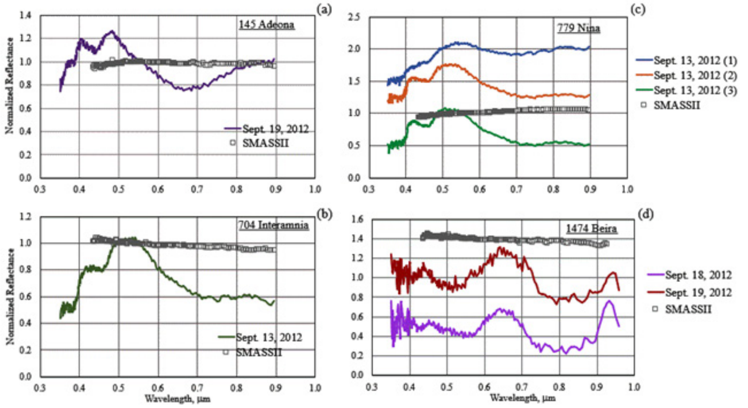

Fig. 1. The RS of four main-belt primitive asteroids, 145 Adeona, 704 Interamnia, 779 Nina, and 1474 Beira, obtained in September 2012, are shown together with their typical ones in standard (calm) conditions from the SMASSII database. We supposed that the detected features may be signs of a thin dust exosphere induced by sublimation of H_2O ice around the asteroids at a high subsolar temperature near perihelium and in the period of high solar activity (e.g., [3–4]).

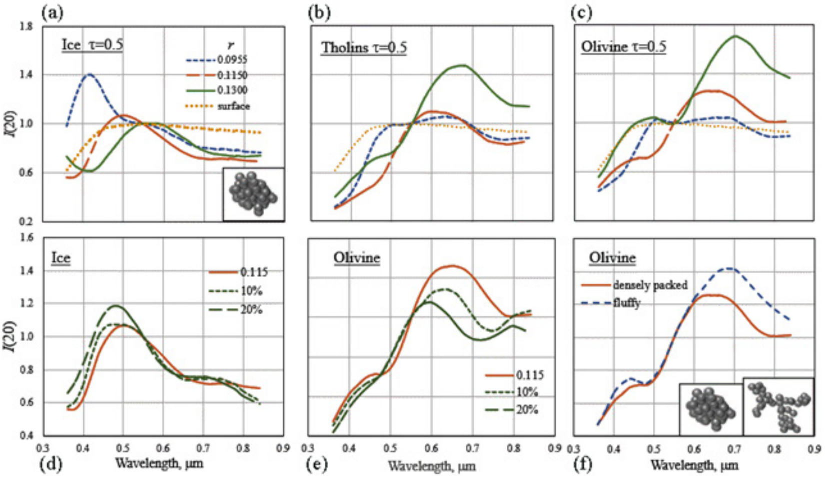

Fig. 2. Model RS of a conditional primitive asteroid (having a mean surface spectral characteristics with geometric albedo of 0.07 at 0.56 µm and a typical phase angle of 20°) enveloped by a thin DE (at optical thickness of 0.5) composed of aggregate particles with submicron constituents (their sizes are given in the right upper or bottom corners of the pictures) and different composition (water ice, tholins, and olivine) [4–5]

OBSERVATIONS OF NEW ASTEROIDS:

Spectrophotometric observations of 8 main-belt asteroids, 46 Hestia, 111 Ate, 117 Lomia, 164 Eva, 324 Bamberga, 372 Palma, 654 Zelinda, and 1021 Flammario, were performed in December 2022 using the 2-m telescope of Terskol Observatory under operation of Institute of Astronomy of Russian Academy of Science (IA RAS). The observatory is situated at high altitude of 3150-m above sea level, making favorable conditions for observations at shorter wavelengths. The telescope is equipped with a prism CCD-spectrometer (WI CCD 1240×1150 pixel) working in the range 0.35–0.97 µm, with $R \approx 100$ resolving power. DECH spectral package was used to reduce CCD data by means of standard procedures (such as flat-field correction and bias and dark subtraction) and to extract asteroid spectra. RS of the asteroids displayed changes related possibly to sublimation activity of ice and the presence of a thin DE, which will be shown and discussed in the presentation.

ON A PROBABLE MECHANISM OF A THIN DE OF AAS

According to our observational and model results [3–5], a thin DE to have ~0.5 optical thickness (call it as DE0.5). Such DE partially transmits sunlight reflected from the surface of asteroid to the observer and adds its own maxima of light scattering (typically in the range between ~0.4 and ~0.65 µm), wavelength positions of which are characteristic of dust particles' sizes from submicron to micron (~0.01÷1.0 µm). Besides, there is a possibility in the case to study not only sizes and structure of the dust particles but also their composition through the refractive index [4–5]. The problem with a thin DE of AAs is to find a mechanism, which could maintain it sufficiently close to the asteroid surface for a relatively long time (from several months to several years, taking into account duration of our observations of some AAs [3–4]). Even in calm conditions, the total effect of the pressure of sunlight and especially radiation pressure (based on exchange of charges between particles and electrons and protons of solar wind) to the smallest particles of DE in a weak gravitation field of AAs (weaker by several orders of magnitude than that of the Earth's) should quickly remove them from the vicinity of AAs. But just the latter factors probably ensure a longer existence of DE on AAs. As is known from lunar space exploration (e.g., [6–9]), an electrostatic field of photoemission nature can detach dust particles of mentioned sizes from the surface and cause them to levitate. At the same time, a photoelectron and charged dust sheath with a thickness from 2–3 tens of centimeters to several meters and a strength of electrostatic field of the order of several volts per meter is formed above the surface of the asteroid near the subsolar point [8–9]. As follows from analytical and 2D numeric modeling (e.g., [8–10]), the thickness of such dust-filled plasma sheath on the illuminated side of an airless body increases to one kilometer at the dawn and dusk regions, where the greatest potential difference (up to ~300 V/m) of the electrostatic field is achieved, it accelerates the movement of the smallest charged dust particles so that they leave the gravitational field of the body. As it is known, the presence and movement of fine dust over the lunar surface was first discovered with the TV-cameras on Surveyor 5, 6, and 7 (1967–1968), at the very beginning of intense lunar exploration in XX century [6–7]. Although it was supposed to, there were previously no direct (observational) confirmations of a thin dusty exosphere presence on asteroids. We assume that electrostatic field and solar radiation pressure on the sunlit side of an AA (which is just observed by spectrophotometric method) can lead to the formation of a thin and relatively stable DE0.5 with a height of ~10–10^3 m (as follows from [8–10] and references therein) consisting of small particles of mentioned sizes (~0.01–1.0 µm) in the form of a close to the surface plasma-dust layer, providing that the rate of injection of dust particles into this layer at sublimation of H_2O ice on AAs exceeds the rate of their ejection by the electrostatic field near the terminator.

Although at a qualitative level, as follows from radiative-transfer theory, separate maxima of light scattering in RS of AAs characteristic of different compounds will be "diluted" by multiple scattering of light at higher optical thickness, so to be of interest of RS modeling of a conditional primitive asteroid enveloped by an intermediate DE (with optical thickness of ~1.5 or DE1.5) and a thick DE (or DE3.0) composed of aggregate particles with submicron constituents to have ideas about the tendency and rate of DE optical thickness influence to RS of AAs.

Acknowledgements:
The authors (VVB, SIB, and MPS) express their gratitude to Russian Science Foundation (grant no. 22-12-00115) for supporting the work.

References:

[1] *Jewitt D., Hsieh H.H.* The Asteroid-Comet Continuum // https://arxiv.org/. 2022. arXiv: 2203.01397.
[2] *Hsieh H.H., Micheli* M., Kelley *M.S.P. et al.* Observational Characterization of Main-belt Comet and Candidate Main-belt Comet Nuclei // The Planetary Science J. 2023. V. 4. No. 3. Art. No. 43. 22 p. DOI: 10.3847/PSJ/acbdfe.
[3] *Busarev V.V., Barabanov S.I., Rusakov V.S., Puzin V.B.* Spectrophotometry of (32) Pomona, (145) Adeona, (704) Interamnia, (779) Nina, (330825) 2008 XE3, and 2012 QG42 and laboratory study of possible analog samples // Icarus. 2015. V. 262. P. 44–57. https://doi.org/10.1016/j.icarus.2015.08.001.
[4] *Busarev* V.V., *Petrova E.V., Irsmambetova T.R.* Simultaneous sublimation activity of primitive asteroids including (24) Themis and (449) Hamburga: Spectral signs of an exosphere and the solar activity impact. // Icarus. 2021. V. 369. Art. No. 114634. 18 p. DOI10.1016/j.icarus.2021.114634.
[5] *Petrova E.V., Busarev V.V.* On the Prospects for Estimating the Properties of Particles in an Active Asteroid Exosphere by Features in the UV and Visible Reflectance Spectra // Solar System Research. 2023. V. 57. Iss. 2. P. 161–174. https://doi.org/10.1134/S0038094623020065.
[6] Criswell D.R. Lunar Dust Motion // Proc. of the 3rd Lunar Science Conf. 1972. V. 3. P. 2671–2680.
[7] *Rennilson J.J., Criswell D.R.* Surveyor observations of lunar horizon-glow // The Moon. 1974. V. 10. P. 121–142.
[8] *Nitter T., Havnes O.* // Earth, Moon, and Planets. 1992. V. 56. Iss. 1. P. 7–34.
[9] *Lee P.* Dust levitation on asteroids // Icarus. 1996. V. 124. P. 181–194.
[10] *Hartzell C.M.* Dynamics of 2D electrostatic dust levitation at asteroids // Icarus. 2019. V. 333. P. 234–242. https://doi.org/10.1016/j.icarus.2019.05.013.

THE STUDY OF MEAN MOTION RESONANCE MULTIPLET FOR NEAR SUN ASTEROIDS

T.Yu. Galushina, O.N. Letner, O.M. Syusina
Tomsk State University, Tomsk, Russia, tatyana.galushina@mail.tsu.ru, oksana.letner@gmail.com, olga_syusina@rambler.ru

KEYWORDS:
near Sun asteroids, mean motion resonances, multiplet, machine analysis, automation.

INTRODUCTION:

The study of mean motion resonances in the dynamics of asteroids and major planets is of great theoretical and applied importance from the point of view of solving the asteroid hazard problem. During such research often there is a need to analyze a large number of time series of resonant arguments, since to complete the picture, it is necessary to consider not only the main argument, but the entire multiplet. In order to facilitate this task, we have developed an algorithm and a program for machine analysis and automatic classification of the behavior of the resonant arguments. The developed automation was implemented in the IDA software [1] and applied to the study of the dynamics of resonant objects with perihelion distances not exceeding 0.15 AU.

STUDY TECHNIQUE:

Mean motion resonances appear when orbital periods of asteroid and planet are commensurable. The resonant (critical) argument is considered as a characteristic of the resonant motion [2–3]

$$\beta = k_1\lambda' + k_2\lambda + k_3\omega' + k_4\omega + k_5\Omega' + k_6\Omega, \qquad (1)$$

where λ is the mean longitude, ω is the perihelion longitude, Ω is the longitude of the ascending node. The apostrophe refers to the asteroid, and the unprimed values denote to the planet. k_1, k_2, k_3, k_4, k_5, k_6 are integers.

The commensurability of orbital periods is determined from the expression $\dot{\beta} = 0$, meaning that the first time derivative of the critical argument is equal to zero. The first time derivative is called the resonant band and is usually denoted as α [4]. In the case of asteroid motion, the secular frequencies $\dot{\omega}'$, $\dot{\omega}$, $\dot{\Omega}'$, $\dot{\Omega}$ are small compared to the orbital frequencies $\dot{\lambda}'$, $\dot{\lambda}$, so the resonance band takes the form

$$\alpha = k_1\dot{\lambda}' - k_2\dot{\lambda}. \qquad (2)$$

Orbital frequencies (mean motions) can be explicitly expressed through the semi-major axes of the asteroid and the planet. This means that the resonance condition (2) with unique k_1 и k_2, but different k_3, k_4, k_5, k_6 will correspond to one and the same values of the semi-major axes. Such a structure is called a resonant multiplet.

The following two condition should be performed during multiplet constructing:

$$k_1 + k_2 + k_3 + k_4 + k_5 + k_6 = 0, \qquad (3)$$

$$k_5 + k_6 = 0, 2, 4, \ldots (4)$$

By the nature of the behavior of the argument β, the stability of the resonance or its absence is estimated. The resonance is stable, if β librates, that is it oscillates around a certain center with an amplitude less 360°. Circulation (or resonance absence) is such behavior when β change from 0 to 360°, not having a certain center. The change from libration to circulation and vice versa points to a mixed type of behavior, in which the resonance is defined as unstable.

The multiplet size depends on the resonance order $|k_1 - k_2|$ and its analysis requires the classification of a significant number of time series, especially in the case of studying a lot of objects. Therefore, we considered it reasonable to use an automation algorithm, the idea of which is described in [5] and is as follows. The values of the argument are divided into subintervals ranging from 0 to 360°, and the hit of each value in the formed cells is fixed. We introduced a number of modifications into this algorithm, in particular, splitting the time interval to determine the mixed types of behavior of resonance arguments.

Using the IDA software, a multiplet of resonant arguments is formed by enumeration of the coefficients k_3, k_4, k_5, k_6. For each such set, using numerical integration, the orbital evolution of objects is constructed at a given time interval. The obtained files of the evolution of resonant arguments are automatically analyzed by the resonant behavior classification program. As a result of the machine analysis, the nature of the argument behavior is determined (circulation, libration, or mixed behavior) and graphs of the arguments depending on time are plotted.

RESEARCH RESULTS:

A preliminary search for mean motion resonances in the motion of asteroids with small perihelion distances using a modified IDA software showed that 33 of them move in the vicinity of resonances with one or several planets simultaneously. The Lobbie integrator was used to numerically integrate the asteroid motion equations. A previous resonant motions study of asteroids with small perihelion distances is described in [6].

For some researched asteroids, resonant multiplets were constructed and analyzed, and, as a result, the behavior of each argument and the type of resonant interaction were determined. The machine analysis of the arguments behavior in course of time showed that for all asteroids within the one multiplet, the resonant arguments are of the same type. The only difference is that for cases of libration, the center of argument oscillation shifts when varying the coefficients k_3, k_4, k_5, k_6.

Figure 1 shows an example of the behavior of some arguments from the 7/2 resonance multiplet of asteroid 431760 2008 HE with Jupiter. For this resonance, the multiplet includes 28 possible variants of the resonance argument. Fig. 1 shows the behavior of four of them. The resonant argument $2\lambda' - 7\lambda + 5\omega'$ is called the main argument and is determined by the ratio of the coefficients $|k_1 - k_2| = k_3$. Its behavior for this case demonstrates the change of circulation to libration and vice versa (mixed type). Fig. 1 shows that the type of resonant behavior does not change when changing the values of the coefficients, but the center of libration of the arguments shifts. This behavior is typical for the entire multiplet.

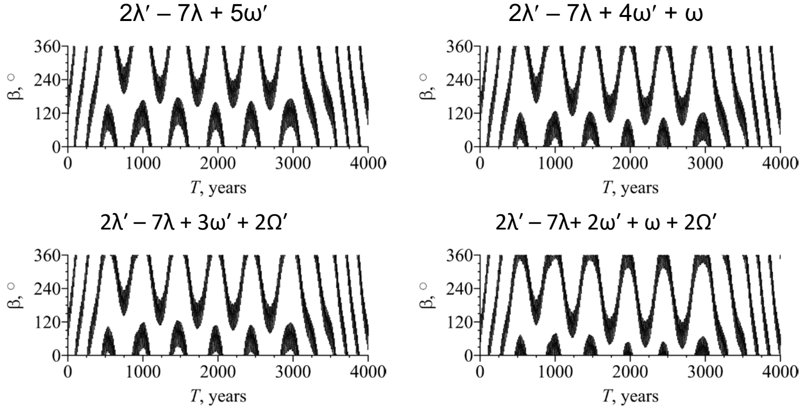

Fig. 1. Behavior of arguments of resonant multiplet corresponding to the 7/2 resonance of asteroid 431760 2008 HE with Jupiter

The analysis of resonant multiplets showed that in most cases it is sufficient to consider the behavior of the main critical argument to identify the features of the resonant interaction of the studied asteroids with planets. The developed algorithm and program for automating the process of classifying the resonant arguments behavior significantly reduced the time costs and the probability of random errors when processing received data.

Acknowledgements:
This work was supported by the Russian Science Foundation (no 19-72-10022; https://rscf.ru/en/project/19-72-10022/).

References:

[1] *Galushina T.Yu., Letner O.N.* Modified version of IDA software and its application to the study of the motion of asteroid 2007 PR10 // Astronomical and Astrophysical Trans. 2021. V. 32. Iss. 4. P. 355–370.
[2] *Murray C.D., Dermott S.F.* Solar system dynamics. Cambridge: Cambridge University Press, 1999. 592 p.
[3] *Nesvorny D., Ferraz-Mello S., Holman M., Morbidelli A.* Regular and Chaotic Dynamics in the Mean-Motion Resonances: Implications for the Structure and Evolution of the Asteroid Belt // Asteroids III / eds. Bottke W.F., Cellino A., Paolicchi P., Binzel R.P. Tucson: Univ. Arizona Press. 2003. P. 379–394.
[3] *Author A.B.* Third example of a cited book. Example Publishing House, 2011. 134 p.
[4] *Grebenikov E.A., Ryabov Yu.A.* Rezonansy i malyye znamenateli v nebesnoy mekhanike [Resonances and small denominators in celestial mechanics]. Moscow: Science, 1978. 128 p. (in Russian.)
[5] *Sekhar A., Asher D.J., Vaubaillon J.* Three-body resonance in meteoroid streams // Monthly Notices of the Royal Astronomical Society. 2016. V. 460. Iss. 2. P. 1417–1427. https://doi.org/10.1093/mnras/stw1086.
[6] *Galushina T.Yu., Letner O.N., Syusina O.M., Niganova E.N.* Influence of the Yarkovsky Effect on Mean Motion Resonances of Asteroids with Small Perihelion Distances // Russian Physics Journal. 2022. V. 65. No. 5. P. 878–885. DOI: 10.1007/s11182-022-02709-y.

ON PERTURBATIONS IN THE ROTATIONAL MOTION OF THE ASTEROID (99942) APOPHIS DURING ITS 2029 EARTH ENCOUNTER

A.V. Melnikov[1], K.S. Lobanova[1,2]
[1] *Central Astronomical Observatory RAS, Saint Petersburg, Russia, melnikov@gaoran.ru*
[2] *Saint Petersburg State University, Saint Petersburg, Petrodvorets, Russia*

KEYWORDS:
near-Earth objects, asteroids, close encounters, rotational dynamics, (99942) Apophis, Yarkovsky effect

INTRODUCTION:
Asteroid (99942) Apophis is considered one of the most dangerous objects in terms of potential Earth collision (see e.g. [1–2]). By means of numerical simulations of the rotational dynamics of Apophis, perturbations in rotational motion of small asteroids during their close encounters with Earth have been studied [3–7].

RESULTS:
It has been established that the close encounter of Apophis with Earth in 2029 may result significant changes in the rotational speed of the asteroid and in the orientation of its rotational axis. The dependences of the change in the period of rotation of the asteroid on both the parameters of the orbit and its rotational state before approaching the Earth are studied in detail. Examples of the obtained dependences of the change in the rotation period of Apophis P with time in the vicinity of the approach point are shown in Figure 1.

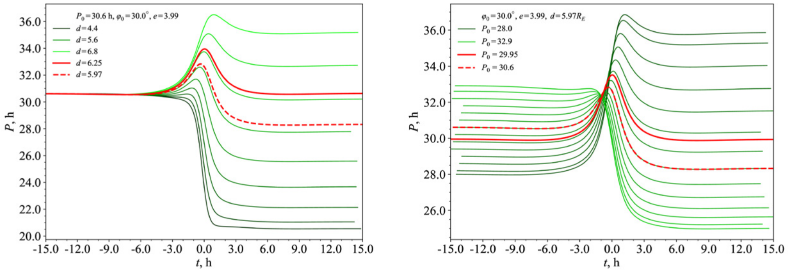

Fig. 1. The change of the rotational period of the asteroid P during its close encounter with Earth, plotted for different values of the pericentric distance d (*left*) and initial period values P_0 (*right*). Solid red line corresponds to the value of P_0 for which $\Delta P = 0$. Dotted red line corresponds to the value of P_0 for Apophis [8]. The moment $t = 0$ corresponds to the point of the closest approach to Earth; R_E is the radius of the Earth

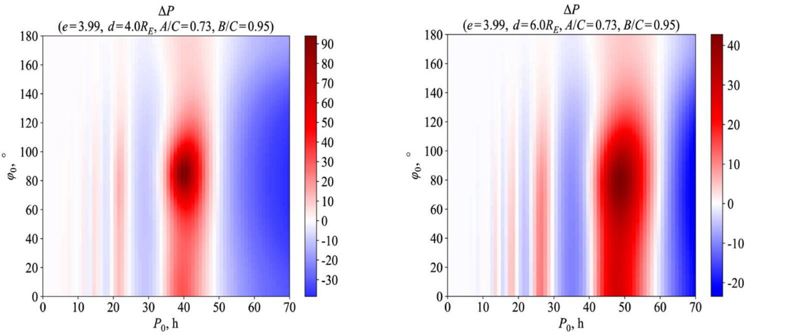

Fig. 2. The dependencies of the value ΔP (in hours) of the change in the rotational period of the asteroid due to its close encounter with Earth on the initial values of the rotational period P_0 and the angle φ_0 between the rotational axis and the orbital plane for different values of the pericentric distance d. A/C and B/C are ratios of the main central moments of inertia of Apophis [7].

The figure shows: the eccentricity e, the pericentric distance $d = a(e - 1)$), the rotation period P_0, and the inclination of the rotation axis to the orbital plane φ_0 of the asteroid until the moment of approach to the Earth. Figure 2 for different values of d shows examples of dependences of the change in the value of the rotation period of the asteroid $\Delta P = P_{final} - P_0$, where P_{final} is the rotation period of Apophis after approaching the Earth, on P_0 and φ_0. It is shown that perturbations in the rotational motion of the asteroid during its close encounter with Earth affect noticeably its further orbital dynamics through the change of the value of the Yarkovsky effect (see also [2–7]).

Acknowledgements:
The study was funded by a grant Russian Science Foundation no 23-22-00306 (https://rscf.ru/project/23-22-00306/).

References:

[1] *Sokolov L.L., Bashakov A.A., Pitjev N.P.* Peculiarities of the motion of asteroid 99942 Apophis // Solar System Research. 2008. V. 42. No. 1. P. 18–27. DOI: 10.1134/S0038094608010036.
[2] *Farnocchia D., Chesley S.R., Chodas P.W. et al.* Yarkovsky-driven impact risk analysis for asteroid (99942) Apophis // Icarus. 2013. V. 224. Iss. 1. P. 192–200. https://doi.org/10.1016/j.icarus.2013.02.020.
[3] *Scheeres D.J., Ostro S.J., Werner R.A. et al.* Effects of Gravitational Interactions on Asteroid Spin States // Icarus. 2000. V. 147. Iss. 1. P. 106–118. https://doi.org/10.1006/icar.2000.6443.
[4] *Souchay J. Lhotka C., Heron G. et al.* Changes of spin axis and rate of the asteroid (99942) Apophis during the 2029 close encounter with Earth: A constrained model // Astronomy and Astrophysics. 2018. V. 617. Art. No. A74. https://doi.org/10.1051/0004-6361/201832914.
[5] *Boldrin L.A.G., Araujo R.A.N., Winter O.C.* On the rotational motion of NEAs during close encounters with the Earth // European Physical J. Special Topics. 2020. V. 229. No. 8. P. 1391–1403. DOI:10.1140/epjst/e2020-900200-5.
[6] *Melnikov A.V.* Rotational Dynamics of Asteroids Approaching Planets // Solar System Research. 2022. V. 56. No. 4. P. 241–251. https://doi.org/10.1134/S0038094622040062.
[7] *Benson C.J., Scheeres D.J., Brozović M. et al.* Spin state evolution of (99942) Apophis during its 2029 Earth encounter // Icarus. 2023. V. 390. Art. No. 115324. https://doi.org/10.1016/j.icarus.2022.115324.
[8] *Pravec P., Scheirich P.,* Ďurech *J. et al.* The tumbling spin state of (99942) Apophis // Icarus. 2014. V. 233. P. 48–60. https://doi.org/10.1016/j.icarus.2014.01.026.

WHAT WE CAN LEARN ABOUT DUST IN COMETS FROM THEIR POLARIMETRY

E. Zubko[1] , G. Videen[2]
[1] *Planetary Atmospheres Group, Institute for Basic Science (IBS), 55 Expo-ro, Yuseong-gu, Daejeon 34126, South Korea;*
[2] *Space Science Institute, 4750 Walnut Street, Boulder Suite 205, CO 80301, USA; evgenij.s.zubko@gmail.com*

KEYWORDS:
Comets; polarization; classification; dust; modeling; retrieval; microphysics

INTRODUCTION:

While initially unpolarized sunlight gets scattered from comets, it acquires a partial linear polarization. Because cometary dust particles are randomly oriented in space, their linear-polarization plane appears oriented in only one of two discrete positions. It either coincides with the scattering plane or appears to be perpendicular to that plane. The former case is referred to as the phenomenon of the *negative polarization* and it manifests itself near backscattering (phase angles $\alpha < 30°$); whereas, the latter one is known as the *positive polarization* that reaches its maximum amplitude at side scattering ($\alpha \sim 80° – 100°$). These two phenomena are widely observed in comets (see, e.g. [1–3] and references therein). As such they provide important clues for understanding the microphysics of cometary dust. However, an interpretation of observations is dependent on the morphology of the model dust particles used. A reliable interpretation is possible only with a realistic model of cometary dust shape, such as the *agglomerated debris particles* shown at the top of Fig. 1. These particles were examined versus laboratory optical measurements of cosmic-dust analogs and they have been proven to be capable of accurate retrievals of microphysics (e.g., [3] and therein). This capability significantly enhances the confidence in the scientific return from observations.

BRIEF SUMMARY OF RESULTS OF POLARIMETRY OF COMET:

All comets reveal the phenomenon of negative polarization at small phase angles $\alpha < 30°$. In the aperture-averaged mode, the negative polarization could be as strong as $P_{min} \approx –3\%$; whereas, the imaging polarimetry demonstrates that in the vicinity of the nucleus, the negative polarization could be twice stronger, $P_{min} \approx –6\%$.

Unlike the negative polarization, the positive polarization shows a dramatic dispersion in comets, with the amplitude of the positive-polarization branch spanning the range from $P_{max} \approx 5\%$ [4] up to 35%, or even larger P_{max} in the case of a disintegrating comet [5]. Comets were classified into three types based on their amplitude of the positive polarization: low-P_{max} comets, high-P_{max} comets, and the Hale-Bopp-type comets [1, 2]. While P_{max} was considered to be a persistent feature of the given comet, recent observations suggest this is not necessarily the case [6]. P_{max}, similar to other light-scattering characteristics of a comet, could be subject to very quick and dramatic variations. An important feature of comets with different P_{max} is that their maximum of polarization occurs at different phase angles. In the low-P_{max} comets, it is observed at $\alpha_{max} \sim 80°$ and in the high-P_{max} comets $\alpha_{max} \sim 95° – 100°$ [1,2].

BRIEF SUMMARY OF THE MODELING RESULTS:

Agglomerated debris particles demonstrate that the negative polarization in comets unambiguously constrains the imaginary part of refractive index in their dust to be $\mathrm{Im}(m) \leq 0.02$ [3]. On the other hand, the location of the positive-polarization maximum $\alpha_{max} > 90°$ observed in the high-P_{max} comets necessarily suggests $\mathrm{Im}(m) > 0.3$ [3]. These two features lead to the conclusion that a coma consists of at least two types of particles [2]. One of them should have a weak material absorption, that is consistent with Mg-rich silicates; whereas, another type necessarily has large $\mathrm{Im}(m)$, resembling carbonaceous materials. It is important to stress that both components have been indeed found *in situ* in comets (see discussion in [2, 3]). However, a mixture of these two components easily reproduces the polarimetric observations of the vast majority of comets; see examples in Fig. 1. Therefore, the dispersion of P_{max} in comets reveals different ratios of silicate and carbonaceous particles in their coma. This ratio presumably may characterize the age of comets.

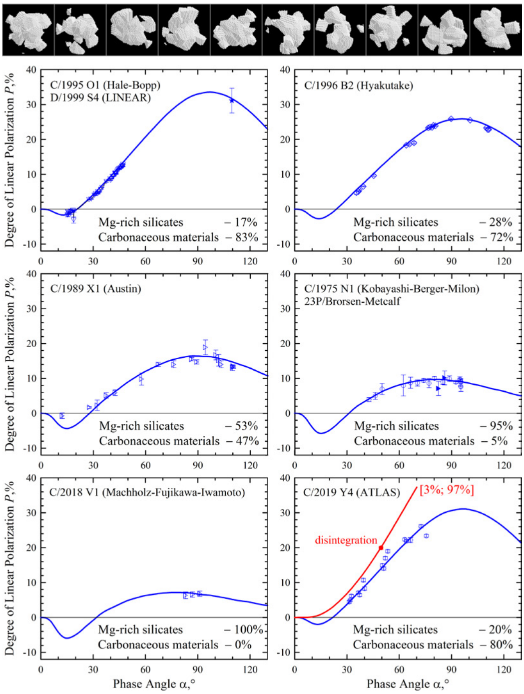

Fig. 1. Ten examples of the agglomerated debris particles (top) and phase functions of the degree of linear polarization measured in several comets in the blue-green part of the spectrum (symbols) with their best fits (lines). The chemical composition of the coma is given in % (vol.) in the legend.

References:

[1] *Hines D.C., Levasseur-Regourd A.-C.* Polarimetry observations of comets: Status, questions, future pathways // Planet. Space Sci. 2016. V. 123. P. 41–50.

[2] *Zubko E., et al.* The positive-polarization of cometary comae // Planet. Space Sci. 2016. V. 123. P. 63–76.

[3] *Zubko E., Videen G.* Polarimetric remote sensing of cometary particles // Light, Plasmonics and Particles / eds. M.P. Mengüç, M. Francoeur. Elsevier, 2023. P. 327–347.

[4] *Zubko E., et al.* Extremely low linear polarization of Comet C/2018 V1 (Machholz–Fujikawa–Iwamoto) // Icarus. 2020. V. 336. Art. 113453

[5] *Zubko E., et al.* Polarization of disintegrating Comet C/2019 Y4 (ATLAS) // MNRAS. 2020. V. 497. P. 1536–1542.

[6] *Chornaya E., et al.* C/2020 S3 (Erasmus): Comet with a presumably transient maximum of linear polarization Pmax // MNRAS. 2023. V. 518. P. 1617–1628.

THE 2.5-METER WIDE FIELD SURVEY TELESCOPE (WFST) DESIGN AND HUNTING FOR NEOS

W.T. Luo on behalf of WFST collaboration
Institute of Deep Space Science, Deep Space Exploration Laboratory, Anhui, China, wtluo@ustc.edu.cn

KEYWORDS:
wide field survey telescope, optical design, survey strategy, NEOs, orbits

INTRODUCTION:

As the first and the largest imaging survey telescope in China, WFST will starts its commissioning by the end of 2023. It is equipped with a 2.5-meter diameter primary mirror, an active optics system, and a mosaic CCD camera with 0.73 gigapixels on the primary focal plane for high-quality image capture over a 6.5-square-degree field of view. Its wide FOV of 6.5 square degree, a depth of *r* band 22.5 mag at 30 seconds exposure as well as high resolution imaging with 0.33”/pix, enables highly efficient Near Earth Objects (NEOs) hunting. Based on the Granvik’s model, WFST will discover thousands of near Earth asteroids every night.

The left panel of Figure 1 shows the ray-tracing simulation of the optical design of WFST, and the right panel is the simulated WFST observation image.

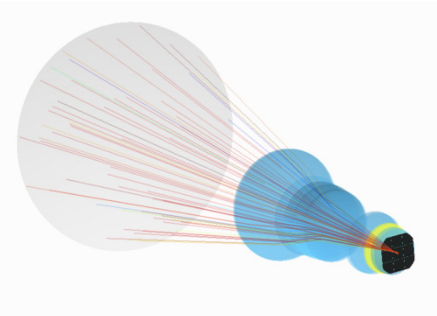

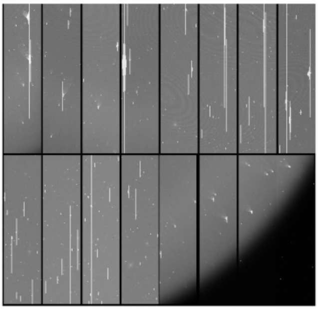

Fig. 1. PHOSIM simulated optical desgin of WFST (*left*); The simulated 90s exposure time of a CCD from the WFST FOV edge (*right*)

References:

[1] WFST collaboration; Scince for The 2.5-meter Wide Field Survey Telescope (WFST) // SCMPA invited. June. 2023 (in print).

[2] *Peterson J., Dutta A, Jernigan G. et al.* PhoSim: A Tool to Simulate Astronomical Images One Photon at a Time // 235th American Astronomical Society meeting. Bull. American Astronomical Society. 2020. V. 52. No. 1. Art. No. 313.03.

DISTANT COMETARY OUTBURSTS: A NON-GRAVITATIONAL MECHANISM OF ORBIT PERTURBATION

D.V. Belousov, A.K. Pavlov
Ioffe Institute, Saint Petersburg, Russia, dom.999.bel@gmail.com

KEYWORDS:
comets, Oort cloud, cometary outbursts, cosmic rays, free radicals, supernovae

INTRODUCTION:

Comet activity has been detected at vast range of heliocentric distances up to 35 AU [1]. At the activity stage, a comet increases unexpectedly its brightness by raising the number of reflecting dust particles in the halo area. The activity of long-period comets at distances above 3 AU, where sublimation of water ice is negligible, can be triggered by amorphous-ice-transition, sublimation of volatile gases and recombination of free radicals [2]. Due to the high efficiency of the last mechanism at very low temperatures, the recombination of radicals could cause detected distant cometary activity and even activity in the Oort cloud.

The main source of long-period comets — Oort cloud — includes many cometary nuclei at heliocentric distances of 10^4–10^5 AU. At such distances, solar radiation is strongly suppressed, and cometary nuclei reside in the hibernation stage with an equilibrium surface temperature of about 10 K. However, comets in the Oort cloud experience episodic heating events by passing O and B stars or supernovae [3]. In addition, galactic cosmic rays constantly bombard cometary nuclei in the Oort cloud. The long-term irradiation at low temperatures contributes to the accumulation of free radicals in cometary ice. By raising the temperature of irradiated ice or when the critical concentration of radicals is obtained, the fast recombination of radicals occurs with a significant energy release [2]. This effect can trigger distant cometary outbursts with the emission of gas and dust.

It is believed that only gravitational mechanisms, as the influence of a passing star, the tidal effect of the galactic disk and the encounter with molecular clouds, affects the stability of cometary orbits in the Oort cloud [4]. However, due to low orbital velocities in the Oort cloud, the expected distant cometary activity can result in significant changes in a comet's orbit. Herein we present a non-gravitational mechanism for changing the orbit of a comet in the Oort cloud.

MODEL:

A jet of gas and dust from a comet surface produce a non-gravitational acceleration. The resulting shift of the cometary orbit towards lower perihelion distances causes comets to fall under the gravitational influences of the giant planets or enter the inner part of the Solar system. We use the classical approach to calculate changes in the parameters of comet's orbit from [4].

To estimate the value of non-gravitational acceleration created by dust and gas flux from the comet surface, we created the model of comet outburst in the Oort cloud [5]. According to our model, the recombination of radicals increases the temperature of a surrounding matter. Upon reaching a critical temperature of amorphous-to-crystalline ice transition, CO gas is released from amorphous ice. Released gas gives rise to high pressure zones beneath the surface. These zones are highly unstable and can be suddenly break up with concomitant dust and gas ejection through cracks. The amplitude of the recoil acceleration is determined by the penetration depth of amorphous-to-crystalline transition front and the area of subsurface cavities in comets. The latter parameter is unknown and can be obtained only from observations of short-period comets (i.e., 67P/Churyumov-Gerasimenko).

RESULTS:

From the model, the mass of ejected material during the outburst is estimated to be in the range of 10^8–10^{10} kg. From Fig. 1, comets with radius <1 km could be ejected from the Oort cloud by one outburst more efficiently than by gravitational mechanisms.

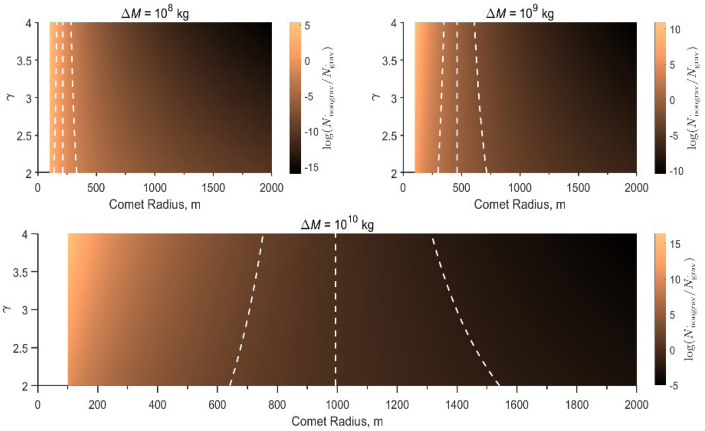

Fig. 1. Comets fluxes from the Oort cloud to the inner part of the Solar system due to gravitational and non-gravitational (cometary outburst) mechanisms. The ratio of fluxes for three masses of ejected material is presented as a function of a comet radius and an exponent in the distribution of comets in the current Oort cloud. The white dotted curves from left to right show the flux ratio 10^2, 10^0, 10^{-2}

CONCLUSION:

Comets in the Oort cloud can experience outbursts with a total ejected mass similar to the observed cometary outburst in the inner Solar system. Although it is impossible to detect activity of comets at Oort cloud distances, we can evaluate the impact of gas and dust jet on the stability of the comet's orbit. The total effect of cometary outbursts during the evolution of the Oort cloud could lead to a decrease in the number of long-period small-radius comets. In addition, cometary activity in the Oort cloud and other distant regions beyond the Kuiper belt can be a source of large amounts of dust and ice particles.

References:

[1] *Jewitt D., Kim Y., Mutchler* M. *et al.* Cometary activity begins at Kuiper belt distances: evidence from C/2017 K2 // The Astronomical J. 2021. V. 161. No. 4. Art. No. 188. 11 p. DOI 10.3847/1538-3881/abe4cf.

[2] *Pavlov A.K., Belousov D.V., Tsurkov D.A., Lomasov V.N.* Cosmic ray irradiation of comet nuclei: a possible source of cometary outbursts at large heliocentric distances // Monthly Notices of the Royal Astronomical Society. 2022. V. 511. Iss. 4. P. 5909–5914. https://doi.org/10.1093/mnras/stac497.

[3] *Stern S.A., Shull J.M.* The influence of supernovae and passing stars on comets in the Oort cloud // Nature. 1988. V. 332. Iss. 6163. P. 407–411. DOI: 10.1038/332407a0.

[4] *Fernandez J.A.* Long-period comets and the Oort cloud // Earth, Moon, and Planets. 2000. V. 89. Iss. 1. P. 325–343. DOI: 10.1023/A:1021571108658.

[5] *Belousov D.V., Pavlov A.K.* Cometary outbursts in the Oort cloud // Asteroids, Comets, Meteors Conference. Flagstaff. USA. 2023. Abs. 2067.

UV-INFLUENCE ON DUST PARTICLES ELECTROSTATIC LIFT-OFF PROCESSES IN EXPERIMENTAL SET-UP

I. Kuznetsov[1], I. Shashkova[1], A. Poroykov[2], A. Zakharov[1], A. Lyash[1], S. Bednyakov[1], G. Dolnikov[1], A. Dubov[1], A. Kartasheva[1], M. Essam[1], E. Kronrod[4], O. Voshchan[1], P. Stoliarenko[3]

[1] *Space Research Institute RAS, Moscow, Russia, kia@cosmos.ru*
[2] *National Research University "Moscow Power Engineering Institute", Moscow, Russia*
[3] *Lomonosov Moscow State University, Moscow, Russia*
[4] *Vernadsky Institute of Geochemistry and Analytical Chemistry RAS, Moscow, Russia*
[5] *Kazan Federal University, Kazan, Russia*

KEYWORDS:
dust, lunar dust, dusty plasma, dust dynamics

INTRODUCTION:
The direct observations of the lunar horizon glow that made more than 50 years ago by the Surveyor-7 automatic spacecraft [1] and Apollo-17 astronauts [2] are one of the most mysterious observations related to Moon and are still under debate. [3–5] and other authors stated that the electric potential of the lunar surface in the terminator region and in the lunar nightside can highly vary and reach as low as minus 4000 V. [6] estimated the possible electric field on the Moon up to 3000 V/cm. Levitation mechanism explanation is based on the idea that the electrically charged surface and electrically charged dust grains repel each other. A very similar phenomenon is proposed for most of the celestial atmosphereless bodies. Solar UV irradiation suggested as one of the main drivers of the particle activity. Due to much lower gravity force, the increasing of the dust dynamics on the asteroids [7, 8] and Martian satellites Phobos and Deimos [9, 10] is predicted. [11] estimated the electric field on asteroids in the range of 500–1500 V/cm. Alongside the theoretical works, there is an experimental simulation approach [12, 13] that can help to solve the dust dynamics mystery.

In this work, we describe the experimental simulation approach to the airless dust particles dynamics. We simulated the several varieties of the electrostatic-field and UV-irradiation (147 nm lightwave) cross-influence on the particle activity.

Acknowledgements:
This work was partially funded by 10th program of the Experimental Laboratory Astrophysics and Geophysics NCPM.

References:
[1] *Rennilson J.J., Criswell D.R.* Surveyor Observations of Lunar Horizon-Glow // Moon. 1974. V. 10. P. 121–142.
[2] *Zook H.A., McCoy J.E.* Large scale lunar horizon glow and a high altitude lunar dust exosphere // Geophysical Research Letters. 1991. V. 18. Iss. 11. P. 2117–2120. https://doi.org/10.1029/91GL02235.
[3] *Stubbs T.J., Vondrak R.R., Farrell W.M.* A dynamic fountain model for lunar dust // Advances in Space Research. 2006. V. 37. Iss. 1· P· 59–66. https://doi.org/10.1016/j.asr.2005.04.048.
[4] *Halekas J.S., Delory G.T., Lin R.P. et al.* Lunar Prospector observations of the electrostatic potential of the lunar surface and its response to incident currents // J. Geophysical Research: Space Physics. 2008. V. 113. Iss. A9. https://doi.org/10.1029/2008JA013194.
[5] *Farrell W., Stubbs T., Vondrak R. et al.* Complex electric fields near the lunar terminator: The near-surface wake and accelerated dust // Geophysical Research Letters. 2007. V. 34. Iss. 14. Art. No. L14201. https://doi.org/10.1029/2007GL029312.
[6] *De B.R., Criswell D.R.* Intense localized photoelectric charging in the lunar sunset terminator region, 1. Development of potentials and fields // J. Geophysical Research. 1977. V. 82. Iss. 7. P. 999–1004. https://doi.org/10.1029/JA082i007p00999.

[7] *Lee P.* Dust Levitation on Asteroids // Icarus. 1996. V. 124. Iss. 1. P. 181–194. https://doi.org/10.1006/icar.1996.0197.
[8] *Yeo L.H., Wang X., Deca J. et al.* Dynamics of electrostatically lofted dust on airless planetary bodies // Icarus. 2021. V. 366. Art. No. 114519. https://doi.org/10.1016/j.icarus.2021.114519.
[9] *Popel S.I., Golub' A.P., Zakharov A.V., Zelenyi L.M.* Dusty plasma near the surface of phobos // J. Experimental and Theoretical Physics Letters. 2017. V. 106. Iss. 8. P. 485–490. https://doi.org/10.1134/S0021364017200115.
[10] *Krivov A.V., Hamilton D.P.* Martian dust belts: Waiting for discovery // Icarus. 1997. V. 128. Iss. 2. P. 335–353. https://doi.org/10.1006/icar.1997.5753.
[11] *Rennó N., Kok J.* Electrical Activity and Dust Lifting on Earth, Mars, and Beyond // Space Science Reviews. 2008. V. 137. P. 419–434. https://doi.org/10.1007/s11214-008-9377-5.
[12] *Wang X., Schwan J., Hsu H.W. et al.* Dust charging and transport on airless planetary bodies // Geophysical Research Letters. 2016. V. 43. Iss. 12. Art. No. 6103. https://doi.org/10.1002/2016GL069491.
[13] *Orger N.C., Toyoda K., Masui H., Cho M.* Experimental investigation on silica dust lofting due to charging within micro-cavities and surface electric field in the vacuum chamber // Advances in Space Research. 2019. V. 63. Iss. 10· P. 3270–3288. https://doi.org/10.1016/j.asr.2019.01.045.

MICROWAVE DISCHARGE EXPERIMENTS ON SAMPLES OF A METEORITE SUBSTANCE AND LUNAR REGOLITH SIMULANTS FOR PLASMA-DUST CLOUD MODELLING

V.D. Borzosekov[1,2], N.S. Akhmadullina[3], A.S. Sokolov[1], T.E. Gayanova[1], V.D. Stepakhin[1], A.V. Knyazev[1], E.V. Voronova[1], E.A. Obraztsova[4], A.D. Rezaeva[1,2], A.V. Ishchenko[5], I.A. Weinstein[5], V.I. Grokhovsky[5], O.N. Shishilov[4,6], N.N. Skvortsova[1]

[1] *Prokhorov General Physics Institute RAS, Moscow, Russia, borzosekov@fpl.gpi.ru*
[2] *Peoples' Friendship University of Russia (RUDN University), Moscow, Russia*
[3] *Baikov Institute of Metallurgy and Materials Science RAS*
[4] *Moscow Institute of Physics and Technology (National Research University), Dolgoprudny, Moscow Region, Russia*
[5] *Ural Federal University, Ekaterinburg, Russia*
[6] *MIREA — Russian Technological University, Institute of Fine Chemical Technologies, Moscow, Russia*

KEYWORDS:
space dust, microwave discharge, plasma-dust cloud, Tsarev meteorite, regolith simulant

INTRODUCTION:
Space dust [1] has a lot of possible sources in the Solar system. Few of them are meteoroids interaction with an atmosphere of an astronomical body [2] and meteoroid impacts [3]. In the both cases, at least at some point of evolution of the process, there exists a plasma dust-cloud. This cloud is a complex medium containing neutral gases (atomic and molecular), plasma, melt and dust particles. The typical range of plasma temperature is 3000–10000 K and the plasma density 10^{13}–10^{17} and depends on many factors (e.g. chemical and geological composition of meteoroid, surface and atmosphere; distance from the meteoroid). For understanding of evolution of space dust, plasma-dust cloud and for study of its interaction with various materials it is necessary to develop experimental methods for modelling of such a medium. One of the possible methods could be implemented with microwave discharge in powder mixtures of metals (or semiconductors) and dielectrics [4]. This method allows fast (tens of microseconds) heating of powder mixtures with melting, evaporation and ejection of the initial substance into the reaction volume. Thus, a plasma-dust cloud with gas temperatures ~5000 K and plasma densities ~10^{14} cm^{-3} is formed. In this work we present the results of the recent experiments on modelling of the plasma-dust cloud with microwave discharge in powder mixtures relevant to space dust: substance of Tsarev meteorite (L5 ordinary chondrite found in 1968 in Volgograd district, USSR); regolith simulant LMS-1D (lunar mare dust simulant produced by Exolith Lab, USA); ilmenite (mineral occurring both on the Earth and on the Moon).

EXPERIMENTAL SETUP:
The experiments were carried out at the MIG-3 gyrotron complex [5] in the GPI RAS (Moscow). Microwave radiation of the 75 GHz 400 kW gyrotron was used for the experiment. Duration of the microwave pulse was up to 8 ms. The microwave radiation was introduced into the plasma chemical reactor [6,7] vertically from the bottom input window (diameter is 120 mm). A powder sample (mass is 1–2 g) in the form of a thin layer (~1 mm) is located on the quartz disk (diameter is 80 mm) within the reactor. The radius of the gaussian microwave beam is about 50 mm at the location of a sample. A quartz tube (diameter is 70 mm, length is 100 mm) is vertically placed on the quartz disk inside the reactor along its axis to limit expansion of the plasma-cloud and contamination of the reactor metallic walls. To monitor physical processes during the experiments the following diagnostics are used: microwave detectors (reflected and transmitted radiation); optical spectrometers (plasma

radiation, solid body thermal radiation); high-speed cameras (fine dynamics of dust-cloud evolution). Post-analysis includes: scanning electron microscopy with energy dispersive X-rays analysis — to study change in the morphology of the particles and to determine elemental composition; transmission electron microscopy — to find nano sized materials synthesized in the experiments; X-ray diffraction analysis — to determine and quantify phase composition; dynamic light scattering — to determine particle size distribution before and after the experiment.

EXPERIMENTAL RESULTS:

Three types of samples (Fig. 1*a*–*c*) were used in the experiments: 1) substance of the Tsarev meteorite was milled 2 times at 600 rpm for 10 min each time with a planetary ball mill Fritsch Pulverisette 7; 2) regolith simulant LMS-1D mixtures with 10 % (mass) Fe fine powder or with 10 % of Mg powder PA-4; 3) commercially available ilmenite mineral (with 3 % rutile fraction and 0.4 % zircon fraction) was grinded manually in an agate mortar for 10 min.

The samples 1 and 3 were in the air atmosphere and the sample 2 was in the argon atmosphere during the experiments. For all three types of samples the microwave discharge was exited with following formation of a plasma-dust cloud (Fig. 2) that lasted (at least as a vapor-dust cloud) substantially longer (up to 100 ms) then the microwave pulse (<8 ms). As microwave breakdown in powder mixtures depends on electromagnetic wave intensity, metal powder concentration, metal particle size (optimal size is about skin depth δ) it was expected to achieve it in the sample 2 (LMS-1D mixture with 10 % Mg powder). For the samples 1 (Tsarev meteorite) and 3 (ilmenite), which do not contain a particular metal powder, the breakdown was much less expected, as it is considered for the discharge to start at the contacts of metal and dielectric particles. It seems that for the sample 1 the abundant mineral inclusions of metals (Fe, Mg, Al, Ni or their alloys) were enough to start the discharge, and for the sample 3 $FeTiO_3$ with semiconducting properties could do the same. It should be noted that microwave discharge plays a crucial role in the experiment. Without it the conventional microwave heating approach (even considering thermal instability growth for dielectrics) do not yield enough temperatures for evaporation of most of the substances for the used in the experiments electromagnetic wave intensities (<20 kW/cm^2) and pulse durations (<8 ms).

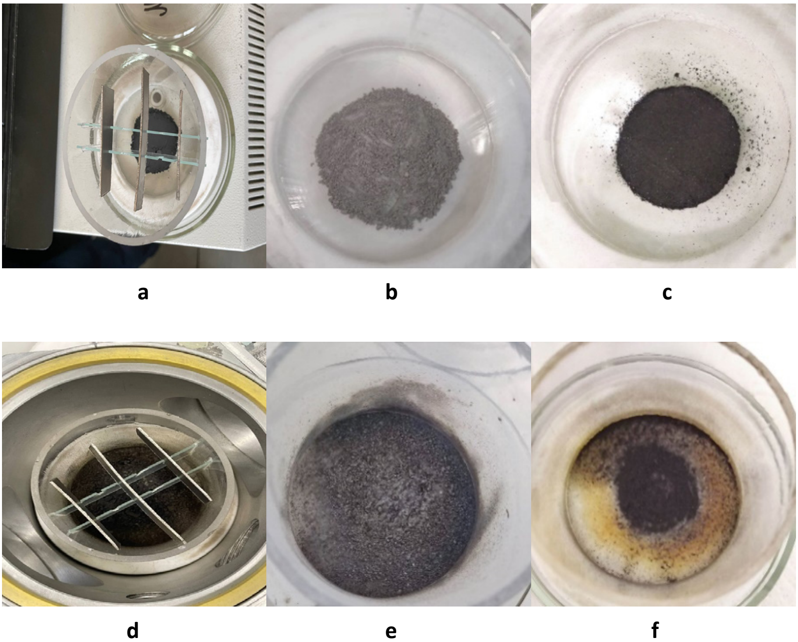

Fig. 1. The samples before (**a**–**c**) and after (**d**–**f**) the experiments: **a**, **d** — Tsarev meteorite; **b e** — LMS-1D regolith simulant with 10 % Mg; **c f** — ilmenite

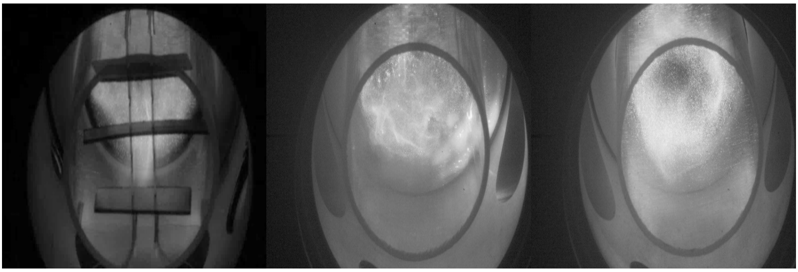

Fig.2. Video frames (exposition ~1 μs) from the high-speed camera Phantom VEO 710L obtained ~20 ms after the microwave pulse: **a** — Tsarev meteorite; **b** — LMS-1D regolith simulant with 10 % Mg; **c** — ilmenite.

CONCLUSIONS:

For the first time a plasma-dust cloud was successfully obtained with microwave discharge in powder mixtures from the space dust relevant samples: Tsarev meteorite, LMS-1D regolith simulant, ilmenite. Microwave absorption, optical emission spectra and plasma-dust cloud dynamics was obtained during the experiments. After the experiments the samples were transferred to post-analysis. Such a result allows further more complicated studies (e.g. abiogenic synthesis of precursors of complex organic molecules from inorganic molecules in a plasma-dust medium, imitation experiments on space dust deposition on various construction materials).

ACKNOWLEDGEMENTS:

The authors express their sincere gratitude to V.V. Kachmar who during her work at the GPI RAS conducted the study of modern commercially available lunar regolith simulants, chose and obtained for the experiments LMS-1D and LHS-1D simulants from Exolith Lab.

References:

[1] *Kuznetsov I.A., Zakharov A.V., Zelenyi L.M. et al.* Dust Particles in Space: Opportunities for Experimental Research // Astronomy Reports. 2023. V. 67. Iss. 1. P. 35–60. DOI: 10.1134/S1063772923010110.

[2] *Bronshten V.A.* Physics of Meteoric Phenomena. Dordrecht; Holland; Lancaster: D. Reidel Publishing Company, 1983. 358 p.

[3] *Gerasimov M.V., Ivanov B.A., Yakovlev O.I., Dikov Yu.P.* Physics and chemistry of impacts // Earth, Moon, and Planets. 1998. V. 80. Iss. 1. P. 205–259. DOI:10.1023/A:1006322032494.

[4] *Skvortsova N.N., Malakhov D.V., Stepakhin V.D. et al.* Initiation of dusty structures in chain reactions under the action of gyrotron radiation on a mixture of metal and dielectric powders with an open boundary // J. Experimental and Theoretical Physics Letters. 2017. V. 106. Iss. 4. P. 262–267. DOI: 10.1134/S0021364017160135.

[5] *Batanov G.M., Belousov V.I., Bondar' Y.F. et al.* A new MIG-3 gyrotron complex for creation and heating of plasma in the L-2M stellarator and the first experimental results // Plasma Physics Reports. 2013. V. 39. Iss. 13. P. 1088–1095. DOI: 10.1134/S1063780X1307012X.

[6] *Batanov G.M., Berezhetskaya N.K., Borzosekov V.D. et al.* The plasma chemical reactor on basis of microwave discharge at mixtures of metal-dielectric powders // Uspekhi Prikladnoi Fiziki (Advances in Applied Physics). 2013. V. 1. No. 5. P. 564–570 (in Russian).

[7] *Sokolov A.S., Akhmadullina N.S., Borzosekov V.D et al.* Plasmochemical system for synthesis of micro- and nanoparticles having controlled compositions and structures on the basis of a microwave discharge in gyrotron radiation // Izvestiya Vysshikh Uchebnykh Zavedenii. Radiofizika. 2022. V. 65. No. 11. P. 927–942.

SIMULATION EXPERIMENTS ON THE DEPOSITION OF CHARGED PARTICLES OF LMS-1D REGOLITH ON THE SOLAR PANELS OF SPACECRAFT

A.S. Sokolov[1], T.E. Gayanova[1], V.D. Borzosekov[1], V.D. Stepakhin[1], N.S. Akhmadullina[2], E.V. Voronova[1], E.A. Obraztsova[3], N.T. Vagapova[4], I.V. Badurin[4], E.S. Loginova[4], N.N. Skvortsova[1]

[1] *Prokhorov General Physics Institute RAS, Moscow, Russia, dmc63@yandex.ru*
[2] *Baikov Institute of Metallurgy and Materials Science RAS, Moscow, Russia*
[3] *Moscow Institute of Physics and Technology (National Research University), Dolgoprudny, Moscow Region, Russia*
[4] *JSC "Research-Production Enterprise "KVANT", Moscow, Russia*

KEYWORDS:
low-temperature plasma, dusty plasma, regolith, gyrotron, microwave radiation, solar panels

In this report we present the results of experiments on depositing charged particles, which imitate the levitating dust on the Moon, on surface of solar panels. The simulation experiment is based on the similarity between the processes that develop in the laboratory experiments with regolith and the processes that occur on the Moon during its bombardment by micro-meteoroids. In the experiments we use the artificial lunar regolith LMS-1D. The LMS-1D Lunar Mare Dust Simulant has been developed by Exolith Lab for dust mitigation experiments and other applications where very fine dust is needed. In these experiments, 10 % pure magnesium was added, as was described in [1] for the generation of ensembles of levitating particles. Under the action of the gyrotron radiation on the regolith, nonlinear physical-chemical processes develop (breakdown, chain plasma chemical reactions, and particle scattering by the Coulomb mechanism), which lead to the appearance of a levitating cloud of particles.

The experimental plasma chemical complex on which these experiments were made is presented on the Figure 1 and described in the work [2].

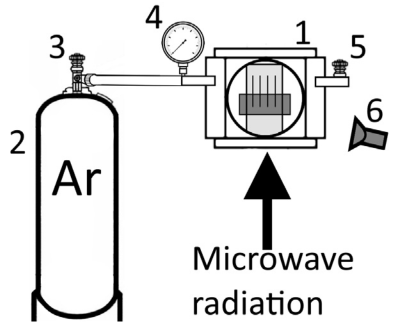

Fig. 1. Plasma chemical complex: **1** — plasma chemical reactor with regolith and solar panels inside, **2** — compressed argon, **3** — gas input valve, **4** — manometer, **5** — gas output valve, **6** — high speed camera

Diagnostics used in the experiment include:

- balanced microwave measurements that allow one to evaluate incident, transmitted and reflected radiation what makes it possible to estimate reaction efficiency;
- spectrometric measurements from which it is possible to determine the temperature of various areas in the reactor;
- high-speed video measurements allow one to observe the dynamics of plasma-dust cloud during the experiment.

Previously, the deposition of regolith particles on metal plates was studied [3–44]. The solar panels were placed above the regolith in the reactor (gyrotron power up to 400 kW, radiation frequency of 75 GHz, microwave pulse up to 8 ms) filled with atmospheric pressure argon. View of placed solar panel is presented on Figure 2.

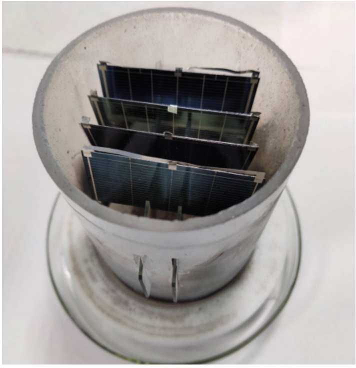

Fig. 2. The view of solar batteries in reactor

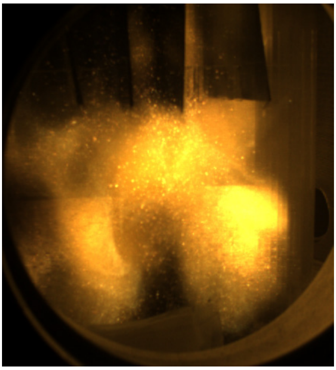

Fig. 3. View of particle cloud in plasma chemical reactor

Levitating particles are observed for hundreds of milliseconds. Figure 3 shows the solar panels against the background of a cloud of particles. The effect of the levitating cloud on the surface of solar panels is studied. Figure 4 shows particles deposited on the solar panel.

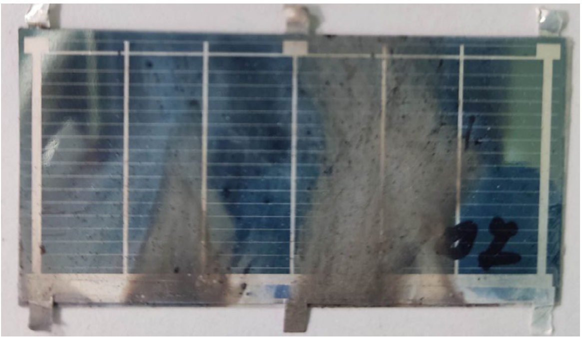

Fig. 4. Regolith particles deposited on the surface of the solar panel

Experimental results are presented on deposition of charged particles that imitate the levitating dust (dusty plasma) on the Moon on solar panels obtained with scanning electron microscopy and presented on Figure 5

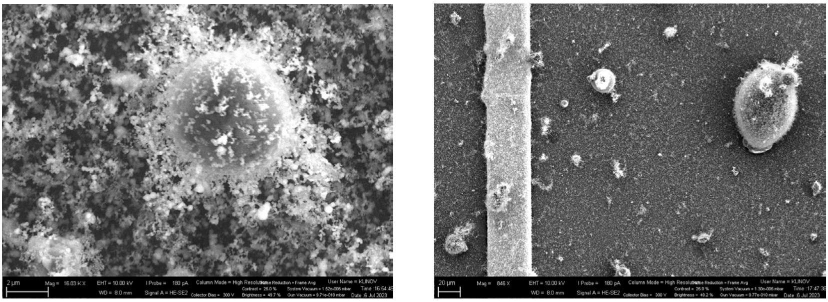

Fig. 5. Micrographs of particles deposited on the surface of the solar panel

The levitating dust obtained under laboratory conditions (ensembles of charged regolith particles) can be used in imitation experiments on creating samples of solar panels with modified surface for further development of methods of its cleaning (under conditions of Lunar missions) for space technology.

Acknowledgements:
The authors express their gratitude to the entire science team participated in the experiments on plasma chemical complex. Also, sincere gratitude to V.V. Kachmar who during her work at the GPI RAS conducted the study of modern commercially available lunar regolith simulants, chose and obtained for the experiments LMS-1D and LHS-1D simulants from Exolith Lab.

References:

[1] *Skvortsova N.N., Maiorov* S.A., *Malakhov D.V. et al.* On the dust structures and chain reactions induced over the regolith by gyrotron radiation // J. Experimental and Theoretical Physics Letters. 2019. V. 109. Iss. 7. P. 441–448. https://doi.org/10.1134/S0021364019070130.

[2] *Sokolov A.S., Akhmadullina N.S., Borzosekov V.D. et al.* Plasmachemical complex of synthesis of micro- and nanoparticles with controlled composition and structure based on microwave discharge in gyrotron radiation // Radiophysics and Quantum Electronics. 2022. V. 64. No. 11. P. 701–709.

[3] *Skvortsova N.N., Stepakhin V.D., Sorokin A.A. et al.* Microwave Simulation Experiments on Regolith (Lunar Dust) Deposition on Stainless Steel // Materials. 2021. V. 14. Iss. 21. Art. No. 6472. https://doi.org/10.3390/ma14216472.

[4] *Skvortsova N.N., Stepakhin V.D., Borzosekov V.D. et al.* Microwave Plasma Imitation Experiments on Deposition of Lunar Dust on Metal Plates // Plasma Physics Reports. 2023. V. 49. No. 1. P. 120–128. https://doi.org/10.1134/S1063780X22601833.

SPECIFIC FEATURES OF DUSTY PLASMA AND WAVE PROCESSES IN THE EXOSPHERE OF MERCURY

Yu.N. Izvekova, S.I. Popel, A.P. Golub'
Space Research Institute RAS, Moscow, Russia, izvekova@iki.rssi.ru

KEYWORDS:
dusty plasma, exosphere of Mercury, electrostatic oscillations, nonlinear waves, dust acoustic solitons.

INTRODUCTION:
Mercury belongs to celestial bodies that have no atmosphere: gas pressure at its surface is $5 \cdot 10^{11}$ times lower than the pressure of the Earth's atmosphere. However, similar to the Moon, there is a rarefied gaseous envelope around Mercury that represents an exosphere and can contain dust particles [1]. The gravity of Mercury is relatively strong, twice stronger than that of the Moon. Therefore, similar trends in dust-particle dynamics can be expected above the surfaces of Mercury and the Moon. In contrast to the Moon where magnetic fields are present locally in the areas of magnetic anomalies or when the Moon crosses the Earth's magnetotail, i.e., the fields are in fact the Earth's magnetic fields observed at the Moon's orbit [2], Mercury has its own magnetosphere [3]. The Mercury's orbit is characterized by the largest orbital eccentricity among all planets of the solar system: its distance from the Sun at perihelion is about two thirds of that at aphelion. So far, Mercury was studied during two space missions: Mariner-10 (https://solarsystem.nasa.gov/missions/mariner-10/in-depth/) in 1970s and Messenger [4] in 2008–2015. The spacecraft of the European BepiColombo mission (https://www.cosmos.esa.int/web/bepicolombo/home) that is supposed to reach the planet in 2025 was launched in 2018. In addition, launching a Russian Mercury-P space probe that is supposed to land on the surface of the planet in 2030s is under discussion.

Wave processes in dusty plasma near the surface of Mercury can be detected by scientific equipment of planning missions and then are of interest [4–7]. The near-surface layers of Mercury's exosphere have a number of common features with those of the exosphere of the Moon, e.g., there are dust particles above the illuminated side of both cosmic bodies that become positively charged due to the photoelectric effect. Mercury has its own magnetosphere that protects the surface from particles of the solar wind. However, the solar wind can reach the surface of the planet near the magnetic poles. Therefore, dust particles of the same size get different charges depending on their localization above the Mercury's surface. A drift wave turbulence can appear in dusty plasma in the magnetic field near the Mercury's surface in the presence of gradient of electron concentration. The solar wind that streams at speeds of about 400 km/s relative to plasma near the surface of the planet can induce longitudinal electrostatic oscillations with frequencies determined by the electron plasma frequency. Nonlinear waves are considered — dust-acoustic solitons and nonlinear periodic waves. The profiles of the potential of high-amplitude solitons and nonlinear periodic waves are obtained, the dependences of the soliton amplitude on the height above the planet's surface and the soliton velocity are obtained. We analyze wave processes taking into account the difference in parameters at aphelion and perihelion of the Mercury's orbit, along with the fact whether the dust particles are located near the magnetic poles or far from them.

DRIFT WAVES AND LONGITUDINAL ELECTROSTATIC OSCILLATIONS:
Wave processes that can occur in the plasma-dust system near the Mercury's surface can be caused by both the presence of the magnetic field and the relative motion of the solar-wind plasma and the near-surface plasma of Mercury. It turns out that a number of possibilities of wave generation in the near-surface plasma that exist in the dusty plasma near the surface of the Moon do not exist on Mercury. Indeed, the hydrodynamic and kinetic

instabilities that are caused by the motion of the Moon relative to the Earth's magnetosphere and lead to generation of the ion-acoustic and dust-acoustic waves were analyzed in the case of the Moon. The possibility of excitation of the lower hybrid waves in lunar dusty plasma is also related to the relative motion of the dusty plasma and the Earth's magnetosphere. No such processes occur in the case of Mercury since the dusty plasma does not move relative to the planet's magnetosphere. The drift waves can also be generated on the Moon. Taking into account that Mercury has its own magnetic field with a magnitude of about 10^{-3} G, it can be expected that the drift turbulence develops in the regions where the magnetic field is directed parallel to the surface and perpendicular to the gradient of the electron concentration directed vertically. In is obtained that the instability development time is substantially smaller than the length of the solar day on Mercury.

The energy distributions of photoelectrons above the Mercury's surface represents a superposition of the distribution function of electrons knocked out by photons with energies close to the work function that have the temperature of about 0.1 eV and the distribution function of photoelectrons associated with the Lyman-alpha line of hydrogen in the spectrum of the solar radiation that have the temperature of about 1 eV [5]. Generation of oscillations in the frequency range of the Langmuir and electromagnetic waves is thus possible in the regions where the solar wind penetrates the exosphere of Mercury, i.e., near the magnetic poles, as a rule. Electromagnetic waves can be generated as a result of relative motion of the near-surface plasma and the solar wind in the regions of magnetic poles where the solar wind can reach the surface of the planet. In the process, the wave frequencies are determined by the concentration of the photoelectrons corresponding to the first peak in the distribution function with energies of about 0.1 eV [6]. The dust-acoustic waves can also exist in the dusty exosphere of Mercury. The difference in plasma parameters at aphelion and perihelion does not impose restrictions on the possibility of generation of oscillations.

NONLINEAR DUST-ACOUSTIC WAVES:
In the dusty exosphere of Mercury, one can expect the development of wave disturbances with a dispersion equation corresponding to the equation for dust-acoustic waves [6]. In the vicinity of the terminator, similarly to the situation on the Moon, one can expect the development of an instability leading to the excitation of dust-acoustic waves of large amplitude. Here we consider nonlinear waves in the form of solitons and periodic structures. The role of solar wind ions in the consideration of wave processes, in particular dusty sound, is insignificant, so the consideration can be reduced to equations describing the dynamics of dust particles and electrons. Dust-acoustic nonlinear waves, including solitons, are described by a system of equations consisting of the Poisson equation for the potential and equations specifying the densities of the plasma components. The search for a solution is carried out using the method of Sagdeev potentials. The dependences of the amplitude of solitons on the height above the planet's surface and propagation velocity are obtained. Potential profiles for solitons and nonlinear periodic waves are constructed. The characteristic amplitudes of solitons and nonlinear periodic waves can reach values of the order of 10^{-3}–10^{-2} esu.

Acknowledgements:
The work was supported by the Foundation for the Advancement of Theoretical Physics and Mathematics "BASIS".

References:
[1] *Domingue D.L., Koehn P.L., Killen R.M. et al.* Mercury's atmosphere: A surface-bounded exosphere // Space Science Reviews. 2007. V. 131. P. 161–186. https://doi.org/10.1007/s11214-007-9260-9.
[2] *Dyal P., Parkin C.W., Daily W.D.* Magnetism and the interior of the Moon // Reviews of Geophysics and Space Physics. 1974. V. 12. P. 568–591. DOI: 10.1029/RG012i004p00568.
[3] *Ness N.F., Behannon K.W., Lepping R.P., Whang Y.C.* The magnetic field of Mercury, 1 // J. Geophysical Research. 1975. V. 80. Iss. 19. P. 2708–2716. DOI: 10.1029/JA080i019p02708.

[4] *Solomon S.C., McNutt R.L., Gold R.E., Domingue D.L.* MESSENGER mission overview // Space Science Reviews. 2007. V. 131. P. 3–39. https://doi.org/10.1007/s11214-007-9247-6.
[5] *Popel S.I., Golub' A.P., Zelenyi L.M.* Dusty plasmas above the sunlit surface of Mercury // Physics of Plasmas. 2023. V. 30. Art. No. 043701. https://doi.org/10.1063/5.0142936.
[6] *Izvekova Yu.N., Popel S.I., Golub' A.P.* Wave Processes in Dusty Plasma near the Mercury's Surface // Plasma Physics Reports. 2023. V. 49. No. 7. P. 912–919. https://doi.org/10.1134/S1063780X23600585.
[7] *Izvekova Yu.N., Popel S.I., Golub' A.P.* Nonlinear dust-acoustic waves in Mercury's exosphere // Plasma Physics Reports. 2023. V. 49. Iss. 10 (in print).

14MS3-SB-13
ORAL

MANIFESTATIONS OF ANOMALOUS DISSIPATION IN DUSTY PLASMAS OF OUR SOLAR SYSTEM: CELESTIAL BODIES WITHOUT ATMOSPHERE

S.I. Popel, L.M. Zelenyi
Space Research Institute RAS, Moscow, Russia, popel@iki.rssi.ru

KEYWORDS:
dusty plasmas, dust particle charging, anomalous dissipation, Moon, Mercury, Phobos, Deimos, comets, dust particle trajectory, damping, “levitating” dust particles

INTRODUCTION:

The main features that distinguish the dusty plasma from ordinary (not containing charged dust particles) plasma is the possibility of self-organization, leading to the formation of macroscopic structures such as a dusty plasma crystal, dusty plasma clouds, droplets, *etc.*, and, in addition, the occurrence of anomalous dissipation [1] leading to new physical phenomena, effects and mechanisms [2–5]. Under natural conditions, the formation of dusty plasma crystals is, as a rule, impossible, and the main attention should be paid to anomalous dissipation associated with dust particle charging. This kind of anomalous dissipation is responsible for the formation of a new kind of shock waves, which are important in the physics of comets, the Earth’s atmosphere during active experiments, in the description of the primary Earth, *etc.* [6]. The effects associated with dust particle charging are important in describing the modulational instability in the dusty plasma [3] and in the consideration of weakly damped solitons [7]. It is well known that in the dusty plasma, electrons and ions are absorbed on the surface of a dust particle, so, naturally, the energy of the dust component is exchanged with the plasma. However, in all the cases listed above, when statements are made about anomalous dissipation associated with dust particle charging, there are manifestations of this effect that characterize the behavior of the dusty plasma. A similar situation arises in the context of describing the dynamics of dust particles in dusty plasmas above surfaces of the celestial bodies like the Moon, Mercury, Phobos, Deimos, and comets [8–14], when anomalous dissipation associated with dust particle charging can lead to damping of oscillations when a dust particle moves over the corresponding surface. Here, we discuss the manifestations of anomalous dissipation in dusty plasmas of our Solar system.

DUST PARTICLE CHARGING FREQUENCY:

We consider the situation when the surface of a celestial body like the Moon, Mercury, Phobos, Deimos, and a comet is illuminated by the solar radiation. In this case, anomalous dissipation in the dusty plasma is characterized by the so-called dust particle charging frequency ν_q, which is determined from the relationship [10–11]

$$\frac{\mathrm{d}\delta q_d}{\mathrm{d}t} \approx \left.\frac{\partial\left(I_e(q_d)+I_i(q_d)-I_{ph}(q_d)+I_{e,ph}(q_d)\right)}{\partial q_d}\right|_{q_d=q_{d0}} \delta q_d \equiv -\nu_q \delta q_d\,,$$

where q_{d0} is the equilibrium charge of a dust particle, δq_d is the dust particle charge variation, $I_e(q_d)$ and $I_i(q_d)$ are microscopic currents of electrons and ions of the solar wind on a dust particle, $I_{ph}(q_d)$ is the photoelectron current from a dust particle due to the interaction of its surface with solar radiation, $I_{e,ph}(q_d)$ is the current of photoelectrons surrounding a dust particle to it,

$$\nu_q \approx \frac{1}{4\sqrt{2\pi}}\cdot\frac{a\nu_{T_e,ph}}{\lambda_D^2}\left(1+\frac{Z_{d0}e^2}{aT_{e,ph}}\right)\exp\left(-\frac{Z_{d0}e^2}{aT_{e,ph}}\right)+\frac{2}{\sqrt{2\pi}}\cdot\frac{a\upsilon_{T_eS}}{\lambda_{DeS}^2},$$

a is the size of a dust particle, Z_{d0} is its charge number ($q_{d0} = Z_{d0}e$), $-e$ is the electron charge, $v_{Te,ph}$ is the thermal speed of photoelectrons, λ_D is the Debye length of photoelectrons near the surface of the celestial body, $T_{e,ph}$ is the temperature of photoelectrons, v_{TeS} is the thermal speed of solar wind electrons, λ_{DeS} is the Debye length of solar wind electrons. The above expression for ν_q has been derived under the conditions of the illuminated part of the Moon.

Calculations [10–14] show that the charged dust particle motion above the surface of a celestial body like the Moon, Mercury, Phobos, Deimos, and a comet is oscillatory, the $2/\nu_q$ value determining the damping of the dust particle oscillations, i.e., damping of dust particle oscillations is caused by anomalous dissipation in dusty plasmas due to charging of dust particles.

THE MOON:

The distinguishing characteristic of the dust-particle-motion trajectory in dusty plasma above the lunar surface consists [8, 10] in the presence of oscillations which are damped due to variation of charges of dust particles, which is consistent with the concept of anomalous dissipation in dusty plasma. The processes causing changes in charge of the dusty particles are too fast relative to the duration of the lunar day. Therefore, the oscillations have enough time to decay for most (~83 %) of the dust particles above the lunar surface illuminated by the Sun, and these dust particles can be considered as "levitating". Only very small particles do not make a transition to the levitation regime during the lunar day, and the effects related to dusty plasma system being nonstationary should be taken into account when studying these particles.

MERCURY AND MARTIAN SATELLITES:

The character of dusty plasmas at other celestial bodies that have no atmosphere, e.g., Mercury or Martian satellites Phobos and Deimos, has a number of characteristics that are similar to those of the dusty plasma at the Moon. However, there are some substantial peculiarities. In particular,

the solar wind is important for formation of dusty plasma on Mercury due to its magnetosphere but only near the magnetic poles [12]. In other Mercury's regions, the solar wind does not have a significant impact on properties of dusty plasma, in contrast to the situation on the Moon. Correspondingly, the value of the dust particle charging frequency is modified (in comparison with that given above). Parameters of dusty plasma above Mercury are different at aphelion and perihelion of its orbit.

Theoretical studies [13–14] revealed that, in contrast to the Moon or Mercury, formation of the dusty plasma system in the near-surface layer above the illuminated part of the Martian satellite surface is nonstationary over almost entire daytime period. Processes of variation of charges of the dust particles that result in damping of their oscillations above the surface of the Martian satellite turn out to be too slow relative to duration of the daytime on the satellite. To obtain exact data on parameters of the dusty plasma system near Martian satellites, it is necessary to get more complete information on the properties of their soil, e.g., the work function, the quantum yield, *etc*. The authors express hope that this information will be obtained in the course of future space missions.

COMETS:

Dusty plasma processes can substantially impact formation of a bow shock as a result of interaction of the comet coma with the solar wind. They can also reveal themselves in the situations when the comet is far from the Sun.

1. The bow shock wave can sometimes be interpreted as a variety of the ion-acoustic shock wave [6]. The presence of charged dust leads to another important type of interaction, namely, interaction of protons of the solar wind with dust particles in the comet coma. For a typical comet nucleus with a radius of ~1 km and relatively dense coma (number density of dust particles exceeding 10^6 cm^{-3}), anomalous dissipation caused by charging of dust particles plays an important role in shock wave formation. Apparently, the nature of such a shock wave is similar to that of the ion-acoustic shock waves [4–5].

2. For a comet exhibiting parameters of the nucleus close to those of the nucleus of the Halley's comet, the dusty plasma in the vicinity of the nucle-

us forms due to electrostatic interactions, i.e., analogous to dusty plasma formation near other bodies without atmosphere (e.g., Martian satellites [13–14]), provided that the distance from the comet to the Sun is at least ~3 AU. Dust particle trajectories are influenced by anomalous dissipation in dusty plasmas due to charging of dust particles. On the contrary, if the comet is closer to the Sun, the dynamics of dust particles is determined by the gas flow from the comet nucleus.

Acknowledgements:
This work was supported by Theoretical Physics and Mathematics Advancement Foundation "BASIS" (grant "Leader") and partially by the National Center for Physics and Mathematics, Project 10: "Investigation of plasma-dusty processes in the exosphere of the Moon and other airless bodies of the Solar System using laboratory modeling methods".

References:

[1] Tsytovich V.N., Morfill G.E., Vladimirov S.V., Thomas H.M. Elementary Physics of Complex Plasmas (Lecture Notes in Physics. 731). Berlin; Heidelberg: Springer, 2008. 370 p. DOI: 10.1007/978-3-540-29003-2.

[2] *Tsytovich V.N.* One-dimensional Self-organised Structures in Dusty Plasmas // Australian J. Physics. 1998. V. 51. P. 763–834.

[3] *Benkadda S., Tsytovich V.N.* Modulational instability in dusty plasmas // Physics of Plasmas. 1995. V. 2. P. 2970–2974. https://doi.org/10.1063/1.871195.

[4] *Popel S.I., Yu M.Y., Tsytovich V.N.* Shock waves in plasmas containing variable-charge impurities // Physics of Plasmas. 1996. V. 3. P. 4313–4315. https://doi.org/10.1063/1.872048.

[5] *Popel S.I., Golub' A.P., Losseva T.V.* Dust Ion-Acoustic Shock-Wave Structures: Theory and Laboratory Experiments // J. Experimental and Theoretical Physics Letters. 2001. V. 74. No. 7. P. 362–366. https://doi.org/10.1134/1.1427122.

[6] *Popel S.I., Gisko A.A.* Charged dust and shock phenomena in the Solar System // Nonlinear Processes Geophys. 2006. V. 13. P. 223–229.

[7] *Popel S.I., Golub' A.P., Losseva T.V. et al.* Weakly dissipative dust-ion-acoustic solitons // Physical Review E. 2003. V. 67. Iss. 5. Art. No. 056402. https://doi.org/10.1103/PhysRevE.67.056402.

[8] *Popel S.I., Golub' A.P., Kassem A.I., Zelenyi L.M.* Dust dynamics in the lunar dusty plasmas: Effects of magnetic fields and dust charge variations // Physics of Plasmas. 2022. V. 29. Iss. 1. Art. No. 013701. DOI: 10.1063/5.0077732.

[9] *Popel S.I., Golub' A.P., Kassem A.I., Zelenyi L.M.* On the Role of Magnetic Fields in the Plasma of Dusty Lunar Exosphere // Plasma Physics Reports. 2022. V. 48. P. 512–517. https://doi.org/10.1134/S1063780X22200065.

[10] *Popel S.I., Golub' A.P.* On Anomalous Dissipation in the Plasma of the Dusty Lunar Exosphere // J. Experimental and Theoretical Physics Letters. 2022. V. 115. Iss. 10. P. 596–601. https://doi.org/10.1134/S0021364022100587.

[11] *Popel S.I.* Manifestations of Anomalous Dissipation in Dusty Plasma Systems // Plasma Physics Reports. 2023. V. 49. P. 70–78. DOI: 10.1134/S1063780X22601456.

[12] *Popel S.I., Golub' A.P., Zelenyi L.M.* Dusty plasmas above the sunlit surface of Mercury // Physics of Plasmas. 2023. V. 30. Art. No. 043701. https://doi.org/10.1063/5.0142936.

[13] *Golub' A.P., Popel S.I.* Nonstationary Processes in the Formation of a Dusty Plasma near the Surface of Phobos // J. Experimental and Theoretical Physics Letters. 2021. V. 113. Iss. 7. P 428–432. https://doi.org/10.1134/S0021364021070079.

[14] *Golub' A.P., Popel S.I.* Non-Stationary Processes during the Formation of Dusty Plasma at the Surface of Deimos, the Satellite of Mars // Plasma Physics Reports. 2021. V. 47. Iss. 8. P. 826–831. DOI: 10.1134/S1063780X21070084.

DUSTY PLASMA CLOUDS IN THE ATMOSPHERE OF MARS: SIGNIFICANCE OF RAYLEIGH-TAYLOR INSTABILITY

Yu.S. Reznichenko[1,2], A.Yu. Dubinskii[1], S.I. Popel[1]
[1] *Space Research Institute RAS, Moscow, Russia, nfkpb@bk.ru*
[2] *Moscow Institute of Physics and Technology (National Research University), Dolgoprudny, Moscow Region, dvju@yandex.ru*

KEYWORDS:
dusty plasma clouds, dust particles, Martian atmosphere, Rayleigh – Taylor instability, growth rate

The presence of dry ice dusty plasma clouds at altitudes of about 100 km is an important feature of the Martian atmosphere. Such clouds were seemingly detected by the SPICAM infrared spectrometer (Mars Express) as well as photographed by the Mars Science Laboratory Curiosity mission in March 2021. The rover Mars Science Laboratory Curiosity took photographs at sunset when dust particles of the clouds were illuminated by the Sun against the dark sky background.

We describe a possible mechanism of dusty plasma clouds formation in the Martian atmosphere [1–5]. We use theoretical base from [6–9] as well as experimental data from [10]. We consider carefully dust particle deceleration because of condensation of supersaturated carbon dioxide vapor. This effect is usually ignored in case of the Earth's dusty plasma system but is important for the atmosphere of Mars. We calculate an altitude dust particle distribution of Martian dusty plasma clouds using our model.

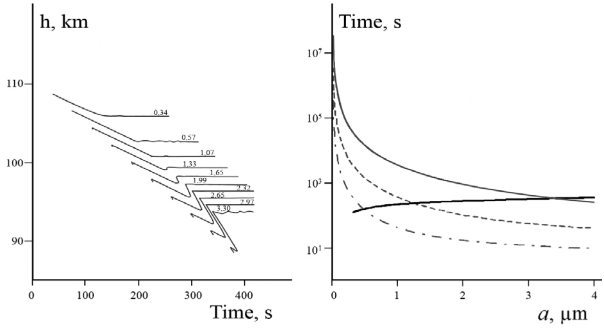

Fig. 1. An altitude dust particle distribution of Martian dusty plasma clouds. Initially dust particles were located at altitudes of 110–120 km (*left*).The instability characteristic development time as well as sedimentation time for different dust particle sizes. The atmosphere parameters correspond to the altitude of 90 km (*right*)

We also show that an important factor for dusty plasma cloud formation on Mars is the Rayleigh – Taylor instability. The upper half-space of a dusty plasma cloud is full of gas and dust mixture while dust number density of the lower half-space is negligible. In such case the Rayleigh – Taylor instability is naturally developed in the gas-and-dust system in the gravitational field. The instability growth rate reaches a maximum value γ for a certain $|k|$-value determining the characteristic instability development time. We show that in case of significant value of dust particle number density this time is more than sedimentation time only for small dust grains. This effect leads to the fact that dusty plasma clouds can exist only with sufficiently small sizes of their constituent dust particles, as well as to the thickness limit of the clouds.

Acknowledgements:
This work was supported in part by the Theoretical Physics and Mathematics Advancement Foundation "BASIS" (grant "Leader").

References:

[1] *Reznichenko Yu.S., Dubinskii A.Yu., Popel S.I.* Formation and Evolution of Dusty Plasma Structures in the Ionospheres of the Earth and Mars // Plasma Physics Reports. 2019. V. 45. P. 928–935. https://doi.org/10.1134/S1063780X19100039.

[2] *Reznichenko Yu.S., Dubinskii A.Yu., Popel S.I.* On dusty plasma formation in Martian ionosphere // J. Physics: Conf. Series. 2020. V. 1556. Art. No. 012072. DOI: 10.1088/1742-6596/1556/1/012072.

[3] *Reznichenko Yu.S., Dubinskii A.Yu., Popel S.I.* Plasma-Dust System in the Martian Ionosphere // Plasma Physics Reports. 2023. V. 49. P. 79–88. https://doi.org/10.1134/S1063780X22601377.

[4] *Reznichenko Yu.S., Dubinskii A.Yu., Popel S.I.* On the Formation of Clouds in the Dusty Ionosphere of Mars // J. Experimental and Theoretical Physics Letters. 2023. V. 117. P. 428–434. https://doi.org/10.1134/S0021364023600398.

[5] *Dubinskii A.Yu., Reznichenko Yu.S., Popel S.I.* On the Kinetic Features of Sedimentation of Dust Particles in the Martian Atmosphere // Solar System Research. 2023. V. 57. P. 214–220. https://doi.org/10.1134/S0038094623020016.

[6] *Klumov B.A., Popel S.I., Bingham R.* Dust particle charging and formation of dust structures in the upper atmosphere // J. Experimental and Theoretical Physics Letters. 2000. V. 72. P. 364–368. https://doi.org/10.1134/1.1331147.

[7] *Klumov B.A., Morfill G.E., Popel S.I.* Formation of structures in a dusty ionosphere // J. Experimental and Theoretical Physics. 2005. V. 100. P. 152–164. https://doi.org/10.1134/1.1866207.

[8] *Dubinskii A.Yu., Popel S.I.* Formation and evolution of dusty plasma structures in the ionosphere // J. Experimental and Theoretical Physics Letters. 2012. V. 96. P. 21–26. https://doi.org/10.1134/S0021364012130048.

[9] *Savel'ev R.S., Rozanov N.N., Sochilin G.B., Chivilikhin S.A.* Relei-teilorovskaya neustoichivost' zapylennogo gaza (Rayleigh-Taylor instability of dusty gas) // Scientific and Technical J. Information Technologies, Mechanics and Optics. 2011. V. 73. P. 18–22 (in Russian).

[10] *Forget F., Montmessin* F., *Bertaux* J.-L. *et al.* Density and temperatures of the upper Martian atmosphere measured by stellar occultations with Mars Express SPICAM // J. Geophysical Research. 2009. V. 114. Iss. A1. Art. No. E01004. https://doi.org/10.1029/2008JE003086.

ENERGY RELEASE OF LARGE IMPACTORS IN THE TERRESTRIAL ATMOSPHERE

O.P. Popova, V.V. Shuvalov, V.V. Svetsov, D.O. Glazachev
Sadovsky Institute of Geosphere Dynamics RAS, Moscow, Russia, o9055610006@gmail.com

KEYWORDS:
large impactors, energy release

INTRODUCTION:

The impact of large (tens of meters and greater) cosmic objects into the atmosphere is typically considered within one of two scenarios, i.e. airburst or crater-forming. Chelyabinsk/Tunguska and Chicxulub are bright examples of these limiting cases. However, there is a wide range of impact parameters when a projectile loses a considerable part of its mass and energy passing through the atmosphere, but the remaining part hits the surface producing crater. Impacts in this impactor size range may be called transitional ones.

The fraction of the kinetic energy released by the impactor into the atmosphere has a decisive influence on the hazardous impact consequences especially for airbursts and transitional scenarios. The energy deposition profile may be used as initial conditions for airblast shock wave hydrocode modeling [1–2] as well as for estimates of thermal and others effects [3].

To replicate the rate of energy deposition inferred from light curves appears to be possible with the help of semi-empirical models in which the meteoroid undergoes catastrophic fragmentation leading to a rapid and dramatic increase in drag and deceleration [4–5]. Another possibility includes modeling of cosmic object interaction with the atmosphere in the frame of different hydrodynamic models, which permits one to determine the energy release.

ENERGY PARTITION:

Semi-empirical models typically assume that the vaporized substance of the meteoroid instantly decelerates and transfers its energy to the air. Numerical hydrodynamical modeling [9] demonstrated that for Tunguska scale impactors the jet consisting of vapors and shock heated air continues to move along the trajectory at high speed even after the complete evaporation of the meteoroid. At first the energy of the meteoroid is converted into the energy of the vapor jet (mainly kinetic), and then the vapor energy is transferred to the air. Most of the energy is released in the air after the meteoroid has completely evaporated and at altitudes lower than the height of complete evaporation. This effect can complicate the application of semi-empirical models for determination of energy deposition curves needed to estimate hazardous effects. This presentation will discuss the features of impactor energy deposition in the atmosphere, and possibilities of semi-empirical models to estimate the energy deposition. And hazardous effects for transitional (between airbursts and crater forming) cases of impacts.

References:

[1] *Artemieva N., Shuvalov V.* Atmospheric shock waves after impacts of cosmic bodies up to 1000 m in diameter // Meteoritics and Planetary Science. 2019. V. 54. Iss. 3. P. 592–608. https://doi.org/10.1111/maps.13229.

[2] *Aftosmis M.J., Nemec* M.*, Mathias D., Berger M.J.* Numerical Simulation of Bolide Entry with Ground Footprint Prediction // 54th AIAA aerospace sciences meeting. 2016. Art. No. 0998.

[3] *Svetsov V.V., Shuvalov V.V.* Thermal radiation and luminous efficiency of superbolides // Earth and Planetary Science Letters. 2018. V. 503. P. 10–16. https://doi.org/10.1016/j.epsl.2018.09.018.

[4] *Popova O., Jenniskens* P.*, Emel'yanenko* V. *et al.* Chelyabinsk airburst, damage assessment, meteorite recovery, and characterization // Science. 2013. V. 342. P. 1069–1073. DOI: 10.1126/science.1242642.

[5] *Wheeler L.F., Register P.J., Mathias D.L. et al.* A fragment-cloud model for asteroid breakup and atmospheric energy deposition // Icarus. 2017. V. 295. P. 149–169. https://doi.org/10.1016/j.icarus.2017.02.011.

[6] *Shuvalov* V., *Svetsov* V., Popova O., *Glazachev* D. Numerical model of the Chelyabinsk meteoroid as a strengthless object // Planetary and Space Science. 2017. V. 147. P. 38–47. https://doi.org/10.1016/j.pss.2017.05.011.
[7] *Robertson D.K., Mathias D.L.* Effect of yield curves and porous crush on hydrocode simulations of asteroid airburst // Journal of Geophysical Research: Planets. 2017. V. 122. Iss. 3. P. 599–613. https://doi.org/10.1002/2016JE005194.
[8] *Robertson D.K., Mathias D.L.* Hydrocode simulations of asteroid airbursts and constraints for Tunguska // Icarus. 2019. V. 327. P. 36–47. https://doi.org/10.1016/j.icarus.2018.10.017.
[9] *Shuvalov V.V., Artemieva N.A.* Numerical modeling of Tunguska-like impacts // Planetary and Space Science. 2002. V. 50. Iss. 2. P. 181–192. https://doi.org/10.1016/S0032-0633(01)00079-4.

MIGRATION OF BODIES EJECTED FROM THE EARTH AND THE MOON

S.I. Ipatov
Vernadsky Institute of Geochemistry and Analytical Chemistry RAS, Moscow, Russia, siipatov@hotmail.com

KEYWORDS:
motion of bodies, ejection of bodies from the Earth and the Moon, probabilities of collisions, planets, the Moon, collision velocities

INTRODUCTION AND CONSIDERED MODEL:
I studied the evolution of the orbits of bodies ejected from the Earth or the Moon. The studies included calculations of the probabilities and velocities of collisions of the bodies with the Earth, the Moon, and the terrestrial planets. Such ejection could often take place during the Earth's accumulation and late heavy bombardment. In each calculation variant, the motion of 250 bodies ejected from the Earth or the Moon was studied for the fixed values of an ejection angle i_{ej} (measured from the surface plane), a velocity v_{esc} of ejection, and a time step t_s of integration. The velocity of rotation of the Earth's surface (0.46 km/s) was not taken into account. The gravitational influence of the Sun and all eight planets was taken into account. Bodies that collided with planets or the Sun or reached 2000 AU from the Sun were excluded from integration. The symplectic code from the SWIFT integration package [1] was used for integration of the motion equations. The considered time step t_s equaled to 1, 2, 5, or 10 days, and the results of calculations with different t_s were compared and gave similar results. The probabilities p_{E} of collisions of bodies with the Earth were about the same for calculations with different t_s. The motion of bodies ejected from the Earth or the Moon under the gravitational influence of all planets was studied during the dynamic lifetime T_{end} of all bodies, which was often about 200–500 million years in the calculation variants. In [2–3] the motion of bodies ejected from the Earth at collisions of bodies-impactors with the Earth was studied during time interval equal to 30 Kyr, and considered initial velocities were perpendicular to the surface of the Earth.

The ejection of bodies from six opposite points of the Earth's surface, as well as from the far point of the Moon, was considered for a number of values of velocities and angles of ejection of bodies. In the *vf* and *vc* series, the motion of the bodies started at most and least distant points of the Earth's surface from the Sun (located on the line from the Sun to the Earth), respectively. In the *vw* and *vb* series, the bodies started from the forward point on the Earth's surface in the direction of the Earth's motion and from the back point on the opposite side of the Earth, respectively. In the *vu* and *vd* series, the bodies started from points on the Earth's surface with the maximum and minimum values of *z* (with the z axis perpendicular to the plane of the Moon's orbit), respectively. In different variants, the values of the ejection angle i_{ej} were 15°, 30, 45, 60, 89, or 90°. The ejection velocity v_{esc} was mainly equal to 11.22, 11.5, 12, 14, or 16.4 km/s, but other values in the range from 11.22 to 11.5 km/s were also considered. For ejection from the Moon located at h equal to $3r_{\mathrm{E}}$, $5r_{\mathrm{E}}$, $7r_{\mathrm{E}}$, or $60r_{\mathrm{E}}$ from the center of the Earth of radius r_{E}, the calculations were also carried out for the velocity v_{esc} equal to 2.5 or 5 km/s. $60r_{\mathrm{E}}$ is the semi-major axis of the present orbit of the Moon. For the Moon, the parabolic velocity is 2.38 km/s. Note that mass m_{ej} of ejected material is smaller at greater velocity v_{esc} of ejection. According to [4], m_{ej} is proportional to $v_{esc}^{-1.65}$.

PROBABILITIES AND VELOCITIES OF COLLISIONS OF BODIES EJECTED FROM THE EARTH WITH THE EARTH AND THE MOON:
The probabilities p_{E} and p_{M} of collisions of bodies with the Earth and the Moon were generally lower at higher velocities v_{esc}. At ejection velocities in

the range of 11.5-14 km/s, the values of p_E and p_M depended less on the ejection point on the Earth's surface. At ejection velocities $v_{esc} \le 11.3$ km/s, i.e., slightly greater than the parabolic velocity, most of the ejected bodies fell back to the Earth. Over the entire considered time interval, with v_{esc} equal to 11.5, 12, and 14 km/s, the values of p_E were approximately 0.3, 0.2, and 0.15–0.2, respectively. The mean velocities v_{colE} of collisions of ejected bodies with the Earth were greater at greater velocities of ejection. The values of v_{colE} were about 13, 14–15, 14–16, 14–20, 14–25 km/s at v_{esc} equal to 11.3, 11.5, 12, 14, and 16.4 km/s.

The Moon was not included in the integration of motion equations of bodies. Based on the arrays of orbital elements of migrated bodies, similar to [5–8], I calculated the probabilities of collisions of bodies with the Moon and the Earth and the ratio k_{EM} of probabilities of collisions of bodies with the Earth to those with the Moon. The probability p_M of a collision of a body with the Moon was calculated as p_E/k_{EM}, where p_E was calculated at integration of motion equations. The probability p_M of a body ejected from the Earth colliding with the Moon was about 15–35 times less than that with the Earth at $v_{esc} \ge 11.5$ km/s. Basically, this probability p_M was in the region of 0.01–0.016 at $v_{esc} \le 11.4$ km/s and 0.005–0.01 at $v_{esc} \ge 12$ km/s. The collision velocities of bodies with the Moon were higher at high ejection velocities and were mainly in the ranges of 7–8, 10–12, 10-16, and 11–20 km/s at v_{esc} equal to 11.3, 12, 14, and 16.4 km/s. At v_{esc} about 12–14 km/s, the probabilities of collisions of bodies with Venus and the Sun usually did not differ by more than a factor of 2 from p_E, the probabilities of collisions of bodies with Mercury were about 0.05–0.08, and those with Mars typically did not exceed 0.01. The probabilities could be different at different i_{ej}, v_{esc} and the point of ejection.

In the considered calculations of the motion of bodies ejected from the Earth, most of the bodies left the Earth's Hill sphere and moved along heliocentric orbits. Bodies ejected from the Earth could participate in the formation of the outer layers of the Moon. In order to contain its current fraction of iron, the Moon must have accumulated most of its mass from the Earth's mantle [9–10]. From the obtained estimates of the probabilities of collisions of bodies ejected from the Earth with the Moon moving in its present orbit, we can conclude that in order for the Moon to acquire most of its mass due to the bodies ejected from the Earth during its repeated bombardment, the total mass of bodies ejected from the Earth during its accumulation should be comparable with the mass of the Earth. Therefore, the bodies ejected from the Earth and falling on the Moon's embryo were probably not enough for the Moon to grow to its present mass from a small embryo moved in its current orbit. This result testifies in favor of the formation of a large lunar embryo near the Earth. In a collision with a body, due to the smaller mass, the Moon would lose a larger fraction of its mass than the Earth. Calculations have shown that the fraction of bodies that fell onto the Earth and the Moon does not depend much on whether these bodies would have been ejected from the Earth or the Moon.

PROBABILITIES OF COLLISIONS OF BODIES EJECTED FROM THE MOON WITH THE EARTH:

At ejection of bodies from the Moon moved in its present orbit (at $h = 60r_E$), a considered time interval T = 10 Myr and $30° \le i_{ej} \le 60°$, p_E was about 0.2–0.25 at v_{esc} = 2.5 km/s, 0.13–0.14 at v_{esc} = 5 km/s, and 0.06–0.07 at $12 \le v_{esc} \le 16.4$ km/s. At $h = 60r_E$ and at the end of evolution ($T = T_{end}$), p_E was about 0.3–0.32 at v_{esc} = 2.5 km/s, 0.2–0.22 at v_{esc} = 5 km/s, and 0.1–0.14 at $12 \le v_{esc} \le 16.4$ km/s. That is, at velocities v_{esc} slightly greater than the parabolic velocity, the values of p_E are approximately the same for ejection from the Earth and the Moon, but for different ejection velocities. At $h = 60r_E$, these values of p_E show the fraction of bodies that could collide with the Earth after their ejection from the Moon, moving along its present orbit. This fraction is approximately the same as for bodies ejected from the Earth, if we take into account the lower minimum velocities of bodies ejected from the Moon. Bodies ejected from the Moon embryo located close to the Earth fall back onto the Earth and the Moon if their initial velocity was less that the corresponding parabolic velocity. At v_{esc} = 2.5 km/s and h equal to $3r_E$ or $5r_E$, the dynamical lifetime of ejected bodies did not exceed 5 days. At v_{esc} = 5 km/s and $h = 5r_E$, the value of p_E was between 0.29 and 0.33 at considered i_{ej} from 30 to 89°. The maximum dynamical lifetime equaled to a few hundreds of Myrs.

CONCLUSIONS:

At ejection velocities about 12–14 km/s, the fraction of bodies ejected from the Earth that fall back onto the Earth was about 0.15–0.2, mean velocities of collisions with the Earth and the Moon were about 14–20 and 10–16 km/s, respectively. The fraction is greater for smaller ejection velocity. The probability of collisions of such bodies with the Moon moved in its present orbit was about 0.01. A large Moon embryo should be formed close to the Earth in order to accumulate material rich in iron.

Acknowledgements:

The studies were supported by the Russian Science Foundation (no. 21-17-00120).

References:

[1] *Levison* H.F., Duncan *M.J.* The long-term dynamical behavior of short-period comets // Icarus. 1994. V. 108. Iss. 1. P. 18–36. https://doi.org/10.1006/icar.1994.1039.

[2] *Gladman B., Dones* L., *Levison* H.F., Burns J.A. Impact seeding and reseeding in the inner Solar System // Astrobiology. 2005. V. 5(4). P. 483–496. DOI: 10.1089/ast.2005.5.483.

[3] *Reyes-Ruiz M., Chavez C.E., Aceves H. et al.* Dynamics of escaping Earth ejecta and their collision probabilities with different Solar System bodies // Icarus. 2012. V. 220. Iss. 2. P. 777–786. https://doi.org/10.1016/j.icarus.2012.06.017.

[4] *Svetsov V.* Cratering erosion of planetary embryos // Icarus. 2011. V. 214. Iss. 1. P. 316–326. https://doi.org/10.1016/j.icarus.2011.04.026.

[5] *Ipatov S.I., Mather J.C.* Migration of trans-Neptunian objects to the terrestrial planets // Earth Moon Planets. 2003. V. 92. P. 89–98. https://doi.org/10.1016/j.icarus.2011.04.026.

[6] *Ipatov S.I., Mather J.C.* Comet and asteroid hazard to the terrestrial planets // Advances in Space Research. 2004. V. 33. Iss. 9. P. 1524–1533. https://doi.org/10.1016/S0273-1177(03)00451-4.

[7] *Ipatov S.I., Mather J.C.* Migration of Jupiter-family comets and resonant asteroids to near-Earth space // Annals New York Academy Sciences J. 2004. V. 1017(1). P. 46–65. DOI: 10.1196/annals.1311.004.

[8] *Ipatov S.I., Mather J.C.* Probabilities of collisions of planetesimals from different regions of the feeding zone of the terrestrial planets with forming planets and the Moon // Solar System Research. 2019. V. 53. Iss. 5. P. 332–361. DOI: 10.1134/S0038094619050046.

[9] Ipatov S.I. Formation of embryos of the Earth and the Moon from the common rarefied condensation and the subsequent growth // Solar System Research. 2018. V. 52, No. 5. P. 401-416. https://doi.org/10.1134/S0038094618050040.

[10] *Marov M.Ya., Ipatov S.I.* Migration processes in the Solar System and their role in the evolution of the Earth and planets // Physics — Uspekhi. 2023. V. 66. Iss. 7. P. 2–31. DOI: 10.3367/UFNe.2021.08.039044.

POSSIBILITY OF SPACE DEBRIS ESCAPE FROM THE EARTH – MOON SYSTEM

T.V. Salnikova, E.I. Kugushev
Lomonosov Moscow State University, tatiana.salnikova@gmail.com, kugushevei@yandex.ru

KEYWORDS:
Chazy classification, three-body problem, hyperbolic-elliptical motion, Hill regions, space debris

INTRODUCTION:

The classification of the final motions of the three-body problem by J. Chazy had a symmetry in the past and in the future [1].

Numerical examples that appeared later by a number of authors asserted the possibility of exchange and capture in the asymmetric case. Finally, V.M. Alekseev proved by qualitative methods that there is an open set of initial conditions of positive measure leading to the exchange for systems with both positive and negative total energy: hyperbolic-elliptic motions have different bodies receding to infinity in the past and in the future.

The non-zero exchange probability in the general case should be discussed separately in specific real situations [2].

PROBLEM SETTING:

There are two applied aspects of final motions in the three-body problem:

1) formation of non-spherical (irregularly shaped) satellites in planetary systems (such as the martian satellites Phobos and Deimos);
2) evolution of space debris.

For justification of the possibility of exchange (interception) in the model of the hyperbolic-elliptic/parabolic-elliptic three-body problem we need to study the following:

3. Mobility (the possibility of arbitrary movements of the system of three bodies).
4. The ratio of speeds when approaching.
5. Computer analysis at medium distances.
6. Sufficient conditions for the stability of the satellite orbit after interception.

THE RESULTS OF NUMERICAL SIMULATION FOR THE EARTH-MOON SYSTEM:

For the second of two applied aspects: 2) possible evolution of debris in the vicinity of the planet under the influence of two types of perturbations from another body, which either flies by (asteroid) or rotates (satellite):

a) the fragment remains near the planet,
b) the fragment goes into the zone of influence of the body,
c) the fragment flies to infinity,
d) the fragment is alternately located near the body and the planet.

Using the properties of the Hill regions, a numerical analysis of space debris evolution has been carried out.

If the Hill regions are closed, then a spontaneous ejection of debris from the Earth-Moon system is impossible. If orbital radii of near-Earth debris are less than 88 500 km, and if orbital radii of near-Moon debris smaller than 3850 km, then the Hill regions are closed; if corresponding radii are grater, then the Hill regions are open.

For orbital radii of near-Earth debris less than 238,000 km (0.62 Earth-Moon distances), and for circumlunar debris smaller than 46 200 km, there is no effect of debris escape. Starting from the indicated values, the system decays. As the radius of the orbits increases, the proportion of debris emitted from the system during 70 years increases.

References:

[1] *Salnikova T., Kugushev E., Pestrikov A.* Possible appearing of the asteroid origin celestial bodies in near-Earth orbits // Acta Astronautica. 2022. V. 204. P. 912–919. https://doi.org/10.1016/j.actaastro.2022.09.011.

[2] *Chazy J.* Sur l'allure finale du mouvement dans le problème des trois corps // J. Mathématiques Pures et Appliquées. 1929. V. 8. P. 353–380.

ON THE DYNAMICS OF METEOROID STREAMS ORIGINATING FROM NEA COLLISIONS

R.V. Zolotarev, B.M. Shustov
Institute of Astronomy RAS, Moscow, Russia, rv_zolotarev@mail.ru

KEYWORDS:
meteoroid, meteoroid stream, NEA, asteroid collisions

INTRODUCTION:

Formation of meteoroid streams usually are associated with comet activity and comet nuclei disruption. Meteoroids are ejected by gas outflow during comet's perihelion passage. Another mechanism is collisions. It works both for comets and asteroids.

During last decade a new type of objects, "active asteroids", draws a lot of attention. Those are asteroids for which coma or tail has been observed at least once [1]. Another type of activity is sublimation-dust activity. Asteroids of this type have no visible coma or tail, but existence of dusty exosphere can be derived from spectral observations [2]. Such activity can be induced by collisions or sublimation process (which can be started with collisional event). Collisions of asteroids were not observed directly, however consequences of recent collisions were observed several times [3]. Estimates show that such collisions should be rather frequent. At any time some large (D > 100 km) asteroids can be "active" [4].

In this work we study the process of formation and evolution of meteoroid stream arising during the collision of Near-Earth asteroid (NEA) with impactors which are essentially Main-belt asteroids (MBAs). Being originated in MBA region NEAs intersect the region during their orbital motion. Collisions are most frequent here due to higher number density of objects in MBA.

MODEL:

FORMATION OF METEOROID SWARM:

We consider the collision of a NEA with a projectile near the aphelion of the NEA orbit. Obviously a projectile is considered to be smaller then the target NEA. Particles of different sizes are formed during collision. We focus on meteoroid size (diameter) in range of 0.1–100 mm. To study dynamics of particles, one need to know geometry of ejection, size and velocity distribution. According to laboratory experiments [5], particle size distribution can be written in form $\mathrm{d}N = C_r r^{-s_r} \mathrm{d}r$, where d$N$ — is number of particles in size interval [r, r+dr], C_r is normalizing constant, s_r lying in range 2.5–4 with average value about 3.3. In these experiments projectile speed varied in wide range (0.9–11 km/s) which corresponds to range of random velocities of MBAs [4]. Velocity distribution in experiments can be approximated with following expression: $v(r) = C_v(r/(1\ \mathrm{cm}))^{-2/3}$ where C_v is constant in range 1–22 (m/s) [5]. Angular distribution of expelled particles can be approximated as uniform in semi-sphere. These initial conditions are similar to those that have been derived in the DART experiment [6].

EVOLUTION OF METEOROID STREAM:

We consider the model asteroid (NEA) at following orbit: perihelion distance q = 0.9 AU, aphelion distance Q = 3 AU, inclination i = 10°. These are close to mean orbital parameters of NEAs with aphelion in the MBA region. The orbit intersects MBA region and approaches Earth orbit which is important to model observable meteor stream parameters. Particles of four radii were considered: 0.05, 0.5, 5.0 and 50 mm. Initial velocities (if we assume C_v = 10) are 342, 74, 16, and 3.5 m/s respectively. Initial velocities were distributed isotropic in the semi-sphere co-directed with the asteroid velocity vector. Further motion of particles was integrated using the REBOUND code [7]. Gravitational perturbations from Solar system planets and radiative forces (radiation pressure and Poiting-Robertson drag) were taken into account.

RESULTS AND CONCLUSIONS:

After ejection meteoroid swarm elongates, stretches along the orbit of the parent body. Lighter particles move relatively faster and form looped quasi-ring structure first. The time of quasi-ring formation depends on particle size.

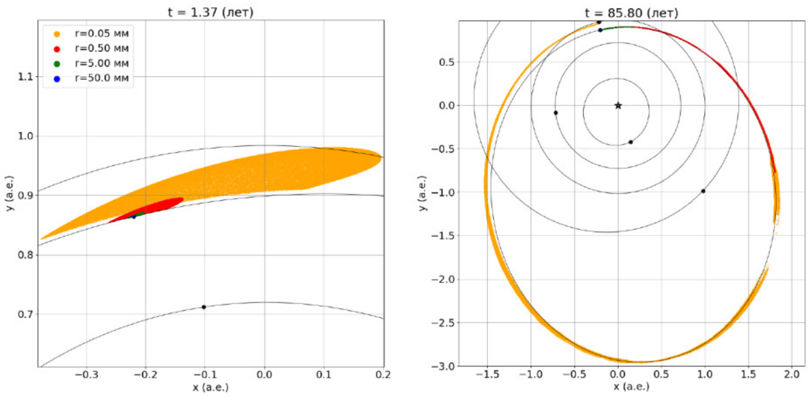

Fig. 1. Meteoroid stream projection on the ecliptic plane in time t = 1.37 yr and t = 85.8 yr. Black asterisk and dots is the Sun, planets and parent body, black lines represents orbits of planets and parent body. Particles of different radius r are shown by colors

As can be seen from the figure small particles are more affected by radiation forces and their orbits are more perturbed and located farthest from parent body orbit than orbits of larger particles. Structure of stream is not regular, there are sections without meteoroids at all (see Fig. 1, *right*). This is caused by close encounters with planets. Such irregularities are difficult to predict for real streams since exact collision time and place are not known.

Ejection of meteoroids and dust during the collision takes place once, opposed meteoroid streams originating from comets, where meteoroid swarm forms every time when comet gets close to the Sun. It specifies the difference in lifetime and observable characteristics of meteoroid streams with different origin mechanisms.

Acknowledgments:

This work is supported by Russian Scientific Foundation, grant no. 22-12-00115.

References:

[1] *Jewitt D., Hsieh H.H.* The Asteroid-Comet Continuum // arXiv e-prints. 2022. arXiv:2203.01397.

[2] *Busarev V.V., Barabanov S.I.,* Puzin V.B. Material composition assessment and discovering 43 sublimation activity on asteroids 145 Adeona, 704 Interamnia, 779 Nina, and 1474 Beira // Solar System Research. 2016. V. 50. No. 281–293. DOI:10.1134/S003809461604002X.

[3] Jewitt D., Weaver H., Agarwal J., Mutchler M., Drahus M. // AAS/Division for Planetary Sciences Meeting Abstracts. 2010. 42. 53.03.

[4] *Shustov B.M., Zolotarev R.V., Busarev V.V., Shcherbina M.P.* Impact Events as a Possible Mechanism to Initiate Sublimation–Dust Activity of Main-Belt Asteroids // Astronomy Reports. 2022. V. 66. No. 11. P. 1098–1110. https://doi.org/10.1134/S1063772922110178.

[5] *Nakamura A., Fujiwara A.* Velocity distribution of fragments formed in a simulated collisional disruption // Icarus. 1992. V. 92. Iss. 1. P. 132–146. https://doi.org/10.1016/0019-1035(91)90040-Z.

[6] *Li J.-Y., Hirabayashi M., Farnham T.L. et al.* Ejecta from the DART-produced active asteroid Dimorphos // arXiv e-prints, 2023, arXiv:2303.01700.

[7] *Rein H., Liu S.F.* REBOUND: an open-source multi-purpose N-body code for collisional dynamics // Astronomy and Astrophysics. 2012. V. 537. Art. No. A128. https://doi.org/10.1051/0004-6361/201118085.

POLARIMETRY OF NEAs AT THE CRIMEAN ASTROPHYSICAL OBSERVATORY AND THE PEAK TERSKOL OBSERVATORY IN 2019–2023

N. Kiselev[1,2], N. Karpov[2], A. Savushkin[1], D. Petrov[1], A. Gorshkov[2], E. Zhuzhulina[1], A. Shein[2], K. Antoniuk[1]

[1] *Crimean Astrophysical Observatory RAS, Nauchny, Russia, kiselevnn42@gmail.com*

[2] *Institute of Astronomy RAS, Moscow, Russia*

KEYWORDS:
NEAs, ground-based observations, polarimetry, albedo, diameters

INTRODUCTION:

The study of near-Earth asteroids (NEAs) holds significant importance for several reasons. NEAs provide valuable insights into the phase dependences of brightness and polarization of airless objects in the solar system, particularly at large phase angles. This complements the data obtained for main belt asteroids (MBAs). In particular, this allows obtaining the most complete, for ground-based observations, phase dependence of the polarization, including characteristics of the polarization maximum. This, in turn, allows for the determination of surface albedo and, as a result, properties of the regolith particle. Additionally, some NEAs may serve as nuclei of extinct comets. Moreover, studying the physical properties of small kilometer-sized NEAs aids in comparing surface properties among asteroids with different origins and degrees of regolith maturity. Given the increased efforts to address asteroid-comet hazards, comprehensive studies of NEAs have gained importance and practical relevance.

OBSERVATIONS AND RESULTS:

To measure the polarization of the ASSBs the 2.6-m (f/16) Shajn telescope of the Crimean Astrophysical Observatory and the 2-m (f/8) telescope of the Peak Terskol Observatory were used. The telescopes are equipped with the same design dual channel photoelectric polarimeters “POLSHAKH”. The red channels were used for observations of the program objects in the *RI* bands. The blue channels provide observations in the *UBV* bands. In 2019–2023, we carried out polarimetric measurements of 8 NEAs, which approached the Earth during the periods allocated for polarimetric observations and which were available in brightness. They are 162082 (1998 HL1), 163373 (2002 PZ39), 52768 (1982 OR2), 159402 (1999 AP10), 2010 (XC15), (2212) Hephaistos, 37638 (1993 VB), and 2006 HV5.

Due to the fact that 6 of them were observed near the maximum, or near the inversion point, or near the minimum of polarization, we determined their albedo ρv using the relations $P_{\max}$ vs albedo, the polarimetric slope h vs albedo, $P_{\min}$ vs albedo [1–2].

$\log \rho v = -0.71 \log P_{\max} - 1.65$ [1],

$\log \rho v = -1.016 \log h - 1.719$ [2],

$\log \rho v = -1.331 \log P_{\min} - 0.882$ [2].

Using equation [3], we have estimated the average sizes of some NEAs.

$\log D = 3.1236 - 0.2H - 0.5 \log \rho v$ [3].

Where H is absolute magnitude of NEA in the V band at unit heliocentric and geocentric distances and zero phase angle, was taken from (http://www.johnstonsarchive.net/astro/spitzerasteroids.html). Polarization and physical parameters of the NEAs are presented in Table 1, where we listed the dynamical class, the range of observed phase angle $\Delta\alpha$, the degree of minimal polarization $P_{\min}$, the inversion angle α_{inv}, the polarimetrical slope h, the degree of maximal polarization $P_{\max}$, the geometric albedo ρ, diameter asteroids D, and the taxonomical class, according to polarization data.

Table 1. Polarization and physical parameters of observed NEAs

NEAs Number	Orb class	$\Delta\alpha$, deg	P_{min}, %	α_{inv}, deg	h, %/deg	P_{max}, %	ρ	D, km	Taxon class
162082 (1998 HL1)	Apollo, PHA	3.5–27.1	−0.48± 0.06	19.0±0.2			0.40±0.19	0.31±0.10	S
163373 (2002 PZ39)	Apollo, PHA	69.2–109.4				4.1±0.3	0.17±0.10	0.48±0.17	S?E
52768 (1982 OR2)	Apollo, PHA	70.5–75.9		20.1±1.9	0.16±0.02		0.17±0.14	1.80±0.99	S?C
159402 (1999 AP10)	Amor	32.1–71.6		20.1±1.9	0.16±0.02		0.35±0.23	1.20±0.29	S?C
2010 (XC15)	Aten, PHA	58.6–65.8				1.82	0.38	0.11	E
(2212) Hephaistos	Apollo	38.3–116.6				7.0	0.15	6.9	S
37638 (1993 VB)	Apollo, PHA	47.4							S?C
2006 HV5	Aten, PHA	73.2							S

The results of our observational campaign are shown in the Fig. 1 for the data in the V and R bands, respectively. The same figures show the synthetic phase-polarization curves of the main taxonomic classes C, S and E, obtained from the Asteroid Polarimetric Database (APDB) (https://data.amerigeoss.org/ru/dataset/asteroid-polarimetric-database-v8-0).

As one can see, data of NEA 162082, (2212) Hephaistos and 2006 HV5 are close to the synthetic polarization curves for the S taxonomic class in both wavelength bands. The polarization data for NEA 159402, 37638 and 52768 complement each other and lie between the synthetic polarization curves for classes C and S in both bands. The data of NEA 163373 are between the synthetic polarization curves for the S and E taxonomic classes. The data of NEA 2010 (XC15) correspond to the synthetic polarization curve for the E taxonomic class, based on the data for NEAs 33342 and 144898 (https://data.amerigeoss.org/ru/dataset/asteroid-polarimetric-database-v8-0). Thus, 2010 (XC15) is the third representative of a rare taxonomic E-class of NEAs which were observed at large phase angles.

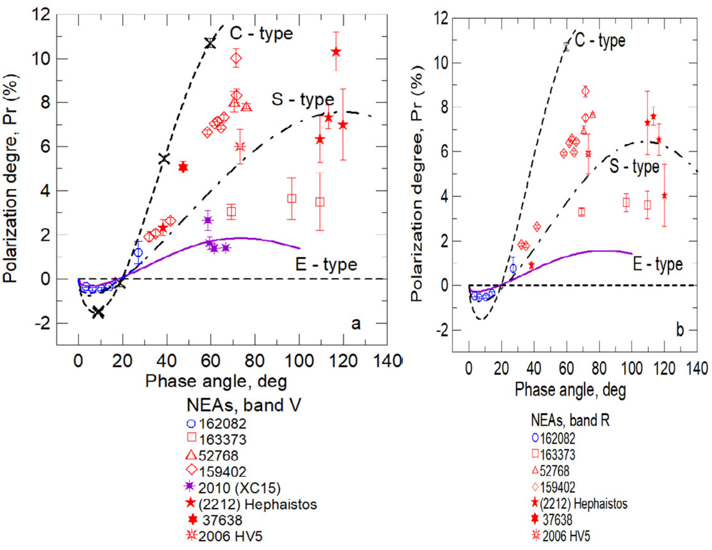

Fig. 1. The polarization phase dependences for observed NEAs in the V and R bands. Dashed, dash-dotted, and solid lines are the synthetic phase-polarization curves for taxonomic asteroids classes C, S and E, respectively.

The modified Sh-matrix method [4, and references therein] was used to interpret the obtained data, in particular, a significant deviation of the polarization of some asteroids from the synthetic phase dependences of the polarization of the main taxonomic C, S and E classes. The computer simulation has shown that different values of the maximum of positive polarization can be explained by different content of highly absorbing carbon matter.

References:

[1] *Lupishko D.F.* Generalized Calibration of the Polarimetric Albedo Scale of Asteroids // Solar System Research. 2018. V. 52. Iss. 2. P. 98–114. DOI: 10.1134/S0038094618010069.

[2] *Bowell E., Zelner B.* Polarizations of Asteroids and Satellites // Planets, Stars and Nebulae: Studied with Photopolarimetry / ed. Gehrels T. 1974. P. 381–404.

[3] *Muinonen K., Belskaya I., Cellino A. et al. A* Three-Parameter Magnitude Phase Function for Asteroids // Icarus. 2010. V. 209(2). P. 542–555. DOI:10.1016/j.icarus.2010.04.003.

[4] *Petrov D.V., Kiselev N.N.* Conjugated Gaussian Random Particles Model and its Application for Interpretation of Cometary Polarimetric Observations // Solar System Research. 2019. V. 53. Iss. 4. P. 294–305. https://doi.org/10.1134/S0038094619040075.

ABOUT THE GTOC XII PROBLEM

A.S. Samokhin, M.A. Samokhina, A.A. Galyaev
Institute of Control Sciences RAS, samokhin@ipu.ru

KEYWORDS:
GTOC, global optimization, trajectory optimization, flight to the asteroid, low thrust

INTRODUCTION:
The GTOC Global Trajectory Optimization Competition was founded by Dario Izzo from ESA in 2005. Since then, 12 editions have already taken place. The audience of participants expands each year, with 102 teams participating for the 2023 competition.

PROBLEM STATEMENT:
In 2035, humanity begins mining minerals from asteroids. For successful mining on an asteroid it is necessary to realize two consecutive rendezvous with the asteroid by the same or two different spacecrafts, controlled by electric engines of low thrust, the value of thrust was limited to 0.6 N. Ten kilograms of payload is extracted from a single asteroid in one year. The number of ships available is highly dependent on the total mass extracted.

Participants were required to extract as much mass as possible. If one of the teams had already flown to a given asteroid, the contribution of the extracted mass to the functionality was reduced.

In total, the participants were offered a choice of 60000 asteroids, the orbital elements of which were set. The starting mass of each spacecraft should not exceed 3 tons, the final mass should not be less than 500 kilograms. The total duration of the mission was limited to 15 years. The asteroids moved in the central Newtonian field of the Sun's gravitational forces. The spacecraft were allowed to perform perturbation maneuvers.

All spacecraft launched from the Earth and automatically dropped the extracted cargo to the Earth at the subsequent passage of it with a relative velocity of less than 6 km/s, at which point the functional was calculated.

SOLUTION METHODS:
For the construction of trajectories with low thrust, the impulse approximation can be taken as a basis, in which the problem of flight to an asteroid, between asteroids, or return to Earth is guaranteed to be solved as a Lambert problem. Our team solved it on the basis of the universal Kepler equation. This allows us to select good asteroids and good start and finish times for them. Then the flight trajectory can be recalculated based on the Lagrangian principle to obtain the values of the targeting parameters — conjugate variables in the impulse formulation.

After that, a transition to the construction of the problem with continuous thrust is possible; for this purpose, an ideally controlled thrust with optimization of the integral of the square of acceleration can be considered first, and then the thrust can be successively constrained in the formulation to satisfy the constraints of the problem.

Thus the problem is reduced to selection of successful sequences of asteroids and optimization of their flyby times, as well as implementation of the selected flyby chains with low thrust, so that the functional of the original problem is as high as possible and the trajectories satisfy all the constraints.

The idea of splitting the problem into search for successful first asteroids, search for last asteroids, and construction of chains of intermediate asteroids is reasonable. Also, mixing asteroids between ships is quite effective - those asteroids that were successfully located relative to each other at the beginning of the mission lose this property when trying to rendezvous at the end.

The report will present the results of solving the problem by different teams.

MAPPING OF HYPERION IN THE TRIAXIAL ELLIPSOID PROJECTIONS

A.I. Sokolov[1], I.E. Nadezhdina[2], M.V. Nyrtsov[1], A.E. Zubarev[2], M.E. Fleis[3], N.A. Kozlova[2]

[1] *Lomonosov Moscow State University, Moscow, Russia, ikionyedi@yandex.ru*
[2] *Moscow State University of Geodesy and Cartography, Moscow, Russia, n_kozlova@miigaik.ru*
[3] *Institute of Geography RAS, Moscow, Russia, fleis.maria@yandex.ru*

KEYWORDS:
Hyperion, geodetic heights, triaxial ellipsoid, shape model, map projections, distortions in projections.

Due to the chaotic rotation of Saturn's satellite Hyperion, there is an ambiguity in determining the body-fixed coordinate system for its mapping [1–2]. In this regard, when compiling the map, the approximating ellipsoid was used, with semi-axes 177.6, 128.5 and 105.6 km, and the coordinate system based on it. In addition to the parameters of the ellipsoid, photogrammetric processing of images obtained by the Cassini spacecraft made it possible to obtain a photomosaic and a shape model of Hyperion.

Geodetic heights relative to the triaxial ellipsoid with the specified parameters were calculated using the shape model. The calculation of heights is based on the joint use of the equation of the normal to the surface passing through a given point, and the equation of the surface itself and the solution of the equation of the sixth degree by the Sturm method [3]. The contour lines displayed on the map were obtained from the calculated heights and are in good matching with the photomosaic.

The Hyperion map was compiled in meridian section projections (cylindrical and azimuthal) of a triaxial ellipsoid, the formulas of which are presented in [4]. The largest features of the surface of this celestial body are clearly visible both in the photomosaic and in contour lines. The choice of map projection is due to the need to correctly display the contours of the relief. When choosing a layout, an analysis was made of the distribution of distortions of various types (the local linear scale along a meridian, the local area scale, the maximum angular deformation) in the projections of the meridian section for Hyperion. The resulting map layout ensures the integrity of the image of the polar regions and the optimization of distortions.

References:

[1] *Nadezhdina I.E., Konopikhin A.A.* Prospects of an integrated approach to small celestial bodies chaotic rotation dynamics study // Izvestiya vysshikh uchebnykh zavedenii. Geodeziya i aerofotos"emka. 2022. V. 66. No. 3. P. 27–41. DOI: 10.30533/0536-101X-2022-66-3-27-41 (in Russian).

[2] *Harbison R.A., Thomas P.C., Nicholson P.C.* Rotational modeling of Hyperion // Celestial Mechanics and Dynamical Astronomy. 2011. V. 110. No. 1. P. 1–16. https://doi.org/10.1007/s10569-011-9337-3.

[3] *Fleis M.E., Nyrtsov M.V., Borisov M.M., Sokolov A.I.* Accurate Calculation of Geodetic Heights of a Celestial Body's Surface Points Relative to the Triaxial Ellipsoid // Doklady Earth Sciences. 2019. V. 486. No. 2. P. 663–668. DOI: 10.1134/S1028334X19060035ю

[4] *Nyrtsov M.V., Fleis M.E., Sokolov A.I.* Meridian section projections: a new class of the triaxial ellipsoid projections // Geodezia i kartografia. 2021. V. 82. No. 2. P. 11–22 DOI: 10.22389/0016-7126-2021-968-2-11-22 (in Russian).

 14MS3-SB-22 ORAL

SATURN'S MAGNETISM IN THE ORIGIN OF DENSE RINGS AND IN THEIR PECULIARITIES RECORDED BY THE CASSINI PROBE. THE TCHERNYI – KAPRANOV EFFECT

V.V. Tchernyi[1], S.V. Kapranov[2], M.V. Belodedov[3]
[1] *Modern Science Institute, Science and International Business Research, Moscow, Russia, chernyv@mail.ru*
[2] *A.O. Kovalevsky Institute of Biology of the Southern Seas RAS, Sevastopol, Russia, sergey.v.kapranov@yandex.ru*
[3] *Bauman State Technical University, Moscow, Russia, m.belodedov@mail.ru*

Keywords:
Saturn's rings origin, magnetic anisotropic accretion, separation of particles inside the rings, diamagnetism of space ice, Saturn's rings peculiarities

We show that Saturn's magnetism makes an important contribution to the origin of dense rings, and also helps to explain and evaluate some of their features, for example, such as the equilibrium separation of ice particles in dense rings, which has not yet been fully explained, and others. Many features of dense rings were observed and measured by the Cassini probe, but could not be explained within the framework of known gravitational theories. There are number of gravitational models of the origin of Saturn rings: a moon of the planet could have been disrupted by a passing celestial body; the rings could have been generated by the pieces separated from moons of the outer planets by collision with comets or meteorites; the ring particles can be debris of a large comet tidally broken by the planet; the rings can be the relic of a protosatellite disk [1–5]. Unfortunately, no theory has provided a convincing explanation for the observed features and peculiarities of Saturn's dense rings among the bodies of the Solar System [6–7]. Cassini measured that the particles of rings mostly consist of water ice, 90–95 % [3–4, 8]. Also Cassini found the ratio of deuterium and hydrogen isotopes for the ice of Saturn's dense rings is the same as for the Earth's ice [9]. This fact indicates the similarity of ice in the rings and Earth's ice. About 20 types of ice are known on Earth. Ice XI is a good analogy and is more suitable for the dense rings of Saturn [10]. It has stable parameters below 73K and it is diamagnetic [11], Figure 1.

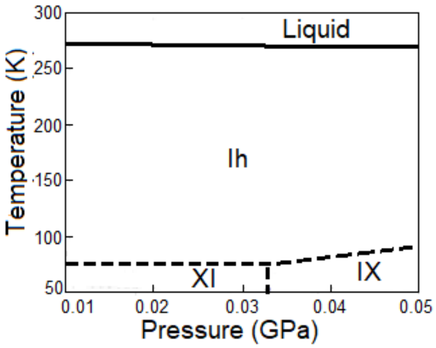

Fig. 1. Low-pressure and the low-temperature part of the phase diagram of ice XI [10]

With these data at hand, we have found a solution to the problem of the interaction of gravitational field and magnetic field of Saturn with diamagnetic ice particles moving in Keplerian orbits around Saturn in a protoplanetary cloud [12]. An interesting fact is that it takes into account the action of magnetic field of Saturn in addition to the action of gravitational field, explains the transformation of a protoplanetary cloud into a disk of stable dense rings, and accounts for strong planar structure of rings located in the magnetic equator of Saturn. This scenario is shown in Figure 2.

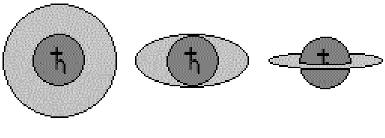

Fig. 2. Evolution of Saturn's protoplanetary cloud into disk-shaped dense rings under the action of the gravitational, centrifugal and magnetic forces: (a) → (b) →(c)

Cassini discovered that Saturn's magnetic equator almost coincides with the geographical one [13]. Saturn's magnetic field has a dipolar structure in the region of dense rings [14]. Finally, we come to a conclusion that Saturn could create its dense rings from the particles and chunks of the protoplanetary cloud by means of its own magnetic field due to the action of an additional third force of diamagnetic expulsion and the mechanism of magnetic anisotropic accretion (Tchernyi – Kapranov effect) [15]. It is worthwhile to note that Saturn has a spherically symmetric gravitational field and an axisymmetric magnetic field. First, a problem of magnetization of spherical ice particle in the external magnetic field was solved, and then, by analogy, the solution was extended to a system of identical uniformly magnetized ice particles with constant number density in an infinite disk-like structure. The equations of collisionless motion of magnetic ice particles orbiting at a constant radius to the center in the gravitational and magnetic fields of the planet are reduced to the equation for the polar angle ϑ_{Sp} of the orbiting particle:

$$\ddot{\theta}_{Sp} + \dot{\theta}^2_{Sp} \cot\theta_{Sp} = \frac{GM_S}{r^3_{Sp}} \cot\theta_{Sp} + \frac{3C\mu_0^2 m_S^2}{2\pi^2 r^8_{Sp} M_p} \cot\theta_{Sp} \cos^2\theta_{Sp}, \tag{1}$$

where G is the gravitational constant, Ms is the mass of Saturn, r_{Sp} is the radial distance between the centers of Saturn and the spherical particle, m_s is the magnitude of magnetic moment of Saturn, M_p is the mass of particle with magnetic moment m_p, and C is the Clausius-Mossotti coefficient for magnetic spheres, which depends on the particle environment. The only solution of equation (1) is singular: $\vartheta_{Sp} = \pi/2$. It accounts for essentially planar structure of Saturn's dense rings and their location in the magnetic equator plane. The relationship for the azimuthal velocity of the particle is

$$\dot{\varphi}_{Sp} = \sqrt{\frac{GM_S}{r^3_{Sp}} + \frac{3C\mu_0^2 m_S^2}{8\pi^2 r^8_{Sp} M_p}}. \tag{2}$$

In equation (2) the gravitational force acting on the orbiting particle is counterbalanced by both the centrifugal force and the force of diamagnetic expulsion. As mentioned, the factor C is a function of the particle environment.

An interesting feature is that ice particles in dense rings are separated in the presence of the gravitational and magnetic fields of Saturn. If there were no repulsive force prevailing over the force of attraction between the particles at short distances, then the particles of the rings would stick together and form a new satellite. In the case of rings, the repulsive force can only have a non-gravitational nature, similar to the magnetic repulsion force [16]**.** The fact that rings along the orbit are not continuous, but consist of separated particles has been proved by J.K. Maxwell [17]. The Newtonian dynamics for a single particle differs from the dynamics for particles assembled in rings. Particles repel each other under the influence of magnetic force and are attracted to each other under the influence of gravity. From the balance of the forces of gravitational attraction and magnetic repulsion, we have derived the expression for the evaluation of equilibrium distance r_0 between the particles in the ring, Fig.3. Of the entire spectrum of theories of the origin of Saturn's rings, the only theory that takes into account the action of the magnetic field allows us to explain and evaluate the separation of particles in the rings. The separation of particles is confirmed by images of rings obtained by the Cassini probe in 2004-2017.

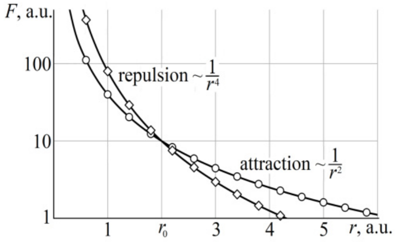

Fig. 3. Dependence of the repulsion and attraction forces on distance between particles

$$r_0 = \left(\frac{R}{r_{Sp}}\right)^3 \frac{m_S}{M_p} \frac{\mu - \mu_0}{\mu + 2\mu_0} \sqrt{\frac{3\mu_0}{4\pi G}}, \tag{3}$$

where R is the particle radius, where μ and μ_0 are magnetic permeability of the particle material and free space.

References:

[1] *Charnoz S., Morbidelli A., Dones L. et al.* Did Saturn's Rings Form during the Late Heavy Bombardment? // Icarus. 2009. V. 199. Iss. 2. P. 413–428. https://doi.org/10.1016/j.icarus.2008.10.019.

[2] *Canup R.M.* Origin of Saturn's Rings and Inner Moons by Mass Removal from a Lost Titan-sized Satellite // Nature. 2010. V. 468. P. 943–946. https://doi.org/10.1038/nature09661.

[3] *Cuzzi J.N., Burns J.A., Charnoz S. et al.* An Evolving View of Saturn's Dynamic Rings // Science. 2010. V. 327. Iss. 5972. P. 1470–1475. DOI: 10.1126/science.117911.

[4] *Esposito L.W.* Composition, Structure, Dynamics, and Evolution of Saturn's Rings // Annual Review of Earth and Planetary Science. 2010. V. 38. P. 383–410. https://doi.org/10.1146/annurev-earth-040809-152339.

[5] *Porco C.C.* Cassini at Saturn // Scientific America. 2017. V. 317. No. 4. P. 78–85. DOI: 10.1038/scientificamerican1017-78.

[6] *Crida A., Charnoz S.* Solar System: Recipe for Making Saturn's Rings // Nature. 2010. V. 468. P. 903–905. https://doi.org/10.1038/nature09738.

[7] *Estrada P., Durizen R., Cuzzi J.* After the Cassini grand finale, is there a final consensus on ring origin and age? // American Geophysical Union meeting. New Orleans. 11–15 Dec. 2017. Art. No. 298112.

[8] *Poulet F., Cuzzi J.N.* The composition of Saturn's rings // Icarus. 2002. V. 160. Iss. 2. P. 350–358. https://doi.org/10.1006/icar.2002.6967.

[9] *Clark R., Brown R.H., Cruikshank D.P. et al.* Isotopic ratios of Saturn's rings and satellites // Icarus. 2019. V. 321. P. 791–802. https://doi.org/10.1016/j.icarus.2018.11.029.

[10] *Hemley R.J.* Effects of high pressure on molecules // Annual Review of Physical Chemistry. 2000. V. 51. P. 763–800. https://doi.org/10.1146/annurev.physchem.51.1.763.

[11] *Tchernyi V.V., Kapranov S.V.* To the problem of the properties of Saturn's rings' ice // *Research Notes of the American Astronomical Society. 2021. V. 5. No. 10. P. 255. DOI 10.3847/2515-5172/ac348c.*

[12] Tchernyi V.V., Kapranov S.V. Contribution of Magnetism to the Origin of Saturn's Rings // The Astrophysical J. 2020. V. 894. No. 1. Art. No. 62. 6 p. DOI 10.3847/1538-4357/ab8475.

[13] Dougherty M., et al. Saturn's magnetic field revealed by the Cassini grand finale // Science. 2018. V. *362. Iss. 6410. DOI: 10.1126/science.aat5434.*

[14] André N., Cao H., Khurana K.K. et al. Identification of Saturn's magnetospheric regions and associated plasma processes: Synopsis of Cassini observations during orbit insertion // Reviews of Geophysics. 2008. V. 46. No. 4. 22 p.

[15] *Tchernyi V.V., Kapranov S.V.* How Saturn could create dense rings after the emergence of its magnetic field. The Tchernyi-Kapranov effect: mechanism of magnetic anisotropic accretion // Physics and Astronomy Intern. J. 2023. V. 7. No. 1. P. 54–57. DOI: 10.15406/paij.2023.07.00284.

[16] *Tchernyi V.V., Kapranov S.V., Belodedov M.V.* The role of Saturn's magnetism in the equilibrium separation of particles of dense rings // Physics and Astronomy Intern. J. 2023. V. 7. No. 2. P. 146–148.

[17] *Maxwell J.C.* On the Stability of the Motion of Saturn's Rings // Monthly Notices of the Royal Astronomical Society. 1859. V. 19. Iss. 8. P. 297–304. https://doi.org/10.1093/mnras/19.8.297.

VYSIKAYLO' CUMULATIVE PLASMA CANNON ON THE PROTECTION OF THE EARTH FROM METEOROIDS

P.I. Vysikaylo
Moscow State Regional University, Moscow, Russia, filvys@yandex.ru

This year marks the 10th anniversary of the destruction Chelyabinsk' meteoroid!

KEYWORDS:
Vysikaylo's plasma cumulative-dissipative structures, coulomb explosion, runaway electrons, impulse advancement of lightning, Schonland's lightning experiments (1934–1937), Vysikaylo's mechanism of meteoroid fragmentation

INTRODUCTION:
De Broglie reported that particles behave like waves. The author proves that de Broglie waves of free electrons in the plasma tail of a meteoroid behave like electromagnetic waves in a quantum resonator (laser) and form a beam (jet) of high-energy electrons directed into the meteoroid. A jet of high-energy electrons formed in the plasma tail behind the meteoroid sprays the meteoroid with the help of a Coulomb explosion (or a series of them). This phenomenon in the plasma cumulative-dissipative structure of Vysikaylo, limited by Coulomb barriers in the plasma tail behind the meteoroid ~20 km long (Fig. 1), is associated with cumulative and dissipative processes of transformation of the mechanical energy of the entire meteoroid into electrical energy and then into the energy of meteoroid destruction and its spray up to positive ions and electrons.

Fig. 1. This is a photograph [5] of the Coulomb explosion [3] that breaks the 2013 Chelyabinsk meteoroid to ions and electrons. This phenomenon is clearly electrical in nature, like the sparking of contacts in a trolleybus or tram, or a cathode spot that "spits out pieces" of the cathode (see [3–4] for more details)

The kinetic energy of the meteoroid is enough for this with a margin. In this phenomenon, as proved in this article, the virial theorem is fulfilled: half of the Coulomb energy (equal to the kinetic energy of the meteoroid) goes to form a beam of high-energy electrons catching up with the meteoroid, and the other half goes to dumping positive ions along the plasma tail behind the meteoroid, in the direction opposite to the motion of the meteoroid. This is how the Vysikaylo's cannon is formed, shooting at the meteoroid. As a recoil in such a cannon, positive ions are ejected in the opposite direction of the meteoroid motion. Based on this idea, we proposed and investigated a new 4D inertial-polarization-quantum cumulative-dissipative **Vysikaylo's mechanism for the fragmentation of meteoroids** and small comets (self-protection of the Earth from meteoroids) into simple ions and electrons. The mechanism is based on the similar coherent behavior of de Broglie waves of electrons in the plasma tail behind the meteoroid and in front of pulsed lightning from negatively charged clouds. The formation of a cumulative electron jet in front of an impulsively moving lightning was studied in detail in the experiments of Schonland et al. in 1934–1937 [1]. The physical explanation of such functioning of lightning (~2 km in size) from negatively charged clouds to positively charged clouds was first given in [2].

COULOMB MECHANISM OF METEOROID FRAGMENTATION: Behind a fast-flying (10–40 km/s) meteoroid or other object in the Earth's atmosphere, the air is heated and strongly ionized. At a meteoroid velocity of 20 km/s, the energy received by air molecules is about 50 eV. This is three times the ionization potential of air molecules. The more mobile electrons leave the ionization region, the more the plasma is polarized and a radially self-cumulating plasmoid (see Fig. 1) is formed in the wake of the meteoroid (the Vysikaylo' cumulative-dissipative structure). A cumulative jet (CJ) of high-energy electrons behaving coherently, like electromagnetic radiation in a laser, accumulates (focuses) the energy stored throughout the plasmoid — in a huge storage capacitor of electrical and kinetic energies (Fig. 2*a*).

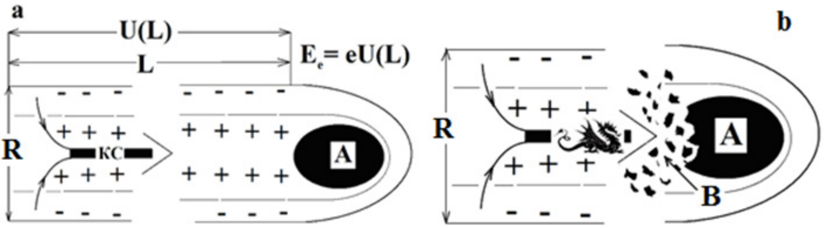

Fig. 2. Two-dimensional scheme: *a* — a Vysikaylo' railgun with a space charge operating on Coulomb (polarization) forces [3–4], and not on Lorentz forces (as in the Artsimovich railgun). "+" and "–" — represent the separation of the space charge (polarization) of the plasma behind a rapidly moving object — A in the medium. Behind body A, a cumulative jet (CJ) of electrons is formed in a positively charged plasma column, converting the potential energy of polarization (the kinetic energy of the meteoroid) into energy CJ; *b* — a new cumulative-plasma mechanism of fractal fragmentation of meteoroids, initiated by Coulomb explosions. This mechanism was proposed by the author in [3–4]. A is a fast moving object in an electronegative medium. B — exploding fragments that form a jet engine behind object A and simultaneously destroy it from behind, thereby supplying the engine with a new high-energy "fuel" with an energy of 200 eV per atom of already solid fuel (at a meteoroid speed ~20 km/s).

The plasmoid grows linearly with the speed of a meteoroid. The flow of high-energy electrons catching up with the meteoroid periodically explodes the meteoroid with a electrons (Coulomb forces) and accelerates its parts, including in the direction of the meteoroid (Fig. 2*b*). We estimated the parameters of the high-energy electron beam for lightning (~2 km) in [2], and for the plasma tail of the Chelyabinsk meteoroid (its length is ~20 km) in [3–4]. According to the Coulomb mechanism proposed by us [3–4] and according to the virial theorem: half of the entire kinetic energy of a meteoroid goes to its destruction and acceleration of its parts by a beam of fast electrons, and the other half goes to discharge positive ions into the upper layers of the atmosphere (up to heights of 70–80 km). In [3–4], we explained all the phenomena observed by eyewitnesses during the complete destruction of the Chelyabinsk meteoroid at an altitude of 23 km.

CONCLUSION: In [3–4] we have proposed for the first time a model of the Coulomb explosion of a meteoroid. The formation of plasma structures, plasmoids, is caused by the radial focusing (cumulation) of a positive charge by returning electrons. The results obtained by us are compared with the experimental observations of Schonland (1934–1937) [1] for the pulse-periodic advance of linear lightning near the Earth's surface. Based on the de Broglie hypothesis: "particles behave like waves", we have shown that de Broglie waves of electrons in plasmoids can behave like electromagnetic waves in quantum generators (lasers) — form longitudinal opposite energy flows from a plasmoid resonator if there is an external electric field. In [3–4] we explained the processes of radial cumulation of all energy-mass-momentum flows to the center of a positively charged plasma structure behind a meteoroid. The escape of free high-energy electrons and the constant growth of a positively charged region behind a moving meteoroid (see Fig. 2*a*) is a generator of an electric field affecting the formation of a beam of high-energy electrons escaping into the meteoroid and a stream of positive ions tending in the opposite direction. Since the charge of electrons is equal to the charge of positive ions, the forces and work of the electric field on the flows of electrons and positive ions are equal. As a result, the virial theorem is realized in the form of two quasi-neutral counter flows to and from the meteoroid. The analogue of a fully reflecting mirror in the case of a plasmoid (see Fig. 1) is the end of the tail, a positively charged plasmoid (at a distance of 20 km from the meteoroid). The analogue of a transparent mirror is the meteoroid itself, which gives rise to another element of a positively charged plasmoid (see Fig. 2*b*). The results we obtained in [3–4] are useful for completely new discoveries, explanations of paradoxes and the development of completely unexpected new technologies - flying on your own plasma tail. After analyzing these visualized phenomena, we come to understand that photographs (see Fig. 1) and videos [5] are undoubtedly worthy of the highest awards and commendations. They completely reverse the “classical” mechanical concepts of many natural phenomena, transferring them from the class of phenomena in the “quasi-liquids” of Chernogor [6] to the class of cumulative-dissipative synergetic (coherent) plasma processes in the Vysikaylo’ cumulative-dissipative structures.

Within the framework of only a mechanical model [6], Chernogor could not explain the whole range of amazing phenomena that occurred during the penetration of the Chelyabinsk meteoroid in 2013 into the Earth’s electronegative atmosphere and recorded in [5] and in photo 1! All these processes can be explained only on the basis of the theory of cumulative-dissipative plasma structures of Vysikaylo, with the involvement of cyclic plasma-chemical processes [3–4]. These processes are significantly enhanced by mechanical processes with explosions and spraying of small fragments up to ions (after the next crushing of the meteoroid) and are accompanied, in turn, by charge separation due to the difference in the masses of electrons and positively charged ions (see Fig. 2). All the kinetic energy of the parts of the meteoroid goes into the internal energy of the plasmoid and then into the electrical energy of the capacitor, which gives it to the electrons escaping from the plasmoid. In this case, the role of electron-electron collisions in the formation of a beam of high-energy electrons escaping into a meteoroid is essential. This follows from the presence of an electrophonic effect observed by a number of witnesses to the event in Chelyabinsk [3–4].

References:

[1] *Loeb L.B.* Fundamental Processes of Electrical Discharge in Gases. J. Wiley and Sons, 1950. 717 p. (*Leb L.* Osnovnye protsessy elektricheskikh razryadov v gazakh. Leningrad: Gosudarstvennoe izdatel’stvo tekhniko-teoreticheskoi literatury, 1950. 672 p. (in Russian)).

[2] *Vysikaylo P.I.* Detailed Elaboration and General Model of the Electron Treatment of Surfaces of Charged Plasmoids (from Atomic Nuclei to White Dwarves, Neutron Stars, and Galactic Cores): Self-Condensation (Self-Constriction) and Classification of Charged Plasma Structures — Plasmoids. Part III. Behavior and Modification of Quasi-stationary Plasma Positively Charged Cumulative-Dissipative Structures (+CDS) with External Influences // Surface Engineering and Applied Electrochemistry. 2013. V. 49(3). P. 222–234. https://link.springer.com/article/10.3103/s1068375513030125.

[3] *Vysikaylo P.I.* Kumuljativnoe oruzhie Zemli protiv meteoroidov. // Prostranstvo i vremja. 2013. No. 3(13). C. 145–153. https://space-time.ru/space-time/article/view/2226-7271provr_st4-14.2013.72 (in Russian).

[4] *Vysikaylo P.I.* Pulse-periodic 4D model of energy cumulation and dissipation processes in a meteoroid tail in Earth’s electro-negative atmosphere // 242nd Meeting of the American Astronomical Society. Albuquerque, New Mexico, 4–8 June 2023. aas242-aas 2023. https://aas242-aas.ipostersessions.com/default.aspx?s=A2-09-05-57-8A-37-5A-F3-92-45-FB-FF-F5-17-F5-4F.

[5] https://dzen.ru/video/watch/63f33808d4b39e3d6a1940b8?f=d2d

[6] *Chernogor L.F.* Plazmennye, elektromagnitnye i akusticheskie effekty meteorita “Chelyabinsk” (Plasma, Electromagnetic and Acoustic Effects Ofmeteorite “Chelyabinsk”) // Inzhenernaya fizika. 2013. No. 8. P. 23–40 (in Russian).

SESSION 4. SMALL BODIES (SB)
POSTER SESSION

AN OVERVIEW OF PLUTO'S ATMOSPHERIC STUDIES

M. Madani
BSN Project, Tehran, Iran, iotamiddleeast@yahoo.com

KEYWORDS:
occultations, planets and satellites, atmospheres Kuiper belt objects

INTRODUCTION:
Pluto and its satellites are the best and most comprehensible of the trans-Neptunian objects (TNOs) due to their well-known complicated and active geological properties [1]. The Hubble Space Telescope observation revealed some features of this dwarf planet. Furthermore, NASA's New Horizons spacecraft made a close flyby of Pluto in 2015 in order to study Pluto and its moon Charon [2]. Since the confirmation of the existence of Pluto's atmosphere based on a 1988 stellar occultation [3], the study of Pluto's atmospheric parameters (pressure, composition, temperature, etc.) has carried on using data from both ground-based and space-based observation. To calculate Pluto's atmospheric pressure, [4] developed a model based on a thermal gradient indicated in a light curve as a scale height. This model is a method for precisely coordinating the data obtained from an occultation light curve. The structure of Pluto's atmosphere was determined in the areas examined by the occultation. Additionally, the conceivable physical conditions of the atmosphere on the supposition were investigated [5]. Later, in 2015, a simple atmospheric model, named DO15, was defined based on the use of both direct ray-tracing and inversion approaches by assuming a spherically symmetric, clear, and pure N2 atmosphere (Dias-Oliveira et al. 2015). This model was suitably fit with light curves from 2012 and 2013 stellar occultations between the heights of 1190 and 1450 km from Pluto's center [6]. Research conducted in recent decades has indicated that Pluto's atmospheric pressure changes are due to the seasonal cycles of Pluto's surface volatiles, which were calculated using atmospheric models [7]. In 1988, atmospheric pressure at a radius of 1215 km (the distance to Pluto's center) was estimated [8]. Atmospheric pressure increased to 6.05±0.32 μbar in 2008 [9]. A drop in Pluto's atmospheric pressure was reported from 2008 to 2010, estimated at 5.64±0.22 μbar [10]. The Stratospheric Observatory for Infrared Astronomy (SOFIA) aircraft, simultaneously with ground-based observatories, observed the 2015 stellar occultation by Pluto at an altitude of about 40 000 ft. [11]. Analysis of the data from SOFIA in optical and near-infrared wavelengths, along with ground-based observations, showed that the atmospheric pressure at half-light altitude was stable from 2011 to 2015 [11]. In 2015, Pluto's atmospheric pressure was observed at its maximum value of about 6.92±0.07 μbar [12]. According to a stellar occultation observation in 2019, Pluto's atmospheric pressure was estimated to be 5.20 μbar, which showed a decrease of approximately 21 % between 2016 and 2019 at the 2.4σ level [13]. This is also studied by the [14].

References:

[1] Spencer J., Grundy W.M., Nimmo F. et al. The Pluto system after New Horizons // The Trans-Neptunian Solar System / ed. D. Prialnik, M.A. Barucci, L. Young. Elsevier, 2020. P. 271–288. DOI: 10.1016/B978-0-12-816490-7.00012-6.

[2] *Stern S.A., Bagenal F., Ennico K. et al.* The Pluto System: Initial Results from Its Exploration by New Horizons // Science. 2015. 350(6258). Art. No. aad1815. https://doi.org/10.1126/science.aad1815

[3] *Hubbard W.B., Hunten D.M., Dieters S.W. et al.* Occultation evidence for an atmosphere on Pluto // Nature. 1988. V. 336. P. 452–454.

[4] *Elliot J.L., Young L.A.* Analysis of stellar occultation data for planetary atmospheres. I. Model fitting, with application to Pluto // The Astronomical J. 1992. V. 103. No. 3. P. 991–1015.

[5] *Elliot J.L., Dunham E.W., Bosh A.S. et al.* Pluto's atmosphere // Icarus. 1989. V. 77. Iss. 1. P. 148–170. https://doi.org/10.1016/0019-1035(89)90014-6.

[6] *Dias-Oliveira A., Sicardy B., Lellouch E. et al.* Pluto's atmosphere from stellar occultations in 2012 and 2013* // The Astrophysical J. 2015. V. 811. No. 1. Art. No. 53. DOI: 10.1088/0004-637X/811/1/53.

[7] *Meza E., Sicardy B., Assafin M. et al.* Lower atmosphere and pressure evolution on Pluto from ground-based stellar occultations, 1988–2016 // Astronomy and Astrophysics. 2019. V. 625. Art. No. A42. https://doi.org/10.1051/0004-6361/201834281.
[8] *Yelle R.V., Elliot J.L.* Atmospheric Structure and Composition: Pluto and Charon // Pluto and Charon / ed. S.A. Stern, D.J. Tholen. 1997. P. 347–390.
[9] *Sicardy B., Bolt G., Broughton J. et al.* Constraints on Charon's orbital elements from the double stellar occultation of 2008 June 22 // The Astronomical J. 2011. V. 141. No. 2. Art. No. 67. DOI 10.1088/0004-6256/141/2/67.
[10] *Young L., Sicardy B., Widemann T. et al.* // 42nd Annual Meeting of the Division for Planetary Sciences of the American Astronomical Society. 2010. Abs. No. 42.
[11] *Bosh A.S., Person M.J., Zuluaga C.A. et al.* // 47th Annual Meeting of the Division for Planetary Sciences of the American Astronomical Society. 2015. Abs. No. 47.
[12] *Sicardy B., Talbot J., Meza E. et al.* Pluto's atmosphere from the 2015 June 29 ground-based stellar occultation at the time of the new horizons flyby // The Astrophysical J. Letters. 2016. V. 819. No. 2. Art. No. L38. DOI: 10.3847/2041-8205/819/2/L38.
[13] *Arimatsu K., Hashimoto G.L., Kagitani M. et al.* Evidence for a rapid decrease of Pluto's atmospheric pressure revealed by a stellar occultation in 2019 // Astronomy and Astrophysics. 2020. V. 638. Art. No. L5. https://doi.org/10.1051/0004-6361/202037762.
[14] *Poro A., Farahani* F.A., *Bahraminasr* M. *et al.* Study of Pluto's atmosphere based on 2020 stellar occultation light curve results // Astronomy and Astrophysics. 2021. V. 653. Art. No. L7. https://doi.org/10.1051/0004-6361/202141718.

TWO-DIMENSIONAL DESCRIPTION OF NONLINEAR WAVE PERTURBATIONS IN THE DUSTY SATURN'S MAGNETOSPHERE

S.I. Kopnin[1], D.V. Shokhrin[2], S.I. Popel[1]
[1] *Space Research Institute RAS, Moscow, Russia, shokhrin3@mail.ru*
[2] *National Research University Higher School of Economics, Moscow, Russia*

Two-dimensional description of nonlinear dust-acoustic waves in the dusty Saturn's magnetiosphere that contains electrons of two types (the hot and the cold ones) obeying the kappa distribution, along with magnetospheric ions and charged dust particles, is presented. The Kadomtsev – Petviashvili equation that describes the nonlinear dynamics of the nearly one-dimensional wave structures is derived for the conditions of the dusty Saturn's magnetosphere. The possibility of propagation of localized wave structures of the dust-acoustic soliton type is analyzed. It is demonstrated that the Kadomtsev–Petviashvili equation has solutions in the form of one-dimensional solitons and two-dimensional N-solitons under the conditions of the Saturn's magnetosphere. The possibility of observation of the discussed solitons during future space missions is discussed.

Acknowledgements:
This research was supported by the "BASIS" Foundation for Advancement of Theoretical Physics and Mathematics.

GAIA DATA RELEASE 3: DISTRIBUTION BY SPECTRAL GROUPS OF NEAR-EARTH ASTEROIDS

M.P. Shcherbina[1,2], D.A. Kovaleva[1], B.M. Shustov[1]
[1] *Institute of Astronomy RAS, Moscow, Russia, mpshcherbina@inasan.ru*
[2] *Sternberg Astronomical Institute Lomonosov Moscow State University, Moscow, Russia*

KEYWORDS:
Gaia Data Release 3, near-Earth asteroids, spectral classes, reflectance spectra, potentially hazardous asteroids

INTRODUCTION:
Based on Gaia Data Release 3 data, which contains asteroid reflection spectra, studies of near-Earth asteroids were conducted. The reflection spectra of about 100 representatives of the Aten, Apollo, and Amor groups were evaluated to identify their spectral class. For 47 asteroids, this assessment was made for the first time. For convenience, the classes were grouped into broader spectral groups. The distribution by spectral groups aligns with results obtained earlier using other data on a larger sample of objects.

DESCRIPTION OF GAIA DATA RELEASE 3:
The Gaia Data Release 3 catalog includes observations of Solar System Objects (SSOs) collected during Gaia's operation from August 5, 2014, to May 28, 2017. This catalog presents visible-light reflectance spectra for 60,518 objects — numbered asteroids: most are in the Main Belt, and near-Earth asteroids (NEAs), Trojans, Hungarias, Hildas, and members of the Jupiter family were also selected [1].

Following classical methods [2], the reflectance spectra of the asteroids were calculated by dividing each wavelength by the average of the mean spectra of several solar analog stars. Solar analogs are stars with physical properties (e.g., mass, metallicity, temperature, age) similar to those of the Sun. However, for the purposes of calculating the spectral reflectance of asteroids, solar analogs are stars whose spectra are similar to those of the Sun. The obtained reflectance spectra were normalized to the reflectance value at 0.55 μm. Then, the reflectance spectra were converted into 16 discrete wavelength channels in the range from 374 to 1034 nm. An example of the final asteroid reflectance spectrum is shown in Figure 1 (the reflectance spectrum for asteroid 155,334).

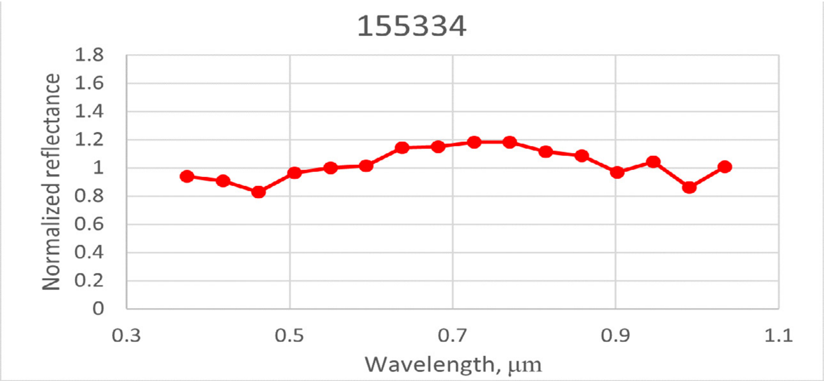

Fig. 1. An example of the final asteroid reflectance spectrum for asteroid 155,334

DESCRIPTION OF THE SELECTED ASTEROID GROUPS:
This paper considers asteroids approaching the Earth, specifically the Aten, Apollo, and Amor groups. These have perihelion distances less than or equal to 1.3 a.u. In the Gaia catalog, the calculated reflectance spectra of near-

Earth asteroids are: Aten group — 4 obj., Apollo group — 49 obj., Amor group — 37 obj. (totaling 91 asteroids).

For each asteroid, additional information (geometric albedo, rotation period, and diameter, indirectly involved in the spectral class estimation) and the spectral class estimation by Tholen or Bus-Binzel taxonomy (SMASSII) were collected, if available in the NASA database. An additional comparison of the results was made for objects previously studied by low-resolution spectrophotometry conducted by INASAN jointly with the SAI MSU at the Terskol Peak Observatory (Terskol branch of INASAN) since 2013. In most cases, the spectral class estimate coincided. Some objects were added, for a total analysis of 107 near-Earth asteroids.

Some asteroids are classified as potentially hazardous. These are asteroids that approach Earth and have orbits that allow them to come within about 0.05 a.u. or less of Earth's orbit (an approximate value due to the difficulty of determining an asteroid's exact position), and whose absolute stellar magnitude does not exceed 22.0. These bodies are classified as potentially hazardous asteroids (PHAs).

DETERMINATION OF THE SPECTRAL CLASS OF ASTEROIDS:

Based on the overall reflectance spectral gradient, absorption bands characteristic of a specific mineral group, and additional information (e.g., geometric albedo), the asteroid's spectral class was estimated.

Given that the definition of subclasses was often very approximate and the situation with several classes of similar mineralogy (quite logical considering the specificity of the data) was often observed, the spectral classes were traditionally divided into large groups, according to their peculiarities:

The C-group includes classes B, C, Cb, Cg, Ch, Cgh (corresponding also to classes B and F according to Tholen's taxonomy). Asteroids of this class have spectra very similar to those of carbonaceous chondrite meteorites (CI and CM).

The S-group includes classes S, A, Q, R, K, L, and the transitional Sa, Sq, Sr, Sk, and Sl. The most suitable analogs are iron-stone meteorites, ordinary chondrites, and achondrites.

The X-group includes classes X, M, E, P (according to Tholen's classification), and transitional ones Xe, Xc, Xk.

Small groups include very rare classes of asteroids: Ld, T, D, V, O.

Some asteroids have a mixed type of surface matter mineralogy, as they simultaneously exhibit features of both high-temperature (S-group) and low-temperature classes (C-group). This result may be indirect evidence of the asteroids' impact history.

It should be noted that for some objects, we gave the first estimate of the spectral class. For 47 asteroids (almost half of the total), this was the first identification of spectral classes.

The results are presented in Table 1 and in the diagram (Figure 2).

Table 1. Distribution of NEA by spectral groups (including PHA)

NEA-group	Total number	C-group	S-group	X-group	Small groups	Mixed type
	of which PHA	*of which PHA*	*of which PHA*	*of which PHA*	*of which PHA*	*of which PHA*
Aten	7	3	1	1	1	1
	4	*2*	*0*	*0*	*1*	*1*
Apollo	57	12	36	1	3	5
	19	*4*	*12*	*0*	*0*	*3*
Amor	45	8	30	0	6	1
	1	*0*	*1*	*0*	*0*	*0*
Total	**109**	**23**	**67**	**2**	**10**	**7**
	24	***6***	13	0	1	4

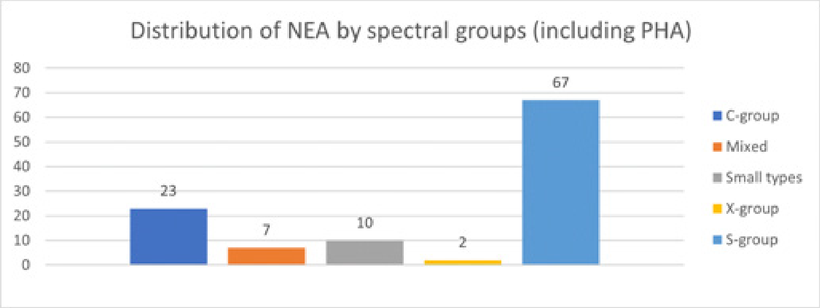

Fig. 2. Distribution of NEA by spectral groups (including PHA)

The results are in good agreement with [3], which presents a sample of more than 1000 NEAs. According to this work, the fractional distribution of the main taxonomic classes (60 % S, 20 % C, 20 % others) remains remarkably constant, even when distributed over asteroid diameters. A similar pattern appears in the GAIA results.

Acknowledgments:
The authors (MPS, BMS) express their gratitude to the Russian Science Foundation (grant no. 22-12-00115) for supporting this work.

References:
[1] *Vallenari A., Brown A.G.A., Prusti T. et al.* Gaia Data Release 3: Summary of the content and survey properties // Astronomy and Astrophysics. 2023. V. 674. Art. No. A1. 22 p. https://doi.org/10.1051/0004-6361/202243940.
[2] *Bus S.J., Binzel R.P.* Phase II of the small main-belt asteroid spectroscopic survey: A feature-based taxonomy // Icarus. 2002. V. 158. Iss. 1. P. 146–177. https://doi.org/10.1006/icar.2002.6856.
[3] *Binzel R.P., DeMeo F.E., Turtelboom E.V. et al.* Compositional distributions and evolutionary processes for the near-Earth object population: Results from the MIT-Hawaii NearEarth Object Spectroscopic Survey (MITHNEOS) // Icarus. 2019. V. 324. P. 41–76. https://doi.org/10.1016/j.icarus.2018.12.035.

ON THE EVALUATION POSSIBILITY FOR THE PROPERTIES OF THE EXOSPHERE OF AN ACTIVE ASTEROID FROM POLARIMETRIC DATA

E.V.Petrova
Space Research Institute RAS, Moscow, Russia, epetrova@cosmos.ru

KEYWORDS:
asteroids, spectropolarimetry, light scattering, aggregate particles

INTRODUCTION:

In recent years it has been found that some objects, being on typical asteroid orbits and definitely composed of nonvolatile materials in general, may demonstrate signs of comet-like activity. About 30 active asteroids (AAs) have been identified so far, and the causes of their activity are currently discussed (e.g., [1]). In some asteroids near perihelion, unusual changes in the shape of spectra in the UV-visible range were registered (e.g., [2]). From the light-scattering modeling, it was obtained that (1) the observed change in the spectrum slope from positive to negative may be caused by scattering on weakly/non-absorbing particles smaller than the wavelength and (2) the spectral features atypical for asteroids may appear due to interference of light scattered by constituents (~0.1 µm in radius) of aggregate particles in the exosphere [3]. However, the obtained set of parameters of exospheric particles is far from being complete. At the same time, the polarization of light scattered by a medium is known to be very sensitive to the properties of particles in this medium. The purpose of this analysis is to evaluate possible influence of the exosphere on the polarization of light scattered by AA, which can be measured in UBVR observations (the wavelengths λ = 0.36, 0.44, 0.54, and 0.68 µm). For this, the light-scattering characteristics of particles of different morphology and composition and the radiative transfer in the system "asteroid surface + exosphere" were calculated.

RESULTS OF SIMULATIONS:

Some examples of the calculated models are presented in Figure 1 and 2, which show how the scattering in the exosphere, containing homogeneous or aggregate particles of different composition, influences the phase func-

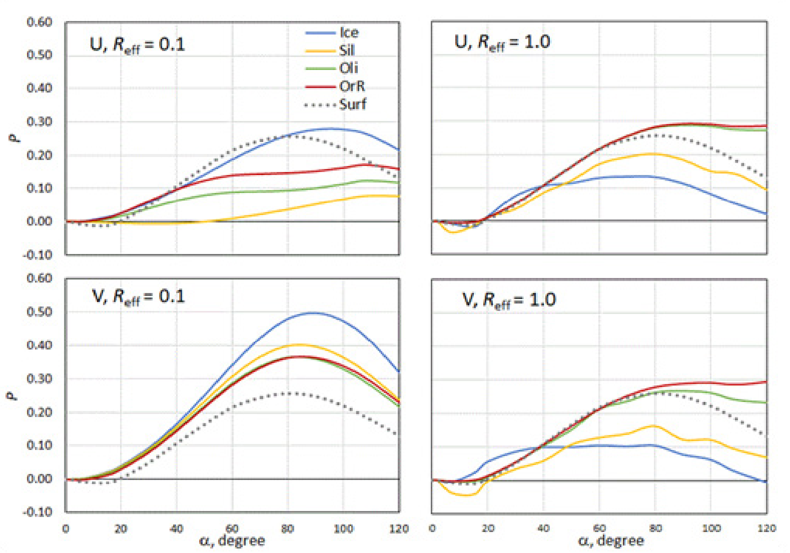

Fig. 1. The linear polarization degree of light P(α) reflected by a model AA with an exosphere, containing a mixture of randomly oriented spheroids with the effective radii Reff = 0.1 or 1.0 µm, the effective variance veff = 0.05, and the aspects ratios E = 0.7–1.3. Models for H_2O ice ("Ice"), astronomical silicates ("Sil"), olivine ("Oli"), and refractory organics ("OrR") (see [4–5] for the refractive indices), as well as for a bare asteroid ("Surf") are shown

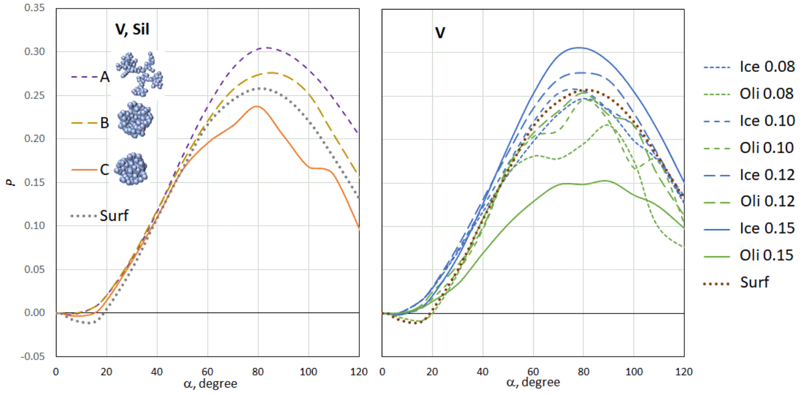

Fig. 2. The linear polarization degree of light $P(\alpha)$ reflected by a model AA with an exosphere composed of aggregates (containing 100 grains). Left: Silicate aggregates are of different porosity, 0.94, 0.72, and 0.54 (for A, B, and C, respectively), and their grains are 0.1 µm in radius. Right: Aggregates of structure C contain ice or olivine grains with radii specified (in microns)

tion of linear polarization of light $P(\alpha)$ reflected by a modeled AA at $\lambda = 0.36$ and 0.54 µm (U and V, respectively). The optical thickness of the exosphere is assumed to be $\tau = 0.5$ at $\lambda = 0.54$ µm and changes along the spectrum according to the scattering cross-sections of particles. The characteristics of the surface are assumed to be the same at all λ. From these diagrams, it can be seen that both the refractive index and the sizes of scattering particles, as well as the sizes of aggregates' constituents, determine the behavior of $P(\alpha)$.

Figure 3 shows the wavelength dependence of polarization of light scattered by AA with an exosphere ($\tau = 0.5$ at $\lambda = 0.54$ µm) at two phase angles. To reveal more clearly the effect of the exosphere, the polarization of the surface is assumed to independent of λ. It is well seen that, at small phase angles, the light scattering in the exosphere mostly weakens the negative degree of polarization or even makes it slightly positive, while at large phase angles it may introduce substantial spectral gradient of both signs depending on the composition and mosphology of scattering particles.

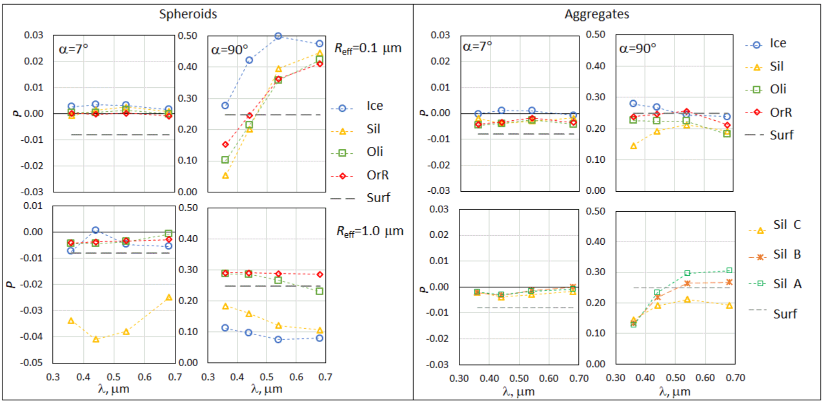

Fig. 3. Spectral changes in the degree of linear polarization of light reflected by AA with an exosphere at $\alpha = 7°$ and 90°. Exospheric particles are randomly oriented spheroids of the specified composition and size (left) and aggregates of the specified composition and structure (right)

CONCLUDING REMARKS:

Light scattering in the exosphere of AA may both weaken the polarization of light coming from the surface and increase it. The effect depends not only on the properties of particles in the exosphere, but also on its optical thickness.

Due to the exosphere, the spectral gradient of polarization may be changed towards both positive and negative values depending on the wavelength range, the refractive index of particles, and their morphology.

At phase angles $\alpha < 30°$, which are characteristic of observations of asteroids in the Main belt, the changes in the polarization of AA caused by scattering in the exosphere are small and, in most cases, differ weakly for particles of different properties, which makes it difficult to estimate them. However, if measurements of the asteroid in a definitely dormant state are also available, the change in polarization compared to the canonical values may indicate the presence of the exosphere.

At phase angles $\alpha > 30°$, the effect of scattering in the exosphere on the polarization of AA is more prominent. This makes it promising to use polarimetry for detecting activity in near-Earth asteroids observed at these phase angles. This effect should be taken into account when estimating the albedo of an asteroid from the polarization maximum (according to Umov's law), if activity may be expected for a given asteroid.

Acknowledgements:
This study is supported by the Russian Science Foundation (grant no. 22-12-00115).

References:

[1] *Hsieh H.H., Novaković B., Kim Y., Brasser R.* Asteroid family associations of active asteroids // Astronomical J. 2018. V. 155. Art. No. 96. 22 p. DOI: 10.3847/1538-3881/aaa5a2.

[2] *Busarev* V.V., *Petrova E.V., Irsmambetova T.R.* Simultaneous sublimation activity of primitive asteroids including (24) Themis and (449) Hamburga: Spectral signs of an exosphere and the solar activity impact. // Icarus. 2021. V. 369. Art. No. 114634. 18 p. DOI10.1016/j.icarus.2021.114634..

[3] *Petrova E.V., Busarev* V.V. On the Prospects for Estimating the Properties of Particles in an Active Asteroid Exosphere by Features in the UV and Visible Reflectance Spectra // Solar System Research. 2023. V. 57. Iss. 2. P. 161–174. https://doi.org/10.1134/S0038094623020065.

[4] *Warren S.G., Brandt R.E.* Optical constants of ice from the ultraviolet to the microwave: A revised compilation // J. Geophysical Research. 2008. V. 113. Art. No. D14220.

[5] *Li A., Greenberg J.M. A* unified model of interstellar dust // Astronomy and Astrophysics. 1997. V. 232. P. 566–584.

[6] *Dorschner J., Begemann B., Henning T., Jaeger C., Mutschke H.* Steps toward interstellar silicate mineralogy. II. Study of Mg-Fe-silicate glasses of variable composition // Astron. Astrophys. 1995. V. 300. P. 503–520.

INSTABILITIES IN METEOROID TAILS ASSOCIATED WITH ION ACOUSTIC MODE

T.I. Morozova, S.I. Popel
Space Research Institute RAS, Moscow, Russia, timoroz@yandex.ru

KEYWORDS:
meteoroids, dusty plasmas, meteoroid tail, modulational interaction, electrophonic sounds, low-frequency perturbations, ion acoustic waves, magnetic field fluctuations.

INTRODUCTION:
Different wave mode can be excited in meteoroid tails. Here ion acoustic mode and instabilities connected with it are considered. Meteoroid flights can lead to the different observational phenomena such as electrophonic noises and magnetic field fluctuations, which can be explained by the development of various instabilities.

DISCUSSION:
The instabilities in meteoroid tails associated with ion acoustic mode are studied. In particular, we study the modulation instability of an electromagnetic wave associated with the ion acoustic mode, as well as the ion acoustic instability excited as a result of the relative motion of the plasma of meteoroid tails and ionospheric plasma. Parameters of meteoroids and dusty plasma of meteoroid tails for which the development of such instabilities can occur are determined.

Conditions for the possibility of the occurrence of ion-wave waves in the tails of meteor-sounds.

The ion acoustic instability excited as a result of the relative motion of the plasma of meteoroid tails and ionospheric plasma is discussed. The conditions for the development of ion-acoustic instability in meteoroid are considered and the conditions for the possibility of the occurrence of ion acoustic waves will be shown. Including the consideration of ambipolar diffusion and interaction with neutrals will be discussed. Perameters of meteor bodies for the possible development of this instability are found.

The modulation instability of electromagnetic waves in meteoroid tails associated with ionic sound is considered. It is shown that its development is possible for a wide range of meteoroids. Growth rates and characteristic times of development of this instability are determined.

It is shown that the modulation instability of electromagnetic waves in meteoroid tails associated with ionic sound can explain the use of electrophonic noise simultaneously with the passage of meteoroids and the rationale for a wider range of frequencies of electrophonic waves than the preliminary study of the author’s modulation instability of electromagnetic waves in meteoroid tails associated with dust acoustic mode [1].

References:
[1] *Morozova T.I., Kopnin S.I., Popel S.I.* Modulation interaction in the dusty plasma of meteoroid tails // Geomagnetism and Aeronomy. 2021. V. 61. No. 6. P. 794–802. https://doi.org/10.1134/S0016793221060116.

MANIFESTATIONS OF MODULATION INSTABILITY IN METEOROID TAILS

T.I. Morozova, S.I. Popel
Space Research Institute RAS, Moscow, Russia, timoroz@yandex.ru

KEYWORDS:
meteoroids, dusty plasmas, meteoroid tail, modulational interaction, electrophonic sounds, low-frequency perturbations, magnetic field fluctuations, lower-hybrid waves, Langmuir waves

INTRODUCTION:
Electrophonic noises from meteoroid flight are very interesting and mysterious phenomena which still do not have definite explanation. In this work it is explained buy the development of modulational interaction of different wave modes that also can explain the arising of magnetic field fluctuations during meteoroid flight [1–2].

DISCUSSION:
Modulational instability of different wave modes in in meteoroid tails is described. It can lead to a number of observational effects in meteoroid tails, such as electrophonic noises [3–5] and arising of fluctuations of magnetic fields. In particular, this can be the modulation instability of electromagnetic waves from the shock wave of a meteoroid associated with the dusty sound mode, as well as the modulation instability of lower hybrid and Langmuir waves. In the first case, waves can be born, which are then transformed into sound waves when they reach the Earth's surface. In the last two cases, magnetic fields can arise, the magnitudes of which are comparable with the observed magnetic fields during experiments with magnetometers, and transverse electromagnetic oscillations can also propagate, which, reaching the Earth's surface, can be perceived as electrophonic noises heard simultaneously with passage of meteoroids. The influence of meteor flares on the parameters of the dusty plasma of meteoroid tails is considered depending on the height of the passage of meteoroids. The characteristic concentrations of dust particles in meteoroid tails during flares with height are estimated. Using the example of the modulation instability of electromagnetic waves associated with the dusty sound mode, it is shown how the concentration of dust particles increased during flares will affect the magnitude of the instability increments and the conditions for its development.

Acknowledgements:
The work was supported by the Foundation for the Advancement of Theoretical Physics and Mathematics "BASIS".

References:
[1] *Kalashnikov A.G.* On observations of magnetic effect of meteors by the induction method // Izvestiya Akademii nauk SSSR. Seriya Geofizicheskaya. 1952. No. 6. P. 7–20 (in Russian).
[2] *Chernogor L.F.* Effekty Lipetskogo meteoroida v geomagnitnom pole (Effects of the Lipetsk meteoroid in the geomagnetic field) // Geomagnetizm i Aeronomiya (Geomagnetism and Aeronomy), 2020. V. 60. No. 3. P. 375–392. DOI: 10.31857/S0016794020030037 (in Russian).
[3] *Trautner R., Koschny D., Witasse O. et al.* ULF-VLF electric field measurements during the 2001 Leonid storm // Proc. Asteroids, Comets, Meteors (ACM 2002) Intern. Conf. July 29 – Aug. 2, 2002, Berlin, Germany / ed. B. Warmbein (ESA SP-500). 2002. Art. No. 161.
[4] *Zgrablić G., Vinković D., Gradečak S. et al.* Instrumental recording of electrophonic sounds from Leonid fireballs // J. Geophysical Research. 2002. V. 107. Iss. A7. P. SIA 11-1–SIA 11-9. https://doi.org/10.1029/2001JA000310.
[5] Keay C.S.L. Progress in Explaining the Mysterious Sounds Produced by Very Large Meteor Fireballs // Scientific Exploration. 1993. V. 7. No. 4. P. 337–354.

CALCULATION OF THE NON-GRAVITATIONAL A2 PARAMETER USING GROUND-BASED OBSERVATIONS OF THE APPARENT CLOSE APPROACHES BETWEEN NEAR-EARTH ASTEROIDS AND GAIA STARS

M.Yu. Khovrichev[1,2], D.A. Bikulova[1]
[1] *Central Astronomical Observatory RAS, Saint Petersburg, Russia, gmymax@gmail.com*
[2] *Institute of Applied Astronomy RAS, Saint Petersburg, Russia, gmymax@gmail.com*

KEYWORDS:
Yarkovsky drift, appulse, apparent close approach, near-Earth asteroid, A2 parameter

INTRODUCTION:
The Yarkovsky drift plays a significant role in the orbital evolution of asteroids. At present time, the A2 parameter has been estimated for about a few hundred asteroids. First of all, this effect can be measured for the near-Earth asteroids due to their relatively small size and observational data coming from ground-based astrometry, radar measurements, and the results of the Gaia space mission. The accuracy of the optical astrometry available from the MPC database is relatively low (about 100–500 mas). Hence, the main expectations and successes are caused by the radar and the Gaia observations [1]. The basic strategy for the calculations is varying the state vector for a certain epoch and A2 parameter according to the observational data fitting procedure (this scheme is described in the papers [2] and [3]). We performed similar calculations by adding high-accurate ground-based measurements coming from the observations of apparent approaches between Gaia stars and near-Earth asteroids (NEA) [4].

OBSERVATIONS AND DATA ANALYSIS:
Observations of appulses for two NEA 2010 XC15 and 2014 HK129 were performed with the MTM-500M telescope (Mountain Astronomical Station of the Pulkovo Observatory) in December 2022. The positional accuracy of these observations was 50 mas. Thanks to the high-precision Gaia star coordinates, we obtain the accurate positions and angular velocities for the several normal places for both NEA. Then we calculate the state vector and A2 parameter value by minimization of the (O-C) vector using the Nelder-Mead procedure [5]. We applied REBOUND [6] and ASSIST [7] software to provide massless particle motion simulations in the gravitational field of the Solar system according to NASA JPL DE431 ephemerides.

CONCLUSIONS:
The combination of the data from the observation of apparent close approaches between NEA and Gaia stars, the results of radar measurements, and low-weighted MPC data allow us to obtain the estimates of A2 parameters for these asteroids. In the case of 2010 XC15, A2 = $(-63.9\pm10.4)\cdot10^{-15}$ au/d^2. It contradicts the previously known value A2 = $-147.3\cdot10^{-15}$ au/d^2 used in NASA JPL ephemerides. The A2 parameter for the 2014 HK129 is equal $(15.5\pm12.1)\cdot10^{-15}$ au/d^2. It has been determined for the first time. But the SNR is close to the unit. Hence, this estimate can be considered as preliminary.

Acknowledgements:
The study was funded by a grant Russian Science Foundation no. 23-22-00306 “The synergy of perturbances between the rotational and orbital motions of the asteroids approaching planets”, (https://rscf.ru/en/project/23-22-00306/).

References:
[1] *Tanga P., Pauwels* T., *Mignard* F. et al. Gaia Data Release 3: The Solar System survey // Astronomy and Astrophysics. 2023. V. 674. Art. No. A12. https://doi.org/10.1051/0004-6361/202243796.

[2] *Dziadura K., Spoto F., Oszkiewicz D. et al.* Computing the Yarkovsky effect for asteroids in Gaia DR3 // 16th European Planetary Science Congress. 2022. Art. No. EPSC2022-649. DOI: 10.5194/epsc2022-649.
[3] *Dziadura K., Oszkiewicz D., Bartczak P.* Investigating the most promising Yarkovsky candidates using Gaia DR2 astrometry // Icarus. 2022. V. 383. Iss. 1. Art. No. 115040. https://doi.org/10.1016/j.icarus.2022.115040.
[4] *Bikulova D.A.* Pulkovo observations of apparent close approaches between near-Earth asteroids and the Gaia stars in 2019-2020 // Planetary and Space Science. 2021. V. 204. Art. No. 105245. https://doi.org/10.1016/j.pss.2021.105245.
[5] *Nelder Jh., Mead R.* A simplex method for function minimization // Computer J. 1965. V. 7. Iss. 4. P. 308–313. https://doi.org/10.1093/comjnl/7.4.308.
[6] *Rein H., Spiegel D.S.* IAS15: a fast, adaptive, high-order integrator for gravitational dynamics, accurate to machine precision over a billion orbits // Monthly Notices of the Royal Astronomical Society. 2015. V. 446. Iss. 2. P. 1424–1437. https://doi.org/10.1093/mnras/stu2164.
[7] *Holman M.J., Akmal* A., *Farnocchia* D. *et al.* ASSIST: An Ephemeris-quality Test-particle Integrator // The Planetary Science Journal. 2023. V. 4. No. 4. Art. No. 69. DOI: 10.3847/PSJ/acc9a9.

ASTEROID CLUSTER OF (338073) 2002 PY38: MEMBERSHIP AND AGE ESTIMATION

M.A. Vasileva[1], E.D. Kuznetsov[1]
Ural Federal University, Yekaterinburg, Russia, vasilyeva.maria@urfu.ru, eduard.kuznetsov@urfu.ru

KEYWORDS:
asteroid cluster, Kholshevnikov metrics, asteroids dynamics, numerical simulation, age

INTRODUCTION:

Asteroid cluster of (338073) 2002 PY38 was discovered in 2020 [1]. It consisted of 3 members: (338073) 2002 PY38, (529915) 2010 TZ97 and 2016 SQ14. We report about 10 new members of this cluster. To estimate the age of this cluster, we performed a numerical modeling into the past.

METHOD:

We used the Kholshevnikov metrics [2] to search new members of asteroid cluster. We calculated the metrics ϱ_2 and ϱ_5 based on the osculating and proper orbital elements, respectively. The orbital elements of asteroids were taken from AstDyS (https://newton.spacedys.com/astdys/).

We performed a modeling of the dynamic evolution of asteroids on a time interval of 5 Myr into the past using the Mercury integrator [3]. The age estimation of the cluster was carried out by analyzing low relative-velocity close encounters between asteroids and minimum values of the metrics ϱ_2 and ϱ_5.

RESULTS:

We found 10 new members of asteroid cluster of (338073) 2002 PY38: 2001 KY82, 2002 FD44, 2006 UL238, 2013 VC79, 2015 RA194, 2015 TO83, 2019 OU6, 2019 SL111, 2022 OQ48 and single-opposition 2021 NV62 (denoted with an asterisk). At present, 13 members are known (Table 1).

Table 1. Osculating orbital elements of the cluster members at epoch 25 February 2023 (MJD 60000.0)

Asteroid	α, au	*e*	*i*, deg	Ω, deg	*ω*, deg
338073	2.1961	0.1765	0.889	159.455	160.998
529915	2.1967	0.1759	0.913	157.558	163.753
2001 KY82	2.1973	0.1761	0.936	155.793	166.257
2002 FD44	2.1971	0.1765	0.929	155.943	166.398
2006 UL238	2.1968	0.1754	0.831	165.449	151.847
2013 VC79	2.1967	0.1766	0.934	156.146	165.957
2015 RA194	2.1958	0.1754	0.828	165.620	151.742
2015 TO83	2.1963	0.1766	0.920	156.873	164.647
2016 SQ14	2.1968	0.1764	0.911	157.815	163.353
2019 OU6	2.1966	0.1747	0.795	168.704	148.060
2019 SL111	2.1965	0.1752	0.798	168.093	147.942
2022 OQ48	2.1962	0.1753	0.819	166.566	150.079
2021 NV62*	2.1958	0.1744	0.784	170.201	144.787

The results of calculating the values of Kholshevnikov metrics for asteroid pairs are shown at the Fig. 1. Values of the metric ϱ_5 less than au$^{1/2}$ for all pair within cluster. The metric ϱ_2 divides the cluster into two subclusters for pairs within which the value ϱ_2<0.01 au$^{1/2}$. Subclusters contain 7 (338073, 529915, 2001 KY82, 2002 FD44, 2013 VC79, 2015 TO83 and 2016 SQ14) and 6 (2006 UL238, 2015 RA194, 2019 OU6, 2019 SL111, 2022 OQ48 and 2021 NV62) asteroids, respectively. Values of the metric ϱ_2 for pairs "asteroid from the first subcluster – asteroid from the second subcluster" are larger and have values from 0.01 to 0.04 au$^{1/2}$.

	338073	529915	2001 KY82	2002 FD44	2013 VC79	2015 TO83	2016 SQ14	2006 UL238	2015 RA194	2019 OU6	2019 SL111	2022 OQ48
338073		1.6	0.9	1.2	1.5	0.1	0.07	0.4	2.3	4.9	2.4	2.0
529915	4.1		1.5	1.6	2.2	1.6	1.5	1.8	3.7	6.4	2.4	3.6
2001 KY82	7.5	3.5		0.3	1.7	1.0	0.8	1.3	2.8	5.3	3.0	2.7
2002 FD44	8.7	4.8	1.5		1.9	1.3	1.2	1.6	3.1	5.4	3.2	3.0
2013 VC79	7.6	3.8	0.7	1.1		1.5	1.5	1.5	1.8	4.7	3.5	2.5
2015 TO83	5.0	1.4	2.6	3.7	2.7		0.2	0.3	2.3	4.9	2.4	2.0
2016 SQ14	3.3	0.9	4.1	5.4	4.3	1.7		0.5	2.4	4.9	2.5	2.1
2006 UL238	14.5	18.4	21.8	23.1	22.1	19.4	17.8		2.2	4.8	2.2	1.8
2015 RA194	14.2	18.1	21.5	22.8	21.8	19.2	17.5	0.5		3.0	4.2	1.5
2019 OU6	17.2	21.0	24.5	25.8	24.8	22.1	20.5	3.0	3.2		6.6	3.3
2019 SL111	20.3	24.1	27.6	28.9	27.8	25.2	23.5	5.8	6.1	3.3		3.3
2022 OQ48	17.5	21.3	24.8	26.1	25.0	22.4	20.7	3.0	3.2	1.4	2.8	
2021 NV62*	25.1	28.9	32.3	33.6	32.6	30.0	28.3	10.6	10.9	7.9	4.9	7.7

$\varrho_2 \times 10^3$	≤ 5	(5,10]	(10,20]	(20,30]	(30,40]	$\varrho_5 \times 10^4$	≤ 1	(1,5]	(5,10]

Fig. 1. Values of Kholshevnikov metrics ϱ_2 (left bottom) and ϱ_5 (top right) in au$^{1/2}$. Different colors represent different ranges of values, multicolor for metric ϱ_2 and gray-scale for metric ϱ_5 (see legend).

We obtained age estimates for each pair of asteroids within the cluster. Estimates based on the analysis of low relative-velocity close encounters between asteroids correspond to estimates based on analysis of minimum values of metrics ϱ_2 and ϱ_5. Age estimates for asteroid pairs within both subclusters are less than 1 Myr. While age estimates for asteroid pairs from different subclusters range from 1 to 3 Myr.

Thus, the rough age estimate of the asteroid cluster of (338073) 2002 PY38 is about 3 Myr. We plan to continue researching this cluster in the future. Simulation of probabilistic evolution taking into account non-gravitational effects, such as the Yarkovsky effect, is necessary to obtain a more reliable age estimate.

We also want to test the hypothesis of a cascading decay of the parent body of the cluster. The parent body decayed into two secondary bodies about 3 Myr ago. Then each of the secondary bodies destroyed about 1 Myr ago.

Acknowledgements:
The work was supported by the Ministry of Science and Higher Education of the Russian Federation via the State Assignment Project FEUZ-2020-0038.

References:

[1] Kuznetsov E.D. et al. A search for young asteroid pairs with close orbits // Solar System Research. 2020. V. 54. P. 236-252.

[2] Kholshevnikov K.V. et al. Metrics in the space of orbits and their application to searching for celestial objects of common origin // Monthly Notices of the Royal Astronomical Society. 2016. V. 462. №. 2. P. 2275-2283.

[3] Chambers J.E. A hybrid symplectic integrator that permits close encounters between massive bodies // Monthly Notices of the Royal Astronomical Society. 1999. V. 304. №. 4. P. 793-799.

APPLICATION OF THE SMALL METEORS ABLATION MODEL TO PERSEID METEORS

V. Efremov[1], O. Popova[1], D. Glazachev[1], A. Kartashova[2]
[1] *Institute of Geosphere Dynamics RAS, Moscow, Russia, efremov.vv@phystech.edu*
[2] *Institute of Astronomy RAS, Moscow, Russia*

KEYWORDS:
Meteors, meteoroids, ablation, Perseids shower

INTRODUCTION:
Meteoroids, along with asteroids and comets, are a source of information about our Solar system, since the material of which they are composed indicates the composition of matter on the early stages evolution of the Solar system. One of the ways to obtain information about the properties of a meteoroid is to study the process of its interaction with the atmosphere. Despite extensive research of meteor phenomena in previous years, the task of accurate determination of meteoroid parameters such as mass, density and material properties is still relevant.

OBSERVATIONS:
For testing of the model, the optical meteor observations of SPOSH cameras in 2016 were used [1]. Perseids meteors shower was chosen for our modeling. The range of absolute magnitudes of meteors was $-6^m...+2^m$. The model used describes the ablation process of small meteor bodies, so meteors no brighter than -2^m were selected.

DESCRIPTION OF THE MODEL:
A model describing the interaction of small meteoroids with the Earth's atmosphere is applied to Perseids. In this model, the mass loss of a meteoroid is determined using the saturated vapor pressure of the assumed meteoroid's substance. The meteoroid is considered in two modifications as a solid [2–3] and a porous object. Porous body model has two modifications. In the first version meteoroid proportionally retains its structure and changes size (porosity is constant). In the second modification, the meteoroid changes its structure as a result of the passage, its porosity changes, but its size practically does not change. An automated method to estimate the physical parameters of a meteoroid by comparing observational and model derived data with known parameters was suggested.

DISCUSSION:
Light curves of a number of meteors were reproduced. Corresponding meteor particles parameters (density/porosity, size/mass) were determined. The choice of porous and solid models has little effect on the mass estimate. Density is determined with a large error. For each model, the size is well defined.

Acknowledgments:
V. Efremov, O. Popova, D. Glazachev were funded by the program "Development of an complex model of the entering cosmic objects action on the internal and external geospheres and assessment of the consequences of these impacts" (no. 1021052706222-8-1.5.4). We thank J. Oberst, A. Margonis for their SPOSH observations.

References:

[1] *Margonis A., Christou A., Oberst J.* Characterisation of the Perseid meteoroid stream through SPOSH observations between 2010–2016 // Astronomy and Astrophysics. 2019. V. 626. Art. No. A25. https://doi.org/10.1051/0004-6361/201834867.

[2] *Efremov V., Popova O., Glazachev D., Margonis A., Oberst J., Kartashova A.* Small Meteor Ablation Model: Applying to Perseid Observations // Contributions of the Astronomical Observatory Skalnate Pleso. 2021. V. 51. No. 3. DOI: 10.31577/caosp.2021.51.3.186.

[3] *Efremov V.V., Popova O.P., Glazachev D.O., Margonis, A., Oberst, J., Kartashova, A.P.* Ablation of small meteor bodies: comparison of solid and porous body models // Vestnik Tomskogo Gosudarstvennogo Universiteta. Matematika i Mekhanika. 2023. No. 81 (in Russian). DOI: 10.17223/19988621/81/10.

CONCEPT OF PLANETARY DEFENSE SYSTEM USING A PROJECTILE ASTEROID

V.A. Zubko, N.A. Eismont, V.A. Zubko, K.S. Fedyaev, A.A. Belyaev
Space Research Institute RAS, Moscow, Russia, v.zubko@iki.rssi.ru

KEYWORDS:
planetary defense concept, projectile asteroid, resonant orbits, potentially hazardous asteroid, colliding trajectory

A planetary defense concept based on deviation of a potentially hazardous asteroid from its initial orbit by a kinetic collision is discussed. The success of the DART mission proved that this approach is practically implementable using a spacecraft as a projectile. But the effectiveness of the approach in this case is limited by the mass of the spacecraft which usually is significantly less than a mass of the targeted asteroid and, therefore, is unable to provide a significant change in parameters of its trajectory. A possible way to solve this problem may consist of using a driven projectile asteroid instead of the projectile spacecraft during the collision with the targeted potentially hazardous asteroid. This projectile asteroid may be preliminary selected in such a way that its mass is much bigger than a mass of the projectile spacecraft, but still low enough to fulfill some small rocket propelled maneuvers amplified by gravity assist maneuvers near the Earth. Possibilities of implementation of such an approach have been confirmed by the authors in the earlier publications.

In order to build a planetary defence system one needs to take into account the necessity of sending the projectile asteroid to a discovered hazardous celestial object in the reasonable time. To satisfy this demand the following scenario is proposed. Initially, the most acceptable projectile asteroid has to be selected. It may be either a small enough asteroid or a boulder taken from the surface of some an appropriate asteroid. Then, the selected projectile asteroid is transferred with gravity assist maneuver to a heliocentric orbit resonant (in the 1:1 ratio) with the orbit of the Earth. The heliocentric orbit of the projectile asteroid should be chosen from a set of resonant orbits differ only by inclination, because it this case the projectile asteroid reaches a vicinity of the Earth two times per year. After this the planetary defence system is ready to use. At each Earth flyby the projectile asteroid may be transferred to the trajectory colliding the targeted hazardous object by gravity assist maneuver if such an object is discovered. A set of possible colliding trajectories corresponding to a bunch of all possible gravity assist maneuvers forms a surface in space, which can be described as a virtual hemisphere (the whole sphere is covered in two flybys) or a virtual cocoon. It should be mentioned here that this cocoon changes in time due to deformation caused by the Sun influence. If during the reasonable period of time the Earth is kept inside of this virtual cocoon, then any object approaching the Earth will intersect the cocoon and, therefore, may be intercepted.

Practically this means that when a potentially hazardous celestial object is discovered and its trajectory is defined, our goal is to find a moment of intersection of the trajectory of the discovered object with the virtual cocoon. The intersection point defines a particular colliding trajectory and the corresponding gravity assist maneuver necessary for transfer the projectile asteroid to this trajectory, which provides a practical way to perform the cinetic collision and to avoid the impact of the potentially hazardous object with the Earth.

Results of modeling the operations of the proposed concept are presented.

SESSION 5. EXTRASOLAR PLANETS (EP) ORAL SESSION

MODELLING ABSORPTION IN LINES OF HYDROGEN AND OXYGEN OF SUPER-HOT MASSIVE JUPITER KELT-9B

I.F. Shaikhislamov[1,2,3], I.B. Miroshnichenko[1], A.V. Shepelin[1], M.P. Golubovskii[1], M.S. Rumenskikh[1], A.G. Berezutskii[1]
[1] *Institute of Laser Physics SB RAS, Novosibirsk, Russia, ildars@ngs.ru*
[2] *Institute of Astronomy RAS, Moscow, Russia*
[3] *Novosibirsk State Technical University, Novosibirsk, Russia*

KEYWORDS:
Hot exoplanets, transit absorption

INTRODUCTION:

Close orbiting hot exoplanets possess a unique feature of hydrodynamic outflow of upper atmospheres. The planetary wind is driven by such important factor of space weather as intensity of ionizing radiation. The escape of upper atmospheres of hot exoplanets is a complex phenomenon, and quantitative interpretation of observational data requires numerical simulations. Kelt-9b appears as a unique planet. Absorption in lines of excited hydrogen Hα (656.3 nm) and excited oxygen (777.4 nm) was observed. The host is a hot star of A-spectral type and has extreme intensity in NUV and optical region and a very weak XUV-radiation. This leads to altogether different mechanism of atmosphere heating via photoionization of excited states, rather than photoionization of the atoms from ground state [1].

RESULTS:

We applied 3D multi-fluid aeronomy code [2] upgrading it to calculate non-LTE population of excited hydrogen atom HI(2), and excited oxygen atom. To calculate levels' populations we included all processes involving photo-excitation, photo-ionization and electron impact, except transitions between different excited states. It was found that excitation of HI(2p) state by stellar radiation at $\lambda \approx 121.6$ nm and subsequent photoionization by photons with $\lambda < 365$ nm is by orders of magnitude more effective in heating of atmosphere than direct photo-ionization by photons with $\lambda < 91.2$ nm. Important factor is trapping of Lyα photons in dense atmosphere which greatly increases population of HI(2p) state. However, the overall heating rate is significantly reduced because the average energy of photo-electrons produced by particular spectra of the host star doesn't exceed 1 eV.

We fitted the calculated absorption in Hα (656.3 nm) and OI (777.4 nm) lines with observations and found good agreement. It allowed us to constrain the basic parameters of Kel-9b and elucidate the details of heating of its upper atmosphere.

References:

[1] *Muñoz A.G., Schneider P.C.* Rapid Escape of Ultra-hot Exoplanet Atmospheres Driven by Hydrogen Balmer Absorption // Athens J. Law. 2019. V. 884. Iss. 2. Art. No. L43. DOI 10.3847/2041-8213/ab498d.

[2] *Shaikhislamov I.F., MiroshnichenkoI B., Rumenskikh M.S. et al.* The impact of intrinsic magnetic field on the absorption signatures of elements probing the upper atmosphere of HD209458b // Monthly Notices of the Royal Astronomical Society. 2021. V. 507. Iss. 3. P. 3626–3637. DOI 10.1093/mnras/stab2366.

THE EMISSION SPECTRUM OF THE HOST STAR AND TRANSIT ABSORPTIONS OF HOT JUPITERS IN THE METASTABLE HELIUM LINE

M. Rumenskikh[1,2,3], I.B. Miroshnichenko[1,4], I.F. Shaikhislamov[1], A.G. Berezutsky[1]

[1] *Institute of Laser Physics of the SB RAS, Novosibirsk, Russia marina_rumenskikh@mail.ru*
[2] *Pushkov Institute of Terrestrial Magnetism, Ionosphere and Radiowave Propagation RAS, Moscow, Russia*
[3] *Institute of Astronomy RAS, Moscow, Russia*
[4] *Novosibirsk State Technical University, Novosibirsk, Russia*

KEYWORDS:
exoplanets, Hot Jupiters, transit spectroscopy, numerical simulation, magnetohydrodynamic

Transit spectroscopy of exoplanets opens up tremendous opportunities for studying the features of the structure, composition, properties, and evolution of atmospheres including the Earth-like ones. Planets beyond the Solar system are numerous counting more than 5 thousand examples. The wide age range of many planets in the vicinity of distant stars will allow us to learn more about the formation of the planets of the Solar system, as well as their environment.

The processes leading to changes in the temperature and composition of the environment of the planets depend significantly both on the composition and other initial conditions of the atmospheres and on the radiation of the parent star. This thesis is confirmed by a number of theoretical studies devoted to the analysis of the effect of the emission spectrum of stars on the rate and features of the outflow of the atmospheric matter of planets [1-4]. The aim of this work is to reveal the relative role of the spectral characteristics of a star radiation in the absorption in metastable helium line HeI(2^3S) also of the planetary matter outflow. For this purpose, numerical simulation of transit absorptions in the atmospheres of so called “control planets” is carried out. «Control planets» characterize by the same gravitational potential and atmospheric composition, but with different radiation spectra of stars. As a result, the essential role of stellar radiation on the population of the metastable helium level and absorption is shown.

Acknowledgements:
The work was supported by the RSF project 23-72-10060.

References:

[1] *Nakayama A., Ikoma M., Terada N.* Survival of Terrestrial $N_2 – O_2$ Atmospheres in Violent XUV Environments through Efficient Atomic Line Radiative Cooling // The Astrophysical J. 022. V. 937. Iss. 2. P. 72. DOI:10.3847/1538-4357/ac86ca.

[2] *Kulikov Y.N., Lammer* H., *Lichtenegger* H.I.M. *et al.* A comparative study of the influence of the active young Sun on the early atmospheres of Earth, Venus, and Mars // Space Science Reviews. 2007. V. 129. P. 207–243. DOI: 10.1007/s11214-007-9192-4.

[3] *Erkaev N.V., Lammer* H, *Odert* P. *et al.* XUV-exposed, non-hydrostatic hydrogen-rich upper atmospheres of terrestrial planets. Part I: atmospheric expansion and thermal escape // Astrobiology. 2013. V. 13. Iss. 11. P. 1011–1029. DOI: 10.1089/ast.2012.0957.

[4] *Oklopčić A.* Helium absorption at 1083 nm from extended exoplanet atmospheres: Dependence on stellar radiation // The Astrophysical J. 2019. V. 881. Iss. 2. Art. No. 133. DOI: 10.3847/1538-4357/ab2f7f

THE ROLE OF EARTH-MASS PLANETS IN THE ORIGIN OF DEBRIS DISKS

O.S. Oleynik[1], V.V. Emel'yanenko[2]
Institute of Astronomy RAS, Moscow, Russia, olgaoleynik93@gmail.com, vvemel@inasan.ru

KEYWORDS:
Debris discs, exoplanets, planetesimals, migration, N-body symplectic integration

INTRODUCTION:
About hundred debris disks were detected by now via μm emission of dust which origin is being actively discussed. Our goal is to test whether an Earth-mass planet can migrate through a planetesimal disk and excite planetesimals enough for dust production via impact collisions. We develop a new model for the dynamical evolution of the planetesimal disk and the exoplanet in terms of their gravitational interaction using N-body symplectic integrations. We find that small-mass planets (even as small as ~0.1 Earth mass) could excite the disk efficiently and provide relative velocities up to several hundred m/s. Our work may also serve as a motivation for further N-body simulations of planet-disk interaction.

MODIFIED METHOD OF ROUND GAUSSIAN RINGS. APPLICATION TO THE TWO-PLANETARY PROBLEM

B.P. Kondratyev[1,2,3], V.S. Kornoukhov[2], E.V. Basova[1]
[1] *Lomonosov Moscow State University, Moscow, Russia, work@boris-kondratyev.ru*
[2] *Sternberg Astronomical Institute Lomonosov Moscow State University, Moscow, Russia*
[3] *Central Astronomical Observatory RAS, Saint Petersburg, Russia*

KEYWORDS:
planets, exoplanets, Gaussian rings, equations of perturbed motion, secular evolution of orbits

A scheme of the modified method of round Gaussian rings, designed to study the secular evolution of orbits in systems consisting of a central star and two planets, is presented. The reason for the secular evolution of the nodes and inclinations of the orbits of the planets is their mutual gravitational attraction. The orbits of the planets are modeled by homogeneous round Gaussian rings, to which the masses, sizes and angles of inclination of the orbits, as well as orbital angular momenta of the planets, are transferred. The method takes into account that, in general, the ascending nodes of the orbits may not coincide. The mutual gravitational energy of the rings W_{mut} is represented as a series in the quadratic approximation in powers of small inclination angles. Using this function W_{mut}, a closed system of four differential equations describing the secular evolution of the planets' orbits is composed. The solution of the equations is obtained in finite analytic form, which simplifies the interpretation of the investigated planetary motions. The method was tested on the example of the Sun-Jupiter-Saturn system; for it, in particular, the difference in the longitudes of the nodes of the orbits of Jupiter and Saturn was calculated as a function of time. New approach is also used to study the precession of nodes in the exoplanetary system K2-36; graphs of all unknown quantities are obtained. It has been established that in the course of evolution the mutual inclination angle of the orbits remains constant, and the librations of the orbits in the inclination angle and in the motion of the nodes occur synchronously.

INTRODUCTION:

In celestial mechanics, three main approaches are used to study secular perturbations of the orbits of planets and satellites. The first approach (analytical) is based on the expansion of the Lagrange perturbation function in a series in terms of small values of eccentricities and inclination angles of the orbits [1–3]. The second approach is related to the numerical integration of the equations of motion of the planets of the solar system [4–5]. Although numerical methods make it possible to carry out calculations with any accuracy, they do not provide a qualitative picture of the phenomena.

The third approach is based on averaging methods [6]. Here, one of the main methods is the Gauss ring method, which is designed to study secular perturbations of the first order. This method is clear and is based on the fact that the perturbing effect of one body on another, under certain additional conditions, is equivalent to the influence of the force field of the gravitating ring (Gaussian ring), obtained by distributing the perturbing mass along an elliptical orbit. With this approach, not only problems with single averaging over the orbit of the perturbing body are considered, but also problems with additional averaging over the orbit of the perturbed body itself. In the latter case, the problem is reduced to studying the interaction of two Gaussian rings.

The one-dimensional density of matter on the Gaussian ring is inverse to the velocity of a planet with the mass M in a given section of its trajectory, and the element of mass is equal to

$$dm = \frac{M(1-e^2)^{3/2}}{2\pi} \cdot \frac{d\upsilon}{(1+e\cos\upsilon)^2}, \tag{1}$$

where υ is the angle of true anomaly; e is the eccentricity of the orbit. In the particular case $e = 0$, the ring turns into a homogeneous round hoop with a spatial potential

$$\varphi(r, x_3) = \frac{2GM}{\pi\sqrt{(R+r)^2 + x_3^2}} K(k), \quad k = \sqrt{\frac{4Rr}{(R+r)^2 + x_3^2}} \le 1. \tag{2}$$

(where x_3 is the applicate of the test point). In the general (non-degenerate) case, the spatial potential of the Gaussian elliptical ring in analytical form was obtained in [7].

With the discovery of exoplanets, interest in Gauss rings has increased. On the basis of elliptic rings, a general method for studying long-period and secular perturbations in problems of celestial mechanics was created [8]. There are two more methods based on the idea of averaging over fast variables of a precessing elliptic Gaussian ring. Thus, averaging the ring precession over the rotation of the apsidal line gives the model of a round two-dimensional disk (R-ring) [9], and additional averaging over the motion of the ring nodes gives the 3D model of the R-toroid [10].

As is known, the problems of studying the secular stability of systems of celestial bodies are very time-consuming and complex, so it is important to search for simplified methods for solving such problems. One of the simplification methods is based on the replacement of elliptic Gaussian rings with circular ones [11–12]. The round ring method has proved to be in demand, since the orbits of some exoplanets do indeed have very small eccentricities. Here it should be emphasized that the application of the round ring method noticeably simplifies the differential equations for the evolution of orbits, and the solutions of these equations can be obtained in analytical form. This offers advantages in the study of exoplanetary systems.

STATEMENT OF THE PROBLEM. MUTUAL ENERGY OF ROUND RINGS:
Let us consider in coordinates $Oxyz$ the system of three bodies "Star — Planet 1 — Planet 2". Let the masses of the planets M_1 and M_2 evenly distributed along their orbits, which are concentric circular Gaussian rings with radii R_1 and R_2. Third body, a star, is located in the center of the rings. The planes of the rings have small angles of inclination i_1 and i_2 to the main reference plane (in the solar system — to the ecliptic); therefore, the angle between the planes $\Delta i'$ will also be small. The ascending nodes of the orbital rings Ω_1 and Ω_2 in the general case do not coincide. The problem is to find the mutual perturbations of the Gaussian rings [11, 14].

The method is based on the use of the function of mutual gravitational energy of rings W_{mut}. This function was found earlier in [11, 14], so here we restrict ourselves to the necessary explanations. By definition, the contribution to energy W_{mut} from two elementary point masses dm_1 and dm_1 located at the points (x_1, y_1, z_1) and (x_2, y_2, z_2) is equal to

$$dW_{mut} = -\frac{G\,dm_1 dm_2}{r_{12}}, \quad r_{12} = \sqrt{(x_2-x_1)^2 + (y_2-y_1)^2 + (z_2-z_1)^2}. \tag{3}$$

where r_{12} is the distance between material points. The full expression of the mutual gravitational energy is found by double integration over both rings. Since $dm_1 = R_1\mu_1 d\upsilon_1$ and $dm_2 = R_2\mu_2 d\upsilon_2$, we have

$$W_{mut} = -G\mu_1\mu_2 R_1 R_2 \int_0^{2\pi} d\upsilon_2 \int_0^{2\pi} \frac{d\upsilon_1}{r_{12}} \tag{4}$$

To find r_{12}, we note that in the specified reference system $Oxyz$, the coordinates of the test point on the circular ring 1 can be represented, see, for example, [1], by the formulas:

$$
\begin{aligned}
x_1 &= R_1\left(\cos\upsilon_1 \cos\Omega_1 - \sin\upsilon_1 \sin\Omega_1 \cos i_1\right);\\
y_1 &= R_1\left(\cos\upsilon_1 \sin\Omega_1 + \sin\upsilon_1 \cos\Omega_1 \cos i_1\right);\\
z_1 &= R_1 \sin\upsilon_1 \sin i_1;
\end{aligned} \tag{5}
$$

similarly represent the coordinates of the test point on the second ring:

$$
\begin{aligned}
x_2 &= R_2(\cos\upsilon_2 \cdot \cos\Omega_2 - \sin\upsilon_2 \cdot \sin\Omega_2 \cdot \cos i_2);\\
y_2 &= R_2(\cos\upsilon_2 \cdot \sin\Omega_2 + \sin\upsilon_2 \cdot \cos\Omega_2 \cdot \cos i_2);\\
z_2 &= R_2 \sin\upsilon_2 \cdot \sin i_2.
\end{aligned} \tag{6}
$$

Substituting formulas (5) and (6) into r_{12} (3) and considering that the radii of the rings are equal

$$
\left.\begin{aligned}
R_1 &= \sqrt{x_1^2 + y_1^2 + z_1^2},\\
R_2 &= \sqrt{x_2^2 + y_2^2 + z_2^2},
\end{aligned}\right\} \tag{7}
$$

we find

$$
r_{12} = \sqrt{2R_1R_2} \cdot \sqrt{a - b\sin\upsilon_1 - c\cos\upsilon_1}. \tag{8}
$$

Here, the coefficients *a, b* and c are determined by the formulas [14]

$$
\left.\begin{aligned}
a &= \frac{R_1^2 + R_2^2}{2R_1R_2} = \frac{1}{2}\left(n + \frac{1}{n}\right) \le 1, \quad n = \frac{r_2}{r_1} \le 1;\\
b &= \left[\cos i_1 \cdot \cos i_2 \cdot \cos(\Omega_1 - \Omega_2) + \sin i_1 \cdot \sin i_2\right]\sin\upsilon_2 -\\
&\quad - \cos i_1 \cdot \sin(\Omega_1 - \Omega_2)\cos\upsilon_2;\\
c &= \cos(\Omega_1 - \Omega_2)\cos\upsilon_2 + \cos i_2 \cdot \sin(\Omega_1 - \Omega_2)\sin\upsilon_2.
\end{aligned}\right\} \tag{9}
$$

Taking into account r_{12} from (8), the formula for mutual energy (4) takes the form

$$
W_{mut} = -G\mu_1\mu_2\sqrt{\frac{R_1R_2}{2}}\int_0^{2\pi} d\upsilon_2 \int_0^{2\pi} \frac{d\upsilon_1}{\sqrt{a - b\sin\upsilon_1 - c\cos\upsilon_1}}. \tag{10}
$$

As shown in [14], expression (10) can be represented by a single integral

$$
W_{mut} = -2\sqrt{2} \cdot G\mu_1\mu_2\sqrt{R_1R_2}\int_0^{2\pi} \frac{d\upsilon_2}{\sqrt{a+p}} K\left(\sqrt{\frac{2p}{a+p}}\right). \tag{11}
$$

Here $p = \sqrt{b^2 + c^2}$.

The integral (11) is not found in a finite form, so we represent it as a series in powers of small angles i_1 and i_2. Finding such a series is a rather labor-intensive operation. As shown in [14], the required series has the form

$$
W_{mut} = W_0 + W_{11}i_1^2 + +W_{22}i_2^2 + W_{12}i_1i_2 \tag{12}
$$

with the coefficients

$$
\left.\begin{aligned}
W_0 &= -\frac{\sqrt{2} \cdot Gm_1m_2}{ð\sqrt{R_1R_2}\sqrt{1+a}} K(k);\\
W_{11} &= W_{22} = \frac{G\sqrt{2} \cdot m_1m_2}{8\pi\sqrt{R_1R_2}\sqrt{1+a}}\left\{\frac{a}{a-1}E(k) - K(k)\right\};\\
W_{12} &= -\frac{G\sqrt{2} \cdot m_1m_2}{4\pi\sqrt{R_1R_2}\sqrt{1+a}}\cos(\Omega_1 - \Omega_2)\left\{\frac{a}{a-1}E(k) - K(k)\right\}.
\end{aligned}\right\} \tag{13}
$$

Here $k=\sqrt{2/(1+a)}\leq 1.$ After transformations, (13) is reduced to the form

$$W_{mut}=-\frac{\sqrt{2}\cdot Gm_1m_2}{ð\sqrt{R_1R_2}\sqrt{1+a}}\left\{\begin{array}{l} K(k)-\frac{1}{8}\left[\frac{a}{a-1}E(k)-K(k)\right]\times \\ \times\left[i_1^2+i_2^2-2\cos(\Omega_1-\Omega_2)i_1i_2\right]\end{array}\right\}. \tag{14}$$

For convenience in numerical calculations, the coefficients of series (14) are further transformed using auxiliary formulas:

$$\left.\begin{array}{lll} a=\frac{R_1^2+R_2^2}{2R_1R_2}=\frac{1}{2}\left(n+\frac{1}{n}\right); & n=\frac{r_2}{r_1}\leq 1; & k=\frac{2\sqrt{n}}{1+n}; \\ a-1=\frac{(1-n)^2}{2n}; & \frac{a}{a-1}=\frac{1+n^2}{(1-n)^2}; & \sqrt{1+a}=\frac{1+n}{\sqrt{2n}}. \end{array}\right\} \tag{15}$$

Then the mutual gravitational energy of two round Gaussian rings in the quadratic approximation in terms of inclination angles will take the form [14]

$$W_{mut}=-\frac{2Gm_1m_2}{ðR_1}\left\{K(n)-\frac{\Delta i'^2}{8(1-n^2)}\left[\frac{1+n^2}{(1-n)^2}E(n)-K(n)\right]\right\}, \tag{16}$$

where the angle of mutual inclination of the rings $Äi'$ is related to the angles of orientation (i1, i2) of the rings relative to the main plane by the relation

$$\cos\Delta i'=\cos i_1\cos i_2+\sin i_1\sin i_2\cos(\Omega_2-\Omega_1). \tag{17}$$

Taking into account the smallness of the inclinations of the rings to the main plane, $\Delta i'$ from (16) is expressed in terms of angles in the coordinate system associated with the ecliptic (unprimed coordinates)

$$\Delta i'^2\approx i_1^2+i_2^2-2i_1i_2\cos(\Omega_2-\Omega_1). \tag{18}$$

Note here: since expression (16) refers to the case where the tilt angles i_1 and i_2 are small, then, their difference $\Delta i = i_2 - i_1$ is also small; nevertheless, the difference between the longitudes of the nodes $\Delta\Omega = \Omega_2 - \Omega_1$ is not necessarily a small value.

EQUATIONS FOR THE SECULAR EVOLUTION OF ORBITS:

In full form, the Lagrange equations for the osculating elements have a complicated form (see, e.g., formulas (8.6) in book [2]). However, in our particular case, when the inclination angles i_1 and i_2 are small and the orbits $e_1 = e_2 = 0$ are circular, these equations are simplified and for elements, for example, the second ring have the form

$$\left.\begin{array}{l} \frac{di_2}{dt}=-\frac{1}{n_2R_1^2n^2\sin i_2}\cdot\frac{\partial\overline{R}_2}{\partial\Omega_2}; \\ \frac{d\Omega_2}{dt}=\frac{1}{n_2R_1^2n^2\sin i_2}\cdot\frac{\partial\overline{R}_2}{\partial i_2}, \end{array}\right. \tag{19}$$

where $\overline{R}_2$ — the perturbing function is equal to the mass-normalized mutual energy of the rings $\overline{R}_2=-W_{mut}/m_2$.

As a result, adding to (19) the equations for the first ring, and taking into account the third Kepler law

$$GM=n_1^2a_1^3=n_2^2a_1^3n^3, \tag{20}$$

where M is the mass of the central body (star); n1 and n2 are the average motions of the planets in orbits, we write the equations of the secular evolution of two round rings in the form [14]

$$\left.\begin{aligned} &\frac{d\Omega_1}{dt} = -\sigma_1\left(1-\frac{i_2}{i_1}\cos\Delta\Omega\right); \quad \frac{di_1}{dt} = -\sigma_1 i_2 \sin\Delta\Omega; \\ &\frac{d\Omega_2}{dt} = -\sigma_2\left(1-\frac{i_1}{i_2}\cos\Delta\Omega\right); \quad \frac{di_2}{dt} = \sigma_2 i_1 \sin\Delta\Omega. \end{aligned}\right\} \tag{21}$$

Here the following notations are introduced

$$\left.\begin{aligned} &\sigma_1 = \frac{n_1}{2\pi(1+n)}\frac{m_2}{M}\left[\frac{1+n^2}{(1-n)^2}E(k)-K(k)\right]; \\ &\sigma_2 = \frac{n_2 n}{2\pi(1+n)}\frac{m_1}{M}\left[\frac{1+n^2}{(1-n)^2}E(k)-K(k)\right]. \end{aligned}\right\} \tag{22}$$

SOLVING EVOLUTION EQUATIONS:
To analyze the equations (21), let us introduce the variables

$$h_1 = i_1\cos\Omega_1; \ \ k_1 = i_1\sin\Omega_1; \ \ h_2 = i_2\cos\Omega_2; \ \ k_2 = i_2\sin\Omega_2. \tag{23}$$

Then equations (21) are transformed to a simpler form

$$\left.\begin{aligned} &\frac{dh_1}{dt} = -\sigma_1(k_2-k_1); \quad \frac{dk_1}{dt} = \sigma_1(h_2-h_1); \\ &\frac{dh_2}{dt} = \sigma_2(k_2-k_1); \quad \frac{dk_2}{dt} = -\sigma_2(h_2-h_1), \end{aligned}\right\} \tag{24}$$

where the coefficients (22) are the frequencies of the secular oscillations. Solutions of the system of differential equations (26) have the form [14]

$$\left.\begin{aligned} &h_1(t) = C_1 + \sigma_1[C_3\cos\sigma t + C_4\sin\sigma t]; \\ &k_1(t) = C_2 + \sigma_1[-C_3\sin\sigma t + C_4\cos\sigma t]; \\ &h_2(t) = C_1 - \sigma_2[C_3\cos\sigma t + C_4\sin\sigma t]; \\ &k_2(t) = C_2 - \sigma_2[-C_3\sin\sigma t + C_4\cos\sigma t]. \end{aligned}\right\} \tag{25}$$

Here the sum of frequencies is entered

$$\sigma = \sigma_1 + \sigma_2, \tag{26}$$

and the integration constants

$$\left.\begin{aligned} &C_1 = \frac{\sigma_1 h_2^0 + \sigma_2 h_1^0}{\sigma_1+\sigma_2}; \quad C_2 = \frac{\sigma_1 k_2^0 + \sigma_2 k_1^0}{\sigma_1+\sigma_2}; \\ &C_3 = -\frac{h_2^0 - h_1^0}{\sigma_1+\sigma_2}; \quad C_4 = -\frac{k_2^0 - k_1^0}{\sigma_1+\sigma_2} \end{aligned}\right\} \tag{27}$$

include the following initial conditions

$$h_1^0 = h_1(0); \ \ k_1^0 = k_1(0); \ \ h_2^0 = h_2(0); \ \ k_2^0 = k_2(0). \tag{28}$$

Substituting (25) into (21), we come to the conclusion that, in the linear approximation, the angle of mutual inclination of the orbits during evolution remains constant

$$\Delta i' = \sqrt{(h_1-h_2)^2 + (k_1-k_2)^2} = \text{const}. \tag{29}$$

SOLUTION FOR ORBITS OF TRANSITING EXOPLANETS:
Since the orbital parameters are estimated, as a rule, for exoplanets discovered by transit, the orbital inclinations of such planets to the picture plane vary near 90º. Therefore, to use equations (21), one must move from the picture plane to such a principal plane that the new orbital inclinations are small, e.g., to the Laplace plane. Alternatively, one can use other equations that work in the case of using the picture plane as the principal plane

Let us choose the picture plane as the main plane. Then not only the mutual inclination of the orbits $\Delta i = i_2 - i_1$, but also the difference of longitudes of the ascending nodes $\Delta\Omega = \Omega_2 - \Omega_1$ will be small values The angle of mutual inclination of the rings in the observer's coordinate system is now expressed through the small parameters from formula (18) in the following form

$$\Delta i'^2 \approx \Delta i^2 + \sin^2 i \cdot \Delta\Omega^2, \quad i = \frac{i_1 + i_2}{2}. \tag{30}$$

Using equations (19), similarly to (21), we obtain the equations of secular evolution of circular orbits for exoplanetary systems

$$\left.\begin{aligned} &\frac{d\Omega_1}{dt} = \sigma_1 \frac{\Delta i}{\sin i}; \quad && \frac{di_1}{dt} = -\sigma_1 \sin i \cdot \Delta\Omega; \\ &\frac{d\Omega_2}{dt} = -\sigma_2 \frac{\Delta i}{\sin i}; && \frac{di_2}{dt} = \sigma_2 \sin i \cdot \Delta\Omega. \end{aligned}\right\} \tag{31}$$

Let's introduce new variables

$$p = \sin i \cdot \Delta\Omega, \; q = \Delta i, \tag{32}$$

to which will be added the average slope from (30) and the average longitude of the ascending node

$$\Omega = \frac{\Omega_1 + \Omega_2}{2}, \tag{33}$$

then equations (31) of the evolution of two circular rings are reduced to the form

$$\left.\begin{aligned} &\frac{dp}{dt} = -\sigma q; && \frac{dq}{dt} = \sigma p; \\ &\frac{di}{dt} = -\frac{\sigma_1 - \sigma_2}{2\sigma} \cdot \frac{dq}{dt}; && \frac{d\Omega}{dt} = -\frac{\sigma_1 - \sigma_2}{2\sigma} \cdot \frac{d}{dt}\left(\frac{p}{\sin i}\right). \end{aligned}\right\} \tag{34}$$

Equations (36) have the following solutions:

$$\left.\begin{aligned} &p(t) = \sigma\left[-C_1^2 \sin(\sigma t) + C_2^2 \cos(\sigma t)\right]; && q(t) = \sigma\left[C_1^2 \cos(\sigma t) + C_2^2 \sin(\sigma t)\right]; \\ &i(t) = C_3^2 - \frac{(\sigma_1 - \sigma_2)}{2\sigma} q(t); && \Omega(t) = C_4^2 - \frac{(\sigma_1 - \sigma_2)}{2\sigma \sin i(t)} p(t), \end{aligned}\right\} \tag{35}$$

where the constants expressed in terms of initial conditions

$$\left.\begin{aligned} &i_0 = \frac{i_1^0 + i_2^0}{2} = i(0); && \Delta i_0 = i_2^0 - i_1^0 = \Delta i(0); \\ &\Omega_0 = \frac{\Omega_1^0 + \Omega_2^0}{2} = \Omega(0); && \Delta\Omega_0 = \Omega_2^0 - \Omega_1^0 = \Delta\Omega(0), \end{aligned}\right\} \tag{36}$$

are written in the form

$$\left.\begin{aligned} &C_1^2 = \frac{\Delta i_0}{\sigma_1 + \sigma_2}; && C_2^2 = \frac{\sin i_0 \Delta\Omega_0}{\sigma_1 + \sigma_2}; \\ &C_3^2 = \frac{\sigma_1 i_2^0 + \sigma_2 i_1^0}{\sigma_1 + \sigma_2}; && C_4^2 = \frac{\sigma_1 \Omega_2^0 + \sigma_2 \Omega_1^0}{\sigma_1 + \sigma_2}. \end{aligned}\right\} \tag{37}$$

From the solution (35), taking into account (30), it follows (as in the first version (29)) that during evolution the angle of mutual inclination of the orbits in the linear approximation remains constant

$$\Delta i' = \sqrt{p^2 + q^2} = \text{const}. \tag{38}$$

Note that the libration frequency components σ_1 and σ_2 from (22), as well as their sum σ from (26), were obtained here in a linear approximation and therefore do not depend on the difference in longitudes of the orbit nodes $\Delta\Omega = \Omega_2 - \Omega_1$.

Note also that the solution of Section "Solution for orbits of transiting exoplanets" is not a particular case of the solution of Section "Solving evolution equations". Indeed, there is a nontrivial transformation between these solutions. Only the invariance of libration periods when transformed to another coordinate system is trivial. Generally speaking, the problem of transforming a solution between coordinate systems is not as trivial as it may seem at first glance; suffice it to note the problem of small denominators.

APPLICATION OF THE METHOD OF CIRCULAR RINGS: THE TWO-PLANET SUN-JUPITER-SATURN PROBLEM:

In the Solar System, the giant planets Jupiter and Saturn are usually considered in the framework of the two-planet problem. The initial data for the orbits of Jupiter and Saturn can be taken, for example, in the book [13].

Table 1. Parameters of the Jupiter-Saturn system, from the book [13]

Parameter	Jupiter	Saturn
e	0.0474622	0.0575481
$M/M_\odot$	$9.54786 \cdot 10^{-4}$	$2.85837 \cdot 10^{-4}$
a, a.e.	5.202545	9.554841
n, grad/year	30.3374	12.1890
i, grad	1.30667	2.48795
Ω, grad	100.0381	113.1334

Using the formulas of Section "Solving evolution equations", the evolution of the longitudes of the ascending nodes and orbital inclinations of the giant planets Jupiter and Saturn was calculated over an interval of 200 000 years. The results of these calculations are shown in Fig. 1 and 2.

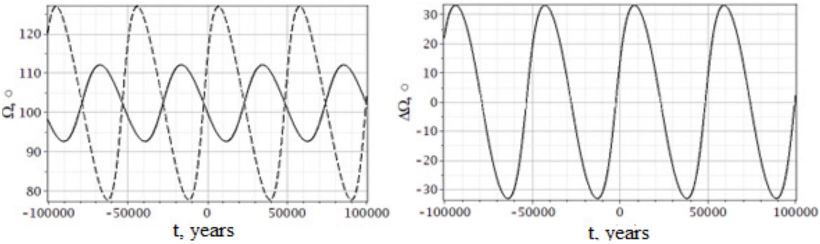

Fig. 1. Dependence of the change in the longitude of the ascending node for Jupiter (solid line) and Saturn (dashes), representing the secular precession of the orbital planes of the giant planets under the action of mutual perturbation (*left*); the difference in the longitudes of the nodes of Jupiter and Saturn's orbit as a function of time (*right*)

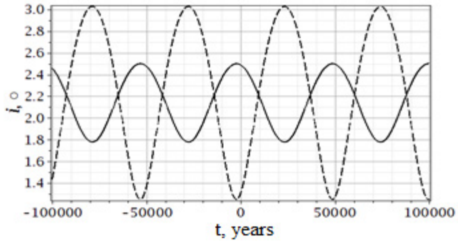

Fig. 2. Time dependence of the inclination (to the ecliptic) of the rings of Jupiter (solid line) and Saturn (dashes)

According to our formulas, the libration period for tilting T_i and moving nodes T_Ω is the same and is approximately $T_\Omega = T_i \approx$ 50 950 years (previously, in [12], where a variant of the problem with matching nodes was studied, was obtained $T_\Omega \approx$ 50 625 years, and the reason for the small difference in 0.5 % is the difference in initial conditions).

EVOLUTION OF ORBITS IN THE SYSTEM OF EXOPLANETS K2-36:

The secular evolution of orbits for a system of two planets around the star K2-36 has not been studied before. The parameters of this system are given in Table 5.2.

Table 5.2. 10 parameters of the K2-36 exosystem. The parameter errors are symmetrized for convenience in estimating the precession period error. The period of precession Tprec of the circular orbits of the planets is calculated by us according to the formula Tprec = 2π/(A11 + A21)Data from articles [15, 16]

System	K2-36
M_*,	0.79±0.01
	3.9±1.1
m_c, M_{Earth}	7.8±2.3
a_b, *au*	0.0223±0.0004
a_c, *au*	0.054±0.001
i_b, grad	84.45±0.063
i_c, grad	86.917±0.061
P_b, days	1.422614±0.000038
P_c, days	5.340888±0.000086
T_{prec}, $\times 10^3$ years	1.3±0.3

As expected, in all three cases of calculations, librations of the angles of inclination and longitude of the ascending nodes of the orbits occur. As can be seen from Fig. 3 and 4, the difference in the longitudes of the nodes affects the shift of the libration graphs, but in a linear approximation does not affect the value of the oscillation period itself.

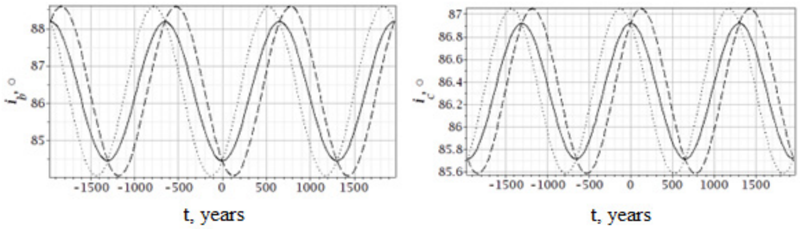

Fig. 3. Time dependence of the orbital inclination for the inner planet K2-36 b (*left*) and the outer planet K2-36 c (*right*). The dotted line corresponds to the value $\Delta\Omega_0 = -\Delta i_0$, the solid line corresponds to the value and the dashed line corresponds to the value $\Delta\Omega_0 = \Delta i_0$.

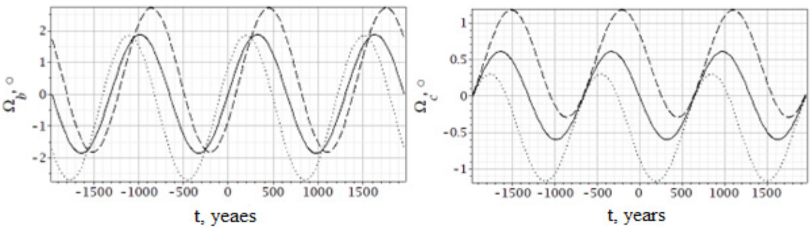

Fig. 4. Longitudes of ascending nodes for planet K2-36 b (left graph) and planet K2-36 c (*right*) versus time. The dotted line corresponds to the value $\Delta\Omega_0 = -\Delta i_0$, the solid line corresponds to the value $\Delta\Omega_0 = 0$, and the dashed line corresponds to the value $\Delta\Omega_0 = -\Delta i_0$.

In addition, it follows from our formulas that the libration periods of the orbits in terms of inclination and node will be the same. For the K2-36 system, these periods are approximately equal to

$$T_{\Omega} = T_i \approx 1306 \text{ years.} \tag{39}$$

References:

[1] *Duboshin G.N.* Nebesnaya mekhanika. Osnovnye metody i zadachi (Celestial Mechanics: Main tasks and methods). M.: Nauka. 1975. 800 p. (in Russian).

[2] *Subbotin M.F.* Vvedenie v teoreticheskuyu astronomiyu (Introduction to theoretical astronomy). M.: Nauka. 1968 800 p. (in Russian).

[3] *Emelyanov N.V.* Dinamika estestvennykh sputnikov planet na osnove nabludenii (Dynamics of natural satellites of planets based on observations). 2019. 576 p. (in Russian).

[4] *Laskar J.* Secular evolution of the solar system over 10 million years // Astronomy and Astrophysics. 1988. V. 198. P. 341–362.

[5] *Simon J.L., Bretagnon P., Chapront J. et al* Numerical expressions for precession formulae and mean elements for the Moon and the planets // Astronomy and Astrophysics. 1994. V. 282. No. 2. P. 663–683.

[6] *Grebenikov E.A.* Metod usredneniya v prikladnyh zadachakh (The Averaging Method in Applied Problems). M.: Nauka. 1986. 256 p. (in Russian).

[7] *Kondratyev B.P.* Potential of a Gaussian ring. A new approach // Solar System Research. 2012. V. 46. No. 5. P. 352–362. DOI: 10.1134/S0038094612040053.

[8] *Kondratyev B.P., Kornoukhov V.S.* Mutual Gravitational Energy of Gaussian Rings and the Problem of Perturbations in Celestial Mechanics // Astronomy Reports. 2020. V. 64. No. 5. P. 434–446 DOI: 10.1134/S1063772920060037.

[9] *Kondratyev B.P.* Two-dimensional generalization of Gaussian rings and dynamics of the central regions of flat galaxies // Monthly Notices of the Royal Astronomical Society. 2014. V. 442. Iss. 2. P. 1755–1766. DOI: 10.1093/mnras/stu841.

[10] *Kondratyev B.P., Kornoukhov V.S.* Study of the Secular Evolution of Circumbinary Systems Using R-Toroid and Gaussian Ring Models // Astronomy Reports. 2021. V. 65. Iss. 7. P. 588–597. DOI: 10.1134/S1063772921080072.

[11] Kondratyev B.P. Teoriya potenciala. Novye metody i zadachi s resheniyami (Potential theory. New methods and problems with solutions). M.: Mir, 2007. 512 p. (in Russian).

[12] *Kondratyev B.P.* Precession of the orbital nodes of Jupiter and Saturn triggered by the mutual perturbation: A model of two rings // Solar System Research. 2014. V. 48. No. 5. P. 366–374. DOI: 10.1134/S0038094614040066.

[13] *Murray C.D., Dermott S.F.* Solar System Dynamics. Cambridge, UK: Cambridge Univ. Press, 1999.

[14] *Kondratyev B.P., Kornoukhov V.S.* Metod kruglykh kolets Gaussa v teorii vozmushchenii (The method of round Gaussian rings in perturbation theory) // Astronomy Reports. 2023. (in Russian).

[15] *Damasso M., Zeng L., Malavolta L. et al.* So close, so different: characterization of the K2-36 planetary system with HARPS-N // Astronomy and Astrophysics. 2019. V. 624. Art. No. A38. DOI: 10.1051/0004-6361/201834671.

[16] *Sinukoff E., Howard A.W., Petigura E.A.* et al. Eleven Multiplanet Systems from K2 Campaigns 1 and 2 and the Masses of Two Hot Super-Earths // The Astrophysical J. 2016. V. 827. No. 1. P. 78. **DOI:** 10.3847/0004-637X/827/1/78.

CALCULATION OF THERMAL ATMOSPHERIC LOSS FOR A HOT EXOPLANET ON ELLIPTIC ORBIT

A.A. Simonova[1,2],V.I. Shematovich[1]
[1] *Institute of Astronomy RAS, Moscow, Russia, simonova@inasan.ru*
[2] *Lomonosov Moscow State University, Moscow, Russia*

KEYWORDS:
hot exoplanets, elliptic orbit, atmospheric mass loss, aeronomic model

INTRODUCTION:

Exoplanets with substantial hydrogen/helium atmospheres have been discovered in abundance, many residing extremely close to their host stars. Their atmospheres are forced by the extreme irradiation levels resulting in the formation of the extended planetary envelopes due to the thermal and non-thermal atmospheric escape. Ongoing atmospheric escape has been observed to be occurring in a few nearby exoplanet systems through transit spectroscopy both for hot jupiters and lower-mass sub-neptunes [1].

Hot sub-neptune-class exoplanet orbiting close to its host star will lose its hydrogen-helium atmosphere over time. This loss is usually calculated using an approximate formula (see, for example, [2–3]) written within the framework of the energy-limited formulation, which assumes that the extreme UV radiation flux is absorbed in a thin atmospheric layer of radius R_{XUV}, where the optical depth for stellar XUV photons is unity. Note that this formula is the ratio of the heating rate of the planet's upper atmosphere (in erg·s^{-1}) when the stellar XUV radiation flux F_{XUV} (in erg·cm^{-2}·s^{-1}) falls on the cross-sectional area πR_{XUV}^2 of the planet's atmosphere, heating it with an efficiency of η_{XUV}, to the gravitational potential of the planet (in erg·g^{-1}) with a correction factor—the tidal parameter—$Kt(\xi)$.

The calculations are carried out according to the following standard procedure: the orbit of a hot exoplanet with given parameters (semi-major axis and eccentricity) was divided into a certain number of sectors. Then, for each sector, the "planet-to-star" distance $r(t)$, the planet's residence time δt in this sector, and the local flux of stellar XUV radiation F_{XUV} were calculated. Next, using approximate formula, the local rate of atmospheric mass loss was calculated for each of the considered sectors. To check the accuracy of the calculation, the number of sectors was doubled and, if the local mass loss rates did not change, then the atmospheric mass loss was calculated over the orbital period.

Estimates of the atmospheric loss over the orbital period of the exoplanet — the model hot sub-neptune, - have shown that the atmospheric loss M_T averaged over the orbital period varies from 5.8×10^{17} g for e = 0.0 to 2.6×10^{18} g for the orbit with e = 0.8, that is, it increases by almost 4.5 times. It is possible to estimate approximately the time of complete atmosphere loss for the considered model sub-neptune — at e = 0.0, this time is about 0.32 billion years, and for e = 0.8 — about 0.07 billion years. Therefore, it is seen that the initial ellipticity of the hot exoplanet's orbit is an important factor in estimating the loss rate of the primary hydrogen-helium atmosphere for sub-neptunes and super-earths. Based on the results obtained and the effects taken into account, it can be assumed that hot sub-neptunes of a given mass can quickly lose their initial hydrogen-helium atmosphere in the case of movement in highly elliptical orbits.

Recently the transit sub-neptune HD 207496b was discovered [4] as part of a large program aimed at describing the characteristics of the exposed cores of planets. This planet may either be an exposed core, or is on the verge of becoming one. It was found that the host star is young, ~0.52 Gyr, allowing to gain insight into planetary evolution, also a planetary mass of 6.1±1.6 M_E, and planetary radius of 2.25±0.12 R_E were derived. This sub-neptune has an eccentric orbit with e = 0.231 [4]. Modeling of the evaporation history of HD

207496b [4] shows that the atmosphere of the planet HD 207496b can be completely evaporated during the time of 1.0±0.6 Gyr from its formation.

The results of numerical calculation of the mass loss rate of the planet's atmosphere using the approximate formula are shown in Figure. The following values were calculated: the period of the planet's orbit, which is $T = 6.0^{d}48$; the average loss of the atmosphere over the period of the planet's rotation M_T, equal to approximately 5.8×10^{15} g, which corresponds to an average atmospheric mass loss rate of 1.1×10^{10} g·s^{-1}. In the case of the considered eccentric orbit, the atmosphere loss time was estimated by averaging over the loss times at several different points along the orbit, shown in Figure. Basing on these values an estimate of ~554 Ma was obtained for the time interval for the complete loss of the sub-neptune HD 207496b H-He atmosphere. It is important to note that this result is in a good agreement with the estimate obtained when modeling through the "photoevolver" pipeline [4]. Consequently, the approximate formula, despite the simplifications adopted in it, allows us to obtain estimates close to the results for more complex models.

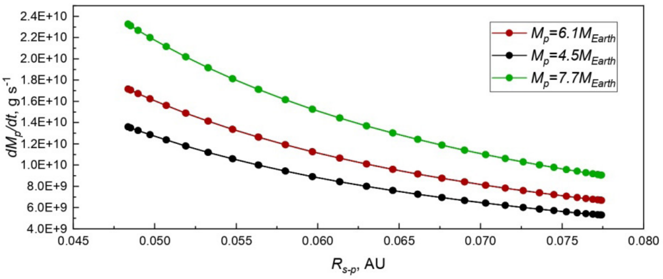

Fig. 1. The dependence of the mass loss rate of the planet's atmosphere on the star-planet distance for sub-neptune HD 207496b assuming different values of the planet's mass [4]

Acknowledgements:
We acknowledge the financial support of the Russian Science Foundation, grant no. 22-22-00909.

References:

[1] *Owen J.E.* Atmospheric Escape and the Evolution of Close-In Exoplanets // Annual Review of Earth and Planetary Sciences. 2019. V. 47. P. 67–90. https://doi.org/10.1146/annurev-earth-053018-060246.

[2] *Lammer H., Selsis F., Ribas I. et al.* Atmospheric Loss of Exoplanets Resulting from Stellar X-Ray and Extreme-Ultraviolet Heating // Astrophysical J. 2003. V. 598. No. 2. P. L121–L124. DOI 10.1086/380815.

[3] Luger R., Barnes R., Lopez E., et al. Habitable Evaporated Cores: Transforming Mini-Neptunes into Super-Earths in the Habitable Zones of M Dwarfs // Astrobiology. 2015. V. 15. Iss. **1**. P. 57–88. https://doi.org/10.1089/ast.2014.1215.

[4] *Barros S.C.C., Demangeon O.D.S., Armstrong D.J. et al.* The young mini-Neptune HD 207496b that is either a naked core or on the verge of becoming one // Astronomy and Astrophysics. 2023. V. 673. Art. No. A4. 18 p. https://doi.org/10.1051/0004-6361/202245741.

KINETIC MODEL OF THE EFFECT OF STELLAR WIND ON THE EXTENDED HYDROGEN ATMOSPHERE OF THE EXOPLANET π MEN C

A.A. Avtaeva, V.I. Shematovich
Institute of Astronomy RAS, Moscow, Russia, nastyaavt@gmail.com

KEYWORDS:
exoplanets, UV observations, stellar wind, aeronomy, atmospheric loss, numerical modeling.

INTRODUCTION:
In this study the kinetic model of the aeronomy of the upper atmosphere of an exoplanet is expanded by taking into account the processes of the effect of stellar wind plasma on the extended hydrogen corona of a hot sub-neptune. For this purpose, previously developed kinetic Monte Carlo models were used to study the precipitation of protons and hydrogen atoms with high energies into planetary atmospheres [1]. The kinetic model is adapted to the upper atmospheres of hot sub-neptunes, allowing us to calculate the deposition rate of stellar wind energy in the planetary corona and to refine the estimates of the of non-thermal atmospheric loss rate due to the influence of the stellar wind of the host star.

In the current studies of the evolution of the atmospheres of hot sub-neptunes, attention is paid only to the thermal processes of atmospheric loss. Non-thermal processes of atmospheric loss are usually not included in aeronomic models, since their consideration requires the use of methods of non-equilibrium kinetics, which is a complex mathematical problem (see, for example, [2]). In our previous studies of non-thermal losses of the atmospheres of hot sub-neptunes [3], it was found that non-thermal atmospheric losses due to exothermic photochemistry can be compared with the rates of thermal losses in the moderate conditions of a host star and these processes should be included in aeronomic models of the upper atmospheres of sub-neptunes.

The object of research in this study, planet π Men c, is in a close-in orbit (distance 0.067 au) around the host star π Men, which belongs to the G0 V class. This is a solar-type star, but younger (~3 billion years) of our Sun, which suggests a higher activity of the star and a significant flow of stellar wind in the direction of the exoplanet. Observations on the HST (Hubble Space Telescope) [4] showed that the hot exoplanet π Men c has an extended atmosphere. This exoplanet has parameters – radius R_p = (2.06±0.03)R_E and mass M_p = (4.52±0.81) M_E, — and average density — 2.82±0.53 g·cm^{-3}, which allows this exoplanet to be classified as a hot sub-neptune. From the volume density estimates, it is assumed that the planet pi Men c is able to hold a significant atmosphere.

In the considered case of low stellar activity for the host star π Men, the energy flux of the undisturbed stellar wind is estimated as ~320 erg·cm^{-2}·s^{-1}. At upper boundary the flux of energetic neutral hydrogen atoms (ENA H) is forming due to the charge exchange of the stellar wind protons in the extended hydrogen corona with rather low efficiency of ~10 %. It penetrates into the upper atmosphere of the hot sub-neptune π Men c with an energy of ~32 erg·cm^{-2}·s^{-1}, which is significantly lower than the UV energy flux of ~1350 erg·cm^{-2}·s^{-1} absorbed in the atmosphere [4–5]. Consequently, atmospheric heating by stellar wind plasma is important only in the outermost regions of the extended hydrogen corona. The energy balance in the thermosphere of a hot exoplanet is determined by the processes of absorption of stellar radiation in the ranges of soft X-rays and hard ultraviolet (1–100 nm) radiation of the host star [4–5].

The calculations carried out for the hot sub-neptune π Men c showed that the energy of a flux of energetic neutral hydrogen atoms penetrating into the atmosphere mainly goes to the heating the hydrogen corona of a hot exoplanet (see Figure 1).

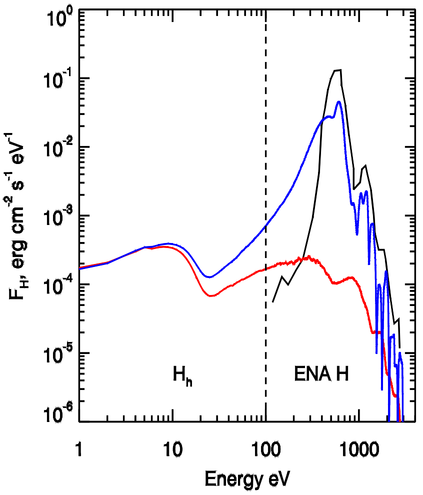

Fig. 1. The calculated energy spectra of the fluxes of suprathermal hydrogen atoms (1eV < E < 100 eV) and ENA H (E > 100 eV) at a distance of 8.0R_p from the center of the exoplanet π Men c are presented. Blue line represents the downward flux of energy of hydrogen atoms, red one represents the upward flux.

Acknowledgements:
We acknowledge the financial support of the Russian Science Foundation, grant no. 22-22-00909.

References:

[1] *Shematovich V.I., Bisikalo D.V., Zhilkin A.G.* A kinetic model for precipitation of solar-wind protons into the martian atmosphere // Astronomy Reports. 2021. V. 65. No. 9. P. 869–875.
[2] *Shematovich V.I., Marov M.Y.* Escape of planetary atmospheres: physical processes and numerical models // Physics-Uspekhi. 2018. V. 61. No. 3. P. 217–246.
[3] Avtaeva A.A., Shematovich V.I. Nonthermal Atmospheric Loss of the Sub-Neptune π Men c Due to Exothermic Photochemistry // Solar System Research. 2022. V. 56. P. 67–75. https://doi.org/10.1134/S0038094622020010.
[4] *García Muñoz A., Youngblood A., Fossati L. et al.* Study of the non-thermal atmospheric loss for exoplanet π Men c // The Astrophysical J. Letters. 2020. V. 888. Art. No. L21. 12 p. https://doi.org/10.1017/S1743921322001855.
[5] *Shaikhislamov I.F., Fossati L., Khodachenko M.L. et al.* A Heavy Molecular Weight Atmosphere for the Super-Earth π Men c // Astronomy and Astrophysics. 2020. V. 639. Art. No. A109. DOI: 10.3847/2041-8213/abd9b8.

THE REFINED METHOD FOR TAKING INTO ACCOUNT OBSERVATIONAL SELECTION FOR PLANETS DETECTED BY THE RADIAL VELOCITY TECHNIQUE

V.I. Ananyeva, A.V. Tavrov, O.I. Korablev
Space Research Institute RAS, Moscow, Russia, a-lada@yandex.ru

KEYWORDS:
exoplanets, statistics, observational selection, numerical methods

When studying the statistics of exoplanets, it is necessary to take into account the effects of observational selection and the inhomogeneity of the data in the exoplanets databases. When considering exoplanets detected using the radial velocity (RV) technique, we proposed an algorithm for taking into account the main inhomogeneities, called the detectability window regularization algorithm [1–2]. Earlier we showed that the de-biased mass distribution of RV exoplanets approximately corresponds to a piecewise power law with the breaks of ~0.14 and ~1.7 MJ (Jupiter mass). The mass distribution of RV planets follows the power laws of: $dN/dm \cdot \alpha \cdot m^{-3}$ (masses of 0.011–0.087 MJ), $dN/dm \cdot \alpha \cdot m^{-0.8\ldots-1}$ (0.21–1.7 MJ), $dN/dm \cdot \propto \cdot m^{-1.7\ldots-2}$ (1.7–13 MJ). There is a minimum of exoplanets in the range of 0.087–0.21 MJ.

The de-biased distributions of RV exoplanets and transiting exoplanets agree with each other in the range of 0.21–13 MJ, but differ somewhat in the low-mass region [3].

To identify the reasons for this difference, we have significantly refined our method. We have taken into account explicitly the number of radial velocity measurements of each star N. We consider RV planets with the orbital periods from 1 to 100 days and with the minimum masses from 0.0061 to 0.21 MJ (2–66.6 Earth mass). We divide each of the domains into 60 bins, which are equal in logarithmic scale. In the middle of each of these cells, we place an artificial planet. For each cell with the artificial planet we compute the semi-amplitude of reflex motion K. We used the Lomb-Scargle periodogram to identify the signal of an artificial planet from the noises that we modeled as Gaussian noise with standard deviation σ. An artificial planet was considered detectable if the false alarm probability (FAP) <1 %. For each artificial planet, we considered 24 implementations of the RV signal with a shift by 15° and then averaged over all implementations. As a result, for each star we received a “single detectability window” — a matrix on the diagram “Orbital period – Minimum mass”, where the value of each element corresponded to the probability of detecting an artificial planet with the given orbital period and mass.

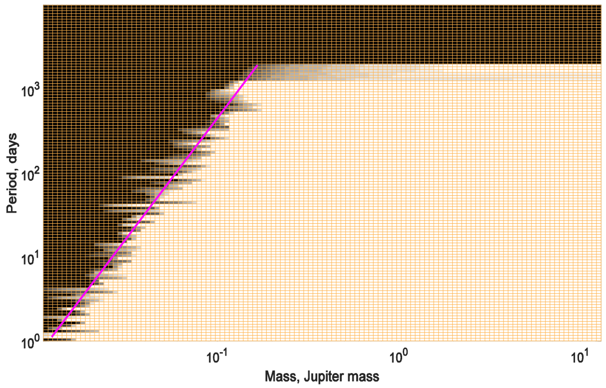

Fig. 1. An example of a single detectability window with the boundary between “detectable” and “undetectable” planets

We approximated the boundary between “detectable” and “undetectable” planets by a power law. We found that for each number of radial velocity measurements N, there exists such a $\gamma(N) = K/\sigma$, which is the threshold value of the detectability of an artificial planet. Thus, a planet is considered detectable if

$K > \sigma\gamma(N)$.

The dependence $\gamma(N)$ was approximated by a power law using the least squares method:

$\gamma(N) = 17.78N^{-2/3}$.

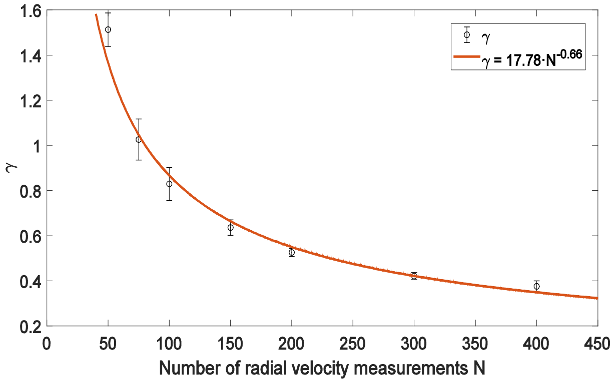

Fig. 2. The dependence of γ on the number of radial velocity measurements

Using of a more accurate method of accounting for observational selection will make it possible to clarify the distribution of small-mass planets.

References:

[1] *Ivanova A.E., Yakovlev O.Ya., Ananyeva V.I. et al.* The “Detectability Window” Method to Take into Account Observational Selection in the Statistics of Exoplanets Discovered through Radial Velocity Measurements // Astronomy Letters. 2021. V. 47. No. 1. P. 43–49. https://doi.org/10.1134/S1063773721010059.

[2] *Ananyeva V., Ivanova A., Shashkova I. et al.* Exoplanets Catalogue Analysis: The Distribution of Exoplanets at FGK Stars by Mass and Orbital Period Accounting for the Observational Selection in the Radial Velocity Method // Atmosphere. 2023. V. 14. Iss. 2. Art. No. 353. https://doi.org/10.3390/atmos14020353.

[3] *Yakovlev O.Ya., Ananyeva V.I., Ivanova A.E., Tavrov A.V.* Comparison of the mass distributions of short-period exoplanets detected by transit and RV methods // Monthly Notices of the Royal Astronomical Society: Letters. 2022. V. 509. Iss. 1. P. L17–L20. https://doi.org/10.1093/mnrasl/slab115.

ONE RELIABLE METHOD FOR STELLAR PARAMETER DETERMINATION BASED ON SPACE PHOTOMETRY AND THE PHOENIX SPECTRAL LIBRARY

Yisi Liu[1], V. Perdelwitz[2]
[1] *Deep Space Exploration Laboratory, Haidian District, Beijing, China, liuyisigj@163.com*
[2] *Hamburger Sternwarte, Hamburg, Germany*

KEYWORDS:
fundamental parameters, atmospheres, catalogues, surveys, exoplanets

To get precise determination of parameters of stars in Galaxy is quite important for exoplanet searching. In order to establish a reliable estimation of stellar parameters such as the effective temperature and so on, we are currently developing an algorithm which compares the absolute fluxes of all Gaia passbands, combined with those from the WISE mission, to PHOENIX spectra. Results have shown that a broader wavelength range enables a reliable determination of these parameters. Furthermore, the effective temperature we derived has a better precision than Gaia's one, which shows the good performance of PHOENIX model.

TELLURIC ABSORPTION CORRECTION AND RADIAL VELOCITY METHOD

A. Ivanova[1], A. Tavrov[1], R. Lallement[2], J.-L. Bertaux[3]
[1] *Space Research Institute RAS, Moscow, Russia, ctf.i.a.e@gmail.com*
[2] *Observatoire de Paris, Paris, Франция*
[3] *Laboratoire Atmosphères, Milieux, Observations Spatiales (LATMOS) Université de Versailles — Saint-Quentin-en-Yvelines (UVSQ), Guyancourt, France*

KEYWORDS:
exoplanets, radial velocity, extrasolar planets, detection, spectroscopy

The radial velocity method is based on the measurement of Doppler shifts of stellar lines caused by the motion of a star around the centre of mass of the star-planet system. Due to the fact that the spectra for radial velocity measurements are obtained from the Earth, the lines produced by the Earth's atmosphere are also displayed in the recorded spectrum. In order to avoid errors, the regions of the spectrum with telluric absorption and the regions close to them are excluded from consideration. Because of the annual motion of the Earth, regions ±30 km/s around telluric lines are excluded from consideration. Telluric lines cover a rather wide range of wavelengths, especially starting at 600 nm. Thus quite large parts of the spectrum, usually with excellent signal-to-noise ratios, are excluded.

It is therefore an important task to correct stellar spectra from telluric absorption, as this can improve the accuracy of radial velocity measurements.

A method for correcting telluric absorption in stellar spectra has been developed. The method was tested on data in the spectral range 380-780 nm for a K2.5V class star. The method is universal and can be applied to a wider spectral range, after a slight modification it can also be applied to cooler stars, e.g. red dwarfs. The method of correction of telluric absorption allows us to use parts of the spectra that were previously unavailable for consideration; this increases the accuracy of measurements of the radial velocity of the parent star, which in turn allows us to find planets, perturbations from which were not previously visible in the data, as well as to make more accurate measurements of the physical and orbital parameters of already discovered exoplanets.

References:

[1] *Ivanova A., Lallement R., Bertaux J.-L.* Improved precision of radial velocity measurements after correction for telluric absorption // Astronomy and Astrophysics. 2023. V. 673. Art. No. A56. 16 p. DOI: 10.1051/0004-6361/202245089.

STATISTICAL EQUILIBRIUM CODE FOR EXOPLANET ATMOSPHERES SIMULATIONS

A.V. Shepelin, M.P. Golubovskii, I.F. Shaikhislamov
Institute of Laser Physics SB RAS, Novosibirsk, Russia, 4.shepelin@gmail.com

KEYWORDS:
exoplanets, atmosphere, plasma, kinetics, NLTE, oxygen, simulation

Exoplanet research — a young and progressive field of science, that uses the full power of modern observational and computing methods to find and study extrasolar planets.

There are many unsolved problems in exoplanet physics, such as formation problems, observation problems, migration problems, composition problems, etc. Atmospheric modeling and comparison with observational data can help us to solve some of these problems.

The most representative information about exoplanets came from their transit spectrum, and mostly, from their atmospheres. In astrophysics, one of the most interesting elements is oxygen. The 777.4 nm neutral oxygen triplet is commonly used to track the formation and main conditions of stars because it has high intensity and low Earth's atmosphere opacity. In 2022 it was first detected in the hot Jupiter KELT-9 b atmosphere [1].

Modeling the interaction of radiation with atmospheres assumes, at least, a joint solution of the radiative transfer and statistical equilibrium equations. Due to a lack of detailed balance in stellar or planetary atmospheres (radiation field deviates from Planck's law, or electrons velocities deviate from Maxwell distribution), local thermodynamic equilibrium (LTE) is inappropriate. We need to take into account the full kinetics of quantum transitions, i.e. use a non-local thermodynamic equilibrium (NLTE) [2].

This report presents LTE and NLTE kinetics library written in C++ (with Python bindings) created as a part of global 3D MHD code [3]. NLTE implements radiative and collisional bound-bound and bound-free transitions with an ability to add and use arbitrary elements and spectra.

References:

[1] *Borsa F., Fossati L., Koskinen T. et al.* High-resolution detection of neutral oxygen and non-LTE effects in the atmosphere of KELT-9b // Nature Astronomy. 2021. V 6. No. 2. P. 226–231. DOI:10.1038/s41550-021-01544-4.

[2] *Sitnova T.M., Mashonkina L.I., Ryabchikova T.A.* Influence of Departures from LTE on Oxygen Abundance Determination // Astronomy Letters. 2013. V. 39. Iss. 2. P. 126–140. DOI: 10.1134/S1063773713020084.

[3] *Shaikhislamov I.F., Khodachenko M.L., Sasunov Yu.L. et al.* Atmosphere expansion and mass loss of close-orbit giant exoplanets heated by stellar XUV. I. Modeling of hydrodynamic escape of upper atmospheric material // The Astrophysical J. 2014. V. 795. No. 2. Art. No. 132. DOI: 10.1088/0004-637X/795/2/132.

MIXING OF PLANETESIMALS IN THE GLISSE 581 PLANETARY SYSTEM

S.I. Ipatov
Vernadsky Institute of Geochemistry and Analytical Chemistry RAS, Moscow, Russia, siipatov@hotmail.com

KEYWORDS:
motion of planetesimals, probabilities of collisions, Glisse 581, exoplanets

INTRODUCTION AND CONSIDERED MODEL:

The extrasolar system Gliese 581 contains the star with a mass equal to 0.307 of the solar mass and five planets (*b, c, d, e,* and *g*). Their masses and semi-major axes and probable range of eccentricities of their orbits are presented in Table 1. In my calculations eccentricities and inclinations of orbits of planets were considered to be equal to 0.250 initial planetesimals were in each calculation variant. The semi-major axes of their orbits were near the semi-major axis of one of the planets and were between a_{min} and a_{max}. The values of a_{min} and a_{max} are presented in Table 1. For an additional disk *h* not corresponded to a planet, a_{min} = 0.25 AU and a_{max} = 0.3 AU. Initial eccentricities of orbits of planetesimals were equal to e_o (0.02 or 0.15). Their initial inclinations equaled to $e_o/2$ rad. Greater eccentricities could be caused by the previous mutual gravitational influence of planetesimals. I studied the evolution of the orbits of planetesimals under the gravitational influence of the star and the planets. Planetesimals that collided with planets or the star or reached 50 AU from the star were excluded from integration. The symplectic code from the SWIFT integration package [1] was used for integration of the motion equations. The considered time integration step t_s equaled to 0.01, 0.04, or 0.1 days. The results of calculations with different t_s were compared and mainly gave similar results. For time interval equal to 10 Myrs, the numbers of collisions of planetesimals with planets (N_e, N_b, N_c, N_g, N_d) are presented in Table 2. The table also includes the number N_{ej} of planetesimals that reached 50 AU from the star (which were considered to be ejected into hyperbolic orbits) and the number N_{el} of planetesimals that were left in elliptical orbits at the considered time.

Table 1. Semi-major axes *a* and eccentricities *e* of orbits and masses *m* (in Earth masses m_E) of exoplanets in Gliese 581 and values a_{min} and a_{max} for considered disks of planetesimals near planets *b, c, d, e,* and *g*

disk	m/m_E	*a*, AU	*e*	a_{min}, a.e.	a_{max}, a.e.
e	1.7	0.02815	0.0–0.06	0.022	0.0344
b	15.8	0.0406	0.020.03	0.0344	0.0563
c	5.5	0.0721	0.0–0.06	0.0563	0.1
g	2.2	0.13	0.0	0.1	0.174
d	6.98	0.218	0.0–0.25	0.174	0.25

PROBABILITIES OF COLLISIONS OF PLANETESIMALS WITH PLANETS:

The aim of the considered calculations was to study the mixing of planetesimals at the late stages of accumulation of planets in the Glisse 581 system. I made the estimates of the fraction of planetesimals that were initially located close to the orbit of one of the planets and then collided with other planets. Earlier I studied mixing of planetesimals migrated from the feeding zones of planets in the Solar System [2–4], Proxima Centauri [5] and Trappist 1 [6] planetary systems. In contrast to [2–5], for calculations for the Glisse 581 system there were no collisions with a star (as in [6]). Below in this paragraph I discuss the data from Table 2 obtained at 10 Myrs. The fraction p_{ej} of ejected planetesimals was greater for disks located more far from the star. For disks corresponded to planets, p_{ej} did not exceed 0.05 and 0.15 at e_o equal to 0.02 and 0.15, respec-

Table 2. The number of collisions of planetesimals with planets during 10 Myrs at integration step t_s equal to 0.01, 0.04 or 0.1 days. Initial eccentricities of orbits of planetesimals were equal to e_o (0.02 or 0.15). The number of initial planetesimals was equal to 250 in each variant. N_{ej} is the number of planetesimals that reached 50 AU from the star. N_{el} is the number of planetesimals that were left in elliptical orbits

disk	e_o	t_s	N_e	N_b	N_c	N_g	N_d	N_{ej}	N_{el}
e	0.02	0.01	**116**	66	5	0	2	3	58
e	0.02	0.04	**106**	80	5	0	0	0	59
e	0.02	0.1	**120**	66	3	1	1	0	59
b	0.02	0.04	7	**111**	16	1	1	2	112
c	0.02	0.04	1	9	**73**	7	6	4	150
g	0.02	0.04	0	6	12	**44**	22	6	160
d	0.02	0.01	0	4	11	8	**104**	9	114
d	0.02	0.04	0	6	4	5	**118**	12	105
d	0.02	0.1	0	3	6	8	**114**	13	106
h	0.02	0.04	0	0	0	0	0	2	248
e	0.15	0.01	**120**	117	4	1	0	1	7
e	0.15	0.04	**105**	125	8	2	1	2	7
b	0.15	0.01	8	**200**	29	3	3	4	3
b	0.15	0.04	17	**183**	38	1	1	7	3
c	0.15	0.01	4	95	**105**	13	16	13	4
c	0.15	0.04	1	85	**111**	16	16	17	4
g	0.15	0.01	0	35	54	**45**	88	21	7
g	0.15	0.04	5	41	52	**34**	83	30	5
d	0.15	0.01	1	14	35	16	**123**	37	24
d	0.15	0.04	1	20	36	21	**118**	30	24
h	0.15	0.01	0	8	10	13	53	68	98
h	0.15	0.04	0	7	8	12	84	82	63

tively. For the disk *h*, p_{ej} was about 0.01 and 0.25–0.4 at $e_o = 0.02$ and $e_o = 0.15$, respectively. Some planetesimals initially located near one of the planets could fall also onto other planets. The largest ratio K_a of the number of planetesimals that fell onto another planet to the number of planetesimals that fell onto the host planet of the initial disk at $e_o = 0.02$ was for planet *e*, which is most close to the star. For disk *e,* the ratio N_b/N_e was about 0.55–0.75 and 0.98–1.2 at $e_o = 0.02$ and $e_o = 0.15$, respectively. At $e_o = 0.02$, the ratio K_a equaled to 0.5 for the disk *g* and was less than 0.15 for the disks *b*, *c* and *d*. At $e_o = 0.15$ for disk *g*, N_g was even about twice less than N_d. At $e_o = 0.15$ the ratio K_a was less than 0.21 for disk *b*, but it was about 0.8–0.9 for the disk *c*. At $e_o = 0.15$ for disk *d*, the ratio N_c/N_d was about 0.3, though planets *c* and *d* were not close to each other. Planetesimals from disk *h* fall onto four planets at $e_o = 0.15$, but they did not collide with any planet at $e_o = 0.02$.

At a current time, the calculations were made for up to a few tens of Myrs and have not yet finished. For these calculation times, the obtained numbers *N* could exceed the numbers presented in Table 2 typically by no more than 2 and were almost the same as in Table 2. For disks close to the star, most of collisions of planetesimals with planets took place during the first 1 Kyr. At $e_o = 0.02$ the ratio k_1 of the total number of collisions of planetesimals with planets during the first 1 Kyr to that during 10 Myrs was between 0.6 and 0.67 for disks *e*, *b*, and *c*; it equaled to 0.3 for the disk *g*, and was between 0.23 and 0.49 for the disk *d*. The latter range was at different t_s. For all other disks, such range of k_1 was narrow for different t_s. At e_o = 0.15 the ratio k_1 was 0.85, 0.8, 0.45, 0.13-0.15, and 0.06-0.08 for disks *e*, *b*, *c*, *g*, *d*, and *h*, respectively.

CONCLUSIONS:

At the late stages of accumulation of planets in the Glisse 581 system, planetesimals from the feeding zone of each planet could fall onto other planets. The fraction of planetesimals ejected into hyperbolic orbits did not exceed 0.05 and 0.15 at initial eccentricities of planetesimals equal to 0.02 and 0.15, respectively. For planetesimals from the feeding zones of planets located close to the star most of collisions of planetesimals with planets were during the first 1 Kyr.

Acknowledgements:

The studies were carried out under government-financed research project for the Vernadsky Institute.

References:

[1] *Levison H.F., Duncan M.J.* The long-term dynamical behavior of short-period comets // Icarus. 1994. V. 108. Iss. 1. P. 18–36. https://doi.org/10.1006/icar.1994.1039.

[2] *Ipatov S.I.* Migration of bodies in the accretion of planets // Solar System Research, 1993. V. 27. Iss. 1. P. 65–79. https://www.academia.edu/44448077/.

[3] *Ipatov S.I.* Probabilities of collisions of planetesimals from different regions of the feeding zone of the terrestrial planets with forming planets and the Moon // Solar System Research. 2019. V. 53. Iss. 5. P. 332–361. DOI: 10.1134/S0038094619050046.

[4] *Marov M.Ya., Ipatov S.I.* Migration processes in the Solar System and their role in the evolution of the Earth and planets // Physics — Uspekhi. 2023. V. 66. Iss. 7. P. 2–31. DOI: 10.3367/UFNe.2021.08.039044.

[5] *Ipatov S.I.* Delivery of icy planetesimals to inner planets in the Proxima Centauri planetary system // Meteoritics and Planetary Science. 2023. V. 58. Iss. 6. P. 752–774. https://doi.org/10.1111/maps.13985.

[6] *Ipatov S.I.* Mixing of planetesimals in the TRAPPIST-1 exoplanetary system // 13th Moscow Solar System Symposium (13M-S3). 2022. Art. Ni. 13MS3-EP-PS-02. P. 378–380.

INVESTIGATION OF DYNAMIC EVOLUTION OF THE COMPACT PLANETARY SYSTEM KEPLER-51

E.D. Kuznetsov, A.S. Perminov
Ural Federal University, Ekaterinburg, Russia, eduard.kuznetsov@urfu.ru, alexander.perminov@urfu.ru

KEYWORDS:
compact planetary system, mean-motion resonances, resonance chains, tides, dynamic evolution, stability

INTRODUCTION:
At present, several dozen compact planetary systems containing more than two planets with masses of the order of the Earth's mass are known[1]. It is shown that the stable evolution of compact planetary systems requires the presence of resonances that prevent close encounters of planets moving in neighboring orbits (see, for example, the five-planet systems Kepler-80 [1], K2-138 [2] and the seven-planet system TRAPPIST-1 [3]). In this case, resonances between pairs of planets can form chains. The longest resonance chain known to date is realized in the TRAPPIST-1 system: 8:5 – 5:3 – 3:2 – 3:2 – 4:3 – 3:2 [4]. In the K2-138 system, five planets form the longest chain consisting of identical 3:2 resonances [2]. On the other hand, simulation results show that in wide systems with massive planets, chains of high-order resonances can lead to the destruction of planetary systems [4].

Antoniadou and Voyatzis [5] demonstrate three possible scenarios safeguarding compact planetary system Kepler-51, each followed by constraints. Firstly, there are the 2:1 and 3:2 two-body mean-motion resonances (MMRs), in which eccentricity $e_b < 0.02$, such that these two-body MMRs last for extended time spans. Secondly, there is the 1:2:3 three-body Laplace-like resonance, in which $e_c < 0.016$ and $e_d < 0.006$ are necessary for such a chain to be viable. Thirdly, there is the combination comprising the 1:1 secondary resonance inside the 2:1 MMR for the inner pair of planets and an apsidal difference oscillation for the outer pair of planets in which the observational eccentricities, e_b and e_c, are favored as long as $e_d \approx 0$.

We consider the compact planetary system Kepler-51 and search for resonances and resonance chains within the errors of determining the orbital periods from observations. For compact systems, an important factor affecting evolution is tidal interaction; therefore, when analyzing the feasibility of the proposed resonance chains, we will model dynamic evolution taking into account tides.

METHODS:
The search for resonances was carried out for the values of the orbital periods of the planets, which varied within the determination error. To determine the resonant combinations of the orbital periods, the ratio of the periods of neighboring planets was represented as a segment of a sequence of convergent fractions. We have obtained a rational approximation of the real ratio of periods. Possible chains of resonances are formed if the resonance values of the periods of the outer and inner orbits in neighboring pairs coincide. The final selection of potential resonance chains is based on an estimate of the frequency of the resonant angle.

We investigated the dynamical evolution of the Kepler-51 compact planetary system using the Posidonius software [6], which allows for tidal interaction.

RESULTS:
We implement a method for searching for resonances within the limits of errors in determining the values of the periods of planetary orbits. In [7] according to the data of the TESS space telescope the refined parameters of the planetary system Kepler-51 were obtained (see Table 1). In Table 1 the mass of the star m_s is given in the masses of the Sun M_S, masses of the planets m_p are given

1 The Extrasolar Planets Encyclopaedia. http://exoplanet.eu/catalog/

in the masses of the Earth M_E, the radius of the star R_s is given in the radii of the Sun R_S, the radii of the planets R_p are given in the radii of the Earth R_E, T are the orbital periods of the planets, e is the eccentricity, g is the argument of the pericenter. T_{conj} moments correspond to the conjunction of the planet with the star. We concluded that the compact three-planetary system Kepler-51 evolves outside the low-order resonances (order of resonance is less than 10).

Table 1. Parameters of the three-planet system Kepler-51 [7]

Parameter	Kepler-51	Kepler-51 b	Kepler-51 c	Kepler-51 d
m_s [M_S]	$0.894^{+0.036}_{-0.048}$			
m_p [M_E]		$2.48^{+1.23}_{-1.04}$	$3.14^{+0.50}_{-0.48}$	$5.22^{+1.17}_{-1.07}$
R_s [R_S]	$0.841^{+0.023}_{-0.021}$			
R_p [R_E]		$6.62^{+0.19}_{-0.17}$	8.98 ± 2.84	$9.04^{+0.25}_{-0.23}$
T [days]		$45.15393^{+0.00036}_{-0.00038}$	$85.31553^{+0.00138}_{-0.00109}$	130.1827 ± 0.0009
$e{\cdot}\cos g$		$-0.019^{+0.009}_{-0.010}$	0.024 ± 0.014	0.014 ± 0.011
$e{\cdot}\sin g$		$-0.059^{+0.019}_{-0.022}$	$-0.048^{+0.027}_{-0.029}$	$-0.037^{+0.022}_{-0.024}$
T_{conj} [BJD – 2457000]		-1285.4040 ± 0.0006	-1274.4886 ± 0.0030	-1304.0693 ± 0.0009

We considered a number of scenarios for the evolution of the Kepler-51 system over 100 Myr using the Posidonius software. We considered the cases of nominal, minimum and maximum star masses for the entire range of orbital periods of the planets at nominal values of planetary orbital eccentricities and zero orbital inclinations. For these initial conditions, we have shown that the system can have a stable evolution in the absence of low-order resonances.

The next stage of our study involves varying the eccentricities of the orbits within the limits of the determination error.

Acknowledgments:
The work was supported by the Ministry of Science and Higher Education of the Russian Federation under the grant 075-15-2020-780 (no. 13.1902.21.0039).

References:

[1] *MacDonald M.G., Ragozzine D., Fabrycky D.C. et al.* Dynamical Analysis of the Kepler-80 System of Five Transiting Planets // The Astronomical J. 2016. V. 152. No. 4. Art. No. 105. 18 p. DOI 10.3847/0004-6256/152/4/105.

[2] *MacDonald M.G., Feil L., Quinn T., Rice D.* Confirming the 3:2 Resonance Chain of K2-138 // The Astronomical J. 2022. V. 163. No. 4. Art. No. 162. 12 p. DOI 10.3847/1538-3881/ac524c.

[3] *Luger R., Sestovic M., Kruse E. et al.* A seven-planet resonant chain in TRAPPIST-1 // Nature Astronomy. 2017. V. 1. Iss. 6. Art. No. 0129. 8 p.

[4] *Murphy M.M., Armitage P.J.* Instability from high-order resonant chains in wide-separation massive planet systems // Monthly Notices of the Royal Astronomical Society. 2022. V. 512. Iss. 2. P. 2750–2757. https://doi.org/10.1093/mnras/stac750.

[5] *Antoniadou K.I., Voyatzis G.* Periodic orbits in the 1:2:3 resonant chain and their impact on the orbital dynamics of the Kepler-51 planetary system // Astronomy and Astrophysics. 2022. V. 661. Art. No. A62. 16 p. https://doi.org/10.1051/0004-6361/20214295.

[6] *Blanco-Cuaresma S., Bolmont E.* Studying Tidal Effects In Planetary Systems With Posidonius. A N-Body Simulator Written In Rust // EWASS Special Session 4 (2017): Star-planet interactions (EWASS-SS4-2017). 2017. DOI: 10.5281/zenodo.1095095.

[7] *Jontof-Hutter D., Dalba P.A., Livingston J.H.* TESS observations of Kepler systems with transit timing variations // The Astronomical J. 2022. V. 164. No. 2. Art. No. 42. DOI: 10.3847/1538-3881/ac7396.

SESSION 5. EXTRASOLAR PLANETS (EP) POSTER SESSION

SIMULATION OF ABSORPTION IN THE Hα LINE OF EXOPLANET KELT-9B

I.B. Miroshnichenko[1,2], S.S. Sharipov[1], I.F. Shaikhislamov[1], M.S. Rumenskikh[1]

[1] *Institute of Laser Physics SB RAS, Novosibirsk, Russia, mib383@gmail.com*
[2] *Novosibirsk State Technical University, Novosibirsk, Russia*

KEYWORDS:
hot Jupiter, Monte Carlo, accident transfer, multi-fluid model, Balmer alpha

INTRODUCTION:

This paper presents the results of modeling the absorption in the Hα line by the atmosphere of exoplanet KELT-9b. For calculations and interpretation of observations, the Monte Carlo model of Lyα photon transfer in the planet's upper atmosphere was used [1]. Atmospheric parameters: temperature and hydrogen atom concentration distribution profiles were calculated on the basis of a self-consistent three-dimensional gas-dynamic model [2]. The simulation was carried out for two different XUV parameters: 5 and 20 $\mathrm{erg \cdot s^{-1} \cdot cm^{-2}}$. As a result, it was found that the variation of the XUV parameter leads to a different nature of absorption in the Ha line: in one case, excited hydrogen is formed mainly due to Lyα photons created in collision reactions, and in the other, in recombination reactions.

Acknowledgments:

The work was carried out within the framework of the Russian Science Foundation project no. 23-72-10060.

References:

[1] *Miroshnichenko I.B., Shaikhislamov I.F., Berezutskii A.G. et al.* Lyα Flux Impact from the Parent Star on Hα Absorption in the Atmospheres of the Hot Jupiters HD189733b and HD209458b // Astronomy Reports. 2021. V. 65. Iss. 1. P. 61–69. DOI: 10.1134/S1063772921010030.

[2] *Shaikhislamov I.F., Khodachenko M.L., Lammer H. et al.* 3D Aeronomy modeling of close-in exoplanets // Monthly Notices of the Royal Astronomical Society. 2018. V. 481. No. 4. P. 5315–5323. ttps://doi.org/10.1093/mnras/sty2652.

OXYGEN 777.4 nm TRIPLET ABSORPTION SIMULATION IN KELT-9B ATMOSPHERE

M.P. Golubovsky, A.V. Shepelin, I.F. Shaikhislamov
Institute of Laser Physics SB RAS, Russia, Novosibirsk, maxym9121@gmail.com

KEYWORDS:
Hot Jupiter, oxygen, non-local thermodynamic equilibrium, hydrodynamics, atmosphere

INTRODUCTION:

In this work we present the results of modeling absorption in oxygen triplet with wavelength 777.4 nm in atmosphere of KELT-9b. The results of modeling are compared with the modeling and observation data from [1]. The atmospheric parameters were calculated on the basis of a self-consistent three-dimensional gas-dynamic model [2].

MODEL:

Modeling of absorption was performed using approximation from [3]. Kinetic model of atom takes into account such processes as photoexcitation, photoionization, radiative deexcitation, recombination, collisional excitation and deexcitation. For calculation required rates were used data about star spectra and information about atom was taken from INASAN database [4]. So, we create atmosphere with three-dimensional gas-dynamic model and calculate the absorption in it using absorption model and kinetic model. Also, the population additionally calculates using LTE model to compare with NLTE.

RESULTS:

Resulting spectrum is shown in Figure 1. The result of simulation in NLTE is close to NLTE result from [1]. The same is true for LTE results, but our results show more effects.

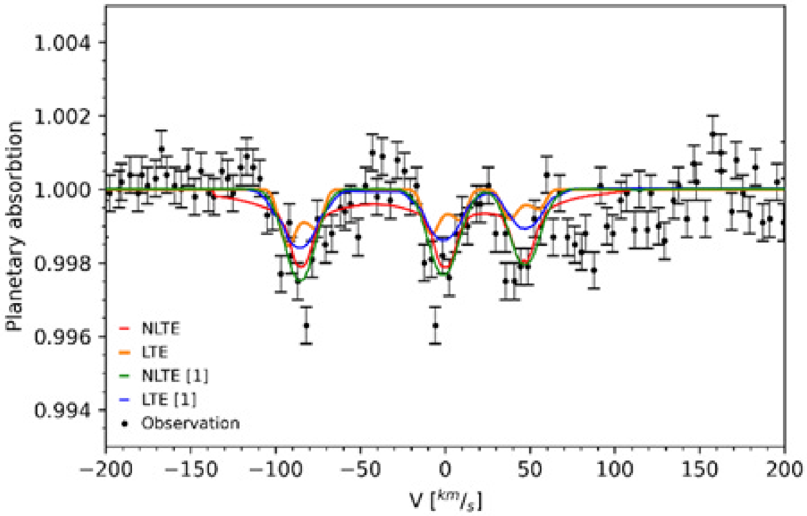

Fig. 1. Comparison of the calculated absorption spectrum with the observational spectrum for exoplanet KELT-9b

Acknowledgments:
This work was carried out as part of the RSF project No. 23-12-00134.

References:

[1] *Borsa F., Luca* F., *Tommi* K. *et al.* High-resolution detection of neutral oxygen and non-LTE effects in the atmosphere of KELT-9b // Nature Astronomy. 2021. V. 6. No. 2. P. 226–231. DOI: 10.1038/s41550-021-01544-4.

[2] *Shaikhislamov I.F., Khodachenko M.L., Lammer* H. *et al.* 3D Aeronomy modelling of close-in exoplanets // Monthly Notices of the Royal Astronomical Society. 2018. V. 481. Iss. 4. P. 5315–5323. https://doi.org/10.1093/mnras/sty2652.

[3] *Tasitsiomi A.* Ly-alpha Radiative Transfer in Cosmological Simulations and Application to a z ~ 8 Emitter // The Astrophysical J. 2006. V. 645. No. 2. P. 792–813. DOI: 10.1086/504460.
[4] *Sitnova T.M., Mashonkina L.I., Ryabchikova T.A.* Influence of Departures from LTE on Oxygen Abundance Determination // https://arxiv.org/. 2013. arXiv:1302.1048.

SIMULATION OF Hα ABSORPTION FOR HOT JUPITER WASP-12B

S.S. Sharipov, I.B. Miroshnichenko, I.F. Shaikhislamov, M.S. Rumenskih
Institute of Laser Physics SB RAS, Novosibirsk, Russia, stas.sharipov@mail.ru

KEYWORDS:
Hot Jupiter, Monte Carlo, radiative transfer, multi-fluid model, Balmer alpha

INTRODUCTION:
In this work, we present the results of modeling the absorption in the Hα line by the atmosphere of hot Jupiter WASP-12b. For calculations and interpretation of observations, the Monte Carlo model of Lyα photon transfer in the planet's upper atmosphere was used [1]. Atmospheric parameters: temperature and hydrogen atom concentration distribution profiles were calculated on the basis of a self-consistent three-dimensional gas-dynamic model [2].

MODEL:
Modeling of radiation transfer in the atmosphere is carried out in the approximation of partially coherent isotropic scattering. The atmosphere of the planet is considered to be spherically symmetric. In the model, one of the main variable parameters is XUV — the flux of ionizing radiation with wavelengths $\lambda < 91.2$ nm at a distance of 1 AU, measured in units of $erg \cdot s^{-1} \cdot cm^{-2}$. Another important input parameter is the emission spectrum of the parent star. The solar radiation spectrum was used in the calculations. The Monte Carlo model makes it possible to reflect the contribution of Lyα photons produced in various processes: collisions, recombination, and stellar emission.

RESULTS:
For exoplanet WASP-12b, a high absorption in the Hα line of about 5 % was detected [3]. In the course of atmospheric simulations, when considering various XUV values, XUV = 60 $erg \cdot s^{-1} \cdot cm^{-2}$ proved to be the most suitable, which most closely matches the observed absorption spectrum. The resulting spectrum with contributions from various processes is shown in Figure 1. According to the results, the main absorption is associated with intense collisional processes in the atmosphere.

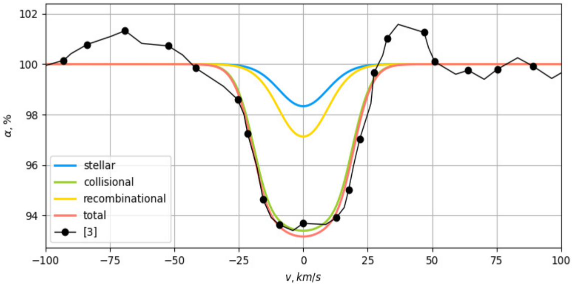

Fig. 1. Comparison of the calculated absorption spectrum with the observational spectrum for exoplanet WASP-12b

Acknowledgments:
This work was carried out as part of the Russian Science Foundation project no. 23-72-10060.

References:
[1] *Miroshnichenko I.B., Shaikhislamov I.F., Berezutskii A.G. et al.* Lyα Flux Impact from the Parent Star on Hα Absorption in the Atmospheres of the Hot Jupiters HD189733b and HD209458b // Astronomy Reports. 2021. V. 65. Iss. 1. P. 61–69. DOI: 10.1134/S1063772921010030.
[2] *Shaikhislamov I.F., Khodachenko M.L., Lammer* H. *et al.* 3D Aeronomy modeling of close-in exoplanets // Monthly Notices of the Royal Astronomical Society. 2018. V. 481. Iss. 4. P. 5315–5323. https://doi.org/10.1093/mnras/sty2652.
[3] *Jensen A.G., Cauley P.W., Redfield S. et al.* Hydrogen and Sodium Absorption in the Optical Transmission Spectrum of WASP-12b // The Astronomical J. 2018. V. 156. No. 4. 13 p. DOI 10.3847/1538-3881/aadca7.

3D AERONOMY OF THE HD 63433 SYSTEM PLANETS AND ABSORPTION IN L$y\alpha$ LINE

A.G. Berezutsky, I.F. Shaikhislamov, M.A. Efimov, M.S. Rumenskikh, M.L. Khodachenko, I.B. Miroshnichenko
Institute of Laser Physics of the SB RAS, Novosibirsk, Russia, 630090, a.berezuckiy@yandex.ru

KEYWORDS:
exoplanet, plasma, stellar wind, absorption, numerical simulations

We study the interaction of the upper atmospheres of planets in the HD 63433 system with the stellar wind on the scale of the entire stellar-planetary system, and also calculate the transit absorption in the HI (Lyα) line. The simulation is carried out using a 3D aeronomic code already used to simulate physical processes in the thermospheres of other exoplanets [1-3] interacting with the stellar wind of their parent stars. So far, numerical simulations of the HD 63433 system have been presented only in [4], where it was assumed that the planets HD 63433b and HD 63433c have fundamental differences: HD 63433c still retains its hydrogen-helium envelope, while HD 63433b probably lost its original atmosphere.

Applied 3D aeronomic modeling of the escaping upper atmospheres of both exoplanets interacting with stellar wind confirmed that they form extended molecular envelopes around the planets and strong outflows with an integral mass loss is $6.7/2.1 \cdot 10^{10}$ g/s which differs slightly from the results obtained in the [4]. A new feature of the considered HD 63433 b and HD 63433 c is that their atmospheric outflows reach significantly supersonic velocities and generate well-pronounced shock waves when they collide with pollutants.

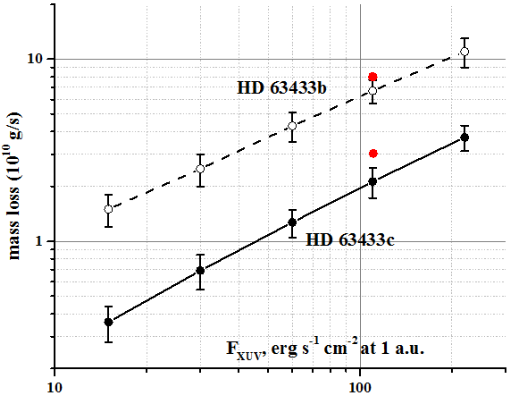

Fig. 1. The integral mass loss of HD 63433b (dashed lines) and HD 63433c (solid lines) as functions of the stellar XUV flux F_{XUV}. The red dots show data taken from [4]

For different values of the stellar XUV flux and the density of pollutants, the spectrally resolved absorption profiles Lya and the corresponding TLS were calculated. The Lya line remains a suitable tool for studying the interaction of planetary wind outflows with stellar wind. It is sensitive to the proton density of stellar wind, and under conditions close to moderate or strong solar wind, the expected extinction would be easily detected in the high velocity blue wing of the line, especially for HD 63433c.

The extinction level in the blue wing of Lya is also sensitive to the stellar XUV flux, and at F_{XUV} ~15 erg·cm^{-2}·s^{-1} per .u. becomes significant for HD 63433c. The dominant mechanism responsible for the absorption of Lya on both exoplanets is related to the resonant broadening of thermal lines. This is due to ENA generated by the charge exchange reaction in the shock layers around the planets, which allows them to be remotely sensed, as in the case of warm Neptunes GJ-436b and GJ-3470b.

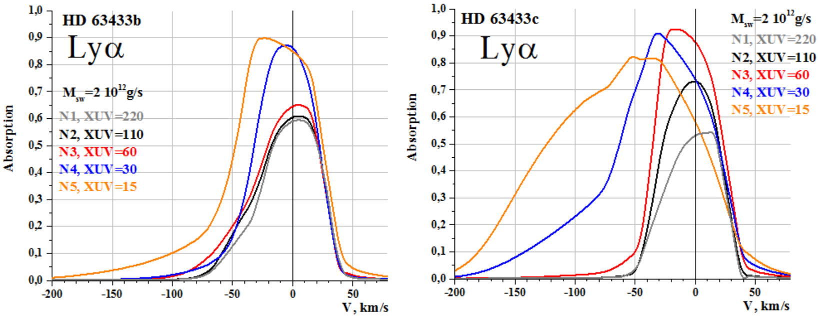

Fig. 2. The calculated Lyα absorption profiles for the transiting HD 63433b (*left*) and HD 63433c (*right*) in the Doppler velocity units, obtained in the simulation runs, with different F_{XUV} (erg·cm^{-2}·s^{-1}] values at 1 a.u., under the fiducial SW conditions

Acknowledgements:
This work was supported by the Russian Science Foundation, project no. 23-72-10060.

References:

[1] *Shaikhislamov I.F., Khodachenko M.L., Lammer* H. *et al.* Global 3D hydrodynamic modelling of absorption in Lyα and He 10830 A lines at transits of GJ3470b // Monthly Notices of the Royal Astronomical Society. 2021. V. 500. Iss. 1. P. 1404–1413. DOI: 10.1093/mnras/staa2367.
[2] *Shaikhislamov I.F., Khodachenko M.L., Lammer* H. et al. Three-dimensional modelling of absorption by various species for hot Jupiter HD 209458b // Monthly Notices of the Royal Astronomical Society. 2020. V. 491. Iss. 3. P. 3435–3447. DOI: 10.1093/mnras/stz3211.
[3] *Khodachenko M.L., Shaikhislamov I.F., Lammer* H. *et al.* Global 3D hydrodynamic modeling of in-transit Lyα absorption of GJ 436b // The Astrophysical J. 2019. V. 885. No. 1. Art. No. 67. 20 p. DOI: 10.3847/1538-4357/ab46a4.
[4] *Zhang M., Knutson H.A., Wang* L. *et al.* Detection of Ongoing Mass Loss from HD 63433c, a Young Mini-Neptune // The astronomical J. 2022. V. 163. No. 2. Art. No. 68. 24 p. DOI: 10.3847/1538-3881/ac3f3b.

PLANETARY MASS-RADIUS RELATION

A. Alizadehsabegh
University of Tabriz, Tabriz, Iran

KEYWORDS:
planetary systems, planets and satellite, fundamental parameters

Both mass and radius parameters for planets, which are the most important properties, are not accessible for most exoplanets. The mass can be calculated through spectroscopic studies, but ways like the transit method are needed to estimate the radius. In order to estimate the radius of the planets, a number of models, including those utilizing different methods, have been studied. It will be a review of recent studies on this relationship with a focus on studies that have used machine learning methods.

EPHEMERIS UPDATES FOR SEVEN SELECTED HATNET SURVEY TRANSITING EXOPLANETS

E. Jahangiri
BSN Project, Transiting Exoplanets Department, Tehran, Iran

KEYWORDS:
planetary systems, planets and satellites, gaseous

We refined the ephemeris of seven transiting exoplanets HAT-P-6b, HAT-P-12b, HAT-P-18b, HAT-P-22b, HAT-P-32b, HAT-P-33b, and HAT-P-52b. We observed 11 transits from eight observatories in different filters for HAT-P-6b and HAT-P-32b. Also, the Exoplanet Transit Database (ETD) observations for each of the seven exoplanets were analyzed, and the light curves of five systems were studied using Transiting light Exoplanet Survey Satellite (TESS) data. We used Exofast-v1 to simulate these ground- and space-based light curves and estimate mid-transit times. We obtained a total of 11, 175 and 67 mid-transit times for these seven exoplanets from our observations, ETD and TESS data, respectively, along with 155 mid-transit times from the literature. Then, we generated transit timing variation (TTV) diagrams for each using derived mid-transit times as well as those found in the literature. The systems' linear ephemeris was then refined and improved using the Markov Chain Monte Carlo (MCMC) method. All of the studied exoplanets, with the exception of the HAT-P-12b system, displayed an increasing trend in the orbital period in the TTV diagrams.

Conclusion:
We conducted a study on seven HATNet survey-selected transiting exoplanets and plotted the TTV diagrams. The goal of this study is to improve the planetary systems' reference ephemerides and to discuss the reasons for the period variations in these systems for future studies. We have presented a new ephemeris for each of the seven exoplanets. For this purpose, we utilised the mid-transit times found in the literature as well as the light curves observed by ETD, TESS, and our ground-based observations. We used 11 mid-transit times from our observations in this study, which were made at eight observatories from 2018 to 2022. Exofast-v1 was used to model the available light curves and extract the mid-transit times. We used the MCMC method to plot new TTV diagrams and refine exoplanets' ephemeris. The TTV diagrams show the orbital periods of exoplanets HAT-P-6b, HAT-P-18b, HAT-P-22b, HAT-P-32b, HAT-P-33b, and HAT-P-52b are increasing, whereas exoplanet HAT-P-12b has a declining tendency. It is probable that the six exoplanets' orbital periods increased since their ephemeris accuracy has become inaccurate over time. According to the new ephemeris for exoplanet HAT-P-6b, it seems that the uncertainties of t and P should be more carefully considered in future investigations and observations.

SESSION 6. ASTROBIOLOGY (AB) ORAL SESSION

CONCEPT OF THERMODYNAMIC INVERSION AS A MODEL OF THE ORIGIN OF LIFE ON PLANETS AND SATELLITES

V.N. Kompanichenko
Institute for Complex Analysis of Regional Problems RAS, Birobidzhan, Russia, kompanv@yandex.ru

KEYWORDS:
origin of life, planet, thermodynamics of systems, entropy, free energy, hydrothermal fluid, bacterial cell, anabiosis

Consideration of the problem of the origin of the biosphere on Earth (or another planet) implies the study of the transition from non-living organic systems to the simplest living cells. It is obvious that the transition between such different types of natural systems could not be carried out instantly, and required some kind of intermediate state, during which systems of the transition type had to combine both some features of non-living chemical systems and certain features of the simplest living systems — populations of microorganisms. Within the framework of the developed inversion concept of the origin of life (TI concept), such a transition is considered primarily from the point of view of the general thermodynamics of systems, through a change in the balance “total entropy contribution (S_c)/total free energy contribution (F_c)” from positive to negative (i.e. through a thermodynamic reversal, or inversion) [1]. According to this approach, the intermediate position of the prebiological system between the inanimate and living states was maintained in an oscillatory mode. Thermodynamically, this situation corresponds to the relative (albeit varying) equality of the entropy and free energy contributions in the system ($S_c \approx F_c$).

The general thermodynamics of the transition cannot give a definite answer to the question of chemical transformations in the system during the transition period and the stages of the origin of metabolism. The sequence of metabolism formation during the origin of life has not yet been reliably established by researchers. There are many conflicting views on this. However, in microbiology, within the framework of the theory of anabiosis, a resting (sleeping) bacterial cell occupies a similar intermediate position between non-living and living: on the one hand, it is no longer able to counteract the growth of entropy, and on the other hand, it retains structural memory of the previous living state. At the same time, the sequence of changes in metabolic processes in the simplest bacterial cell, entering the state of anabiosis and leaving it, has been well studied. The restoration of metabolism in an anabiotic cell proceeds in the following general direction: the appearance of weak respiration, an increase in membrane fluidity, an acceleration of the movement of lipids and membrane proteins → restoration of the structure of the protein-synthesizing apparatus of the cell → restoration of the genetic apparatus of the cell and the beginning of the growth cell cycle [2]. From the foregoing follows the idea of the potential correlation of these processes — prebiological and bacterial, the consideration of which is the subject of this report. It substantiates the general sequence of the formation of metabolism in the process of the emergence of life, based on the correlation of these two intermediate states between non-life and life. In both types of processes, the further development of metabolism from the initial intermediate state proceeded against the general background of an increase in the reserves of free energy in the system (through “stepwise activation”), contradictory tendencies towards heterogeneity and cooperation, and the prevalence of synthesis over destruction (or polymerization over hydrolysis). These analogies emphasize the legitimacy of the correlation.

According to the inversion concept, life originated in a pulsating updraft of hydrothermal fluid. In general, this process included the following steps. 1) Accumulation of dispersed organic matter at the prebiological stage of the Earth’s evolution through astrocatalysis and inflow from space, as well as synthesis and re-synthesis in geospheres under the influence of cosmic radiation, spark discharges and thermal energy. 2) Involvement of organic matter in the water cycle on the planet with subsequent self-assembly of three-dimensional prebiological microsystems of predominantly lipid-protein composition in the ascending hydrothermal fluid. 3) Formation of protocells: the transition of microsystems to an intermediate state between non-life and life through an active response to fluctuations in physico-chemical parameters in the environment (i.e. to periodic stress [3]), including the appearance in them of a weak energy-giving process of respiration for due to redox reactions and local watering of the membrane. 4) The formation of living subcells in the process of formation of a non-enzymatic antioxidant system and the emergence of a protein-synthesizing apparatus. 5) The formation of living cells (correlates with progenotes according to C. Woese [4]) with the emergence of the growth cycle of cells and the formation of the genetic apparatus.

Thus, the stages of the origin of life on Earth are conserved in the stages of the exit of a bacterial cell from anabiosis and are repeated each time during the anabiotic process. Since the TI concept is based on the fundamental concepts of thermodynamics — entropy, free energy and information - then in general terms it can also be applied to explain the origin of life on other cosmic bodies.

References:

[1] *Kompanichenko V.N.* Thermodynamic Inversion: Origin of Living Systems. Cham, Switzerland: Springer, 2017. 275 p.

[2] *Kompanichenko V., El-Registan G.* Advancement of the TI concept: defining the origin-of-life stages based on the succession of a bacterial cell exit from anabiosis // AIMS Geosciences. 2022. V. 8. Iss. 3. P. 398–437. DOI: 10.3934/geosci.2022023.

[3] *Kompanichenko V., Kotsyurbenko O.* Role of Stress in the Origin of Life // Life. 2022. V. 12. Iss. 11. Art. No. 1930. https://doi.org/10.3390/life12111930

[4] *Woese CR.* Bacterial evolution // Microbiology Reviews. 1987. V. 51. P. 221–270. DOI: 10.1128/mr.51.2.221-271.1987.

NON-THERMAL NITRIC OXIDE FORMATION IN POLAR REGIONS OF N_2-O_2 ATMOSPHERES

V.I. Shematovich[1], D.V. Bisikalo[1,2], G.N. Tsurikov[1]
[1] *Institute of Astronomy RAS, Moscow, Russia, shematov@inasan.ru*
[2] *National Center of Physics and Mathematics, Sarov, Russia*

KEYWORDS:
terrestrial planet, auroral event, kinetic modeling, nitric oxide as an atmospheric biomarker

INTRODUCTION:

The study of the origin of atmospheric nitrogen and its stability gives an idea of the uniqueness of the habitat on Earth. As it was pointed out in the recent paper [1], the detection of an N_2-O_2 atmosphere on an exoplanet orbiting in the habitable zone around a solar-type star could be a strong sign of the presence of a developed aerobic extraterrestrial biosphere. The idea of using NO as a potential biomarker is widely discussed (see, e.g., [1]), because its formation and loss processes strongly depend on the presence of molecular nitrogen and oxygen as the main components in terrestrial-type atmospheres. The possibility of observing nitric oxide on exoplanets was recently discussed [2], where it was indicated that under favorable conditions, nitric oxide can be detected in exoplanetary atmospheres using modern space missions such as the WSO-UV and ARIEL space telescopes. The NO radical is a direct indicator of the atmosphere dominated by N_2 and O_2, since its formation is a consequence of the presence of molecular nitrogen and oxygen as the main components in the atmosphere of the planet. To approach this problem it is necessary to use a set of kinetic Monte Carlo models which allow us to follow the evolution of the N_2–O_2 upper atmospheres of the sub-Neptune and exo-Earth families to estimate possible manifestations of life.

A numerical kinetic Monte Carlo model [3] was used to calculate the steady-state energy distribution functions of the suprathermal N(4S) atoms in the polar upper atmosphere formed due to the precipitation of high-energy auroral electrons into the N_2-O_2 atmospheres of the rocky planets in the solar and exosolar planetary systems. This model describes on a molecular level the collisions of the hot N(4S) atoms and atmospheric gas taking into account the stochastic nature of collisional scattering at suprathermal kinetic energies. It was found that the electron impact dissociation of N_2 is an important source of suprathermal N atoms [4] that increases significantly the non-thermal production of nitric oxide in the auroral regions. As it was estimated, when suprathermal nitrogen atoms are taken into account, the NO column density can potentially increase by a factor of 3, 7, and 32 at mean kinetic energies of E_0 = 1, 2, and 5 keV for precipitating electrons, respectively, compared with the case when hot N(4S) atoms are not supplied to the input (see Figure 1).

The consequences of the excess NO production during the auroral events in the polar atmosphere are twofold. First, it is necessary to keep in mind that auroral electron precipitation is a sporadic event in the Earth's polar atmosphere. Therefore, the calculated non-thermal NO production caused by the auroral electron precipitation is also a sporadic input into the odd nitrogen chemistry in the polar regions. Nevertheless, the disturbed solar activity conditions are widely and often observed and usually are accompanied by auroral electron precipitation in the polar lower thermosphere. Such events as was shown in this study could result in the significant increase in NO column density by the non-thermal source of nitric oxide. Second, the presented study of non-thermal NO production caused by the auroral electron precipitation results in the further understanding of the input of the hot fraction to the odd nitrogen chemistry in the N2-O2 atmospheres of terrestrial-type exoplanets. This problem is very important for estimating the possibility of the space observations of potential atmospheric biomarkers such as NO (for example, the γ-bands of this molecule, 205–248 nm) [1–2]. If terrestrial exoplanets located close-in to the host star are considered, then auroral electron precipitation can be much more powerful than on Earth, which, in turn, will increase non-thermal NO production and significantly improve the detection of nitric oxide in the atmospheres of these planets.. In addition, the lack of an exoplanet's own magnetic field and the presence of only an induced one can also be a reason for high electron fluxes and, as a result, a sufficiently high production of NO to detect this molecule. Therefore, we will continue our studies of the non-thermal NO production in the N_2-O_2 atmospheres of hot sub-Neptunes and exo-Earths orbiting in the potential habitable zones of their host stars. The developed kinetic Monte Carlo models [3–4] will be used to calculate the distribution of nitric oxide formed by both thermal and non-thermal sources in the upper atmosphere of the terrestrial-type exoplanet depending on the stellar activity and to assess the possibility of observing nitric oxide as a potential atmospheric biomarker.

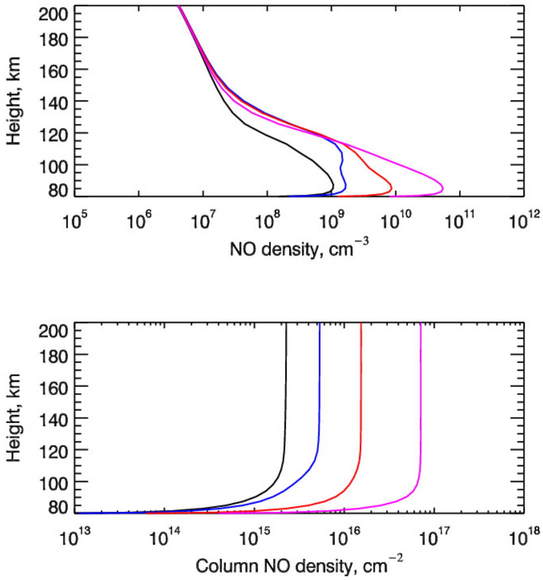

Fig. 1. (*top panel*) Height profiles of the NO number density calculated in the odd nitrogen chemistry model without (black line) and with taking into account the input of the suprathermal N(4S) atoms through the reaction Nh(4S) + O_2 → NO + O. Height profiles of NO number density were calculated for the considered Cases A (E_0 = 1 keV, blue lines), B (E_0 = 2 keV, red lines), and C (E_0 = 5 keV, magenta lines) of the auroral electron precipitation. (*bottom panel*) Height profiles of NO column densities calculated in the odd nitrogen chemistry model without (black line) and with taking into account the input of the suprathermal N(4S) atoms. The color palette is the same as at the top one.

Acknowledgements:
We acknowledge the financial support of the Russian Science Foundation, grant no. 22-12-00364.

References:

[1] *Sproß L., Scherf M., Shematovich V.I. et al.* Life is the Only Reason for the Existence of N_2-O_2-Dominated Atmospheres // Astronomy Reports. 2021. V. 65. Iss. *4.* P. 275–296. DOI: 10.1134/S1063772921040077.

[2] *Tsurikov G.N., Bisikalo D.V.* On the Possibility of Observing Nitric Oxide on Terrestrial Exoplanets Using the WSO-UV Observatory // Astronomy Reports. 2023. V. 67. Iss. 2. P. 125–143. DOI: 10.1134/S1063772923020087

[3] *Shematovich V., Bisikalo D., Tsurikov G.* Non-Thermal Nitric Oxide Formation in the Earth's Polar Atmosphere // Atmosphere. 2023. V. 14. Iss. *7.* P. 1092–1104. https://doi.org/10.3390/atmos14071092.

[4] *Bisikalo D., Shematovich V., Hubert B.* The Kinetic Monte Carlo Model of the Auroral Electron Precipitation into N_2-O_2 Planetary Atmospheres // Universe. 2022. V. 8. Iss. *8.* P. 437–446. https://doi.org/10.3390/universe8080437.

SEARCHING FOR EXTRATERRESTRIAL THERMOPHILES ON ICY MOONS WITH SUBGLACIAL OCEANS?

S. Bulat[1,2], A. Shvetsov[1], J-R. Petit[3]

[1] *Petersburg Nuclear Physics Institute named by B. P. Konstantinov of National Research Centre "Kurchatov Institute", Gatchina, Leningrad Region, Russia, bulatsergey28@gmail.com*

[2] *Institute of Physics and Technology, Ural Federal University, Ekaterinburg, Russia*

[3] *University Grenoble Alpes, CNRS, IRD, INP-G, IGE (UMR 5001), Grenoble, France*

KEYWORDS:
Subglacial Antarctic Lake Vostok, extremophiles, thermophiles, DNA contamination, Oxford Nanopore sequencing, Jovian Europa, Saturnian Enceladus

INTRODUCTION:
The objective was to search for microbial life in the subglacial Antarctic Lake Vostok by analyzing the natural accretion ice obtained by deep ice coring during the Russian campaign toward entering the lake. The ice samples to study originated from ice type I [1] and contained mineral inclusions, amongst which the biggest one cm-sized was present (dubbed "Bolshaya Kamina" — BK). The study aimed to re-evaluate previous microbial finds obtained with Sanger sequencing using the high throughput Oxford Nanopore sequencing technology.

Lake Vostok is a giant (270×70 km, 15 800 km^2 area), deep (up to 1.3 km) freshwater liquid body buried in a graben beneath a 4-km thick East Antarctic Ice Sheet with the temperature near ice melting point (around –2.5 °C) under 400 bar pressure. It is exceptionally oligotrophic and poor in chemical ions, under the high dissolved oxygen tension (320–1300 mg/L) range, with no light, and sealed from the surface biota about 15 Ma ago [1].

SANGER RESULTS:
The common Sanger sequencing technique previously discovered thermophiles in the subglacial Lake Vostok in analyzing bacterial 16S rRNA genes [2–4]. The ice samples included accretion ice segments at 3561 and 3607 m depth, containing sediment inclusions. As a result, in both samples, the facultative thermophilic chemolithoautotroph *Hydrogenophilus thermoluteolus* of *beta-Proteobacteria*, which originated from hot springs, was discovered. This finding suggested that a geothermal system exists beneath the cold-water body of Lake Vostok.

NANOPORE RESULTS:
To clarify the presence of thermophiles in Lake Vostok, the accretion ice segments from 3607 m (borehole 5G-1; the above-mentioned thermophile was detected here [2]), 3608 m (5G-1; 3608BK), 3607 m (5G-3 — 2 segments), and 3709 m (5G-3N) were retested by high throughput nanopore sequencing using the same genomic DNA and broader-in-cover degenerate primers for the v3-v4 region 16S rRNA genes. The nanopore controls (sham DNA isolation/negative PCR, nanopore reagents) were for the first time applied.

A dozen 1 Ma reads were obtained for all five samples' amplicons, but only one sample, 3608 BK, showed the thermophiles in records. For this sample of 1,643,669 reads analyzed, 1,445,557 (88 %) reads were classified. Numerous contaminants were discarded, and 279 (0.02 %) reads were assigned (88–96 % similarity) to moderate thermophile *Meiothermus hypogaeus* NBRC 106114 (*Deinococcus-Thermus*), isolated from a hot spring in Japan. In addition, 27 reads were recorded for thermophile *Meiothermus ruber*, originating from another hot spring, Kamchatka. No reads for this find were recorded in other ice samples and controls. This could mean that a new thermophile of *Deinococcus-Thermus* was discovered in the native accretion ice (naturally frozen water) of Lake Vostok. The *Hydrogenophilus thermoluteolus* remained not detected due to different primers in use.

CONCLUSION:

The high throughput Oxford Nanopore sequencing technology provides a very efficient tool to record/prove in detail the microbial content of the subglacial Antarctic water reservoirs. Newly discovered meio-thermophile might represent ingenious cell populations inhabiting faults offshore the subglacial Lake Vostok and could provide unforeseen prospects in searching for extra-terrestrial life on Jupiter and Saturn's icy moons.

References:

[1] *Bulat S., Petit J.-R.* Vostok, Subglacial Lake // Encyclopedia of Astrobiology // eds. Gargaud M. et al. Springer; Berlin; Heidelberg, 2022. P. 1–7. https://doi.org/10.1007/978-3-642-27833-4_1765-3.

[2] *Bulat S., Alekhina I.A., Blot M. et al.* DNA signature of thermophilic bacteria from the aged accretion ice of Lake Vostok, Antarctica: implications for searching for life in extreme icy environments // Intern. J. Astrobiology. 2004. V. 3. Iss. 1. P. 1–12. DOI: 10.1017/S1473550404001879.

[3] *Lavire C., Normand Ph., Alekhina* I. *et al.* Presence of *Hydrogenophilus thermoluteolus* DNA in accretion ice in the subglacial Lake Vostok, Antarctica, assessed using *rrs*, *cbb* and *hox* // Environmental Microbiology. 2006. V. 8. Iss. 12. P. 2106–2114. DOI: 10.1111/j.1462-2920.2006.01087.x.

[4] *Bulat S.* Microbiology of the subglacial Lake Vostok: first results of borehole-frozen lake water analysis and prospects for searching lake inhabitants // Philosophical Transactions of the Royal Society A. 2016. V. 374. Iss. 2059. Art. No. 20140292. https://doi.org/10.1098/rsta.2014.0292.

RESISTANCE OF BACTERIA BACILLUS LICHENIFORMIS OF "EXPOSE-R2" SPACE EXPERIMENT TO THE EXTREME SPACE FACTORS

A.A. Guridov, S.A. Kharin, S.V. Poddubko
Institute for Biomedical Problems RAS, Moscow, Russia, gaa1707@mail.ru

KEYWORDS:
ISS, Bacillus, spore-forming bacteria, astrobiology, planetary protection, panspermia, EXPOSE-R2, ultraviolet, radiation

INTRODUCTION:

The experience of long-term operation of orbital space complexes shows that the specifically changed environment of spacecraft allows us to consider habitable compartments as a kind of ecological niche for the development and functioning of a microbial community formed from organisms of various physiological and taxonomic groups, among which there are so-called technophiles — microorganisms that cause damage to materials different chemical composition, as well as potentially dangerous for humans types of opportunistic pathogens capable of growing on artificial substrates.

Important role in the formation of the above microbial community belongs to spore-forming bacteria of the genus *Bacillus* [1]. The ability of these bacteria to form endospores, resting forms resistant to various adverse factors, make *Bacillus* the dominant link or a kind of core of the microbial community of the internal environment of orbital space complexes. Viable bacteria have even been previously shown to occur on the outside of the ISS in dust samples collected from the surface of the station [2]. Spore-forming bacteria have a long history of use as model organisms for studying astrobiology, including the origin of life, evolution and survival in extreme environments, and interplanetary transfer of life via natural processes and human activities.

THE PURPOSE OF THE STUDY:

The purpose of this study is to determine the limits of resistance of bacteria *Bacillus licheniformis* to ultraviolet (UV) and radiation under the independent action of these factors on different strains of this bacterial species after exposure to open space conditions in the framework of the EXPOSE-R2 experiment. In the course of the EXPOSE-R2 experiment, dormant forms of microorganisms were exposed outside the International Space Station (ISS) inside metal trays under the influence of space radiation, as well as the full extraterrestrial spectrum of solar UV radiation of various intensities for samples of the upper layer of the trays (Figure 1). After a 15-month exposure, the microorganisms were transported to Earth for research. Among various biological objects, B*. licheniformis 24* was used in this experiment. The *Bacillus licheniformis 24* strain was previously isolated from the internal surfaces of the Russian Segment ISS.

In the EXPOSE-R2 experiment, 4 variants of different combinations of conditions for exposure to microorganisms were tested: Dark – Mars (*md*) – Martian atmosphere conditions with UV radiation screening; UV – Mars (*mu*) – conditions of the atmosphere of Mars under the influence of UV radiation; Dark –Space (*sd*) – conditions of outer space when shielding UV radiation; UV – Space (*su*) – conditions of outer space when exposed to UV. Similar combinations were reproduced in a control model study on Earth. Of all the strains studied in the Biodiversity experiment, *B. licheniformis 24* was the only survivor in all variants of the experiment, including terrestrial controls. The generations obtained from spores of the original *B. licheniformis 24* strain after isolation on a nutrient medium in the laboratory were considered new strains that had been adapted to the above exposure conditions on Earth and in space.

Fig. 1. External view of trays — equipment for exposing bacteria on the outside of the ISS

RESULTS:

To obtain the value of lethal doses of UV, the following radiation doses were chosen: 0,5; 1,0 and 1,2 kJ/m^2. According to the results obtained, some "space" strains of *B. licheniformis* were able to withstand exposure to high doses (1 kJ/m^2) of pulsed UV radiation. The strains that showed the highest resistance to outer space factors and were exposed to cosmic UV in the EXPOSE-R2 experiment later turned out to be less viable compared to the original *B. licheniformis 24* strain, i.e. partially lost resistance to short-wave UV. On the other hand, the strain of *B. licheniformis 24 sd* that survived in this experiment, which was not exposed to cosmic UV, turned out to be more viable than the original strain; acquired additional resistance to UV.

To obtain the value of lethal doses of radiation exposure of strains, the following doses of radiation doses of 5, 10, 15, 20 and 25 kGy were chosen. Some space strains of *B. licheniformis* were able to withstand exposure to high doses (20 kGy) of γ-radiation. The maximum lethal dose for endospores of *Bacillus* rarely exceeds 16 kGy [3]. The highest survival rate under radiation exposure was shown for spores exposed to space environmental factors, the least viable was the original *B. licheniformis 24* strain. It should be noted that two of the three strains most resistant to the maximum radiation dose of 20 kGy turned out to be *B. licheniformis* strains *24 sd* and *24 md*, these are strains that were in the dark layer of trays during the space experiment on the outer side of the ISS. It should be noted that two of the three strains most resistant to the maximum radiation dose of 20 kGy turned out to be *B. licheniformis* strains *24 sd* and *24 md*, these are strains that were in the dark layer of trays during the space experiment on the outer side of the ISS.

CONCLUSION:

A result that deserves great attention is, firstly, the viability of *B. licheniformis 24* spores after the EXPOSE-R2 space experiment. Secondly, higher rates of resistance of the *B. licheniformis 24 sd* strain to both ultraviolet and radiation in post-flight studies. Thus, this work demonstrates the ability of *B. licheniformis* to survive against key lethal factors for bacteria in outer space in the long term. The higher viability of spores that survived in open space is most likely associated with the activation of intracellular adaptive mechanisms. Apparently, this intrapopulation variability is able to persist for several generations.

Using the obtained results in relation to interplanetary flights of unmanned spacecraft, and first of all to the flight to Mars, the duration of which is approximately 300 days, we can draw a preliminary conclusion. Spore-forming bacteria of the genus *Bacillus*, located on such surfaces of the spacecraft, where there is a shadow zone from UV, with a high degree of probability will survive during such a flight, being on Mars already adapted to its extreme conditions.

These data clarify the astrobiological potential of these bacteria and are of importance when discussing the theory of panspermia — the idea that life can be distributed throughout the universe, from planet to planet; as well as invaluable practical importance in the field of microbiological monitoring and antimicrobial protection of the habitat of manned space complexes; as well as for developing the concept of planetary protection, based on the need to prevent the transfer of life forms, including the development of measures for the biological control of extraterrestrial substrates delivered to Earth and returned parts of spacecraft.

The work was carried out with the funding of the basic theme of the Russian Academy of Sciences no. 65.5.

References:

[1] *Pierson D.L.* Microbial contamination of spacecraft // Gravitational and Space Biology Bulletin. 2001. V. 14. Iss. 2. P. 1–6.
[2] *Deshevaya* E.A.*, Shubralova E.V., Fialkina S.V. et al.* Microbiological Investigation of the Space Dust Collected from the External Surfaces of the International Space Station // BioNanoScience. 2020. V. 10. No. 1. P. 81–88. DOI: 10.1007/s12668-019-00712-1.
[3] *Helfinstine S.L., Vargas-Aburto C., Uribe R.M. et al.* Inactivation of Bacillus endospores in envelopes by electron beam irradiation // Applied and Environmental Microbiology. 2005. V. 71. No. 11. P. 7029–7032. DOI: https://doi.org/10.1128/AEM.71.11.7029-7032.2005.

DEVELOPMENT OF BIOMINING TECHNOLOGY USING ASPERGILLUS NIGER: APPLICATION TO THE LUNAR PROGRAM

D.D. Barbashin[1,2], D.D. Mironov[2,3], A.E. Ivanova[1,4], V.S. Cheptsov[1,5]

[1] *Lomonosov Moscow State University, Soil Science Faculty, Moscow, Russia, fen.157@mail.ru*
[2] *Vernadsky Institute of Geochemistry and Analytical Chemistry RAS, Moscow, Russia*
[3] *Institute of Environmental Engineering, RUDN University, Moscow, Russia*
[4] *Severtsov Institute of Ecology and Evolution RAS, Moscow, Russia*
[5] *Space Research Institute RAS, Moscow, Russia*

KEYWORDS:
Moon base, lunar regolith, astrobiology, biomining, lunar program, biological leaching

INTRODUCTION:

In the coming decades, major national and private space agencies are planning manned missions to the Moon, and by 2050 it is planned to create a habitable base there [1]. However, there is still an important unsolved problem of cost-effective provision of the Lunar Base with resources.

Biological leaching using fungal cultures could potentially be one of the solutions to the problems of mining in the regolith when building a lunar base. The mechanism of fungal biological leaching consists in the formation of acids, which then convert metals from the crystal lattice of minerals into a soluble form [2]. Previously, the dissolution of solid particles under the action of acetic and salicylic acids was shown on a sample of lunar soil [3], while the measured concentrations of elements in solution after 81 days of the experiment in a vessel with lunar dust were higher than with terrestrial basalt of a similar granulometric composition. Therefore, biological leaching technologies using various fungal cultures can potentially be successfully applied on the Moon.

Compared to the traditionally used in industry bacterial leaching, biological leaching using fungal cultures has a number of advantages: reduced toxicity of the leach product due to the formation of complexes with organic acids, growth at high pH values, that is, no special conditions are required for the leaching of magmatic rocks (lunar regolith), a fast leaching process [2, 4–5]. Fungal biomining is suitable for mining using organic waste as a substrate [2], which can serve as a good way to dispose of waste on the Moon. *Aspergillus niger* is often used to leach waste and poor ores [2], so this species can potentially be used for biomining of lunar rocks and was chosen for our study.

MATERIALS AND METHODS:

To test the effectiveness of the proposed technology, experiments were carried out on the biological leaching of a chemical-mineralogical analogue of lunar regolith VI-LH1. The content of main oxides in the sample is presented in Table 1. According to X-ray diffraction analysis, the main minerals are plagioclase (labradorite, andesine), which accounts for 80 % (Table 2), biotite, and quartz. Pyroxene and ilmenite are also common, pyrrhotite, apatite, and chromite are represented as accessory minerals, olivine and magnetite are relatively rare, and hornblende is presumably also found.

An *Aspergillus niger* KBP.F-110 was used as a biological leaching agent. Strain KBP.F-110 was chosen due to its high production of organic acids. The synthesis of the following organic acids (mg/g of absolutely dry mass of mycelium) was demonstrated for the studied culture during culturing on a liquid Czapek medium: gluconic (694.0), lactic (186.2), succinic (59.3) [6].

Table 1. Chemical composition of VI-LH1 (chemical-mineralogical analogue of lunar regolith)

Oxide	Content, wt. %
LOI	1.06
Na_2O	4.25
MgO	0.83
Al_2O_3	23.74
SiO_2	52.69
P_2O_5	0.81
K_2O	1.20
CaO	10.20
TiO_2	0.49
MnO	0.06
FeO(t)	4.64
Sum	99.98

Biological leaching was carried out in sterile Petri dishes with 10 g of analog regolith calcined for 6 hours at 250 °C. For one-stage leaching, 5 ml of a spore suspension consisting of Czapek's medium with pH 6.5 and 10^6 per ml of *A. niger* spores was directly added to Petri dishes with analog until 120 % of the total moisture capacity was reached [7]. For two-stage leaching, 5 ml of the medium filtrate was added to Petri dishes after a week of cultivation of the *A. niger* strain [4]. The temperature was maintained in the range of 22-25 °C. Three samples for analysis were taken from the general pool at 7 and 14 days. Additionally, an experiment was carried out on the leaching of metals using solutions of organic acids in concentrations similar to those produced by the studied strain of *A. niger*.

The efficiency of leaching was analyzed by indirect methods (by analyzing the solid part): XRF and the elemental composition of minerals using SEM. Before analysis, the samples were calcined for 1 h at 250 °C. Then washed three times with 10 ml of distilled water, precipitating undissolved particles between washes by centrifugation at 3000 rpm.

RESULTS:

Comparison of the content of oxides Al, Ti, Fe(III), Mn, Mg in the labradorite sample measured using XRF did not show statistically significant differences between the control, one-stage and two-stage bioleaching. Measurement of the elemental composition of various minerals using SEM (Figure 1) also showed no statistical differences.

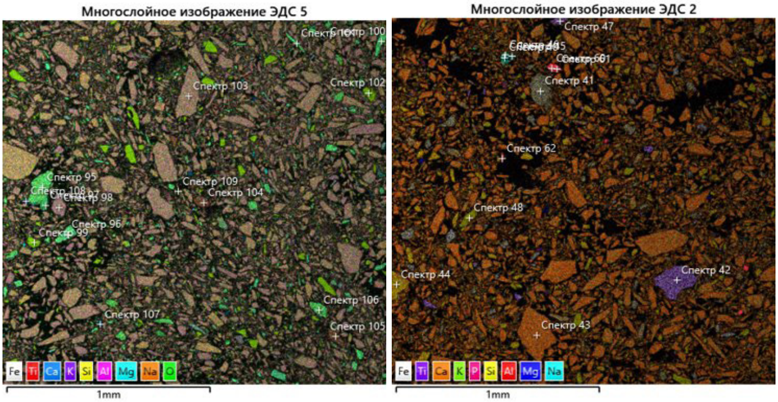

Fig. 1. Scanning electron microscopy results before (*left*) and after (*right*) the experiment. It is noted that such elements as titanium, magnesium, aluminum, and iron are practically not extracted at the current parameters of the experiment

Weak leaching may be due to the short duration of the experiment and incorrectly selected pulp density. To obtain the correct parameters for the operation of the technology, it is supposed to test experiments using different pulp densities and longer time intervals.

Also, we could get incorrect results due to indirect analysis (by the difference in the content of elements in the solid part between control and experimental samples). To obtain more accurate results, it is necessary to use methods of direct analysis of the resulting solutions.

References:

[1] *Marov M.Y., Slyuta E.N.* Early steps toward the lunar base deployment: Some prospects // Acta Astronautica. 2021. V. 181. P. 28–39. https://doi.org/10.1016/j.actaastro.2021.01.002.

[2] *Dusengemungu L., Kasali* G., *Gwanama* C. *et al.* Overview of fungal bioleaching of metals // Environmental Advances. 2021. V. 5. Art. No. 100083. https://doi.org/10.1016/j.envadv.2021.A100083.

[3] *Keller W.D., Huang W.H.* Response of Apollo-12 lunar dust to reagents simulative of those in the weathering environment of Earth // Proc. Lunar Science Conference. 1971. V. 2. P. 973.

[4] *Karavaiko G.N., Rossi J., Agate A., Grudev S., Avakyan Z.A.* Biotechnologies of metals: a practical guide / Center for Intern. Projects of the State Committee for Science and Technology. M., 1989. 374 p.

[5] *Anjum F., Bhatti H.N., Ghauri M.A. et al.* Bioleaching of copper, cobalt and zinc from black shale by Penicillium notatum // African J. Biotechnology. 2009. V. 8. No. 19. DOI:10.4314/AJB.V8I19.65211.

[6] *Smirnov V.F., Smirnova O.N., Anikina N.A. et al.* Deistvie biotsidov na soderzhanie organicheskikh kislot u gribov-destruktorov tekhnicheskikh izdelii, ekspluatiruemykh v usloviyakh tropicheskogo klimata (V'etnam) (The effect of biocides on the content of organic acids in fungi-destructors of technical products operated in a tropical climate (Vietnam)) // Corrosion: materials, protection. 2020. Iss. 6. P. 39–48. DOI: 10.31044/1813-7016-2020-0-6-39-48 (in Russian).

[7] *Bespalova A.Yu., Marfenina O. E., Motuzova G.V.* Communities of microscopic fungi in background and contaminated alpha-humus podzols and their impact on copper mobility // Eurasian Soil Science. 2006. V. 39. No. 2. P. 228–236.

PLANETARY PROTECTION OF MARS IN MISSIONS FOR SEARCHING POSSIBLE LIFE FORMS

E.A. Deshevaya[1], N.M. Khamidullina[2], S.V. Fialkina[1], D.V. Zakharenko, S.N. Ustinov[2], O.I. Orlov[1], V.N. Sychev[1]
[1] *Institute of Biomedical Problems RAS, Moscow, Russia*
[2] *Lavochkin Association, Khimki, Moscow Region, Russia*

KEYWORDS:
planetary protection, bacterial spores, bioburden, clean room, sterilization and decontamination procedures

INTRODUCTION:

The concept of planetary protection (PP) was first set forth in a statement of the 19th General assembly of the Committee on Space Research (COSPAR) in 1964 and then embodied in mission classification and PP principles. PP is applied without fail to the missions with landing on planets to exclude harm to or transformations of life forms that may exist there.

Risks of technical panspermia (transfer of living organisms/bio-structures from one planet to another) in missions of automatic spacecrafts (AS) are assessed using the quantitative probabilistic approach that sets the upper limit of microbial contamination of the descending module containing the instruments for life search (mission IVb according to the COSPAR classification). Surface density of contamination must not exceed 300 bacterial spores/m^2 and bio-instruments must be sterile. Total surface bioload prior to launch must not exceed 3105 bacterial spores.

The report discusses as the COSPAR, so original methods and practices proposed by the authors to comply with the PP requirements at every stage of spacecraft assembly and testing. Cleanness test was performed by a procedure described in this paper.

The prerequisites for successful PP are [1–2]:

- development and application of compatible sterilization and decontamination procedures (radiation, thermal and gas sterilization, pulsed UV combined with alcohol wiping)
- assembly in a clean room with the use of chemical and physical decontamination procedures
- sterile clothing, observance of work rules
- regular microbiological sampling of spacecraft components and instruments, and clean room surfaces
- prevention of recontamination on the stages of spacecraft assembly and testing.

As a result of PP requirements implementation, the reserve of the number of bacterial spores on the eve of the prelaunch campaign made up no more than 83% of admissible level.

References:

[1] *Deshevaya E.A., Khamidullina N.M., Chasovskikh A.V., Kharin S.A.,Novikova N.D., Sychev V.N.* Possibilities of radiation sterilization during the Exomars mission // Aviation, Space, and Environmental Medicine. 2016. V. 54. No. 5. P. 65–72.

[2] *Deshevaya E.A., Fialkina S.V., Guridov A.A., Shashkovsky S.G., Kireev S.G., Khamidullina N.M., Zakharenko D.V.* Application of pulsed UV technologies to ensure microbiological purity in the preparation of missions requiring planetary protection // Aviation, Space, and Environmental Medicine. 2023. V. 57. No. 1. P. 67–74.

SURVIVAL OF MICROORGANISMS OVER TWO YEARS OF EXPOSURE IN THE NEAR-ISS SPACE

E.A. Deshevaya[1], S.V. Fialkina[1], E.V. Shubralova[2], L.M. Vasiliak[3], V.Ya. Pecherkin[3], V.A. Scherbakova[4], A.M. Nosovsky[1], O.I. Orlov[1]

[1] *State Scientific Center of the Russian Federation — Institute of Biomedical Problems RAS, Moscow, Russia, deshevaya@imbp.ru*
[2] *Central Research Institute of Machine Construction, Korolev, Mosow Region*
[3] *Joint Institute of High Temperatures RAS, Moscow, Russia*
[4] *Skryabin Institute of Biochemistry and Physiology of Microorganisms RAS, Pushchino, Moscow Region*

KEYWORDS:
space experiment Test, impact of cosmic factors, bacterial spores, *Aurobasidium pullulans*, international space station (ISS)

INTRODUCTION:
One of the purposes of space experiment Test was to detect microorganisms or bio-structures in the aggressive medium surrounding the International space station. Biological investigations were divided into two parts:

- the first part consisted of collecting and delivery to the ground-based laboratory samples from the ISS outer surfaces for studying the composition of DNAs of bio-structures and looking for viable microorganisms. Space dust gathered from the ISS modules contained DNAs of bacteria, archaea and fungi. Microbial DNAs were found in 75 % dust samples collected in sterile devices; 50 % of the samples had viable units of bacterial and fungal spores [1].
- the second part consisted of testing viability of microorganisms. The idea was to find out how long microorganisms belonging of different taxonomic groups would survive exposure to the variety of open space factors. Cultures of bacteria, archaea and fungi were challenged by fast vacuum and UV-radiation over a one-year period. As a result of data analysis, bacteria *Bacillus velezensis* (group *Bacillus subtilus*), fungus *Aureobasidium pullulan*, and *Methanosarcina mazei S-6t* and were chosen for integration in devices Test-Exponat [2]. The devices had been attached to Russian modules Pirs and Poisk differing in illumination level and orientation over time periods of one and two years since 2017.

The experiment showed that all the microorganisms inoculated on cotton swabs survived the two-year of exposure to the physical space factors without protection.

Non-spore forming Archaea demonstrated that in open space microorganisms can transform into a specific dormant state with formation of cyst-like cells with a multilayer thickened membrane [3].

Specific population variability in 30 % Aureobasidium pullulans subcultures, that had never been reported earlier, manifested itself by enhanced resistance to radiation following two-year space exposure.

In summary, the investigations showed that microorganisms could survive on cotton surfaces protecting from UV given a more steady and, probably, low temperature and vacuum transforming in a specific state of space dehydration/ partial lyophilization or auto-conservation.

References:

[1] *Tsygankov O.S., Grebennikova T.V., Deshevaya E.A., Morozova* M.A.*, Novikova N.D., Polikarpov N.A., Syroeshkin A.V., Shubralova E.V., Shuvalov V.A.* Issledovaniya melkodispersnoi sredy na vneshnei poverkhnosti mezhdunarodnoi kosmicheskoi stantsii v eksperimente “Test”: obnaruzheny zhiznesposobnye mikrobiologicheskie ob”ekty (Study of the environment finely dispersed on the outer surface of the international space station and detection of microbiological objects in space experiment “Test”) // Kosmicheskaya tekhnika i tekhnologii. 2015. V. 8. No. 1. P. 31–41 (in Russian).

[2] *Deshevaya E.A., Pecherkin V.Ya, Vasiliak L.M. et al.* Vyzhivanie mikroorganizmov na testovykh ob”ektakh pri vakuumirovanii (Survival of microorganisms on test objects during vacuumization) // Aviakosmich. i ekolog.med. 2018. V. 52. No. 2. P. 54–59. DOI: 10.21687/0233-528X-2018-52-2-54-59/ (in Russian).
[3] *Oshurkova V.I., Deshevaya E.A., Suzina N.E., Shubralova E.V., Shcherbakova V.A.* Methanogenic archaea in space // Aviation, Space, and Environmental Medicine. 2021. V. 55. No. 1. P. 63–69.

EXOBIOLOGICAL STUDIES IN THE INTERESTS OF ENSURING PLANETARY QUARANTINE

V.K. Ilyin, S.V. Poddubko
Institute of Biomedical Problems RAS, Moscow, Russia, ms2023@cosmos.ru

KEYWORDS:
exobiology, planetary quarantine, microbiology

One of the main goals of space exploration is to study the evolutionary development of celestial bodies - planets and their satellites, comets, etc., in order to answer a number of important natural and scientific questions: what are the laws of the formation and development of planets, how did life arise in the Universe and whether it exists outside the Earth, whether there are prerequisites for its emergence and development on other celestial bodies, etc. Paradoxically, the very development of astronautics can jeopardize this entire expensive research program due to possible irreversible changes in the natural evolutionary development of celestial bodies, if a number of measures are not provided to prevent space pollution by terrestrial life forms. No less, but, from the point of view of the inhabitants of the Earth, a much more serious danger is the quite probable possibility of contamination of the Earth by extraterrestrial or transformed under the conditions of other planets or outer space by terrestrial pathogenic microorganisms brought by returning spacecraft from another planet or from outer space. In this regard, it is extremely important to understand whether terrestrial microorganisms, which inevitably contaminate space technology, are capable of maintaining their viability in outer space for a long time and what changes occur to them under these conditions. Obtaining such data is not only of natural scientific interest, but also of invaluable practical importance for the development of a planetary protection concept based on the need to prevent the transfer of life forms, including the development of measures for the strictest biological control and assessment of the potential pathogenicity of extraterrestrial substrates delivered to Earth and returned parts of space devices. The most important direction of research is to ensure planetary quarantine or, if we formulate this concept more broadly, taking into account the above, planetary protection. The presence of sustainable life forms can cause unauthorized anthropogenic spread of terrestrial organisms to other celestial bodies and, conversely, infection of the Earth with alien forms.

Currently, within the framework of the Russian scientific program, space research is being carried out with resting forms of organisms belonging to various taxonomic groups. These are experiments on the ISS RS, ongoing, completed and promising. The “Plasmid” experiment, dedicated to the study of the features of the horizontal transfer of factors of the genetic heredity of bacteria, belongs to the completed ones. The ongoing experiments include the Test experiment, conducted jointly with TsNIIMASH, dedicated to the study of the outer surface of the ISS for the presence of biological objects and biogenic substances, as well as the Bioisk experiment, dedicated to the study of the properties of pro- and eukaryotes under exposure conditions in outer space. A significant group of studies is made up of experiments on unmanned spacecraft of the Bion-M series. They provide for the possibility of exposure of bio-objects in outer space on the scientific equipment “Exobiofrost” and “Meteorite“, including in the conditions of passage through the dense layers of the atmosphere.

The results obtained indirectly confirm the influence of space flight conditions on the mechanisms of protection of biological forms from the impact of damaging factors inherent in outer space. Since space flight conditions include a large number of different physicochemical factors, some of which cannot be fully reproduced in laboratory conditions on Earth, it becomes very difficult to identify specific ways and mechanisms for changing physiological, biochemical processes, even, at first glance, in the most simple laboratory organism - a bacterial cell. However, the results obtained relate to such a relevant topic in space research as the coexistence of microorganisms and humans in a closed environment (especially in relation to long-term manned flights in the exploration of other space bodies), and, therefore, deserve close attention in further research.

IRRADIATION OF METHYL CYANIDE (CH_3CN) WITH 200 keV AT 15 K TEMPERATURE

S. Jheeta
NoRCEL — Network of Researchers on the Chemical Emergence of Life, Leeds, United Kingdom, sohan@sohanjheeta.com

KEYWORDS:

Methyl cyanide is the simplest organic nitrile (although the hydrogen cyanide, HCN, being the simplest nitrile; however, its cyanide anion is not classed as organic, ergo is not considered as nitrile) and is widely present in the dark molecular clouds and celestial bodies as shown in the bullet points below:

- Identified in 1971 in molecular clouds: Sagittarius Sgr A and Sgr B [1].
- As of 2006 there are no less than 83 molecular clouds in which methyl cyanide has been discovered [2].
- Also, it is detected in comet Kohoutek [3].
- Interest for astrobiology as it is the simplest of organic nitriles.
- Important in the formation of ring compounds — eg thiamine.

We have irradiated methyl Cyanide with 200 keV of protons (H+) at 15 K temperature and so we report here breakdown products. These products may have been relevant during the chemical evolution of life on this planet.

References:

[1] *Solomon P.M., Jefferts K.B., Penzias A.A., Wilson R.W.* Detection of Millimeter Emission Lines from Interstellar Methyl Cyanide // Astrophysical J. 1971. V. 168. Iss. 3. P. L107–L10. DOI: 10.1086/180794.

[2] *Purcell C.R., Balasubramanyam R., M.G. Burton et al.* A CH^3CN and HCO^+ survey towards southern methanol masers associated with star formation // Monthly Notices of the Royal Astronomical Society. 2006. V. 367. Iss. 2. P. 553–576. https://doi.org/10.1111/j.1365-2966.2005.09921.x.

[3] Ulich B.L., E.K. Conklin Detection of Methyl Cyanide in Comet-Kohoutek // Nature. 1974. V. 248. Iss. 5444. P. 121–122. DOI: 10.1038/248121a0.

MAIN DIRECTIONS AND PROSPECTS FOR THE DEVELOPMENT OF ASTROBIOLOGY IN RUSSIA

O.R. Kotsyurbenko
Yugra State University, Khanty-Mansiysk, Khanty-Mansiysk, Russia, kotsor@mail.ru
Network of Researchers on the Chemical Evolution of Life, Leeds, United Kingdom

Keywords:
astrobiology, Puschchino, Dubna, IKI, Roscosmos

Astrobiology is the fundamental discipline of a wide range of scientific knowledge. One of the main features of astrobiology is the deep integration of various, primarily natural science disciplines such as biology, chemistry, physics, mathematics, as well as philosophy and culture.

In the modern scientific world, astrobiology becomes more significant in the educational space and more attractive for young ambitious scientists as a direction of their professional activities and career. On the basis of the principle of integration of education and science in the USA and the European Union, associations and institutional structures have already been created that are actively working towards the development of astrobiology. Training courses in astrobiology are held in various higher educational institutions. Finally, astrobiology is rapidly entering the media space and begins to actively influence society, generating interest in the further exploration of outer space and expanding the general scientific horizons.

The examples are the NASA Astrobiology Institute — NAI (1998), the European Astrobiology Institute — EAI (2019) and the European Astrobiology Network Association EANA (2001). Within the framework of the above entities, working groups of astrobiologists of various directions are created, scientific and educational programs including the organization of expeditions, workshops and summer schools are planned. Astrobiologists are actively involved in preparing scientific proposals that compete with projects from other scientific fields for funding. The most important tool for the integration of astrobiologists is regular meetings within the framework of international and national conferences and meetings, where the results of research and development prospects are discussed.

Astrobiology in Russia is currently also going through a stage of gradual integration with closer interaction between scientific groups and coordination of research. Modern Russian astrobiology is developing in various directions. Russian scientists participate in national and international projects that provide for astrobiology research.

In Russia, the organization of astrobiology seminars and conferences is carried out mainly by four entities: Institute of Physicochemical and Biological Problems of Soil Science of the Russian Academy of Sciences in Pushchino - all-Russian conferences on astrobiology, the Institute for Space Research RAS in Moscow (IKI RAS) — annual conferences on research Solar System with a section of astrobiology, the Joint Institute for Nuclear Research (JINR) in Dubna — conferences on astrobiology and space radiobiology and Roscosmos together with some other institutions — the annual international conference on space biology and aerospace medicine.

Each conference has its own specificity in relation to its attendees. A combined analysis of all astrobiology research presented at conferences shows that the main objects of study related to astrobiology are moderately and extremely cold ecosystems due to peculiarities of the geographical location of the country, most territories of which are in a cold climate including vast expanses of permafrost.

A quite large segment of astrobiology priority areas is associated with astronomical research and experiments on board orbital space stations, which reflects Russia's position as one of the leading space nations.

Finally, a significant part of theoretical and experimental research is related to various aspects of the problem of the origin of life, traditionally attractive issue initiated by the Russian scientist Oparin.

An important condition for the sustainable development of any scientific direction in the modern world is the interconnection of its components such as research activities, education and practice applications. With regard to astrobiology, the most important component for its development is education. At the moment, there are already conditions for the introduction of astrobiology courses into the curricula of universities for the preparation of specialists at the master's level, the need for which is gradually but steadily growing.

A more difficult aspect is the innovative developments that could enable astrobiologists to gain significant financial independence, since the main subject of study in astrobiology provided by the government. However, the possibility of combining the fundamental and practical research can be promising. The instrumental base of astrobiologists including all innovative developments for the study and detection of biological objects outside the earth, can be successfully applied to terrestrial ecosystems, for example, in such areas as ecology or medicine.

Finally, it is extremely important to use electronic resources for the effective exchange of scientific information, messages about job vacancies in the field of astrobiology research, organization of joint projects, holding online conferences and discussing all relevant issues, as well as to participate in various international communities and associations related to astrobiology. NoRCEL is an example of a network where the above activities can be effectively realized.

Finding a common language between scientists of different directions, united within the framework of astrobiology, often having a different type of scientific thinking and using different methodological approaches to obtaining results, is a powerful tool for fruitful cooperation and obtaining new knowledge.

ASTROPHYSICAL SOURCES OF RADIATION AND HABITABILITY IN THE UNIVERSE

X.C. Abrevaya[1,2,8,9], P. Odert[3], M. Leitzinger[3], O.J. Oppezzo[4], E. Guenther[5], M. Patel[6], G.J.M. Luna[7], A.Hanslmeier[3]

[1] *Instituto de Astronomía y Física del Espacio, UBA-CONICET, Argentina, abrevaya@iafe.uba.ar*
[2] *Facultad de Ciencias Exactas y Naturales, UBA, Argentina*
[3] *Institute of Physics, University of Graz, Austria*
[4] *Comisión Nacional de Energía Atómica, Argentina*
[5] *Thüringer Landessternwarte Tautenburg, Karl-Schwarzschild Observatorium, Germany*
[6] *Faculty of Science, Technology, Engineering and Mathematics, The Open University, UK*
[7] *Universidad Nacional de Hurlingham — CONICET, Argentina*
[8] *Argentinian Research Unit in Astrobiology (Astrobio.ar), Argentina*
[9] *Invited scientist, Institute of Physics, University of Graz, Austria*

KEYWORDS:
astrobiology, life, microorganisms, laboratory experiments, interdisciplinary research, planets

INTRODUCTION:
Astrobiology is dedicated to the exploration of the universe to unveil the possibility of finding life outside the Earth. The development of different technical advancements allows us to do this search with more detail and characterize different regions of our galaxy and planets to determine their potential to host life (i.e.: galactic habitability and planetary habitability). In this context, astrophysical sources of radiation (e.g.: stellar radiation) are one of the fundamental factors to be studied, as radiation can have an impact on different scales in the universe being beneficial or detrimental to life through direct or indirect effects. In this talk, we will present a brief review of the current knowledge on the topic of the influence of astrophysical sources of radiation on life. In addition to it, we are going to focus on some particular cases of experiments under laboratory conditions to simulate extraterrestrial radiation environments which are used to investigate the biological impact of stellar radiation, particularly from very energetic events such as flares and superflares. These laboratory simulation experiments are useful as an approximation to obtain some answers about the effects of radiation at planetary scales.

LIFE IN THE UNIVERSE: EXTRATERRESTRIAL WATER, CYANOBACTERIA AND DIATOMS

R.B. Hoover[1], A.Yu. Rozanov[2]

[1] *NASA-Emeritus, U.S. Space and Rocket Center, Alabama, USA, RichardBHoover@Icloud.com*

[2] *Joint Institute for Nuclear Research, Astrobiology Sector, Dubna, Moscow Region, Russia*

KEYWORDS:
life, biomolecules, diatoms, cyanobacteria, comets, meteorites, microfossils, JWST

INTRODUCTION:

Does life exist only on Earth or is it widely distributed throughout the Universe? This is the fundamental question of Astrobiology. Scientific discoveries have recently provided data that challenges the long accepted hypothesis that biology is restricted to planet Earth. All known forms of life have an absolute requirement for the co-existence of water, an energy source and only 20 of the 118 chemical elements. Hydrogen is the most abundant element and water (H_2O) is the most abundant chemical compound in the Universe. Water comprises ~70 % of the mass of every living cell. In 1954, the late Sir Fred Hoyle [1] predicted the formation of a spinless resonant state of Carbon-12 with excitation energy of 7.65 MeV by the triple-alpha process in superhot helium-burning red giant stars. The *Hoyle State* was confirmed by experimental observations [2] and explains the formation in hot stars of stable Carbon (^{12}C), Oxygen (^{16}O), Nitrogen (^{14}N) and Silicon (^{28}Si) atoms. Life-critical CHON particles, silicates and heavy elements are sent into space by supernova explosions to form interstellar dust. The JWST used the Einstein Ring phenomenon to detect large organic Polycyclic Aromatic Hydrocarbons (PAH) on dust in the galaxy (SPT0418-47) over 12 billion light years from Earth [3]. The elements C, H, O, N comprise over 98 % of all living cells and the empirical composition (normalized to nitrogen) of the dry weight of bacterial cells [4] is closely approximated by the relation $C_4H_7O_2N_1$. Most of the biology of Earth inhabits thin films of water in cracks within deep, hot crustal rocks and obtain energy from serpentinization processes or lithotrophic metabolism of Hydrogen released by the decay of the long-lived radiogenic elements. Because of the biogeochemical carbon, oxygen, nitrogen cycles, the C/O and C/N ratios increases over geological time periods after cell death providing a mechanism for distinguishing indigenous ancient microfossils from modern terrestrial biological contaminants [5].

Hoover et al. [6] showed that the infrared properties of the organic silica polymer (Fig. 1*a***)** of diatom shells exhibited a close correspondence to that of the observed infrared spectrum of interstellar dust toward the hot supergiant infrared source GC-IRS 7 in the galactic center (Fig. 1*b*) and the Trapezium nebula (Fig. 1*c*) was very different from inorganic silicates (Fig. 1*d*). These results suggest the existence of a cosmic microbiological system in which microorganisms with polymeric silica shells similar to diatoms may exist in interstellar dust, comets and icy moons.

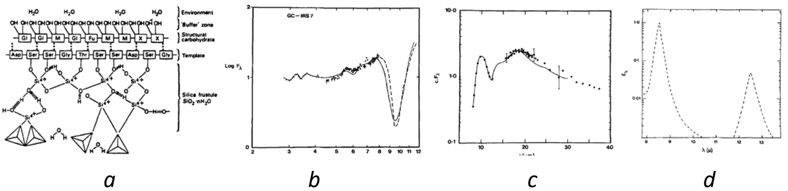

a *b* *c* *d*

Fig. 1. Measured IR spectra of the **a.** organic silica shells of diatoms (solid line) as compared with the IR data (dots) of interstellar dust toward **b.** the hot supergiant GC-IRS 7 and **c.** the Trapezium nebula lacks sharp peaks at 8.7 and 12.7 microns **d.** exhibited by inorganic silicates suggest existence of a cosmic microbiological system

The PUMA mass spectrometer on board VEGA-1 detected a diversity of organics (including nucleobases adenine and xanthine) in Halley comet dust [7]. Simonia and Cruickshank [9] found previously unidentified lines in the spectra of several comets that match the spectra of large, complex biomolecules (e.g., chlorophyll, luciferin, luciferase and green fluorescent protein) essential for photosynthesis and bioluminescence that represent definitive signatures of life. It is now known that the vast majority of living prokaryotic organisms inhabit crustal rocks of the deep hot biosphere as proposed by Gold [9]. Carbonaceous meteorites have been found to contain a vast array of biomolecules, including the biogeochemical breakdown products of chlorophyll (pristine, phytane); proteinogenic amino acids (some with significant *L*-excess); nucleobases and ribose with ($\delta^{13}C_{vs.\ VPDB}$) values proving they are indigenous and extraterrestrial [10–12]. These meteorites contain a subset of only 12 of the 20 life-critical amino acids and 4 of the 5 nucleobases. The missing life-critical biomolecules prove that the meteorites are not contaminated with modern terrestrial microorganisms [13]. The biomolecules in comets and indigenous microfossils in meteorites invalidate paradigms of the endogenous origin of life on Earth and the requirement of surface liquid water oceans for biology.

MATERIALS:

Murchison CM2 #E4806; Dr. William Birch, Museum Victoria, Melbourne

Orgueil CI1 Org #9418; Dr. Edmée Ladier, Musée Victor Brun, Montauban

INSTRUMENTS AND METHODS:

At NASA/MSFC the FEI Quanta 600 FESEM and TESCAN MAIA3 Triglev Field Emission Microscopes produced images, EDS spot data and 2D x-ray maps of element compositions of diverse microstructures found in freshly fractured uncoated surfaces of the meteorites. At PIN(RAS) and JINR, the meteorite samples were gold coated prior to study with the thermal emission TESCAN VEGA-3 SEM. A propane torch was used to flame sterilize all tools, trays, SEM stubs and tweezers for mounting the meteorite fragments.

RESULTS:

In 1996, Scanning Electron Microscopy studies at NASA/MSFC in the United States and at the Borissiak Paleontological Institute (RAS) in Russia resulted in the independent discovery of recognizable fossils of cyanobacteria embedded in freshly fractured interior surfaces of the Murchison CM2 meteorite [14–15]. Subsequent investigations have revealed a great diversity of cyanobacteria, diatoms [16]. EDS data on C/O and C/N ratios show the forms in the volume *The Orgueil Meteorite* (*Atlas of Microfossils*) [17] are ancient and indigenous rather than modern terrestrial biocontaminants. Figure 2 provides examples of cyanobacteria and diatoms embedded in **a.** the Murchison CM2 and **b.** and **c**. the Orgueil CI1 carbonaceous meteorite.

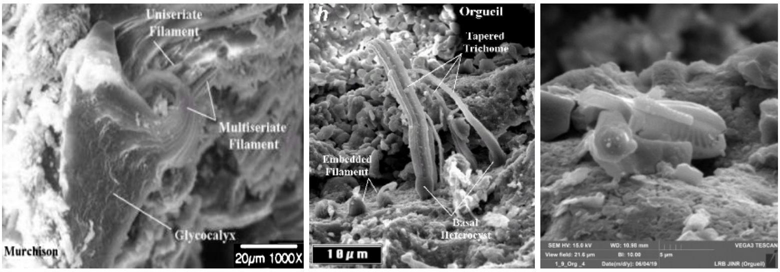

Fig. 2. a. Filaments of cyanobacteria (~*Microcoleus* sp., *Phormidium* sp. and *Nostoc* sp.) in Murchison; **b.** embedded filaments (~*Calothrix* sp) and **c.** partial pennate diatom in the Orgueil CI1 meteorite

CONCLUSIONS:

Life is abundant on planet Earth wherever water coexists with a small group (~20) of life-critical bogenic elements and a source of energy. Most of the biology of Earth inhabits thin films of water in cracks within deep, hot crustal rocks. In the dark regimes of cold deep oceans and polar ice caps or deep hydrothermal vents or hot crustal rocks, diatoms and cyanobacteria do not rely on the usual machinery of photosynthesis. Instead thay alter Photosystem II to consume methane or other organics. Hydrogenase enzymes allow lithotrophic metabolism of hydrogen from decay of neutrons released by long-lived radiogenic^{40}K, $^{23\ 8}$U, and ^{232}Th which could maintain oceans in liquid state the frozen crusts of comets, icy moons or rogue planets. Complex biomolecules have been found in the spectra of comets and in returned samples from asteroid Ryugu and microfossils are embedded in carbonaceous meteorites that are probably the remains of comets. The close agreement of the IR spectra of interstellar dust with bacteria and the organic silica of diatom shells; the detection of PAHS in distant galaxies; the presence of amino acids (some with significant *L*-excess) in Ryugu samples and meteorites and the detection of recognizable indigenous microfossils of diatoms and cyanobacteria in the Orgueil and Murchison meteorites provide clear and convincing evidence for the existence of extraterrestrial life. Therefore, it is concluded that Life and Biospheres are not strictly terrestrial but rather are widely distributed throughout the Universe.

REFERENCES:

[1] *Hoyle F. On Nuclear Reactions Occurring in Very Hot Stars. I. the Synthesis of Elements from Carbon to Nickel // The Astrophysical J. Supplement Series. 1954. V. 1, P. 121-146. DOI: 10.1086/190005.*

[2] *Cook C.W., Fowler W.A., Lauritsen* C.C., *Lauritsen* T. B^{12}, C^{12}, and the Red Giants // Physical Review. 1957. V. 107, P. 508-515. DOI: 10.1103/PhysRev.107.508.

[3] *von Stockar U., Liu J.* Does microbial life always feed on negative entropy? Thermodynamic analysis of microbial growth // Biochimica et Biophysica Acta. 1999. V. 1412. Iss. 3. P. 198–211. (Table 1). DOI: 10.1016/s0005-2728(99)00065-1.

[4] *Spilker J.S., Phadke K.A., Aravena M. et al.* Spatial variations in aromatic hydrocarbon emissions in a dust rich galaxy // Nature. 2023. V. 618. Iss. 7966. P. 708–711. DOI: 10.1038/s41586-023-05998-6.

[5] *Hoover R.B.* Ratios of Biogenic Elements for Distinguishing Recent from Fossil Microorganisms // Proc. SPIE. 2007. V. 6694, Art. No. 66940D_1-66940D_20. 20 p. https://doi.org/10.1117/12.742285.

[6] *Hoover R.B., Hoyle F., Wickramasinghe* N.C. *et al.* Diatoms on Earth, Comets, Europa and in Interstellar Space // Earth, Moon, and Planets. 1986. V. 35. P. 19–45. DOI: 10.1142/9789814675260_0043.

[7] *Kissel J., Krueger F.* The organic component in dust from comet Halley as measured by the PUMA mass spectrometer on board Vega-1 // Nature. 1987. V. 326. Iss. 6115. P. 755–760. DOI: 10.1038/326755a0

[8] *Simonia I, Cruikshank D.P.* Organic Molecules in the Icy Bodies of Planetary Systems — Accepted Notions and New Ideas // Open Astronomy. 2018. V. 27. Iss. **1.** P. 341–355. https://doi.org/10.1515/astro-2018-0038.

[9] *Gold T.* The deep, hot biosphere // *Proc. National Academy of Sciences USA. 1992. V.* 89. Iss. 13. P. 6045–6049. doi: 10.1073/pnas.89.13.6045.

[10] *Ehrenfreund P., Glavin D.P., Botta O. et al.* Extraterrestrial amino acids in Orgueil and Ivuna: Tracing the parent body of CI type carbonaceous chondrites // *National Academy of Sciences USA.* 2001. V. 98. Iss. 5. P. 2138–2141. https://doi.org/10.1073/pnas.05150289.

[11] *Callahan M.P., Smith K.E., Cleaves II H.J. et al.* Carbonaceous meteorites contain a wide range of extraterrestrial nucleobases // *National Academy of Sciences USA.* 2011. V. 108. Iss. 34. P. 13994–13998. https://doi.org/10.1073/pnas.11064931

[12] *Furukawa Y., Chikaraishi Y., Ohkouchi N. et al.* Extraterrestrial ribose and other sugars in primitive meteorites // Earth, Atmospheric and Planetary Sciences. 2019. V. 116. Iss. 49. P. 24440–24445. https://doi.org/10.1073/pnas.1907169116.

[13] *Hoover R.B.* Fossils of Cyanobacteria in CI1 Carbonaceous Meteorites // J. Cosmology. 2011. V. 13. P. 7070–7111.

[14] *Hoover R.B.* Meteorites, Microfossils and Exobiology // Proc. SPIE. 1997. V. 3111. P. 115–136. https://doi.org/10.1117/12.278766.

[15] *Zhmur S.I., Rozanov A.Yu., Gorlenko V.M.* Lithified Remnants of Microorganisms in Carbonaceous Chondrites // Geochemistry International. 1997. V. 35. P. 58–60.

[16] *Hoover R.B., Rozanov* A., *Krasavin* E. *et al.* Diatoms in the Orgueil Meteorite // Paleontological J. 2018. V. 52. Iss. 13. P. 1647–1650. DOI: 10.1134/S0031030118130051.

[17] *Rozanov A.Yu., Hoover R.B., Krasavin E.A. et al.* The Orgueil Meteorite: Atlas of Microfossils. M.: JINR, 2020. 134 p. (in Russian).

STRATEGY FOR USING FLUORIMETRIC METHODS IN THE SEARCH FOR EXTRATERRESTRIAL LIFE FORMS

A.B. Rubin[1], I.V. Konyukhov[1], S.I. Pogosyan[1], V.V. Sorokin[2], D.A. Skladnev[2], S.P. Karlov[3]

[1] *M.V. Lomonosov Moscow State University, Faculty of Biology, Department of Biophysics. 119234, Moscow, Leninskie Gori, 1, bld.24, rubin@biophys.msu.ru.*

[2.] *Winogradsky Institute of Microbiology, 117312, Moscow, 60 Let, Oktjabrja pr-t, 7, bld. 2, 6 Moscow Polytechnic University*

[3] *Moscow Polytechnic University, 107023, Moscow, Bolshaya Semenovskaya st., 38*

KEYWORDS:
light, photosynthesis, pigment, fluorescence, nanoparticles, metabolism

Exchange of substances and energy with the environment – a fundamental property of a living organism that can be used for extraterrestrial life search. Organic substances, the “blocks” from which life is built, can be formed abiogenically under the influence of harsh environmental factors. Therefore, the presence of organic molecules in space is a necessary sign of life, but not sufficient. A more reliable sign of life is the presence of a continuously functioning system of metabolic reactions.

Many microorganisms, when silver ions are added to the external medium, form silver nanoparticles (NP). NP are detected and quantified by their fluorescence in the violet region. The reduction of silver from cations occurs under the influence of certain reducing agents, both organic and inorganic. In particular, NP are formed without the participation of living cells when interacting with organic matter of abiogenic origin. However, this formation proceeds relatively quickly, producing a relatively small particle size, and without constant replenishment of new reducing agents, it stops 10-20 minutes after the appearance of silver ions.

When silver ions come into contact with living organisms, the formation of NP can last for hours due to the constant release of cellular metabolites. NP gradually increase in size, which is manifested in changes in the absorption spectra of the particles and their fluorescence spectra. Thus, a long-term increase in the intensity of the fluorescence signal of silver NP after the addition of silver ions to the medium may indicate the presence of cellular metabolism in this medium.

USING FLUORIMETRIC METHODS TO SEARCH FOR EXTRATERRESTRIAL PHOTOSYNTHETIC ORGANISMS

I.V. Konyukhov[1], S.I. Pogosyan[1] , G.K. Garipov[2], A.B. Rubin[1]

[1] *M.V. Lomonosov Moscow State University, Faculty of Biology, Department of Biophysics. 119234, Moscow, Leninskie Gori, 1 building 24, room 120, vanka.kon@gmail.com*

[2] *M.V. Lomonosov Moscow State University, Skobeltsin Institute of Nuclear Physics. 119234, Moscow, Leninskie Gori, 1 buillding 20, garipov@eas.sinp.msu.ru*

KEYWORDS:
Light, photosynthesis, pigment, fluorescence excitation, fluorescence induction

Light is the main energy source for maintaining life on Earth. In living organisms, light energy is used in the form of electronic excitation in aromatic groups of pigments. Further photochemical energy transformation is accompanied by its partial loss in the form of fluorescence, which serves as the basis for the detection of pigments on Earth and in space. When the pigment molecules are isolated from each other (in solution), upon illumination (excitation), a stationary level of fluorescence is established in a short time corresponding to the lifetime of the excited state (0.1...10 ns). However, in a complex biological system, illumination triggers the movement of electrons: first, from the excited pigment molecule to the primary acceptor, and then the electrons flow from one carrier to another (Fig. 1), which results in a multi-stage fluorescence intensity increase (Fig. 2, control conditions). In different known organisms this process occurs in times ranging from 50 milliseconds to 2 seconds, and the quantum yield of fluorescence increases from the initial values by 1.5 - 5 times.

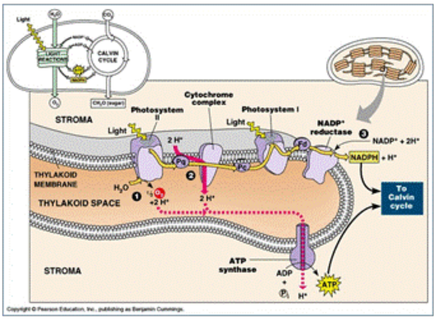

Fig. 1. Photosynthetic energy conversion system of terrestrial organisms.

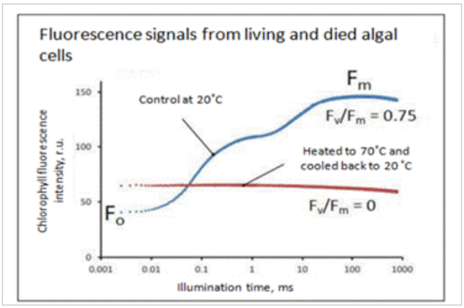

Fig. 2. Fluorescence induction curves in the working solar energy conversion system (control) and in its inactivated state. Inactivation is caused by short-term heating and is due to the irreversible denaturation of photosynthetic proteins. The fluorescence of the pigments is preserved, but the multi-stage nature of the curve disappears.

When the integrity of the energy conversion system is violated, which can be done in a controlled space experiment under the influence of high temperature, inhibitors or high-intensity light, the phenomenon of fluorescence induction is either not observed at all (Fig. 2, changes in the curve as a result of thermal damage), or the curve becomes single-step.

Registration of pigments fluorescence (the fact of the presence of pigments in space) and registration of multi-stage fluorescence induction (a sign of a living system) can be carried out remotely, and also using additional test influences, in order to distinguish "living" from "non-living".

SESSION 6. ASTROBIOLOGY (AB) POSTER SESSION

BACTERIAL TOLERANCE TO THE INFLUENCE OF SODIUM PERCHLORATE: ESTIMATION IN EXTREME ECOTOPES COMMUNITIES

D.D. Barbashin[1,2], V.S. Cheptsov[1,3], A.A. Belov[1]
[1] *Lomonosov Moscow State University, Soil Science Faculty, Moscow, Russia, fen.157@mail.ru*
[2] *Vernadsky Institute of Geochemistry and Analytical Chemistry RAS, Moscow, Russia*
[3] *Space Research Institute RAS, Moscow, Russia*

KEYWORDS:
Mars; perchlorate brines; prokaryotes; potentially habitable niche; astrobiology

INTRODUCTION:

Perchlorates become a topic for scientific discussion in recent decades due to their detection in Martian regolith [1]. The importance of this discovery is in the ability of perchlorates to adsorb water from the atmosphere causing the formation of liquid films [2] with the eutectic freezing temperatures ranging from –34 to –74 °C [3]. Calculations shows that perchlorate brines can remain liquid for at least a few hours during Martian day [4]. It has been indirectly confirmed by spectral studies of the Martian surface [5]. All the mentioned allows to assume this brines one of the potentially habitable niches on Mars [6].

In recent years, a number of perchlorate-tolerant microorganisms have been described. However the limiting concentrations of perchlorates at which bacterial growth is possible were found only for a few strains. Thus limiting concentrations for the most bacterial species have not been established [7–8]. The most perchlorate-resistant microorganisms known so far have been discovered over the past few years [9]. The detection of microorganisms more resistant than currently known is important for understanding the possibility of microbial viability in the Martian regolith. The most promising is the study of microorganisms isolated from extreme habitats, since they showed high resistance to various stress-factors, including the presence of perchlorates in situ or in vitro [10].

MATERIALS AND METHODS:

The study was performed for 5445 strains of aerobic heterotrophic bacteria isolated from 50 soil and sediment samples, collected in different arid ecotopes all over the world.

The estimation of bacterial strains ability to grow in the presence of high concentrations of sodium perchlorate was carried out by culturing in liquid R3A medium [11] supplemented with various concentrations of sodium perchlorate. For all studied strains, a test was conducted for tolerance to 7.5 % sodium perchlorate in the medium. The resulting cultures were tested to determine the survival limit of perchlorate presence *in vitro*. At this stage, the gradient of the studied concentrations ranged from 10.0 to 12.5 % with a step of 0.5 % $NaClO_4$ in culture medium. The incubation period ranged from 14 to 28 days, at the end of which growth was determined visually.

RESULTS:

During the screening of 5445 bacterial strains, 215 cultures have shown tolerance to presence of 7.5 % sodium perchlorate in the culture medium. Representatives of the *Nocardia, Pseudomonas, Bacillus, Rhodococcus, Arthrobacter, Massilia, Micrococcus*, and *Kocuria* genera demonstrated the highest resistance to perchlorate presence. For limiting concentrations detection, 81 out of 215 resistant strains were used.

During the evaluation of limiting concentrations, 6 strains were found being tolerant to 12.5 % sodium perchlorate in the medium. 4 of the 6 most resistant strains belong to the genus *Bacillus*, and the rest to *Kocuria*. Representatives only of 2 species are described in the literature able to growth with such high concentrations: *Halomonas venusta* and *Planococcus halocryoph-*

ilus, capable of growing at comparable concentrations of 12.2 and 13.6 % sodium perchlorate, respectively [9]. During further research, we may find strains capable to grow at higher concentrations of perchlorate than those currently described.

The analysis of the pure cultures tolerance showed that a relatively high percentage of the strains isolated from different arid soils and sediment were resistant to high concentrations of sodium perchlorate: up to 12.3 and 6 % of strains were able to growth at 7.5 and 10 % perchlorate in the medium, respectively. At the same time, the studied salts are not found on Earth in concentrations higher than hundredths of a percent [12], so such a high resistance of microorganisms can be explained by adaptation to various impacts that causes similar to perchlorates influences. Perchlorates affects bacterial cells through osmotic and oxidative stress [13], so the perchlorate tolerance is evolving as a result of the bacterial adaptation to specific ecological niche. Based on experimental data, it was assumed that the perchlorate-resistant bacteria occurrence in different ecotopes could be associated with the presence of environmental factors leads to oxidative stress. Additional studies are needed to find out the which factor (osmotic or oxidative stress) is responsible for inhibiting the growth of bacterial cells.

References:

[1] *Hecht M.H., Kounaves S.P., Quinn R.C. et al.* Detection of perchlorate and the soluble chemistry of martian soil at the Phoenix lander site // Science. 2009. V. 325. Iss. 5936. P. 64–67. DOI: 10.1126/science.1172466.

[2] *Kounaves S.P., Chaniotakis N.A., Chevrier V.F. et al.* Identification of the perchlorate parent salts at the Phoenix Mars landing site and possible implications // Icarus. 2014. V 32. P. 226–231. DOI: 10.1016/j.icarus.2014.01.016.

[3] *Marion G.M., Catling* D.C., *Zahnle K.J., Claire M.W.* Modeling aqueous perchlorate chemistries with applications to Mars // Icarus. 2010. 2010. V. 207. Iss. 2. P. 675–685. DOI: 10.1016/j.icarus.2009.12.003.

[4] *Chevrier V.F., Hanley J., Altheide T.S.* Stability of perchlorate hydrates and their liquid solutions at the Phoenix landing site, Mars // Geophysical Research Letters. 2009. V. 36. Iss. 10. Art. No. L10202. https://doi.org/10.1029/2009GL037497.

[5] *Ojha L., Wilhelm M.B., Murchie* S.L. *et al.* Spectral evidence for hydrated salts in recurring slope lineae on Mars // Nature Geoscience. 2015. V. 8. Iss. 11. P. 829–832. DOI: 10.1038/ngeo2546.

[6] Carrier B.L. et al., Mars extant life: what's next? Conference Report // Astrobiology 2020. V. 20. No. 6. P. 785–814. https://doi.org/10.1089/ast.2020.2237.

[7] *Nuding D.L., Gough* R.V., *Venkateswaran* K.J. *et al.* Laboratory investigations on the survival of *Bacillus subtilis* spores in deliquescent salt Mars analog environments // Astrobiology. 2017.V. 17. Iss. 10. P. 997–1008. DOI: 10.1089/ast.2016.1545.

[8] *Cheptsov V., Belov A., Soloveva O. et al.* Survival and growth of soil microbial communities under influence of sodium perchlorates // Intern. J. Astrobiology. 2021. V. 20. Iss. 1. P. 36–47.

[9] *Heinz J., Krahn T., Schulze-Makuch D.* A new record for microbial perchlorate tolerance: fungal growth in $NaClO_4$ brines and its implications for putative life on Mars // Life. 2020. V. 10. Iss. 5. P. 53. https://doi.org/10.3390/life10050053.

[10] *Belov A.A., Cheptsov V.S., Vorobyova E.A.* Soil bacterial communities of Sahara and Gibson deserts: Physiological and taxonomical characteristics // AIMS Microbiology. 2018. V. 4. No. 4. P. 685–710. DOI: 10.3934/microbiol.2018.4.685.

[11] *Reasoner D.J., Geldreich E.E.* A new medium for the enumeration and subculture of bacteria from potable water // Applied and Environmental Microbiology. 1985. V. 49. Iss. 1. P. 1–7.

[12] *Calderón R., Palma* P., *Parker* D *et al.* Perchlorate levels in soil and waters from the Atacama Desert // Archives of Environmental Contamination and Toxicology. 2014. V. 66. Iss. 2. P. 155–161. DOI: 10.1007/s00244-013-9960-y.

[13] *Rzymski P., Poniedziałek* B., *Hippmann* N., *Kaczmarek* Ł. Screening the Survival of Cyanobacteria Under Perchlorate Stress. Potential Implications for Mars *in situ* Resource Utilization // Astrobiology. 2022. V. 22. Iss. 6. P. 672–684. DOI: 10.1089/ast.2021.0100.

EFFECT OF LOW INTENSITY IONIZING RADIATION AND MAGNETIC FIELDS ON THE FUNCTIONAL STATUS OF PLANTS

M.A. Grinberg[1], E.A. Mareev[2], V.A. Vodeneev[3]
[1] *Lobachevsky State University, Nizhny Novgorod, Russia; Institute of Applied Physics, Russian Academy of Sciences, Nizhny Novgorod, Russia; mag1355@yandex.ru;*
[2] *Lobachevsky State University, Nizhny Novgorod, Russia; Institute of Applied Physics, Russian Academy of Sciences, Nizhny Novgorod, Russia; mareev@ipfran.ru;*
[3] *Lobachevsky State University, Nizhny Novgorod, Russia; Institute of Applied Physics, Russian Academy of Sciences, Nizhny Novgorod, Russia; v.vodeneev@mail.ru.*

KEYWORDS:
ionizing radiation, magnetic fields, plants, photosynthesis, signal systems

INTRODUCTION:
The study of the influence of space factors on the functioning of living organisms that can be part of artificial ecosystems during long-term missions is of paramount importance due to the growing interest in the exploration of near space, in particular, with the active development of the Russian Orbital Station (ROS) project, the renewal of the Russian Lunar program, the international community's close attention to the exploration of Mars. These factors include, in particular, changed levels of ionizing radiation, electromagnetic environment, and gravity. Currently, most works in the field of space biology are focused on determining the survival of living organisms under the influence of adverse factors of space flight of various intensity [1–2]. Morphometric indicators are traditionally the basis for assessing the effect of a factor [3]. In the present work, we demonstrate that signaling systems are significantly more sensitive to factors such as increased levels of ionizing radiation and extremely low frequency electromagnetic fields.

MATERIALS AND METHODS:
The experiments were carried out on 14-16-day-old wheat (*Triticum aestívum* L.) plants. During the entire growing period, the plants were exposed to an increased level of ionizing radiation or extremely low frequency alternating magnetic fields. Control plants were grown under similar conditions in the absence of additional external factors. An increased level of ionizing radiation was created using point sources of β-radiation based on ^{90}Sr and ^{90}Y salts. The dose rate at leaf level was about 31 μGy/hour. An increased level of the magnetic field was set using Helmholtz rings. The frequency of the alternating magnetic field was 14.3 Hz, the field magnitude was 18 μT.

The condition of plants was assessed based on morphometric indicators, photosynthesis activity and electrical activity parameters. The length and weight of plants were used as morphometric indicators. Photosynthesis activity was recorded by PAM fluorometry. Electrical activity was assessed by the parameters of reactions caused by additional stimuli (heating, changes in illumination) using macroelectrode technique.

RESULTS:
The experiment used factors of low intensity. No statistically significant effects on plant growth and weight were found for either ionizing radiation or magnetic fields. A weak stimulating effect of both factors on the key indicator of the light stage of photosynthesis, the quantum yield of photosystem 2, was found. A significantly more pronounced effect was shown for signaling systems. Ionizing radiation enhances heat-induced electrical signals, and a magnetic field increases the amplitude of light-induced electrical reactions.

In general, the results indicate that already low intensities of space flight factors can affect the growth and development of plants, in particular, their ability to form adaptations to stress conditions.

Acknowledgements:
The study was carried out as part of the project "Experimental Laboratory Astrophysics and Geophysics" of the National Center for Physics and Mathematics.

References:

[1] *Baranova E.N., Levinskikh M.A., Gulevich A.A.* Wheat Space Odyssey: "From Seed to Seed". Kernel Morphology // Life. 2019. V. 9. Iss. 4. Art. No. 81. https://doi.org/10.3390/life9040081.
[2] *Zhang Z., Xue Y., Yang J. et al.* Biological Effects of Hypomagnetic Field: Ground-Based Data for Space Exploration // Bioelectromagnetics. 2021. V. 42 Iss. 6. P. 516–531. DOI: 10.1002/bem.22360.
[3] *De Micco V., Arena C., Pignalosa D., Durante M.* Effects of Sparsely and Densely Ionizing Radiation on Plants // Radiation and Environmental Biophysics. 2011. V. 50. Iss. 1. P. 1–19. DOI: 10.1007/s00411-010-0343-8.

2D AND 3D PARAMETER RELATIONSHIPS FOR W UMA-TYPE SYSTEMS REVISITED

M. Khodadadilori
Amirkabir University of Technology, Tehran, Iran, atilaporo@bsnp.info

KEYWORDS:
stellar evolution, fundamental parameters of stars, astronomy data analysis

Two-dimensional (2D) relationships for P-Mv(system), P-L, M-L, and q-L(ratio), as well as three-dimensional (3D) relationships for MPq, RPq, and LPq, were investigated for binary star systems. The sample used is related to 118 contact binary systems whose absolute parameters were calculated based on the Gaia Data Release 3 (DR3) parallax. We reviewed previous studies on 2D relationships and updated six equations. Therefore, the Markov chain Monte Carlo (MCMC) and machine learning methods were used, and the outcomes were compared. We also investigated six 3D relationships by fixing the orbital period and mass ratio, and models were obtained based on the machine learning approach. We compared the results of the obtained 3D models with the outcomes obtained for seven contact systems that were studied by spectroscopic light curves. The results show that our models agree with the results of these studies by \sim85%. Our models suggested that there are significant relationships among parameters, although the models obtained from 3D relationships show better results.

 14MS3-AB-PS-04
POSTER

SCANNING FOR HABITABLE SYSTEMS ON BEHALF OF FUTURE INTERSTELLAR MISSIONS

A.N. Safronov
Obukhov Institute of Atmospheric Physics RAS, Moscow, Russia, safronov_2003@mail.ru

KEYWORDS:
ensemble-averaged stellar reactor, stellar abundance, Hypatia stellar catalog, stellar nucleogenesis, habitability

INTRODUCTION:

The problem of interstellar travels has been of interest to humanity for a long time. After Yuri Gagarin's first flight into space in 1961, the illusion of a rapid discovery of interstellar space appeared. Although the 60-year period of cosmonautics development has led to significant achievements in space exploration by using satellites and space stations, such research has practically not gone beyond the Solar System. The size of modern rockets and the amount of fuel in them significantly limit the range of spacecraft flights. Important limitations of manned space research are two problems: firstly, the lack of new principles and approaches in the development of jet propulsion and, secondly, understanding of the direction of further interstellar missions.

This study focused on studying the possibility of the emergence of life in stellar systems located in the vicinity of the Sun. As it is known, all biological species on Earth have a unique DNA code (Deoxyribonucleic Acid), which determines the full diversity of biological species. DNA includes the following elements: C, O, N, and P. A new concept of DNA-stars was introduced, in which the spectrums of C, O, N, and P elements were recorded together. The possibility of synthesis of Na, Mg, S, K, Fe, Co, Cu, Zn, Ca, Mn and Mo regulating the growth and development of elementary biological forms is also discussed.

However, these elements are synthesized on different stars. For example, according to the B^2FH model [1], C and N are synthesized during the death of low-mass stars; O, Na, and K — during the explosion of massive stars; Mn, Fe, Co and Cu are synthesized mainly during the explosion of white dwarfs. The synthesis of different elements on different stars makes it impossible to raise biological forms on these stars.

This study shows that these models, such as B^2FH, have several defects. With the exception of the defect mentioned in [2] concerning the frequency of neutron stars mergers, firstly, there is no invariance of the distribution of elements in the Solar System; secondly, it is the absence of invariance of elements on the neighboring stars; thirdly, it is the absence of enriched stars, in particular, stars consisting entirely of Th and U, and, fourthly, the absence of a significant number of elements in interstellar space. The error is visible even in the name of the Galactic Chemical Evolution (GCE) models, so these models are not Galactic Chemical Transport (GCT) models. Especially for angry opponents, the simplest textbook transfer task is given below in Table 1. This task has no solution within the framework of modern astrophysics.

The absence of bands of uranium, cesium, and iodine in the solar spectrum led to the paradox of "*exclusive delivery*" of these elements to Earth by "*aliens from exoplanets*". This phenomenon was called the "*exclusive delivery*" paradox, since iodine, cesium, and uranium were delivered from neutron stars bypassing the Sun, as well as other planets such as Venus and Mars. If we are talking about "*exclusive distributed*", we can suspect an alien in every pharmacist, who sold us a bottle of iodine. It is clear that such conclusions arising from the GCE models can cause a smile. Note that the absence of the transport equation in the Galaxy Chemical Evolution (GCE) models, such as the B^2FH and K^2L models, is only the tip of the iceberg.

Table 1. The simple task for GCE models verifications

"The solar reactor is weak and can synthesize mainly hydrogen and helium. According to B^2FH and K^2L models, the thorium can be synthesized in neutron stars (NS), which have a strong reactor. The nearest NS is RX J1856.5 − 3754, which is allocated at 167 pc from the Sun. In the Solar System was recorded 1 gram of thorium. How much of thorium has been produced by the NS donor-star?"

The synthesis of various elements on different stars made it impossible to create biological forms on remote stars. Therefore, first of all, it was necessary to show that the B^2FH and K^2L models of the synthesis of chemical elements incorrectly describe the processes occurring on stars, please see Table 2.

Thus, there are four main drawbacks in the theories of B^2FH and K^2L:

- The invariance of element distributions in the Solar System is not recorded.
- Invariance of element distributions on neighborhood stars is also not recorded.
- This is the absence of super-mega-enriched stars, called as donor-stars.
- There is no significant amount of heavy traces in interstellar space.

Table 2. Different approaches to investigation of stellar nucleogenesys

Stellar Enriched Process is :	
Nuclear Fusion (self–enriched process)	this study
Nuclear Fusion (in donor star) + Interstellar Transfer from donor star to acceptor star*	B^2FH and K^2L

* However, the transfer equation in the GCE models is *mysteriously* absent

- The goal of the study is to find an answer to the next two questions:
- How are the chemical elements necessary for the origin of life synthesized on stars?
- In which stellar systems it is necessary to look for signs of life?

RESULTS:

In this study, terrestrial and solar abundances were compared with the stellar abundances of stars located in the region of 200 pc of the solar neighborhood. To study the dynamics of processes occurring in these stars, it introduces the concept of an ensemble–averaged stellar reactor. According to the effective temperature value, four stellar classes are identified, for which the correlation coefficients and standard deviation are counted. The statement about the possibility of transferring heavy elements, synthesized by stars over long distances in space has been completely refuted. There is no immutability of the distribution of elements on neighboring stars and in the Solar System. It is shown that the chemical elements are mainly synthesized inside each star reactor. The theory of the buoyancy of elements is generalized to stars.

The causes of the explosion of stars and the physical explanation of the existence of the critical limits of Chandrasekhar are proposed.

In the vicinity of the Sun, the spatial distribution of superheated stars with a sufficient temperature of more than 6500 K was analyzed. It was suggested that stars overheat due to a shift in the parameters of nuclear processes occurring inside stars, which leads to the synthesis of transuranic elements, the achievement of a critical nuclear mass, and then to the explosion of the star. Based on the content of chemicals, a list of stars is determined on which the origin of life is possible.

In this study, the possibility of the emergence of life in other star systems, located at a distance of ~200 pc from the Solar System was investigated. For the origin of life, the synthesis of chemical elements, such as C, N, O and P, which are necessary for the formation of DNA and biological organisms, is important. The stars, in spectra of which these elements are represented are called DNA-stars. Based on chemical compounds, a new method for searching for habitable star systems has been developed and a list of 48 DNA-stars in the solar neighborhood, on which life is possible, has been determined. These stars make up only 1.3 % of the total number of studied stars. Moreover, only three stars of the 48 stars selected belong to the same spectral class as our Sun (G2V). The closest to the Solar System is the DNA star with the number HIP 15510 from the Hypatia Stellar Catalog (HSC). This star belongs to the G8V spectral class and is located at a distance of 6 pc from the Solar System. Finally, nine stars have been identified that have the greatest chemical similarity to our solar spectrum (Table 3).

Further, as it is currently known, of these nine stars only one (HIP 24681) has six planets. This star belongs to the spectral class G0, it has an effective temperature of 5879 K, and is located at a distance of 46.09 pc from the Sun. At the moment, we can only express the hope that in the future the planetary properties of not only the remaining nine stars with a high–affinity rank but all the remaining 47 DNA-stars, allocated in the neighborhood of the Solar System, will be investigated. The abundances of life origin elements for selected T-stars are presented in Table 4. The most similar to Sun in the chemical composition are the following stars: HIP 42356 (5910 K, G2V), HIP 48423 (5673 K, G5), HIP 24681 (5879 K, G0), HIP 16852 (5991 K, F9IV/V), HIP 108859 (6091 K, F9V), HIP 47592 (6165 K, F8V), HIP 96895 (5790 K, G1.5V), and HIP 64150 (5748 K, G3IV). The spectra of these stars have a different number of registered elements, so their mutual rating may change as new information becomes available.

The spatial distributions of studying T-stars were presented in Fig. 1*a*, *b* in the Right Ascension and Declination coordinate system (J2000). The referenced 48 DNA–stars are shown in Fig. 1*a* and Fig. 1*b*, by grey points in both Figures. As wrote above in this study it was found that from 48 DNA-stars, only three stars belong to the G2V spectral class, namely HIP 20800 (66.85293, 46.85315), HIP 35209 (109.15178, 1.87877), and HIP 42356 (129.53545, 26.04898). These stars were drawn by blue stars in Fig. 1*a*. These stars are located at a distance from the Sun of 30.25, 41.74, and 44.35 pc, correspondingly. These stars' masses are equal to 1.03, 1.08, and 1.06 M_0 and radiuses — 1.29, 1.25, 1.23 R_0. The nearest star to Sun from 48 DNA-stars is the star HIP 15510 (49.98189, –43.0698), located at a distance of 6 pc and belonging to the G8V spectral class (5433.8 K); this star was drawn by magenta color in Figure 1a.

We also draw the T-stars, which have abundances similar to the Solar System. The parameters of these stars are following: C, N, O, and P abundances are not Null, and Δ abundances are less than 0.2 and above than –0.2. Below, such stars are called T-starts. The RANK of T-stars was determined as the total account of elemental abundances from Li to U, which does not have value in the range of (–0.2, 02) of Earth abundance. The position of T-stars was shown in Fig. 1*b* as red stars.

Table 3. The stellar property of nine T-stars, which have abundances similar to Earth. For selection, the next filter was used: C, N, O, and P abundances are not Null, and < 0.2 and > –0.2 of Earth abundance. The minimum abundance RANK corresponds to the best coincidence of stellar saturation to saturation of the Solar System; see Table 4

Stellar property									
Number	1	2	3	4	5[a]	6	7	8	9
HIP Name	59280	48423	64150	96895	24681	42356	16852	108859	47592
Temp, K	5409	5673	5748	5790	5879	5910	5991	6091	6165
Radius, R_O	0.90	0.93	1.10	1.25	1.46	1.23	4.22	1.19	1.25
Ra	182.41	148.07	197.21	295.45	79.42	129.54		330.79	145.56
Declination	40.25	49.19	5.21	50.53	7.35	26.05	0.40	18.88	–23.92
Distance, pc	25.09	33.17	26.36	21.14	46.09	44.35	13.96	48.30	14.81
Spectrum	G8IV/V	G5	G3IV	G1.5V	G0	G2V	F9IV/V	F9V	F8V
RANK	16	2	7	7	3	1	6	6	6

[a] Currently, planet properties are known only for one star, namely HIP 24681.

Table 4. The abundances of life origin elements for nine selected stars. The RANK is a total account of total elementary abundances, which does not have value in the range of (–0.2, 02) of the Earth abundance

Element abundance									
Number	1	2	3	4	5[a]	6	7	8	9
HIP Name	59280	48423	64150	96895	24681	42356	16852	108859	47592
C	0.10	0.07	0.10	0.15	0.19	0.16	0.06	0.03	0.08
N	0.01	–0.02	–0.01	0.09	0.07	0.12	0.05	–0.09	–0.07
O	–0.08	0.04	0.04	0.10	0.13	0.10	0.02	0.04	0.06
P	0.19	0.08	0.11	0.07	0.05	0.15	–0.08	0.01	0.08
Na	0.10	–0.09	0.02	0.10	0.07	0.06	–0.05	–0.05	–0.05
Mg	0.16	0.01	0.08	0.18	0.15	0.13	0.05	0.12	0.06
S	0.32	0.13	0.04	0.10	0.05	0.12	–0.03	–0.07	–0.09
K	0.11	0.06	0.17	0.11	0.15	0.17	0.16	–0.06	
Ca	0.21	0.20	0.08	0.13	0.16	0.20	0.00	0.11	0.01
CaII	0.35	0.24	0.17	0.35	0.17	0.30	0.07	0.29	0.07
Fe	0.20	0.17	0.08	0.12	0.16	0.16	–0.01	0.06	0.00
Mn	0.11	–0.01	–0.02	0.00	0.09	0.06	–0.16	–0.14	–0.17
Co	0.34		0.09	0.14	0.31		0.00	0.08	0.01
Cu	0.21		0.05	0.00	0.04		–0.24	–0.16	–0.23
Zn	0.05		–0.04	0.02	0.01	0.10	–0.10	–0.17	–0.19
Mo				0.10					
RANK	16	2	7	7	3	1	6	6	6

[a] Currently, planet properties are known only for one star, namely HIP 24681.

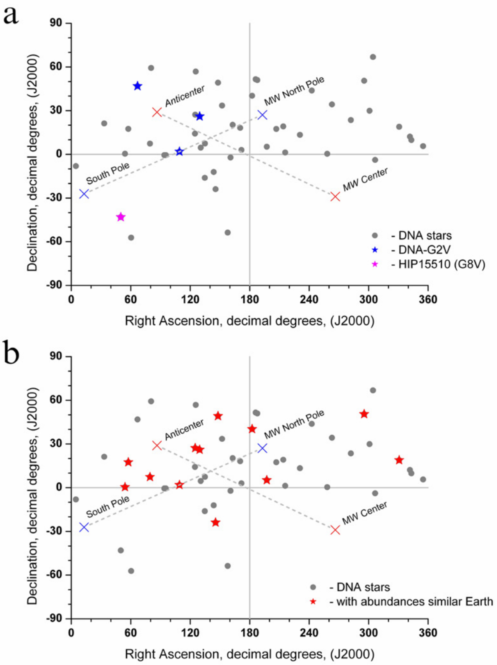

Fig. 1. (a) Three stars belong to the G2V spectral class, as our Sun, were shown by blue and one star, closest to the solar system, which belongs to the other G8V class, were presented by purple color; (b) The T-stars, which have abundances similar to the solar system, were presented by red colors. On both figures as background, the 48 DNA stars, in the spectrum of which C, N, O and P elements were found is drawn by grey color

The details of these studies could be found in [3]–[5]. The stellar nucleogenesis of elements necessary for the life origin was investigated in [3]. Scanning for habitable stellar systems in the solar neighborhood was described in [4]. In [5] it was studying the spatial distribution of overheated stars nearby the Sun, which provided for a synthesis of heavy chemical elements.

References:

[1] *Burbidge E.M., Burbidge G.R., Fowler W.A., Hoyle F.* Synthesis of the Elements in Stars // Reviews of Modern Physics. 1957. V. 29. P. 547–650. DOI:10.1103/revmodphys.29.547.

[2] *Kobayashi C., Karakas A.I., Lugaro M.* The Origin of Elements from Carbon to Uranium // The Astrophysical J. 2020. V. 900. No. 2. Art. No. 179. DOI: 10.3847/1538-4357/abae65.

[3] *Safronov A.N.* Life Origin in the Milky Way Galaxy: I. Stellar Nucleogenesis of Elements Necessary for the Life Origin // MDPI Preprints.org. 2023. Art. No. 2023050202. DOI: 10.20944/preprints202305.0202.v1.

[4] *Safronov A.N.* Life Origin in the Milky Way Galaxy: II. Scanning for Habitable Stellar Systems on Behalf of Future Space Missions // MDPI Preprints.org. 2023. Art. No. 2023050005. DOI: 10.20944/preprints202305.0005.v1.

[5] *Safronov A.N.* Life Origin in the Milky Way Galaxy: III. Spatial Distribution of Overheated Stars in the Solar Neighborhood // MDPI Preprints.org. 2023. Art. No. 2023050006. DOI: 10.20944/preprints202305.0006.v1.

INFORMATION

INFORMATION

address:
Space Researh Institute (IKI)
Profsoyuznaya street 84/32
post code 117997
metro station: Kaluzhskaya
Moscow, Russia

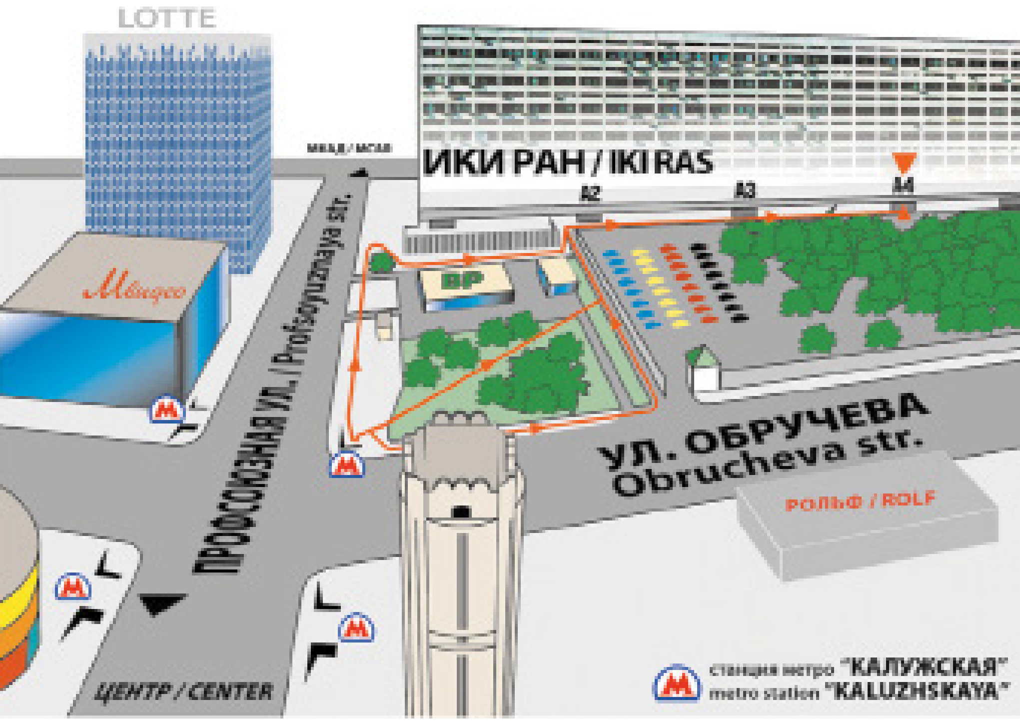

ИКИ РАН

площадь академика Келдыша
метро «Калужская», первый вагон из центра, по тоннелю – прямо, по второму поперечному тоннелю – направо, выход на площадь, далее по стрелкам на схеме

IKI RAS

You should get off at “Kalyzhskaya” metro station using the southern exit. After leaving a station lobby through glass doors you should go straight to the end of the tunnel, then take right and use the stairs to get to the surface. From this point you may follow either arrow on this map

MOSCOW METRO SCHEME

СХЕМА МОСКОВСКОГО МЕТРОПОЛИТЕНА

REGISTRATION AND INFORMATION DESK

location: IKI, entrance A-4

time:
9 october, 9:00–18:00

10 -13 october, 10.00-18.00

ORAL SESSIONS

location:

- IKI conference hall, second floor
  Sessions: Mars, Moon and Mercury, Venus , Small Bodies, Astrobiology
  9–13 october
- IKI Room 200, second floor
  Session Extrasolar Planets
  13 october

POSTER SESSIONS

online discussion

COFFEE BREAKS, WELCOME PARTY, RECEPTION

location:

- IKI Winter Garden, second floor
  Coffee Breaks
- IKI conference hall, second floor
  Welcome Party
- IKI exhibition hall, ground floor
  Reception

INTERNET ACCESS AND WIFI

there is Internet access in and near the conference hall

SOCIAL PROGRAM

	BOLSHOI	OPERETTA	HELIKON	MMDM	NOVAYA OPERA	KREMLIN
8.10	**14.00** ballet, Historic stage **SHOPENIANA**			**18:00** Svetlanov Hall **ORCHESTRA CAGMO, SYMPHONY LINEAGE II**	**18:00** opera, premiere **THE FLYING DUTCHMAN, R.VAGNER**	**14.00** ballet **SWAN LAKE**
9.10				**19:00** concert, Svetlanov Hall **LEGENDARY ROCK HITS**		
10.10		**19.00** operetta **BAYADERA**		**19.00** concert, Svetlanov Hall **GALA CONCERT OF THE ARTIS FUTURA IN-TERNATIONAL FOUNDATION**	**18:00** opera, premiere **THE FLYING DUTCHMAN, R.VAGNER**	
11.10		**19.00** musical **DOG IN THE MANGER**	**19.00** opera **IVAN IV IN THE FRAME-WORK OF THE FESTIVAL "TO SEE THE MUSIC"**	**19.00** concert, Svetlanov Hall **VAN GOGH. LETTERS TO MY BROTHER** **20:00** dramatics, Theatre Hall **LOVE LETTERS , PERFORMANCE BASED ON THE PLAY BY ALBERT R. GURNEY**	**19:00** opera **LIUCHIYA DI LAMMERMUR**	**19.00** ballet **GISELLE**
12.10	**19:00** opera, Historic stage **MAZEPA** **19.00** opera, New stage **PEARL SEEKERS**	**19:00** operetta, premiere **THE MERRY WIDOW**	**19.00** opera **IVAN IV IN THE FRAME-WORK OF THE FESTIVAL "TO SEE THE MUSIC"**	**19:00** consert №3, Svetlanov hall **ORKESTRA CAGMO** **19:00** Theater Hall **"GERSHWIN FOREVER!" O. LUNDSTROM ORCHESTRA** **19:00** Chamber Hall **TENORS XXI CENTURY**	**18:00** opera, premiere **THE FLYING DUTCHMAN, R. VAGNER**	**19.00** ballet **SPARTAK**
13.10	**19.00** opera, Historic stage **MAZEPA** **19.00** opera, New stage **PEARL SEEKERS**	**19.00** musical **THE COURTESAN**		**19:00** Svetlanov hall **CONCERTO GRANDIOSO. «CLASSICO»,**		**19.00** consert **95TH ANNIVERSARY OF THE ACADEMIC SONG AND DANCE ENSEMBLE OF THE RUSSIAN ARMY NAMED AFTER A.V. ALEXANDROV**
14.10	**19.00** opera, Historic stage **MAZEPA** **19.00** opera, New stage **PEARL SEEKERS** **19.00** ballet, New stage, **JIZELLE**	**13:00, 19:00** operetta **QUEEN OF CHARDASH**		**15:00** consert, Svetlanov hall **THE BEST RHAPSODIES OF THE WORLD WITH FABIO MASTRANGELO** **19:00** consert, Svetlanov Hall **MAD DANCES WITH FABIO MASTRANGELO**	**19:00** lyrical scenes in seven paintings **"EUGENE ONEGIN", P.I. TCHAIKOVSKY,**	**18:00** consert **SHAMAN**

BOLSHOI	https://bolshoi.ru	BOLSHOI THEATRE
OPERETTA	https://mosoperetta.ru/	OPERETTA THEATRE
HELIKON	https://www.helikon.ru/	HELIKON OPERA
MMDM	https://www.mmdm.ru/	MOSCOW INTERNATIONAL PERFORMING ARTS CENTER
NOVAYA OPERA	https://novayaopera.ru/	NOVAYA OPERA
KREMLIN	https://kremlinpalace.org/	STATE KREMLIN PALACE

LUNCH POINTS NEAREST TO IKI

1. **ИНСТИТУТ КОСМИЧЕСКИХ ИССЛЕДОВАНИЙ РАН**,
   столовая, 1 этаж, секция А3
   SPACE RESEARCH INSTITUTE,
   Food center, Ground Floor, Section A3
2. **ТЦ “КАЛУЖСКИЙ”**,
   ул. Профсоюзная, 61А, зона ресторанов, 2 этаж
   “KALUZHSKIY” Market Center,
   Profsoyuznaya Street, 61A, 2 Floor
3. **КАФЕ”АНДЕРСОН”**,
   ул. Обручева, 30/1
   CAFÉ “ANDERSON”,
   Obrucheva street, 30/1
4. **ИНСТИТУТ ПРИКЛАДНОЙ МАТЕМАТИКИ РАН,**
   столовая, 1 этаж
   INSTITUTE OF APPLIED MATHEMATICS,
   Food center, Ground Floor